PROCEEDINGS

MICROSCOPY AND MICROANALYSIS 1996

Microscopy Society of America
54th Annual Meeting

Microbeam Analysis Society
30th Annual Meeting

Microscopical Society of Canada/
Société de Microscopie du Canada
23rd Annual Meeting

MINNEAPOLIS, MINNESOTA

11-15 August 1996

Edited by
G. W. Bailey
J. M. Corbett
R. V. W. Dimlich
J. R. Michael
N. J. Zaluzec

PUBLISHER'S NOTICE

Back Volumes

- San Francisco Press is offering all MSA, AEM (Analytical Electron Microscopy), and MAS (Microbeam Analysis Society) proceedings published before 1990 at a special low price of **$10 each**, while they last. The following volumes are available:

  MSA: 1983, 1987, 1988, 1989 at $10 each

  AEM: 1981, 1984, 1987 at $10 each [Note: XII ICEM (International Congress for Electron Microscopy) vol. 2 (see below) also serves as the 1990 AEM]

  MAS: 1976, 1977, 1979, 1980, 1981, 1982, 1986, 1987, 1988, 1989 at $10 each

- Proceedings published in 1990 through 1995 are offered at half price, as follows:

  MSA 1990 (XII ICEM), four volumes, also available individually: (1) imaging sciences, (2) analytical sciences, (3) biological sciences, (4) materials sciences, $32.50 each, $130 the set

  MSA 1991, $32.50

  MSA 1992, two parts (also contains MAS 1992 papers), $65 the set

  MSA 1993, 1994, $40 each

  MAS 1990, 1991 at $32.50 each

  MSA 1995 (published by Jones & Begell), $50

Add postage and handling of $3 for first book, $2 for each additional book (foreign orders, $6 and $4); Californians add sales tax. (No credit cards.)

Copies of this 1996 Proceedings are available to members of MSA, MAS, and MSC/SMC *who send prepayment by personal check* at $56 (a 20% discount from the list price); orders from organizations are filled at the list price, $70.

Also available from San Francisco Press:

Electron Microscopy Safety Handbook (Barber & Mascorro, Eds.), 2nd ed. (1994), $15

Electron Microscopy and Alzheimer's Disease (J. Metuzals, Ed.), $10

Early History of the Electron Microscope (L. Marton), 2nd ed. (1994), $15

Electricity and Medicine: History of Their Interaction (Rowbottom & Susskind), $30

Microstructure of Materials (K. M. Krishnan, Ed.), Gareth Thomas *Festschrift*, $30

Send orders to:

San Francisco Press, Inc., Box 426800, San Francisco, CA 94142-6800, USA

MICROSCOPY SOCIETY OF AMERICA

Established 1942

OFFICERS 1996

Executive Council

President	Margaret Ann Goldstein
President Elect	C. Barry Carter
Past President	Terence E. Mitchell
Secretary	Barbara A. Reine
Treasurer	Ronald M. Anderson
Directors	Mary Grace Burke
	Stanley L. Erlandsen
	Ronald Gronsky
	Ernest Hall
	Peter Ingram
	Conly L. Rieder
	John D. Shelburne

Appointed Officers

Archivist	Rachel A. Horowitz
Telecommunications Committee Chair	Nestor J. Zaluzec
Certification Board Chair	Karen Klomparens
Education Committee Chair	JoAn Hudson
International Committee Chair	Chang Mo Sung
JMSA Editor-in-Chief	Jean-Paul Revel
JMSA Co-Editor	Ray W. Carpenter
Long-Range Planning Committee Chair	Robert M. Glaeser
Membership Committee Co-Chairs	Ralph M. Albrecht
	Linda L. Horton
Placement Officer	John H. L. Watson
Proceedings Editor	G. William Bailey
Public Policy Committee Chair	Michael Isaacson
Sustaining Members Committee Chair	Robyn Rufner
Technologists' Forum	Sandra Silvers
1996 Local Arrangements Chair	Ev Osten
1996 Program Chair	Nestor J. Zaluzec
1996 Program Vice Chair	Ruth V. W. Dimlich

Business Office/Meeting Manager
Lawrence M. Maser

MICROBEAM ANALYSIS SOCIETY

Established 1966

OFFICERS 1996

Executive Council

President	Dale E. Johnson
President Elect	Joseph R. Michael
Past President	Jon McCarthy
Secretary	Inga Holl Musselman
Treasurer	Harvey A. Freeman
Directors	Joseph D. Geller
	Paul F. Hlava
	Richard W. Linton
	John F. Mansfield
	Gregory Meeker
	Carol Swyt

Appointed Officers

Archivist	Gordon Cleaver
Computer Activities Committee Chair	John F. Mansfield
Computer Activities Committee Co-Chair	Paul Carpenter
Corporate Liaison Committee Chair	Thomas G. Huber
Education Committee Chair	Phillip E. Russell
Finance Committee Chair	Gordon Cleaver
Historian	Arthur A. Chodos
International Liaison	David B. Williams
Long-Range Planning Committee Chair	John A. Small
Membership Services	Scott Wight
JMSA Associate Editor	Charles E. Lyman
MicroNews Editor	Ryna Marinenko
Sustaining Members Committee Chair	Jack L. Worrall

MAS Business Office
William S. Thompson

MSA SUSTAINING MEMBERS

MAS SUSTAINING MEMBERS

4pi ANALYSIS INC.
ADVANCED MICROBEAM INC.
AMRAY INC.
CAMECA INSTRUMENTS INC.
CHARLES EVANS & ASSOCIATES
DAPPLE SYSTEMS
DENTON VACUUM INC.
EDAX INTERNATIONAL
ELECTRON MICROSCOPY SCIENCES/DIATOME US
ETP-USA/ELECTRON DETECTORS INC.
FEI COMPANY
FISONS INSTRUMENTS
GATAN INC.
GELLER MICROANALYTICAL LABORATORY
HESSLER TECHNICAL SERVICES
JEOL-USA INC.
RJ LEE INSTRUMENTS LTD.
LEHIGH UNIVERSITY
LEICA INC.
MATERIALS ANALYTICAL SERVICES INC.
McCRONE ASSOCIATES INC.

MICRON INC.
MICROSPEC CORP.
NISSEI SANGYO AMERICA LTD./HITACHI
NORAN INSTRUMENTS INC.
OSMIC INC.
OXFORD INSTRUMENTS INC.
PARK SCIENTIFIC INSTRUMENTS
PHYSICAL ELECTRONICS INC.
PHILIPS ELECTRONIC INSTRUMENTS
PRINCETON GAMMA-TECH
SEM/TEC LABORATORIES INC.
SMALL WORLD
SOFT-IMAGING SOFTWARE CORPORATION
SPECTRA-TECH/NICOLET
SPI SUPPLIES/STRUCTURE PROBE INC.
C. M. TAYLOR CO.
TOPCON TECHNOLOGIES INC.
TOPOMETRIX CORPORATION
XEI SCIENTIFIC
CARL ZEISS INC.

MSC/SMC CORPORATE MEMBERS

ALCAN ARVIDA RES. & DEV. CENTRE
ANALYCHEM CORPORATION LTD.
BAL-TEC PRODUCTS INC.
BIO-RAD LABORATORIES (CANADA) LTD.
CANBERRA PACKARD CANADA
CARSEN MEDICAL & SCIENTIFIC CO. LTD.
DELAWARE DIAMOND KNIVES
DIMENSION LABS INC.
EDAX INTERNATIONAL
EDGECRAFT CORPORATION
EDWARDS HIGH VACUUM LTD.
ELECTRON MICROSCOPY SCIENCES
ELECTRON OPTIC SERVICES INC.
ELECTROSCAN CORPORATION
EMLAB EQUIPMENT INC.
ENERGY BEAM SCIENCES
ESSO RESOURCES
FISONS INSTRUMENTS
GATAN INC.

JEOL-USA INC.
LAB-6 INC.
LECO INSTRUMENTS LTD.
LEICA CANADA INC.
MARIVAC LTD.
MICROSCIENCE ENTERPRISES
NIKON CANADA INSTRUMENTS
NISSEI SANGYO CANADA INC.
OSRAM SYLVANIA LTD./LTEE
PELCO INTERNATIONAL
PHILIPS ELECTRONICS LTD.
POLAROID CANADA INC.
SOQUELEC LTD./LTEE.
SPECTRA RESEARCH CORPORATION
SPI SUPPLIES CANADA
SYSTEMS FOR RESEARCH CORPORATION
TOPOMETRIX
WORKERS COMPENSATION BOARD
CARL ZEISS CANADA LTD.

MICROSCOPY SOCIETY OF AMERICA

1996 DISTINGUISHED SCIENTIST AWARDS

JOHN SILCOX
Physical Sciences


MYRON C. LEDBETTER
Biological Sciences

John Silcox is the David E. Burr Professor of Engineering and Director of the Materials Science Center at Cornell University. He holds a Ph.D. degree in physics (1961) from the University of Cambridge and has been at Cornell since 1961. He is a past-president of MSA and has served on the Solid-state Sciences Committee of the National Research Council, as chair of the Materials Advisory Committee of the NSF Division of Materials Research, and as chair of the Executive Committee of the Division of Materials Physics of the American Physical Society. He spent sabbatical leaves in France and the U.K. in 1967-68 (as a Guggenheim fellow), at Bell Laboratories in 1974-75, and at Arizona State University in 1983. His research interests include electron microscopy, microspectroscopy, and microdiffraction of materials by field-emission gun-scanning transmission electron microscopy. The aim of his research is to establish quantitative procedures at the atomic (or near-atomic) length scale that can be applied to forefront materials science problems.

Myron C. Ledbetter became interested in microscopy at the age of eight with a gift of a student microscope from his parents. He had to postpone learning electron microscopy during his undergraduate studies in botany at Oklahoma State University; he engaged in graduate studies in botany at the University of California at Berkeley, and at Columbia University. His studies under Ed Matzke at Columbia were supported by the Boyce Thompson Institute in Yonkers, N.Y. Training in electron microscopy came at Rockefeller University with Keith R. Porter, an association that continued at Harvard. With Porter, he improved methods of examining fine structure of plants and found microtubules in plant cells. Also at Harvard, he invented thin-film apertures with Robert Dell, coauthored an atlas of plant-cell fine structure with Keith Porter, and studied plant surfaces by scanning electron microscopy; and he performed studies using cluster ions with Lewis Friedman while at the Brookhaven National Laboratory.

BURTON MEDAL
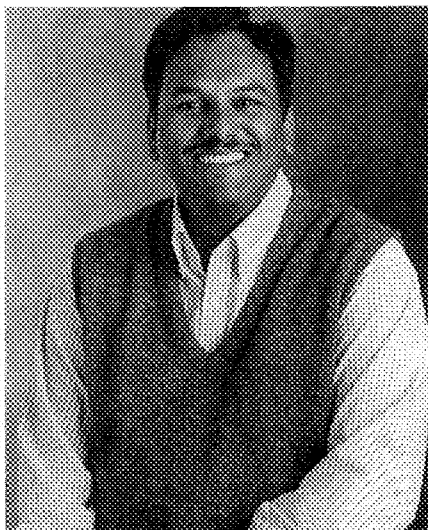
VINAYAK P. DRAVID

Vinayak P. Dravid received the undergraduate B.Tech. degree in Metallurgical Engineering from IIT Bombay, India in 1984. After one year of industrial experience in ferrite manufacturing, he joined the graduate program of Lehigh University and received the Ph.D. in Materials Science and Engineering in 1990. He then joined the faculty of Materials Science and Engineering at Northwestern University, and was promoted to Associate Professor with tenure in 1995. He also serves as director of the newly formed Electron Probe Instrumentation Center (EPIC). His research and teaching interests revolve around nanoscale phenomena in materials, with emphasis on synergistic applications of advanced electron microscopy techniques to problems of interfaces in composites, electronic materials, and nanostructured materials. He is a recipient of the NSF Young Investigator Award, IBM Faculty Development Fellowship, and Exxon Educational Foundation Award. He also serves on the editorial board of the *Journal of Microscopy* and of *Microscopy, Microanalysis and Microstructure.* In his spare time, he enjoys visiting as well as hosting high school and college teachers/students to foster an appreciation for the discipline of Materials Science and Engineering through the medium of electron microscopy, as well as the role that scientists and engineers play in society.

THE MORTON D MASER
MSA DISTINGUISHED SERVICE AWARD

MSA OUTSTANDING TECHNOLOGIST AWARD

JOE A. MASCORRO

DAVID W. ACKLAND
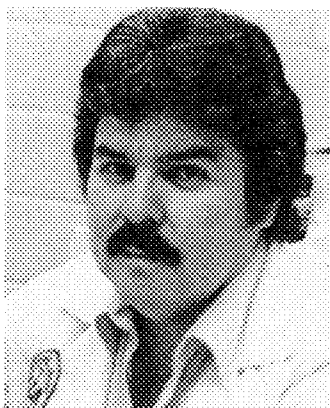
Joe A. Mascorro is a Research Assistant Professor of Anatomy at the Tulane University School of Medicine in New Orleans, LA. He began his career in electron microscopy in 1962 as a research technician at the University of Texas Medical Branch in Galveston. He advanced to the rank of Research Scientist before leaving Galveston for Tulane Medical School in 1972, where he has remained since. His research has centered around two principal areas: the occurrence and probable function of neuroendocrine chromaffin cells within various autonomic ganglia, and the innovation of alternative embedding procedures in biological electron microscopy in order to devise media with specific viscosity characteristics for specific purposes. He has authored or co-authored over 80 scientific publications, including abstracts, manuscripts, and invited chapters, and has served as reviewer for several scientific journals and editorial boards. He has chaired the MSA Technologists' Forum and served on the MSA Speaker's Bureau and as Chairman for the MSA Sustaining Members and Exhibitors Committee.

David Ackland was born and educated in England, where he studied Mechanical Engineering. In 1969 he worked in the electron microscopic facility at Tube Investment Research Laboratories, Cambridge, under the direction of Drs. Melford and Duncomb. In 1973 he moved to the electron microscope section of the Metallurgy Department at Cambridge University, where he managed the electron microscope suite. He came to the USA in 1980 to oversee the installation and operation of the KRATOS 1500kV TEM and auxiliary equipment at the National Center for Electron Microscopy at Berkeley. In 1987 David moved to the Department of Material Science and Engineering at Lehigh University, where he is now manager of the electron microscopy facility. One of his major projects at Lehigh has been the complete renovation of the microscope facilities to enable the installation of new generation electron microscopes, especially the VG 1113603 STEM. He went to England to help perform factory tests on this unique instrument. He has given lectures on electron microscopy laboratory management at Lehigh and in Venezuela.

E. M. Hunt
Georgia Institute of Technology
Materials Science and Engineering
Atlanta, Georgia

B. N. Johnson
Michigan State University
Department of Zoology
East Lansing, Michigan

K. S. Katti
University of Washington
Materials Science and Engineering
Seattle, Washington

M. M. Lipp
University of California—Santa Barbara
Department of Chemical Engineering
Santa Barbara, California

H. E. Lippard
Northwestern University
Materials Science and Engineering
Evanston, Illinois

D. L. Polis
University of Pennsylvania
Materials Science and Engineering
Philadelphia, Pennsylvania

R. A. Ristau
Lehigh University
Materials Science and Engineering
Bethlehem, Pennsylvania

M. A. Schofield
University of Wisconsin—Milwaukee
Laboratory for Surface Studies
Milwaukee, Wisconsin

S. Subramanian
Cornell University
Materials Science and Engineering
Ithaca, New York

I-Fei Tsu
University of Wisconsin—Madison
Materials Science and Engineering
Madison, Wisconsin

MSA DISTINGUISHED SCIENTIST AWARD

Biological Sciences		Physical Sciences	
1975	Keith Porter	1975	Robert Heidenreich
1976	L. L. Marton	1976	Albert Crewe
1977	Robley Williams	1977	James Hillier
1978	Thomas Anderson	1978	V. E. Cosslett
1979	Daniel Pease	1979	John Cowley
1980	George Palade	1980	Gareth Thomas
1981	Sanford Palay	1981	Vladimir Zworykin
1982	Richard Eakin	1982	Benjamin M. Siegel
1983	Hans Ris	1983	Otto Scherzer
1984	Cecil Hall	1984	Sir Charles Oatley
1985	Gaston Dupouy	1985	Ernst Ruska
1986	F. O. Schmitt	1986	Peter Hirsch
1987	Marilyn Farquhar	1987	Jan LePoole
1988	Morris Karnovsky	1988	Hatsujiro Hashimoto
1989	Don W. Fawcett	1989	Elmar Zeitler
1990	Audrey M. Glauert	1990	Gertrude F. Rempfer
1991	Hugh E. Huxley	1991	Archie Howie
1992	Fritiof Sjöstrand	1992	Oliver Wells
1993	Jean-Paul Revel	1993	Ken Smith
1994	Andrew Somlyo	1994	Dennis McMullan
1995	Shinya Inoué	1995	David B. Wittry

MSA BURTON MEDALIST

1975	James Lake
1976	Michael Isaacson
1977	Robert Sinclair
1978	David Joy
1979	Norton B. Gilula
1980	John Spence
1981	Barbara Panessa-Warren
1982	Nestor Zaluzec
1983	Ronald Gronsky
1984	David B. Williams
1985	Richard Leapman
1986	J. Murray Gibson
1987	Ronald Milligan
1988	A. D. Romig, Jr.
1989	Laurence D. Marks
1990	W. Mason Skiff
1991	Joseph R. Michael
1992	Kannan Krishnan
1993	Joseph A. N. Zasadzinski
1994	Jan M. Chabala
1995	Joanna L. Batstone

MSA DISTINGUISHED SERVICE AWARD

1992	Ronald Anderson
	G. W. "Bill" Bailey
	Frances Ball
	Blair Bowers
	Deborah Clayton
	Joseph Harb
	Kenneth Lawless
	Morton Maser
	Caroline Schooley
	John H. L. Watson
1993	E. Laurence Thurston
1994	Richard F. E. Crang
1995	Raymond K. Hart

MSA OUTSTANDING TECHNOLOGIST AWARD

1993	Ben O. Spurlock
1994	Bernard J. Kestel
1995	Kai Chien

MSA PAST PRESIDENTS

1942	G. L. Clark[1]		1969	W. C. Bigelow
1943	R. Bowling Barnes[2]		1970	Russell Steere
1944	R. Bowling Barnes		1971	Robert M. Fishe
1945	James Hillier		1972	Daniel C. Pease
1946	David Harker		1973	Benjamin Siegel
1947	William G. Kinsinger		1974	Russell J. Barne
1948	Perry C. Smith		1975	Gareth Thomas
1949	F. O. Schmitt		1976	Etienne de Harv
1950	Ralph W. G. Wyckoff		1977	T. E. Everhart
1951	Robley C. Williams		1978	Myron Ledbette
1952	R. D. Heidenreich		1979	John Silcox
1953	Cecil E. Hall		1980	Michael Beer
1954	Robert G. Picard		1981	John Hren
1955	Thomas F. Anderson		1982	Lee Peachey
1956	William L. Grube		1983	David Wittry
1957	John H. L. Watson		1984	J. David Robert
1958	Max Swerdlow		1985	Dale Johnson
1959	John H. Reisner		1986	Robert Glaeser
1960	D. Gordon Sharp		1987	Linn W. Hobbs
1961	D. Maxwell Teague		1988	Jean-Paul Revel
1962	Keith R. Porter		1989	Ray Carpenter
1963	Charles Schwartz		1990	Keith R. Porter
1964	Sidney S. Breese		1991	Charles Lyman
1965	Virgil G. Peck		1992	Patricia Calarco
1966	Walter Frajola		1993	Michael S. Isaac
1967	Joseph J. Comer		1994	Robert R. Carde
1968	John H. Luft		1995	Terence E. Mitc

---

[1]Chair of committee to arrange first meeting
[2]Temporary (pre-constitution).

AVRIL V. SOMLYO

ANDREW P. SOMLYO

Avril V. Somlyo grew up in Saskatoon, Canada, and attended the University of Saskatchewan. She received the Ph.D. in Physiology from the University of Pennsylvania in 1976, where she rose through the ranks to Research Professor in 1982. In 1988 she moved to the University of Virginia as Professor of Pathology and Professor of Molecular Physiology and Biological Physics. Dr. Somlyo's research has been focused on the contractile apparatus, its regulation, and the upstream pathways leading to activation in smooth muscle. Electron-optical techniques have played a major role in her research. She has received the Ciba-Geigy Award for Hypertension Research in 1991 and the Louis and Artur Lucian Award for Research in Circulatory Diseases in 1995. She serves on various Editorial Boards, including *FEBS Letters, Journal of Biological Chemistry, Cell Calcium, NIPS,* and the *Journal of Physiology-Cell Physiology.*
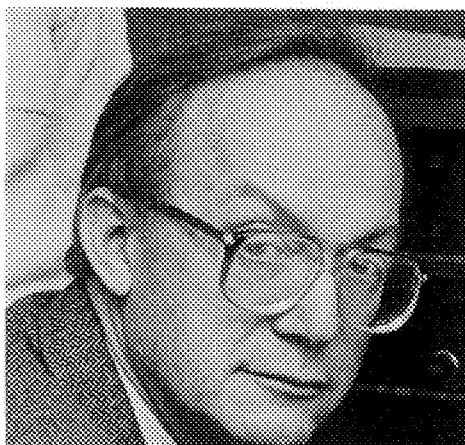
Andrew P. Somlyo was born in Budapest, Hungary, and received the M.D. degree from the University of Illinois in 1956. He was Professor of Physiology and Pathology and Director of the Pennsylvania Muscle Institute at the University of Pennsylvania. Since 1988 he has served as Chairman and Charles Slaughter Professor of Molecular Physiology and Biological Physics and Professor of Medicine (Cardiology) at the University of Virginia. In addition to his studies of the cellular biophysics of muscle, he has participated in the development and biological applications of analytical electron microscopy. He is a recipient of the Ciba-Geigy Award for Hypertension Research (1991); the Distinguished Scientist Award for the Biological Sciences, Microscopy Society of America (1994); and the Louis and Artur Lucian Award for Research in Circulatory Diseases (1995). He was Visiting Professor at Shanghai Medical University in China (1988) and British Heart Foundation Visiting Professor at Hammersmith Hospital in London, U.K. He is a member of the Alpha Omega Alpha Medical Honor Society, and honorary member of the Hungarian Physiological Society and of the Microscopy Society of America.
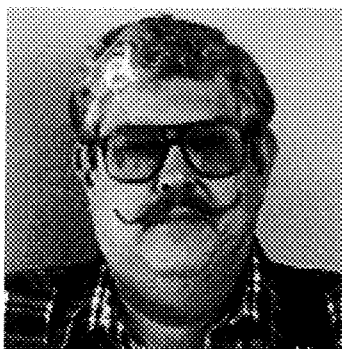
PAUL F. HLAVA

Paul Hlava is a Senior Member of Technical Staff at Sandia National Laboratories in Albuquerque, New Mexico, where he is in charge of the electron microprobe facility. He received the B.S. in Geology in 1964 from the University of Wisconsin, Madison. After some postgraduate studies there, he taught Earth Science at Wisconsin State University, River Falls. In 1974 he graduated from the University of New Mexico with an M.S. in Geology and went directly to Sandia's electron microprobe laboratory. Hlava's research interests are in the electron microprobe analysis of minerals, ceramics, metals, and joining technologies (welds, solders, and brazes), especially systems that are diffiicult to analyze. He has discovered and/or helped to characterize several new mineral species. He has been a member of MAS since 1975, a director (1994-1996), in charge of the tour speaker program since 1990, and has served on numerous program committees. He had a major role on the LAC of the 1986 MAS/EMSA meeting in New Mexico. Paul has been a member of his local group, NMMBUG, since 1974 and president for most of the past ten years.

MAS DISTINGUISHED SCHOLAR AWARDS

L. Cho
Kansas State University
Microbeam Molecular Spectroscopy Laboratory
Manhattan, Kansas

M. T. Johnson
University of Minnesota
Chemical Engineering and Materials Science
Minneapolis, Minnesota

D. Drouin
Université de Sherbrooke
Département de génie mécanique
Sherbrooke, Quebec

V. J. Keast
Lehigh University
Materials Science and Engineering
Bethlehem, Pennsylvania

P. C. Liu
Northwestern University
Materials Science and Engineering
Evanston, Illinois

MAS PRESIDENTIAL AWARDS

	Science		Service
1977	R. Castaing	1977	P. Lublin
1978	K. F. J. Heinrich	1978	D. R. Beaman
1979	P. Duncumb	1979	M. A. Giles
1980	D. B. Wittry	1980	A. A. Chodos
1981	S. J. Reed	1981	R. Myklebust
1982	R. Shimizu	1982	J. Doyle
1983	J. Philibert	1983	D. Newbury
1984	L. S. Birks	1984	J. I. Goldstein
1985	E. Lifshin	1985	M. C. Finn
1986	R. Myklebust	1986	V. Shull
1987	O. C. Wells	1987	D. C. Joy
1988	J. D. Brown	1988	C. G. Cleaver
1989	J. Hillier	1989	W. F. Chambers
1990	T. E. Everhart	1990	C. E. Fiori
1991	J. I. Goldstein	1991	T. G. Huber
1992	G. Lorimer	1992	E. Etz
	G. Cliff	1993	H. A. Freeman
1993	D. E. Newbury	1994	J. L. Worrall
1994	D. C. Joy	1995	R. W. Linton
1995	G. Bastin		

MAS K. F. J. HEINRICH AWARDS

1986	P. Statham	1991	A. D. Romig, Jr.
1987	J. T. Armstrong	1992	S. Pennycook
1988	D. B. Williams	1993	P. E. Russell
1989	R. Leapman	1994	J. R. Michael
1990	R. W. Linton	1995	N. Lewis

MAS PAST PRESIDENTS

1968	L. S. Birks		1982	R. Myklebust
1969	K. F. J. Heinrich		1983	R. Bolon
1970	R. E. Ogilvie		1984	D. C. Joy
1971	A. A. Chodos		1985	D. E. Newbury
1972	K. Keil		1986	C. G. Cleaver
1973	D. R. Beaman		1987	C. Fiori
1974	P. Lublin		1988	W. F. Chambers
1975	J. W. Colby		1989	D. B. Wittry
1976	E. Lifshin		1990	A. D. Romig, Jr.
1977	J. I. Goldstein		1991	J. T. Armstrong
1978	J. D. Brown		1992	D. B. Williams
1979	D. F. Kyser		1993	T. G. Huber
1980	O. C. Wells		1994	J. Small
1981	J. R. Coleman		1995	J. McCarthy

1996 MICROSCOPICAL SOCIETY OF CANADA/
SOCIETE DE MICROSCOPIE DU CANADA AWARDS

MSC/SMC GERARD T. SIMON STUDENT AWARDS

M. M. G. Barfels
University of Toronto
Department of Medical Biophysics
Toronto, Ontario

C. Blais
Ecole Polytechnique de Montréal
Center for Microscopy and Characterization Materials
Montréal, Quebec

MSC/SMC PAST PRESIDENTS

|				
1972-1975	A. F. Howatson		1984-1985	J. M. Sturgess
1975-1977	E. J. Chatfield		1985-1987	D. A. Craig
1977-1979	G. T. Simon		1987-1989	R. F. Egerton
1979-1981	G. H. Haggis		1989-1991	P. J. Lea
1981-1983	F. P. Ottensmeyer		1991-1993	G. L'Esperance
1983-1985	D. O. Northwood		1993-1995	L. Arsenault

Margaret Ann Goldstein
MSA President

Dale E. Johnson
MAS President
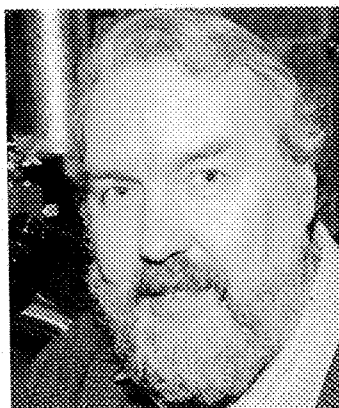
James M. Corbett
MSC/SMC President

LOCAL ARRANGEMENTS
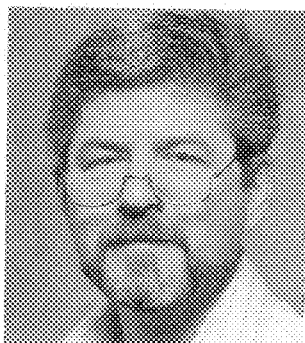
Ev Osten
Local Arrangements Chair
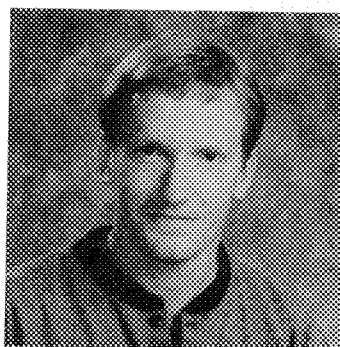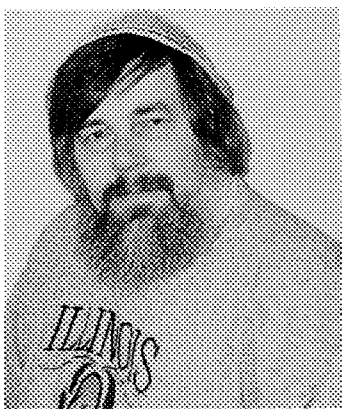

Dwight D. Erickson
Local Arrangements Treasurer

Mike Coscio
Local Arrangements Vice Chair
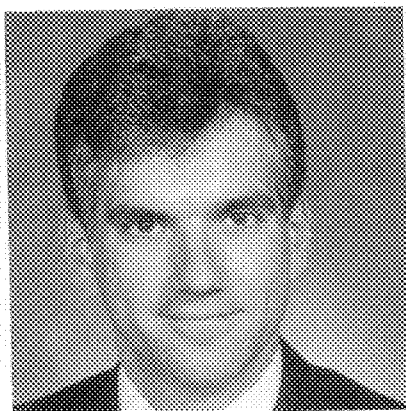

Stan E. Erlandson
Local Arrangements Vice Chair

PROGRAM

Nestor J. Zaluzec
Chair

Ruth V. W. Dimlich
Vice Chair

Joseph R. Michael
Co Chair

MICROSCOPY AND MICROANALYSIS 1996

PROGRAM COMMITTEE

FOREWORD

MARGARET ANN GOLDSTEIN
President, Microscopy Society of America

DALE E. JOHNSON
President, Microbeam Analysis Society

JAMES M. CORBETT
President, Microscopical Society of Canada/
Société de Microscopie du Canada

The Proceedings of this Annual Meeting contain papers of members from the three societies. A new meeting format, indicated by the title *Microscopy and Microanalysis '96,* emphasizes our common research interests and attempts to eliminate some unwanted overlap. The MSA Presidential Symposium acknowledges the keen interest in the microscope-computer interface and explores the challenges of generating and displaying 2-D and 3-D images in the biological and physical sciences.

We thank the Program Committee for their efforts over several years to achieve a combined meeting style that reflects the close cooperation between MSA and MAS and with MSC/SMC. Special thanks go to Program Chair '96 Nestor Zaluzec and Program Chair '97 Ruth Dimlich of MSA, Joe Michael of MAS, Jim Corbett of MSC/SMC, and the members of their committee from all three societies. Imagination and many hours of careful and hard work by dedicated volunteers make a superb scientific program possible.

We also thank our volunteers on the Local Arrangements Committee, headed by Ev Osten. The successful coordination of planned scientific sessions, social events, committee meetings, and informal exchanges with colleagues from around the world is accomplished by the dedicated work of the LAC.

Congratulations to Myron Ledbetter for the MSA Distinguished Scientist Award in the Biological Sciences, to John Silcox for the MSA Distinguished Scientist Award in the Physical Sciences, to Vinayak Dravid for the MSA Burton Award, to Joe Mascorro for the MSA Morton D Maser Distinguished Service Award, and to David Ackland for the MSA Outstanding Technologist Award. Congratulations also to Avril Somlyo and Andrew Somlyo for the MAS Presidential Sciences Awards, and to Paul Hlava for the MAS Presidential Service Award. We also congratulate our winners of the ten MSA Presidential Student Awards, the five MAS Distinguished Scholar Awards, and the two MSC/SMC Gerard T. Simon Student Awards.

May we all find the joy of a new learning experience and the fellowship of good companions at this meeting.

Houston, Texas
August 1996

TITLES AND ORDER OF SESSIONS

PRESIDENTIAL SYMPOSIUM
CHALLENGES OF GENERATING AND DISPLAYING IMAGES
WITH EMERGING TECHNOLOGIES

MICROSCOPIC ANALYSIS OF ANIMALS WITH ALTERED GENE EXPRESSION
AND *IN SITU* GENE AND ANTIBODY LOCALIZATIONS

HIGH-RESOLUTION ELEMENTAL MAPPING OF
NUCLEOPROFEIN INTERACTIONS

PLANT BIOLOGY AND PATHOLOGY

QUANTITATIVE HREM ANALYSIS OF PERFECT AND DEFECTED MATERIALS

COMPUTATIONAL METHODS FOR TEM IMAGE ANALYSIS

HIGH-RESOLUTION FESM IN MATERIALS RESEARCH

FRONTIERS IN POLYMER MICROSCOPY AND MICROANALYSIS

OXIDATION AND CORROSION

MICRO XRD AND XRF

MOLECULAR MICROSPECTROSCOPY AND SPECTRAL IMAGING

TUTORIAL: PHYSICAL SCIENCES

TUTORIALS: BIOLOGICAL SCIENCES

ADVANCES IN CONFOCAL AND MULTIDIMENSIONAL LIGHT MICROSCOPY

ANALYTICAL ELECTRON MICROSCOPY IN BIOLOGY

MAS PRESIDENTIAL SYMPOSIUM: COMPOSITIONAL IMAGING IN BIOLOGY

CORRELATIVE MICROSCOPY IN BIOLOGICAL SCIENCES: ADVANCES AND APPLICATIONS

GRAIN-BOUNDARY MICROENGINEERING

SURFACES AND INTERFACES

TELEPRESENCE MICROSCOPY IN EDUCATION AND RESEARCH

MSA EDUCATIONAL OUTREACH

DEVELOPMENTS IN INSTRUMENTATION

QUANTITATIVE ELECTRON PROBE MICROANALYSIS

FRONTIERS OF ANALYTICAL ELECTRON MICROSCOPY

IMAGE ANALYSIS IN THE BIOLOGICAL AND PHYSICAL SCIENCES

TECHNOLOGISTS FORUM: MOVING TO DIGITAL MICROSCOPY

CRITICAL ISSUES IN CERAMIC MICROSTRUCTURES

MSC/SMC PRESIDENTIAL SYMPOSIUM

MODULATED STRUCTURES, QUASI CRYSTALS, AND SUPERCONDUCTORS

DYNAMIC ORGANIZATION OF THE CELL

PATHOLOGY

MICROBIOLOGY

HIGH-RESOLUTION BIOLOGICAL AND CRYO SEM

MATERIAL SCIENCES AND BIOLOGY APPLICATIONS OF
LEAKY-VACUUM SEM

SCANNING-PROBE MICROSCOPY: INSTRUMENTATION AND APPLICATIONS

FUNCTIONAL MAGNETIC RESONANCE IMAGING FROM
MOLECULES TO HUMANS

NEW LABELS FOR BIOLOGICAL MICROSCOPY

BIOLOGICAL TECHNIQUES

BIOLOGICAL ULTRASTRUCTURE

ELECTRONIC MATERIALS

PHASE TRANSITIONS IN METALS AND ALLOYS

SPECIMEN PREPARATION: PHYSICAL SCIENCES

MICROBEAM MASS SPECTROMETRY

MICROSCOPY SOCIETY OF AMERICA
S
M · A
FOUNDED 1942

MICROBEAM
Analysis Society

MSC
SMC

CHALLENGES OF GENERATING AND DISPLAYING IMAGES WITH EMERGING TECHNOLOGIES--PRESIDENT'S SYMPOSIUM

THREE WAYS TO LOOK AT MUSCLE

by Margaret Ann Goldstein, Baylor College of Medicine, Department of Medicine, Houston, TX 77030

A pictorial history of muscle morphology from the 1960's to the 1990's shows the successive addition of new methodology and the combination of analytical techniques with descriptive approaches. These powerful images express the relationships between the cell components required for cycles of contraction and relaxation.

Although electron micrographs are used as pictures to illustrate a story, they are precise descriptions containing analyzable data. The vast quantities of information contained in a single image has been the impetus to make better procedures and technologies to extract and display selected information. One of the simplest methods of feature extraction that is still widely used is cropping images to limit the field of view. Selective staining allows visualization of long-range ordering of specific features in images from HVEM. Optical diffraction and optical reconstruction provide for enhancement of order, and stereological approaches allow for quantitation in studies of muscle protein lattices.

The advent of the microscope-computer interface and the software to analyze, assemble and display images brings a whole new range of possibilities and potential difficulties. Small portions of a muscle lattice or individual protein filaments can be studied in greater detail in 3-d. Computer techniques are used to reproduce earlier techniques such as optical diffraction (by Fourier analysis), and Markham rotation (by image averaging). Difference Fourier analysis can be used to quantitate subtle differences between labeled and unlabeled muscle treated with antibodies. The information contained in a series of 2-d electron micrographs in shades of gray can be combined to reconstruct a 3-d object. A tiny portion of a muscle which was originally in 3-d and in color, may now be rendered in 3-d and displayed in color. Features not imaged in electron micrographs of cross or longitudinal sections of the muscle are visible in the 3-d reconstruction.

The pace of the progression of methods from the 60's to the 80's was a slower one and few people looked at the process. Now more people must once again confront the limits of the human eye and brain as we examine the new imaging and display technologies, shape our future direction and communicate to a larger and larger audience the wonders of microscope images.

Fig. 1. Three images of longitudinal sections of the Z band in relaxed rat soleus muscle. Each image depicts a different level in the imaging and analysis of this protein lattice. The scale bars in these images are 10 nm.

a) An electron micrograph shows a projection of the lattice. Thin filaments enter the Z band from the top and bottom of the figure. Inside the Z band, they are interconnected by a poorly visualized net of cross-connecting Z-filaments. In this part of the figure, protein appears dark against a white background.
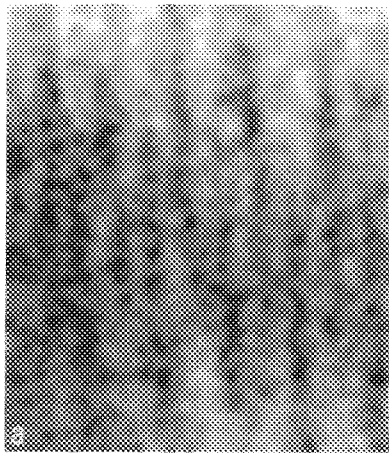
b) A stereo pair showing part of a 3-d reconstruction of the Z band and nearby I band generated by computerized electron tomography. Depicted is the intersection region of two orthogonal 10 nm sections. The cross-connecting Z-filaments appear more distinct. Also visible is the Z band relaxed interconnecting body (Z-RIB). These filamentous structures run parallel to the thin filaments and are shown hatched. In this part of the figure, protein is shaded white against a dark background.

c) An interpretation of the connectivity visualized in b. The extensions of the thin filaments are diagonally striped, the Z-RIB is cross-hatched, and cross-connecting Z-filaments appear in grey. Connections between the thin filaments in the I band appear at the top and bottom of the figure in a darker grey.
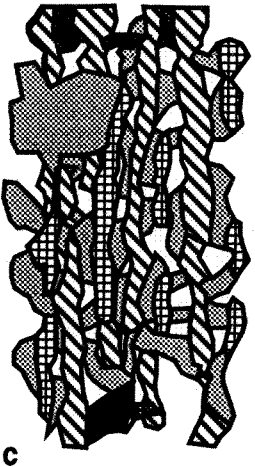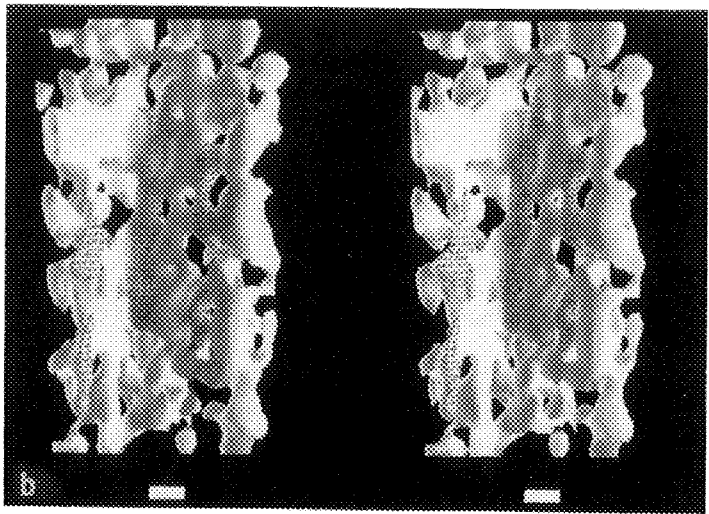
GENERATING AND COMPARING THREE-DIMENSIONAL IMAGES OF STRUCTURES OBTAINED BY ELECTRON MICROSCOPY AND OTHER METHODOLOGIES

D.J. DeRosier

Rosenstiel Basic Medical Sciences Research Center, Brandeis University, Waltham, MA 02254-9110

"Subtract the mind,...and the eye is open to no purpose, which before did see." "Before my eye can see the painting on the wall, this must...be borne into my phantasy, to be assimilated by my understanding." (both attributed to 14th century philosopher-mystic, Meister Eckhart).

Images of models provide a way to look at structures. A well-executed model can embody the results of many studies in a way that our minds easily grasp. We learn from them, and we teach from them. They are especially important in structural studies because comprehension of spatial relationships is key to our understanding. The computer, with its ability to generate, color and animate three-dimensional objects, is a source of both good and evil when producing images of models.

Models are really analogies intended to illustrate particular attributes of a structure. A "dangerous pitfall is hidden in the very nature of analogies themselves. Every grade [of analogy] can be traced between remote analogies, and analogies which are so close that they pass into identities, and - paradoxically enough - it is often the remote analogies which have the greatest value, while it is the close analogies of which we have to beware. The misuse of an analogy by pressing it to the point at which it is confused with an identity, is one to which biological thought is particularly liable." (Agnes Arber, 1953).

Models may possess incidental features that are not relevant to the structure studied. In early models, actin subunits were represented by spheres, and consequently models of the actin filament had more symmetry than the real filament: namely, the models lacked polarity, a biologically critical attribute of filament structure. A model of the filament made from spheres attempts to illustrate the positions of the centers of masses of the subunits. It need not and does not represent accurately other aspects of the structure; for example, the nature of the intersubunit contacts. The danger is that incidental features of the model can constrain our thinking along incorrect lines. The more lifelike the model, the more likely we are to accept it as the structure rather than as a limited analogy for the structure. In the construction of model, we can really only illustrate particular aspects of a structure; for example, the surface topography. I have selected examples from three-dimensional reconstructions from electron micrographs to illustrate the power and problems of using models and to show how the the computer can be used to improve the situation.

The end result of a three-dimensional reconstruction is a three-dimensional density distribution. Prior to the use of computers, people often displayed their maps in the form of solid models cut out of wood or plastic. The model was intended to show the surface features of the structure. Sometimes segments of the model were cut away to reveal inner details. Photographs of the model made it easy to visualize the structure: the organization of its subunits, the symmetry of the structure, and even the domain structure within the subunit.

How can such images and models objectively derived from electron micrographs lead us astray? The answer is that the models generated from the maps require some decision about which aspects of the map are to be displayed. The three-dimensional map resulting from the processing of electron micrographs does not specify directly the position of the outer surface of the structure. Some people produce a surface so that the volume enclosed represents the expected volume of the subunit. Others

generate use a smaller volume in order to enhance the appearance of domains within the subunit. These choices affect what we perceive when we view such a surface representation. We might see no connectivity between subunits that are in contact because we chose an outer surface that doesn't reveal the connectivity. Or vice versa. Further, the surface can be affected by noise in the map or by disorder in the structure. The surface does not show us which features in the map are strong (i.e.., correspond to high density) and are therefore reliable. It does not show us those which are weaker, and are therefore less reliable.

With the computer, we generate such surface representations easily and quickly, but with the computer's ability to render transparent, colored surfaces, we can generate images that better represent the three-dimensional density distribution than merely creating digital versions of our wooden analogues. We can show the outer surface in one transparent color and the strong (internal) features as a second surface in a different color. Although no one has done it, we could as an alternative vary the color of the surface to represent the precision to which we can place the surface based on an analysis of errors in the map. This would be akin to coloring parts of an atomic model according to the temperature factors of the atoms.

In an increasing number of instances, we have intermediate resolution maps of macromolecular complexes (e.g.., the actin filament) produced using electron microscopy, and we have atomic models of isolated subunits (e.g.., the actin monomer) obtained by X-ray crystallography or nuclear magnetic resonance spectroscopy. The computer allows us to dock the atomic model of the subunit into the map of the complex thereby generating an atomic model for the complex. We can display the result by superposing a transparent surface representation of the map on the atomic model of the complex. With such a display, we can judge the fit of the atomic model to the map; we can see what parts of the atomic model stick out from the surface and what parts inside the surface are devoid of atoms from the model.

While we can use the computer to generate other kinds of useful static images (such as ones in which different parts of a structure are rendered in different colors), what may well be used most is the computer's ability to animate. What better way to visualize a complicated model than to watch it as it rotates or to explore its structure by traveling through the model. Animated sequences provide a better grasp than stereo images do, and animation provides access to individuals who do not see in stereo. But animation also provides a way to convert differences in space to differences in time. For example, to see conformational changes in actin made under different conditions, one could generate an animated sequence in which one conformational form merges into the other. The changes, which may be hard to pinpoint by comparing static images, are easily picked out as movement of the parts in animated sequences. The danger is that we come to think of the movements seen in the animation as the real pathway of the conformational change.

Perhaps in a future electronic journal, such animated sequences will be included as a figure in a paper, but for now we can make them available using the internet.

THE IMPACT OF IMAGING TECHNOLOGIES IN MATERIALS ENGINEERING

R. Gronsky

Department of Materials Science and Mineral Engineering, and Materials Sciences Division, E.O. Lawrence Berkeley National Laboratory, University of California, Berkeley, CA 94720-1760

Materials Engineering is widely acknowledged as a "hyper-discipline" spanning the fundamental sciences (Physics, Chemistry and Biology) with all of the traditional engineering pursuits (Civil, Electrical, Mechanical, Metallurgical, Nuclear...). A healthy materials engineering program in fact demands interaction among basic science and technology, all classes of materials, and the intrinsic elements of the field, parochially known as properties, performance, structure (including composition) and synthesis (including processing). Advanced characterization techniques are obviously critical to this integration, and new imaging technologies have accelerated the process of characterizing materials at all relevant length scales, communicating large data sets to practicing engineers, and refining manufacturing methods with image-based technologies. The importance of imaging technologies was forecast by the National Research Council in a highly regarded 1989 report[1] "Material Science & Engineering for the 1990's: Maintaining Competitiveness in the Age of Materials," which included prominent mention of all microscopy methods. Since then, the success and challenges associated with imaging technologies have increased dramatically.

Biomaterials In the biomaterials field, which is projected to be a $5 billion dollar industry[2] before the year 2000, imaging technologies are most evident. Cross-modal medical imaging (MRI, CAT..) localizes the results of disease or trauma that might be remedied by implantable structures, developed under condition of strict microstructural control, and monitored for degradation products by non-invasive *in-situ* means. Products include biochemical sensors requiring high spatial resolution characterization of structure and composition, orthopedic prostheses and repairs, sometimes processed to possess pore structures that mimic natural bone, and wound-management devices, including artificial skin composed of bi-layer silicone elastomers and glycosaminoglycan interspersed with collagen. The last of these is especially dependent upon microstructural characterization. Implantable materials systems, such as the cochlear implant for hearing restoration (direct stimulation of the auditory nerve), or heart-assist devices (long fatigue life), require some of the highest standards in materials selection, design, and integration, with the added dimension of biocompatibility. In addition, the irradiation sensitivity of many candidate biomaterials[3] requires strict attention to low-dose imaging methods, rapid scan image acquisition, and sometimes extensive image processing to avoid or circumvent artefacts. Forward-looking projects on fully implantable therapeutic "agents" for medicinal delivery or chelation of toxins and viruses will place even more demands upon our ability to image *in-situ* functionality.

Nanoelectronics Previously known as microelectronics, this field is driven by processing speed, capacity, portability, and dependability, for which structural and compositional characterization at the highest levels of spatial resolution are essential. Just as electron-optical imaging components are now integrated into semiconductor fabrication lines, the diagnostics of failed devices requires sophisticated focused ion beam registration and accurate mechanical methods of material removal to isolate individual junctions exhibiting breakdown so that they might be analyzed for the root cause of failure.[4] Images of atomic constituents, devices, circuits, and packages are being acquired and stored

6

at escalating rates, with mounting pressure to decrease turn-around time back to the fab line for corrective measures to restore zero-defect manufacturing yield. In this industry, imaging has literally become a manufacturing process. The information storage field has also fostered new alliances with many imaging technologies, including those that map magnetic domains at high spatial resolution (spin-polarized electron detectors, differential phase contrast imaging, holographic reconstruction), which are most useful when combined with information regarding both the atomic structure and local composition of the recording media. And in the mammoth telecommunications industry, new families of photoresists, improved dry processing, new dielectrics, and new metallization technologies will be needed to achieve the nanoscale integration needed for tomorrow's applications. All have imaging components.

Transportation Although dominated in recent history by the need for energy efficiency (higher strength alloys for weight savings, surface coatings for reduced friction and wear, alternative materials for compatibility with alternative fuels), the transportation industry has broadened its materials-based engineering activities to encompass more complex issues. These include life-cycle (is the vehicle re-cyclable?), passenger safety (crash-worthiness), and zero-emission propulsion (fuel cells and batteries). The development of new materials for more challenging applications, such as higher engine operating temperatures[5] to achieve higher thermodynamic efficiency, and the improvement of existing materials to meet new federal guidelines, as in automotive catalytic converters,[6] is intimately linked to precision microstructural characterization. Other imaging technologies coupled to on-board global positioning system (GPS) hardware will be needed to employ such proposed "intelligent vehicle" concepts as automatic convoying, crash prevention, and remote traffic control.

What Next? Manufacturing technologies that rely upon rapid prototyping are moving to optical-based imaging and three-dimensional shaping with essential imaging components. In some applications, the laser/photodetector that "reads" an existing component also "writes" its full 3-D morphology into photo-sensitive or thermal-sensitive media for consolidation into a prototype part, and a "transfer function" for the process is based upon imaging theory. Intelligent processing systems will furthermore utilize "image banks" with interactive virtual cameras under operator control to view and dry-run a manufacturing process from any line-of-sight perspective needed to understand and optimize control. When linked to virtual reality modeling language (VRML) data files, on-line process control can acquire even more increased precision by interactive comparisons with simulations and real-time feedback.

References

[1] "Materials Science and Engineering for the 1990's: Maintaining Competitiveness in the Age of Materials," National Research Council, National Academy Press, Washington, D.C. (1989).
[2] "Advanced Materials and Processing: Fiscal Year 1993 Program," Federal Office of Science and Technology Policy, National Institute of Standards and Technology, Gaithersburg, MD, (1992).
[3] M. Goldman, R. Ranganathan, L. Pruitt, and R. Gronsky, *Trans. 21st Ann. Mtg. Soc. Biomaterials*, **21**, 111 (1995).
[4] J.B. Liu, B. Tracy, and R. Gronsky, *Microscopy Research and Technique* **26**, 162 (1993).
[5] R.W. Beye and R. Gronsky, *Acta Met. et Mater.*, **42** (4), 1373 (1994).
[6] Z.Weng-Sieh, R. Gronsky, and A.T. Bell, in *Proc. Microscopy & Microanalysis 1995*, G.W. Bailey, M.H. Ellisman, R.A. Hennigar, and N.J. Zaluzec, (Eds.), Jones & Begell Publishing, N.Y., p. 400, (1995).

RADIOACTIVE AND NON-RADIOACTIVE *IN SITU* HYBRIDIZATION TECHNIQUES

I. Durrant

Life Sciences Research and Development, Amersham International, White Lion Road, Amersham, Buckinghamshire, HP7 9LL, UK

In situ hybridization is a powerful technique that has found multiple applications in the biological sciences. The most widely used technique is in the analysis of mRNA species in cell populations. This is particularly useful for the analysis of relative amounts, site of transcription, timing and induction of transcription. Recent advances have lead the technique into the areas of relative quantification, dual signal detection and disease diagnosis. DNA targets can also be visualised by *in situ* hybridization both in cells and tissues and on isolated chromosomes and nuclei. There are a variety of systems that can be used to detect hybridization signals *in situ*. These choices are based in two areas, probe type and label type and this selection process holds true for both radioactive and non-radioactive systems.

Probe selection is important and plays a part in the overall success of the application (see Table 1). RNA probes and oligonucleotide probes are the most widely used in cells and tissues whereas DNA probes are routinely used for chromosome and nuclei targets. RNA probes are used due to the higher sensitivity obtained but oligonucleotide probes are gaining in popularity due to ease of use. The lower sensitivity seen with these probes, due to lower labelling capacity, can be overcome by use of probe cocktails.

Traditionally *in situ* hybridization probes have been based on radioactive labels. Radioactive labels may still offer the highest sensitivity but the signal may take a significant length of time to develop, particularly when the highest possible resolution is required. Within radioactive methods, isotope selection is a key feature. The difference between the available isotopes and nucleotide formulations and labelling methods has been investigated (see Table 2). The choice has been widened recently by the availability of ^{33}P labelled nucleotides [1].

Non-radioactive techniques are also highlighted by a variety of choices. Here the choice of label and the choice of detection process have to be made together (see Table 3). The standard system used in most applications utilizes alkaline phosphatase conjugated anti-hapten antibodies in conjunction with a coloured enzyme reaction product [2]. Antibody conjugates can also be made with gold and peroxidase labels and these may find use in particular applications. In addition fluorescence may be used as a detection system and it is the method of choice for cytogenetic studies.

The criteria applied to the selection of the most appropriate detection system (see Figure 1) should be based on the balance required, in the individual experimental system, between speed of result, sensitivity of detection and the resolution of the signal.

References
1. I. Durrant et al., *Histochemical Journal*, 27 (1995) 89.
2. I. Durrant et al., *Histochemical Journal*, 27 (1995) 94.

Table 1: Criteria for selection of probe type for *in situ* hybridization

	Advantages	Disadvantages
RNA probes	High stability hybrids Single stranded Free of vector sequence	Sub-cloning required Danger of RNase contamination
DNA probes	No sub-cloning required Choice of labelling methods	Probe denaturation required Less stable hybrids
Oligonucleotide probes	No cloning required Easy to make and label High specificity	Less well labelled and lower sensitivity

Table 3: Detection methods for non-radioactive probe labels

Probe labels	Detection methods	Features
Fluors Fluorescein Rhodamine Cy Dyes	Direct fluorescence microscopy	Potential high sensitivity, speed, resolution. Excellent for chromosomes and nuclei
Haptens Fluorescein Biotin Digoxigenin	Through antibodies conjugated to peroxidase, phosphatase or gold	Alk.phos. used widely for mRNA, peroxidase for DNA, gold for high resolution
Enzymes Peroxidase Phosphatase	Enzyme assay using colour or light based reaction products	Not widely used as direct labels. Light reaction for peroxidase has potential.

Table 2: Properties of isotopes commonly used for radioactive *in situ* hybridization

Isotope	^{32}P	^{33}P	^{35}S	^{125}I	^{3}H
Energy of emission (MeV)	1.71	0.249	0.167	0.035	0.018
Half life (days)	14.3	25.4	87.4	60.0	12.4 years
Resolution (μm)	20-30	15-20	10-15	1-10	0.5-1.0
Application	Macroscale *in situ* Optimization of parameters	Localization at the cellular level	Localization at the cellular level	Sub-cellular localization	Sub-cellular localization
Advantage of label	Detection using x-ray film Rapid analysis	Short exposure Low background	Short exposure Medium resolution	High sensitivity Short exposure, Good resolution	High resolution
Disadvantage of label	Low resolution			Gamma emitter	Long exposure time

Figure 1: Flow diagram for the selection of appropriate methods for different *in situ* hybridization applications

Application

Cells and tissue section — Chromosomes and nuclei

Medium / high sensitivity — Medium / low sensitivity

Radioactive label — Non-radioactive label

Choice of label type — Choice of probe type — Choice of fluorescent label

Choice of probe type — Choice of hapten label — Choice of labelling method

Probe labelling reaction — Probe labelling reaction — Probe labelling reaction

Hybridization — Hybridization — Hybridization

Detection — Antibody conjugate — Direct detection — Antibody conjugate

Film   Emulsion — Colour   Gold   Light — Microscopy

9

A Morphologic Approach to Understanding Molecular Events During Development

D. P. Witte
Department of Pathology, Children's Hospital Medical Center, and the University of Cincinnati College of Medicine, Cincinnati, Ohio, 45229

Through the combined technologies of *in situ* hybridization and transgenic mouse analysis major advances have been made in the understanding of developmental biology. Recent advances in understanding embryogenesis have been accomplished by determining specific gene activation during development, determining the cell specificity of individual activated genes, characterizing the cis regulatory elements of the developmentally regulated genes, and disrupting the activity and functions of these genes during critical stages of development through targeted mutation. *In situ* hybridization provides highly specific and sensitive detailed information of both the spatial and temporal pattern of endogenous gene expression during embryogenesis. The regulatory elements that determine the tissue specific and temporal related expression pattern of these embryonic genes are then identified and characterized by *in situ* hybridization through the generation of transgenic mice which carry gene constructs with reporter genes, such as CAT, luciferase, or lac Z, linked to the flanking DNA sequences that exert either positive or negative influence over the expression of the gene in question. Finally once the expression patterns and regulatory elements have been characterized targeted ablation of the developmentally regulated gene can determine or provide important insight into function.

The mammalian Hox genes are an important family of developmentally regulated genes that are organized in four clusters and encode important transcription factors which determine the mammalian body plan. As an example of the type of molecular approach described above to better understand developmental gene regulation we have recently characterized the homeobox genes Hoxa11 and Hoxd11 and the developmental defects that result from targeted ablation of these genes.[1,2]

In situ hybridization using S^{35} labeled single stranded RNA probes were used to localize the mRNA in mouse embryos for both the Hoxa11 gene and its paralogue Hoxd11 (Figure A, B). Hoxa11 transcription patterns were defined in the developing limbs, kidney and stromal cells of the primitive reproductive tract. Similar *in situ* hybridization analyses of the paralogue gene, Hoxd11, showed an identical expression pattern.

Targeted mutation of Hoxa11 resulted in sterility and limb defects. Similarly targeted mutation of the Hoxd11 gene also resulted in a similar phenotype. Suprisingly there were no significant renal abnormalities in either mutant mouse lines. By breeding the two strains together double mutant mice were generated which had dramatic phenotypes. In the double mutants the radius and ulna of the forelimb were almost entirely eliminated (Figure C,D) and severe kidney defects (Figure E,F) resulted in perinatal deaths. These results illustrate the strong correlation between the observed expression pattern of these Hox genes as determined by the *in situ* hybridizatin and the resultant phenotype following targeted gene mutation. The overlapping expression patterns of these two Hox paralogue genes and the quantitative, synergistic interactions between these genes further exemplify potential redundancy in some critical developementally regulated genes.

1.   Hsieh-Li HM, Witte DP, Weinstein M, Bradford W, Small K, and Potter SS.
      Development 121:1373-1385, 1995.
2.   Davis AP, Witte DP, Hsieh-Li HM, Potter SS, and Capecchi MR.
      Nature 375:791-795, 1995.
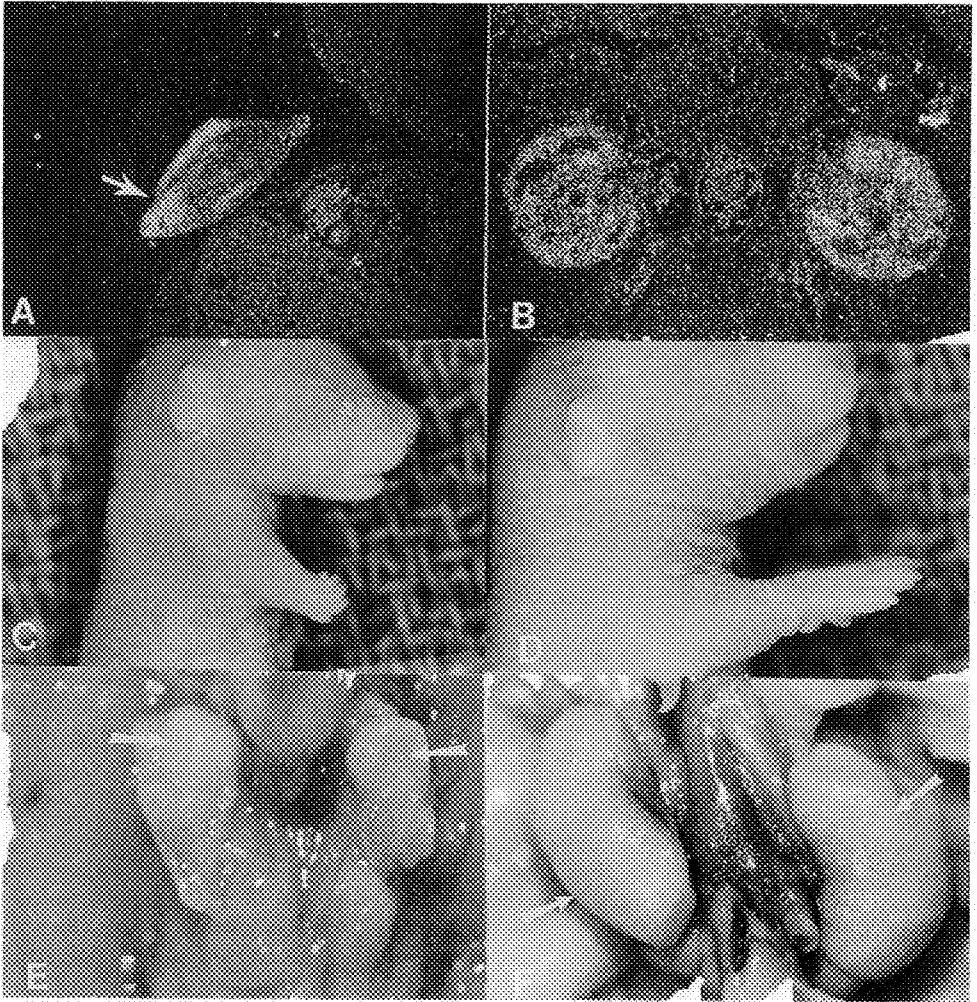
Panel A. In situ hybridization of d11 mouse embryo showing positive signal (bright white grains) for Hoxd11 mRNA in distal aspect of forelimb (arrow).

Panel B. In situ hybridization of d11 mouse embryo showing positive signal for Hoxd11 gene expression in metanephric kidneys.

Panel C. Gross photograph of a newborn mouse double mutant for Hoxa11/Hoxd11. Note the lack of distal limb development.

Panel D. Gross photograph of wild type littermate of mouse in panel C with normal limb development.

Panel E. Gross photograph of d20 mouse embryo double mutant for Hoxa11/Hoxd11. The kidneys are severely hypoplastic (arrows)

Panel F. Wild type littermate of embryo shown in panel E. The normal size kidneys are indicated by the arrows.

MOLECULAR AND MICROSCOPIC ANALYSIS OF ALTERED GENE EXPRESSION IN TRANSGENIC AND GENE TARGETED MICE

W. K. Jones and J. Robbins

Division of Molecular Cardiovascular Biology, Children's Hospital, Cincinnati, OH 45229

Two myosin heavy chains (MyHC) are expressed in the mammalian heart and are differentially regulated during development. In the mouse, the α-MyHC is expressed constitutively in the atrium. At birth, the β-MyHC is downregulated and replaced by the α-MyHC, which is the sole cardiac MyHC isoform in the adult heart. We have employed transgenic and gene-targeting methodologies to study the regulation of cardiac MyHC gene expression and the functional and developmental consequences of altered α-MyHC expression in the mouse.

We previously characterized an α-MyHC promoter capable of driving tissue-specific and developmentally correct expression of a CAT (chloramphenicol acetyltransferase) marker in the mouse[1]. Tissue surveys detected a small amount of CAT activity in the lung (Fig. 1a). The results of *in situ* hybridization analyses indicated that the pattern of CAT transcript in the adult heart (Fig. 1b, top panel) is the same as that of α-MyHC (Fig. 1b, lower panel). The α-MyHC gene is expressed in a layer of cardiac muscle (pulmonary myocardium) associated with the pulmonary veins (Fig. 1c)[2]. These studies extend our understanding of α-MyHC expression and delimit a third cardiac compartment.

We have disrupted the α-MyHC by homologous recombination in embryonic stem cells (Fig. 2a). Mice heterozygous for the disrupted allele (+/-) were shown to have a reduced level of ventricular α-MyHC expression relative to age and sex matched wild type littermates (+/+). This reduction is documented at the level of transcription and translation (Fig. 2b, upper and lower panels respectively). Fig. 2c shows that α-MyHC expression is similarly reduced during embryonic and fetal development. Physiologic analysis *ex vivo* revealed that the +/- hearts are functionally compromised (data not shown). These data suggest a relationship between cardiac function and the level of α-MyHC protein. Reasoning that the MyHC deficit might lead to detectable changes in myofibrillar structure, electron micrographs of longitudinal sections through adult ventricular myocardia were compared. In the +/- mice (Fig. 3b), the average sarcomeric length was 45% as compared to the control (Fig. 3a). The Z-discs are diffuse, often wavy and sometimes broken. Well defined M lines, present in the centers of the wild type sarcomeres, are reduced to faint, diffuse lines in the +/- muscle. Myofilament disarray and numerous gaps are present in the internal architecture of the sarcomeres. These results suggest that serious disruption of the sarcomere due to reduced α-MyHC expression underlies the altered cardiac function in +/- animals.

Homozygosity for the α-MyHC gene ablation causes embryonic lethality around day 12 post coitum (p.c.). Histologic analyses revealed disorganization of developing trabeculae in +/- (Fig. 4b) and -/- (Fig. 4c) hearts at day 11 p.c. SEM analyses indicate gross abnormalities of the ventricular wall and outflow tract in -/- hearts at day 11 p.c. (Fig. 5c). Specifically, cardiac looping is incomplete, the walls of the ventricles and outflow tract are thin and the outflow tract remains undivided. A subset of these defects are detected in +/- hearts (Fig 5b), though these animals survive to adulthood. We conclude that homozygous disruption of the α-MyHC gene results in embryonic lethality, associated with early cardiac defects.

References
1. A. Subramaniam et al., (1991) J. Biol. Chem. **266**: 24613-24620.
2. W. K. Jones et al., (1994) Developmental Dynamics **200**:117-128.
3. This work was funded by NIH grants HL46826, HL41496, HL22619, HL52318 to J. R. and American Heart Association grant SW-95-22-I to W. K. J.
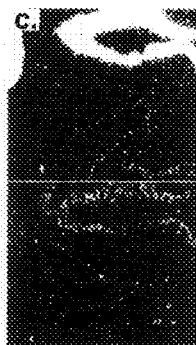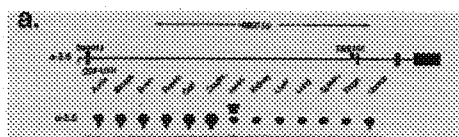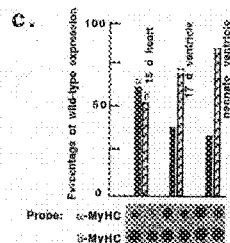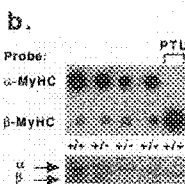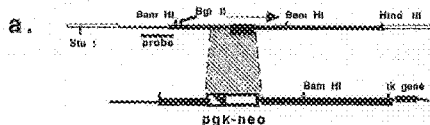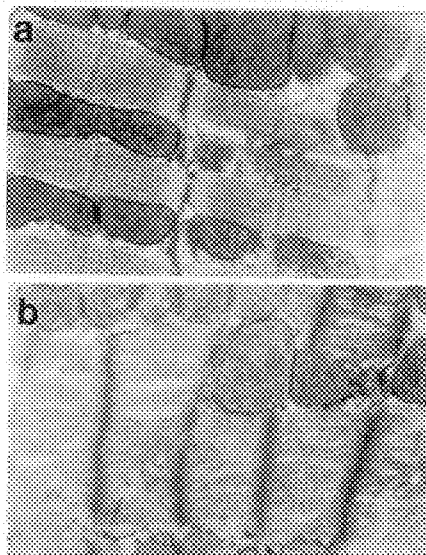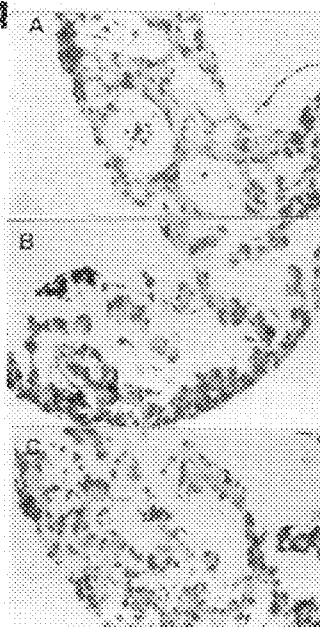
FIG. 1 Expression of an α-MyHC transgene. a CAT assay of transgenic tissues. b *In situ* hybridizations with α-MyHC and CAT riboprobes (upper and lower respectively). c. *In situ* hybridization analysis of lung (α-MyHC probe).
FIG. 2 Targeted disruption-deletion of the α-MyHC gene (a) MyHC gene expression in adult (b) and in embryos (c).
FIG. 3 TEM analysis of heart muscle from +/+ (a) and +/- (b) adult animals.
FIG. 4 Histological Sections of embryonic ventricles. a +/+ ventricle; b +/- ventricle; c -/- ventricle.
FIG. 5 SEM analysis of 11 day p.c. embryonic hearts. a +/+; b +/-; c -/- hearts.

13

QUANTITATIVE MICROSCOPIC COMPARISON OF THE ORGANIZATION OF THE LUNG IN TRANSGENIC MICE EXPRESSING TRANSFORMING GROWTH FACTOR-α (TGF-α)

C. G. Plopper,* C. Helton,* A. J. Weir,* J. A. Whitsett,** and T. R. Korfhagen**

*Department of Anatomy, Physiology & Cell Biology, School of Veterinary Medicine, University of California, Davis, CA 95616
**Division of Neonatology, Children's Hospital Medical Center, Cincinnati, OH 45229

A wide variety of growth factors are thought to be involved in the regulation of pre- and postnatal lung maturation, including factors which bind to the epidermal growth factor receptor. Marked pulmonary fibrosis and enlarged alveolar air spaces have been observed in lungs of transgenic mice expressing human TGF-α under control of the 3.7 KB human SP-C promoter.[1,2] To test whether TGF-α alters lung morphogenesis and cellular differentiation, we examined morphometrically the lungs of adult (6-10 months) mice derived from line 28, which expresses the highest level of human TGF-α transcripts among transgenic lines.[2] Total volume of lungs (LV) fixed by airway infusion at standard pressure was similar in transgenics and aged-matched non-transgenic mice (Fig. 1). Intrapulmonary bronchi and bronchioles made up a smaller percentage of LV in transgenics than in non-transgenics (Fig. 2). Pulmonary arteries and pulmonary veins were a smaller percentage of LV in transgenic mice than in non-transgenics (Fig. 3). Lung parenchyma (lung tissue free of large vessels and conducting airways) occupied a larger percentage of LV in transgenics than in non-transgenics (Fig. 4). The number of generations of branching in conducting airways was significantly reduced in transgenics as compared to non-transgenic mice. Alveolar air space size, as measured by mean linear intercept, was almost twice as large in transgenic mice as in non-transgenics, especially when different zones within the lung were compared (Fig. 5). Alveolar air space occupied a larger percentage of the lung parenchyma in transgenic mice than in non-transgenic mice (Fig. 6). Collagen abundance was estimated in histological sections as picro-Sirius red positive material by previously-published methods.[3] In intrapulmonary conducting airways, collagen was 4.8% of the wall in transgenics and 4.5% of the wall in non-transgenic mice. Since airways represented a smaller percentage of the lung in transgenics, the volume of interstitial collagen associated with airway wall was significantly less. In intrapulmonary blood vessels, collagen was 8.9% of the wall in transgenics and 0.7% of the wall in non-transgenics. Since blood vessels were a smaller percentage of the lungs in transgenics, the volume of collagen associated with the walls of blood vessels was five times greater. In the lung parenchyma, collagen was 51.5% of the tissue volume in transgenics and 21.2% in non-transgenics. Since parenchyma was a larger percentage of lung volume in transgenics, but the parenchymal tissue was a smaller percent of the volume, the volume of collagen associated with parenchymal tissue was only slightly greater. We conclude that overexpression of TGF-α during lung maturation alters many aspects of lung development, including branching morphogenesis of the airways and vessels and alveolarization in the parenchyma. Further, the increases in visible collagen previously associated with pulmonary fibrosis due to the overexpression of TGF-α are a result of actual increases in amounts of collagen and in a redistribution of collagen within compartments which results from morphogenetic changes. These morphogenetic changes vary by lung compartment.

References

1. T.R. Korfhagen, et al., *Proc. Natl. Acad. Sci. USA* (1990) 87:6122.
2. T.R. Korfhagen, et al., *J. Clin. Inbest.* (1994) 93:1691.
3. J. Lakritz, et al., *A. J. Bet. Res.* (1995) 56:11.

1. FIXED LUNG VOLUME
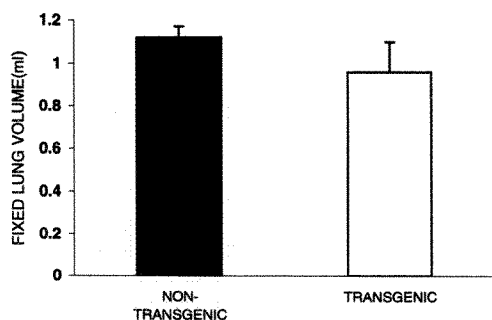
2. PERCENTAGE OF LUNG OCCUPIED BY AIRWAYS
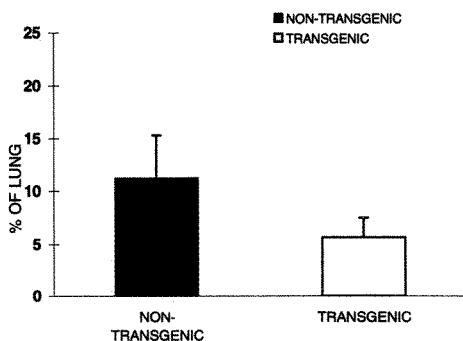
3. PERCENTAGE OF LUNG OCCUPIED BY BLOOD VESSELS

*P<0.05 AS COMPARED TO NON-TRANSGENIC
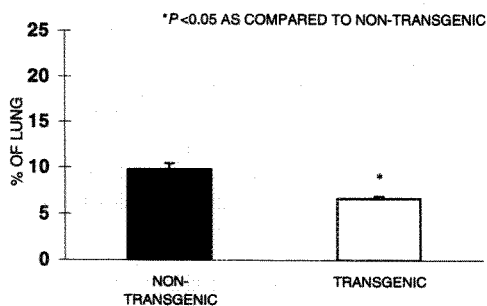
4. PERCENTAGE OF LUNG OCCUPIED BY PARENCHYMA

*P<0.05 AS COMPARED TO NON-TRANSGENIC

5. ALVEOLAR AIRSPACE SIZE

*P<0.05 AS COMPARED TO NON-TRANSGENIC
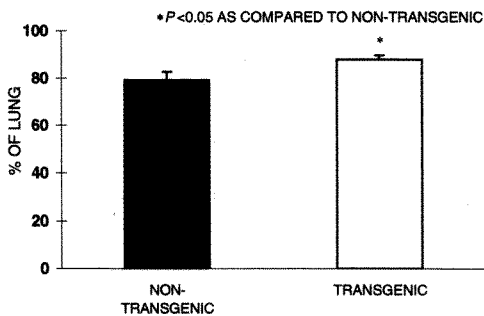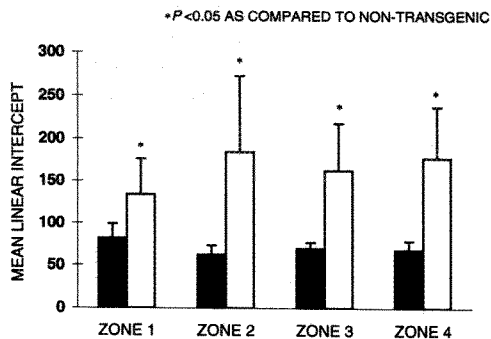
6. ALVEOLAR AIRSPACE AS PERCENTAGE OF LUNG PARENCHYMA

*P<0.05 AS COMPARED TO NON-TRANSGENIC

15
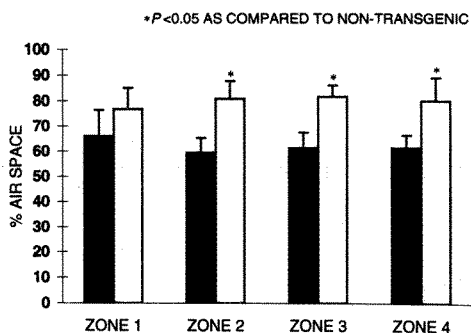
DETECTION OF NUCLEIC ACIDS IN CELLS OR TISSUE SECTIONS USING *IN SITU* POLYMERASE CHAIN REACTION (PCR)

J. R. Hully, K. R. Luehrsen, K. Aoyagi, C. Shoemaker, and R. Abramson

Department of *In Situ* PCR, Applied Biosystem Division, Perkin Elmer, Foster City, CA

The development of PCR technology has greatly accelerated medical research at the genetic and molecular levels. Until recently, the inherent sensitivity of this technique has been limited to isolated preparations of nucleic acids which lack or at best have limited morphological information. With the obvious exception of cell lines, traditional PCR or reverse transcription-PCR (RT-PCR) cannot identify the cellular source of the amplified product. In contrast, *in situ* hybridization (ISH) by definition, defines the anatomical location of a gene and/or it's product. However, this technique lacks the sensitivity of PCR and cannot routinely detect less than 10 to 20 copies per cell. Consequently, the localization of rare transcripts, latent viral infections, foreign or altered genes cannot be identified by this technique. *In situ* PCR or *in situ* RT-PCR is a combination of the two techniques, exploiting the sensitivity of PCR and the anatomical definition provided by ISH[1]. Since it's initial description considerable advances have been made in the application of *in situ* PCR, improvements in protocols, and the development of hardware dedicated to *in situ* PCR using conventional microscope slides[2-5]. Our understanding of the importance of viral latency or viral burden in regards to HIV, HPV, and KSHV infections has benefited from this technique, enabling detection of single viral copies in cells or tissue otherwise thought to be normal. Clearly, this technique will be useful tool in pathobiology especially carcinogenesis, gene therapy and manipulations, the study of rare gene transcripts, and forensics[6].

The protocol can be divided into three stages, the initial preparation of the tissue or cells, followed by thermal cycling and finally detection of the amplicon by conventional ISH or, if it has been labeled during PCR, by immunocytochemistry. Tissue preparation is the most critical step for optimal *in situ* PCR and consists of fixation, embedding & cutting, mounting and permeablization. Fortunately, most of the well known cross-linking or denaturing fixatives are applicable for *in situ* PCR. Reproducible results have been reported using formalin or paraformaldehyde as long as the pH is neutral. Alcohol-based fixatives are superior for nucleic acid integrity but morphological preservation is not as good as the cross-linking fixatives. Unfortunately, many investigators are using archival tissue where fixation may be unknown or sub-optimal. In addition, the deleterious effect of time, often measured in years, on the integrity of the nucleic acids within these tissue is poorly understood.

As with any protocols involving PCR, contamination needs to be avoided during embedding and cutting. Similarly, RNase activity must be minimized if performing *in situ* RT-PCR. Attachment of the sections or cells to the slide is of vital importance as they must withstand the subsequent proteolytic digestion and

thermal cycling. The permeablization is designed to expose enough of the target sequence for the primers and DNA polymerase but not enough that the target is lost during the reaction or subsequent PCR. Furthermore, retention of the amplicon is highly desirable to avoid potential diffusion to neighboring cells. Most permeablization protocols involve limited digestion using proteases such as proteinase K or pepsin but good results have been achieved using mild hydrolysis or microwaves. As yet there is no universal protocol which is applicable to all tissues. Generally, each cell type and the fixation conditions determine the degree of permeablization. This needs to be determined empirically. The thermal cycling itself will permeablize tissues and therefore a consideration when optimizing the protocol. The reaction conditions for thermal cycling are similar to those used for solution PCR except many groups report that higher concentrations of Mg^{2+} and AmpliTaq DNA polymerase give better results. These components are thought to be sequestered by the silane coating on the slide and/or the tissue itself. Most of the reaction parameters can be determined by solution PCR using DNA or RNA from the tissue in question. Optimal T_Ms for the primers, however, are generally a few degree higher than those found by solution PCR. For *in situ* RT-PCR various combinations of viral reverse transcriptase and DNA polymerases have been used successfully but the one buffer/one enzyme system using rTth DNA polymerase and manganese ions is the best system. This protocol avoids the need for the standard two step RT-PCR but more importantly, the reverse transcription is performed at higher temperatures, usually at the optimal T_m for the downstream primer, thereby reducing any secondary structure of the target mRNA or non-specific cDNAs.

Sufficient amplification of the target, usually achieved after 25 to 30 cycles, should be readily detected by conventional ISH using a non-isotopic probe. An alternative is the label the amplicon during PCR, for example by including digoxigenin-dUTP in the reaction, such that the amplicon can be detected by routine immunocytochemistry. Although such an approach, known as direct *in situ* PCR, eliminates the need for ISH it is very sensitive to primer-independent DNA synthesis and mispriming leading to non-specific labeled products. Such false positives are avoided by using conventional ISH.

As with any emerging technique there is a need for absolute controls to guard against false positives and false negatives as well as the interpretations of the results. This talk will review the current protocols paying special attention to the key steps of fixation, permeablization, thermal cycling, and review the obligatory controls. Examples of *in situ* PCR, *in situ* RT-PCR will be shown for various tissues or cells.

1. A.T. Haase, A. T. et al., Proc. Natl. Acad. Sci. USA 87(1990)4971.
2. O. Bagasra et al., Cell Vision 1(1994)324.
3. J. Gu, J. Cell Vision 1(1994)8.
4. P. Komminoth et al., Verh. Dtsch. Ges. Path. 78(1994)146.
5. K.R. Luehrsen et al., Cell Vision 2 (1995)348.
6. J.J. O'Leary et al., J. Pathol. 178(1996)11.

ANALYSIS OF MYOFIBRILLAR ORGANIZATION AND DEGENERATION BY FLUORESCENCE CONFOCAL MICROSCOPY

Mark A. Sussman

Division of Molecular Cardiovascular Biology, The Children's Hospital Research Foundation, 3333 Burnet Avenue, Cincinnati, OH 45229-3039

Myofibrillar degeneration is an important pathological process in progressive cardiomyopathy leading to heart failure. Loss of myofibrils *in vivo* has been observed in both adaptive cardiac responses (i.e. hypertrophy) as well as in chemotherapeutic use of antitumor drugs with cardiotoxic side effects (i.e. doxorubicin). The molecular mechanism(s) of myofibrillar degeneration are poorly understood in comparison with the sequence of events involved in myofibrillar assembly and organization. Maintenance of myofibril integrity is dependent upon a variety of factors, including contractile protein stoichiometry and protein kinase activity.

The repeating sarcomeric architecture of myofibrils is well suited to structural analysis, since disruption of normal organization is easily visualized by fluorescence microscopy. Many antibodies are available for use in observation of myofibril structure (see Table at right). Confocal microscopy provides advantages in studies of myofilament organization by allowing for direct and accurate measurement of distances to within 0.2 μm and the ability to perform vertical sectioning through individual cells. This vertical (Z-axis) sectioning can be used to select the focal plane within the cell for observation, resulting in higher resolution images by reducing fluorescent signals from above and below the plane. Image analysis software enables the user to create projections of optically sectioned cardiomyocytes which can be rotated to reveal interior structural relationships previously unobserved with single sections or conventional epifluorescence microscopy. Examples of image analysis will highlight useful features such as distance measurement, periodicity, pixel intensity, colocalization of dual labels, and three dimensional reconstruction.

protein	labeled structure	antibody/source
sarcomeric markers		
actin	thin filaments	C4, HUC 1-1: Dr. Jim Lessard 5C5: Sigma # A2172 phalloidin: Sigma # P 1951
tropomyosin	thin filaments	CH1: Sigma # T9283
troponin T	thin filaments	JLT-12: Sigma # T6277
tropomodulin	thin filament ends	rabbit polyclonal - personal stock
α-actinin	Z-discs	EA-53: Sigma # A7811
myosin	thick filaments	RBT 76250: Accurate Antibodies
titin	epitope overlies Z-disc	T11: Sigma # T9030
cytoskeletal markers		
tubulin	microtubules	TUB 2.1: Sigma # T4026
vinculin	costameres	VIN-11-5: Sigma # V4505
desmin	overlies Z-discs	DE-U-10: Sigma # D1033
cytosolic markers		
DNase I	G actin pool	Molecular Probes # D 970
calmodulin	Ca++ pool	mixture: Sigma # C 7055

Studies using these techniques are underway to characterize the process of myofibril degeneration in isolated neonatal rat cardiomyocytes, which provide an excellent model system for studies of myofibril organization. Culture conditions can be manipulated to affect myofibril organization ands effects can be assessed on a single cell level. This flexibility allows for experimental designs which are not possible in an *in vivo* context. Transgenic animals with altered myocardial contractile protein expression are also being studied in order to understand how the functioning heart responds to and compensates for loss of function resulting from myofibril degeneration.
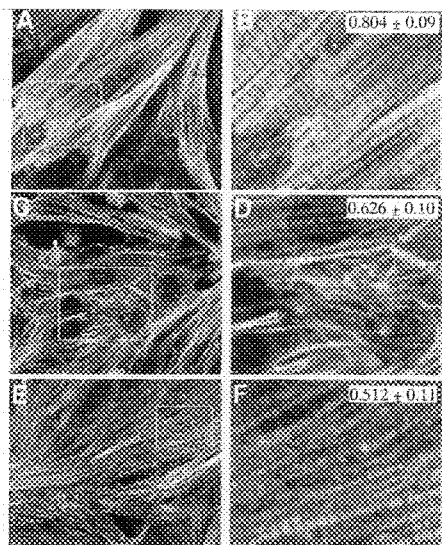
Figure 1
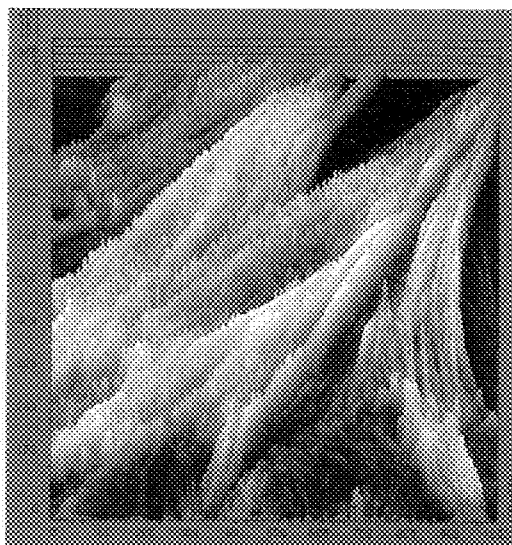
Figure 2
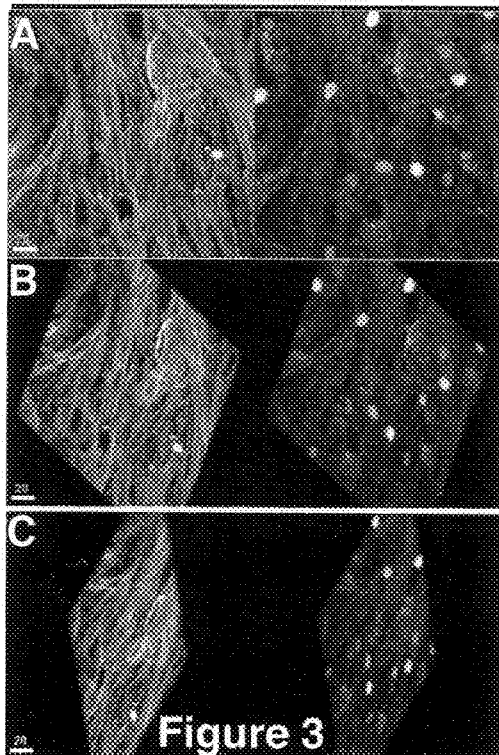
Figure 3
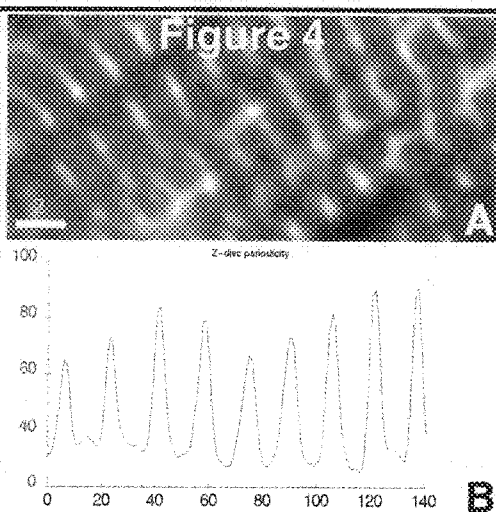
Figure 4

Figure 1. Measurement of actin filament length in normal (A,B) and degenerating myofibrils (C-F).

Figure 2. Fish net plot to show pixel intensity analysis of cardiomyocytes shown in Fig. 1A.

Figure 3. Projection rotations of cardiomyocytes with labeled actin filaments (left) and nuclei (right).

Figure 4. Fluorescent labeling of Z-discs in cardiac myofibrils (A) with corresponding plot of distance vs. pixel intensity (B).

19

MAGNETIC RESONANCE ANALYSIS OF MOUSE EMBRYOS WITH ALTERED GENE EXPRESSION

B.R. Smith

Department of Radiology, Duke University Medical Center, Durham, NC 27710

Techniques to assess and analyze phenotypes of experimentally altered animals have not kept pace with our ability to manipulate the genome. Assessment of the shape, position, and timing of the appearance of anatomical structures is indispensable to identifying and understanding the mechanisms of normal and abnormal morphogenesis. Tools are needed to effectively diagnose the condition of the hundreds of experimentally altered animals being produced.

Magnetic resonance (MR) microscopy is a non-destructive technique capable of generating three-dimensional images of developing structures from whole embryos. It facilitates the evaluation of complex anatomical structures by allowing them to be studied in any plane of sectioning for cut-away views and from any angle for surface views.

MR microscopy has been used to assess the following mutant mouse embryos and mouse embryos with altered gene expression: Splotch [1,2], Curly-tail [1], Loop-tail [1], TS 16 [3], HOX 2.2 transgenic [4], MARKS knockout [5], LH-2 knockout [6], and Dlx-2 knockout [7]. Imaging was performed on a modified 9.4 Tesla GE NMR Instruments Omega system with echo times of 6 ms and repetition times of 200 ms [8]. Three-dimensional spin warp encoding was performed on isotropic 256^3 data arrays (256 image slices with 256 by 256 pixels in each slice) yielding voxel resolutions ranging from 23 microns in each axis for the smallest embryos to 130 microns for the larger fetuses and neonates. Data were volume rendered on Silicon Graphics workstations using Vital Image's VoxelView_ULTRA 2.0 software. Image data representing every slice in each of the three orthogonal sectioning planes were converted to Quicktime movies and recorded on compact disc (CD) for distribution to the collaborating researchers. These image data were then accessible on standard desktop computers.

MR microscopy succeeded in generating three-dimensional image data free of the sectioning and registration artifacts often associated with reconstructions based on optical microscopy. The following anatomical structures were visualized based on contrast properties inherent to the tissues being studied: skeletal elements and their cartilaginous anlaga, active growth plates along the developing long bones, lung, kidney, thyroid, the cranial and spinal neural tube, individual dorsal root ganglia, stomach, intestine, retina, esophagus, and skeletal muscle.

1. Elwood Linney, Duke University, Durham, NC
2. Eric Effmann, Children's Hospital, Seattle WA
3. Roger Reeves, Johns Hopkins Medical School, Baltimore, MD
4. Michael Underhill and David Cash, Duke University, Durham, NC
5. Perry Blackshear, Duke University, Durham, NC
6. Forbes D. Porter, NICHD, NIH, Bethesda, MD
7. Roger Pederesen and John Rubenstein, University of California, San Francisco, CA
8. BR Smith et al., Proc. Natl. Acad. Sci., USA, 91:3530-3533, 1994.

Figure 1
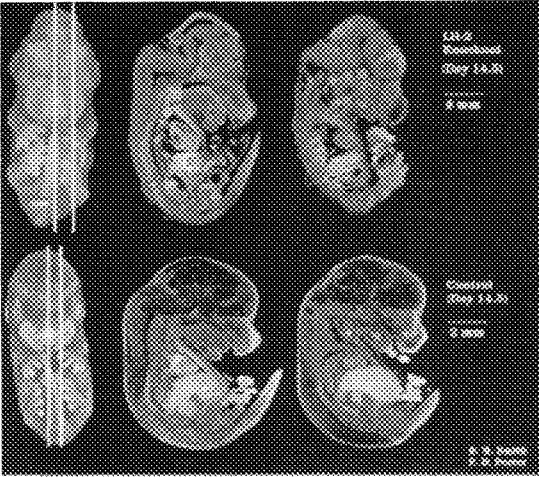
Figure 2
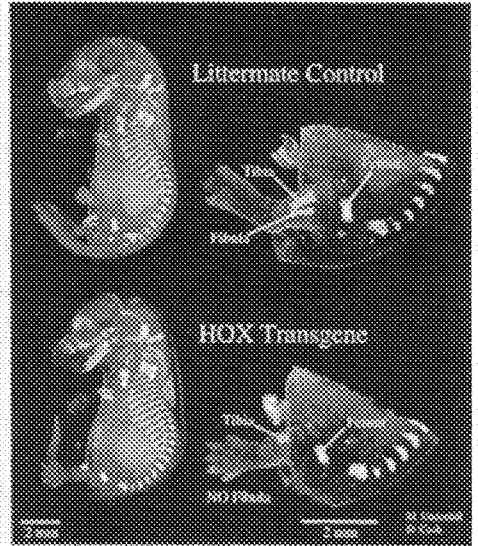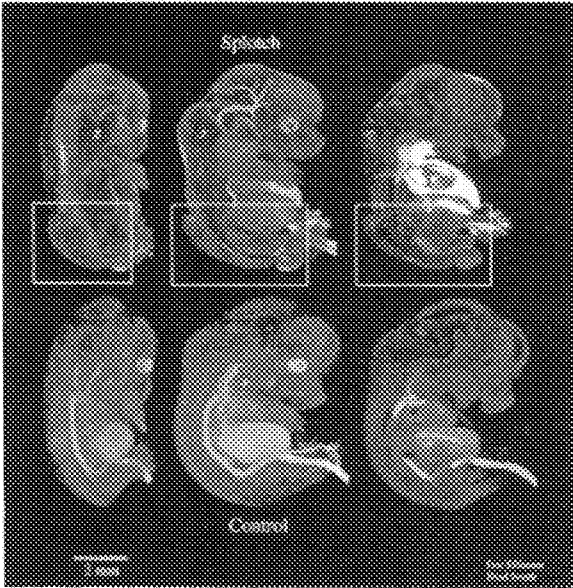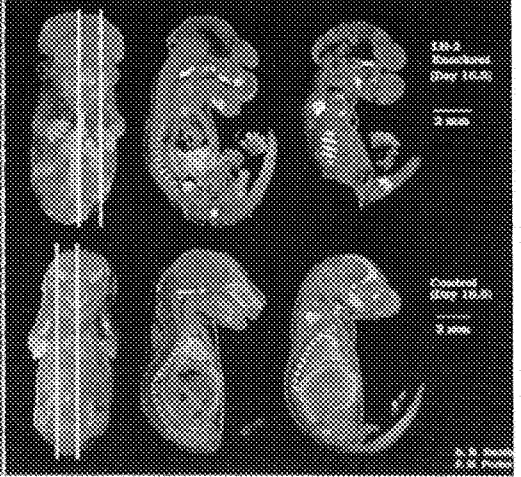
Figure 3

Figure 4

Three-dimensional magnetic resonance microscopy of the following genetically altered animals:

Fig. 1 Embryonic day 14.5 LH-2 knockout (homologous recombination) and control mouse embryos.
Fig. 2 Embryonic day 16.5 LH-2 knockout (homologous recombination) and control mouse embryos.
Fig. 3 Embryonic day 12.5 Splotch mutant and control mouse embryo with vasculature staining.
Fig. 4 Embryonic day 16.5 HOX 2.2 transgenic embryo and control.

21

ANALYSIS OF GENE EXPRESSION DIRECTED BY A THYMIC LOCUS CONTROL IN TRANSGENIC MICE: MECHANISMS AND APPLICATION TO VECTORS FOR GENE THERAPY

BJ Aronow, CA Ley, KC Ess, and DP Witte

Division of Developmental Biology, Children's Hospital Medical Center, University of Cincinnati, Cincinnati, OH 45229

The formation of peripheral T cells from thymocyte progenitors is an intricate developmental process that requires the organized and coordinate expression of multiple genes. Adenosine deaminase (ADA) is an example of a gene that is subject to strong developmental regulation in T-cell precursors and is essential for the subsequent formation of T-cells in humans. We have sought to understand the mechanisms of ADA gene regulation from a basic point of view as well as to employ this to potential vectors for gene therapy.

Using transgenic mice have shown that the first intron of the ADA gene contains a powerful locus control region that directs high level gene expression within cortical thymocytes. Based on extensive mutational analysis of the regulatory region and analyses of gene expression that include quantitative gene expression, in situ hybridization, and biochemical characterizations of chromatin structure, we have demonstrated that the intronic locus control region (LCR) consists of a hierarchically structured 2300 base pairs of DNA sequence (Figure 1). The LCR is composed of a series of regulatory elements that include a centrally positioned 300 base pair classical enhancer domain within which there is a critical 30 base pair enhancer core. Within this core, there is a single binding site for the transcription factor c-Myb that is required for activity of the enhancer core, the enhancer, and the intact LCR. Beyond the 300 bp enhancer core on either side the LCR contains novel and puzzling 1 kb non-enhancer sequences that we have termed facilitators. These sequences enable gene copy proportional expression by facilitating the ability of the enhancer to function in chromatin. The effects of the facilitators are evidenced by their ability to allow for insertion-site-independent and gene-copy-proportional expression and they prevent variegated expression among similarly differentiated cell types (Figure 2). Thus, total gene expression does not indicate proper cell type specific expression. The facilitators also allow for the formation of a strong tissue and cell type specific DNAse I hypersensitive site at the enhancer. This suggests that the formation of a discrete organized chromatin structure as a function of developmental differentiation requires extensive DNA sequences, only some of which are of the enhancer type. The capabilities of the facilitators to activate a chromatin domain may also suggest their potential usefulness in vectors for gene therapy of both ADA deficiency and possibly other human genetic diseases. However, the distance and non-enhancer nature of the facilitators suggest that they may act differently than conventional regulatory elements. In support of this, the facilitators obey a strict position and orientation rules with respect to the enhancer.

To gather clues to the mechanism by which the locus control region functions we have searched for regulatory factors that act on the LCR. We have recently shown that the single site for c-Myb plays a critical role in the function of the entire LCR and that c-Myb is expressed at very high levels by developing T-cells. High power immunofluorescent localization of c-Myb in T-cell nuclei indicates that the protein is highly localized to discrete intranuclear microbodies (Figure 3). This is consistent with the requirement for ordered structure in the LCR. We hypothesize that c-Myb in close association with other transcription factors together mediate a program of gene expression that is likely critical for the production of mature T cells from thymocyte progenitors.

To test the ability of the facilitated ADA regulatory domain to function in gene therapy vectors we constructed retroviruses that contain human ADA minigenes with both facilitator and enhancer segments in a minimal retroviral backbone that consists of LTR, psi, and cloning vector sequences. Of a series of constructs generated, two were capable of retroviral transmission and produced abundant human ADA in transduced T-cells. However, only one form of the minigene seemed to allow the function of the LCR in transgenic mice. This suggests that additional rules for LCR function need to be determined and that complex regulatory behavior may only be ascertained by using detailed transgenic analyses.

Figure 1

I II III IV V VI

ADA GENE

0 1 5
kb

1 2 3 4 6 7 10 12

HS II HS III

Alu.1
SphI NF-kB Pu-rich EcoRI µE5 ETS PflMI Dra III rpt. X 21 T's SphI
AP-1 LEF-1 AP-1 TCF-1 Tth 111
c-Myb MAZ
Alu.2 Alu.3

5' facilitator segment   enhancer domain   3' facilitator segment
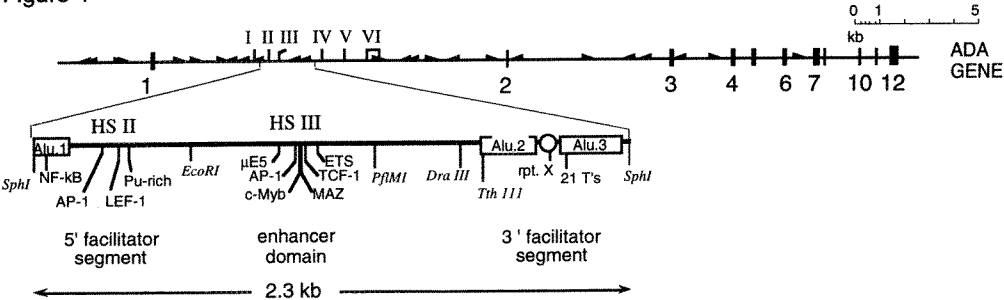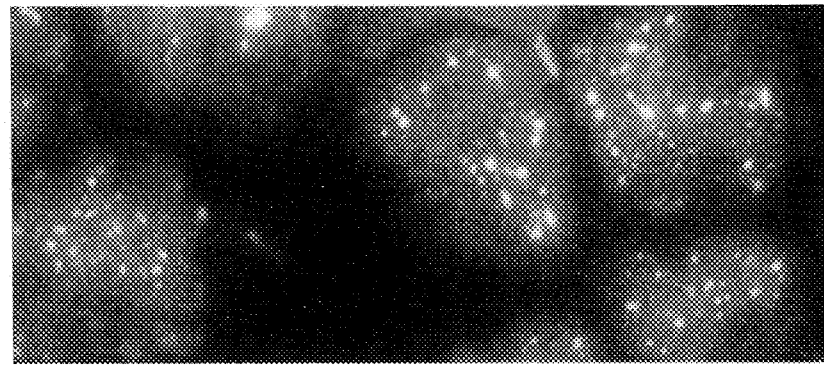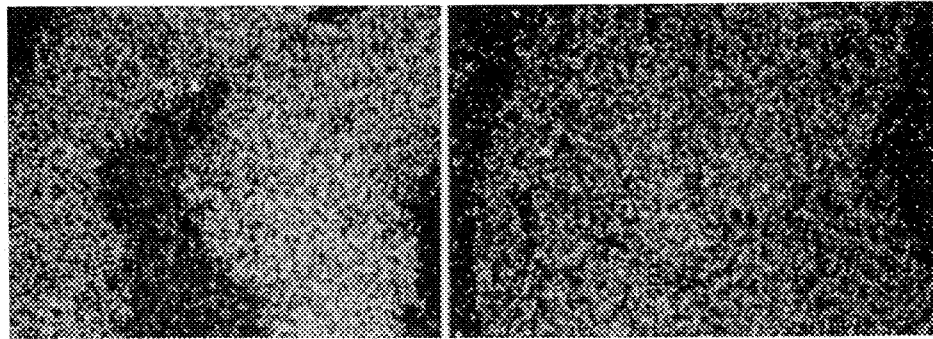
2.3 kb

Figure 2

Figure 3

Figure 1. The structure of the human ADA gene and its 2.3kb thymic locus control region.

Figure 2. Appropriate and inappropriate expression of CAT reporter gene: transgenic mouse thymus with intact versus facilitator-mutated LCR. In situ hybridization, 100x. Note the uniformity versus variegated expression of mRNA (white signal from dark field silver grains) over the cortical thymocyte region.

Figure 3. Immunofluorescent localization of c-Myb protein in the nucleus of thymocytic T-cells, 1000x. White dots represent IF, nucleus is counter-stained with propidium iodide.

FLUORESCENT MOLECULES AS DIRECT AND INDIRECT LABELS FOR *IN SITU* HYBRIDIZATION

Ian Durrant

Life Sciences Research and Development, Amersham International, White Lion Road, Amersham, Buckinghamshire, HP7 9LL, UK

In situ hybridization has traditionally been performed with radioactive probes. Over recent years effort has been spent in elucidating non-radioactive alternatives for a variety of molecular biology systems. Non-radioactive *in situ* hybridization is possible, but to date the systems available have, in general, delivered lower sensitivity and higher backgrounds than traditional methods. We have studied a variety of alternative labelling and detection processes; different systems may be required for different applications.

Fluorescein has been developed as a new label for all aspects of non-radioactive *in situ* hybridization. Separate systems have been investigated for DNA, RNA and oligonucleotide probes (see Figure 1). These probes can be applied to frozen sections, paraffin sections, whole mounts, cells and chromosomes. The standard non-radioactive detection system utilizes alkaline phosphatase as an end point to produce a coloured reaction product precipitated at the point of hybridization. This gives both good resolution and sensitivity. Other options becoming available, based on different enzymes and other formats of detection, include peroxidase and gold in conjunction with colour, chemiluminescence and direct and indirect fluorescence. These alternatives have been investigated using the fluorescein based probe labelling systems.

Fluorescence based detection systems are gaining in popularity in many areas of biological research. As a detection system fluors offer a number of advantages, in particular the high sensitivity, the speed of detection and the multiple target detection capability using the range of colours available.

A number of fluorescent dyes have become established in biological detection applications; notably fluorescein and rhodamine derivatives. These dyes were initially used as labels of antibodies and have been widely used in the fields of immunochemistry and flow cytometry. Subsequently, we utilised suitable derivatives of these dyes to attach directly to nucleotides so that fluorescent nucleic acid probes can be synthesised. This eased the ability to perform multiple hybridizations on the same slide and has enabled initial investigations into quantification of results to be performed in an analogous manner to experiments performed on immunochemistry samples.

New dyes are now becoming available that can also be attached to antibodies and to nucleotides. These dyes, notably the cyanine based compounds, have the advantage of being available with narrow excitation and emission spectra and are significantly more photo stable than those currently in use. The cyanine based dyes (CyDyes™) can be individually modified so that they fluoresce at distinct points across, and beyond, the visible range in a set of 5-6 dyes (see Table 1).

These dyes have been used successfully in the above applications. This work, like that with the traditional dyes, began with immunochemistry and flow cytometry systems where the new dyes are already well established. The use of the CyDyes has been extended into fluorescent *in situ* hybridisation applications and have been used to label probes for chromosome copy number and for chromosome painting. Recently the use of these new dyes, and the traditional dyes, has been investigated in other molecular biology systems, notably mRNA detection, detection of apoptosis *in situ* and for direct detection of nucleic acid on blots and in gels. As the optics and image analysis systems progress these dyes will become increasingly useful in a wide range of biological techniques.

Probe type

DNA	RNA	Oligonucleotide
Random prime labelling (High probe yield and no purification needed)	Transcription labelling (Compatible with SP6, T7 and T3 polymerases)	3' end labelling (Short tail length and no purification needed)

Hybridization
Hybridization buffer
formulated to give high
signal-to-noise

Detection

Light	Colour	Gold
Specialist technique with high sensitivity	Routinely used technique with good resolution and sensitivity	Specialist technique with high resolution

Figure 1: Features of optimized non-radioactive *in situ* hybridization systems for mRNA analysis

Table 1: Features of novel fluorescent Cy Dye compounds compared to fluorescein

Dye	Colour	Absorbance max (nm)	Emission max (nm)
Cy2	Green	489	506
Cy3	Orange	550	570
Cy3.5	Scarlet	581	596
Cy5	Far Red	649	670
Cy5.5	Near infra red	675	694
Cy7	Near infra red	743	767
Fluorescein	Green	494	520

MH27 BINDS TO SEVERAL TYPES OF EPITHELIAL JUNCTIONS BY EM-IMMUNCYTOCHEMISTRY IN THE NEMATODE *C. ELEGANS*

David H. Hall

Department of Neuroscience, Albert Einstein College of Medicine, Bronx, NY 10461

The monoclonal antibody MH27 was used to test a post-embedding method for EM immunocytochemistry in the nematode *C. elegans*. Primary antibody localization was performed on LR Gold thin sections of lightly fixed *him-5* adult animals, followed by a gold-linked anti-mouse IgG secondary antibody (AuroProbe, Amersham Life Science) and viewed on a Philips CM10 electron microscope. Methods for fixation, embedding, sectioning and antibody procedures followed those of Selkirk et al. (1990) and Hall (1995). Relatively few examples of immunolabelling have been previously demonstrated in *C. elegans* at the EM level. We have previously found that LR White embedment was unsuitable, as it causes severe shrinkage in nematode tissues. Selkirk and coworkers showed that LR Gold was preferable for EM-immunocytochemistry, and used it to localize several surface antigens. Okamoto and Thomson (1985) previously demonstrated successful results with post-embedding labeling of Epon embedded material, but we anticipate that many antigens will not be well exposed in an Epon thin section.

MH27 was generated during a search for specific antibodies to muscle proteins (Francis and Waterston, 1985). The antibody is now widely used for immunofluorescence studies to demarcate the boundaries of the hypodermal cells, and has proven useful to follow cellular development during embryogenesis and larval stages in *C. elegans* and other nematode species (Fitch and Emmons, 1995). We were interested to learn the ultrastructural localization of the MH27 antibody, as well as to further develop this technique for *C. elegans* tissues. We used the *him-5* strain so that both male and hermaphrodite animals could be sampled.

We obtained strong labelling of several types of cell junctions with low background using 1/4500 dilutions of the ascites fluid, at room temperature for 150 min, followed by a 1/20 dilution of the gold-linked secondary antibody. Fixation for 60 minutes on ice in either 2% glutaraldehyde or in 2% paraformaldehyde, 0.1% glutaraldehyde, gave satisfactory results. No labelling of muscle cells has been noted in thin sections.

Adherens junctions were intensely labelled in several tissues, including intestine, seam cells and hypodermis. In the intestine, a continuous narrow band of apical adherens junctions link adjacent pairs of intestinal cells. In seam cells and hypodermis, apical junctions again link adjacent cells as a continuous narrow band along the body wall, but immunolabelling is less intense than in intestinal cells. Because these tissues are present ubiquitously along the length of the animal, such junctions are easily scored in almost any thin section. By immunofluorescence, similar MH27 labelling has been found between structural cells of several sensory structures in the nose (amphid), tail (phasmid) and adult male tail (rays). All of these sites show prominent adherens junctions in serial thin sections, but are less easy to find for EM-immunocytochemistry. Gap junctions are known to lie very near to the apical adherens junctions in both intestine and hypodermis, but were not labelled by MH27.

A novel type of intercellular junction was heavily labelled between epithelial cells in the spermatheca. Septate junctions immediately adjacent in the same membranes showed no labelling. The labelled junctions show extensive sinuous zones of parallel contact, and appear rather tightly apposed. In thin sections of well-fixed tissue, these regions show no cytoplasmic densities characteristic of adherens junctions, and the "gap" between apposed membranes is much wider than in tight junctions or gap junctions. The intercellular cleft is slightly electron-dense but shows no obvious septation. These junctions are somewhat similar to the "septate-like junctions" which have previously been described between neurons in the mollusc *Navanax* (Hall, Spray and Bennett, 1983), but the spermathecal junctions are much more extensive.

The high antigenicity and ubiquitous nature of adherens junctions in intestine and hypodermis along the length of the nematode make the MH27 antibody particularly useful when testing EM immunochemical procedures in *C. elegans*. The growing body of cellular detail regarding the development of *C. elegans* and the many specific antibodies to nematode proteins now available will make this technique valuable for exploring gene expression in both wild type and mutant strains of this model organism.

References

1. M.E. Selkirk et al., *Molecular & Biochemical Parasitology*, 42 (1990)31.
2. D.H. Hall, in *Caenorhabditis elegans: Modern Biological Analysis of an Organism*, H.F. Epstein and D.C. Shakes (eds.), Academic Press, (1995)396.
4. H. Okamoto and J.N. Thomson, *Journal of Neuroscience*, 5, (1985)643.
5. G.R. Francis and R.H. Waterston, *Journal of Cell Biology*, 101, (1985)1532.
6. D. Fitch and S. Emmons, *Developmental Biology*, 170 (1995)564.
7. D.H. Hall et al., *Neurocytology*, 12, (1983)831.
8. MH27 mouse ascites fluid was generously provided by Jim Waddle and Ross Francis (Washington University, St. Louis).

FLUORESCENCE, CONFOCAL, AND INTERMEDIATE VOLTAGE ELECTRON MICROSCOPY OF CENTRACTIN LOCALIZATION IN TRANSFECTED PtK2 CELLS

Elizabeth A. Holleran,* Gladys Gray-Board,*** Erika L.F. Holzbaur,** and Lee D. Peachey***

*Cell & Molec. Biology Graduate Group, School of Medicine, **Dept. of Animal Biol., School of Veterinary Medicine, and ***Dept. of Biology, School of Arts & Sciences, University of Pennsylvania, Philadelphia, PA 19104-6018

Centractin (Arp 1) is an actin-related protein that shares 53% sequence identity with conventional actin and is predicted to have a similar core structure for nucleotide binding[1]. Biochemical studies of centractin, named for its apparent localization to the centrosome[2], reveal that it is a member of a stable macromolecular complex, dynactin[3]. The dynactin complex consists of at least 9 polypeptides[4,5,6] and has been implicated in activating dynein mediated vesicle transport along microtubules[4]. Ultra-structural analysis, by rotary shadowing electron microscopy with antibody decoration, reveals that within the context of the dynactin complex, centractin forms a 37 nm filament resembling the structure of an actin filament with capping protein and p62 localizing to opposite ends[6].

We have used transient transfection assays to investigate the effects of overexpression of centractin in cells. Mammalian PtK2 cells were transiently transfected with centractin cloned in the pcDNA3 vector under the control of a CMV promoter. The cells were transfected for 24 hours using Ca^{2+}/DNA co-precipitates. The transfection efficiency was as high as 41% as determined by direct counting of immunostained cells. Cells were fixed at time points ranging from 18 to 24 hours post washing using 1% formaldehyde plus 1% Triton X-100 (5 min), 0.05% glutaraldehyde (5 min), 1% formaldehyde (5 min), and 0.05% sodium borohydride to block free aldehyde groups (3x5 min). Immunofluorescence employed an affinity-purified, rabbit polyclonal antibody to centractin followed by a Texas Red-labeled secondary antibody. Epifluorescence microscopy revealed that all of the cells overexpressing centractin contained centractin structures with novel morphology. Two distinct patterns were observed consistently: filamentous centractin localized throughout the cytoplasm (Figure 1a) and perinuclear centractin accumulations (Figure 1b). The perinuclear accumulations appear to be highly three dimensional and curved in structure (confirmed by confocal microscopy), and often have associated filamentous structures (Figure 1b). The addition of 33 micromolar nocodozole (30 min. at 4°C) to the transfected cells results in thinner centractin filaments (Figure 1c).

To determine in greater detail the structure of these novel centractin accumulations, cells were plated and transfected on gold EM finder grids on coverglasses coated with a formvar film. Following immunostaining as described above, these grids were examined using a Leica TCS confocal laser scanning microscope (Figure 2a). Subsequently the grids were further fixed with 1% glutaraldehyde (10 min), postfixed in 1% osmium tetroxide (10 min), stained in 1% uranyl acetate (10 min), removed from the coverglasses, and critical point dried.[7] The grids then were examined in the intermediate voltage electron microscope (IVEM) at 400 kV, and the same cells were located with the aid of the finder marks on the grids. The perinuclear structures that immunostained for centractin in the confocal images could easily be identified in the same cells in the IVEM. Their morphology was consistent in shape and localization of the Golgi apparatus. Further work, in progress, will focus on exploring the exact nature of these structures.

References

1. Kabsch and Holmes, (1995) FASEB 9, 167-174
2. S.W. Clark and D.I. Meyer, Nature 359 (1992) 246-250
3. J.P. Lees-Miller et al., Nature 359 (1992) 244-246
4. Gill et al., J. Cell Biol. 115 (1991) 1639-1650
5. Paschal et al., J. Biol. Chem. 268 (1993) 15318-15323
6. Schafer et al., J. Cell Biol. 126 (1994) 402-412
7. H. Ishikawa et al., Proc. 12th Int. Congr. Electron Micros. (1990) 178-179
8. This work was supported by Grants GM48661 and RR02483 from the National Institutes of Health, U.S.A.
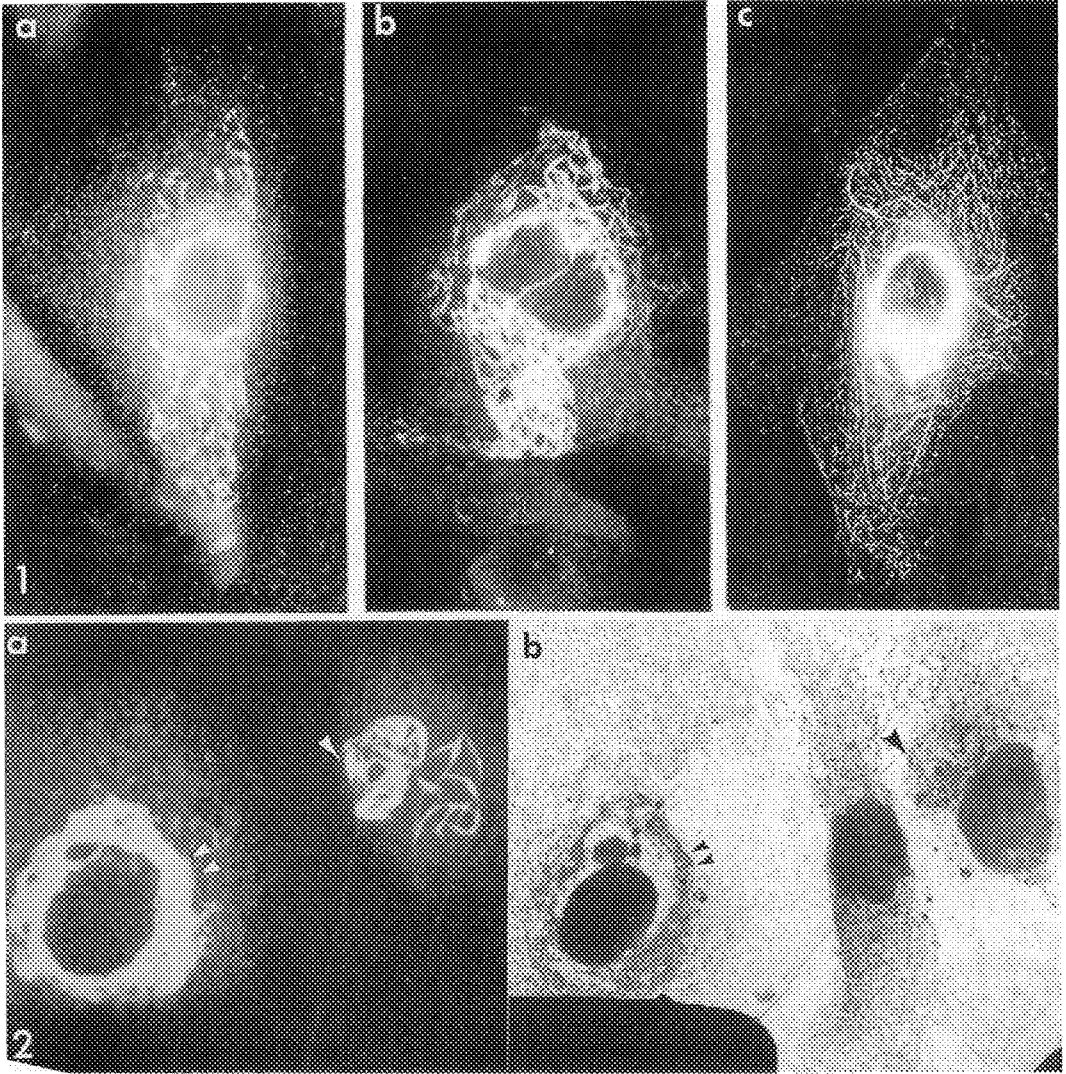
FIG. 1-Epifluorescence micrographs of transfected cells; a) a cell showing centractin staining distributed as short, filamentous structures throughout cytoplasm; b) a cell showing mainly perinuclear accumulation of centractin; c) a cell treated with nocodozole, with finer centractin filaments in the cytoplasm. x3000.

FIG. 2-a) Confocal fluorescence image (in-focus projection of 15 z-slices at 0.2 micrometers spacing) of two transfected cells showing predominantly perinuclear localization of centractin. The cell on the right shows filamentous centractin structures overlying and adjacent (arrow) to the nucleus. x1800; b) intermediate voltage electron micrograph of the same field. Three cells are seen, but only the outer two cells correspond to the transfected cells seen in the confocal image. The arrow indicates the region of centractin accumulation adjacent to the nucleus in the cell on the right. The double arrow points to the perinuclear staining region in the other cell. These regions show a structural pattern consistent with the structure and location of the Golgi apparatus. x2000.

29

AN ULTRASTRUCTURAL COMPARISON OF HEPATOCYTES FROM ADH⁺ AND ADH⁻ PEROMYSCUS MANICULATUS

J. T. Ellzey,* D. Borunda** and B. P. Stewart*

*Department of Biological Sciences, University of Texas at El Paso, El Paso, TX 79968-0519
**Department of Fishery and Wildlife Sciences, Box 30003, Dept. 4901, New Mexico State University, Las Cruces, NM 88003

Genetically alcohol deficient deer mice (ADH^N/ADH^N) (obtained from the Peromyscus Genetic Stock Center, Univ. of South Carolina) lack hepatic cytosolic alcohol dehydrogenase. In order to determine if these deer mice would provide a model system for an ultrastructural study of the effects of ethanol on hepatocyte organelles, 75 micrographs of ADH^+ adult male deer mice (n=5) were compared with 75 micrographs of ADH^- adult male deer mice (n=5). A morphometric analysis of mitochondrial and peroxisomal parameters was undertaken.

The livers were perfused with 0.1M HEPES buffer followed by 0.25% glutaraldehyde and 2% sucrose in 0.1M HEPES buffer (4C), removed, weighed and fixed by immersion in 2.5% glutaraldehyde in 0.1M HEPES buffer, pH 7.4, followed by a 3,3'diaminobenzidine (DAB) incubation,[1] postfixation with 2% OsO_4 , *en bloc* staining with 1% uranyl acetate in 0.025M maleate-NaOH buffer, dehydrated, embedded in Poly/Bed 812-BDMA epon resin, sectioned and poststained with uranyl acetate and lead citrate. Photographs were taken on a Zeiss EM-10 transmission electron microscope, scanned with a Howtek personal color scanner, analyzed with OPTIMAS 4.02 software on a Gateway2000 4DX2-66V personal computer and stored in Excel 4.0.

The ultrastructure of the ADH^+ hepatocytes (Fig. 1) was compared with the ultrastructure of the ADH^- hepatocytes (Fig. 2). A Student t-test showed no significant differences between the volume density or surface density of peroxisomes or mitochondria from ADH^+ and ADH^- deer mice hepatocytes. The mean volume density (V_V) of peroxisomes from ADH^+ mice was 2.18% (S.D.=0.005) and 2.31% (S.D.=0.005) for the ADH^- mice. The surface density of peroxisomes from ADH^+ deer mice hepatocytes was 0.33 $\mu m^2/\mu m^3$ (S.D.=0.084) and 0.33 $\mu m^2/\mu m^3$ (S.D.=0.079) from ADH^- deer mice hepatocytes. The volume density of mitochondria from ADH^+ deer mice hepatocytes was 23.9% (S.D.=0.035) and 23.7% (S.D.=0.024) for ADH^- deer mice hepatocytes. The surface density of mitochondria for ADH^+ deer mice hepatocytes was 1.43 $\mu m^2/\mu m^3$ (S.D.=0.178) and 1.42 $\mu m^2/\mu m^3$ (S.D.=0.159) for ADH^- deer mice hepatocytes. Therefore, we concluded that ADH^+ and ADH^- adult deer mice provide a good model system for future studies of the effects of ethanol on hepatocytes.

References

1. K. Beier and H. D. Fahimi, *Cell Tissue Res.*, 246(1986)635-640.
2. The authors gratefully acknowledge the assistance of Melchor Ortiz, Biostatistics Laboratory.
3. This research was undertaken in the Analytical Cytology Core Facility, Biological Sciences, the University of Texas at El Paso and funded by M.A.R.C. grant #6M08048 and NIH grant #RR08124-03.
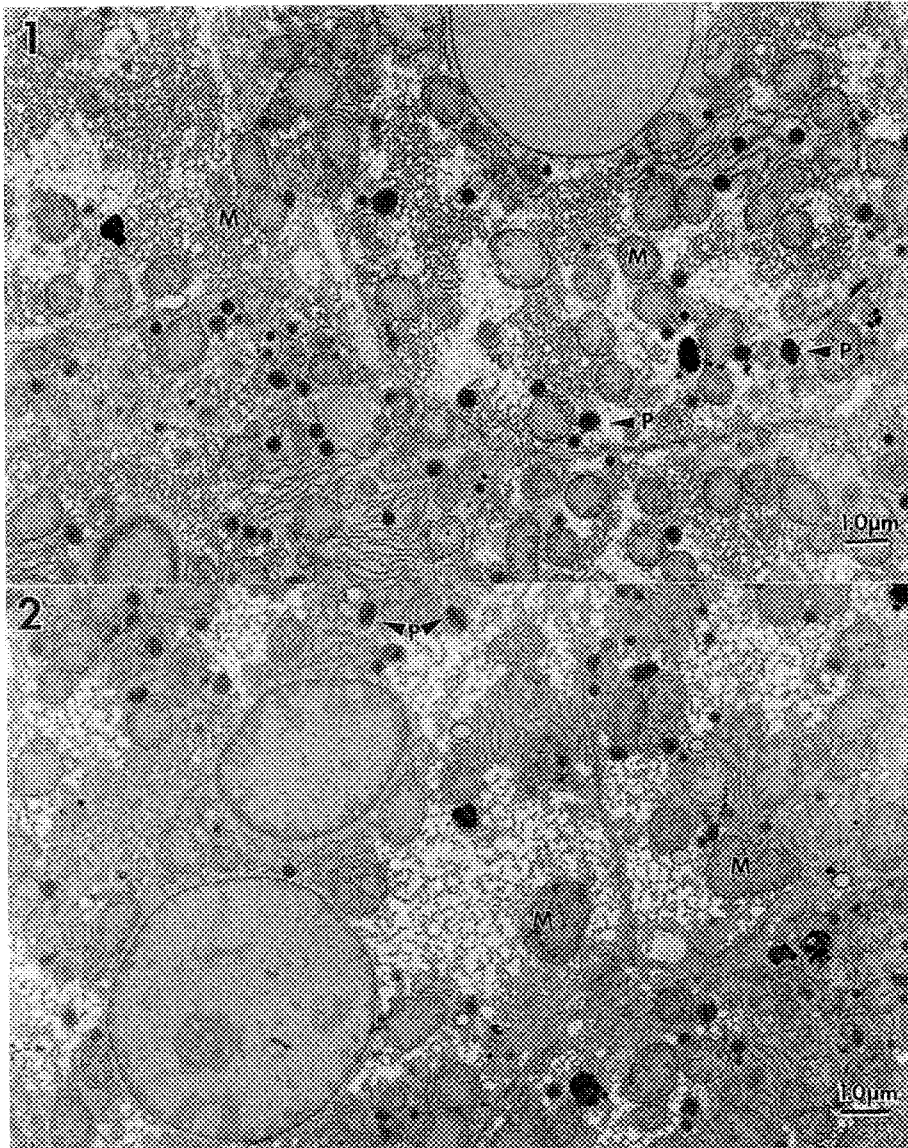
FIG. 1 TEM of <u>Peromyscus maniculatus</u> ADH$^+$ hepatocytes. M = mitochondria; P = peroxisomes.
FIG. 2 TEM of <u>Peromyscus maniculatus</u> ADH$^-$ hepatocytes. M = mitochondria; P = peroxisomes.

IN SITU LOCALIZATION OF PPAR GAMMA AND UNCOUPLING PROTEIN IN MOUSE EMBRYO SECTIONS USING DIGOXIGENIN-LABELED RIBOPROBES

C. Jennermann*, S. A. Kliewer**, and D. C. Morris*

*Department of Molecular Pharmacology
**Department of Cell Biology
Glaxo Wellcome, Inc., Research Triangle Park, NC 27709

Peroxisome proliferator-activated receptor gamma (PPARg) is a member of the nuclear hormone receptor superfamily and has been shown *in vitro* to regulate genes involved in lipid metabolism and adipocyte differentiation.[1] By Northern analysis, we and other researchers have shown that expression of this receptor predominates in adipose tissue in adult mice, and appears first in whole-embryo mRNA at 13.5 days postconception.[2] *In situ* hybridization was used to find out in which developing tissues PPARg is specifically expressed.

Digoxigenin-labeled riboprobes were generated using the Genius™ 4 RNA Labeling Kit from Boehringer Mannheim. Full length PPAR gamma, obtained by PCR from mouse liver cDNA, was inserted into pBluescript SK and used as template for the transcription reaction. Probes of average size 200 base pairs were made by partial alkaline hydrolysis of the full length transcripts. The *in situ* hybridization assays were performed as described previously with some modifications.[3] Frozen sections (10 μm thick) of day 18 mouse embryos were cut, fixed with 4% paraformaldehyde and acetylated with 0.25% acetic anhydride in 1.0M triethanolamine buffer. The sections were incubated for 2 hours at room temperature in pre-hybridization buffer, and were then hybridized with a probe concentration of 200μg per ml at 70° C, overnight in a humidified chamber. Following stringent washes in SSC buffers, the immunological detection steps were performed at room temperature. The alkaline phosphatase labeled, anti-digoxigenin antibody and detection buffers were purchased from Boehringer Mannheim. The sections were treated with a blocking buffer for one hour and incubated with antibody solution at a 1:5000 dilution for 2 hours, both at room temperature. Colored precipitate was formed by exposure to the alkaline phosphatase substrate nitrobluetetrazoliumchloride/ bromo-chloroindlylphosphate.

Our initial results showed that PPARg is expressed in adipose depots in the interscapular and thoracic region. In developing and neonate animals these areas are known to contain brown adipose tissue (BAT). BAT is involved in the dissipation of energy in the form of heat in newborn and cold-exposed animals, and defects in BAT function are thought to be involved in the development of diabetes and obesity in several animal models.[4] In order to establish that the tissue in which PPARg was localized was actually brown fat, the in situ hybridization protocol was used to localize mitochondrial uncoupling protein (UCP), a protein specific to BAT which is involved in the heat generating function of that tissue. The pBS-KS plasmids containing a 1.2 kB RI fragment of rat UCP were used to generate riboprobes and in serial sections UCP and PPARg were colocalized to these BAT sites (Figures 1-4). These data suggest a role for PPARg in BAT function and in vivo regulation of brown adipocyte differentiation.

References

1. P. Tontonoz, et al, *Genes Dev.*, 8 (1994) 1224
2. S. Kliewer et al., *Proc. Natl. Acad. Sci.*, 91 (1994) 7355
3. N. Schaeren-Wiemers and A. Gerfin-Moser, *Histochemistry*, 100 (1993) 431
4. J. Himms-Hagen, in *Obesity* (eds. P. Bjorntorp and B. N. Brodoff), J. B. Lippincott Co., Philadelphia (1992) 15
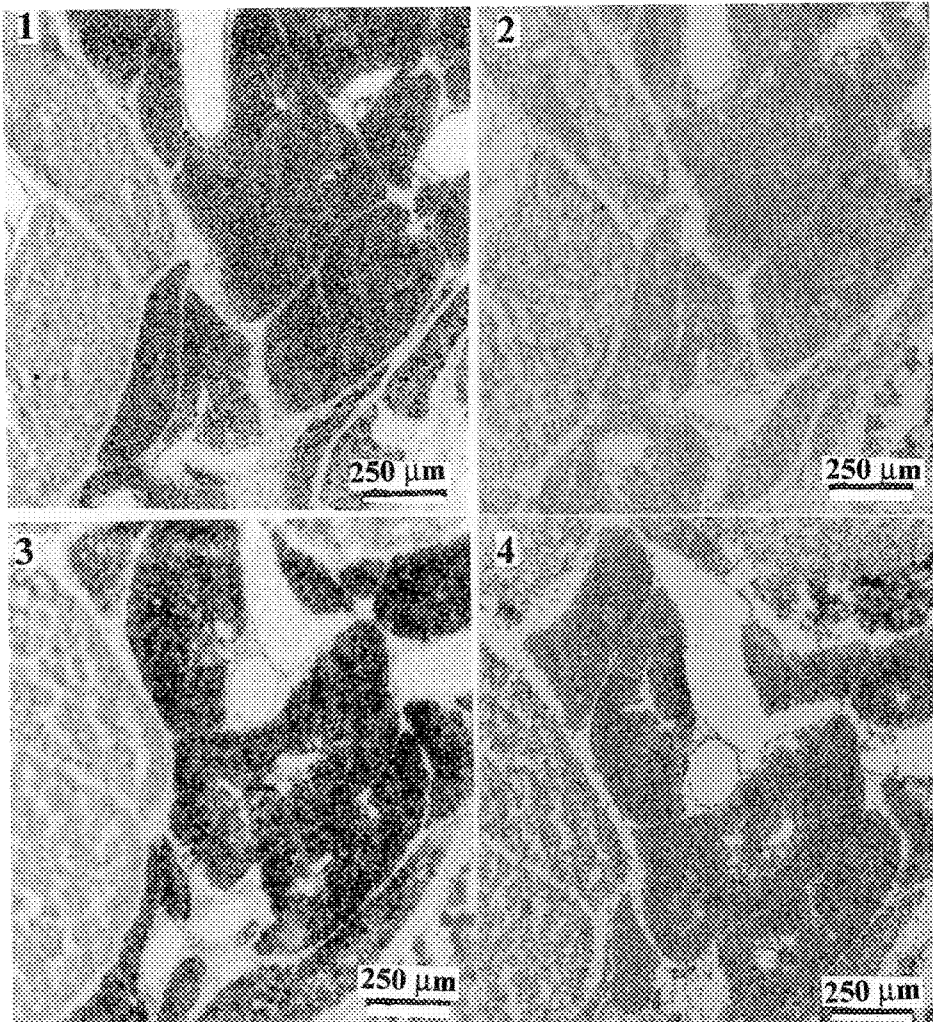
FIG. 1 PPARgamma antisense probe localized to adipose tissue in day 18 mouse embryo.
FIG. 2 PPARgamma sense probe control on serially cut section.
FIG. 3 UCP antisense probe localized to same brown adipose on serially cut section.
FIG. 4 UCP sense probe control on serially cut section.

DESMOSOMAL DISORGANIZATION AND EPIDERMAL ABNORMALITIES IN A TRANSGENIC MOUSE EXPRESSING MUTANT DESMOGLEIN-3.

Qian-Chun Yu, Elizabeth Allen, and Elaine Fuchs

Howard Hughes Medical Institute, Department of Molecular Genetics and Cell Biology, University of Chicago, Chicago, IL 60637

Desmosomes are special adhesion structures connecting epithelial cells. The formation of desmosome plaques requires the participation of multiple molecules including desmoplakin (DP), plakoglobin (PG), desmocollins (DSC), and desmogleins (Dsg). It is known that Dsg has functional domains involved in cell-cell adhesions and plaque-cytoskeleton interactions. Functional modulation of Dsg is known to be related to some skin disorders exhibiting desmosome abnormalities. To better understand the role of Dsg 3 in the assembly of epidermal desmosomes and its possible relation to cutaneous disorders, we generated a transgenic mouse model which, driven by a keratin 14 promoter, expressed high levels of a truncated Dsg 3, Dsg3ΔN, in the lower epidermal keratinocytes.

Skin samples of different body sites were collected, at different ages, from both control mouse and mutant animals exhibiting phenotypic skin changes for histology, immunohistochemistry, and ultrastrucutral studies. Specimens for conventional TEM studies were fixed in 4% paraformaldehyde and 2.5% glutaraldehyde, post-fixed in 1% O_sO_4, and embedded in LX-112. For immunoelectron microscopy, samples were fixed in 2% paraformaldehyde and 0.05% glutaraldehyde, dehydrated in ethanol at -25°C, embedded in Lowicryl K4M medium, and polymerized at -25°C with UV light. Ultrathin sections were labeled with several antibodies against DP, PG, DSC, and E-cadherin. All sections were stained with uranyl acetate and lead citrate before examining with a JEOL-CX microscopy operated at 60 kv.

All the transgenic mice expressing mutant Dsg3ΔN showed apparent swelling of their paws, flaky skin, and infarction of their tail-tip. Light microscopy of toluidine blue stained semithin sections revealed a dramatic widening of the intercellular spaces in the transgene-expressing cells of the epidermis, particularly in paw skin. In ultrathin sections examined by TEM, there were frequent disruptions of desmosomes, with an overall decrease in the number of desmosomes in affected areas. Numerous aberrant desmosomes with irregular or assymetric plaques, or simply "thikened membrane contacts" were also present in these cells. In keratinocytes that had lost most of their desmosomal connections, keratin networks were often collapsed into aggregates. Immunoelectron microscopy using antibodies against the several desmosome-associated antigens demonstrated various changes of molecular disorganizations within the desmosomes in affected epidermis. While the majority of the normal desmosomes are labeled specifically with antibodies against DP, PG, and Dsc, many aberrant desmosomes in the mutant mouse showed absence of labeling on only one side of the plaque, often with small aggregates of label, or no labeling. Some of the plakoglobin labels are found in the cytoplasm. Our results indicate that the presence of mutant Dsg 3 in the epidermis affected the assembly of desmosomes, and abnormalities in epidermal differentiation.

References:
1. Garrod DR, Current Opin Cell Biol 5:30-40, 1993
2. Koch PJ, et al. Eur J Cell Biol 53:1-12, 1990
3. Allen E, Yu QC, Fuchs E, J Cell Biol, 1996 In press
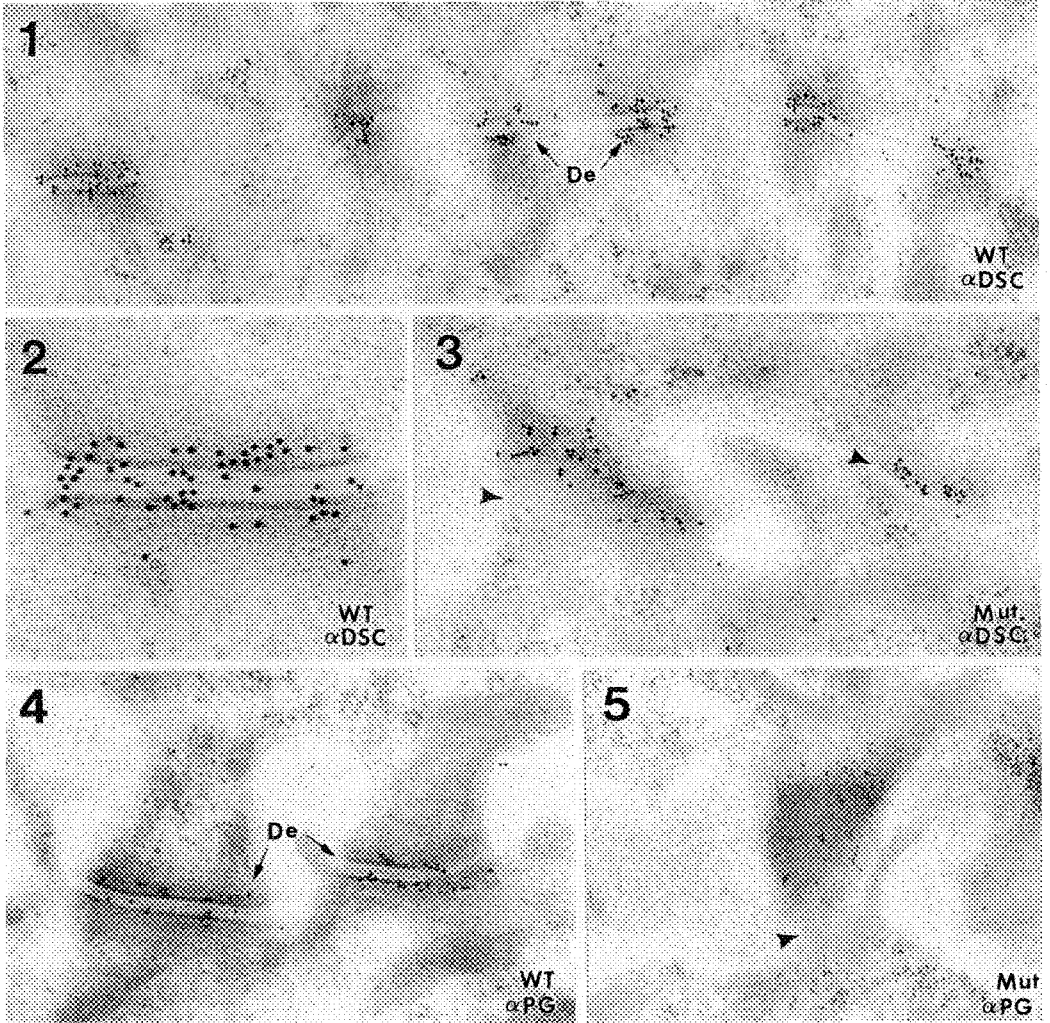
Figure 1. ImmunoEM of Dsc in normal skin, showing numerous desmosomes labeled with αDsc.
Figure 2. High Magnification view of normal desmosome labeled with αDsc.
Figure 3. High Mag view of mutant desmosome labeled with αDsc.
Figure 4. High Mag of normal desmosome labeled with αPG.
Figure 5. High Mag view of mutant desmosomes labeled with αPG.

35

AN EARLY DEVELOPMENTAL MARKER FOR RADIAL GLIA IN RAT SPINAL CORD

V. Kriho[*], H.-Y. Yang[*+], C.-M. Lue[+], N. Lieska[*], and G. D. Pappas[*]

[*] Department of Anatomy and Cell Biology, University of Illinois at Chicago, Chicago, IL 60612
[+] Department of Anatomy, National Cheng Kung University, Tainan, Taiwan, R.O.C.

Radial glia have been classically defined as those early glial cells that radially span their thin processes from the ventricular to the pial surfaces in the developing central nervous system.[1] These radial glia constitute a transient cell population, disappearing, for the most part, by the end of the period of neuronal migration.[2,3] Traditionally, it has been difficult to definitively identify these cells because the principal criteria available were morphologic only.

Using immunofluorescence microscopy, we have previously defined a phenotype for radial glia in rat spinal cord based upon the sequential expression of vimentin, glial fibrillary acidic protein and an intermediate filament-associated protein, IFAP-70/280kD.[4] We report here the application of another intermediate filament-associated protein, IFAP-300kD, originally identified in BHK-21 cells, to the immunofluorescence study of radial glia in the developing rat spinal cord.[5]

Results showed that IFAP-300kD appeared very early in rat spinal cord development. In fact by embryonic day 13, IFAP-300kD immunoreactivity was already at its peak and was observed in most of the radial glia which span the spinal cord from the ventricular to the subpial surfaces (Fig. 1). Interestingly, from this time, IFAP-300kD immunoreactivity diminished rapidly in a dorsal to ventral manner, so that by embryonic day 16 it was detectable only in the maturing macroglial cells in the marginal zone of the spinal cord and the dorsal median septum (Fig. 2). By birth, the spinal cord was essentially immuno-negative for this IFAP. Thus, IFAP-300kD appears to be another differentiation marker available for future studies of gliogenesis, especially for the early stages of radial glia differentiation.

References

1.   Rakic, P., J. Comp. Neurol. 145(1972)283.
2.   Rakic, P., Anat. Embryol. 156(1991)115.
3.   Fedoroff, S., Astrocytes, Vol.1, eds. Fedoroff, S. and Vernadakis, A., Academic Press, New York(1986)35.
4.   Yang, H.-Y., Lieska, N., Shao, D., Kriho, V. and Pappas, G.D., J. Neurocytol. 22(1993)558.
5.   Yang, H.-Y., Lieska, N. and Goldman, R.D., J.Cell Biol. 100(1985)620-631.
6.   The authors wish to thank Nicholas Kriho for his photographic work. This research was supported by NIH grant NS28931 and National Science Council, Taiwan, R.O.C., grant NSC85-2331B006-084.

Fig. 1   Immunofluorescence
Localization of IFAP-300kD in Rat
Spinal Cord at Embryonic day
13.
Radial glia are extensively
labelled.

Fig. 2   Montage Micrograph
Demonstrating IFAP-300kD
Immunofluorescence Staining of
Embryonic Day 16 Rat Spinal
Cord.
The IFAP rapidly began to
disappear in cells from the
dorsal (D) to ventral (V) cord,
with IFAP-300kD remaining only
in some cells in the marginal
zone and the dorsal median
septum.
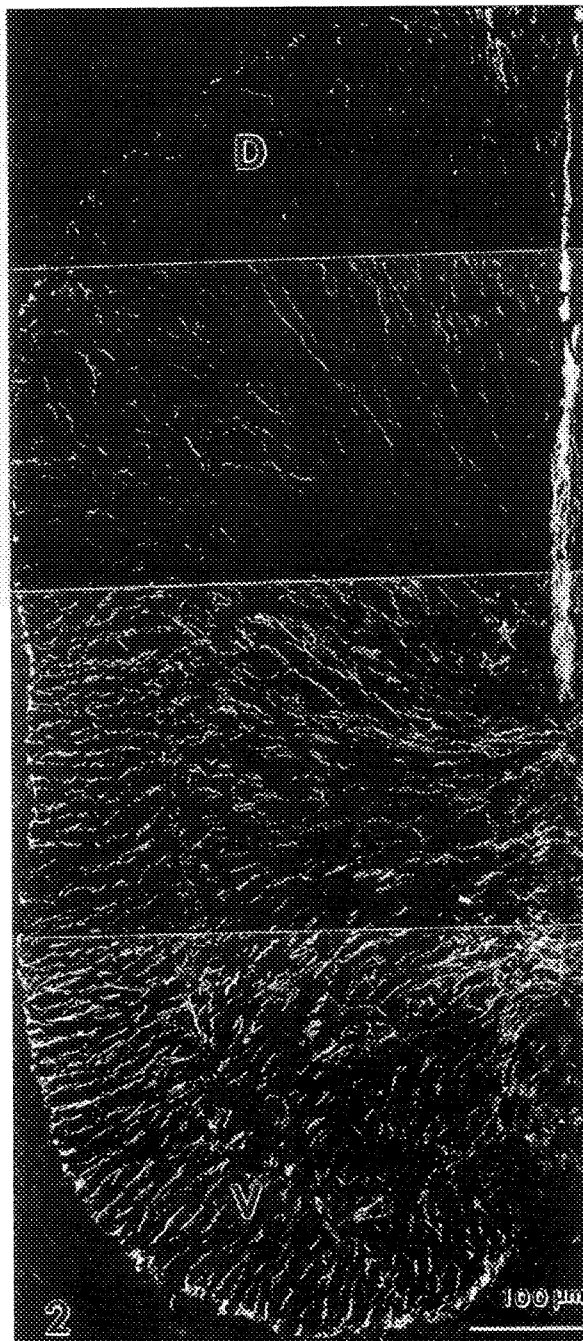
Can Microwave Ovens Reduce Immunocytochemical Labeling Times?

Linda Iadarola and Paul Webster

Center for Cell Imaging, Yale University School of Medicine, Department of Cell Biology, 333 Cedar Street, New Haven CT 06520-8002   *http://info.med.yale.edu/cellimg*

In recent years the use of microwave ovens in biomedical microscopy laboratories has contributed to reducing the times of fixation (1) and resin embedding (2). Reports of the use of microwaves for histochemsitry and immunocytochemistry (3) led us to investigate the possible use of a microwave oven to reduce immunocytochemical labeling protocols.

The application of specific antibodies to thawed cryosections of aldehyde-fixed material is becoming more accessible to research and service laboratories. These detection methods, routinely performed in our laboratory, were used to study the effect of microwaves on labeling protocols using affinity purified, polyclonal antibodies and protein A-gold.

Cells containing 3-(2,4-dinitroanilino)-3-amino-N-methyldipropylamine (DAMP), a compound which accumulates in low pH compartments, were aldehyde-fixed, cryosectioned and then labeled with rabbit antibodies to dinitrophenol (which bind to DAMP) and 10nm protein-A gold. Regular sequential labeling protocols (4) were compared with protocols using a microwave oven operating at 100% power, where the antibody incubation and washing times were reduced. The effect of microwaves on the labeling efficiency was investigated using simple quantitative methods. The protocol which produced reduced incubation times with no loss of labeling efficiency was then applied to sections in the absence of microwaves. The effect of reducing the final methyl cellulose-uranyl acetate contrasting step was also investigated.

The reduced incubation times we investigated, using microwaves, significantly reduced the total labeling time (Fig 1). The labeling efficiency or background label was not affected by this reduction in labeling time (Fig 2). However, if the reduced incubation and washing times were applied to labeling protocols in the absence of microwaves, the labeling efficiency was similar to that found when the microwave oven was used (Fig 2, Fig 3). The contrasting step could also be reduced from 10 min to 15 sec (Fig 4).

We have found that labeling times for DAMP visualization and subsequent washing steps can be shortened without a significant reduction of labeling efficiency or increase in non-specific label (background). Microwaves played no role in this time reduction.

References
1. G. R. Login et al., J. Histochem. Cytochem. (1986) 34 381-397.
2. R. T. Giberson and R. S. Demaree Jr., Microsc. Res. Tech. (1995) 32:246-254.
3. D. Hopwood *et al.*, Histochem. J. (1984) 16:1171-1191.
4. G. Griffiths, Fine Structure Immunocytochemistry, Springer Verlag Heidelberg, (1993) 165.

Figure 1:

Treatment	Microwave Protocol	Normal Protocol
0.15%glycine	15 sec.	5 min
1% BSA	5 min.	10 min.
Anti-DNP	1+3, 1+3 min	30 min.
PBS wash	2 x 15 sec.	5 x 3 min.
protein A-gold	15 min.	15 min.
PBS wash	2 x 15 sec.	5 x 5 min.
Water wash	2 x 15 sec.	5 x 1 min.
Contrasting	15 sec.	10 min.
Total	30 min.	155 min.

Figure 2:

Treatment	Label (gold/nm^2)	Background (gold/nm^2)
Microwave	14.9 ±3.7	0.029 ±0.003
Normal	12.5 ±3.0	0.038 ±0.001
Microwave Time (no microwave)	14.0 ±1.7	0.029 ±0.006

3A

3B
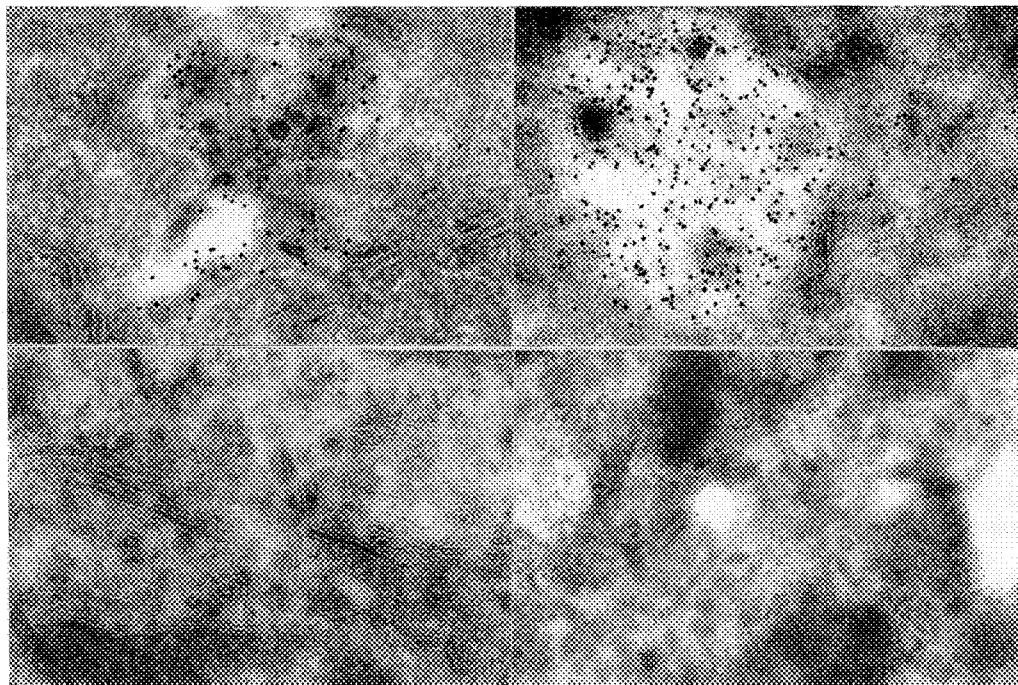
4A

4B

FIG 1. Comparison of labeling protocol times.
FIG 2. Specific signal and background label (gold/unit area) for each protocol.
FIG 3. Anti-DNP on cryosections (10nm gold). Normal (A) and Microwave (B) protocols
FIG 4. Methyl cellulose-uranyl acetate 15 sec. incubation. In microwave (A), on bench (B).
Print magnifications 3A - 52,000x; 3B - 52,000; 4A - 59,000; 4B - 47,000

ULTRASTRUCTURAL LOCALIZATION OF ANTIGENS BY CAPILLARY ACTION IMMUNOCYTOCHEMISTRY

László G. Kömüves

University of California San Francisco, VA Medical Center, San Francisco CA 94121

Light microscopic immunohistochemistry based on the principle of capillary action staining is a widely used method to localize antigens.[1] Capillary action immunostaining, however, has not been tested or applied to detect antigens at the ultrastructural level. The aim of this work was to establish a capillary action staining method for localization of intracellular antigens, using colloidal gold probes.

Post-embedding capillary action immunocytochemistry was used to detect maternal IgG in the small intestine of newborn suckling piglets. Pieces of the jejunum of newborn piglets suckled for 12 h were fixed and embedded into LR White resin. [2,3] Sections on nickel grids were secured on a capillary action glass slide (100 μm wide capillary gap, Bio-Tek Solutions, Santa Barbara CA, distributed by CMS, Houston, TX) by double sided adhesive tape. Immunolabeling was performed by applying reagents over the grids using capillary action and removing reagents by blotting on filter paper. Reagents for capillary action staining were from Biomeda (Foster City, CA). The following steps were performed: 1) wet the surface of the sections with automation buffer twice, 5 min each; 2) block non-specific binding sites with tissue conditioner, 10 min; 3) apply first antibody (affinity-purified rabbit anti-porcine IgG, Sigma Chem. Co., St. Louis, MO), diluted in probe diluent, 1 hour; 4) wash with automation buffer three times, 5 min each; 5) apply gold probe (goat anti-rabbit IgG conjugated to 10 nm colloidal gold, Zymed Laboratories, South San Francisco, CA) diluted in probe diluent, 30 min; 6) wash with automation buffer three times, 5 min each; 7) post-fix with 5% glutaraldehyde in PBS for 10 min; 8) wash with PBS twice, 5 min each; 9) contrast with 1% OsO_4 in PBS for 15 min; 10) wash with PBS followed by distilled water for 5 min each; 11) stain with 2% uranyl acetate for 10 min; 12) stain with lead citrate for 2 min; 13) wash with distilled water three times, 1 min each. The glass slides were separated, and the grids were air-dried, then removed from the adhesive tape. The following controls were used to ensure the specificity of labeling: i) omission of the first antibody; ii) normal rabbit IgG in lieu of first antibody; iii) rabbit anti-porcine IgG absorbed with porcine IgG.

Post-embedding capillary action immunocytochemistry using colloidal gold probe resulted in a specific labeling (Fig. 1.). Compared to sections labeled with the conventional method, the labeling intensity was higher. Furthermore, as many as twenty grids can be processed simultaneously using one pair of glass slides. This advantage results in increased uniformity and time-saving. This work is the first to show that capillary action staining can be successfully used for ultrastructural localization of antigens, and forecasts the possibility of fully automated EM immunolabeling.

References
1. J.A. Reed et al., *Biotechniques*, 13 (1992) 434.
2. L.G. Kömüves and J.P.Heath, *J. Histochem. Cytochem.* 40 (1992) 1637.
3. L.G. Kömüves et al., *Histochemical J.* 25 (1993) 19.
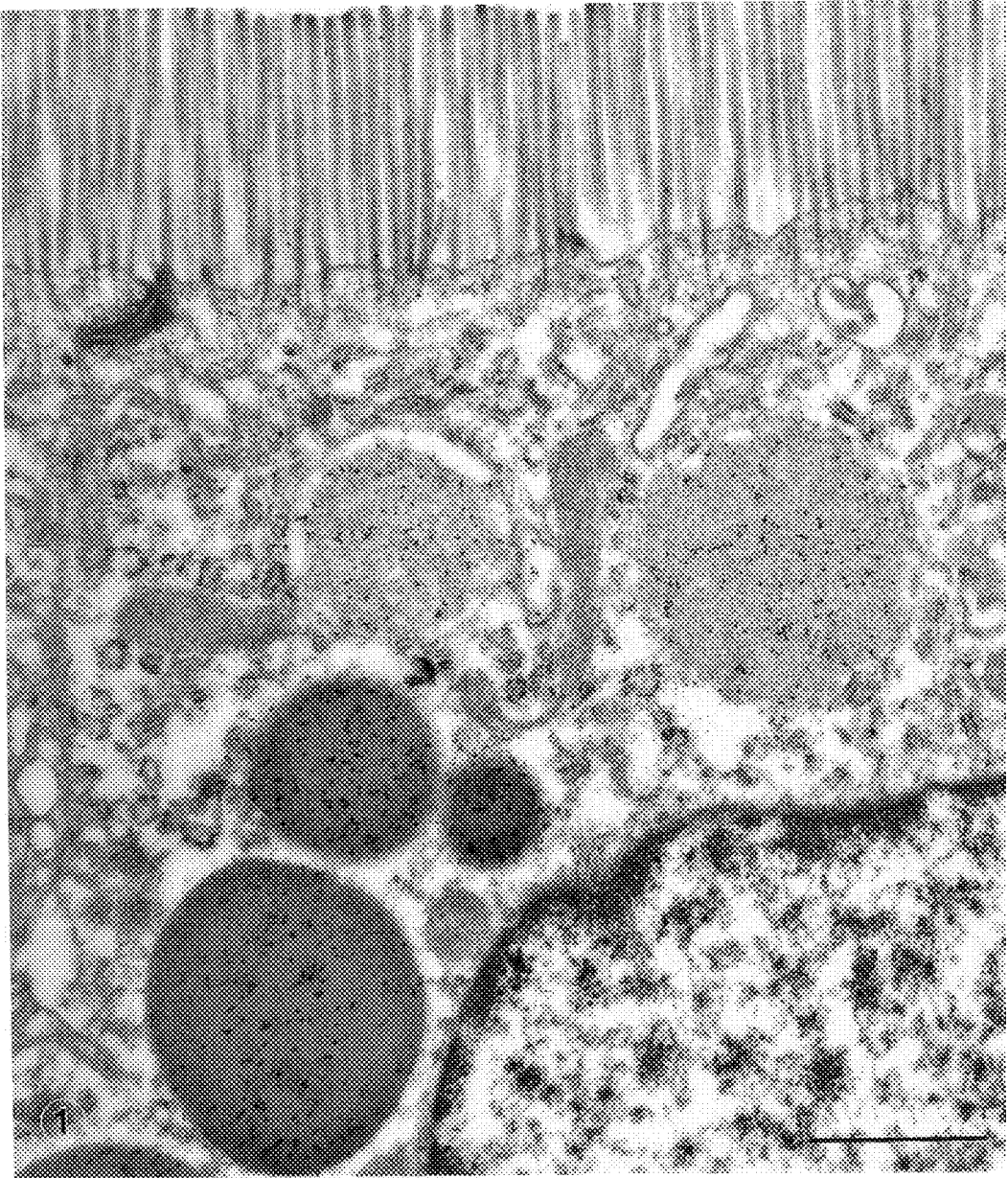
FIGURE 1. Localization of maternal IgG in the enterocytes of newborn suckling piglet
Maternal IgG is localized in apical vesicles and granules of endocytic origi
Final magnification: x 28,000, bar = 1 μm.

41

ENZYMATIC DIGESTION IS ALSO AN EFFECTIVE ANTIGENICITY-RESTORING METHOD FOR IMMUNOHISTOCHEMISTRY AT THE ELECTRON MICROSCOPE (EM) LEVEL

P. Ahmadi[*], Z. Qu[*], R. Kayton[‡], D. Andersern[†], W. D. Spangler[*], S. R. Plank[*] and J. T. Rosenbaum[*]. From the Departments of [*]Medicine, [†]Pathology and [‡]C.R.O.E.T, The Oregon Health Sciences University, Portland, OR 97201

Introduction: Immunohistological study using EM technique offers several advantages over light microscopy (LM) such as unequivocal identification of cell type by morphology and accurate subcellular localization of antigenic molecules of interest. These are mainly attributed to fixation with strong cross-linking reagents and embedding in resin-based media. However, they also are associated with a major drawback -- greatly reduced antigenicity or completely abolished accessibility to tissue antigen due to extensive cross-linking and the hydrophobicity of the resin [1]. As a result, the success rate of immunolabeling of routinely processed tissue for EM is far lower than that for LM using paraffin sections. Yet the process is far more laborious. To circumvent this problem, various etching or de-plasticizing methods have been introduced. However, most of them invariably lead to deterioration of the tissue morphology[1, 2]. A trade-off between morphology and antigenicity is generally considered necessary. Here we demonstrate that a brief enzymatic digestion prior to immunolabeling the routinely processed tissue samples for EM greatly improves the success rate of the immunostaining without noticeable effect on morphology. Our results suggest that enzymatic digestion is an effective antigenicity-restoring method for EM.

Experimental Design and Methods: Human synovium and rat skin were fixed in 4% paraformaldehyde alone or with 1% glutaraldehyde for 4 - 12 hours at 4 C, dehydrated through graded ethanol and propylene oxide, and embedded in araldite. A rat peripheral nerve sample fixed in 5% glutaraldehyde, post fixed in OsO_4, and embedded in Spurr was also used. Ultra thin sections were cut and laid on coated nickel grids. The sections were incubated with 2% crystal bovine serum albumin to block non-specific binding sites, and then with various primary antibodies at 12 - 50 µg/ml (see Table). The sections were then incubated with a secondary antibody conjugated with 5-nm gold particles. The antigen-antibody complex was visualized by TEM. To test if enzymatic digestion restores the tissue antigenicity, tissue sections were exposed to a selective enzyme prior to blocking step and labeled by antibodies that otherwise gave no specific staining. To determine the general feasibility of the enzymatic digestion method, 3 different enzymes were tested. Irrelevant immunoglobulins were used to replace the specific primary antibodies in control groups.

Results and Discussion: All bFGF-specific antibodies gave weak to moderate staining in endothelial cells and fibroblasts without enzymatic digestion (Fig. 1a). Brief enzymatic digestion greatly increased the staining intensity in these cells by 2 of the 3 antibodies tested. In addition, the digestion also resulted in strong labeling of cytoplasmic granules of mast cells (Fig. 1b). Most striking was the intense positive labeling of the 5% glutaraldehyde- and OsO_4-fixed sample (Table). The staining pattern was consistent with our previous findings at the LM [3]. While the antibody to chondroitinase sulfate gave strong specific labeling after the enzymatic treatment, no staining was observed without digestion (Fig. 1c and 1d). The positive staining was abolished by substitution of the primary antibodies with irrelevant immunoglobulins. In the tested conditions, enzymatic digestion did not seem to cause apparent morphological deterioration. Our results suggest that enzymatic digestion may be very useful for antigen-restoration for EM. Given the simplicity of this technique and its well documented application on paraffin sections for LM, we think that it deserves further exploration.

References
1. M.A. Hayat, ed.: Colloidal Gold (1989):35.
2. J.M. Polak and L.M. Vandell, ed.: Immunolabeling for Electron Microscopy (1984).
3. Z. Qu, et al.: The American Journal of Pathology (1995) 147:564.
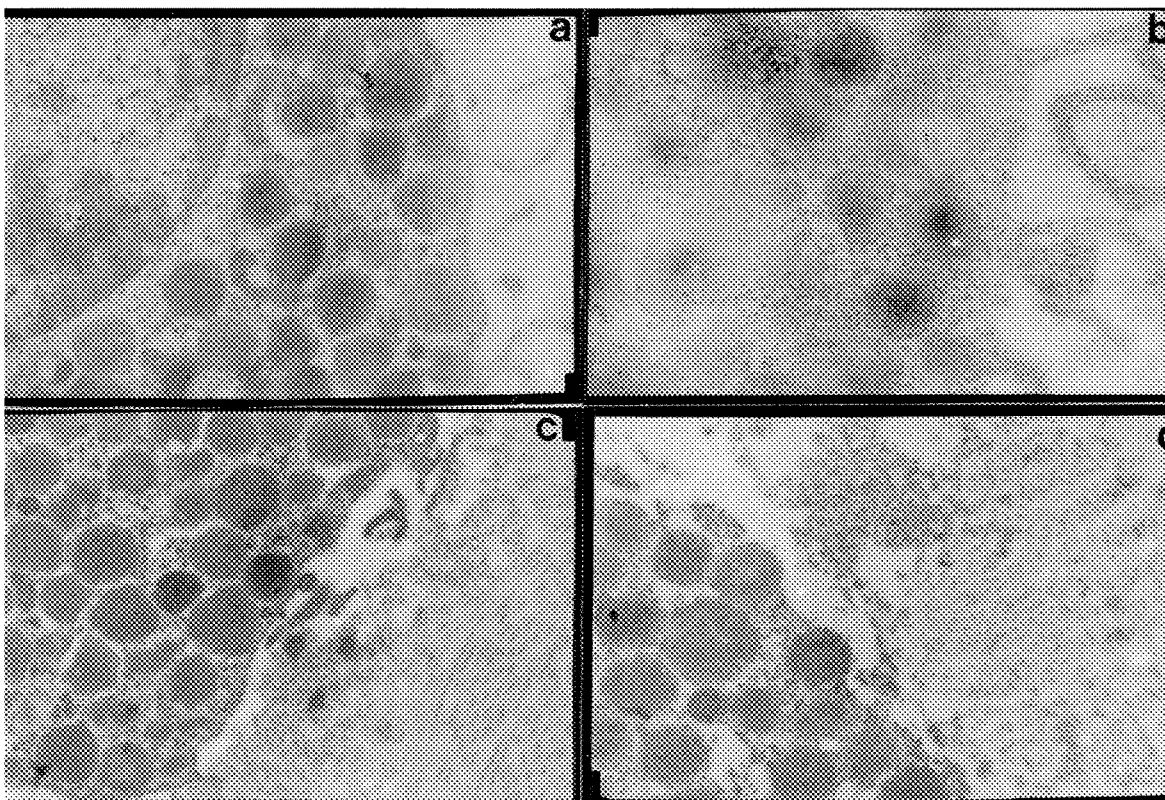
Figure 1. Immunogold labeling of mast cells adjacent to peripheral nerve by anti-bFGF without (a) or with enzymatic digestion (b), and by anti-chondroitin sulfate without (c) and with (d) digestion.

Table. Effects of Enzymatic Digestion on Immunolabeling

Antibodies* Specific for	Enzymatic Digestion†	Intensity of Immunolabeling	
		No Digestion	With Digestion
Basic FGF (A)	Hyaluronidase 15 min.	+	++++
Basic FGF (B)	Hyaluronidase 15 min.	+	++++
Basic FGF (C)	Hyaluronidase 15 min.	++	++
Chondroitin S	Chondroitinase ABC	---	++++

* Anti-basic fibroblast growth factor (basic FGF) (A) was a mouse monoclonal antibody. Anti-bFGF (B, C) and anti-chondroitin sulfate were polyclonal antibodies raised in rabbit. The anti-bFGF antibodies were also tested in human lung, nasal polyp, and rat dermal granuloma and peripheral nerve tissues.
† Enzyme solutions were prepared as described elsewhere [3]. Proteinase K solutions was from Dako Corp..

SUBCELLULAR LOCALOZATION OF TFPI IN HUMAN UMBILICAL VEIN ENDOTHELIAL CELLS (HUVEC)

Randi Olsen* Paul Webster** and John Bjarne Hansen***

*Department of Electron Microscopy and ***Department of Medicine, Institute of Clinical Medicine,University of Tromsø, Norway and **Center for Cell Imaging, Yale Univeristy, School of Medicine

Tissue factor pathway inhibitor (TFPI) is a serine protease inhibitor which regulates tissue factor (TF) induced blood coagulation by inhibiting the action of factor VIIa-TF complexes and factor Xa. In plasma, more than 80 % of the TFPI is bound to lipoproteins, 10 -20 % is carrier free, whereas platelets contains a small amount of TFPI. A major pool is probably assosiated with the vascular endothelium (1). This pool may have a crucial regulatory function because the endothelial surface serves as a binding site for factor VII/VIIa, mediating the activation of the extrinsic coagulation system.

The normal distribution of TFPI within human umbilical vein endothelial cells (HUVEC) was examined on ultrathin cryosections labeled with specific antibodies and colloidal gold probes (2,3). Label was seen associated with the cell surface and with many intracellular structures. The surface label was patchy, the signal intensity varied between cells and between different parts of the same cell. Intracellular TFPI was found in many compartments including the Golgi complex (fig.1) a finding that was expected as these cells are the main site of TFPI synthesis, and endocytic organelles. Anti TFPI-antibodies were seen over organelles that also contained 3-(2,4-Dinitroanilino)-3'-amino-N-methyldipropylamine (DAMP), a compound that accumulates in organelles with low lumenal pH. DAMP was visualized using anti-DNP antibodies (fig.2). Structures that contained exclusively TFPI or DAMP were also seen, suggesting that TFPI did not enter all endocytic organelles and was not exclusively localized to low pH compartments. The TFPI-antibodies also colocalized with specific markers of endosomes (MPR) (fig.3) and lysosomes (LAMP-1) (fig.4)(4). TFPI colocalized with both, demonstrating the appearence of TFPI also in these endocytic compartments.
To demonstrate the presence of TFPI in early endosomes, a compartment involved in recycling to the plasma membrane, the TFPI was colocalized with antibodies to the transferrin reseptor (TfR). Both polyclonal and monoclonal antibodies to the human TfR colocalize with TFPI in membranous organelles. (fig.5). This demonstrates the possibility that TFPI could be rapidly recycled to the cell surface.

We have established:
-    TFPI is synthetized in endothelial cells and associated with its cell membrane.
-    TFPI is internalized by the endothelial cells and directed to lysosomes for eventual degredation.
-    The possibility that some of the internalized TFPI enters a compartment involved in membrane reecycling to the cell surface.

REFERENCES
1. Broze, GJ Jr. Tissue Factor Pathway Inhibitor. *Thromb. Haemostas.* (1995) 74: 90-93.
2. Griffiths, G, *Fine Structure Immunocytochemistry.* (1993) Springer Verlag Berlin Heidelberg New York
3. Liou, W and Slot *JW,Proc. of the 13th Int. Congr. on Electron Microscopy,*(1994)3A:253-254
4. Kornfeld, S and Mellman, I. The Biogenesis of Lysosomes. *Annu Rev. Cell Biol.* (1989) 5: 483-525.
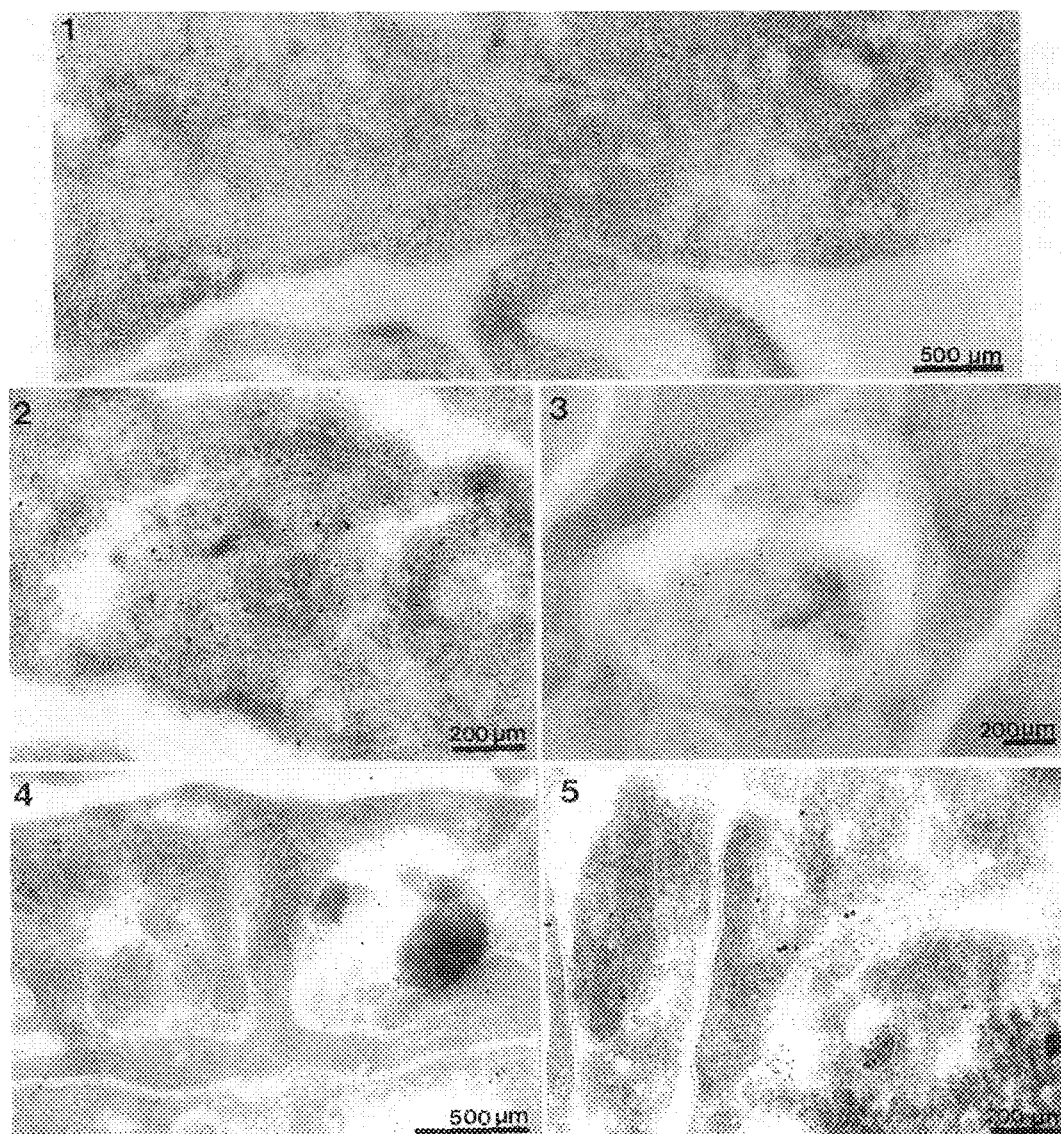
FIGURES

Cryosections of HUVEC showing TFPI (large gold particles)

1) over the cell surface and many cytoplasmic organelles, including Golgi,
2) colocalized with DAMP in intracellular organelles,
3) colocalized with cathion-independent mannose phosphate receptor,
4) colocalized with human LAMP-1 and
5) colocalized with human transferrin receptor.

NMR, CRYSTALLOGRAPHY, AND ELECTRON MICROSCOPY OF NUCLEOPROTEIN COMPLEXES

F.P. Ottensmeyer

Ontario Cancer Institute and Department of Medical Biophysics, University of Toronto, Toronto, Ontario, M5G 2M9, Canada

The *forte* of electron microscopy in biology is its unique ability to elucidate the very diverse structures of biological specimens at a range of sizes, with relationships within tissue sections, between and within cells, subcellular organelles, and macromolecules, for the latter with increasingly finer detail. It is the relationship between molecules that is the essence of biology, and it is here that a major emphasis in effort has been placed in recent years in terms of structure determination, not only in electron microscopy, but also in fields with complementary structural approaches, such as the classical x-ray crystallography and the much more recent NMR spectroscopy. The spatial relationship between nucleic acids and proteins is only one facet of this effort, albeit a most important one.

Conventionally electron microscopy has a spatial resolution of about 20 Å in stained biological specimens, but has succeeded with near-atomic resolutions in several cases.[1,2] NMR spectroscopy *per force* has to start at atomic dimensions, since its inter-nuclear signals are only available at short range. It builds outward mathematically to molecular dimensions. In the process the technique has permitted the elucidation of detailed interactions, not only between atoms on the same molecule, but in a number of instances between atoms of interacting macromolecules. One such case is the interaction between the tryptophan repressor protein with a symmetric 20-base-pair DNA consensus sequence that comprises the *trp* operator, both in the presence and in the absence of feedback inhibition by the amino acid tryptophan.[3] The complex, with a molecular weight of 37 kDa, consisting of an intertwined repressor dimer on the DNA duplex, is small by electron microscopic standards as well as by biochemical standards of average protein size. Yet it is one of the largest structures solved by NMR techniques, and required special approaches that included isotopic labelling of specific combinations of amino acids as well as labelling of one or other of the nucleic acid or protein components. However, one very important advantage over other techniques, including crystallography, is the fact that the NMR analysis occurs in aqueous solution in conditions that permit a free association and dissociation of components and that should approximate conditions *in vivo* quite closely.

X-ray crystallography over the last few years has yielded a profusion of results on specific protein/nucleic acid interactions, some of which are straight binding interactions, others with catalytic potential. Thus structures of truncated forms of the Myc-binding Max protein and of the upstream binding factor (UBF) have been solved as complexed with the E-box sequence CAGGTG.[4] In both cases the DNA remained in the standard straight B-form. More interestingly, in the complexes of two forms of the TATA-binding protein (TBP) with the adenovirus late promoter TATAAAG or with the yeast CYC1-52 TATATAAA, the DNA enters in the standard B-form, then undergoes an abrupt transition to an unprecedented partially unwound form of the right-handed double-helix induced by binding to a saddle-like eight-stranded antiparallel beta-sheet structure, and the insertion of two phenylalanines into the first T:A base step, the interaction in total resulting in a bend of about 100°.[4]

An even more intricate interaction is the complex of the 5-adenosyl-L-methionine transferase *M.HhaI* with its DNA substrate, in which the target cytosine base is flipped out of the DNA double-helix via the minor groove into the catalytic site of the enzyme.[5] At the same time the side chains of two amino acids, Gln237 and Ser87, from two different loop regions of the protein insert into the hole left by the flipped base. However, the details are not always so exquisite, depending on the diffracting qualities of the crystal, when crystals are formed at all. As indicated above, holoproteins are frequently truncated to remove appendages which at times prevent crystallization. Moreover, for structures larger than about 200 kDa, the solution of the crystal structure is still quite difficult even when crystals form.

Thus there is a clear need for an electron microscopic approach for the solution of the 3D structure of a multitude of biological structures. Many structures of interest have not been crystallized as 3D or even as 2D arrays, and most structures of interest, particularly protein/protein and protein/nucleic acid complexes are too large to be tackled successfully by the solution techniques of NMR spectroscopy. A spate of techniques have been applied and are being refined for 3D structure determination by EM: 2D crystal approaches[1,2], uses of symmetry in natural or artificial particles[6,7], random conical approaches for molecules with preferred orientations[8], and angular reconstitution for completely random orientations.[9,10] Thus the location and orientation of tRNA on the A-, P-, and E-sites of the ribosome have been determined by elegant reconstruction and subtraction methods, even without the specific identification of the nucleic acid by such EM techniques as electron spectroscopic imaging.[11] In two dimensions the latter approach has delineated the internal signal of 7SL RNA in the signal recognition particle[12], of the 16S and 28S rRNA in the ribosomal subunits[13], of the tRNA and 5S RNA in RNP storage particles[14], as well as of DNA in its complex with upstream binding factor (UBF)[15]. In 3D the DNA phosphorus signal has now been determined both in the inactive and in the active nucleosome.[16,17] The clearly accelerating pace in the application of these techniques bodes well for the use of electron microscopy toward the determination of the structure of nucleoprotein complexes in particular and indeed of macromolecular complexes in general.

1. R. Henderson *et al.* (1990) J. Mol. Biol. 213, 899-929.
2. W. Kühlbrandt *et al.* (1994) Nature 367, 614-621.
3. C. Arrowsmith *et al.* (1994) J. Mol. Biol. 238, 592-614.
4. S.K. Burley (1994) Curr. Opinions Struct. Biol. 4, 3-11 (a review).
5. X. Cheng (1995) Curr. Opinions Struct. Biol. 5, 4-10.
6. P.L. Stewart *et al.* (1991) Cell 67, 145-54; (1993) EMBO J. 12, 2589-2600.
7. N. Unwin (1993) J. Mol. Biol. 229,1101-1124.
8. M. Radermacher *et al.* (1987) J. Microscopy 146, 113-122.
9. G.J. Czarnota *et al.* (1994) J. Struct. Biol. 3, 35-46.
10. I.I. Serysheva *et al.* (1995) Nature Struct. Biol. 2, 18-23.
11. R.K. Agrawal *et al.* (1996) Science 271, 1000-1002.
12. D.W. Andrews *et al.* (1987) EMBO J. 6, 3471-3477.
13. A.P. Korn *et al.* (1983) Eur. J. Cell Biol. 31, 334-340.
14. D.W. Andrews (1985) Ph.D. Thesis. University of Toronto, Toronto, Canada.
15. D.P. Bazett-Jones *et al.* (1994) Science 264, 1134-1137.
16. G. Harauz & F.P. Ottensmeyer (1984) Science 226, 936-940.
17. G.J. Czarnota *et al.* (1996) These Proceedings.

HIGH RESOLUTION MAPPING OF NUCLEIC ACID CONTAINING COMPLEXES *in vitro* AND *in situ*

D. P. Bazett-Jones, and M.J. Hendzel

Department of Anatomy, The University of Calgary, Calgary, AB, Canada T2N 4N1

Structural analysis of combinations of nucleosomes and transcription factors on promoter and enhancer elements is necessary in order to understand the molecular mechanisms responsible for the regulation of transcription initiation. Such complexes are often not amenable to study by high resolution crystallographic techniques. We have been applying electron spectroscopic imaging (ESI) to specific problems in molecular biology related to transcription regulation[1]. There are several advantages that this technique offers in studies of nucleoprotein complexes. First, an intermediate level of spatial resolution can be achieved because heavy atom contrast agents are not necessary. Second, mass and stoichiometric relationships of protein and nucleic acid can be estimated by phosphorus detection, an element in much higher proportions in nucleic acid than protein. Third, wrapping or bending of the DNA by the protein constituents can be observed by phosphorus mapping of the complexes. Even when ESI is used with high exposure of electrons to the specimen, important macromolecular information may be provided. For example, an image of the TATA binding protein (TBP) bound to DNA is shown in the Figure (top panel). It can be seen that the protein distorts the DNA away from itself and much of its mass sits off the DNA helix axis. Moreover, phosphorus and mass estimates demonstrate whether one or two TBP molecules interact with this particular promoter TATA sequence.

Immunofluorescent microscopy of the interchromatin space of the vertebrate cell nucleus, the site of pre-mRNA transcription, processing, indicates that it is functionally compartmentalized[2]. To understand the complex higher-order assemblies responsible for compartmentalization, it is necessary to investigate combinations of interactions between proteins and mucleic acids. Element-specific mapping with ESI has proven particularly useful for understanding the complex architecture of the interchromatin space[3], including the specific imaging of proteins by nitrogen mapping at 415 eV energy loss (middle panel of Fig.). Protein-based structures produce signals in net nitrogen but not net phosphorus maps whereas nucleic acid-based structures produce signals in both maps. We are applying these methods to understand the biochemical basis of maintaining interchromatin granule cluster (IGC) structure. IGCs are intranuclear accumulations of approximately 25 nm mass-dense particles, identified as sites of pre-mRNA splicing factor and poly(A) pre-mRNA accumulation[4]. We have investigated nucleic acid organization both within and between individual particles of the IGC. Although nucleic acid linkers are found between individual particles, we have direct evidence for a protein-based structural framework within the IGC (compare Net P and Net N, bottom panel of Fig., also note the IGC indicated by long arrow in centre panel). Currently, we are investigating the possibility that similar structures are involved in the organization of the remainder of the interchromatin space.

References:
1. Bazett-Jones, D.P. et al. (1994) Science 264, 1134-1137.
2. Moen, P.T. et al. (1995) Hum. Mol. Genet. 4, 1779-1789.
3. Hendzel, M.J., Bazett-Jones, D.P. (1996) J. Microscopy (in press).
4. Hendzel, M.J., Bazett-Jones, D.P. (1995) Chromosoma 103, 509-516.
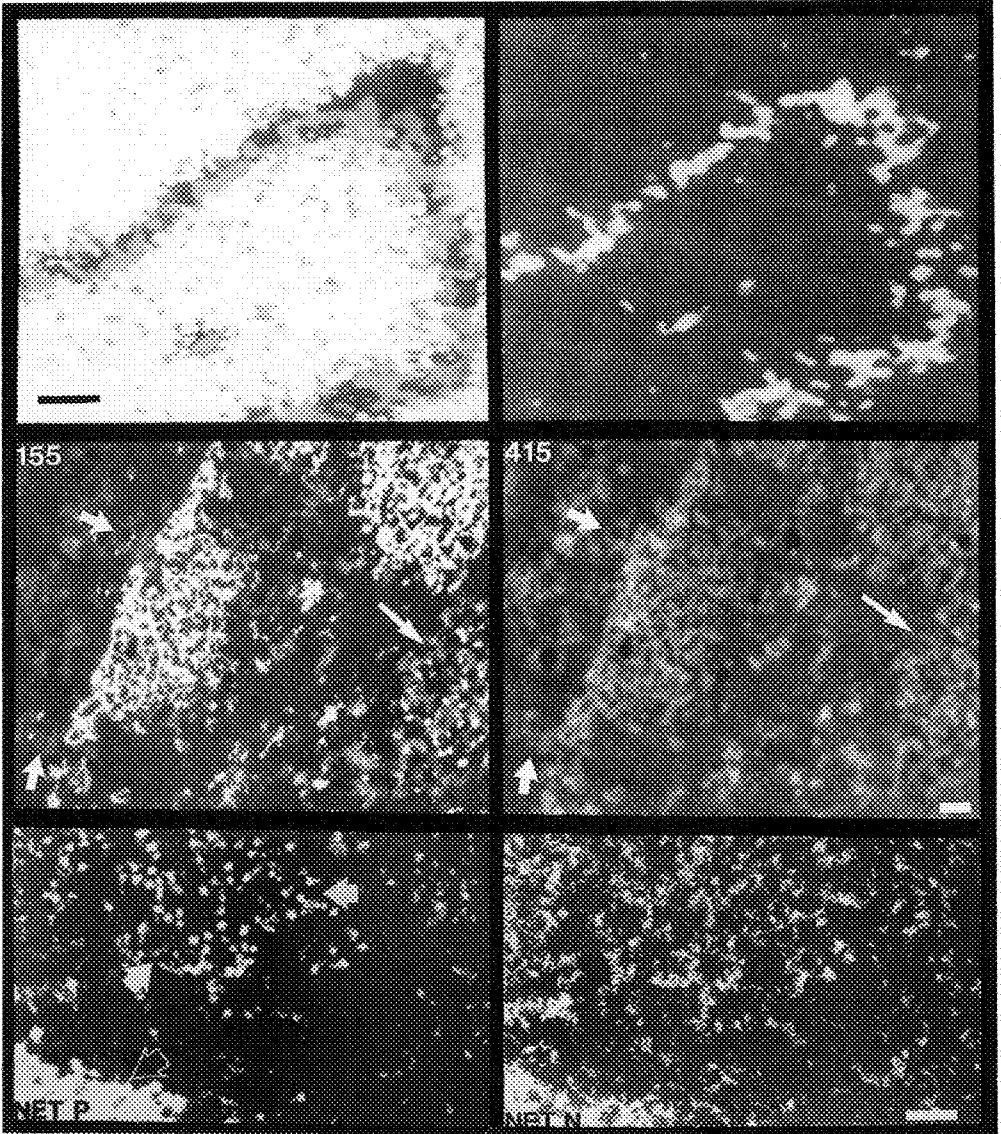
Top Panel- TBP:DNA complex. Net P image (grey) is superposed on mass image (black)(left). Net P image shown in reverse contrast (right). Scale bar, 6.0 nm.

Middle Panel- P-enhanced (left), N-enhanced (right) of cell nucleus. Nucleic acid-containing and protein-based structures can be identified with this image pair and the pair in the bottom panel. Short arrows indicate nuclear pore complexes, long arrow indicates an IGC. Scale bar, 100 nm.

Bottom Panel- Net P and Net N maps showing an IGC, between filled arrows. Note 25 nm beads in the P map and fibres in the N map. Scale bar, 210 nm.

THE USE OF AN INTERNAL STANDARD IN THE APPLICATION OF QUANTITATIVE IMAGE-EELS IN BIOLOGY

S. Abolhassani-Dadras[*], G.H. Vázquez-Nin[*,**], O.M. Echeverría[*,**] and S. Fakan[*]

[*]Centre of Electron Microscopy, University of Lausanne, 27 Bugnon, CH-1005 Lausanne, Switzerland
[**] Laboratory of Electron Microscopy, Department of Biology, Faculty of Sciences,
National Autonomous University of México, México City, D.F. 04510, Mexico

The energy filtering transmission electron microscope (EFTEM) is employed to examine the possibility of using ribosomes as internal standard for a quantitative in-situ study of phosphorus content of nuclear constituents in a biological section. The problems that can arise from different steps of such an experimental approach are discussed.

Salivary gland cells from fourth instar larvae of *Chironomus thummi* are selected as test specimens because of their appropriate structure. The nucleus of these cells contains two types of granules, one of which (known as Balbiani ring granule, Brg) has an RNA size known from radioactive phosphorus labelling and subsequent isolation, allowing one to estimate its phosphorus content.[1] The other type of granule (known as small RNP granule) has been recently discovered and its phosphorus content is not known.[2] The EFTEM method is used to verify the phosphorus content of these two nuclear constituents.

Salivary glands are fixed in 2.5% glutaraldehyde in 0.1M cacodylate buffer, pH 7.3, for one hour at room temperature. They are dehydrated in ethanol, embedded in Epon, and cut to 20-40 nm sections. No post fixation or specific stain are used for contrast enhancement. A Zeiss 902 microscope (prism-mirror-prism filter), equipped with a SIT camera and a Kontron AT personal computer for image acquisition and data treatment are utilised.

Prior to image acquisition, specimen thickness (t/λ) is controlled from the plasmon peak; specimens have often a (t/λ) of the order of 0.1 - 0.15 (Fig. 1).[3] Images are obtained from the SIT camera between 55 and 155 eV energy losses at 10 eV intervals with a slit opening of 12 eV. Care is taken to image always a part of the nucleus and a part of the cytoplasm, so that the conditions of experimentation regarding the electron dose and element evaporation would be the same for the standard (i.e. the ribosomes) and the RNP granules (Fig. 2).

Two images at 250 eV energy loss are obtained before and after image acquisition in order to check for drift. They are also utilised to select objects that are appropriate for "Image-EELS": in the case of each constituent and specifically in the case of ribosomes, objects that have at least a half of their diameter within the section (the shape of all three constituents are approximated to spheres) are chosen. Ribosomes being the reference structures, those showing the highest intensity of signal at the phosphorus L_{23}-edge are considered to correspond to items with their total volume in the section. This value of signal intensity is used as reference for estimation of phosphorus concentration and hence phosphorus content of the two nuclear constituents. Assuming that ribosomes contain about 5200 phosphorus atoms, then an average phosphorus content for the Brg is 43000 atoms and for the small RNP granules, 3600 atoms.

The examination of results has shown that this method and reliability of its results depend on the appropriate specimen preparation and careful data acquisition. Although no evidence about the contribution of exogenous phosphorus has been found, it seems logical for a quantitative study that phosphorus containing salts and solutions should be preferentially avoided. Accuracy of thickness measurement and correct selection of constituents for Image-EELS are of prime importance. The phosphorus edge being very near the tail of the plasmon peak, the variation of signal intensity is always larger than the dynamic range of acquisition systems as that described above, contrast adjustment needed, causes a "flattening" of spectra (Fig. 3). Figure 4 shows the type of spectrum obtained from the same section as in figure 3, benefiting from a system with a higher dynamic range and a slow scan CCD camera; we can observe the typical inverse exponential shape of spectra (data acquisition between 100 and 200 eV energy loss).[4] However, taking advantage of ribosomes as internal standard offers the possibility of employing simple systems without much problem, since
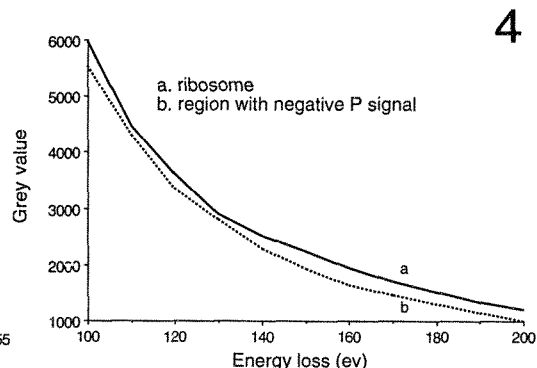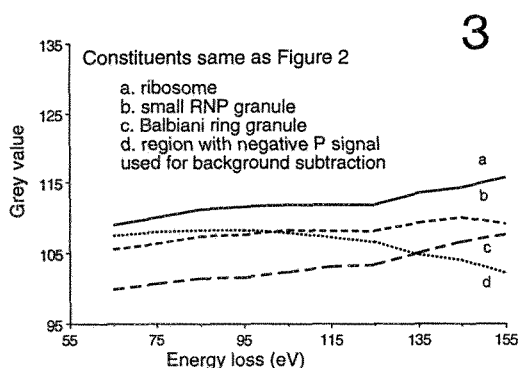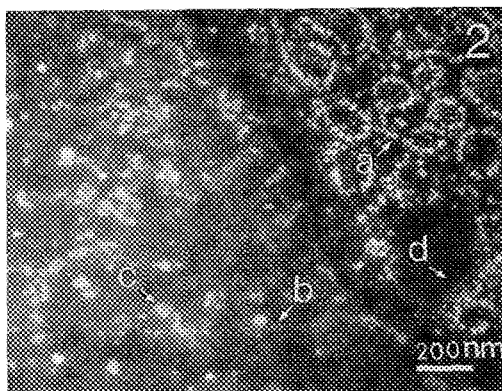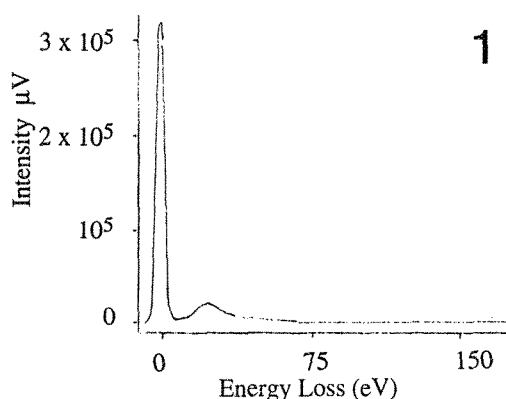
FIG. 1 Zero-loss and plasmon peak of a section employed for quantitative analysis.
FIG. 2 Micrograph of an area where Image-EELS can be done, $\Delta E = 250$ eV.
FIG. 3 Image EELS spectra obtained with a Zeiss 902 and a SIT camera.
FIG. 4 Image EELS spectrum obtained with a Zeiss 912 and a Gatan slow scan CCD camera.

any modification of the shape of Image-EELS spectrum would be the same for all constituents provided that acquisition is carried out under identical conditions. Areas near the nuclear membrane where both the ribosomes and the nucleoplasm are observed in the same time satisfy this condition.

References

1. Wurtz T. et al., *Proc. Nat. Acad. Sci. USA*, 87 (1990), 831.
2. Vázquez-Nin, G.H. et al., *Chromosoma*, 102(1993), 693.
3. Reimer, L. (1995) Energy Filtering Transmission Electron Microscopy. *Springer Series in Optical Sciences* (ed. by P.W.Hawkes), Vol. 71, Springer-Verlag, Berlin, Heidelberg.
4. The authors gratefully acknowledge Dr. J. Mayer, Max Planck Institut, Stuttgart and Gatan GmbH, München, for the use of Zeiss EM 912 Omega microscope equipped with a Gatan 679 slow scan CCD camera and for image acquisition of data shown on Figure 4.
5. This work was supported by the Swiss National Science Foundation.

CHALLENGES OF THREE-DIMENSIONAL RECONSTRUCTION OF RIBONUCLEOPROTEIN COMPLEXES FROM ELECTRON SPECTROSCOPIC IMAGES - RECONSTRUCTING RIBOSOMAL RNA

D.R. Beniac[*], G.J. Czarnota[+], T.A. Bartlett[*], F.P. Ottensmeyer[+], and G. Harauz[*]

[*] Department of Molecular Biology and Genetics, Biophysics Interdisciplinary Group, University of Guelph, Guelph, Ontario, Canada, N1G 2W1
[+] Division of Molecular and Structural Biology, Ontario Cancer Institute, 610 University Avenue, Toronto, Ontario, M5G 2M9.

Transmission electron microscopy has been dominant in structural studies of the ribosome and its constituent ribonucleic acids and proteins. Ribosomal RNA (rRNA) has central importance in the architecture of this complex and in protein synthesis. Our work has entailed using electron spectroscopic imaging (ESI) to probe the tertiary structure of rRNA *in situ* in a prokaryote (*Escherichia coli*) and in a eukaryote (*Thermomyces lanuginosus*). ESI uses only electrons which have lost a specific amount of energy due to specific inner-shell ionisation interactions with the specimen to form an elemental map [8]. In nucleoprotein complexes, a map of the phosphorus distribution represents primarily a projection of the phosphate backbone of the nucleic acid component [1]. The visualisation of rRNA *in situ* in the intact ribosomal subunit by ESI was demonstrated almost a decade ago to be feasible [7]. Our work on quantitative image analysis of ES images of *E. coli* and *Th. lanuginosus* ribosomal subunits [2,3] has presented unique challenges and has resulted in new algorithmic developments generally applicable to such images. These innovations include a singular pretreatment procedure [6], the use of mutual correlation functions rather than cross correlation functions to reduce the effect of low spatial frequency components [9], and angular determination using iterative quaternion-assisted angular reconstitution to compute a three-dimensional reconstruction [5,6]. These investigations have produced direct information regarding ribosomal rRNA localisation in the ribosomal subunits of *E. coli* and *Th. lanuginosus*, and the position of non-conserved sequences [2,3].

References

1. Bazett-Jones DP, Ottensmeyer FP (1981). Science 211, 169-170.
2. Beniac DR, Harauz G (1993). Micron 24, 163-171.
3. Beniac DR, Harauz G (1995). Mol Cell Biochem 148, 165-181.
4. Boublik M, *et al.* (1984). Proc 42nd EMSA Meeting, 690-691.
5. Czarnota GJ, *et al.* (1994). J Struct Biol 113, 35-46.
6. Farrow, NA, Ottensmeyer FP (1993). Ultramicroscopy 52, 141-156.
7. Korn AP, *et al.* (1983). Eur J Cell Biol 31, 334-340.
8. Ottensmeyer FP (1984). J Ultrastruct Res 88, 121-134.
9. van Heel M, *et al.* (1992). Ultramicroscopy 46, 307-316.
10. This work was supported in part by the NSERC of Canada.

Figures are representative galleries of (top left) large and (bottom left) small ribosomal subunits from *Thermomyces lanuginosus*, and (top right) large and (bottom right) small ribosomal subunits from *Escherichia coli*. These images have only been pretreated by "farrowing" [6] to remove the background carbon film and normalise intensities within each population of particles. Micrographs were recorded at 150 eV energy loss, and comprise information both on the overall structure of the complex as well as on the distribution of phosphorus within each particle. The phosphorus distribution can be assumed to represent the path of the rRNA backbone, since the number of (any) phosphorylated proteins is negligibly small.
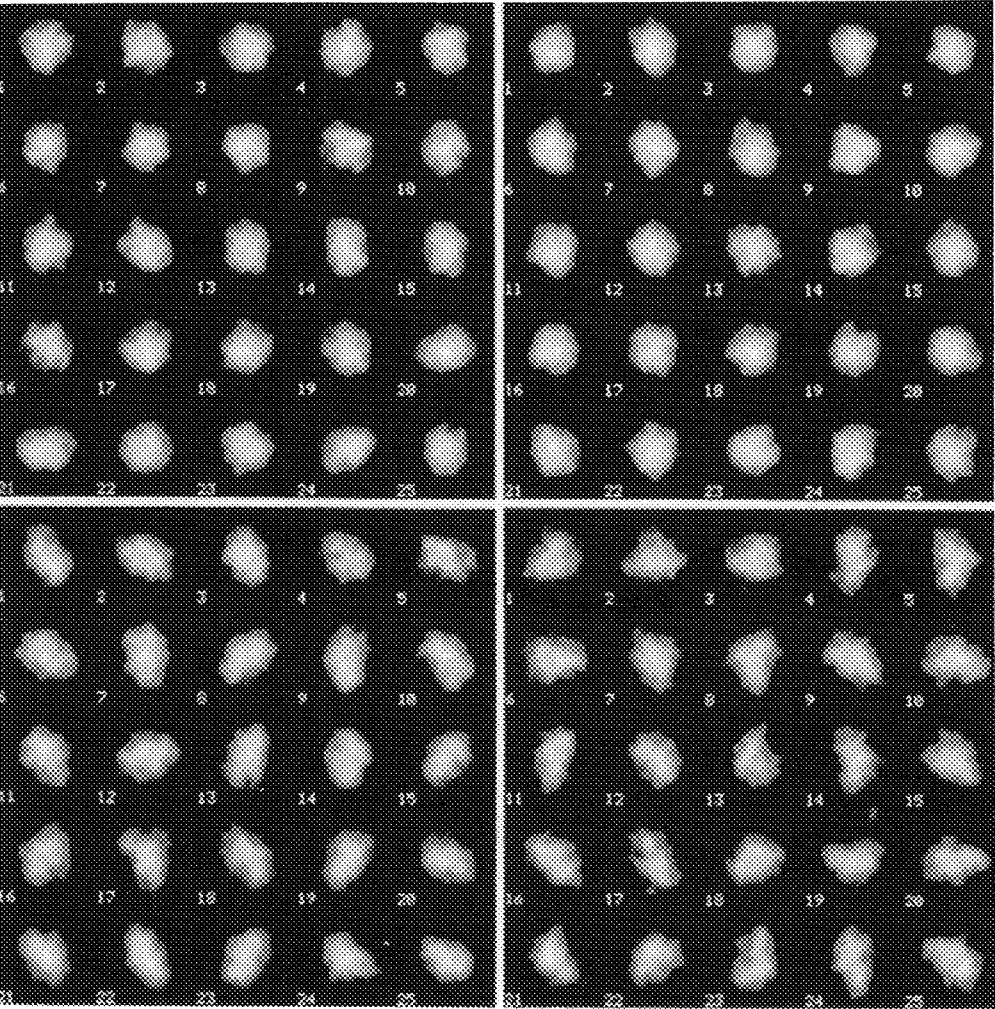
THREE-DIMENSIONAL IMAGING OF NUCLEOSOMES FROM TRANSCRIPTIONALLY ACTIVE GENES USING ELECTRON SPECTROSCOPIC IMAGING

G.J. Czarnota, D.P. Bazett-Jones,* and F.P. Ottensmeyer, Ontario Cancer Institute and Department of Medical Biophysics, University of Toronto, Toronto, Ontario, M5G 2M9, Canada, *Department of Medical Biochemistry, University of Calgary, Calgary, Alberta, T2N 4N1, Canada

The three-dimensional structure of the nucleosome was determined using particles purified from transcriptionally active genes (1) in conjunction with electron spectroscopic imaging (1,2), and quaternion-assisted angular reconstitution procedures (2-4). The results reveal a configuration which is very different from the canonical compact crystallographic structure for this fundamental chromosome subunit, implying a structural disruption of the nucleosome with the activation of gene expression in accord with numerous physico-chemical observations (1).

Previous analyses of nucleosomes purified from transcriptionally quiescent genes have indicated numerous structural states dependent on factors *in vitro* which modify charge based interactions in nucleoprotein complexes (2,5). Nucleosomes from transcriptionally active genes undergo chemical alterations *in vivo* which similarly modify charge based interactions (5). In order to investigate the effects of the gene expression associated chemical alterations on nucleosome structure, particles were purified from transcriptionally active genes using mercury affinity chromatography (1). These nucleosome particles are hyperacetylated with respect to particles from transcriptionally quiescent genes. Here additionally, sulphydryls normally buried within the protein core of the transcriptionally inactive particle are exposed to chemical modifying agents thus facilitating purification as described.

Chromatographically purified hyperacetylated particles with exposed sulphydryls were subsequently imaged using spectroscopic electron microscopy (Figs.1 & 2). Contrast enhanced darkfield micrographs were obtained by imaging with electrons scattered at an energy loss of 150 eV. This selected for electrons scattered inelastically by the phosphorus in the nucleosomal DNA. Additional darkfield images were obtained using electrons with an energy loss of 100 eV. Elemental maps of the phosphorus of nucleosomal DNA were subsequently calculated by an image subtraction procedure. Three-dimensional reconstructions were calculated using the contrast enhanced nucleosome images. A putative three-dimensional phosphorus map was also reconstructed using parameters calculated from the contrast-enhanced images. In total, the three-dimensional reconstruction indicates a structure for the transcriptionally active nucleosome which has an open C-shaped configuration (Fig. 3). The particle has an asymmetric mass distribution implying a disruption of the constituent nucleosomal proteins. The indicated conformation is consistent with a sulphydryl exposing structure. Additionally, the three-dimensional phosphorus map in conjunction with the two-dimensional phosphorus maps indicates a DNA configuration similar to that of a bent spring (Fig. 4). Moreover, these changes in nucleosomal structure which accompany the activation of gene expression are concordant with the recognized genetic and structural dynamism of this macromolecular nucleoprotein complex.

References
1. D.P. Bazett-Jones, E. Mendez, G.J. Czarnota, F.P. Ottensmeyer and V.G. Allfrey (1996) *Nuc. Acids Res.* **24**, 321.
2. G.J. Czarnota and F.P. Ottensmeyer (1996) *J. Biol. Chem.* **271**, 3677.
3. N.A. Farrow and F.P. Ottensmeyer, *J. Opt. Soc. Am. A.* **9** (1992), 1749.
4. G.J. Czarnota, D.W. Andrews, N.A. Farrow and F.P. Ottensmeyer (1994) *J. Struct. Biol.* **133**, 35.
5. van Holde, K.E. (1988) *Chromatin*, Springer-Verlag New York Inc., New York.
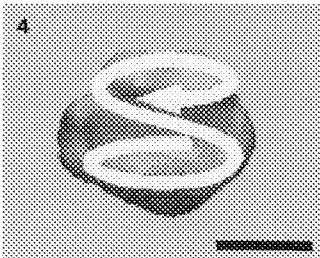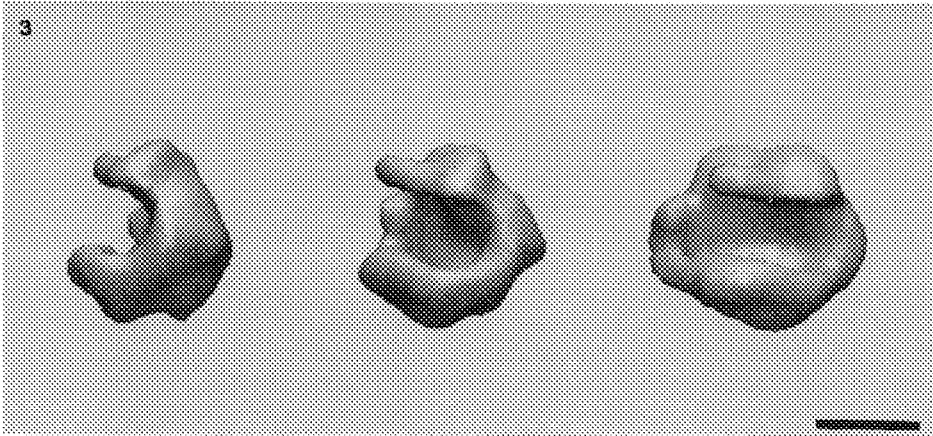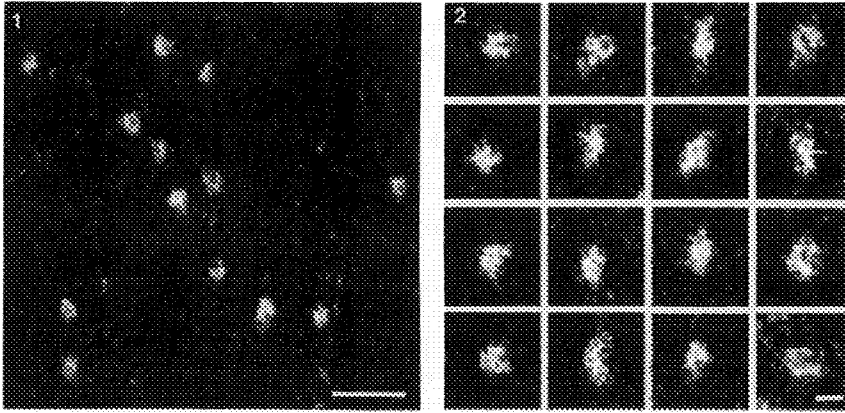
Fig. 1 Phosphorus contrast enhanced electron spectroscopic images of nucleosome particles. Scale bar represents 400 Å.

Fig. 2 Individual nucleosome particles imaged by spectroscopic electron microscopy. Images are phosphorus contrast enhanced. Scale bar represents 100 Å.

Fig. 3 Three views of the three-dimensional reconstruction of the transcriptionally-active nucleosome particle. The lower domain is more massive than the upper. Left to right views are related by subsequent 45° rotations. Scale bar indicates 50 Å.

Fig. 4 A preliminary model of the inferred DNA trajectory in the transcriptionally active nucleosome based upon phosphorus maps. A three-dimensional phosphorus map at a higher signal to noise ratio is currently being calculated. Scale bar represents 50 Å.

55

PHOSPHORUS-MAPPING OF ISOLATED VIRUSES BY ENERGY SPECTROSCOPIC IMAGING (ESI): AN EXPERIMENTAL APPROACH TO DISCRIMINATE MASS-EFFECTS FROM THE ELEMENT SIGNAL

K. Richter[*], H. Tröster[*], A. Haking[*], P. Schultz[**], P. Oudet[**], J. Witz[***], W. Probst[****], E. Spiess[*], H. Spring[*] and M. Trendelenburg[*]

[*] German Cancer Research Centre (DKFZ, 0195) INF 280, D-69120 Heidelberg, Germany
[**] IGBMC and [***] IBMC F-67085 Strasbourg, France
[****] Leo Electron Microscopy-GmbH, D-73446 Oberkochen, Germany

ESI uses the fact that the probability of an electron beam loosing a certain amount of energy by inelastic scattering is a function of the elemental composition of the specimen. However, to extract precise information about the elemental distribution from the specimen, the background intensity at the element sensitive energy-loss must be known. Since background increases with mass-thickness, adequate background-estimation is a crucial prerequisite for element mapping in isolated particles as otherwise the element signal conflicts with the contrast in mass-thickness.

To control the mass effect, a double layer of carbon film is used as an internal probe for phosphorus detection of the RNA in TYMV (turnip yellow mosaic virus). Phosphorus detection was performed at the P-L_{23}-edge above 132 eV (energy-windows: 155/120/90 eV; window-size dE=15eV; irradiation dose per image approx. 10^5 e/nm^2 EM Leo 912; detection device slow-scan ccd 14 bit). Virus particles (diameter 25 nm, ratio Protein/RNA 3/2; 6000 bases; ca. 20 P-atoms/pixel) and carbon film (thickness 10 nm) have about the same mass thickness. A second set of images taken before the P-edge (120/100/75 eV) was acquired as a negative-control for phosphorus. ESI-signals calculated from this set of images are interpreted as mass-thickness. Four methods of background subtraction as implemented in the image-processing program ESIVISION 2.0 were compared: Power-law resp. exponential law are three-window methods, differential law resp. jump-ratio are two-window methods. The P-map results from the definition of a detection mask containing the high-intensity-pixels of the calculated phosphorus distribution. The corresponding thresholding was done interactively trying to bring the viruses into the foreground while excluding the double-layer of pure carbon film from the detection mask.

The following conclusions can be drawn from this experiment: 1. All four methods detect phosphorus more sensitive than mass. 2. In behalf of mass-thickness detection, the three-window methods underestimate the background in thicker specimen regions (i.e. the double layer of carbon), while the two-window methods underestimate the background in thinner regions (i.e. the single layer of carbon). The three-window exponential law is not able to separate perfectly the element signal from the mass-signal in the P-map. The strongest separation between element and mass contrast, as judged from the net element distribution maps (not shown), is obtained by the three-window power law followed by the two-window differential law. 3. Since none of the four methods is capable to suppress the background completely, it will always be possible to arrange the thresholds for the detection mask in a way to bring some structure into foreground. Working with the three-window power-law, the use of an internal mass-probe enables to set the thresholds under exclusion of mass-detection. The lack of the element signal in the phosphorus-negative map further confirms the interpretation of the P-map as a pure phosphorus distribution.
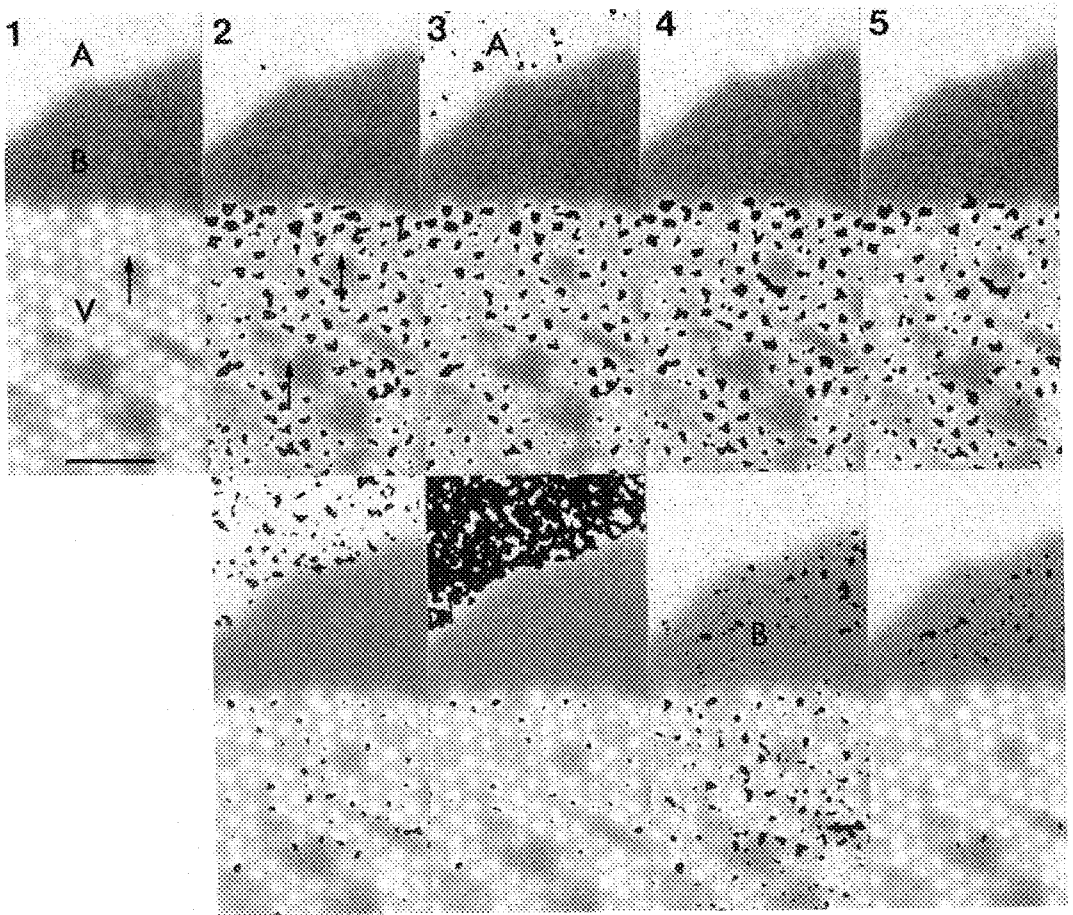
FIG.1 Phosphorus sensitive image of the series (dE=155 eV). V area of viruses, A double-layer, B single layer of carbon film. The arrow points to a single virus. Scale bar 100 nm.

FIG.2-5 ESI-detection of virus-RNA by the phosphorus-signal. Each pair contains the P-map (at 155 eV; upper row) and the mapping before the phosphorus-edge (at 120 eV; lower row). The map is a binary image (black) in overlay with FIG.1.

FIG.2 Three-window power law: The viruses in the P-map are well separated from the background. The detection mask in the non-phosphorus control highlights the mass-thick regions indicating that mass-contrast is part of the calculated element-distribution. Note that some viruses are not detected in the P-map (arrow). They are supposed to contain no RNA.

FIG.3 Three window exponential law: The viruses in the P-map are not completely separable from the mass-signal represented by region A.

FIG.4 Two-window differential law: The P-map is a clear detection of the viruses. In contrast to FIG.2-3, the non-phosphorus mapping is sensitive to thin regions (B).

FIG.5 Two-window jump ratio: The signal over the viruses in the P-map is much weaker than with the other methods. The suppression of mass-thick regions is stronger than in FIG. 4.

THE STRUCTURE OF FROZEN-HYDRATED MEMBRANE SKELETONS OF HUMAN RED BLOOD CELLS

Li Yang and Robert Josephs

Laboratory for Electron Microscopy and Image Analysis, Department of Molecular Genetics and Cell Biology, The University of Chicago, Chicago, IL 60637

The red cell membrane skeleton is a two-dimensional network of structural proteins attached to the cytoplasmic surface of the erythrocyte membrane. The major components of the skeletal network are spectrin, actin and band 4.1. Reversible shape changes in the red cell are believed to be mediated by changes in the conformation of spectrin. In this study cryo electron microscopy was used to examine membrane skeletons that were embedded in a thin layer of vitreous ice supported by a fenestrated carbon film. This avoids drying and flattening effects and the attendant changes in salt concentrations and pH associated with negative staining.

Ghosts derived from normal human red cells were incubated with 4 volumes of 2.5% Triton X-100 in 5 mM sodium phosphate (pH 7.6) for 1 hour at 4°C. Membrane skeletons were isolated on a discontinuous density gradient of 10% and 60% sucrose and dialyzed against 1 mM sodium phosphate buffer (pH 8) containing 0.1 mM DTT for 4-6 hours. Skeletons were applied to carbon-coated fenestrated films that had been treated with 1% Alcian blue and rinsed thoroughly with distilled H_2O and frozen in liquid ethane. The specimens were examined at -172°C in a Philips CM10 microscope.

Figure 1 presents a cryo electron micrograph of spread membrane skeletons in 1 mM sodium phosphate buffer (pH 8.0) containing 0.1 mM DTT. The frozen-hydrated membrane skeleton is organized into a polygonal lattice of actin junctional complexes crosslinked by spectrin tetramers, which are usually sinusoidal. The actin junctional complexes appear as short rods or globules. We attribute the variable appearance of these complexes to variations in the orientation of the actin complexes (in negatively stained specimens the actins are flattened on the grid whereas in frozen hydrated specimens the actin complexes are free to assume any orientation). There are generally 6 to 8 spectrin tetramers radiating from each junctional complex. Each actin junctional complex is crosslinked to 5 or 6 its nearest junctional complexes by either a single spectrin tetramer or two separate spectrin tetramers (Figure 2).

The average end-to-end distance of spectrin tetramers is 179.65 nm (SD 9.44 nm). The average contour length of spectrin tetramers is 212.06 nm (SD 8.91 nm). The average period and amplitude of the sinoid is 61.84 nm (SD 5.26 nm) and 7.26 nm (SD 1.14 nm) respectively.

The significant feature in the images of frozen-hydrated membrane skeletons is that spectrin tetramers usually display sinusoidal shapes, whereas negatively stained spectrins are usually straight.[1,2] The number of cycles in each spectrin tetramer ranges from 2.5 to 3.25 (average=2.9). Because a sine is the two-dimensional projection (side-on) view of a helix, we speculate that the spectrin tetramer may be a helical molecule in the membrane skeleton.[3]

References

1. S. C., Liu, L. H., Derick, and J. Palek, 1987. J. Cell Biol. 104, 527-536.
2. A. M. McGough and R. Josephs, Proc. Natl. Acad. Sci. USA 87(1990)5208
3. This work was supported by NIH Grant HL22654
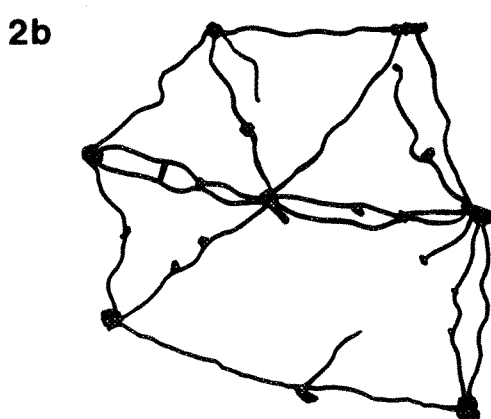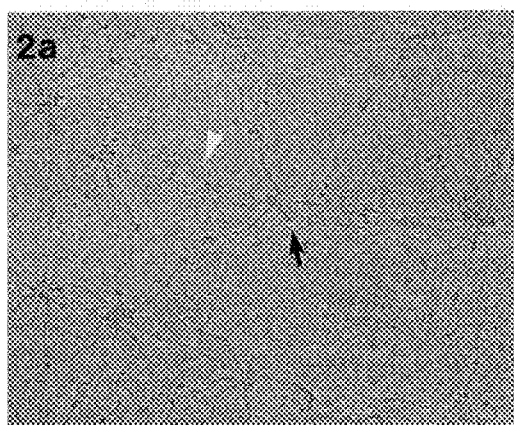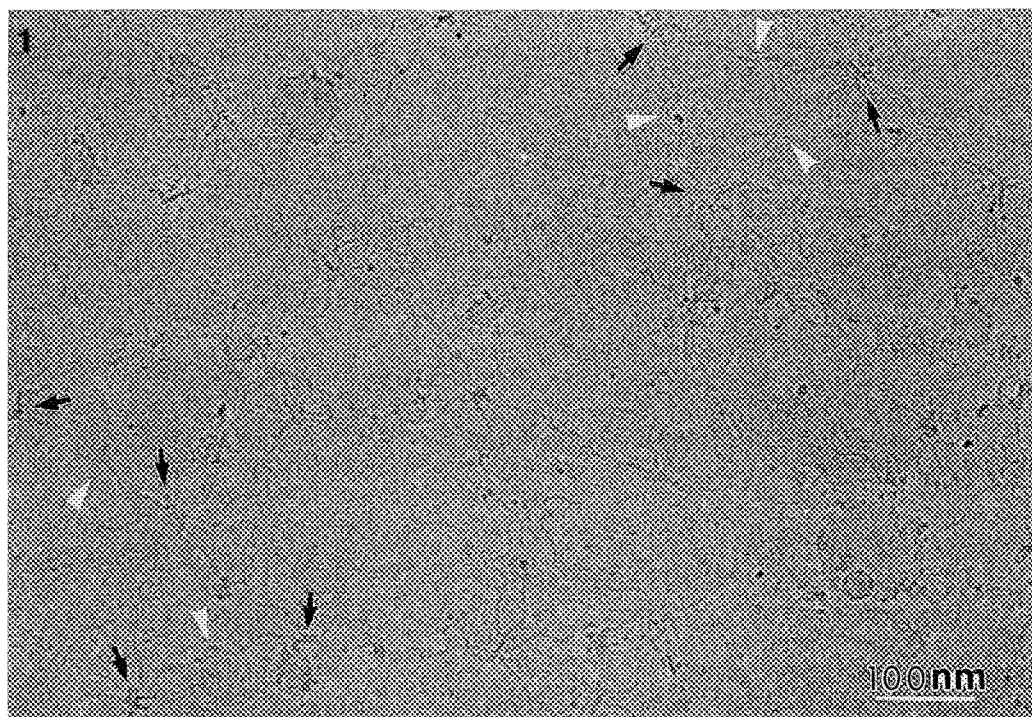
Figure 1. Cryo electron micrograph of a membrane skeleton suspended in 1 mM sodium phosphate (pH 8) containing 0.1 mM DTT. The actin junctional complexes (indicated by arrows) are crosslinked by sinusoidal spectrin tetramers (indicated by arrow heads) to form a triangulated network.

Figure 2. Each actin junctional complex is crosslinked to 5 or 6 its nearest actin complexes by either a single spectrin tetramer or two separate spectrin tetramers. (2b) is a schematic diagram of (2a). The arrow indicates the actin junctional complex to which 5 or 6 adjacent complexes are connected. The arrow head indicates the two separate spectrin tetramers that crosslink the same two complexes.

THE STRUCTURE OF MYELIN BASIC PROTEIN DETERMINED BY HIGH-RESOLUTION ELECTRON MICROSCOPY AND MOLECULAR MODELLING

D.R. Beniac, R.A. Ridsdale, M.D. Luckevich, T.A. Tompkins*, and G. Harauz

Molecular Biology & Genetics, University of Guelph, Guelph, Ontario, Canada, N1G 2W1.
*Present address: Lallemand Inc., Laboratoire R&D, 6100, Royalmount, Montréal, Québec, Canada, H4P 2R2

Multiple sclerosis (MS) is characterised by the active degradation of the myelin sheath, and is thought to be precipitated by an autoimmune response to one or more of the sheath's protein components. Myelin basic protein (MBP) is generally considered to be the antigen responsible for autoimmunity and is one of the most abundant proteins of the sheath [1,2]. Knowledge of the tertiary structure of MBP, and its organisation on lipid layers and within the compacted myelin multilayers, is essential to understanding the organisation of the myelin membrane and the mechanisms of development of autoimmunity in MS. MBP has hitherto not proved crystallisable for structural studies by X-ray diffractometry despite much effort in this area. We have initiated high-resolution electron microscopical analyses of MBP. When imaged as individual particles, a recurring motif is that of a "C" shape in projection, of approximately 2 nm in thickness and 8 nm in length (Figure a - field of view; Figure b - class averages after single particle analysis; Figure c - 3D reconstruction). The total length of this particle is less than would be expected if the polypeptide chain were fully extended. Crystallisation experiments on MBP using monolayers of lipid mixtures (phosphatidylcholine, phosphatidylserine, dioleoyl phosphatidylethanolamine, galactocerebroside) yielded microcrystalline structures with a repeating pattern of packed protein molecules of size 5 nm, with an arm width of 2 nm and total length of 10-11 nm (Figure d). Molecular modelling of MBP based on the schemes proposed by Stoner [3] and Martenson [4], and using coordinates of the β sheet backbone of bacteriochlorophyll A protein and energy minimisation of intervening segments, yielded a compact structure of size and appearance consistent with the electron microscopical data (Figure e). The bend of the C shape appears due to a natural curvature in the β sheet. These results are fully congruous with MBP having a regular secondary structure and domains that are potentially flexible with respect to one another. Energy minimisation experiments were performed on this model structure after specific post-translational modifications such as phosphorylation of specific sites (*e.g.*, Ser7, Thr98) and conversion of arginine residues to citrullines. These results are consistent with biochemical data on accessibility of these sites to modification, and provide a framework for hypothesising scenarios of myelin sheath degradation in MS [5].

References

1.   R. Smith (1992). J. Neurochem. 59, 1589-1608.
2.   S.M. Staugatis *et al.* (1994). BioEssays 18, 13-18.
3.   G.L. Stoner (1984). J. Neurochem. 43, 433-447.
4.   R.E. Martenson (1986). J. Neurochem. 46, 1612-1622.
5.   This work was supported by the Multiple Sclerosis Society of Canada.
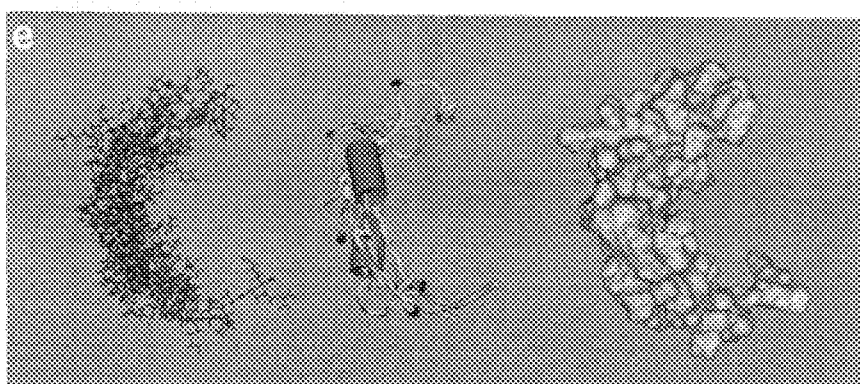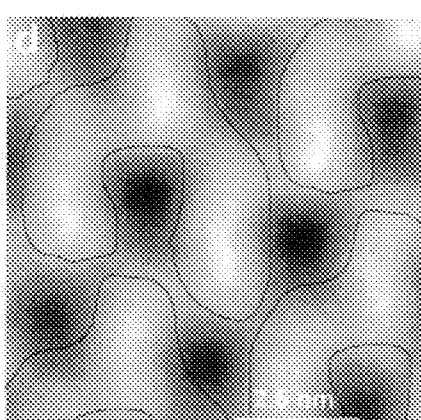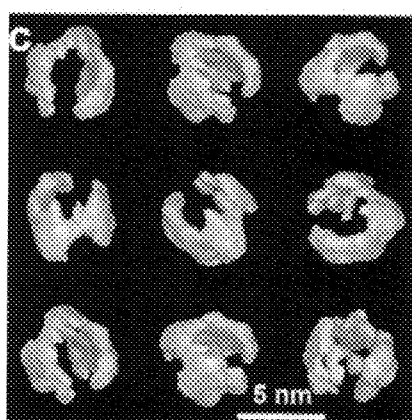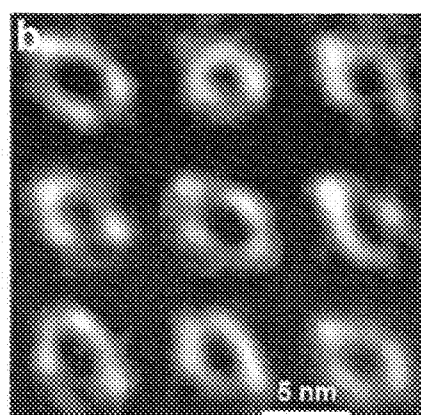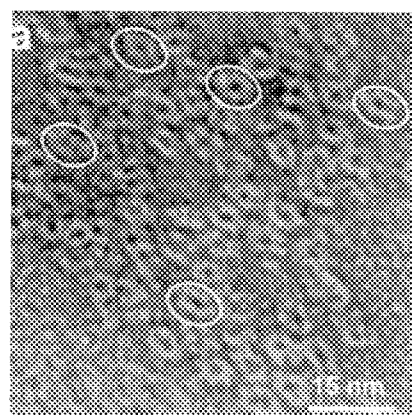
STRUCTURE OF RATTLESNAKE VENOM LECTIN DETERMINED BY SINGLE-PARTICLE HIGH-RESOLUTION ELECTRON MICROSCOPY

Peter D. Moisiuk, Daniel R. Beniac, Ross A. Ridsdale, Martin Young[+], Bhushan Nagar[*], James M. Rini[*], and George Harauz

Department of Molecular Biology and Genetics, University of Guelph, Guelph, Ontario, Canada, N1G 2W1
[+]Division of Biological Sciences, National Research Council, 100 Sussex Drive, Ottawa, Ontario, Canada, K1A 0R6
[*]Departments of Molecular and Medical Genetics and Biochemistry, University of Toronto, Toronto, Ontario, Canada, M5S 1A8

Venom from the rattlesnake *Crotalus atrox* contains a mixture of enzymes that induce a localized effect leading to hemorrhaging, necrosis and edema. As a member of the crotalid family of snake venoms, *Crotalus atrox* venom contains a C-type lectin that will agglutinate blood cells in a Ca^{2+}-dependent fashion [1,2]. The lectin is a hydrophilic protein, consisting of two covalently linked, 135 amino acid residues, identical subunits that are rich in aspartic acid, glutamic acid and lysine. Sequence homology with known carbohydrate recognition domains (CRDs) indicates that rattlesnake venom lectin (RSLV) contains a CRD motif that is not linked to accessory domains [1,3]. Preliminary X-ray diffraction and sedimentation analysis has indicated that lectin from *Crotalus atrox* forms decamers composed of two five-fold symmetric pentamers [3]. Single particles of RSVL imaged at -171°C displayed two distinct orientations on the specimen support (Figure a) following incubation in a crystallization Teflon well, coated with a lipid monolayer consisting of phosphatidylcholine and monosialoganglioside [4]. When lying in an end-on orientation, the lectin exhibited a "pentagonal ring" with an outer diameter of 6.7 nm and an inner hollow core of 1.7 nm. A side orientation was also seen, whereby a thickness of 5.8 nm was measured for the lectin. Image processing of 2280 single particles placed in 100 classes (Figure b) led to 3D reconstructions of RSVL (Figure c). Density limited 3D reconstructions showed the lectin to be made of two five-fold symmetrical rings covalently linked between the five subunits that constitute each ring of this homodimer. These results are consistent with sedimentation and preliminary X-ray diffraction analysis on the shape of RSVL and provide the framework for structural verification by 2D electron crystallography [3].

References

1.   Hirabayashi J, Kusunoki T, Kasai K-I (1990) J. Biol. Chem. 266, 2320-2326
2.   Gartner TK, Ogilvie ML (1984) Biochem. J. 224, 301-307
3.   Rini JM (1995) Annu. Rev. Biophys. Biomol. Struct. 24, 551-577
4.   Mosser G, Brisson A (1991) J. Struct. Biol. 106, 191-198

Figure a - Single particles of RSVL in varying orientations on specimen support.

Figure b - 100 classes of single particles averaged from a population of 2280

Figure c - 3D reconstructions of RSVL. Top row modelled at a molecular weight of 163 kDa. Density threshold on reconstruction is increasing as the bottom row is approached.
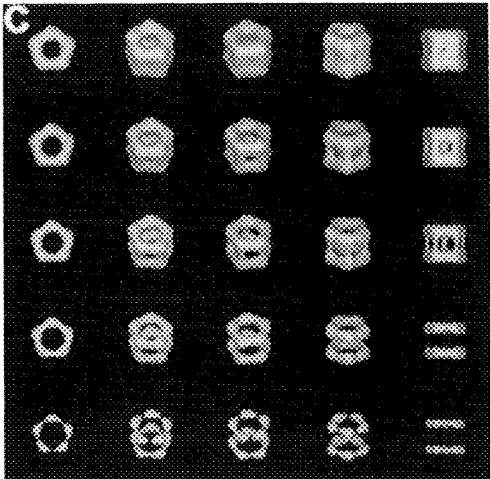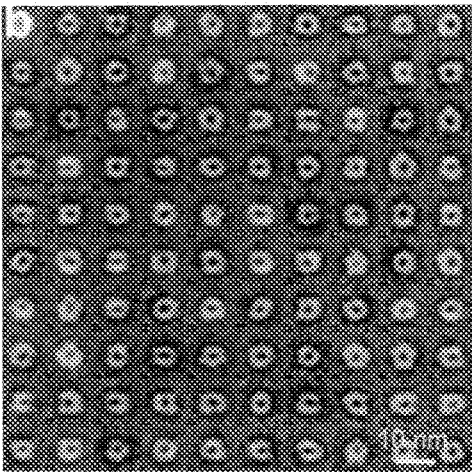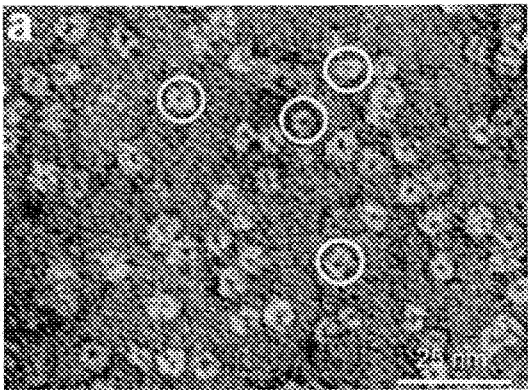
HIGH RESOLUTION ROTARY SHADOWING OF HERPES SIMPLEX VIRUS HELICASE PROTEINS

R. C. Moretz* and James J. Crute**

Departments of *Analytical Sciences and **Immunological Diseases, Boehringer Ingelheim Pharmaceuticals, Inc. Ridgefield, CT 06877

Herpes viruses cause numerous human diseases. Herpes Simplex viruses (HSV1 and HSV2), varicella zoster virus (VSV),cytomegalovirus (CMV), and Epstein-Barr Virus (EBV) cause conditions ranging from peripheral sores (HSV, VSV), generalized viremia (CMV) and recurrent malaise (EBV). The common targets for HSV are neurons in the CNS, peripheral nerve cells or plexuses of sensory ganglia in highly innervated epithelium (e.g. lips, genitals).

Interfering with the mechanisms of infection and virus production depends on the ability to target specific stages of viral reproduction. Helicases are enzymes that are essential for the duplication of viral DNA. The origin binding protein (OBP) helicase (encoded by the DNA replication gene UL9) binds to sequences in DNA at the three replication origins. These origins are points within the HSV chromosome where DNA replication initiates. The protein is a 83kDa polypeptide which exists as a dimer. Although the role of the UL9 helicase in HSV DNA replication has not been exactly determined, by analogy to other eukaryotic origin binding replication proteins, the binding and enzymatic action of the UL9 helicase to the origin sequences may initiate the assembly of a multiprotein replication complex. Helicase-primase (the product of the DNA replication genes UL5, UL8 and UL52) acts to unwind double-stranded DNA at growing replication forks. The helicase-primase activity is expressed by a 213kDa heterodimer consisting of the 99kDa UL5 and 114kDA UL52 subunits. ICP8 (SSB--UL29 gene product) is a single-stranded binding protein of 122kDa that complexes with OBP (two SSB/OBP dimer). Each of these gene products has been expressed in insect cells with a recombinant baculovirus and purified to near homogeneity. Assays have been established for the screening of compounds that could inhibit the helicase activity of HSV1 helicases. Analysis of helicase/DNA substrate complexes under different conditions will be facilitated by a better understanding of the structure of the individual proteins.

Purified protein was diluted to 25µg/ml in high salt buffer in the presence of 50% glycerol and sprayed onto freshly cleaved mica. The mica was placed on the stage of a Cressington CFE-50 and dried in vacuo for 5min. Samples were rotary shadowed with 0.2nm Pt or W/Ta at 5° incident angle, followed by stabilization with 2.5 to 3.0nm C. Replicas were floated onto water, picked up on bare Cu grids and examined in a Hitachi H-7000 at 30,000x to 50,000x.

OBP consists of globular subunits (fig. 1). At concentrations of 1mg/ml OBP helicase is purified as a dimer, but at lower concentrations (such as those used for TEM sample preparation), both monomers and dimers are found. Images of the SSB protein show single assymmetric molecules with a closed 'C' shape (fig. 2). In the absence of ATP, TEM of the helicase-primase subassembly shows the presence of both subunits as well as the heterodimer of the helicase-primase subassembly (fig. 3a). With ATP added to the preparation, only the open 'C'-shaped heterodimer is found (fig. 3b).

High resolution TEM of rotary shadowed HSV helicases and the single-stranded binding protein has shown that there are distinct structures that will be distinguishable during analysis of the protein-protein and protein/ssDNA complexes involved in HSV helicase activity.
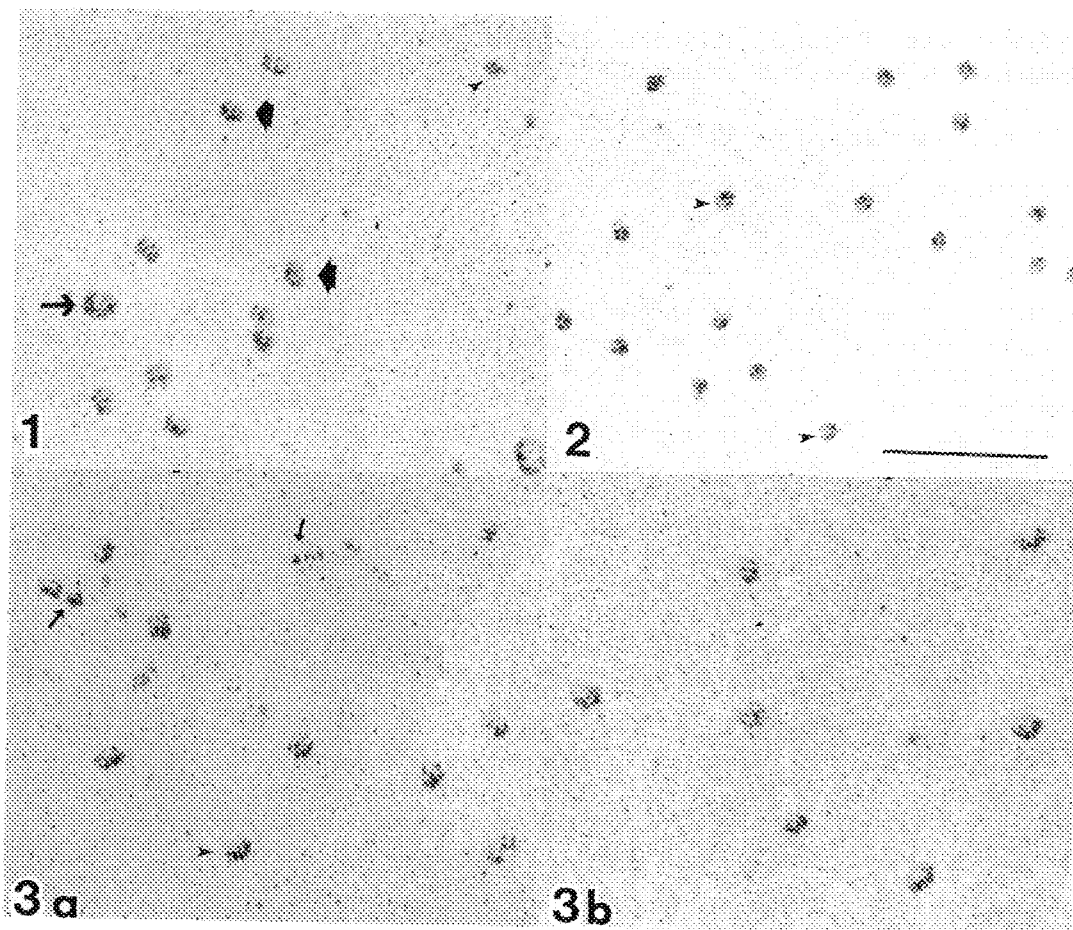
Figure 1. OBP molecules are visualized as monomers (➤), dimers (◗) and multimers (➔) in these preparations. Larger aggregates are occasionally seen, but not shown in this field. Figure 2. SSB is primarily seen as monomers. The small cleft is visible in some of the molecules (➤) but is more obvious when viewed in stereo (not shown). Figure 3. (a) Helicase-primase subassembly prepared without ATP shows both the complete assembly (➤) with the 'C' shape as well as the individual subunits (→); (b) in the presence of ATP only intact subassemblies are seen with the characteristic 'C' configuration. Magnification bar equals 100nm.

DIFFERENTIAL CONTRAST IMAGING OF HIGH RESOLUTION TEM MICROGRAPHS OF ROTARY SHADOWED HETERODOUPLEX PROTEIN COMPLEXES

R.C. Moretz*, James J. Crute*, K.-R. Peters**

*Departments of Analytical Sciences and Immunological Diseases, Boehringer Ingelheim Pharmaceuticals, Inc., Ridgefield, CT 06877
**Molecular Imaging Laboratory, University of Connecticut Health Center, Farmington, CT 06030

The resolution attainable from rotary shadowed molecules is limited by sample preparation method, the distribution of the metal through the shadowing procedure and the grain structure of the metal film. Utilizing very thin metal coats (less than a few 0.1 nm measured perpendicular to the substrate) and metals that form small grain sizes improves the resolution. Differential hysteresis (DH) processing of the micrograph data offers the opportunity to utilize the full range of contrast information present in the images and to improve the structural analysis and interpretation of high resolution rotary shadowed macromolecules. A protein complex of interest that shows varying structures in the presence or absence of ATP was prepared by glycerol spray onto freshly cleaved mica. The mica was placed on the stage of a Cressington CFE-50 and dried in vacuo for 5 min. Samples were rotary shadowed with 0.2 nm W/Ta (measured on the support) at 5° incident angle, followed by stabilization with 2.5 to 3.0 nm C. Replicas were examined in a Hitachi H-7000 with a LaB_6 gun at 100 kV at direct magnifications of 100,000x. Micrographs were taken on Kodak type 4489 EM film at one f-stop higher than for standard silver halide printing to provide a full gray scale data file during digitization.

TEM negatives were digitized at 300 dpi to 14-bit gray scale using an AGFA Arcus II flat-bed scanner with FotoTune 2.08 software. The scanned data were acquired with linear lookup tables as positives and were handled as 16-bit gray level TIF files. The digital data were processed in a PiXISION AP128 image workstation (JEOL USA, INC., Peabody, MA) for differential contrast imaging. The processing utilizes DH properties of the image for segmentation of contrast patterns[1].

The protein complex is a heterodimer of two subunits of 99 kDa and 114 kDa and was evenly dispersed (Fig. 1). The original image had an intensity range (IR) 1-11,189 and was scaled to 8-bit. It did not reveal most of the fine metal contrast (a) that could be observed after DH imaging of selected contrasts (b). After 3x bicubic zoom still no detailed contrast could be visualized (c). A very low noise component (d) of less than 1% IR proved high quality of the scanned digital data. The fine structure of the metal film generated a contrast pattern of 3.5% IR (e) over the whole sample surface that obscured fine molecular detail. The significant metal generated detail contrast was observed at a contrast range of 3.5% IR (f) delineating the shadow around the particles and decorating the smallest details on the molecules. Geometrical metal accumulation on the side of the molecules provided the major contrast of 92% IR and imaged the major topographic features (g). This contrast imaged the polymeric state of the molecules. The smaller metal contrast component provided an accurate size and shape which was not seen in the major contrast component or in the original image. Both contrasts constituted the pertinent information and when reconstituted (3+1) into a composite DH image (b,h) was free of noise or inherent metal film structures. The composite image provided all important contrasts for quantification of the polymeric qualities of the aggregates, i.e., shape (U-shape), size and multimeric state.

1. K.-R. Peters, *Proc. Microscopy Microanalysis 1995*: 642-643
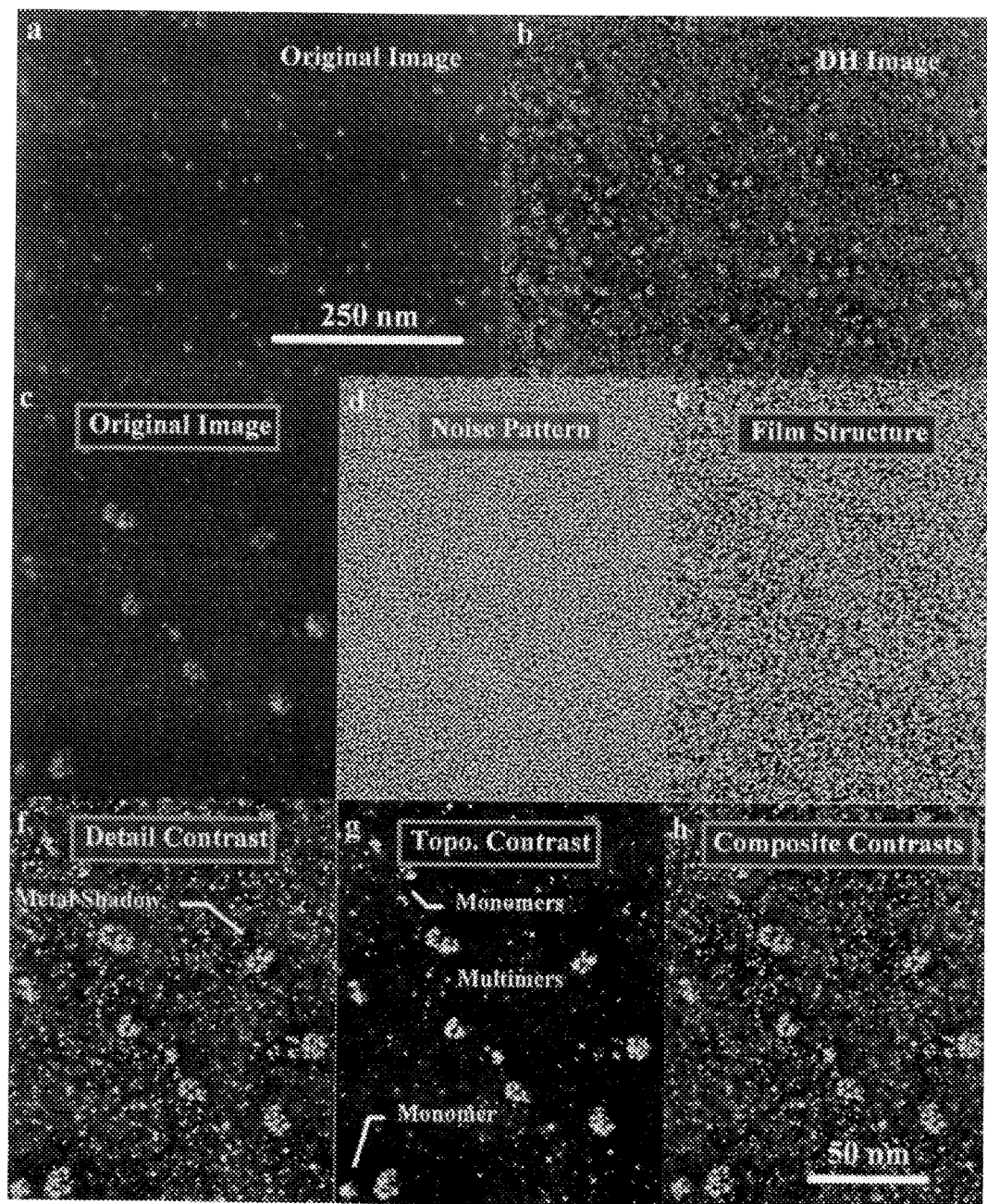
Fig. 1.- (a-h) TEM micrograph of metal coated heteroduplex protein complexes. For specifics see Text.

VISUALIZATION OF CO-AXIALLY COILED dsDNA IN BACTERIOPHAGE T7 CAPSIDS BY CRYO-ELECTRON MICROSCOPY

Naiqian Cheng[*], Mario E. Cerritelli[*], Alan H. Rosenberg[**], Frank P. Booy[*] and Alasdair C. Steven[*]

[*]Laboratory of Structural Biology, National Institute of Arthritis, Musculoskeletal, and Skin Diseases, National Institutes of Health, Bethesda, MD 20892; [**]Biology Department, Brookhaven National Laboratory, Upton, NY 11973

The packaging of viral DNA into a pre-formed procapsid structure and its subsequent release from the mature virion during infection, constitutes one of the basic phenomena of the viral life-cycle which still remains to be understood. The DNA must package at a high density into the head to allow efficient utilization of the space available, overcome the mutual electrostatic repulsive forces between the strands, and be readily available for release upon infection. Cryo-electron microscopy has proven to be an invaluable tool for visualizing the internal organization of the packaged DNA inside viral capsids[1]. We report on the effectiveness of this technique in examining the packaging of the ~ 40,000 bp double-stranded DNA genome inside the capsids of bacteriophage T7.

A mutant of T7, which completely deletes the tail genes, was purified from lysates of infected E. coli BL21 cells by cesium chloride centrifugation, followed by dialysis against phage dilution buffer (0.2 M NaCl, 2 mM Tris-Cl, pH 8, 0.2 mM EDTA). Samples of the purified phage, at a protein concentration of ~ 3 mg/ml, were quench-frozen in liquid ethane and transferred into a Gatan 626 cryo-holder. Frozen-hydrated samples were visualized in a Philips CM20FEG using low dose techniques. Micrographs were recorded relatively close to focus, with the first zero of the phase contrast transfer function in the range of $(1.9 \text{ nm})^{-1}$ to $(2.7 \text{ nm})^{-1}$.

The T7 heads produced in this infection contain DNA but lack tail structures. Electron micrographs of negatively stained preparations show the core, which is attached to the inner surface of the connector vertex, as centered in the majority of cases. This indicates that these phage have a tendency to orient preferentially on the grid to give a view along the 5-fold symmetry axis that passes through the connector vertex. This observation was confirmed by determining the orientations of the same T7 mutant phage imaged in the frozen-hydrated state using the common-lines procedure[2].

The cryo-images (Fig. 1) show clear spiral or ring shaped patterns that have strong contributions in the spatial frequency range that corresponds to the ~ $(2.6 \text{ nm})^{-1}$ liquid crystalline side-by-side packing of the DNA duplexes (Fig. 2). In all the viral particles which have this specific orientation (a view down the connector vertex), a distinct pattern of spiral-like concentric curves is evident. This pattern is enhanced by correlation averaging (Fig. 3), implying that the DNA is packaged in a rather consistent manner from particle to particle[3], and its appearance is in agreement with an axial winding of the packaged DNA around the core[4,5].

REFERENCES

1. Booy, F. P., Trus, B. L. et al., EMSA (1992) pp. 452-453.
2. Crowther, R. A., Proc. R. Soc. London B (1971) 261, 221-230.
3. Cerritelli, M. E., Cheng N. et al., Biophys. J (1996) 70, 363.
4. Richards, K. E., Williams et al., J. Mol. Biol. (1973) 78, 255-259.
5. Earnshaw, W. C. and Harrison, S. C., Nature (1977) 268, 598-602.
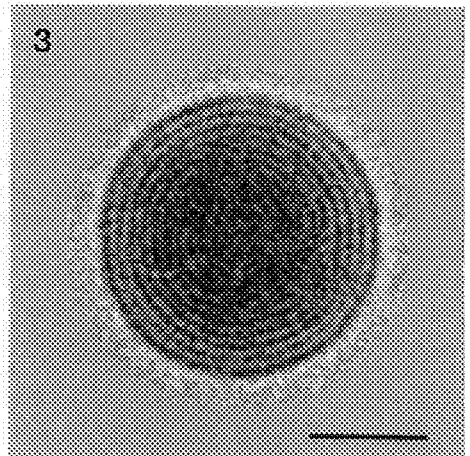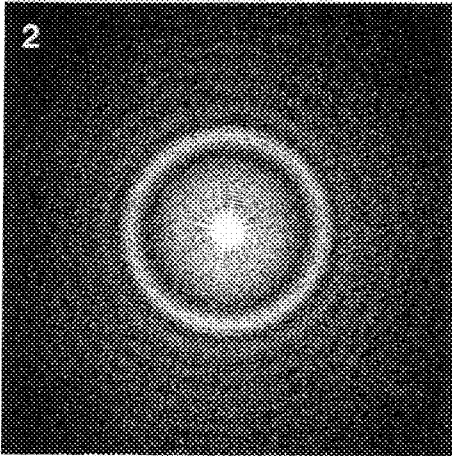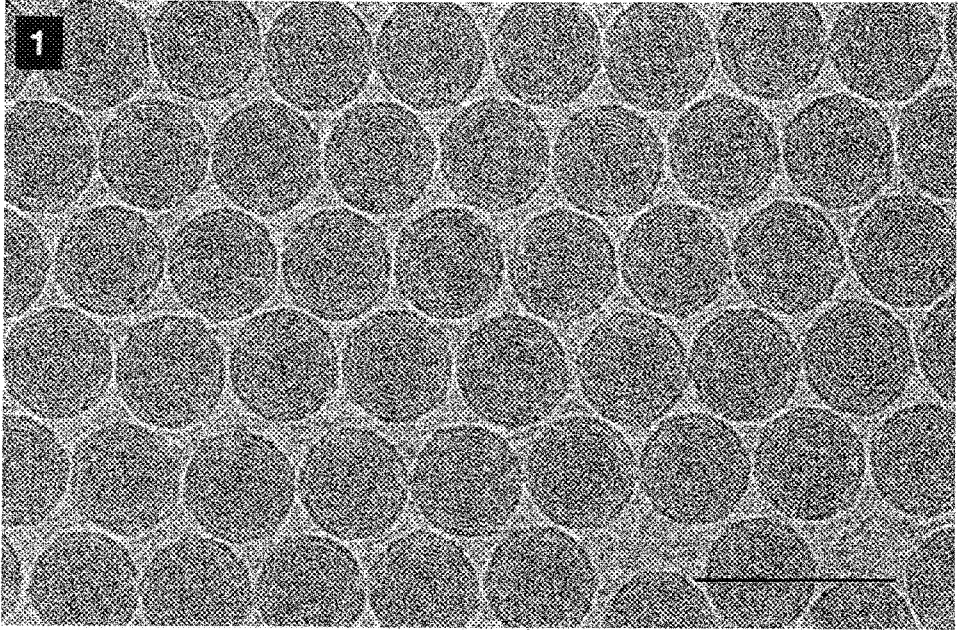
Fig.1: Cryo-electron micrograph of bacteriophage T7 virions, showing the spiral-like concentric curve motif of encapsidated DNA duplexes. Bar = 100 nm.

Fig. 2: Optical diffraction pattern of Fig. 1 reveals a strong ring that corresponds to the 2.6 nm spacing of the DNA strands.

Fig. 3: Computer averaged representation of 21 spiral views. The spacing between the observed rings, the outermost of which is the protein shell, agrees with the expected 2.6 nm spacing of the DNA strands. Bar = 25 nm.

LOCATION OF SUBUNITS IN THE ACETYLCHOLINE RECEPTOR BY ANALYSIS OF ELECTRON IMAGES OF TUBULAR CRYSTALS FROM *TORPEDO MARMORATA*

David A. Burkwall,[*] Robert Josephs,[*] Jennifer Holly,[*] David Richman[**] and Robert Fairclough[**]

[*]Laboratory for Image Analysis and Electron Microscopy, Department of Molecular Genetics and Cell Biology, The University of Chicago, 920 East 58th Street, Chicago, Illinois 60637
[**]Department of Neurology, University of California Davis, Davis California

The nicotinic acetylcholine receptor(AChR) is a membrane protein containing four different homologous polypeptide chains[1] (two copies of an α-subunit and single copies of β, γ, and δ). These subunits assemble about a central cavity, which is thought to delineate the ion-selective channel. In tubular crystals from *T. marmorata* receptors normally exist as dimers, paired through disulphide bonds between the δ-subunits. Conflicting reports still arise concerning the relative locations of these subunits around the central axis. It has been proposed that the β-subunit lies between the two α-subunits[2] or that the γ subunit lies between the two α-subunits.[3] Here we examine the locus of two subunit-specific labels, mAb 383C and 247G, bound to receptors and averaged in each case from over 5,000 molecules.

mAb 383C and 247G were produced from Torpedo-AChR immunized rats. Alpha-bungarotoxin can block the binding of these mAbs to the AChR. 383C also inhibits binding to the AChR by carbamylcholine whereas 247G does not. Complexes of 383C with Torpedo AChR bind no bungarotoxin whereas the complexes formed with 247G bind half as many toxins as untreated receptors. Studies have mapped the 383 epitope to α-subunit residues 187-199, which are also affinity labeled by acetylcholine. The 247G epitope specifically modifies (eliminate) the high affinity tubocurarine binding (6) at the α–γ subunit interface. In AChR enriched membranes each of the mAbs binds to a single site on each AChR. The binding of 383C inhibits the binding of 247G, and binding of 247G inhibits the binding of 383C.

Electron micrographs of tubes were selected for analysis based on their optical diffraction pattern. The lattice was straightened using the procedure of Kubalek et al(2) and Henderson et al(4). Several different reference images were used and compared to get the best possible straightened images. A cross-correlation map was produced based on the comparison of the reference image with the whole image, with peaks being generated at positions of best match. Deviations from the ideal lattice were calculated and applied to correct the original lattice. The fourier transforms of straightened images based on the different reference images were compared based on the size of the reflections and their intensity. The other side of the image was then lattice passed and the same procedure followed.

The fourier transforms of the corrected images were used to obtain structure factors which were combined to form an averaged set for unlabeled and labeled tubes. The images combined were all the same size and were scaled to the same average amplitudes before being averaged. Difference maps were then obtained to identify the positions of the ligands in the crystal lattice.

References:
1. A. Brisson & N. Unwin, J. Cell Biol. 99 (1984) 1201
2. E. Kubalek et al., J. Cell Biol. 105 (1987) 9.
3. S. Hamilton et al., Biochemistry 24 (1985) 2210
4. R. Henderson et al., Ultramicroscopy 19 (1986) 147.
5. Gomez, C.M. and Richman, D.P. Proc. Natl. Acad. Sci. USA. 80 (1983) 4089.
6. Mihovilovic, M. and Richman, D.P.J. Biol. Chem. Vol. 259 (1984) 15051.
7. Mihovilovic, M. and Richman, D.P J. Biol. Chem. 262, (1987) 4978.
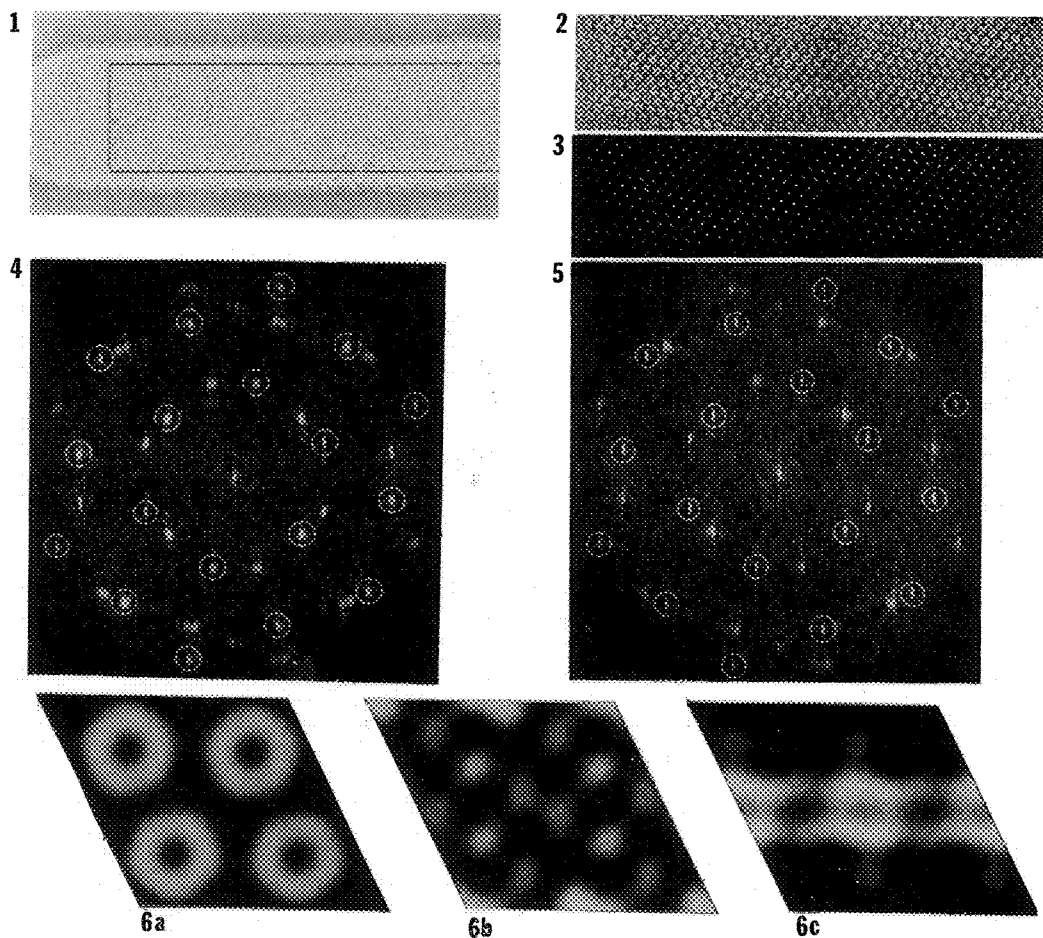
Fig 1. A tube containing negatively stained acetylcholine receptors. The area selected for processing is outlined.

Fig 2. Fourier filtered image of the area selected in figure 1.

Fig 3. Cross correlation map used in the straightening procedure.

Fig 4. Fourier transform of the unstraightened tube. Note that the reflections are somewhat blurred due to the disorder in the tube.

Fig 5. Fourier transform of the straightened tube. In figs 4 and 5 the reflections corresponding to the side being straightened are enclosed in circles. The superlattice reflections are not indicated in order to minimize congestion.

Fig 6. Electron density maps calculated from structure factors obtained from the Fourier transforms.
a. Native
b. Difference map between native and 383C.
c. Difference map between native and 247G.

COMPARISON OF POLYMERIZATION OF DEOXY-SICKLE CELL HEMOGLOBIN IN HIGH AND LOW CONCENTRATED PHOSPHATE BUFFERS

Zhiping Wang, Yimei Chen and Robert Josephs

Laboratory for Image Analysis and Electron Microscopy, Department of Molecular Genetics and Cell Biology, The University of Chicago, 920 East 58th Street, Chicago, Illinois 60637

Substitution of Val for Glu-ß6 in the ß-globin chain of hemoglobin (Hb) results in deoxy-sickle hemoglobin (HbS) forming fibers which cause sickle cell anemia.[1] We have previously determined the three-dimensional structure of the HbS fiber from electron micrographs and synthesized a model depicting the contacts stabilizing the fiber.[2] In order to test the contacts predicated by the model we are preparing site directed mutants. However high concentrations of hemoglobin (ca. 160 mg/ml) are required for polymers to form. Quantities of the order of 10-20 mg are available from most site directed mutant preparations. Increasing the phosphate buffer concentration to 1.5 M can reduce the concentration of HbS required for polymerization. However the use of high concentrations of phosphate buffer to induce polymerization has been criticized because there is little data relating the structure of fibers formed in high phosphate to the structure of fibers formed under physiological conditions.[3, 4]

Accordingly we have characterized the structures formed in high phosphate to determine if they are similar to those formed under physiological conditions. Experiments involving stirred solutions (25mg/ml HbS, 1.5 M potassium phosphate at pH 6.2-7.0) were carried out in a humidified oxygen-free nitrogen tent. Hemoglobin S preparation and negative staining have been described.[5] Electron microscopy was carried out with a Philips CM120. Optical transforms were recorded using a folded optical diffractometer and measurements from electron micrographs and optical transforms were made using a digital Nikon model 6C microcomparator.

HbS was polymerized in 1.5 M phosphate at a concentration of 25 mg/ml. Fibers form first (Figure. 1) and after about 10 hours they begin to form other types of structures such as bundles, macrofibers(Figure 2), macrofiber bundles and crystals which have the same appearance as the corresponding particles formed in low phosphate buffer (~160 mg/ml HbS, 0.05 M potassium phosphate at pH 6.2-7.0). In addition optical diffraction of the micrographs of fibers, bundles, macrofibers and macrofiber bundles reveals characteristic spacings of $1/32\text{Å}^{-1}$ and $1/64\text{Å}^{-1}$ respectively which are the same as those obtained in low phosphate. Electron micrographs and optical diffraction patterns of HbS crystals in high and low phosphate (viewed down the a, b and c-axis) are similar and have the same unit cell dimensions (a=64 Å, b=185 Å, c=53 Å). On the basis of these preliminary studies, the pathways of polymerization in high and low phosphate buffers are similar and HbS fibers and other species formed in high phosphate appear to have the same structures as those formed in low phosphate.

References

1. W. A. Eaton et al., *Advances in Protein Chemistry*, 40(1990)63-297
2. S. J. Watowich et al., *J Structural Biology*, 111(1993)161-179
3. K. Adachi et al., *Blood Cells*, 8(1982)213-24
4. K. Adachi et al., *The Journal of Biological Chemistry*, 254(1979)7765-71
5 T. E. Wellems et al., *Journal of Molecular Biology*, 135(1979)651-74
6. This work was supported by NIH grant HL22654
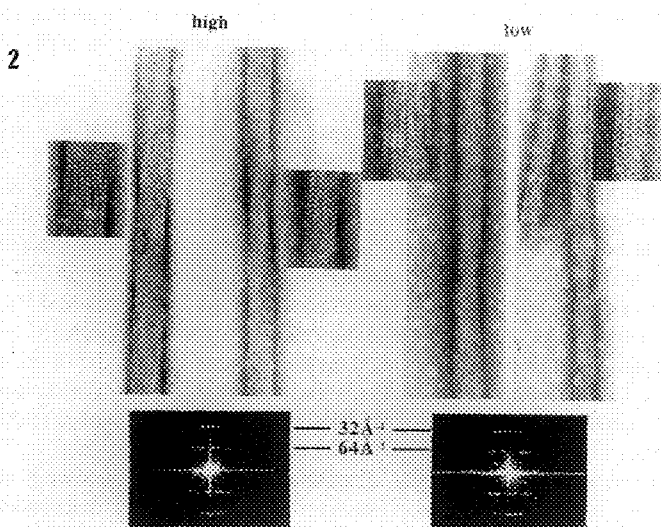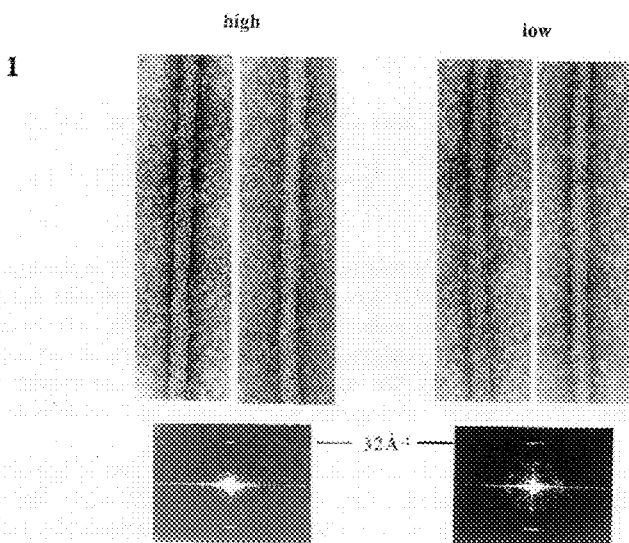
Figure 1. Electron micrographs of negatively stained HbS fibers formed in high (1.5 M) and low (0.05 M) phosphate buffers

Figure 2. Electron micrographs of negatively stained HbS macrofibers with 6 rows and 4 rows of double strands formed in high (1.5 M) and low (0.05 M) phosphate buffers.

BIOLOGICAL CRYSTALS FORMATION STUDIED BY HTREM AND IMAGE ANALYSIS

P. HOULLE[*], F.J.G. CUISINIER[*], J.C. VOEGEL[*] AND P. SCHUTZ[**]

*Centre de Recherches Odontologiques, INSERM Unité 424, 1, Place de l'Hôpital, 67000 Strasbourg, France
** Institut de Génétique et de Biologie Moléculaire et Cellulaire, CNRS / INSERM / ULP, 1, rue Laurent Fries, 67404 Illkirch, France

High resolution electron microscopy (HREM) allows the determination of the molecular crystal structure by comparing HREM images with simulated images. Direct comparison was not possible for small crystalline areas such as nanometer-sized particles or for thin crystals with weak image contrast. To overcome these problems, we used numerical image analysis to gain access to the structure informations within these minute crystals. We used this approach for the characterization of the initial mineralization steps during human amelogenesis, chicken bone and human dentine crystals growth.

Our method consists in HREM associated with both numerical image analysis and image simulation techniques (EMS) Image analysis was performed using the IMAGIC statistical. Nanoparticle subimages, 128 x 128 pixels in size, were extracted from the original micrographs by interactive selection. A circular mask with a radius of 50 pixels was applied. The mean intensity of each subimage was set to zero and its internal variance was normalized to 10. Double direct alignment procedures were used to align the images in rotation and translation against an alignment reference extracted from the data set. An average image was finally calculated to improve the signal to noise ratio.

A roundish amorphous area in human dentine (Fig. 1) was also found due to a slight contrast change at the border. Five nanoparticles (A, B, C, D, E) situated on the margin of this area were identified and individually analyzed with numerical diffractograms (A to E in Fig.2). The five patterns indicate that all the nanoparticles were observed along the [001] zone axis of HA. This observation suggest that all selected nanoparticles were similarly orientated. The signal to noise ratio of individual images was however too low to distinguish the less prominent reflections. We therefore aligned in rotation and in translation the nanoparticle images (A to E in Fig.1). The calculated average image (1 in Fig.1) highlights the common features to all images and its Fourier transform (M in Fig.2) shows more clearly the weak. This result allows us to perform a HREM simulated image of hydroxyapatite which was surimposed on the average image (3 in Fig1). In that case, the good correspondence between both images clearly indicate that the dentine nanoparticles have a structure related to HA. Similar analyses were also performed on human enamel and chicken bone nanometer-sized particles.

The rule that emerged from these observations is that all nanometer-sized particles were observed along the same zone axis. The good correspondence between this image and a calculated image obtained with the [001] HA characteristics indicate that our supposition was true and that dentine nanoparticles have a structure related to HA. This observation should constitute a strong indication for a substrate mediation of the nucleation process. The presence of the same nucleation mechanism in enamel, bone and dentine indicates that such a process is ubiquitous in vertebrate calcified tissues.
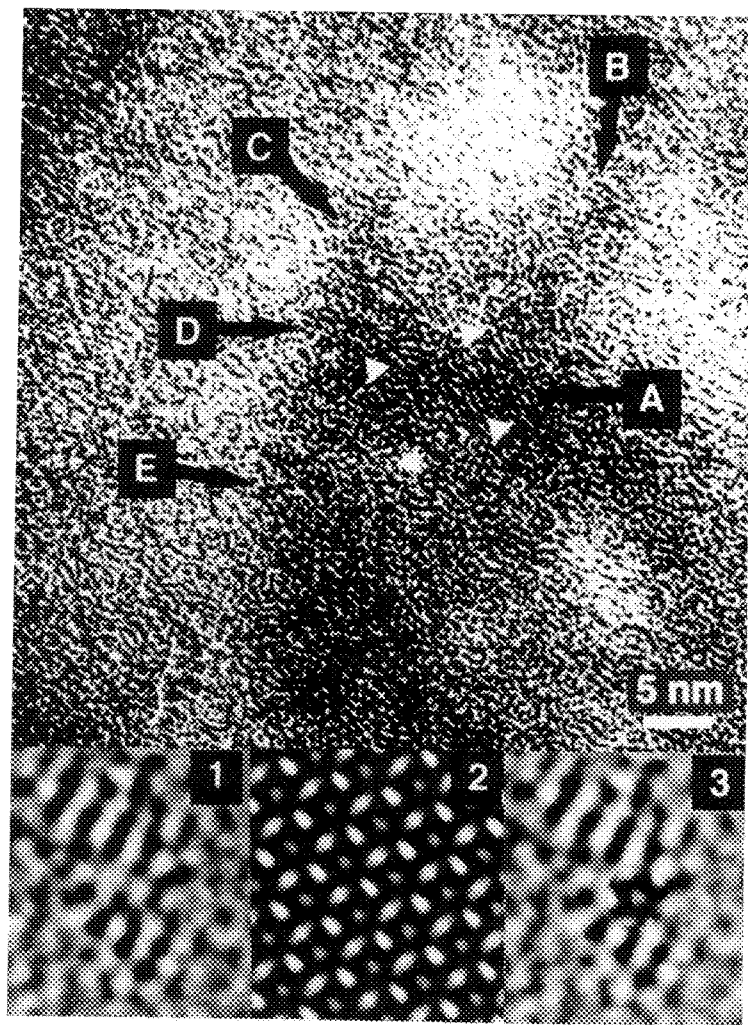
Fig. 1
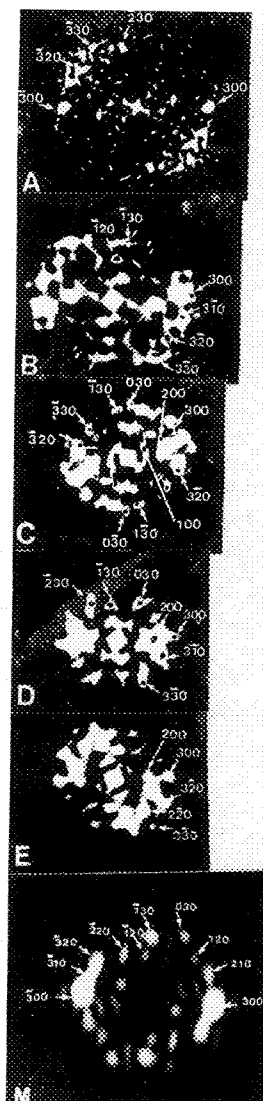
Fig. 2 →

Fig 1 :A voluminous round amorphous area with 5 nanometer sized particles (A, B, C, D, E), bar = 5 nm, an average image of the 5 nanoparticles (1), a simulation image of HA along [001] zone axis (2), simulated image of HA (objective lens defocalization = 5nm^{-1}, crystal thickness = 56nm, beam tilt = [2,0,0] and aperture shift = [0.5,0,0]) surimposed on the average image(3).

Fig 2 : numerical diffractograms corresponding to the 5 nanoparticles (A to E)) and to the average image (M), all diffractograms are characteristic of [100] zone axis of HA

CRYO-ANALYTICAL MICROSCOPY: MULTIPLE APPLICATIONS FOR PLANT STRUCTURE AND PHYSIOLOGY

C.X. Huang,[1] L.E.C. Ling,[1] M.E McCully,[2] M.J Canny [2]

[1]Carleton University Research Facility for Electron Microscopy; [2] Biology Department, Carleton University, Ottawa, Canada K1S 5B6

Carleton University's cyo-analytical SEM facility deals with a very wide range of specimens from all the sciences. One of its major specializations is the study of plant structure and function[1], as illustrated by reference to particular research programs, for example: Stabilization of structures that cannot be preserved by conventional fixation and embedding methods. Many plant tissues are constructed of extremely fragile cell walls containing large vacuoles with high turgor pressures within, interspersed with large volumes of air or fluid. Plants which grow under water are a conspicuous example, requiring large internal open channels for the transport of gases to and from the roots. Other fragile tissues and those having cell walls that are impermeable to solvents and resins have been preserved in roots of desert monocotyledons, and in tree roots. Fluids in spaces between cells. We have pioneered the discovery that many intercellular spaces in plant tissues, always believed to contain air, are in fact filled with fluid[2]. These spaces in sugarcane stems (Figs. 1&2) have been shown to contain both strong sugar solution, and an endophyte that lives on this sugar and fixes atmospheric nitrogen[3]. The large air spaces (aerenchyma) in some roots, always considered an aeration system, have been shown to contain water some of the time, and to enhance diffusion of solutes in roots. We have also discovered that roots, always considered to be organs for collecting water from soil, also excrete water to the soil at night[4]. Distribution of nutrient ions in plant tissues. Quantitative analysis of nutrient ions (especially potassium) in individual cells of roots, stems and leaves are opening up new perspectives on the acquisition, use and transport of ions in plants[5,6]. Bubbles of air and water. The processes by which water is transported in plants have again become highly controversial, and the question of whether the conducting pipes contain only water, or mixtures of water and air, are being answered by rapid freezing of the conducting tissues after various experimental treatments. Mucilages. Carbohydrate polymers with very high water contents are common components of many plants They become a unnaturally hydrated, or are dispersed in conventional preparations. We have characterized the reactions of root and bacterial mucilages to soil water, and shown how they operate to organize soil particles around roots (the rhizosphere) into coherent structures and aggregates. Phytoremediation. Plants are being used increasingly to scavenge heavy metal contaminants (e.g.., lead, cesium, radioactive isotopes) from contaminated sites. Our analyses at the single cell level show where these elements accumulate in roots, stems and leaves (e.g. Figs. 3&4), and on what time scale.

References
1. C.X. Huang et al., *Microscopy Research and Technique* 28(1994)67.
2. M.J. Canny & C.X. Huang, *Physiologia Plantarum* 87(1993)561.
3. Z. Dong et al., *Plant Physiology* 104(1994)1139.
4. M.E. McCully, *Physiologia Plantarum* 95(1995)217.
5. M.J. Canny, *Philosophical Transactions of the Royal Society of London*, B, 348(1995) 457
5. M.E. McCully, *Protoplasma* 183(1994)116
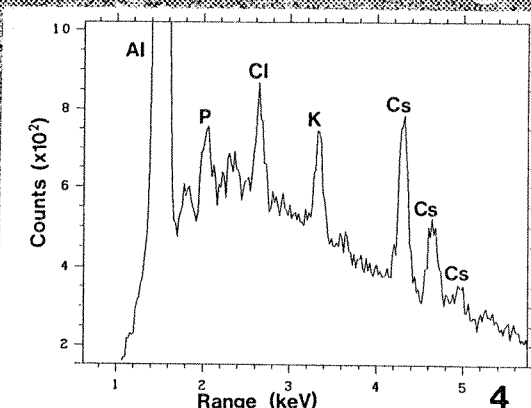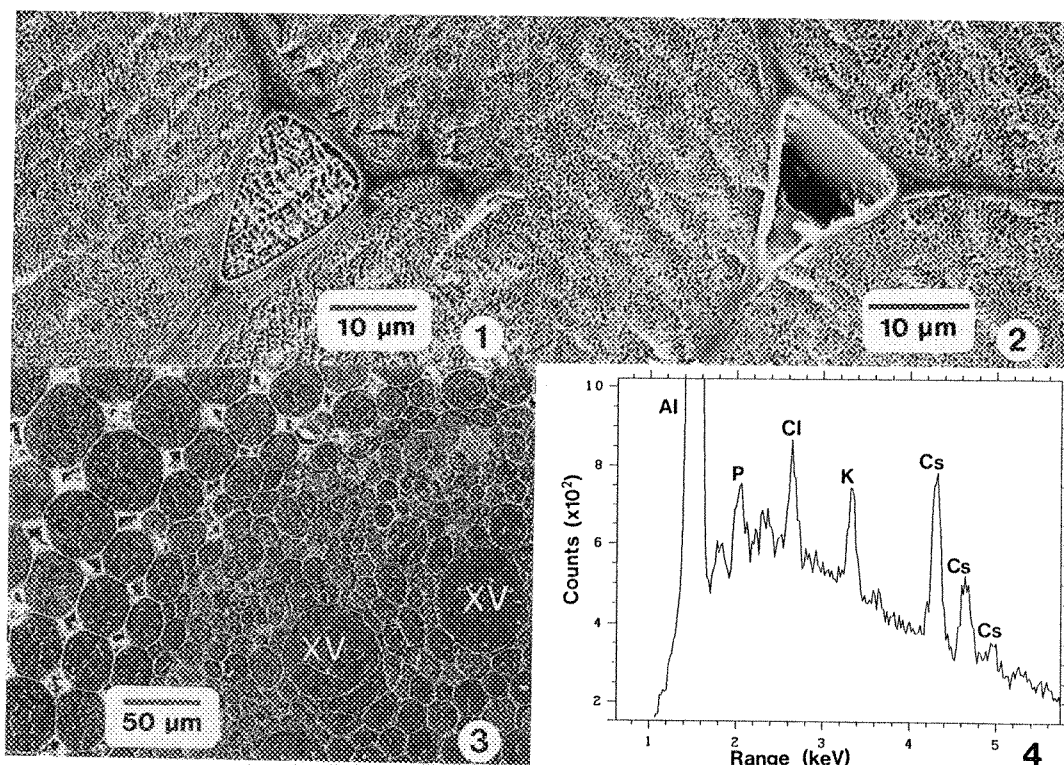
Figures 1 & 2 show portions of sugarcane stems quick-frozen and examined by cryo- SEM after a smooth transverse face was planed in a cryomicrotome then coated with Al. In both micrographs an intercellular 'space' is surrounded by parenchyma cells. This microscopy has shown that in a normal cane many of the intercellular spaces are filled with solution (Fig. 1) which is absent if the stem is centrifuged before freezing (Fig. 2). Light element analyses of the contents of the spaces *in situ* gave a carbon content of ca. 13%. This agreed closely with the 12% sucrose analyzed chemically in the fluid extracted by centrifugation.

Figure 3 is a similar preparation to those in Figs. 1 & 2 but of a root of water hyacinth. This plant can accumulate metals from contaminated water. In this case it has accumulated cesium as well as normal nutrient elements. EDX analyses of individual cells shows that specific cells associated with the vascular tissue accumulate the highest concentrations of cesium.

Figure 4 shows a typical spectrum obtained from parenchyma cells adjacent to large xylem vessels (XV) as labeled in Fig. 3.

77

HIGH-PRESSURE FREEZING AND FREEZE SUBSTITUTION FIXATION OF THE PLANT PATHOGENIC FUNGUS *EXOBASIDIUM VACCINII*

Elizabeth A. Richardson and Charles W. Mims

Departments of Botany and Plant Pathology, University of Georgia, Athens, GA 30602-7271

Members of the small fungal genus *Exobasidium* are all plant pathogens. Most species are noted for their ability to produce large fleshy galls on leaves and flower parts. They produce their hyphae and specialized absorbing structures known as haustoria inside these galls and their sexual reproductive structures (basidia) on gall surfaces. The objective of this study was to examine the feasibility of using high pressure freezing (HPF) followed by freeze-substitution (FS) fixation to prepare *Exobasidium* induced galls on *Rhododendron* sp. for study with transmission electron microscopy (TEM). HPF fixation followed by FS fixation is considered to be the best method for preserving large samples of plant tissue for TEM.[1,2] This approach has shown promise for the examination of host-pathogen relationships in fungal diseases of plants.[3-5]

Approximately 0.5 mm² pieces of infected leaf tissue were placed in 15% dextrane which served as a cryoprotectant. Samples were frozen in the Balzers HPM 010 High Pressure Freezing Machine, transferred to substitution fluid and processed for study using the methods of Hoch.[6] Thin sections cut with a diamond knife were collected on slot grids and allowed to dry onto formvar coated racks.[7] Sections were post-stained with uranyl acetate and lead citrate prior to examination.

Our results show that it is possible to obtain good to excellent preservation of fungal structures within gall tissue. The mycelium of *E. vaccini* developed within intracellular spaces of gall tissue and consisted of well-developed septate hyphae (Fig. 1). Nuclear migration from one hyphal compartment to the next was observed (Fig. 2). Some hyphal compartments gave rise to haustoria (Figs. 3,4). These structures appeared to be similar to those demonstrated previously in other species of *Exobasidium*.[8,9] Haustoria were branched to lobed structures that penetrated the host cell wall and invaginated the plasma membrane. Developing basidia were observed beneath the epidermis of the gall (Fig. 6). Synaptonemal complexes were found in the nuclei of young basidia (Fig. 5). The contents of older basidia (Fig. 6) were very well preserved. Basidia eventually ruptured the epidermis of the gall and become exposed on the gall surface.

References

1. S. Craig and L. A. Staehelin, European J. Cell Biology (1988)46, 80.
2. D. Studer *et al.*, Scanning Microscopy Supplement (1989)3, 253.
3. K. Mendgen *et al.*, in Electron Microscopy of Plant Pathogens, Eds. K. Mendgen and D. E. Leseman, Heidelburg: Springer Verlag (1991)31.
4. K. Welter and K. Mendgen, Protoplasma (1988)147, 91.
5. R. Bauer *et al.*, Canadian J. of Botany (1995)73, 867.
6. H. C. Hoch, in Ultrastructure Techniques for Microorganisms, Eds. H. C. Aldrich and W. J. Todd, New York: Plenum (1986)183.
7. C. R. Rowley and D. T. Moran, Ultramicroscopy (1975)1, 151.
8. C. W. Mims, Mycologia (1982)74, 188.
9. C. W. Mims and N. L. Nickerson, Canadian J. of Botany (1986)64, 1338.
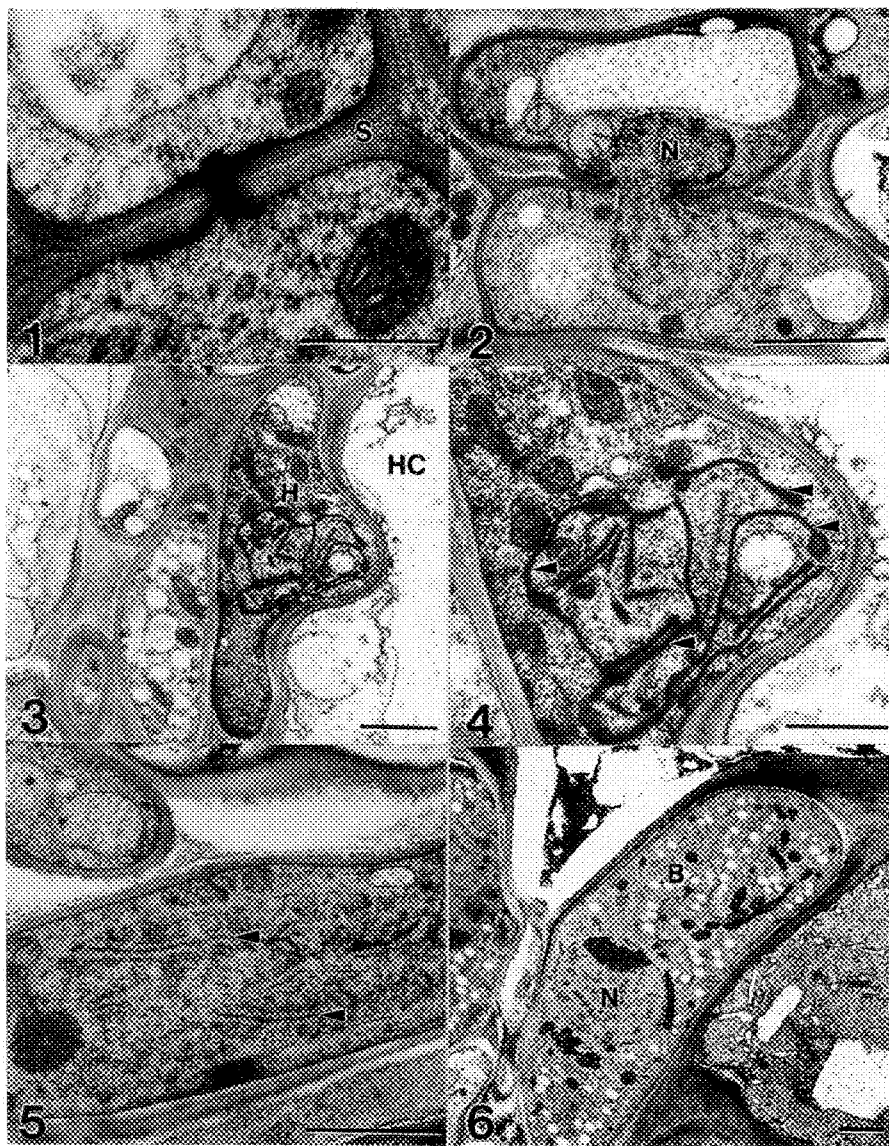
Fig. 1. Median longitudinal section of a septum (S) of *E. vaccini*. Bar = 0.25 μm.

Fig. 2. Example of a nucleus (N) moving from one hyphal compartment to the next. Bar = 1 μm.

Fig. 3. Low magnification view of a haustoria (H). The host cell is shown at HC. Bar = 1 μm.

Fig. 4. High magnification view of the haustorium from Fig. 3. Note the membranous inclusions (arrowheads) in the haustorium. Bar = 0.5 μm.

Fig. 5. Symptomenal complexes (arrowheads) in a meiotic nucleus. Bar = 1 μm.

Fig. 6. Low magnification view of a young basidium (B). The nucleus is shown at (N) and a host epidermal cell at HC. Bar = 1 μm.

A COMPARISON BETWEEN ONE NON-INVASIVE AND THREE INVASIVE PROCEDURES USED IN THE PREPARATION OF PLANT MATERIAL FOR X-RAY MICROANALYSIS

Patrick Echlin

Multi-Imaging Centre, School of Biological Sciences, University of Cambridge, CB2 3DY England

It is generally accepted that accurate quantitative elemental x-ray microanalysis of bio-organic material depends critically on the way the sample is treated before it is analysed. It is axiomatic that preparative procedures which change the local permeability of samples are going to be less useful than procedures which do not affect this critical property of cells and tissues, particularly if highly diffusible electolytes are the focus of any investigation. Thus we generally eschew ambient temperature methods in favour of low temperature techniques which either slow down or halt diffusion processes. As part of a larger study on the distribution and local concentration of aluminium in the developing leaves of tea plants, which under some circumstances can be as high 30,000ppm, a comparative study has been carried out to assess the effectiveness of four preparative techniques in retaining this element in the cell walls and vacuoles of older tea leaves which are know to contain more aluminium than younger leaves.

The four methods consist of a chemically invasive procedure which has proved succesful in retaining small organic molecules *in situ* for immunocytochemical studies; two chemically invasive procedures which have been reported to retain diffusible elements *in situ* for x-ray analytical studies and one non-chemical procedure which has been shown to retain diffusible elements in situ for x-ray analytical studies. The four procedures are as follows;
1. Quench cooled unfixed samples fractured, coated and analysed frozen hydrated at 90K[1];
2. Quench frozen unfixed samples freeze substituted in di-ethyl ether at 190K[2];
3. Quench frozen unfixed samples freeze substituted in tetrahydrofurane at 200K[3];
4. Fixed tissue partially dehydrated and embedded during progressive lowering of temperature[4].
Older leaves, 140-160mm long, were taken from a single tea plant grown in soil with a neutral pH.
Method 1. A 1 x 2 x 0.2mm piece of inter-vein tissue was cut from the mid-region of the leaf, quench cooled in melting nitrogen at 64K, fractured at 10^{-6} torr and sputter coated with 5nm of chromium at 10^{-2} torr, both at 100K, and bulk frozen hydrated material examined and analysed at 10^{-6} torr and 100K.
Method 2. 1 x 2 x 0.2mm strips of inter-vein tissue were cut from the mid vein region of the leaf, quench cooled in melting propane at 84K and freeze substituted for 21 days at 188K in absolute diethyl ether held over 0.3nm molecular sieve. Following substitution the material was infiltrated for a week at 293K under anhydrous conditions with Spurrs Low Viscosity Resin, placed in deep capsules and polymerized at 343K. The block faces were trimmed to reveal the embedded leaf.
Method 3. 1 x 2 x 0.2mm strips of inter-vein tissue were cut from the mid vein region of the leaf, quench cooled in melting propane at 84K and freeze substituted for 7 days at 203K in absolute tetrahydrofurane held over 0.4nm molecular sieve. Following substitution the material was infiltrated for a 1 week at 293K under anhydrous conditions with Spurrs Low Viscosity Resin, placed in deep capsules and polymerized at 343K. The block faces were trimmed to reveal the embedded leaf.
Method 4. 1 x 2 x 0.2mm strips of inter-vein tissue were cut from the mid vein region of the leaf, fixed for 1h at 277K with a mixture of 2% paraformaldehyde + 0.05% glutaraldehyde in 50mM PIPES buffer

at pH 7.2, dehydrated over a 3h period to 80% ethanol during which time the temperature was slowly lowered to 248K and infiltrated with LR White acrylic resin which was polymerized at 248K. The block faces were trimmed to reveal the embedded leaf.

The trimmed and smooth block faces of the three resin embedded samples were coated with ca. 1.5nm of evaporated carbon and were examined and analysed at 293K. The instrumental conditions for all four samples was 10keV and a beam current of 130pA in a Philips XL30 Hot FEG SEM using an Oxford Instrument ISIS ultra-thin window germanium ED spectrometer. The analysis was carried out using the Oxford Instruments PBQuant analytical programme at a magnification of x1000 for the analysis of the vacuolar contents and x10,000 for the analysis of the cell walls using a 3 x 3mm reduced raster for 100s which gave between 2-300cps. There were no signs of beam damage on the any of the four specimens

Cell Compartment	Method 1	Method 2	Method 3	Method 4
Upper Epidermis Cell Wall	0.048	0.038	0.027	0.021
Upper Epidermis Cell Vacuole	0.028	0.012	0.015	0.009
Palisade Cell Vacuole	0.039	0.004	0.003	0.010
Spongy Mesophyll Cell Vacuole	0.039	0.005	0.015	0.009
Bundle Sheath Cell Vacuole	0.045	0.004	0.006	0.003
Xylem Tracheid Cell Lumen	0.019	0.014	0.013	0.003
Lower Epidermis Cell Wall	0.057	0.015	0.022	0.019
Lower Epidermis Cell Vacuole	0.031	0.007	0.004	0.012
Embedding Resin (Background)	-	0.012	0.012	0.016
Embedding Ice (Background)	0.015	-	-	-

Table 1. Peak/ Local Background ratios for aluminium in old tea leaves from three samples.

If one accepts that any P/B values below 0.020 are outside the detectable limit for this sample and analytical procedure, it is clear that much of the data obtained using Methods 2, 3, and 4 are invalid. This is not surprising for the data obtained using Method 4 which has been designed for use with immunocytochemical studies. It is surprising however to discover that the two methods (2 & 3) which have been designed for use with the x-ray microanalysis of diffusible elements have failed miserably to retain the small amounts of aluminium which are known to be present in the tissues of tea plants. These findings are even more surprising when compared to the data obtained from the non-invasive cryopreparative method which shows that aluminium is present in both the cell walls and, to a lesser extent, in the vacuoles of the tea leaves. All the indications suggest that the aluminium located in the cell walls is probably bound to the structural polysaccharides. Clearly we have to re-evaluate the effectiveness of chemically invasive preparative procedures as a method to retain the particular elements which are present in small amounts in plant material

1. Echlin, P. (1992) Low Temperature Microscopy and Analysis. Plenum Press. New York
2. Orlovich, D.A. & Ashford, A.E. (1995) Journal of Microscopy 180 117-126.
3. Pälsgärd, E., Lindh, U. & Roomans. G. (1994) Microscopy Research and Technique 28 254-258.
4. Paul Monaghan (personal communication)

SCANNING ELECTRON MICROSCOPY OF EARLY INFECTION OF DYERS WOAD, *ISATIS TINCTORIA* BY GERMLINGS OF *PUCCINIA THLASPEOS*

M. T. Binns*, G. R. Hooper**, B. R. Kropp***, D. R. Hansen***, and S. V. Thomson***

*Department of Agronomy and Horticulture, Brigham Young University, Provo, Utah 84602
**Department of Botany and Range Sciences, Brigham Young University, Provo, Utah 84602
***Department of Biology, Utah State University, Logan, Utah 84322-5305

Dyers Woad (*Isatis tinctoria*) is an introduced noxious weed of crop and rangeland in northern Utah. A native rust fungus (tentatively identified as *Puccinia thlaspeos*) is being investigated as a possible biological control agent of the weed. In order to effectively use the rust in a bio-control program, it is necessary to understand its epidemiology and characteristics.

Weeds were inoculated by suspending previously infected weed leaf fragments over test plants. Teliospores on these fragments produced basidiospores which dropped onto the weed seedling leaf surfaces. Inoculated leaves were prepared for SEM by fixation in 2% cacodylate buffered glutaraldehyde, post fixed in 2% buffered osmium tetroxide and dehydrated through ethyl alcohol and critical point dried. Mounted specimens were sputter-coated with gold. Some tissues were freeze fractured in 100% alcohol and fragments were critical point dried, coated and mounted for SEM (1).

Basidiospores are roughly ovoid, 9-10 μm in diameter with a prominent hilum, or attachment scar (Fig. 1). Spores are firmly adhered to the epidermal surface and germinate by a germ tube varying in length from 2 to 14 μm (Fig. 2, 3). A slight swelling at the end of the tube demarks the appressorium (Fig. 3)—below which the fungus penetrates the cell. The entire rust germling (spore, germ tube and appressorium) adheres tightly to the epidermis and appears to either dissolve cuticular waxes or mechanically disrupt them. Shortly after spore germination, and movement of its contents into the germ tube, the original spore collapses (Fig. 3).

Unlike many species of fungi, this rust does not enter the plant through stomata, nor penetrate the leaf between cells. All observed penetration was directly through cell walls—even when the germ tube was very near stomatal openings (Fig. 2). Once inside the leaf, the fungal hypha ramifies between cells throughout the leaf (Fig. 4). *Puccinia thlaspeos* is similar to some other microcyclic rusts in this behavior (2). Even though this fungus becomes systemic it does not penetrate leaf veins nor move through xylem vessels or tracheids.

References

1. O'Donnell, K.C. and G.R. Hooper. 1977. *Mycologia* 69: 309-320.
2. Gold, Randall E., and Kurt Mendgen. 1991. pp 67-99. In: *The Fungal Spore and Disease Initation in Plants and Animals.* Plenum Press, New York.
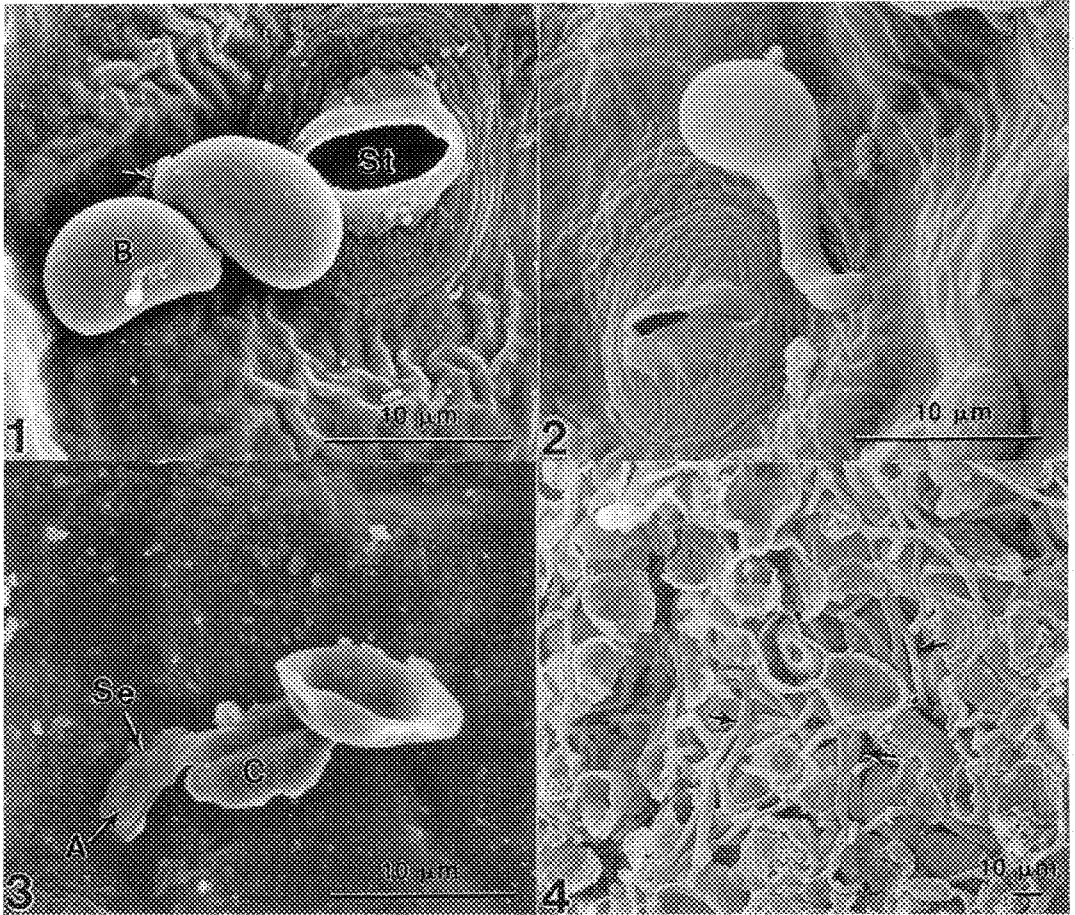
FIG. 1   Rust basidiospores on Dyers Woad leaf surface. St = stomate; B = basidiospore;
            Arrow indicates hilum (attachment scar).
FIG. 2   Germinated basidiospore (germling) near stomate.
FIG. 3.   Collapsed, germinated basidiospore. Note disruption of leaf cuticle. A = appressorium ;
            C = cuticle; Se = septum.
FIG. 4   Cross section (freeze fractured) of infected leaf. Note abundant intercellular hyphae.
            Arrows indicate hyphae.

SEM Study of Phytoliths Produced by Grasses Indigenous to the Desert Experimental Range in Southwestern Utah

Melanie R. Carver*, Terry Ball**, John S. Gardner*** and Kali M. Erickson***

*Provo High School, 1125 N. University Ave., Provo, UT 84602
**Dept. Of Ancient Scripture, 303D JSB, Brigham Young University, Provo, UT 84602
***Microscopy Laboratory, 128 WIDB, Brigham Young University, Provo, UT 84602

The USDA Desert Experimental Range Station located in southwestern Utah has been conducting an ongoing investigation into the effects of grazing on the ecology of the region.[1] The study reported herein is a preliminary effort to determine if phytolith analysis can be used to gain insight into the ecology of the region prior to the 60 year period over which records have been kept.

Phytoliths are solid deposits of silicon dioxide that form at specific intracellular and extracellular locations in many plant taxa. Grasses produce phytoliths with morphological characteristics diagnostic of their taxa. When a plant dies, its phytoliths resist decomposition thereby becoming micro-fossils of the plant that produced them. Micro-fossil phytoliths provide archaeobotanical and ecological information because they remain in the same soil horizon at which decay occured.[2] In this study phytoliths produced by four grasses indigenous to the Experimental Range were analyzed. Phytoliths extracted from soil samples of different grazing treatments at the Range were then analyzed to determine if any similar to those produced by the four grasses could be identified in the soil. If so, then phytolith analysis could prove to be a viable research tool for those studying the paleoecology of the Range.

Phytoliths produced by *Oryzopsis hymenoides, Hilaria jamesii, Sporobolus cryptandrus,* and *Aristida purpurea* were extracted from fresh tissue and prepared for SEM evaluation following the methods of Ball, et.al. [3] Extraction of phytoliths from soil samples was accomplished using the heavy liquid flotation method described by Piperno [4]. The SEM analysis was conducted using a 5 KV accelerating potential at a working distance of 10 mm.

Phytoliths produced by these grasses include those formed by the silicification of trichomes, silica cells, stomata, vascular tissue, and epidermal long cells. The most characteristic or diagnostic of these were silica cells. In *A. purpurea , H. jamesii,* and *S. cryptandrus* the silica cells were bilobate in shape, while in *O. hymenoides* they were round to trapezoid in shape (Figs. 1 and 2). Both of these characteristic shapes were found among phytoliths extracted from the soil samples (Figs. 3 and 4). Additional study and comparison of phytoliths found in indigenous taxa and soils of the Range, employing computer-assisted image and statistical analysis, are planned to further develop phytolith analysis as a research tool for the area.

References

1. Blaisdell, J. P., and R. C. Holmgren. 1984. USDA General Technical Report INT-163.
2. Rovner, I. 1971. Quaternary Research, 1:345-359.
3. Ball, T. B., J. D. Brotherson, and J. S. Gardner. 1993. Can. J. of Botany. 71:1182-1192.
4. Piperno, D. R. 1988. Phytolith Analysis: An Archeological and Geological Perspective. Academic Press, Inc.: San Diego, CA. 120-124.
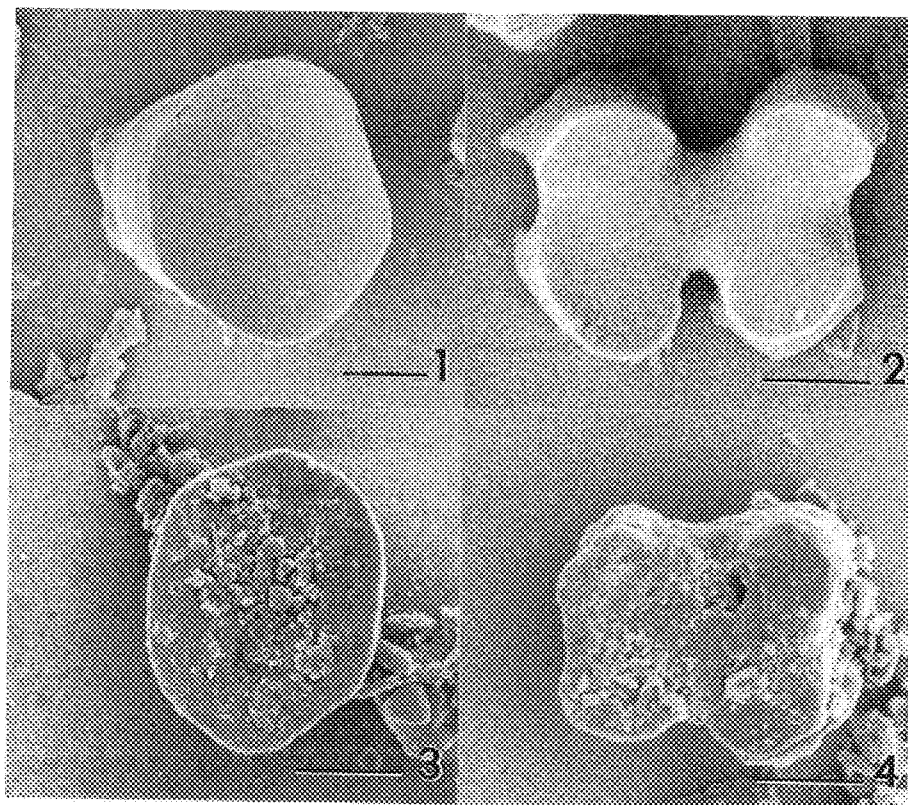
Figs. 1-4. SEM images of Phytoliths. Bars = 5 μm.

Fig. 1. Trapezoid shaped silica cell phytolith extracted from fresh tissue of *O. hymenoides*.

Fig. 2. Bilobate shaped silica cell phytolith extracted from fresh tissue of *H. jamesii*.

Fig. 3. Trapezoid shaped silica cell phytolith extracted from soil.

Fig. 4. Bilobate shaped silica cell phytolith extracted from soil.

STOMATAL MORPHOLOGY AND DISTRIBUTION OF *PINUS KORAIENSIS*

Zhu Hua Ning and Kamran Ken Abdollahi

Southern University and A&M College, Baton Rouge, LA 70813

Stomata are the important channels for the necessary exchange of gases between the plants and the surrounding earth. Stomata open and close in response to environmental and physiological signals, thus helping the plant maintain a balance between its water losses and its oxygen and carbon dioxide requirements. This paper reports the study on stomatal morphology and distribution of *Pinus koraiensis*, a five needle pine tree with a natural distribution in Northeastern China.

Needle samples were collected from one-year-old seedlings. They were cut into 1mm lengths and fixed overnight at 4^0C in 4% glutaraldehyde buffered with 0.07M cacodylate at pH 7.2-7.4. After being rinsed with the same buffer, they were post-fixed for 1 hour in 1% osmium tetroxide in the same buffer and dehydrated in a graded ethanol series.[1] Afterward, tissues were dried in a DCP-1 critical point dryer and coated in a Hummer II sputter coater. Stomatal morphology and distribution were examined under a Hitachi S-405A scanning electron microscope.

Like other pines, *Pinus koraiensis* needle bore sunken stomata to allow a pocket of moist air to be trapped between the surface of the needle and the guard cells of the stomata to insure the gas exchange could occur with a minimum transpiration loss of water. The aperture which could be seen on the surface of a needle was not real stomatal chamber, but marked the opening to the front chamber above the stoma (Fig.1). The front chamber was formed by the subsidiary cells of the stoma arched over the sunken stoma (Fig.2). Often the front chamber was lined with hair-like wax giving a white appearance to the stoma (Fig.3). The guard cells were concealed in surface view by subsidiary and other epidermal cells. The real stomatal chamber was beneath the guard cells (Fig.2). The stomata occurred in longitudinal rows with an average of 8 rows per needle. All stomatal rows were distributed on two adaxial surfaces of the needle.

Reference

1. K.L. Klomparens et al., *Procedures for Transmission and Scanning Electron Microscopy for Biological and medical Sciences*. 2nd ed. Ladd Research Ind. Burlington, VT, 1986.

FIG. 1- Surface view of a needle with longitudinal stomatal rows. x705.
FIG. 2- Cross-section of a stoma shows detailed structure. s, subsidiary cell, f, front chamber, g, guard cell, c, stomatal chamber, x1500.
FIG. 3- Surface view of a needle with longitudinal stomatal rows. Note the front chamber of a stoma was covered with wax. x500.
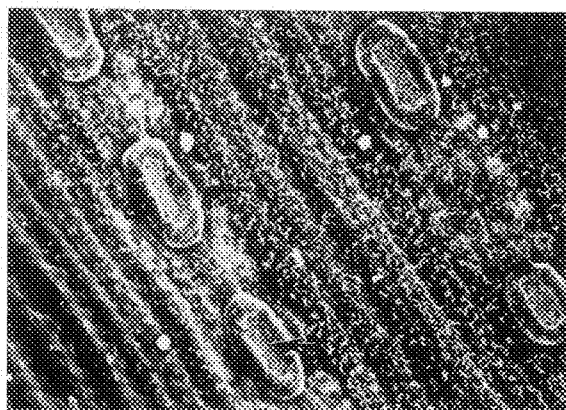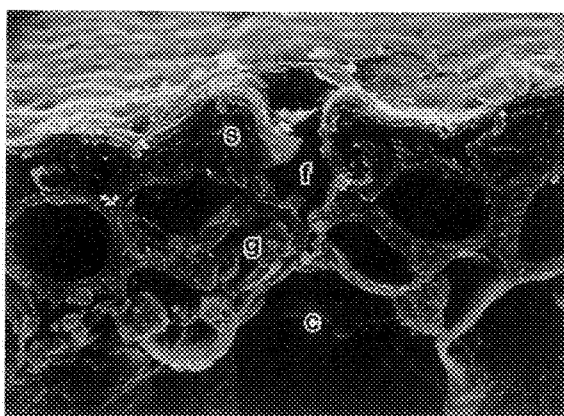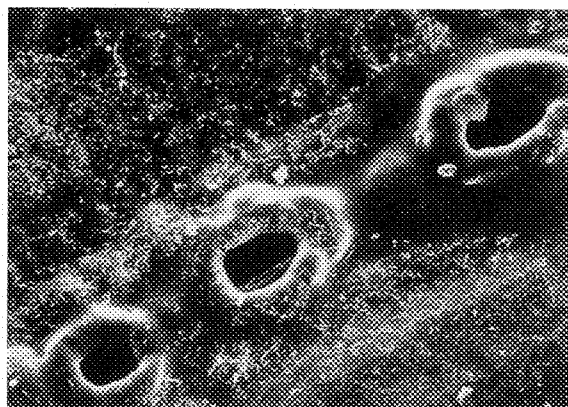
CHARACTERIZATION OF THE EFFECT OF HEAT STRESS ON MATERNAL AND EMBRYONIC TISSUES OF MAIZE (*Zea mays* L.) KERNELS USING SCANNING ELECTRON MICROSCOPY (SEM)

P. D. Commuri and R. J. Jones

Department of Agronomy and Plant Genetics, University of Minnesota, St. Paul, MN 55108

Heat stress during the early formative stages of maize (*Zea mays* L.) kernel development is detrimental to subsequent growth and grain yield. During this period, even a brief exposure to temperature above the optimum (25°C) can result in significant yield losses. The mechanisms involved in this response are not well understood, but appear to be associated with a thermally induced shift in hormone balance (cytokinin/ABA), which results in a reduction in kernel sink capacity (i.e. number of endosperm cells and starch granules formed) and the disruption of sugar metabolism and starch biosynthesis.[1,2,3,4] However, the effect of heat stress on the morphology and ultra-structure of kernel component tissues (pedicel, pericarp, endosperm, and embryo) has not been studied. Therefore, the objective of our current study was to characterize heat stress induced changes in the pericarp (maternal) and the embryo (embryonic) tissues using SEM.

Kernels of the single cross hybrid A619xW64A were *in vitro* cultured at 3 days after pollination (DAP) on an agar based sucrose (16%) media containing essential nutrients, vitamins and amino acids.[3] At 5 DAP, kernels were heat stressed (35°C, day/night) for 2, 4, 6, or 8 days and subsequently transferred to 25°C and retained there until physiological maturity. Control kernels were kept at 25°C continuously. At physiological maturity (31 DAP) kernel component tissues were weighed, sections were made and used for SEM.

Two days of heat stress did not significantly affect normal kernel development as is indicated by the fresh weight accumulation profiles (Fig. 1). However, 4 or more days of heat stress caused 30 to 100% of the kernels to abort. In kernels exposed to 4 or 6 days of heat stress, kernel growth appeared to recover to some extent when they were transferred to 25°C (Fig. 1). The extent of recovery was dependent on the duration of stress. However, it is clear that 8 days of heat stress completely disrupts kernel development and growth does not resume at 25°C (Fig. 1). Heat stress affected maternal and embryonic tissues differently. Two through 8 days of stress increased the thickness of the pericarp by 1.5 to 12-fold (Fig. 3B, 3C, 3D, 3E) as compared to the controls (Fig. 3A). As the duration of heat stress increased, the number of pericarp cell layers was increased, cell walls became thicker, and as a result fresh weights were increased (Fig. 2A). In contrast, heat stress disrupted normal embryo growth (Figs. 4 and 2B). Two or 4 days of heat stress caused only modest changes in the morphology (Fig. 4) and fresh weights (Fig. 2B), whereas, the embryos of 6 and 8 day heat stressed kernels were malformed and shrivelled (Figs. 4D and 4E) as compared to the controls (Fig. 4A). The results clearly show that the effect of heat stress on the morphology and ultra-structure of maize is dependent on the duration of the stress and that kernel components differ in their heat sensitivity. It appears that in maize kernels heat stress stimulates cell expansion (e.g. pericarp) but disrupts cell division (e.g. embryo).

References

1. R. J. Jones et al., *Crop Science*, 25 (1985)830.
2. R. J. Jones et al., *Crop Science*, 24 (1984)133.
3. R. J. Jones et al., *Crop Science*, 21 (1981)761.
4. N. Cheikh and R. J. Jones, *Plant Physiology*, 106 (1994)45.
5. The authors gratefully acknowledge the use of facilities at the MAES, Electron Optical Facility, University of Minnesota, and technical assistance by Gilbert Ahlstrand. This research was supported by US Department of Agriculture, National Research Initiative grant No. 92-37100-7440. Minnesota Agricultural Experiment Station paper no. 22,305, Scientific Journal Series.
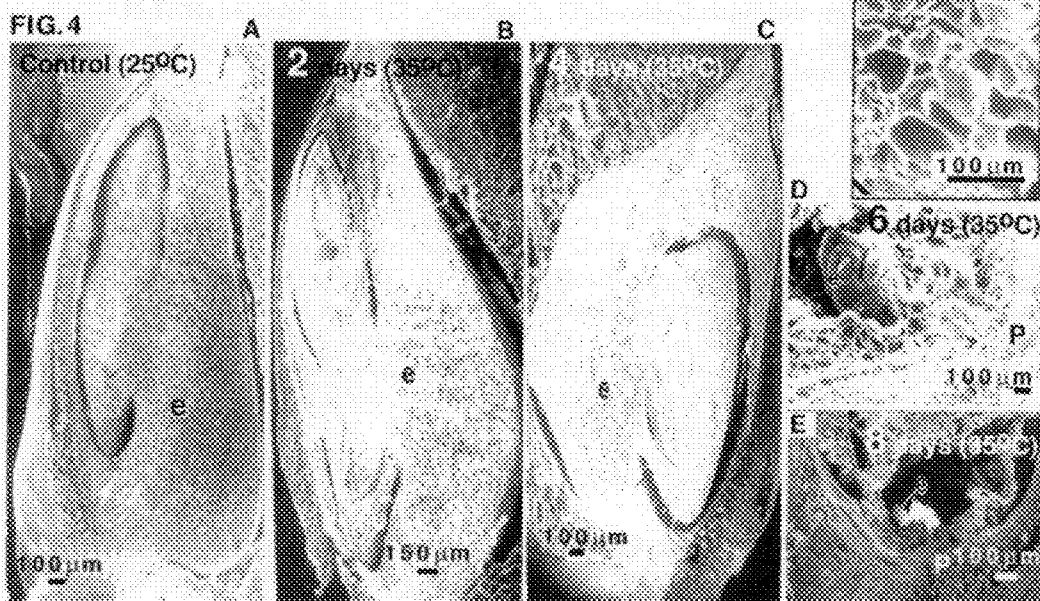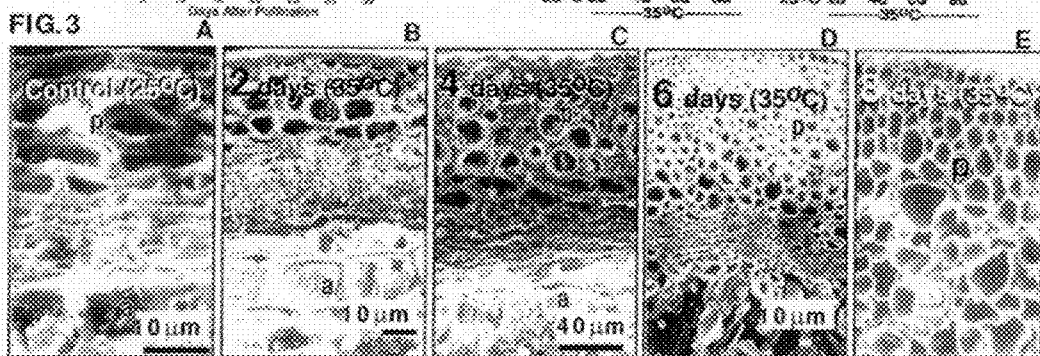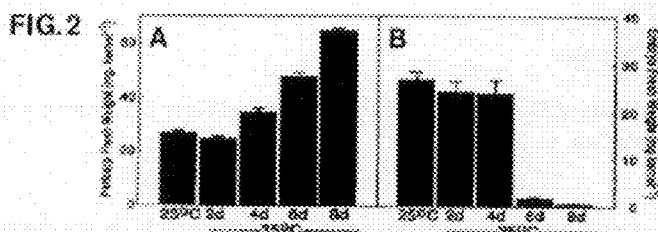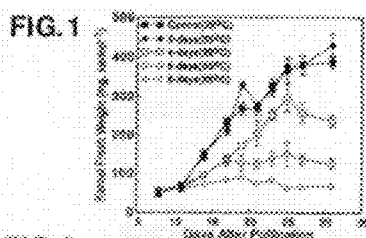
FIG. 1 Effect of heat stress on kernel fresh weight accumulation.
FIG. 2 Effect of heat stress on pericarp (A) and embryo (B) fresh weight accumulation.
FIG. 3 Effect of heat stress on pericarp growth. p=pericarp; a=aleurone layer.
FIG. 4 Effect of heat stress on embryo growth. e=embryo; p=pericarp.

CYTOCHEMICAL LOCALIZATION OF CHLORIDE IN THE LEAVES OF *Ruppia maritima* L

A.D. Barnabas

Department of Botany, University of Durban-Westville, Private Bag X54001, Durban 4000, South Africa

Ruppia maritima L. is a submerged halophyte which occurs frequently in estuaries where sodium chloride is the dominant salt. Unlike terrestrial halophytes, *R. maritima* does not possess any specialized salt-secreting structures such as salt glands. Knowledge of salt tolerance mechanisms in this plant is important to our understanding of its biology. In the present study, the subcellular distribution of chloride ions in leaf blade epidermal cells of *R. maritima* was determined.

Chloride ions in the cells were localized by precipitation with silver, resulting in the formation of silver chloride ($AgCl_2$) deposits[1]. Leaf samples were fixed in a mixture of osmium and silver acetate under red safe light conditions to prevent reduction of silver by light. The material was dehydrated and embedded in a chloride-free resin[2]. Leaf samples fixed only in osmium were used as controls. Transmission electron microscopy (TEM) and energy dispersive X-ray (EDX) microanalysis using a Joel 6100 SEM with a Noran Voyager 2100 EDX microanalyser, were used to study $AgCl_2$ distribution. Ultrathin sections for TEM were examined unstained. EDX microanalysis was performed on thick sections of resin-embedded material mounted on glass slides.

Electron-dense deposits were concentrated in the cell walls especially in the outer tangential and radial walls and within extracytoplasmic spaces bordering these walls (Figs. 1,2). There was a sparse distribution of these deposits within the vacuoles (Figs. 1,2). Control sections of leaf material fixed only in osmium were free of electron-dense precipitates. Spot EDX microanalysis of electron-dense deposits showed that they consisted of $AgCl_2$, silver and chlorine being present in all the precipitates analyzed (Fig. 3). X-ray mapping confirmed the presence of these ions predominantly outside the protoplast in the walls, and distributed only sparsely within the vacuoles (Figs. 4-6). There was thus a good correlation with the distribution of $AgCl_2$ deposits seen in Figures 1 and 2. The results indicate that salt control in *R. maritima* is probably associated with the plasma membrane which prevents excessive amounts of chloride ions from entering the protoplast of the cells[3].

References

1.   M.M. Smith et al., *Journal of Experimental Botany,* 33(1982) 886.
2.   C.K. Pallaghy, *Australian Journal of Biological Science,* 26(1973) 1015.
3.   The author gratefully acknowledges the financial support of the University of Durban-Westville and Foundation for Research and Development (FRD), South Africa.
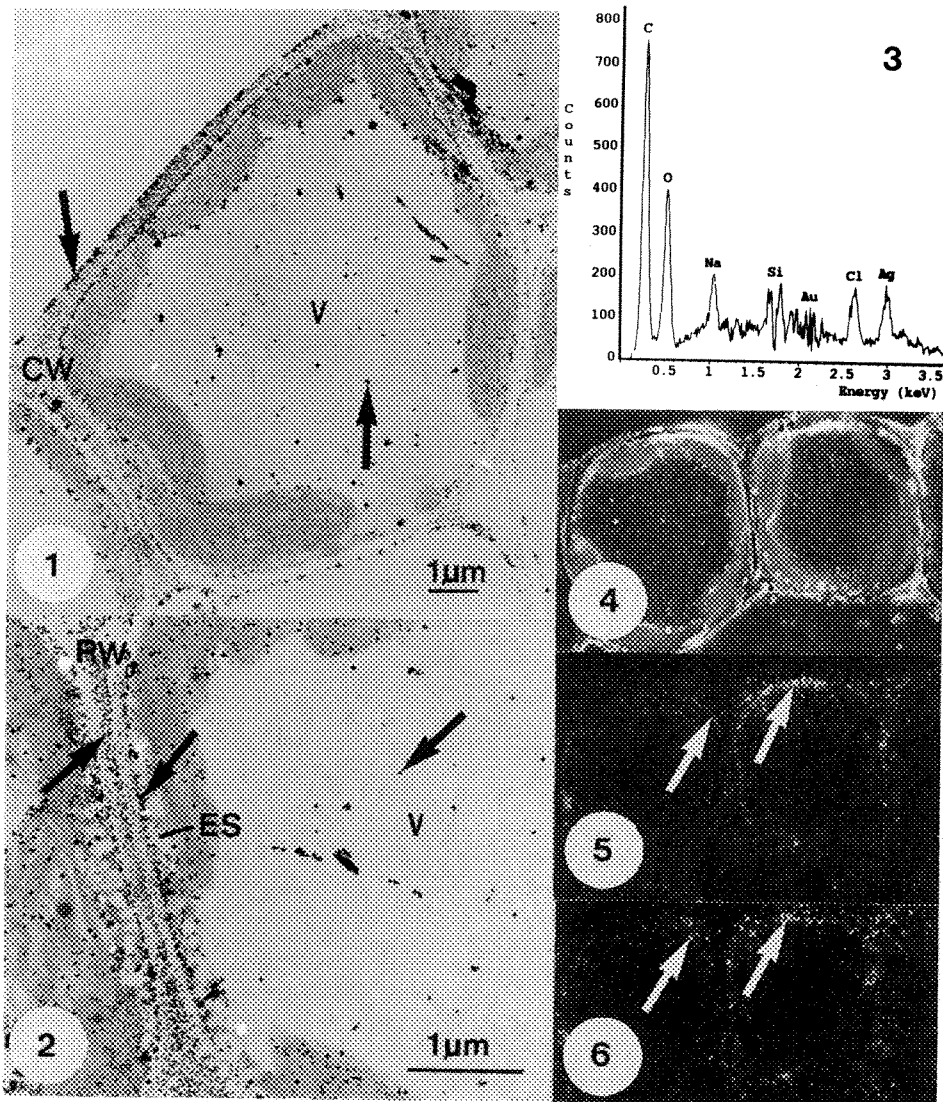
FIG. 1. TEM image showing distribution of AgCl$_2$ deposits (arrows) predominantly in cell walls (CW) and sparsely within vacuole (V).

FIG. 2.   TEM image of portion of cell depicting AgCl$_2$ deposits (arrows) in radial wall (RW), extracytoplasmic space (ES) and vacuole (V).

FIG. 3. X-ray spectrum indicating silver and chlorine in electron-dense deposits.

FIG. 4.   SEM image of resin section of epidermal cells analyzed to produce X-ray maps (Figs. 5,6).

FIG. 5. X-ray map showing distribution of silver ions (arrows).

FIG. 6. X-ray map showing distribution of chlorine ions (arrows).

LOCALISATION OF HYPERACCUMULATED NICKEL IN *STACKHOUSIA TRYONII* USING ELECTRON-PROBE MICROANALYSIS

I. Noell* and D. Morris**

*Zoology Department, James Cook University, Townsville, Qld 4811, Australia
**Biology Department, Central Queensland University, Rockhampton, Qld, Australia

Proton microprobe and electron probe X-ray microanalysis (EPXMA) simultaneously measure and map elemental content, and hence are excellent tools for investigating the distribution and function of elevated Ni levels in hyperaccumulating plants (Ni concentration >1000 μg g^{-1} dry weight).[1,2] Five major hypotheses have been proposed for the function of Ni hyperaccumulation.[3] Our research focuses on the hypothesis that Ni defends against herbivore or pathogen attack and examines the movement of Ni from soil through plant to herbivore in *Stackhousia tryonii*, the only known hyperaccumulator in eastern Australia. Using a JEOL JXA-840-A electron probe microanalyzer with Moran Scientific Analysis software, we located features of high mean atomic number in whole leaves and cross-sections through backscattered-electron imaging (BEI), then we used EPXMA to identify the elements present and to prepare semi-quantitative x-ray maps of seven key elements.

A leaf cross-section BEI (Fig 1b) revealed a large epidermal cell containing numerous backscattered-electron-bright spheres about 1 μm in diameter, whose topology was visible in secondary electron mode (Fig. 1a). The spheres overwhelmingly consisted of Ni (Fig. 2), containing Ni concentrations at least 12 times higher than found in the interspherical areas. Mg showed the same ten-fold increase as Ni in the spheres, whereas K, S, and Ca concentrations were about 8, 5.5, and 4.5 times larger respectively.

We also examined leaf surface exudates which we believe are responses to a natural wound made by a herbivore. An energy dispersive X-rays map of Ni (Fig. 4b) produced a shield-shaped pattern identical to that defined by the backscattered-electron bright exudate (Fig. 4a). Si, however, was co-deposited only in the more central portion of the exudate (Fig. 4c). The prominence of stomates in the BEI suggested a possible route for the movement of Ni from the epidermal storage cell to the leaf surface. Also, occasional single stomates in undamaged areas of a leaf showed backscattered-electron-bright exudates (Figs. 3a-b), which appeared thin in comparison to the larger (wound?) exudates that included many stomates (Fig. 4a). Initial spot analyses indicated that Ni:Si ratios of the two exudates contrasted strongly: approximately 1:10 in the single stomate exudate and 7:1 in the larger exudate. We anticipate developing, on the basis of these preliminary observations and the continued applications of microanalytic methods, a more complete account of Ni movement in *S. tryonii*.

References

1. J. Mesjasz-Przyblowicz et al., *Nuclear Instruments and Methods in Physics Research*, B 89 (1994) 208-212.
2. Freudenrich et al., *Journal of Structural Biology*, (1994)112, 173-182
3. R.S. Boyd and S.N. Martens, in *The Vegetaion of Ultramafic (Serpentine) Soils*, edited by A.J.M. Baker et al., (1992), 279-289.
4. The authors gratefully acknowledge Bob Riel, Advanced Analytical Centre, James Cook University (JCU), for his excellent photographic and technical assistance. We also thank Dr. Ann LeFurgey (Duke University) for her encouragement and support, and Rob Parsons and Heather Winsor, Advanced Analytical Centre, and Kelvin De Waele, Computer Center, JCU, for their technical assistance. This work was supported by internal research funds, Zoology Department, JCU.
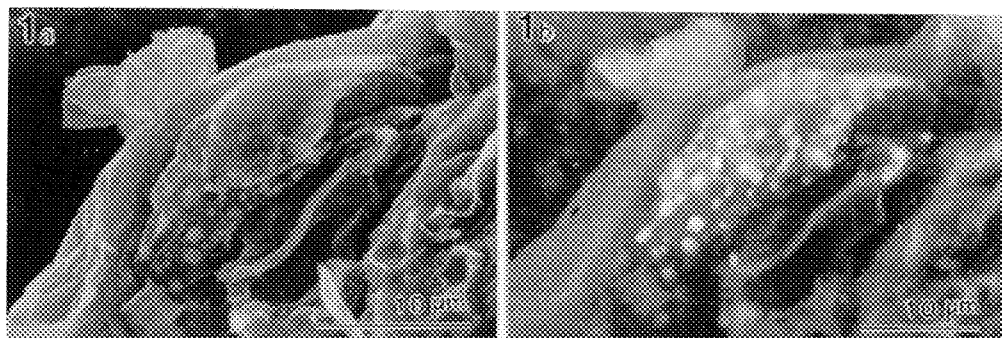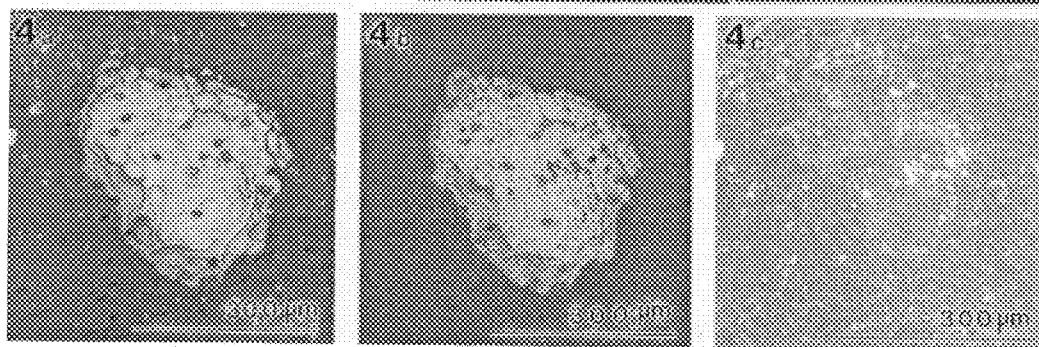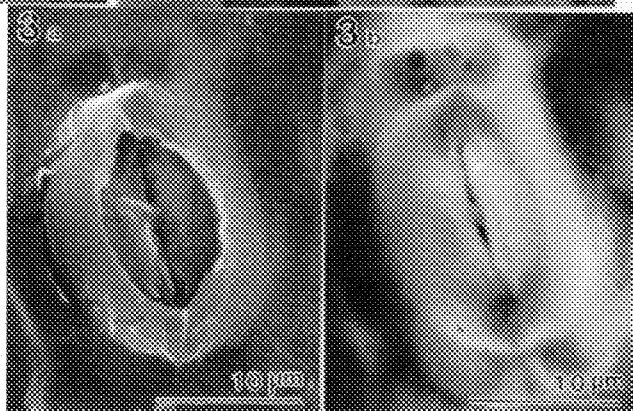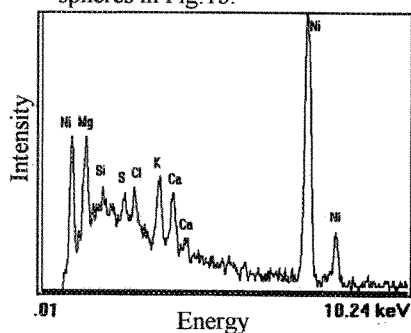
FIG. 1. (a) Secondary electron image (SEI) of nickel storage cell and (b) backscattered-electron image (BEI) showing backscattered-electron-bright spheres within cell, x 2000.

FIG. 2. Energy dispersive X-ray spectrum (EDS) taken at 15kV.

FIG. 3. (a) SEI of stomate with nickel exudate and (b) BEI showing exudate as backscattered-electron-bright, x 3500.

FIG. 4. Digital images of leaf surface (wound?) exudate: (a) BEI. (b) Semi-quantitative EDS x-ray map for nickel and (c) for silicon, x 160. Grey scale depicts white in region of highest content, black in region of lowest content, each element scaled independently of the other.

QUANTITATIVE HREM USING NON-LINEAR LEAST-SQUARES METHODS

Wayne E. King and Geoffrey H. Campbell

Chemistry and Materials Science Department, University of California, Lawrence Livermore National Laboratory, Livermore, CA 94550

Non-linear least-squares methods have been coupled with high resolution image simulation to determine the critical electron microscopic imaging parameters, such as thickness and defocus, from experimental high resolution electron optical images of yttrium aluminum garnet (YAG). For a quantitative fit between experimental and simulated images we seek to minimize the residual image $f_i(x)$ at each pixel,

$$f_i(x) = \left[f_i^{obs} - f_i^{calc}(x) \right] \big/ W_i , \tag{1}$$

where f_i^{obs} is the intensity value of the ith pixel in the experimental image, $f_i^{calc}(x)$ is the intensity value of the ith pixel in the simulated image based on the image model x, and W is the image that represents the uncertainty associated with measurement of the ith pixel in the experimental image.[1,2]

This problem has been addressed in the current work using the MINPACK-1 non-linear, least-squares optimization code[3] coupled with the EMS image simulation code.[4] MINPACK-1 employs the Levenberg-Marquardt algorithm[5] to solve the non-linear, least-squares problem.

A YAG grain boundary was prepared for electron optical observation along <001>. The sample was observed at high resolution in the JEOL-4000EX at Sandia National Laboratories, Livermore. Images at three defocus values were recorded. As-developed films were digitized using a $1024 \times 1024 \times 14$ bit CCD array camera at a pixel density comparable to the sampling for HREM image simulation. To determine the critical electron optical image parameters, images were warped to remove aberrations in the imaging system. Unit cell images were extracted from the experimental images.

The result of one of the optimizations is shown in Fig. 1. The image at left is the average experimental image. The image at center is the simulation and the image at right is the normalized residual image from Eq. 1. The normalized residuals lie primarily between -1.3 and +1.3 indicating that while the fit is reasonably good (an ideal fit would have a range between -1 and +1), there are systematic variations of the model from the experiment. The white spots in the simulated image have been broadened to match the experiment by applying an unrealistic defocus spread: 71 nm. Results of the optimization at three defocus values confirm that (1) there is significantly more detail in the simulated image than in the experimental image, (2) this results in the optimization procedure seeking an unrealisti-

cally large value of the defocus spread, and (3) additional electron optical effects must be accounted for in the simulation before an acceptable fit can be obtained.

References
1. W. E. King and G. H. Campbell, *Ultramicroscopy*, 51, (1993)128.
2. W. E. King and G. H. Campbell, *Ultramicroscopy*, 56, (1994)46.
3. J. J. Moré, B. S. Garbow, and K. E. Hillstrom, (Argonne National Laboratory, 1980).
4. P. Stadelmann, *Ultramicroscopy*, 21, (1987)131.
5. J. J. Moré, in *Lecture Notes in Mathematics*, edited by G. A. Watson, Springer-Verlag, Berlin, 630(1977)116.
6. The authors acknowledge useful discussions with Dr. M. A. O'Keefe and Dr. P. Stadelmann. This work performed under the auspices of the Division of Materials Science of the Office of Basic Energy Sciences, U. S. Department of Energy, and the Lawrence Livermore National Laboratory under contract No. W-7405-Eng-48.
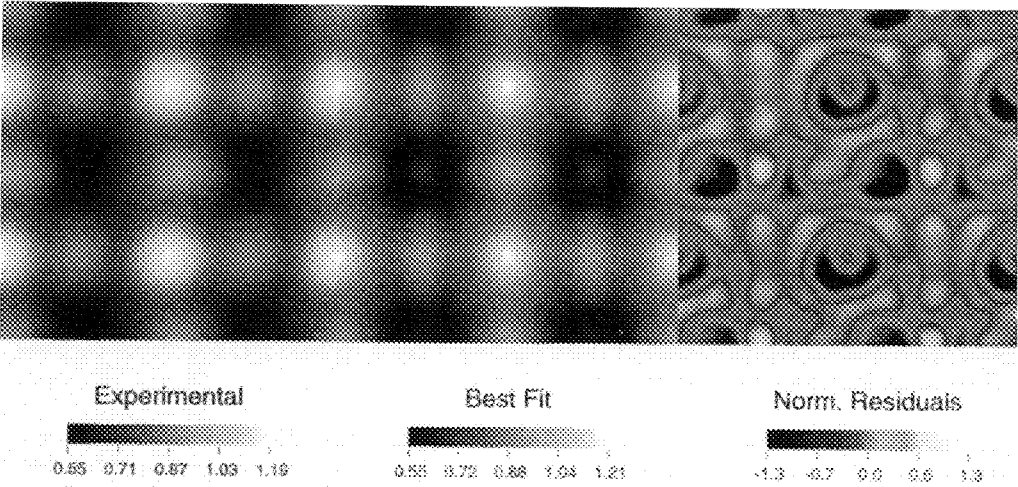
FIG. 1. Experimental image (at left), best-fit simulated image (at center), and normalized residuals image from Eq. 1 at right.

QUANTITATIVE DETERMINATION OF IMAGING PARAMETERS AND COMPOSITION FROM HIGH-RESOLUTION TRANSMISSION ELECTRON MICROSCOPY LATTICE IMAGES

D. Stenkamp

Institut für Werkstoffwissenschaften, Lehrstuhl für Mikrocharakterisierung
Universität Erlangen-Nürnberg, Cauerstr. 6, D-91058 Erlangen, Germany

A quantitative method for the direct determination of defocus $\triangle f$, local sample thickness t and local composition x from high-resolution transmission electron microscopy (HRTEM) lattice images of wedge-shaped samples is described. The method is applicable to a wide class of crystalline materials comprising elemental semiconductors, elemental metals and substitutional random alloys composed of these elements. The proposed method relies on the functional dependence of linear and non-linear image Fourier coefficients on the parameters defocus $\triangle f$, sample thickness t and composition x. This relationship is analytically derived by application of the Bloch wave formalism and the non-linear imaging theory to the HRTEM imaging process. Influences of inelastic electron scattering and partially coherent illumination conditions are taken into account explicitly.

Starting with a 5×5 Bloch wave matrix equation for zone axes $\langle 100 \rangle$, $\langle 110 \rangle$ and $\langle 111 \rangle$, crystal symmetry elements are exploited and suitable matrix reduction techniques are applied. Thereby the number of Bloch waves effectively contributing to the exit wave function is reduced to two. The superposition of these two Bloch waves results in a periodic thickness dependence of the amplitudes $U(\vec{g}, t)$ for the undiffracted beam $\vec{g}_0$ and for the first-order diffracted beams $\vec{g}_1$. The period of this oscillation ξ (extinction distance) is given by the wave vector difference of the two Bloch waves. The same thickness periodicity is also obtained for the relative beam phase $\triangle\theta(\vec{g}_1, t)$ which exhibits the characteristic of an arcustangens function for varying t. Due to the uniform thickness periodicity of $U(\vec{g}, t)$ and $\triangle\theta(t)$, the linear and non-linear first-order image Fourier coefficients $J_1(t, \triangle f)$ and $J_2(t)$ are also periodic functions in t. When $J_1(t, \triangle f)$ and $J_2(t)$ are taken as components of a 2-D vector, ellipses with characteristic geometries are obtained for varying thickness. The phase angle of these ellipses is given by $2\pi t/\xi$ and their geometrical center and eccentricity sensitively depends on $\triangle f$ and x.

Based on this relationship between J_1 and J_2, a precise determination of defocus and sample thickness from digitized HRTEM lattice images of wedge-shaped samples becomes feasible. For this purpose the image is divided into small image cells for which values of J_1 and J_2 are determined by local Fourier analysis. Afterwards, an ellipse is fitted to the data and $\triangle f$ is determined from the geometrical parameters of the obtained ellipse. Finally, the sample thickness for each image cell is determined from the phase angle of the corresponding data pair (J_1, J_2). An example for the application of this method is given in Fig. 1 and 2. Fig. 1 depicts a 7-beam HRTEM lattice image of pure Si taken at 400 keV along [110] (JEOL4000EX). Fig. 2 shows the set of resulting data points (J_1, J_2) as obtained by a Fourier analysis of individual image cells in Fig. 1. The cell dimension is given by the smallest projected unit cell. Also shown is an ellipse as is obtained by a fit to the experimentally obtained data. From the parameters of this ellipse an image defocus of -55 ± 3 nm is yielded. By determination of the individual phase angle for

each experimental data point (J_1, J_2), a value for the local sample thickness of each image cell is directly obtainable.

For the determination of local composition values at interfaces, the method utilizes the finding that the (J_1, J_2) ellipses for different compositions do not coincide. Thereby it becomes possible to determine values for t and x independently over the full range $0 \leq x \leq 1$. Moreover, even interfaces for which the composition is known only for one side of the interface or for which the compositional transition is broader than the field of view can be quantitatively analysed.

References

1. D. Stenkamp and H.P. Strunk, *Inst. Phys. Conf. Ser. No 146*, (1995)17.
2. D. Stenkamp and H.P. Strunk, *Appl. Phys.*, A62(1996).
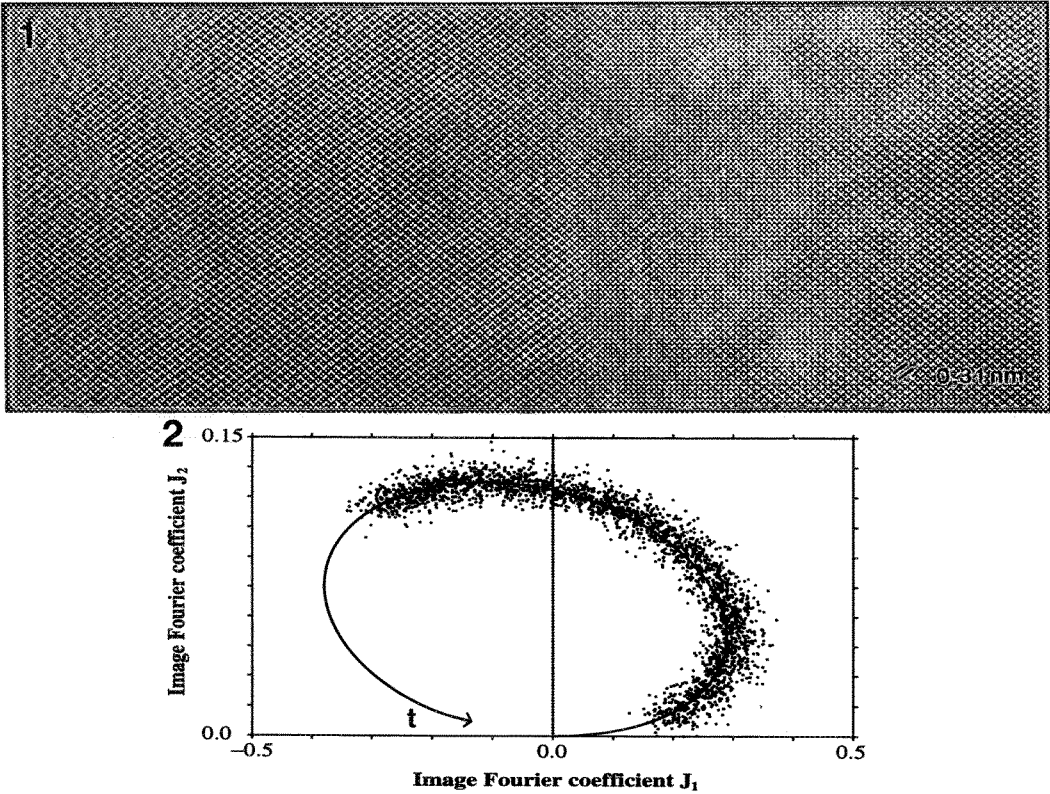
FIG. 1 Experimental 7-beam [110] lattice image of pure Si at 400 keV.
FIG. 2 Plot of image Fourier coefficients (J_1, J_2) for individual image cells in FIG. 1. From the parameters of the fitted ellipse (solid line) a defocus $\triangle f = -55 \pm 3$ nm is determined.

QUANTITATIVE χ^n ANALYSIS OF HREM IMAGES WITH APPLICATIONS TO PLANAR DEFECTS

H. Zhang and L. D. Marks

Department of Materials Science and Engineering, Northwestern University, Evanston, IL 60208

A number of different methods have been suggested in the literature for using HREM in a quantitative fashion, including R factors and cross-correlation analyses. The problem with many of these is that it is difficult to realistically gauge the errors involved when they are applied to real systems. For instance, R-factors defined by:

$$R^n = \Sigma \, |I_c - I_e|^n / \Sigma I_e^n$$

(where n=1 or 2 and I_c is the calculated image, I_e the experimental data) assume a signal independent error. Furthermore, the absolute value of R is strongly dependent upon background levels which is misleading.

Here we will discuss the approach based upon probabilistic χ^n methods defined by:

$$\chi^n = 1/m \, \Sigma \, |I_c - I_e|^n / \sigma^n$$

where σ is the error and m the number of degrees of freedom. The later must be independently determined for each picture, and the error in any measurement can then be strictly determined by a change in the calculated image such that $\Delta \chi m = 1$ (for 68% confidence level) and $\chi = 1$ for a good fit.

To illustrate this, Figure 1 shows calibration measurements of the error distribution comparing the mean of a small region of an experimental image with individual regions, for two different defoci. It is clear that the errors are not Gaussian (n=2), but have longer tails (n=1).

To show how this approach is applied to real experimental data, Table 1 shows the results of quantitative fitting the structure of planar defects in and infinite layer superconductor[1,2]. In this case it is possible to determine not just the location of the Sr atoms, but more importantly the error in the measurement.

This, and similar semi-quantitative work on modulated superconductor structures[3,4] will be discussed.

References

1.   H. Zhang et al., Nature 370, 352 (1994)
2.   H. Zhang et al., Ultramicroscopy 53, 103 (1995).
3.   O. Chmaissem et al., Phys. Rev. B52 (1995) 15636.
4.   H. Zhang et al., Physica C 255 (1995) 257.

1a

No filtering (defocus 0 nm)

1b

No filtering (defocus 46 nm)
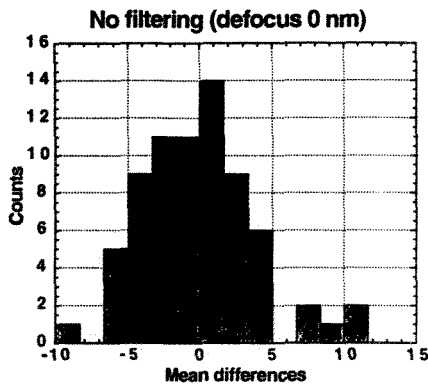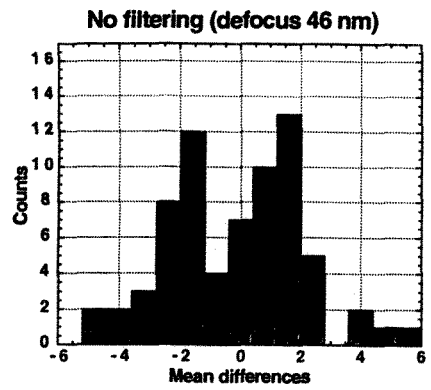
TABLE 1.- Atomic positions of the defect in fraction of the unit cell dimension. Unit cell for the defect is 3.9 x 3.9 x 7.4 $\AA^3$ (xyz)

	Cu	O(2)*	O(3)	Sr(1)	Sr(2)
x	0	0	0.5	0	0.5
y	0	0	0.5	0	0.5
z	0	0.29	0.5	0.58(±.01)	0.78(±.02)

*half occupancy

FIG.1 The distribution of the mean differences of an averaged small region with individual regions of experimental images for two different defoci: a) 0 nm, b) 46 nm.

MONTE-CARLO ESTIMATIONS FOR THE PRECISION OF ITERATIVE STRUCTURE REFINEMENT IN QHREM

G. Möbus

Max-Planck-Institut für Metallforschung, Institut für Werkstoffwissenschaft,
Seestr. 92, D-70174 Stuttgart, Germany

1. Introduction: Quantitative high-resolution TEM (QHREM) serves for the determination of structures of crystal defects. The structure retrieval problem is usually considered to be solved when a simulated image calculated from a model structure matches with high quality to the experimental image. Often, however, surprisingly large (and continuous) shifts of individual atomic columns are possible before the simulation looses its similarity to the experiment. Therefore, we propose printing structure retrieval results as "atomic ball pictures" with the radius of the ball as a circle of confidence (replacing the chemical atomic radius otherwise used for these pictures). Statistical methods are necessary to derive the proper radius of the circles which are element and site specific [1-3]: Monte-Carlo based strategies are highly suitable for this purpose. As a model system we use two bulk sections from a micrograph of a Cu/Sapphire interface [4] (Fig. 1). For interface properties see [5].

2. Test (i): Evaluation of multiple equivalent cells in perfect crystal areas.
A field of 11 cells in sapphire and one monolayer of Cu is selected near the interface (Fig. 2) where the structure is assumed to be perfect and known. Refining all atomic positions by global optimization (simulated evolution, [6]) leads to a distribution of distances around the perfect lattice positions (Fig. 4), visualized by Gaussians. All error sources which are spatially constant in the image are included. Interface-related errors are to be treated separately.

3. Test (ii): Evaluation of multiple added noise patterns on a single cell.
The experimental image is modified by adding several (here: 36) intensity patterns (average subtracted) cut from the amorphous edge on the same micrograph. The iterative structure refinement is applied to all these experimental reference images in parallel with one selected atomic column to be variable. The 36 best fit results of the coordinates x and y are collected as histogram plots in Fig. 3.

4. Test (iii): Distribution of image agreement around different atomic sites.
The hypersurface $Q = Q(\{x_i, y_i\})$ describes the matching quality with respect to the atomic coordinates. This surface might differ in terms of its curvature and anisotropy for different elements and sites. During the random walk involved in the optimization strategy of simulated evolution many trial structures are calculated besides the best fit. To examine such a hypersurface approximately in sapphire (Fig. 5a), all calculated quality values are printed at the actual positions of the 5-fold atomic ensemble on a discretized field (Fig. 5 b,c).

Overall, we arrive at precision values of 0.06 Å (copper), 0.15 Å (aluminum), 0.2Å (oxygen) based on σ (half width). Secure limits are twice as high (Fig. 5d).

1. D. Hofmann and F. Ernst, *Ultramicroscopy*, **53**, (1994), 205.
2. G. Möbus and M. Rühle, *Ultramicroscopy*, **56**, (1994), 54.
3. T. Höche, *Ph.D. thesis, University of Stuttgart*, (1994).
4. G. Dehm, M. Rühle, G. Ding and R. Raj, *Phil.Mag.B*, **71**, (1995), 1111.
5. G. Dehm, C. Scheu and M. Rühle, this volume.
6. G. Möbus and G. Dehm, *Ultramicroscopy*, submitted
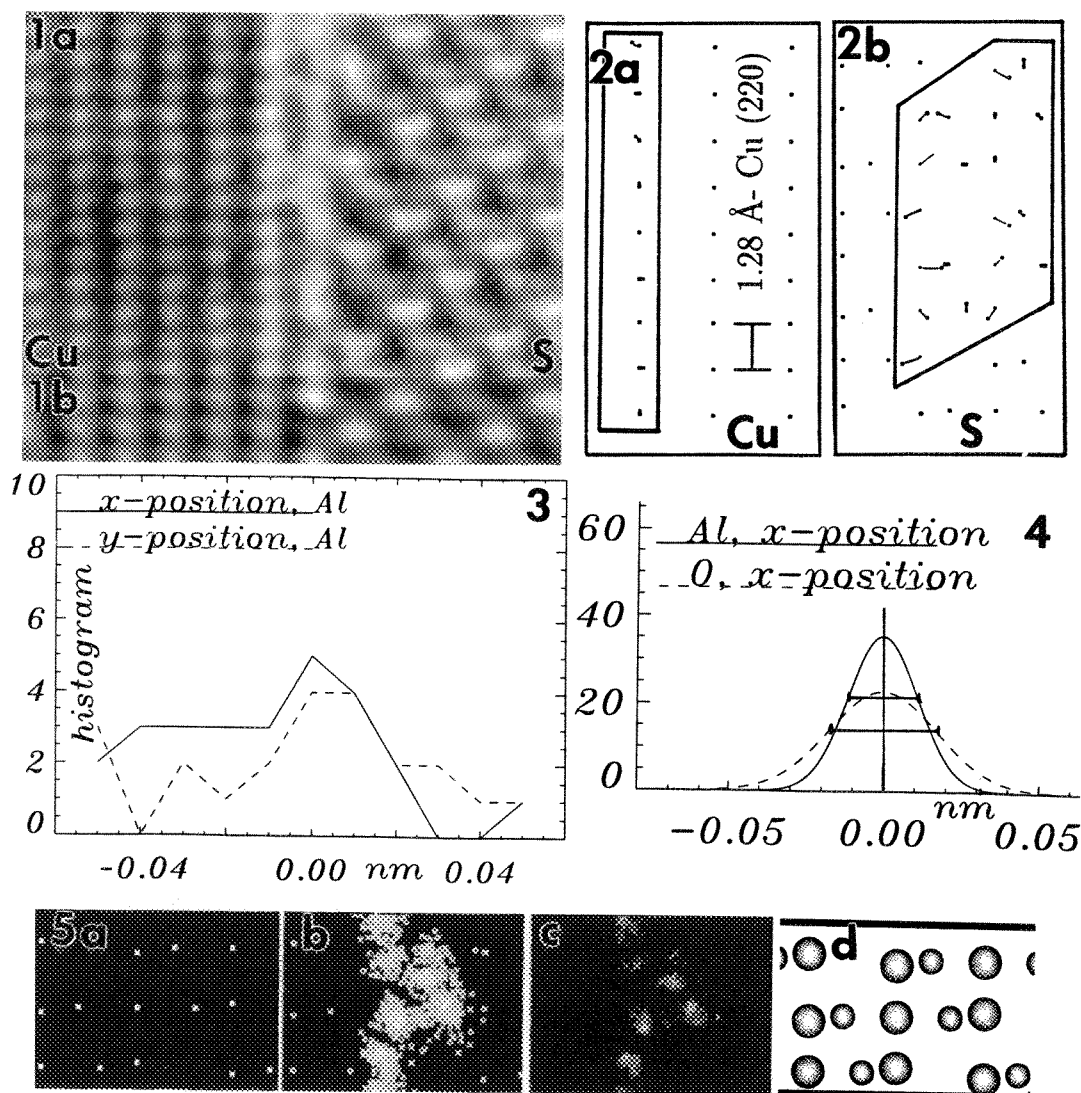
FIG. 1. - (a) Experimental image (ARM1250-Stuttgart; courtesy Dr. G. Dehm) of a Cu-sapphire interface with zone axis of $< 211 >$ in Cu and $< 2\bar{1}\bar{1}0 >$ in sapphire (S); (b) simulated inset.

FIG. 2. - Atom positions before and after optimization: (a) Section of perfect Cu with 9 columns moved (box), (b) section of pefect sapphire with 4 unit cells (box).

FIG. 3. - Location of a single Al-column refined with 36 added noise patterns (amorphous edge).

FIG. 4. - Standard deviations σ after refining 22 Al and 33 O atoms from sapphire as in fig. 2b.

FIG. 5. - Refinement of a single unit cell in sapphire: (a) perfect coordinates, (b) distribution of all trials, (c) distribution of best models based on correlation, (d) atom ball model with radii indicating the confidence level after Fig. 4.

TECHNIQUES FOR QUANTITATIVE HREM ANALYSIS OF STRUCTURE AND DISPLACEMENTS AT INTERFACIAL STEPS, FACETS AND FACET JUNCTIONS

U. Dahmen[1], S. Paciornik[2], D. Michel[3] and M. Hÿtch[3]

[1]National Center for Electron Microscopy, LBNL B72, Berkeley CA 94720,
[2]DCMM, PUC-Rio, Brazil
[3]CECM-CNRS, 15, rue Georges Urbain, F94407 Vitry sur Seine Cedex, France

Quantitative High Resolution Electron Microscopy (QHREM) has made considerable recent advances in the analysis of localized atomic structure, especially in flat, periodic interfaces. This is largely due to the increased speed and sophistication of computer algorithms that compare experimental and simulated images, and to strategies for refining this comparison. However, defects such as dislocations, disclinations or steps often lead to elastic distortion fields in the experimental image that are not included in the simulations of an idealized interface. In the presence of such defects, it is difficult to separate the short-range atomic structure immediately at the core of the interface from the longer-range displacement fields due to steps and dislocations.

In this work we describe quantitative techniques to measure atomic structure and displacement fields in these two different regimes, and to refine the structure of the core when defects lead to deviations from ideal periodic conditions. For the regime of the localized structure, we have introduced a template matching technique which measures the precise location and similarity of structural units characteristic for an interface structure [1]. In the regime of longer-range displacement fields, the moiré technique [2] and the closely related geometrical phase technique [3] have been shown to be useful quantitative tools.

Figure 1 illustrates the template matching method on the image of a stepped grain boundary in rutile [4]. The locations of characteristic structural units with a fivefold motif (white frame) were detected by calculating a cross-correlation map between the structural unit templates and the image. The peaks in this map (b) show the boundary to be made of steps and terraces. The steps are associated with DSC lattice dislocations which cause a 2° misorientation from the exact $\Sigma 5$ coincidence orientation, leading to a systematic variation of the apparent unit structure across the width of a terrace. This is illustrated in figure 2 where the similarity between any two structural units in a single terrace has been calculated. The largest difference was found between structural units nearest the dislocations associated with each step, the smallest difference at the center of the terrace. Image simulations were carried out for the ideal periodic $\Sigma 5$ misorientation, but comparisons between simulated and experimental images were confined to the structural unit to avoid systematic errors resulting from such local variations, and from the associated 2° change in misorientation. With this procedure, it was possible to determine the normal component of the rigid body shift with an accuracy of ± 0.04Å.

To measure longer-range displacement fields at and around interfaces, a moiré pattern generated by comparison with a reference lattice gives an accuracte magnified view of the distortions for each set of lattice planes. This technique is particularly useful when large areas extending over hundreds of lattice fringes are being analyzed. Figure 3 illustrates this technique for a high resolution image of a complex junction of a 90° grain boundary with a twin boundary and a small angle boundary made of individual dislocations. The initial high resolution image is relatively featureless (a) and difficult to analyze even when greatly enlarged. In (b) and (c), two moiré images with 10x magnification are generated digitally by adding a reference wave with a period 10% shorter than the average lattice. The resulting moiré patterns show a magnified view of two sets of {111} planes. It is apparent that grains 1 and 2 are rotated by 2° (20° in the moiré pattern). The dislocations are visible as extra half planes in (b) and do not disturb the lattice planes in (c). An excellent quantitative measure of the local displacement can be obtained from such images, especially for infinite magnification of the

moiré pattern, when the reference lattice has the same wavelength as the average lattice in the image. Such an image can be produced by single sideband reconstruction of the "geometric phase" of a lattice image [3], in which a component of the displacement is mapped as the gray level in the image.

References
1. S. Paciornik, R. Kilaas, J. Turner and U. Dahmen, Ultramicroscopy, in press
2. C.J.D. Hetherington and U. Dahmen, Scanning Microscopy Suppl. 6, 405-415 (1992)
3. M.J. Hÿtch and J.P. Chevalier, Ultramicroscopy 58, 97 (1995), M. Hÿtch and U. Dahmen, Ultramicroscopy, to be submitted
4. U. Dahmen, S. Paciornik, I.G. Solorzano and J.B. Vandersande, Interface Science, 2, 127 (1994)
5. This work is supported by the Director, Office of Energy Research, Office of Basic Energy Sciences, Materials Sciences Division of the U.S. Department of Energy under Contract No. DE-ACO3-76SFOOO98.
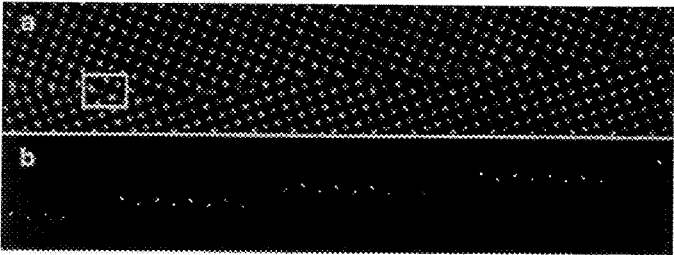
Figure 1: High resolution image of a stepped near-$\Sigma 5$ (210) tilt grain boundary in TiO_2 (a) and map (b) of peaks in cross correlation value between image and small framed template containing structural unit with pentagonal motif. Each terrace contains five structural units of this type.
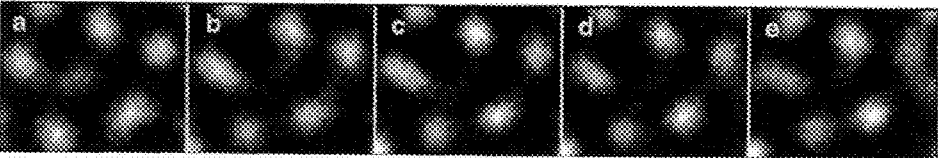
Figure 2: Magnified view of five structural units in a terrace showing a systematic change due to DSC lattice dislocations at steps causing 2° misorientation from exact $\Sigma 5$ value. Quantitatively, the change is measured by the value of cross correlation coefficients between structural unit pairs: a/b=0.85, b/c=0.96, c/d=0.97, d/e=0.92, a/c=0.81, b/d=0.94, c/e=0.89, a/d=0.77, b/e=0.82, a/e=0.6.
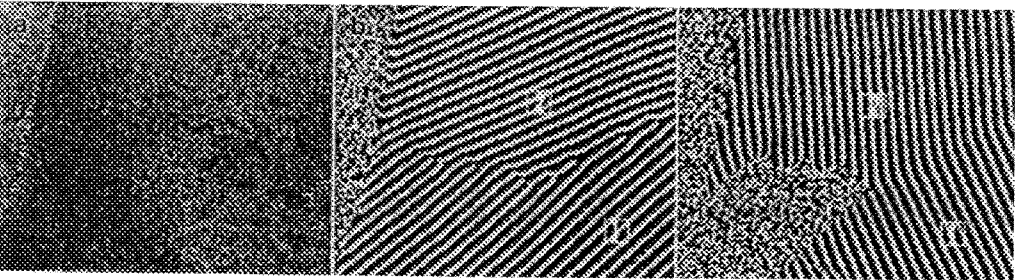
Figure 3: Digital moiré patterns (b,c) generated from a high resolution image (a) of a complex grain boundary junction by single sideband reconstruction [3]. The reference wave was chosen to yield a moiré magnification of 10x. The 2° rotation between grains 1 and 2 (20° in the moiré) is readily apparent. The rotation is due to a set of dislocations parallel to the common close packed planes, visible in (b). Fringe spacing is 23Å.

QUANTITATIVE STRUCTURE DETERMINATION OF INTERFACES THROUGH Z-CONTRAST IMAGING AND ELECTRON ENERGY LOSS SPECTROSCOPY

S. J. Pennycook*, P. D. Nellist*, N. D. Browning**, P. A. Langjahr*** and M. Rühle***

*Solid State Division, Oak Ridge National Laboratory, P.O. Box 2008, Oak Ridge, TN 37831-6030
** Dept. Physics (M/C 273), University of Illinois at Chicago, Chicago, IL 60607
***Max-Planck-Institüt für Metallforschung, Institute für Werkstoffwissenschaft, 70174 Stuttgart, Germany

The simultaneous use of Z-contrast imaging with parallel detection EELS in the STEM provides a powerful means for determining the atomic structure of grain boundaries. The incoherent Z-contrast image of the high atomic number columns can be directly inverted to their real space arrangement, without the use of preconceived structure models. Positions and intensities may be accurately quantified through a maximum entropy analysis. Light elements that are not visible in the Z-contrast image can be studied through EELS; their coordination polyhedra determined from the spectral fine structure.[1] It even appears feasible to contemplate 3D structure refinement through multiple scattering calculations.[2]

The power of this approach is illustrated by the recent study of a series of $SrTiO_3$ bicrystals,[3] which has provided significant insight into some of the basic issues of grain boundaries in ceramics. Figure 1 shows the structural units deduced from a set of 24°, 36° and 65° symmetric boundaries, and 24° and 45° asymmetric boundaries. It can be seen that apart from unit cells and fragments from the perfect crystal, only three units are needed to construct any arbitrary tilt boundary. For symmetric boundaries, only two units are required, each having the same Burgers' vector of a<100>. Both units are pentagons, on either the Sr or Ti sublattice, and both contain two columns of the other sublattice, imaging in positions too close for the atoms in each column to be coplanar. Each column was therefore assumed to be half full, with the pair forming a single zig-zag column. For asymmetric boundaries, crystal geometry requires two types of dislocations; the additional unit was found to have a Burgers' vector of a<110>. Such a unit is a larger source of strain, and is especially important to the transport characteristics of cuprate superconductors. These zig-zag columns avoid the problem of like-ion repulsion; they have also been seen in TiO_2 and $YBa_2Cu_3O_{7-x}$ and may be a general feature of ionic materials.

That the a<100> structural units are in fact the cores of lattice dislocations is suggested by Fig. 2. Here, misfit dislocation cores are seen located at the interface between $SrTiO_3$ and a $SrZrO_3$ epitaxial film, prepared by spin coating $SrTiO_3$ substrates with organic precursors followed by high temperature heat treatment to form the epitaxial layer.[4] The dislocations are located close to the interface, probably at steps, and also comprise pentagons that appear to include a pair of half columns.

Further quantitative deductions from such images would require the accurate modelling of several second order effects, including the surface relaxation around a dislocation core, the effect of the inevitable small tilt across a grain boundary, and the change in atomic vibration amplitude of lower coordinated atoms in a dislocation core. This latter effect would probably require a first principles calculation in itself, and it would seem more fruitful to take the approximate models suggested by the images as starting points for a full theoretical analysis.

At present, simultaneous Z-contrast imaging and EELS is limited to the 2.2Å resolution of the 100 kV HB501UX STEM. The greatly increased penetration of the 300 kV HB603 STEM, and its demonstrated 1.26Å probe size, would greatly extend the range of materials on which this strategy could be applied, including charge transfer effects at metal-ceramic interfaces or between monolayer catalyst rafts and their supports.[5]

References

1. M. M. McGibbon et al., Science, 266(1994)102.
2. D. J. Wallis and N. D. Browning, these proceedings.
3. N. D. Browning et al, Interface Science, 2(1995)397.
4. P. A. Langjahr et al., Mat Res Soc Symp Proc Vol 401, in press.
5. This research was sponsored by the Division of Materials Sciences, U.S. Department of Energy, under contract DE-AC05-96OR22464 with Lockheed Martin Energy Research Corp.

1. **Unit Cells and Fragments: Spacer Units**

A $\frac{A}{2}$

(100) Boundary

A* $\frac{A^*}{2}$

(110) Boundary

● Sr

◍ Half-occupied Sr

⊛ Ti-O

◓ Half-occupied Ti-O

∘ O
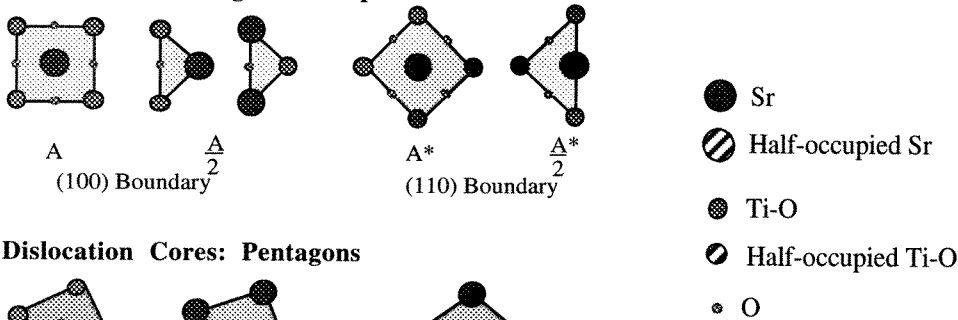
Dislocation Cores: Pentagons

B   B#   C
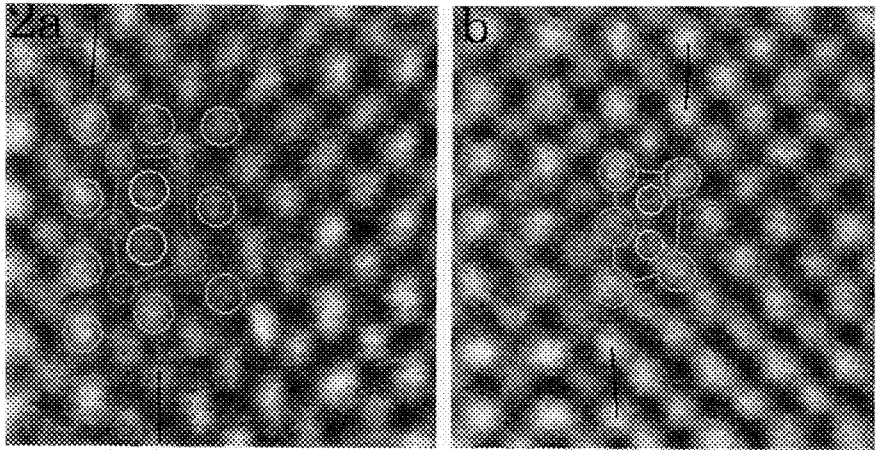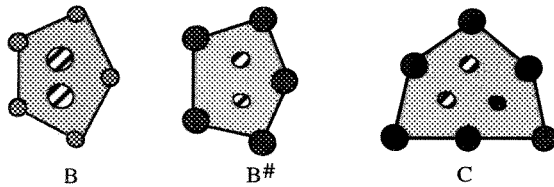
FIG. 1.--Structural units for SrTiO$_3$ deduced from Z-contrast images and EELS.

FIG. 2.--Structure of misfit dislocation cores at a SrTiO$_3$ / SrZrO$_3$ interface, showing the same structural units, with half columns apparent on the (a) Sr and (b) Zr sublattices. Lines show estimated interface location, SrTiO$_3$ is to the left.

ATOMIC STRUCTURE DETERMINATION OF NIO-ZRO$_2$(CaO) AND NI-ZRO$_2$(CaO) INTERFACES USING Z-CONTRAST IMAGING AND EELS

E.C. Dickey*, V.P. Dravid*, P. Nellist**, D.J. Wallis***, N. D. Browning***, S.J. Pennycook**

* Department of Materials Science, Northwestern University, Evanston, IL 60208
**Solid State Division, Oak Ridge National Laboratory, Oak Ridge, TN 37831
*** Dept. Physics (M/C 273), University of Illinois at Chicago, Chicago, IL 60607

Combining atomic-resolution imaging with spatially resolved electron energy loss spectroscopy (EELS) is a powerful approach to probing the geometric, chemical and electronic aspects of internal interfaces.[1,2] By elucidating these interrelated constituents of interface structure, one can begin to understand the influence of the interface atomic structure on relevant bulk material properties, deducing atomic structure/property relationships. The combined Z-contrast and EELS approach was applied to two types of heterophase interfaces: oxide-oxide (NiO-ZrO$_2$) and metal-oxide (Ni-ZrO$_2$). The interface structure will be discussed in light of these experiments and compared to previous HREM results.

The NiO-ZrO$_2$ interfaces are planar, low-energy boundaries formed during the solidification of a NiO-ZrO$_2$ eutectic system.[3] Fig. 1 is a Z-contrast image of one such boundary taken on the 300kV VG-HB603 STEM at Oak Ridge National Laboratory. Individual columns of cations are directly imaged as high-intensity sites due to the incoherent nature of the imaging process and the Z-dependence of high-angle scattering. Consistent with interpretation of previous HREM results, the geometric structure of the interface is atomically abrupt with the two phases sharing a common oxygen plane. As a consequence of this geometry, a cation-anion sequence of planes is maintained across the boundary. Interplanar spacings at and near the boundary are measured to within about 0.2Å revealing any local relaxations normal to the interface. Since the Z-contrast image is only a projected image, results from an orthogonal zone axes will be presented to reveal the three-dimensional interface structure. Near atomic-resolution EELS was performed on a 100kV VG-HB501UX. Using the Z-contrast image to position the probe, line profiles of the oxygen K-edge, Ni L$_{2,3}$ edge, and Zr M$_{2,3}$ were collected in steps of interplanar distance across the boundary. The resulting chemical profiles, presented in fig. 2, define the chemical width of the boundary to less than 5 Å, less that three planar spacings. The fine structure of the oxygen K-edge was also probed across the boundary (see fig. 3). The O K-edge fine structures in the bulk NiO and ZrO$_2$ are distinct because of different oxygen coordinations— octahedral in NiO and tetrahedral in ZrO$_2$. Changes in the fine structure near and at the boundary indicate atomic relaxation which alters aspects of the electronic structure.

The Ni-ZrO$_2$ interfaces result from the reduction of a NiO-ZrO$_2$ eutectic, facilitated by an inherent electrochemical potential across the boundary in reducing atmospheres.[4] Fig. 4 is a Z-contrast image of this metal-ceramic boundary. Once again, the image shows the geometric structure of the interface as atomically abrupt. Although the lattice mismatch between the Ni (111) and the ZrO$_2$ (200) is 16.7%, no localized dislocation cores are observed and the interface appears incommensurate. Preliminary interpretation of Z-contrast images and EELS results indicate that the system is not in equilibrium so that two types of interface structures are observed: one in which the ZrO$_2$ terminates with an oxygen plane and the other with a metal planes. Implications of these results will be discussed.

References
1. N.D. Browning, M.F. Chisholm, and S.J. Pennycook, *Nature*, **333** (1993) 143-146.
2. P.E. Batson, *Nature*, **366** (1993) 727-728.
3. G. Dhalenne and A. Revcolevschi, *J. Crystal Growth*, **69** (1984) 616-618.
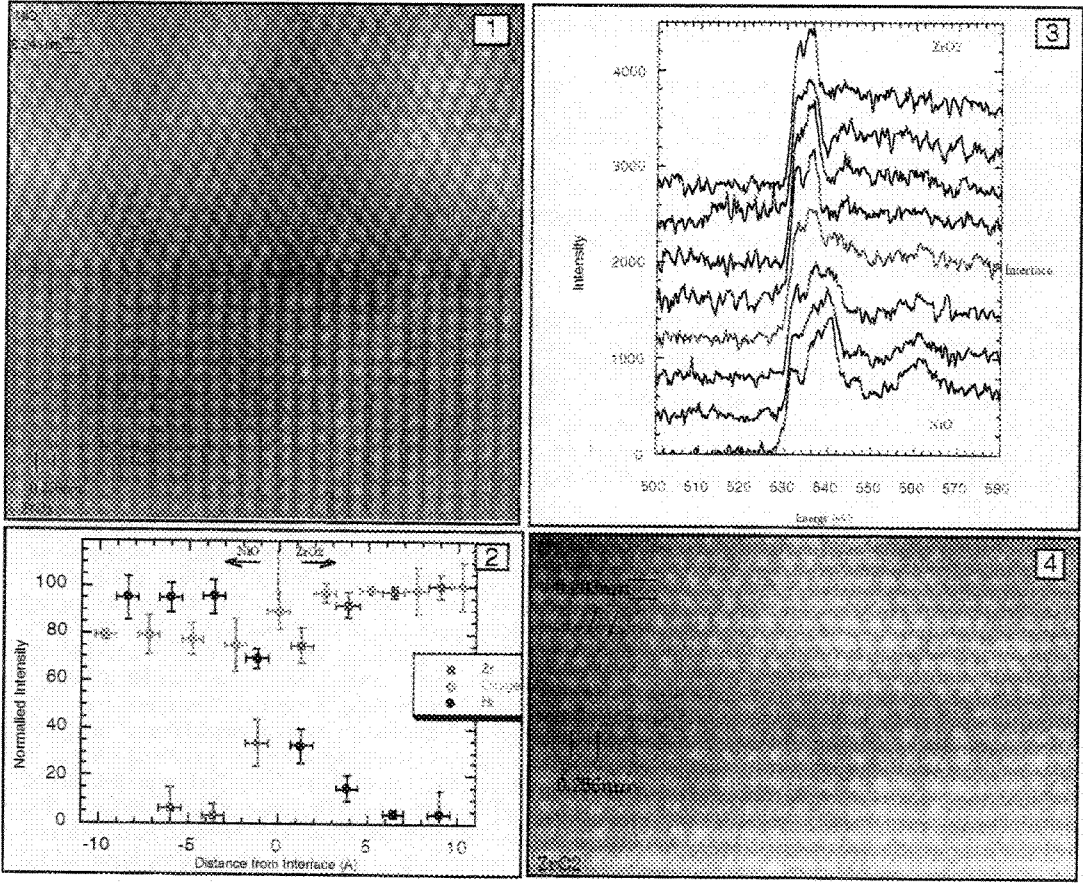
Fig 1: Z-contrast image of NiO-ZrO$_2$ interface shows a geometrically abrupt interface.

Fig. 2: EELS intensity profiles across NiO-ZrO$_2$ interfaces define the chemical width to less than 5Å.

Fig. 3: Oxygen K-edge profile across NiO-ZrO$_2$ interface taken in steps of interplanar spacing reflect the atomic configurations at and near the boundary.

Fig. 4: Z-contrast image of Ni-ZrO$_2$ interface shows a geometrically abrupt interface.

CHARACTERIZATION OF THE (01̄10) α-Ti/γ-TiH INTERFACE USING HIGH-RESOLUTION TRANSMISSION ELECTRON MICROSCOPY (TEM) AND ELECTRON ENERGY LOSS SPECTROSCOPY (EELS)

M. M. Tsai and J. M. Howe

Department of Materials Science and Engineering, University of Virginia, Charlottesville, VA 22903

Precipitation of γ-TiH in α-Ti-H alloys involves a hcp → fct lattice transformation with hydrogen as an interstitial diffusing element. Results obtained from a previous TEM study have shown that the lengthening rate of γ-TiH is diffusionally controlled at 25°C, and possibly interfacially controlled at temperatures of 50°C and higher.[1] Therefore, it is essential to ascertain the presence or absence of hydrogen atoms at the interface. TEM foils from a 800 ppm wt.% Ti-H alloy were analyzed using high-resolution TEM and image simulations in order to determine the effects of hydrogen on high-resolution images of the α-Ti/γ-TiH interface, and EELS was used to determine the whether the hydride structure was fully formed up to the interface.

The models of the α-Ti/γ-TiH interface shown in Figure 1 were created using CrystalKit.[2] MacTempas was used to simulate the interface based on the models in Figure 1 and the results are shown in Figure 2.[3] TEM foils were examined in a JEOL 4000EX high-resolution TEM along the [0001] zone axis so that the (01̄10) interface could be imaged edge-on. The filtered image shown in Figure 3 was produced using the fast Fourier transform (FFT) and inverse FFT functions found in DigitalMicrograph™.[4] The EELS spectra in Figure 4 and the electron spectroscopic image (ESI) in Figure 5 were obtained in a JEOL 2010F field emission TEM equipped with a Gatan Imaging Filter (GIF).

The models shown in Figure 1 are identical to interface models I and III respectively, as discussed by Bourret et al.[5] The difference between Figure 1a and b is the absence of hydrogen atoms between the titanium atoms in the hydride phase at the interface. The objective lens defocus values used in the simulated images varied from -30.0 nm to -60.0 nm in -5.0 nm increments, with the thickness ranging from 1.0 nm to 15.5 nm in 2.5 nm increments. The projected potential of the models is shown in Figure 2a, and the simulated images based on Figures 1a and b for a sample thickness of 3.0 nm and an objective lens defocus of -45 nm are shown in Figures 2b and c respectively. The simulated images appear to be identical, indicating that the presence or absence of hydrogen near the interface has very little effect on high resolution images of the interface. Figure 3 shows an experimental filtered image of the interface superimposed with a simulated image from Figure 2. It appears that the simulated images in Figure 2 are also in agreement with experimental images, and that the (01̄10) α-Ti/γ-TiH interface can be simulated. Figure 4 shows EELS spectra of α-Ti and γ-TiH taken on both sides of the interface. The energy difference of the plasmon peaks of the phases was used to produce an ESI of the hydride shown in Figure 5. It appears that the hydride structure is fully formed up to the interface, as demonstrated by the constant intensity of the hydride phase up to the interface. This is supported by the intensity profile taken across the interface, as shown in Figure 6. The drop off in the intensity is sharp and indicates the position of the interface in the image.

References

1. M. M. Tsai and J. M. Howe, *Metal. Trans.*, 26A(1995)2219.
2. CrystalKit Software, RKCS, Berkeley, CA.
3. R. Kilaas, Proc. *45th Ann. Meeting of EMSA*, ed. G. W. Bailey, (1987)66.
4. Digital Micrograph™ Software, Gatan Inc., Pleasanton, CA 1995.
5. A. Bourret et al., *Scripta Metall.*, 20(1986)861.
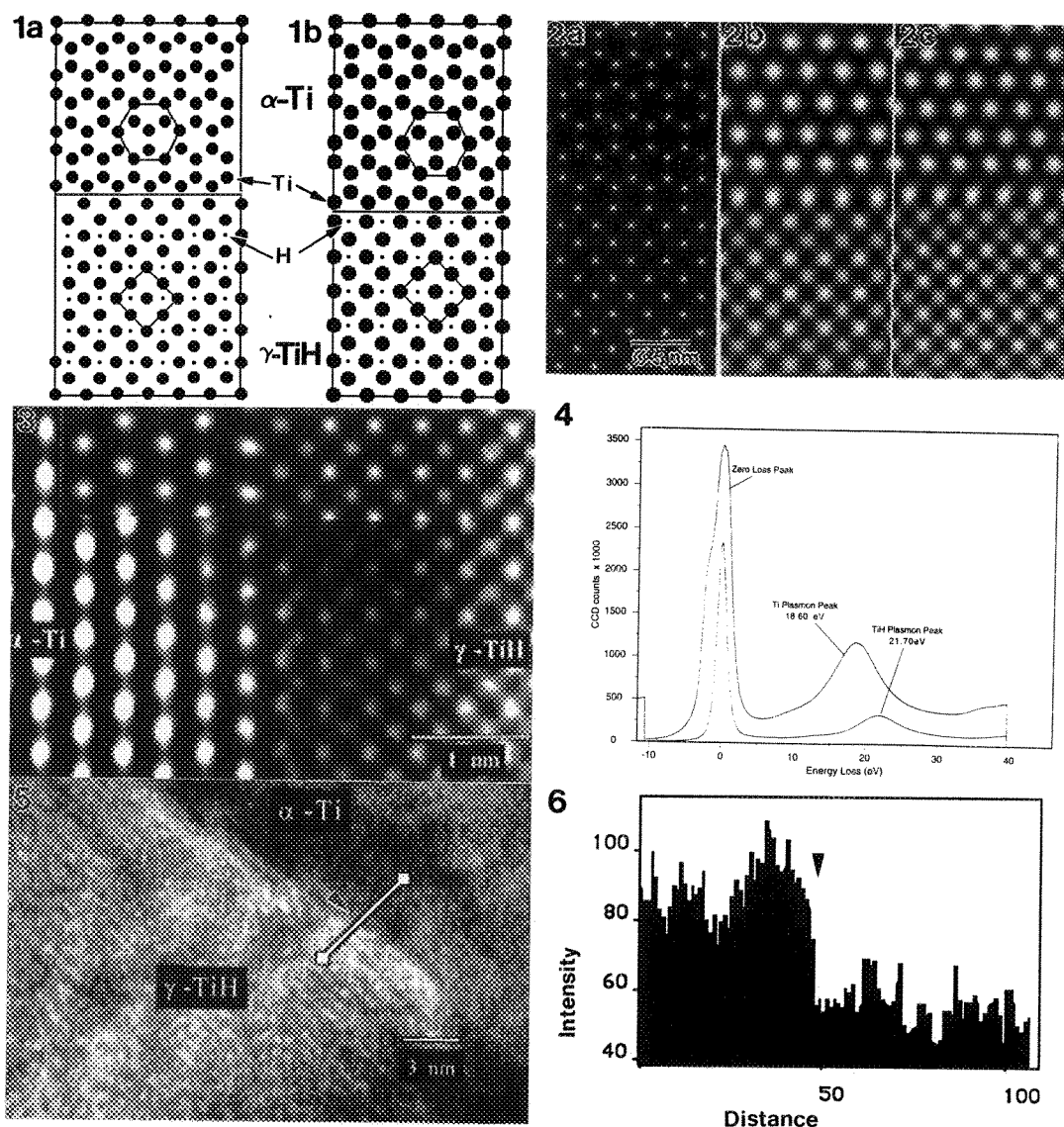
Figure 1. Interface models created using CrystalKit. In (a) hydrogen atoms are present at the interface but not in (b).

Figure 2. Simulated high-resolution TEM images based on the models in Figure 1. (a) is the projected potential of the images. (b) and (c) are simluated images with thickness of 3 nm and defocus of -45 nm, and correspond to Figures 1a and b respectively.

Figure 3. Experimental filtered image using DigitalMicrograph on which Figure 2b is superimposed.

Figure 4. Composite EELS spectra of α-Ti and γ-TiH with their respective plasmon peaks.

Figure 5. Electron spectroscopic image of γ-TiH obtained using GIF with a 2 eV slit. The bar indicates the position at which an intensity profile was taken. The arrow points to the position of the interface.

Fiigure 6. Intensity profile across the interface. The arrow corresponds to the arrow in Figure 5.

109

DETERMINATION OF THE INTERFACE STRUCTURE OF CdTe(111) ON Si(100) USING Z-CONTRAST IMAGING AND EELS

D.J. Wallis[*][1], P. D. Nellist[**], S. Sivananthan[*], N.D. Browning[*] and S.J. Pennycook[**]

[*]Dept. of Physics, University of Illinois at Chicago, 845 W. Taylor, Chicago, IL 60607-7059.
[**]Oak Ridge National Lab, Solid State Division, P.O. Box 2008, Oak Ridge, TN 37831-6031.

The epitaxial growth of dissimilar materials, or hetroepitaxy, is of great technological interest for a variety of reasons. Perhaps the most obvious of these is that high quality, large area substrates are unavailable for many materials. It is therefore necessary to resort to growing the material of interest on a dissimilar substrate. However, this procedure introduces its own problems, such as differences in crystal structure and mechanical properties of the substrate and film materials. Understanding the structural aspects of this growth process is a critical step towards the production of high-quality and reliable integrated device structures.

One system of current interest for application into diverse electron-optical devices is HgCdTe. HgCdTe is a semiconductor whose band gap may be tailored by the concentration of Hg giving it applications as X-ray and g-ray detectors and also in solar cells. The first stage in developing integrated technology for this material is the production of a high-quality substrate. For this task, CdTe seems an ideal choice. However, CdTe itself does not exist in a form that immediately lends itself for use as a substrate and hence must be prepared by heteroepitaxy.

A prime candidate for use as a substrate in heteropitaxial preparation of high-quality CdTe films is silicon. Silicon technology provides large, good quality, single crystals at relatively low cost and offers the promise of incorporating the deposited material's electronic properties with standard integrated circuit technology to give truly monolithic integration. However, the growth of CdTe on Si represents an extreme problem since the lattice mismatch for these two materials is 19.3%. Recently, the epitaxial growth of CdTe(111) on Si(001) has been achieved using MBE techniques.[2] The quality of such films, which is of vital importance in producing good devices, is influenced by the use of surfactants such as As, and slight misorientations of the silicon substrate surface away from the [001] direction.[2] From this, it is clear that the atomic structure at the CdTe/Si interface has a pervasive influence in determining the properties of the entire film.

The interface structure at the CdTe(111)/Si(100) interface has been investigated using Z-contrast imaging in a VG HB-603 STEM and Electron Energy Loss Spectroscopy (EELS) in a VG HB-501 STEM. Fig 1 shows a Z-contrast image of the CdTe/Si interface. Due to the incoherent nature of the Z-contrast imaging process each atomic column may be considered to scatter independently allowing individual columns to be identified.[3] The intensity of the columns also provides evidence for the chemical nature of individual columns since image intensity is related to the mean square atomic number of a column. Thus, the CdTe film can be identified since it is much brighter than the Si substrate. The 1.3Å resolution of the HB-603 allows the "dumbbells" in both silicon and CdTe to be resolved and on careful inspection the polarity of the CdTe "dumbbell" may be discerned in the bulk of the film. This polarity is maintained right up to the CdTe/Si interface showing that the film is Te terminated at the substrate.

The atomic features immediately below the CdTe film show a "dumbbell" like structure aligned with the Si [100] direction, however, the spacing of these atoms is much larger than the 1.36Å bulk spacing of the Si dumbbells. EELS spectra collected from individual planes at this interface (fig 2) show that the planes immediately below the film contain a high concentration of Te atoms. These quantitative results indicating that during the growth process Te diffuses approximately 4 planes into the Si surface. This Te rich region therefore provides a buffer layer on which the CdTe film is grown. The spectra also show that diffusion of Cd into the Si substrate is limited to less than half a

monolayer in a single plane. This is an important factor for understanding the growth processes and also demonstrates that the spatially extended Te signal does not occur due to probe tails or delocalization effects. Additionally, in fig 1 it can be seen that the majority of relaxation necessary to accommodate the 4% misfit of Si (100) and CdTe(111) takes place in a single monolayer immediately below the deposited film.

In addition to Te, a strong oxygen signal is detected just below the interface in the Si substrate (fig 2). This signal is confirmed not to be due to a surface oxide layer since no oxygen can be detected in the bulk of the substrate. However, oxygen may occur at this interface for two reasons: incomplete cleaning of the Si surface before growth of the CdTe film, or preferential oxidation of the interface during specimen preparation. Subsequent studies on this sample suggest that preferential oxidation at the interface occurs since the oxygen K-edge intensity is seen to grow over time. The effects of oxidation on the interface structure are seen to be negligible in the image as the crystallinity of the interface is maintained. Also of interest is that the quality of CdTe films may be enhanced if As is introduced into the growth chamber immediately before deposition of the film.[2] The precise role of this As in the growth process is as yet undetermined. In the sample studied, no arsenic could be detected suggesting that it acts as a surfactant which aids the initial growth of the film and is then removed.

In conclusion Z-contrast imaging and EELS have allowed the atomic structure at a hetroepitaxy interface to be studied. These combined techniques provide unique details of the atomic structure and chemical composition at the interface. These details are vital to allow an understanding of the growth mechanism of such systems and offer clues which will allow improvements in the quality of the films produced.[4]

References

1. Contact address, ORNL, Solid State Division, P.O. Box 2008, Oak Ridge, TN 37831-6031.
2. Chen Y.P. et al, Journal of Electronic Materials 22 951-957 (1993).
3. Jesson D.E. and Pennycook S.J., Proc. R. Soc. Lond. A, 449 273-293 (1995).
4. The authors acknowledge the help of J.T. Luck for specimen preparation. This work was funded by NSF grant No. DMR-9503877.
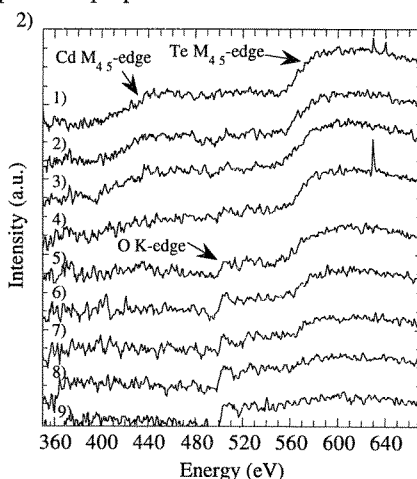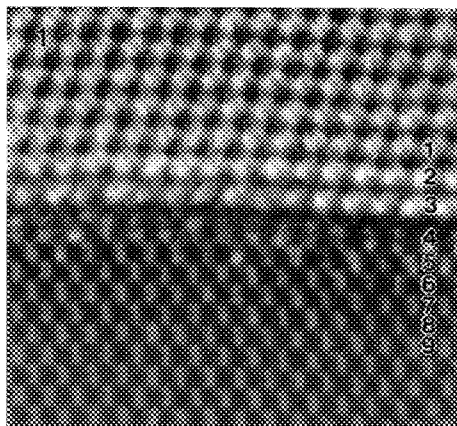
FIG 1. Band-pass filtered Z-Contrast image of the interface for CdTe(111)/Si (100).
FIG 2. EELS spectra collected plane by plane across the CdTe/Si interface. The spectrum numbers correspond to the numbered planes in fig 1.

PSEUDO ABERRATION FREE FOCUS FOR ATOMIC RESOLUTION IMAGING OF TWO ADJOINING CRYSTALS

H. Hashimoto*, H. Endoh**, M. Hashimoto*** and M. Song*

* Faculty of Engineering, Okayama University of Science, Okayama 700, Japan
**Faculty of Industrial Art, Kyoto Institute of Technology, Kyoto 606, Japan
*** Faculty of Engineering, Setsunan University, Neyagawa, Osaka 572, Japan

The atomic structure images of two crystals on both sides of the interface made by conventional TEM are not so easy to be recorded at the same focus without the effect of spherical aberration of imaging lenses even though the spacings of the crystal lattices of both crystals are within Scherzer focus limit, because the specimen is generally larger than 10nm thickness and cannot be treated as weak phase objects and Bragg reflected waves from tow crystals generally cannot be in phase at the image plane. In TEM, the shift of the phases of several Bragg reflected waves from a crystal due to the spherical aberration (coefficient Cs) can be compensated by the defocus (Δf), which was named as aberration free focus (AFF) [1] . The current images of crystals on both sides of an interface are formed by the waves reflected from one or two kinds of lattice planes with low indexes. The relative phase of these waves also can be compensated by a focus named as pseudo-AFF. The present paper concerns to the P-AFF which·is given by setting phase shift to be $2m\pi$, as

$$\Delta f = m(2d^2/\lambda) + (Cs\lambda^2/2d^2) \qquad \text{or} \qquad (\lambda^3/4d^4) Cs - (\lambda/2d^2)\cdot \Delta f = m \qquad (1)$$

where λ : wave length, d: the lattice spacings d1, d2, · ·, $m = \pm 1, \pm 2, ...$ P - AFF images are formed on both sides of the focussing point which located from Gaussian image plane with the distance of $Cs\lambda^2/2d^2$, and with the period of $2d^2/\lambda$ which is the Fourier Images(Fig. 1) . In the P - AFF conditions, intensity maxima of those Fourier images with certain order superimpose exactly. In equation (1), which is a linear equation for Cs and Δf, the values of Cs and Δf for satisfying two equations with the values d = d1 and d2 can be obtained for certain values of m. Fig.2 is the values of Cs and Δf in AFF condition for the images of Al_2O_3 crystal projected along $[1\bar{1}\cdot 0]$. The values of m1 and m2 are for $d1(1\bar{1}\cdot 2) = 3.48$Å and $d2(1\bar{1}\cdot \bar{4}) = 2.55$Å. These values are the intersection of two lines in Cs - Δf diagram of equation (1) as shown in Fig. 3. Fig. 4 shows the projection of Al atoms, electron intensity at the bottom surface of Al_2O_3 crystal of 50nm in thickness and the images formed by the electron waves with degree of coherence (q: beam divergence, Δ : chromatic defocus value) [2] . Figs. 5 and 6 are P - AFF and AFF diagrams of MgO(d(200) = 0.210nm) and $MgAl_2O_4$ (d(220) = 0.285 nmd(400) = 0.202nm), respectively. By superposing Figs. 5 and 6, it is seen that P - AFF conditions for these two crystals are realized at A in Fig. 5 which is Cs = 9.0mm, Δf = 50.0nm. The projected atom position and calculated P - AFF images of MgO and $MgAl_2O_3$ are seen in Fig. 7. Similar relation holds for $MgAl_2O_4$ (d(220) = 0.2857nm) and Al_2O_3 (d($1\bar{1}2$) = 0.3481nm, d($1\bar{1}\bar{4}$) = 0.255nm) crystals. That is Cs = 9.41mm, Δf = 42.5nm, which is the condition indicated by A in Fig. 3. By changing specimen position in z-direction Cs can be changed 9.0mm ~ 9.4mm and by changing Δf from 50.0nm to 42.5nm the images of three crystals MgO/ $MgAl_2O_4$/ Al_2O_3 [3] on both sides of two interfaces can be recorded without the effect of spherical aberration.

REFERENCES:
[1] H. Hashimoto, H. Endoh et al: Chemica Scripta, Proc. Nobel Symposium 14 (1978-79) 23.
[2] K Ishizuka: Ultramicroscopy 5 (1980) 55.
[3] D. Hesse, R. Scholz et al: Int. Nat. Symp. HV and HREM, Sttutgart Feb. (1994)
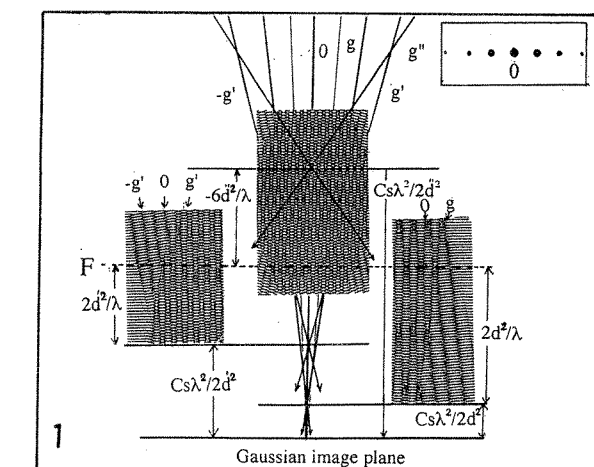
Al_2O_3	$d_{1\bar{1}2} = 0.348, d_{1\bar{1}\bar{1}} = 0.255$ (nm)		
m_1	m_2	$C_s(mm)$	$\Delta f(nm)$
1	2	1.15133	-134.538
0	1	8.25755	92.075
1	3	9.40887	- 42.314
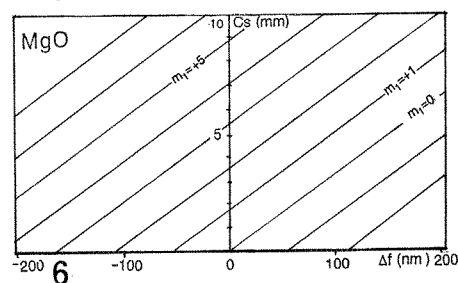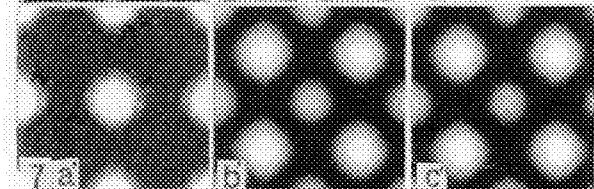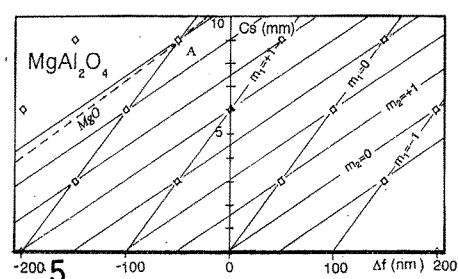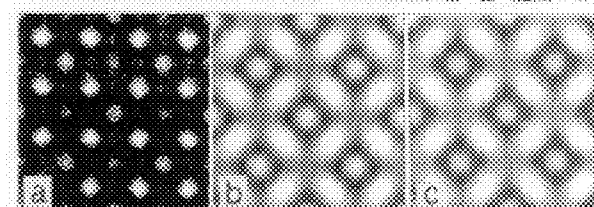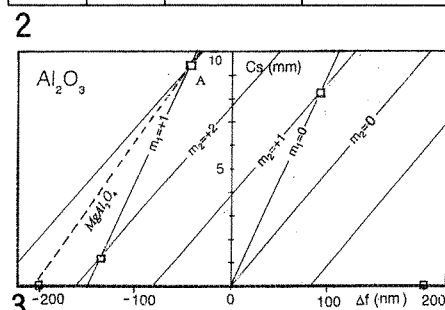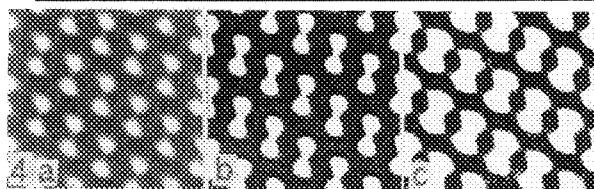
FIG.1 AFF construction.

FIG.2 AFF condition for Al_2O_3 in $[1\bar{1}\cdot 0]$ projection.

FIG.3 AFF diagram for Al_2O_3 in $[1\bar{1}\cdot 0]$. P-AFF condition for Al_2O_3/ $MgAl_2O_4$; is at A.

FIG.4 Al_2O_3 in $[1\bar{1}\cdot 0]$ projection. (a) Al atom position. (b) electron intensity at bottom,   (c) AFF image; q=0.1, Δ=1nm, Cs=1.15mm, Δf=134.54nm (overfocus), thickness 50nm.

FIG.5 AFF diagram for $MgAl_2O_4$ [001] . P-AFF condition for $MgAl_2O_4$/ MgO iis at A.

FIG.6 AFF diagram for MgO [001] .

FIG.7 PAFF images of $MgAl_2O_4$/ MgO. (a), (a´) atom positions, (b), (b´) electron intensities at bottoms,   (c), (c´) P-AFF images. Cs=9.00mm, Δf=50.0nm (overfocus), thickness 50nm.

113

QUANTIFICATION OF ORDER IN THE LIQUID AT A SOLID-LIQUID INTERFACE BY HIGH-RESOLUTION TRANSMISSION ELECTRON MICROSCOPY (HRTEM)

J. M. Howe

Department of Materials Science and Engineering, University of Virginia, Charlottesville, VA 22903

A number of different theoretical approaches have been used to model the atomic structure and properties of solid-liquid interfaces.[1] Most calculations indicate that ordering occurs in the first several layers of the liquid, adjacent to the crystal surface. In contrast to the numerous theoretical investigations, there have been no direct experimental observations of the atomic structure of a solid-liquid interface for comparison. Saka et al.[2] examined solid-liquid interfaces in In and In-Sb at lattice-fringe resolution in the TEM, but their data do not reveal information about the atomic structure of the liquid phase. The purpose of this study is to determine the atomic structure of a solid-liquid interface using a highly viscous supercooled liquid, i.e., a crystal-amorphous interface.

A 40 μm thick amorphous $Pd_{80}Si_{20}$ alloy ribbon was partially crystallized to form a mixture of Pd_3Si and Pd_9Si_2 phases.[3] Samples for HRTEM were prepared by ion milling and HRTEM was performed on small Pd_3Si crystals in an exact [01$\bar{1}$] zone-axis orientation. A through-focus series of images of a (211) crystal-amorphous interface was taken in about 3.0 nm increments on a JEOL 4000EX top-entry microscope operating at 400 kV. An atomic model of a (211) Pd_3Si solid-$Pd_{80}Si_{20}$ liquid interface was constructed by growing an amorphous $Pd_{80}Si_{20}$ liquid on a Pd_3Si seed crystal using an algorithm based on the dense random packing of hard spheres.[4] Simulated HRTEM images were calculated using the TEMPAS multislice program.[5] Experimental and calculated HRTEM images were digitized and analyzed using the fastFourier transform (FFT) and image profile routines available in Digital Micrograph™ software.[6]

The atom positions in one slice of the unit cell of the (211) interface used in the HRTEM image simulations are shown in Fig. 1a. The location of the interface between the last (211) plane of the Pd_3Si crystal and the $Pd_{80}Si_{20}$ liquid phase is indicated by arrowheads and a line. A simulated HRTEM image of the interface in Fig. 1a for a specimen thickness of 5.5 nm and a defocus of -40.0 nm is shown in Fig. 1b. In the image, the positions of high atomic density are dark. A corresponding experimental HRTEM image of a (211) solid-liquid interface is shown in Fig. 1c. There is excellent matching between the simulated and experimental HRTEM images. Sighting along the arrows to the right of the experimental image in Fig. 1c indicates evidence of partial conformation of the liquid to the crystalline solid over several interplanar spacings in both the simulated and experimental HRTEM images.

The (211) solid-liquid interface in Fig. 1c was digitized and the intensity profile in Fig. 2 was obtained by summing intensities horizontally in the image, so there is a direct correspondence between the image position and the intensity profile across the the interface in Figs. 1c and 2. Since the atomic columns in the Pd_3Si phase are dark, the interface between the last crystalline plane and the adjacent liquid is at the position indicated by arrowheads in Fig. 2. Examination of the intensity profile shows that there is a distinct difference in the mean intensities of the crystal and liquid phases (indicated by a thin, dark line), which are about 18,000 and 27,000, respectively. The mean intensity changes abruptly over only one or two planes at the interface. In contrast, there are five layers in the liquid, labelled 1 through 5 in Fig. 2, that display the same periodicity as the interplanar spacing in the crystalline Pd3Si phase parallel to the interface, although the mean image intensity in this area is nearly equal to that of the liquid far from the interface (on the far right in Fig. 2). These features provide strong experimental evidence of order in the liquid at the solid-liquid interface. A FFT of a 256 x 256 area of the liquid phase immediately adjacent to the interface in Fig. 1c was performed and the resulting diffraction pattern is shown in Fig. 3. The pair of spots indicated by arrows correspond to the (211) interplanar spacing parallel to the interface. The presence of the spots in the FFT provides further indication of order in the liquid at the interface in the HRTEM image.

The results from this study demonstrate that analysis of the intensities in HRTEM images of thin specimens using intensity profiles and FFTs provides an experimental method to determine the atomic structure of solid-liquid interfaces. Application of these techniques to a Pd_3Si (211) solid-liquid interface in amorphous $Pd_{80}Si_{20}$ alloy shows that order extends four to five interplanar spacings into the liquid phase adjacent to the crystal surface, in agreement with most theoretical calculations.[7]

References

1. F. Spaepen, in *Solid State Physics, Vol. 47*, Academic Press, San Diego (1994) 1.
2. H. Saka et al., *Ultramicroscopy*, 39 (1991) 110.
3. W. H. Brearley, P.-C. Shieh and J. M. Howe, *Metall. Trans.*, 22A (1991) 1287.
4. P.-C. Shieh, C. O. Stanwood and J. M. Howe, *Ultramicroscopy*, 35 (1991) 99.
5. R. Kilaas, in *Proc. 45th Ann. Meeting EMSA*, San Francisco Press, CA (1987) 66.
6. *Digital Micrograph™ User's Guide*, Gatan, Inc., Pleasanton, CA (1994).
7. This research was supported by the National Science Foundation under grant DMR-9302439.
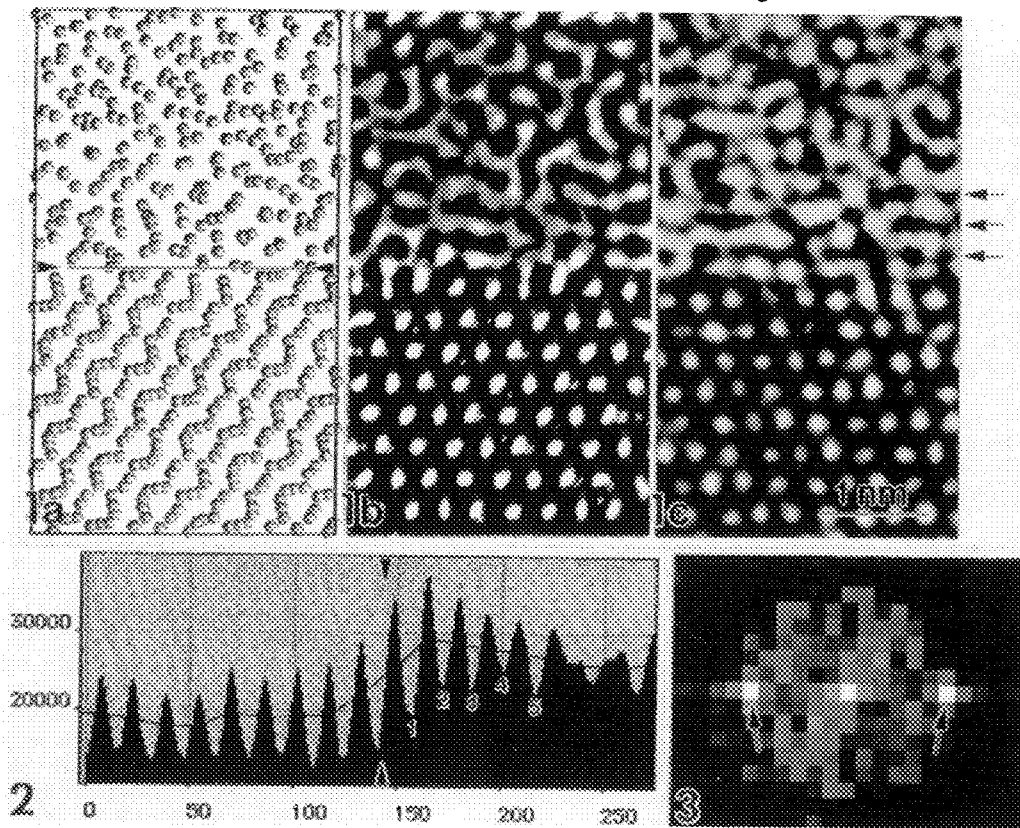
FIG. 1 - (a) Atomic model of the (211) solid-liquid interface used in the image simulations. (b) Simulated HRTEM image of the (211) crystal-liquid interface in a [01 1̄] zone axis. (c) Experimental HRTEM image of a (211) interface viewed along a [01 1̄] zone axis.

FIG. 2 - Intensity profile across the interface in Fig. 1c with the solid on the left and liquid on the right.

FIG. 3 - Diffraction pattern obtained by FFT of the liquid next to the (211) crystal surface in Fig. 1c.

RIGID-BODY TRANSLATION (RBT) OF A NiO-ZrO$_2$(cubic) BICRYSTAL AND ITS IMPLICATIONS FOR INTERFACE ATOMIC STRUCTURE

E.C. Dickey, V.P. Dravid

Department of Materials Science and Engineering, Northwestern University, Evanston, IL 60208

Any internal interface between two crystalline materials can be described by five macroscopic and three microscopic degrees of freedom.[1] The five macroscopic, or geometric, degrees of freedom describe the relative orientations of the two crystalline lattices and interface plane. For the case of low-energy NiO-ZrO$_2$ boundaries this is defined by the orientation relationship: NiO(111)//ZrO$_2$(100), NiO[1$\bar{1}$0]//ZrO$_2$[010].[2] The three microscopic degrees of freedom describe the relative in-plane and out-of-plane RBT (T_x,T_y,T_z); these RBTs are geometric mechanisms by which the interface can relax to a low-energy configuration. The combination of these eight degrees of freedom describes completely the bicrystallography. This paper investigates the RBT associated with NiO-ZrO$_2$ interfaces as measured from HREM and Z-contrast images (see fig. 1).

Consider first the in-plane RBT associated with NiO-ZrO$_2$ interfaces. Fig. 2 is a schematic representation of the intersecting (a) projected point symmetries and (b) three-dimensional symmetries along the interface plane of NiO-ZrO$_2$. The maximum possible point symmetry of the bicrystal is 2mm and maximum whole-pattern symmetry is m. Dravid showed through CBED experiments that the bicrystal does indeed maintain this maximum possible symmetry yielding a monoclinic bicrystal, and by symmetry arguments, this corresponds to zero in-plane RBT.[3] Although the bicrystal symmetry has been completely defined, it has not provided a unique solution for the interface structure. Six possible configurations remain which maintain the maximum bicrystal symmetry. Each model corresponds to a different plane in the FCC stacking sequence of NiO terminating at the interface. For issues of bonding and interfacial energy, it important to distinguish these six models, because each results in a distinct atomic configuration at the interface. It was appreciated long ago that geometric descriptions of interfaces are necessary but not sufficient for understanding the energetics of interfaces.[4] But, in the case of NiO-ZrO$_2$, the bicrystallography restricts the interface configurations to six possibilities (excluding local relaxations). The relative in-plane displacements of the two lattices were measured from both HREM and Z-contrast images. Both imaging techniques have advantages and disadvantages for measuring RBTs: HREM can suffer from artifacts due to crystal tilt, astigmatism and beam tilt which will shift the lattice images from the actual lattice position. While Z-contrast images do not incur these problems, they can suffer from scan distortions and have a poorer signal-to-noise ratio and pixel resolution than HREM images.

Out-of-plane RBT, or volume expansion, for a grain boundary is defined as the excess free volume at the boundary, a thermodynamic quantity. Volume expansion of a heterophase interface, however, is a more elusive concept because it lacks any obvious reference structure. It can be defined in geometric terms, however, as the relative displacement of the two lattices with respect to some reference displacement (d_0), defined here as the average of the two interplanar spacings parallel to the boundary: $d_0=(d_1+d_2)/2$. The out-of-plane RBT for NiO-ZrO$_2$ was measured from both Z-contrast and HREM images. Several techniques were used to measure this RBT, including the lattice displacement method as proposed by Stobbs and coworkers and later modified by Merkle and Buckett.[5,6,7,8] The lattice displacement technique is a real space measurement in which peak positions are obtained by a center-of-gravity calculation and fit to a linear function which represents the lattice. Not only have we used this technique to measure the out-of-plane RBT, but we have used a modified version in which the peak positions are found through a maximum-entropy routine. A new technique is also explored. In this method, the image or a line profile taken pependicular to the boundary is multiplied by a Hanning window and then Fourier transformed. The wave vector and phase are obtained from the maximum pixel in the FT and its largest neighbor; this results in a expression for the cosine wave that best fits the bulk lattice (see fig. 4). The applicability and usefulness of the different RBT measurement techniques to Z-contrast and HREM images will be discussed, and results obtained from both imaging techniques will be compared.

References

1. See for example: D. Wolf, in *Materials Interfaces*, D. Wolf, S. Yip, Eds. (Chapman and Hall, London, 1992) 716.
2. V.P. Dravid, C.E. Lyman, M.R. Notis, A. Revcolevschi, *Ultramicroscopy*, **29** (1989) 60-70.
3. V.P. Dravid, M.R. Notice, C.E. Lyman and A. Revcolevschi, Mat. Res. Soc. Symp. Proc. Vol. 159, 1990 Materials Research Society, 95-100.
4. A.P. Sutton and R.W. Balluffi, *Acta Metall.*, **35** 9 (1987) 2177-2201.
5. G.J. Wood, W.M. Stobbs, D.J. Smith, *Phil. Mag.* **A 50**, no. 3 (1984) 375-391
6. W.M. Stobbs, G.J. Wood, D.J. Smith, *Ultramicroscopy* **14** (1984) 145-154.
7. K.L. Merkle, *Ultramicroscopy* 40 (1992) 281-290
8. M.I. Buckett, K.L. Merkle, *Ultramicroscopy* **56** (1994) 71-78

Fig. 1: Orientation relationship of NiO-ZrO$_2$ (cubic) bicrystal

Fig. 2: Schematic showing maximum symmetry for NiO-ZrO$_2$ bicrystal (a) projected point symmetry (b) 3-D symmetry

Fig. 3: New method for determining out-of-plane RBT utilizes the Fourier transform to measure the relative positions of the bulk lattices.

SIMULATED CHEMICAL IMAGING OF InGaAs/ InAlAs INTERFACES

G. Mountjoy[*], P.A. Crozier[*], P.L. Fejes[**], R.K. Tsui[***] and G.D. Kramer[***]

[*]Center for Solid State Science, Arizona State University, Tempe, AZ 85287-1704
[**]Motorola Inc., Materials Research and Strategic Technologies, Mesa, AZ 85202
[***]Motorola Inc., Phoenix Corporate Research Laboratories, 2100 E. Elliot Rd., Tempe, AZ 85284

For many semiconductor devices, a detailed knowledge of interface composition on an atomic scale is important for understanding the device performance. One technique for obtaining such knowledge is "chemical imaging".[1,2] This technique has previously been applied to Si/Ge and GaAs/AlAs interfaces. Recently, there has been interest in constructing quantum wells using the $(In_{0.532}Ga_{0.468})As/$ $(In_{0.522}Al_{0.478})As$ system (hereafter InGaAs/ InAlAs), which is lattice-matched to InP (lattice constant of 5.869Å).[3]

The chemical imaging technique uses high resolution electron microscopy (HREM) images taken under special conditions of microscope defocus df, and specimen thickness t. Under the correct conditions, the images contain features which are linearly dependent on composition x. For heterogeneous structures (e.g. InGaAs/InAlAs), a change in x affects <200> beams preferentially. In this case, imaging in the <100> orientation is favorable, because four <200> beams occur. It is necessary to define a function of the image intensity h(I) which is proportional to x for some values of t and df. Here we follow the approach of Thoma and Cerva[2] and use h(I) equal to the <200> frequency component of the image intensity (I_{200}) normalized relative to I_{200} for x=0 and x=1. The resolution of h(I) is limited to one <200> period, or 1/2 unit cell (2.93Å).

The chemically sensitive quantity I_{200} has been calculated for the <100> orientation using 9 beam imaging theory.[2] It depends on the diffracted beam amplitudes and phases, which have been calculated for different values of t and x using the Molecular Simulations Inc. CERIUS multislice program (where the composition is $(InGa)_x(InAl)_{1-x}As$). The multislice calculations used 80x80 beams, 4 slices per unit cell, Debye-Waller factors of $B=0.7Å^2$ and an absorption potential equal to 7% of the elastic potential. Figure 1 shows the results for InGaAs and InAlAs. As expected, the <200> beams are significant in the former, but weak in the latter. The 9 beam calculation of I_{200} used parameters for a 4000EX 400kV HREM microscope. Figure 2 shows the relationship between h(I) and x for t=14nm and df=-50nm. The relationship is linear which means that chemical imaging of InGaAs/InAlAs interfaces is feasible for these conditions. Figure 2 also shows that for uncertainties of ±2nm in t and ±10nm in df, the value of x corresponding to a particular value of h(I) has an uncertainty of 20%.

To simulate the application of the chemical imaging method, h(I) has been derived from a simulated image of sharp and diffuse InGaAs/InAlAs interfaces in the <100> orientation, with a signal to noise ratio (S/N) of 10. An 8x8 pixel sampling of each 1/4 unit cell was used. Figure 3a shows the simulated image, and figure 3b shows the derived values of h(I). The derived values of h(I) agree with the actual composition to within 5%. The inaccuracies may be due to inaccuracies in I_{200} calculated from 9 beam imaging theory, or due to interface effects in the image. (One of the assumptions of chemical imaging is that I_{200} for one 1/4 unit cell is independent of the composition of neighboring 1/4 unit cells.) However, figure 3b shows that these effects are less significant than the error in h(I) due to experimental uncertainties in t and df (see figure 2).[4]

References

1. A. Ourmazd et al, *Ultramicroscopy* 34 (1990) 237
2. S. Thoma and H. Cerva, *Ultramicroscopy* 38 (1991) 265
3. R.P. Leavitt and J.L. Bradshaw, *J. Appl. Phys.* 76 (1994) 3429
4. This work was supported by the HREM Industrial Associates Program of Arizona State University (ASU) and was performed in the Center for HREM at ASU.

1

2

3a

3b
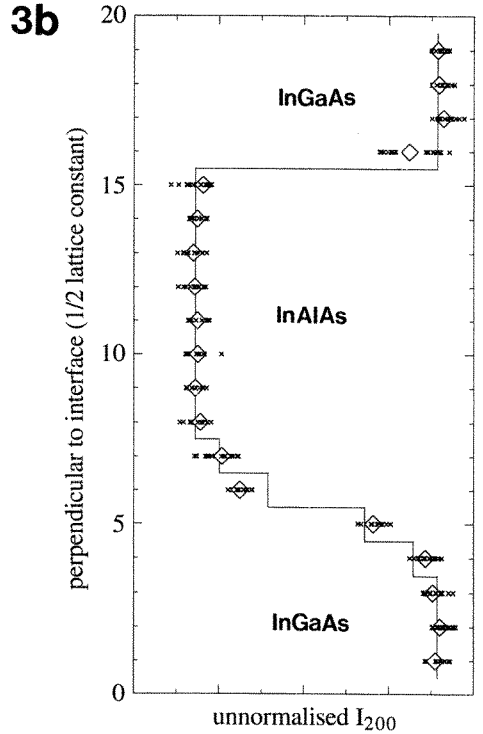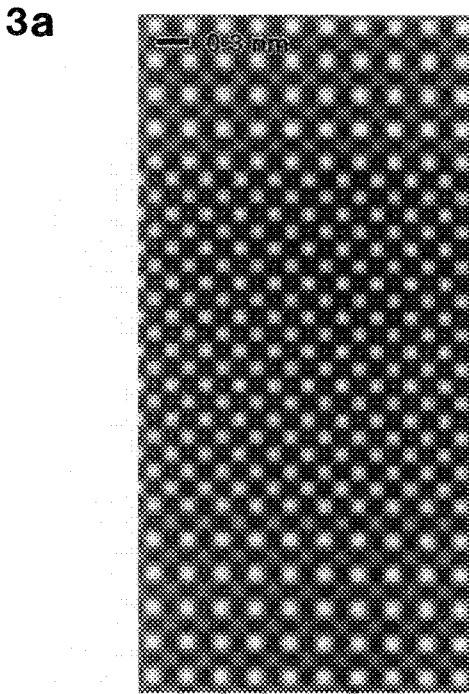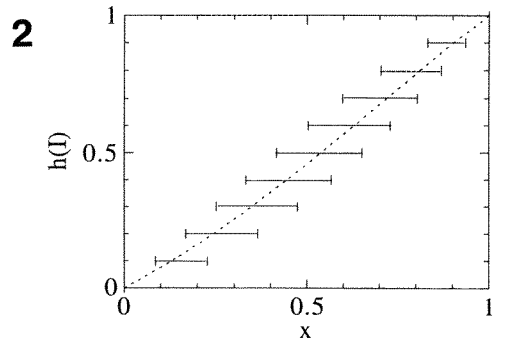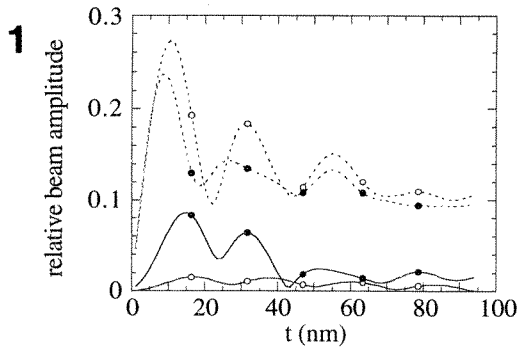
FIG. 1 - <200> (solid line) and <220> (dotted line) beam amplitudes for <100> orientation in InGaAs (solid circle) and InAlAs (empty circle).

FIG. 2 - Relationship between the normalized <200> frequency component of image intensity h(I) and x in $(InGa)_x(InAl)_{1-x}As$, for chemical imaging conditions (t=14±2nm, df=-50±10nm).

FIG. 3 - (a) Simulated HREM image of sharp (upper) and diffuse (lower) 1d interfaces between InGaAs and InAlAs (central layer) in <100> orientation, for chemical imaging conditions, with S/N=10.
(b) Values of h(I) derived from image shown in figure 3a. Crosses show variation along interface due to noise, diamonds show average along interface, and line shows actual values of x.

HIGH RESOLUTION ELECTRON MICROSCOPY OF InGaAs/InAlAs INTERFACES

G. Mountjoy[*], P.A. Crozier[*], P.L. Fejes[**], R.K. Tsui[***] and G.D. Kramer[***]

[*]Center for Solid State Science, Arizona State University, Tempe, AZ 85287-1704
[**]Motorola Inc., Materials Research and Strategic Technologies, Mesa, AZ 85202
[***]Motorola Inc., Phoenix Corporate Research Laboratories, 2100 E. Elliot Rd., Tempe, AZ 85284

Recently, quantum wells (QW) have been constructed using the $(In_{0.532}Ga_{0.468})As/ (In_{0.522}Al_{0.478})As$ system (hereafter InGaAs/InAlAs), which is lattice matched to InP (lattice constant of 5.869Å).[1] In order to understand the properties of such QWs, it is important to have knowledge of the structure and composition of interfaces. For III-V materials, compositional changes affect the <200> frequency component of the high resolution electron microscopy (HREM) image intensity (I_{200}). This underlies the "chemical imaging" approach.[2] Simulations for InGaAs/InAlAs interfaces suggest optimum conditions of microscope defocus df=-50nm and sample thickness t=14nm in the <100> orientation.[3] A double-QW structure, consisting of InGaAs/ InAlAs/ InGaAs layers with nominal thicknesses of 4nm/ 2nm/ 4nm (respectively), and embedded in InAlAs layers, has been studied. All the layers were grown by molecular beam epitaxy at 500°C on a <100> InP substrate, with 60s growth interrupts between layers in the QW region.

A standard sample preparation method has been used to prepare a <100> cross section sample, with efforts to counteract the following problems. InP is very brittle and prone to damage during mechanical thinning. To reduce this, a composite sample of facing layers was sliced to thickness ≥0.8mm using a diamond saw with low weight and speed. The slice was ground to thickness ≥100μm using ≤15μm grit, then dimpled to thickness ≥20μm using a cloth wheel and ≤3μm diamond paste, with low weight and speed. The ion milling of InP is known to cause segregation of In.[4] To reduce this, a Baltec ion mill was used with 5kV Ar ions incident at angles ≤10°, and LN_2 cooling of the sample holder. There is differential (greater) ion milling of InP relative to InGaAs and InAlAs. To reduce this, a single ion beam was used perpendicular to the layers, and the sample orientation was rocked by ±20°.[5]

A 4000EX 400kV microscope has been used to acquire HREM images of the QW. The InGaAs layers were examined to find the thinnest area with good I_{200} contrast (t≈40nm, estimated from <000> beam thickness contours). Figure 1 shows part of the HREM image obtained with defocus set to maximize the I_{200} contrast in InGaAs. As expected, I_{200} is strong in InGaAs and negligible in InAlAs. Figure 2 shows the boundaries of dominant I_{200} contrast (as judged by eye), which are assumed to enclose the InGaAs layers . Using the boundaries in figure 2, the InGaAs/InAlAs/InGaAs layer widths have been estimated to be 3.57nm/ 1.68nm/ 3.60nm with standard deviations of 0.45nm/ 0.40nm/ 0.35nm (respectively). Some of the variation in width may be due to roughness of the interfaces. In addition, the micrograph showed regions where InGaAs appears to intrude into InAlAs (e.g. see figure 1).

For general values of t and df, the relationship between I_{200} and x is not well defined. Figure 3 shows the values of $|I_{200}|$ in InGaAs for different values of df and t. At maxima in $|I_{200}|$, I_{200} is a monotonic function of x, thus the boundary of I_{200} contrast does represent a specific (albeit undetermined) composition 0<x<1. However, figure 4 shows that the exact relationship between I_{200} and x is very sensitive to variations in t (except in the case of chemical imaging, i.e. t=14nm), and this means the boundary composition may vary within a single image if the sample has non-uniform thickness.

References

1. R.P. Leavitt and J.L. Bradshaw, *J. Appl. Phys.* 76 (1994) 3429
2. S. Thoma and H. Cerva, *Ultramicroscopy* 38 (1991) 265
3. G. Mountjoy et al, *Proc. 54th Ann. MSA Meeting* (1996)
4. N.G. Chew and A.G. Cullis, *Ultramicroscopy* 23 (1987) 175
5. A. Barna A., *MRS Symp. Proc.* 254 (1992) 3
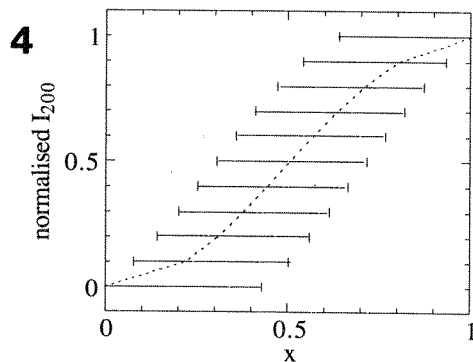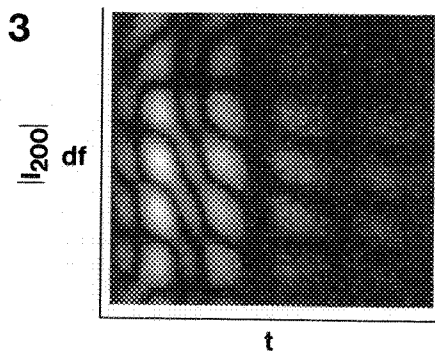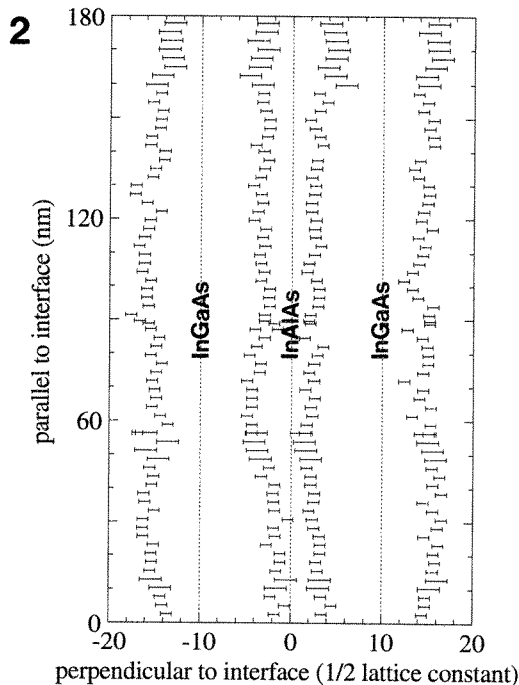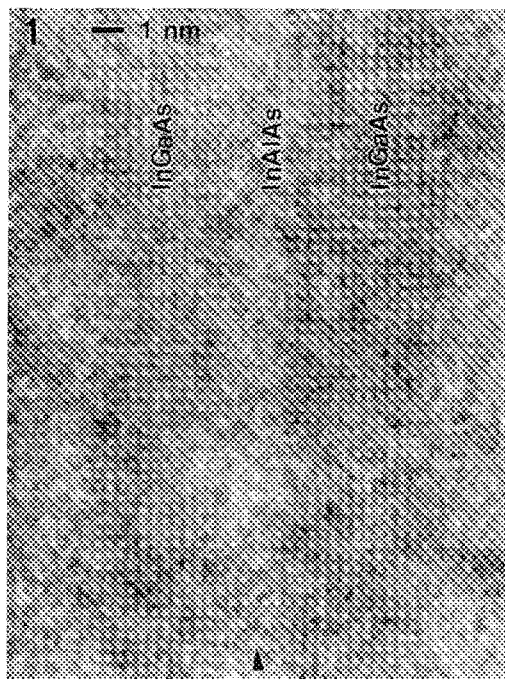
FIG. 1 - HREM image of InGaAs/InAlAs/InGaAs quantum well (with t≈40nm) in <100> orientation. Arrow denotes region where InGaAs appears to intrude into InAlAs.

FIG. 2 - Boundaries of regions with strong <200> contrast in micrograph shown in figure 1. These regions correspond to the InGaAs layers.

FIG. 3 - Map of $|I_{200}|$ in images of InGaAs for -200nm<df<100nm (vertical) and 0nm<t<95nm (horizontal). Bright regions denote maxima.

FIG. 4 - Relationship between normalised I_{200} and x in images of $(InGa)_x(InAl)_{1-x}As$ for df=-60nm and t=34nm (a maxima in $|I_{200}|$ for InGaAs). Error bars show effect of ±2nm variations in t.

HRTEM INVESTIGATION OF THE INTERFACE BETWEEN AlN AND SiC

M.A. O'Keefe, F.A. Ponce✧ and E.C. Nelson

National Center for Electron Microscopy, University of California, LBNL B72, Berkeley, CA 94720
✧Xerox Palo Alto Research Center, 3333 Coyote Hill Road, Palo Alto, CA 94304

Epitaxial thin films of the group III nitrides play an increasingly important role in the fabrication of high-efficiency light emitting diodes in the range between yellow and blue.[1] Growth of such films on sapphire requires the use of low temperature buffer layers of AlN[2] or GaN.[3] Silicon carbide has a much closer lattice parameter match than sapphire to AlN, and promises to produce better AlN layers. Since the atomic arrangement at the interface between AlN and SiC determines the degree of perfection of the epitaxial layer, we have attempted to determine the structure of this interface by high-resolution transmission electron microscopy. Devices were grown by MOCVD[4]; AlN was deposited on the Si-face of α-6H SiC, followed by GaN.[5] The specimen was cut for HRTEM observation in the <1 1̄20> SiC projection, mechanically thinned to 20µm and ion-milled to electron transparency. Observations were made using the NCEM JEOL ARM-1000 operated at 800keV. Images were obtained at a specimen thickness of 85Å (determined by extrapolation to the first extinction distance of the wedge). The most-useful defocus was -1050Å at which the important spacings from both SiC and AlN are passed with the same phase (fig.1).

The atomic arrangement at the interface is shown in fig.2, where both the SiC and AlN are viewed in the <1 1̄20> projection with a {1 1̄00} plane vertical, and the SiC (0006) basal plane and AlN (0002) basal plane horizontal. Interplanar separations of AlN and α-6H SiC are shown in Table 1. Four possible interface models were constructed from the arrangement shown, by substituting the appropriate atoms (in the positions marked with "?" in fig.2), and adjusting separations to conform to the relevant bond lengths and interplanar spacings (table 1). Model **A** has Al in the top "?" layer and C in the lower one; model **B** has Al in the top layer and N in the lower one; model **C** has N in the top layer and C in the lower one; model **D** has N in the top layer and Al in the lower one. In the two latter models the Al and N positions in the AlN are reversed from those in the other two models, i.e. the AlN is "upside down".

Results of image simulations from the four interface models are shown at two defocus values, "black atom" (optimum) and "white atom" defocus (fig.3). Even for a specimen as thick as 85Å, the "black atom" images (fig.3b) show contrast that is approximately proportional to the projected potential in the models; the unresolved atom pairs show as black areas and the tunnels as white areas. Since SiC and AlN have only 1% difference in interplanar spacing (table 1), tunnels on both sides of the interface appear almost the same. Similarly, optimum-defocus images of models **A** and **B** show this "standard" at the interface, since values of their interplanar distances and paired atomic numbers are close to those for SiC and AlN (table 1). For model **C**, however, the interface atom pair (C-N) has a lower potential (Z=13) than the surrounding Al-N and Si-C pairs (Z=20), so dark areas in the interface plane are less black and white areas from adjacent tunnels "bleed" into them. For model **D**, stronger white spots at the interface (fig.3b) are due to the larger spacings in this model (table 1) producing a local lowering of the charge density at the interface. At 85Å thickness, the "white atom" images (fig.3c) are cleaner[6,7] than optimum defocus images (fig. 3b) due to less intrusion by second-order interferences[8], and the interface can clearly be identified by the change in stacking sequence from 6H to 2H (tunnels are dark). Images from models **A** and **B** show the observed stacking (fig.3c), whereas those from models **C** and **D** show features that are not present in the experimental image (fig.4). Our conclusion is that C-N and Si-Al bonds are not present at the interface, and that Si-N and C-Al bonding cannot be distinguished under the experimental conditions.[10]

1. S. Nakamura et al., *Jpn. J. Appl. Phys.* **34** (1995) L797.
2. H. Amano et al., *Appl. Phys. Lett.* **48** (1986) 353.
3. S. Nakamura, *Jpn. J. Appl. Phys.* **30** (1991) L1705.
4. T. Sasaki and T. Matsuoka, *J. Appl. Phys.* **64** (1988) 4531.
5. F.A. Ponce et al., *Appl. Phys. Lett.* **67** (1995) 410.
6. M.A. O'Keefe, *Proc. 3rd Pfefferkorn Conf. on Electron Optical Systems,* Ocean City, MD (1984) 209.
7. M.A. O'Keefe, U. Dahmen and C.J.D. Hetherington, *Mat. Res. Soc. Symp. Proc.* **159** (1989) 453.
8. M.A. O'Keefe, *Ultramicroscopy* **47** (1992) 282.
9. M.A. O'Keefe and Velimir Radmilovic, *50th Ann Proc. EMSA,* Boston, Massachusetts (1992) 116.
10. Work supported by the Department of Commerce Advanced Technology Program (70NANB2H1241), by ARPA (MDA972-95-3-0008), and by the Office of Energy Research, Office of Basic Energy Sciences, Material Sciences Division of the U.S. Department of Energy, under contract No. DE-AC03-76SF00098.

Model	Bond Type	Sum of Z	Bond Length (Å)	Interplanar Distance (Å)
A	Al-C	19	2.06	2.55
B	N-Si	21	1.74	2.38
C	N-C	13	1.47	2.35
D	Al-Si	27	2.43	3.06
AlN	Al-N	20	1.89	2.49
SiC	Si-C	20	1.88	2.516
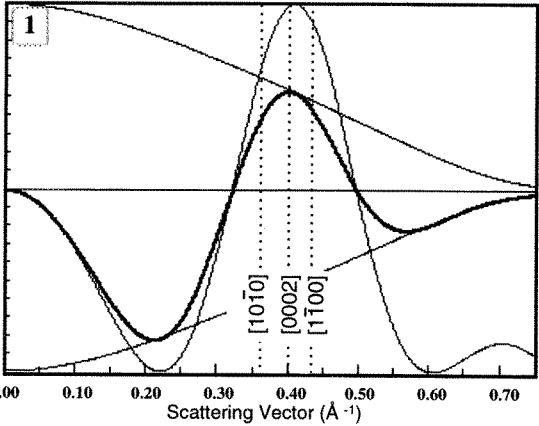
Table1. Interface bonds and AlN and SiC bonds.
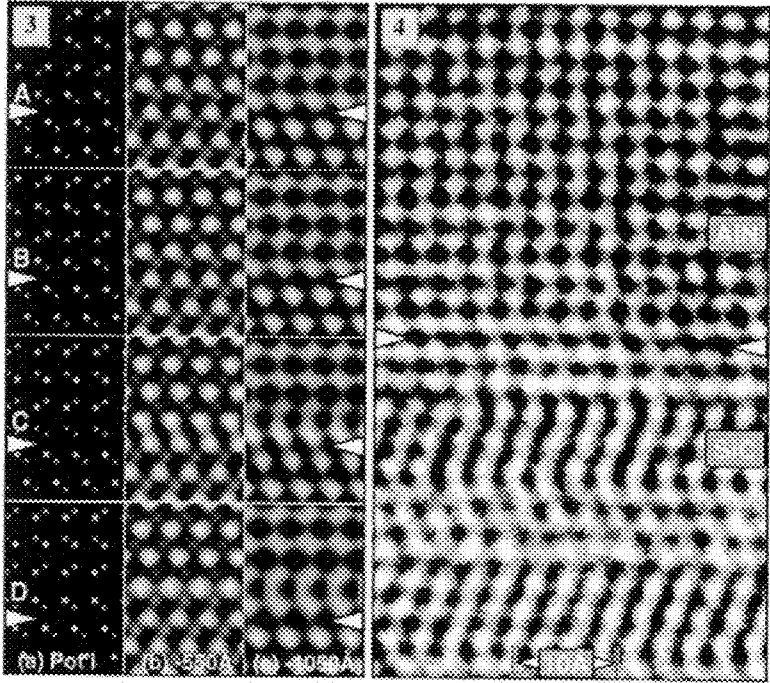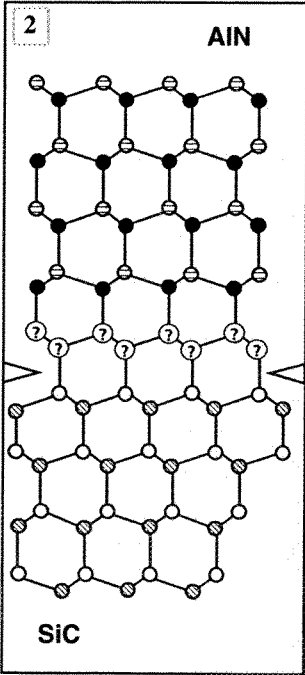
Fig. 1. Contrast transfer function for JEOL ARM-1000 at 800keV and -1050Å defocus. Information in the spatial range of 2.3Å to 2.7Å is transferred strongly and with the same phase.

Fig. 2. Schematic diagram of the model interface between AlN (at the top) and α-6H SiC (bottom). Four possible models of the interface were studied (table 1). Bonding atoms at the interface are Al-C (model **A**), N-Si (model **B**), N-C (model **C**), and Al-Si (model **D**). Arrows indicate the interface.

Fig. 3. Projected potentials (a) and simulated images from the four models at a "black atom" defocus value (b) of -550Å (√1.5 Scherzer) and a "white atom" value (c) of -1050Å. Images simulated at 85Å thickness for JEOL ARM-1000 at 800keV (C_S=2mm, Δ=150Å, α=0.64mrad). Arrows mark interface.

Fig. 4. Experimental image at 85Å thickness for JEOL ARM-1000 at 800keV. Arrows mark interface. The SiC portion of the image shows that the crystal is slightly tilted.[9]

123

PINNING OF 90° DOMAIN BOUNDARIES AT INTERFACE DISLOCATIONS IN BaTiO$_3$/LaAlO$_3$ {100}

Z.-R. Dai[1,2], Z.L. Wang[3] and X.F. Duan[1] and J. Zhang[4]

[1] Beijing Laboratory of Electron Microscopy, Chinese Academy of Sciences, P.O. Box 2724, Beijing 100080, China
[2] Department of Materials Physics, University of Science and Technology Beijing Beijing 100083, China.
[3] School of Materials Science and Engineering, Georgia Institute of Technology, Atlanta Georgia 30332-0245, USA
[4] Advanced Technology Materials, Inc., 7 Commerce Drive, Danbury, CT 06810; currently at: Motorola, Inc., 3501 Ed Bluestein Boulevard, MD: K-10, Austin, TX 78721 USA

Epitaxially grown BaTiO$_3$ thin films have potential applications in microelectronics and integrated photonics [1]. The ferroelectric property of this material is largely determined by the domain structure. It is believed that the structure of the substrate would have profound effect on the quality of BaTiO$_3$ epitaxial thin films. This paper reports our studies on the pinning of 90° domain boundaries at interface dislocations.

Epitaxial BaTiO$_3$ thin films were deposited on single crystalline LaAlO$_3$ (100) substrates at 800 °C by metal-organic chemical vapor deposition (MOCVD). Cross-section specimens of the films were studied at 200 kV using an JEOL 2010 high-resolution transmission electron microscope (HRTEM).

From an HRTEM image (Fig. 1), the film is epitaxially grown on an LaAlO$_3$ substrate. Dislocations are seen at the substrate-film interface, as indicated by dark arrowheads. The intervals between the dislocations are not even, indicating inhomogeneous strain distribution along the interface. Straight 90° domain boundaries in BaTiO$_3$, as indicated by white arrowheads, are parallel to (011) and (0-11) planes and are directly linked to interface dislocations. The domain boundaries have a 45° angle with the interface. An enlarged, digitally processed image is shown in Fig. 2, exhibiting a clear domain boundary as indicated by a dark line. Relative tilt of lattice planes between the two regions on both sides of the boundary can be seen, as indicated by white lines. Figure 3 shows a processed image of the region around an interface dislocation. The Burgers vector of the dislocation is determined to be b[010], an edge type.

BaTiO$_3$ has a cubic perovskite-type structure (a = 0.4012 nm) above 120 °C. Below 120 °C, it is tetragonal (a = 0.3992 nm, c = 0.4036 nm). The tetragonal BaTiO$_3$ phase has ferroelectric property because of the spontaneous polarization along the c-axis. The c-axis in one domain is parallel to the a-/b- axis of another domain, resulting in the formation of a 90° domain boundary. At room temperature, LaAlO$_3$ has a perovskite-like structure with a slight rhombohedral distortion (a = 0.3788 nm, α = 90°4'). LaAlO$_3$ experiences a phase transition from a rhombohedral to a cubic structure (a = 0.381 nm) at 435 °C.

When the film undergoes a structure transition from cubic to tetragonal during cooling from the growth temperature, strain is produced in the film due to lattice mismatch and differences in thermal expansion coefficients between the film and the substrate, domain boundaries are formation to accommodate strain in the film. The lattice mismatch is 5.3% at growth temperature (800 °C). At room temperature, the lattice mismatch is still 5.3% if the c-axis of the film is perpendicular to the interface, but lattice mismatch is 6.5% if the a-axis of the film is perpendicular to the substrate. Therefore, lattice mismatch experiences a jump at the domain boundary, resulting in accumulated strain at the boundary region. Also, the different lattice mismatches in the two adjacent domains will result in different intervals of interface dislocations. Domain boundaries are believed to be formed at the transition temperature 120 °C, and they might move freely at this temperature towards the sites having lower energy. When a domain boundary is directly linked to an interface dislocation, the strain fields of the two might partially cancel out, resulting in lower energy. Thus, the domain boundary is likely to be "pinned" at an interface dislocation.

In conclusion, it has been shown that the interface dislocation is a source for pinning the 90° domain boundary. A proper control on the density of interface dislocations, by selecting a proper substrate with specific lattice constants and structure, can control the density and size of 90° domain boundaries in the grown film. This may have an important impact on the property and performance of the ferroelectric films.

[1] W. Ousi-Benomar, et al., J. Mater. Res. 9 (1994) 970.
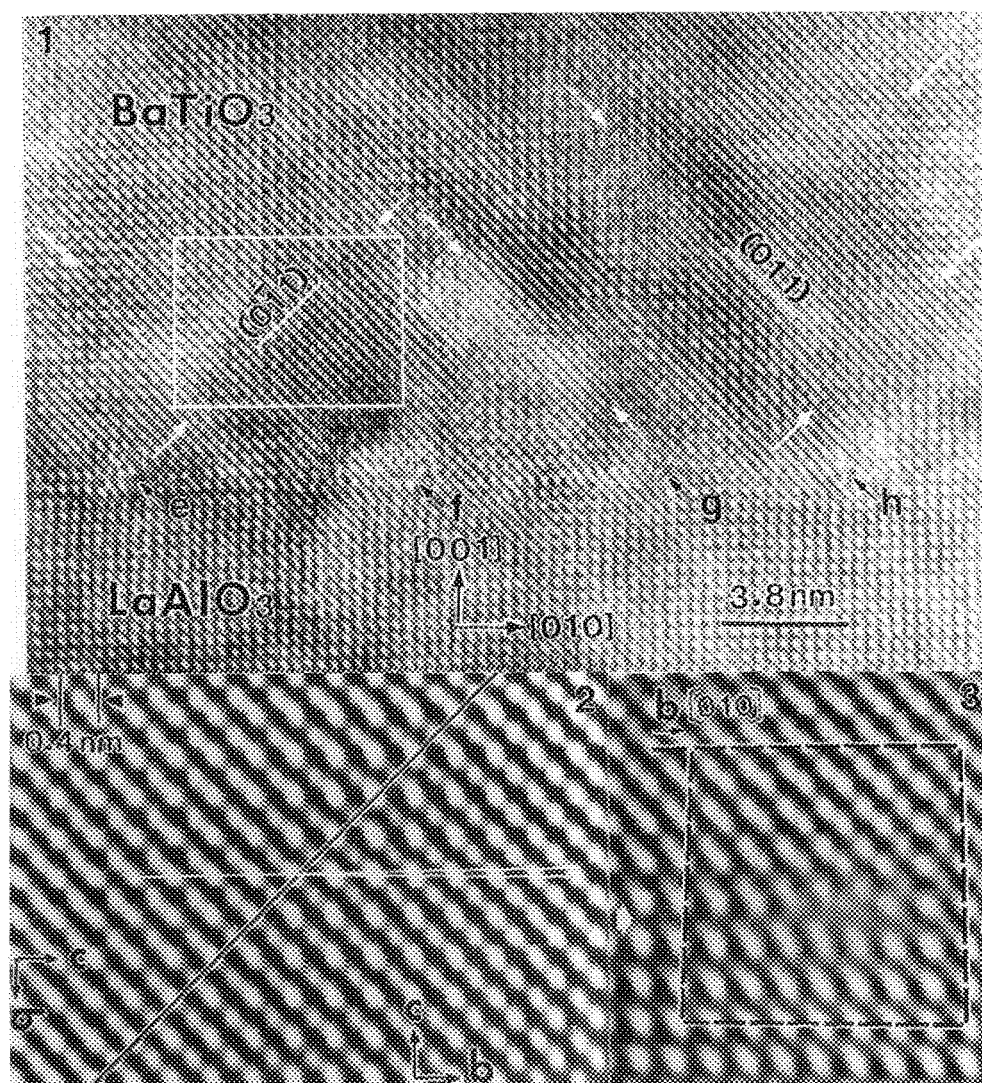
FIG. 1 A cross-sectional HRTEM image of an epitaxial BaTiO3 thin film grown on LaAlO3 {100} substrate, showing that the 90° domain boundaries are directly associated with interface dislocations.
FIG. 2 An enlarged, Fourier filtered image of the region enclosed by a square in Fig. 1.
FIG. 3 An enlarged, Fourier filtered image of the region around an edge dislocation. The Burgers circuit around the dislocation is indicated by lines.

COMPUTER SIMULATION OF TRANSMISSION ELECTRON MICROGRAPHS BY MICROSCOPE FOR WINDOWS

V.-T. Kuokkala

Centre for Electron Microscopy, Tampere University of Technology, FIN-33101 Tampere, Finland

microScope for Windows™ is a transmission electron micrograph simulation program for brightfield and darkfield images of dislocations and stacking faults, based on the dynamical two-beam theory and the column approximation. The program is a modification of the original programs of Head *et al.*, which have been rewritten in Visual Basic™ 4.0 for Microsoft® Windows™ 3.1.[1] microScope for Windows™ also includes routines needed to prepare data for the actual calculation of the image, and to calculate and display a rocking curve for any pixel of the previously computed brightfield or darkfield image. On a 120 MHz Pentium, microScope for Windows™ calculates a true gray scale (256 gray level) image consisting of 19840 pixels in about 10 seconds (version 2.3). A 300 dpi laserprinter screendump at the end of the calculation of an image is shown in Fig. 1.

microScope for Windows™ can be used for several different purposes. The main scientific application is the identification of defects, such as dislocations, by image matching using experimental images where defects are best visible instead of using the common invisibility rules. Compared with the older simulation programs, the computed image quality of microScope for Windows™ is significantly improved which makes the visual matching of experimental and computed images much easier and much more reliable. Some examples of the high quality of images simulated by microScope for Windows™ are given in Fig. 2, which shows theoretical images of dislocations and stacking faults reproduced using a Polaroid Digital Palette Film Recorder (corresponds to a photograph taken from the computer screen). Calculated images can be printed on any printing device supported by Windows™ (*e.g.*, laser printers).

microScope for Windows™ can also be used to simulate images under diffracting conditions where the intensity and contrast in experimental images is extremely low, making focusing rather difficult. The simulation and display of low intensity images is not different from that of normal high intensity images since the 'exposure' parameters can be changed after actual calculation to obtain optimum brightness and contrast for the image. This could be useful, for example, in dark field and weak beam work where focusing and adjustment of exposure parameters is often a problem.

A third application field where microScope for Windows™ has been successfully applied is teaching of transmission electron microscopy to university students. Using the program it is extremely easy to demonstrate quickly how the contrast of a defect is affected by changes in the diffraction conditions, properties of the defect or elastic or geometrical properties of the specimen. The program installation files are available free of charge at foundry.me.tut.fi using anonymous ftp.

References

1. A.K. Head et al., *Computed electron micrographs and defect identification*. North-Holland Publ. Co., Amsterdam (1973).
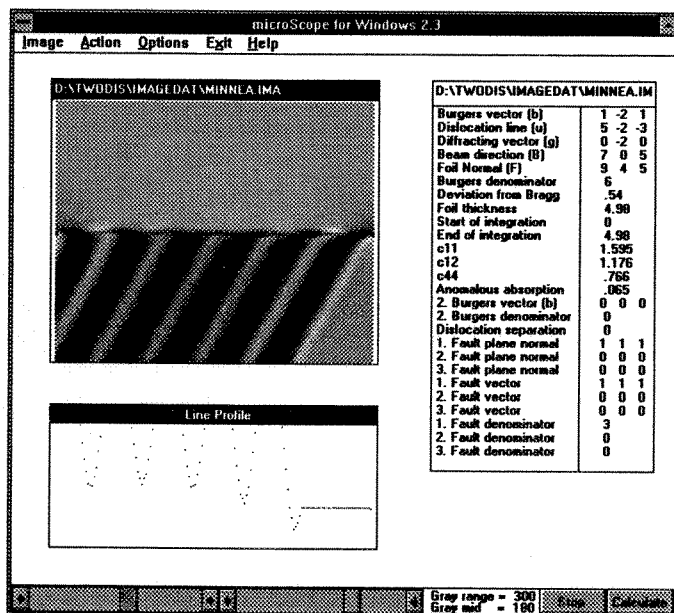
FIG.1. Screendump of microScope for Windows™ after completing the calculation of the image of a stacking fault.
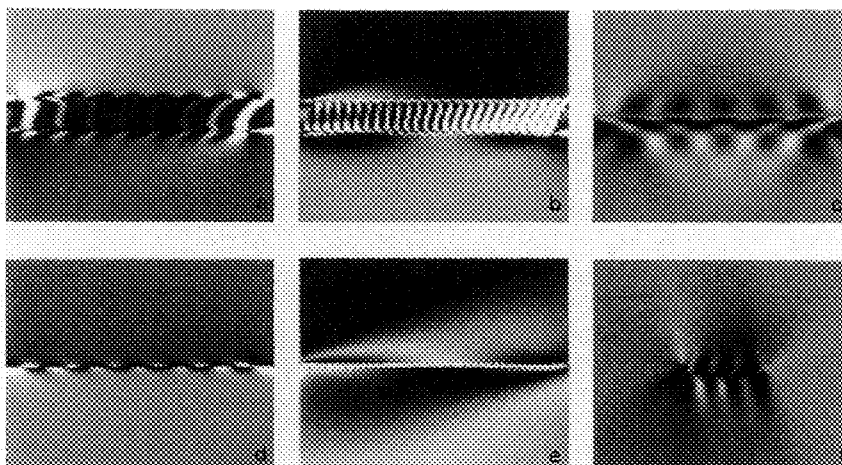
FIG. 2. Examples of images calculated by microScope for Windows. a) Shockley partial dislocations bordering a stacking fault in a Cu-Al alloy, BF image, b) DF image of the same stacking fault at a large deviation from the Bragg condition, c) [110] dislocation in β-brass, d) 1/6[211] partial dislocation in a Cu-Al alloy, e) 'weak-beam' image of a stacking fault in stainless steel, and f) [111] dislocation in β-brass.

CALCULATION OF MANY-BEAM DYNAMIC ELECTRON DIFFRACTION WITHOUT HIGH-ENERGY APPROXIMATION

B. R. Ahn* and N. J. Kim**

* Research Institute of Industrial Science & Technology, P.O.BOX 135 Pohang, 790-600, Korea
**Pohang University of Science & Technology, Pohang 790-784, Korea

High energy approximation in dynamic theory of electron diffraction involves some intrinsic problems. First, the loss of theoretical strictness makes it difficult to comprehend the phenomena of electron diffraction. Secondly, it is difficult to believe that the approximation is reasonable especially in the following cases: 1) when accelerating voltage is not sufficiently high, 2) when the specimen is thick, 3) when the angle between the surface normal of the specimen and zone axis is large, and 4) when diffracted beam with large diffraction angle is included in the calculation. However, until now the method to calculate the many beam dynamic electron diffraction without the high energy approximation has not been proposed. For this reason, the authors propose a method to eliminate the high energy approximation in the calculation of many beam dynamic electron diffraction. In this method, a perfect crystal with flat surface was assumed. The method was applied to the calculation of [111] zone axis CBED patterns of Si.

If potential distribution is periodic, Schroedinger equation can be transformed into dispersion equation.[1]

$$[K^2 - (\mathbf{k} + \mathbf{g}_h)^2] c_h + u_{h\text{-}h'} c_{h'} = 0 . \tag{1}$$

If the surface of crystal is flat, $\mathbf{k}_t = \mathbf{K}_t$. Therefore, equation (1) becomes

$$[K^2 - (\mathbf{K} + \mathbf{g}_h)^2 - 2 (\mathbf{K} + \mathbf{g}_h)_z \gamma - \gamma^2] c_h + u_{h\text{-}h'} c_{h'} = 0 , \tag{2}$$

where $\gamma = kz - Kz$. Equation (2) can be rewritten in a matrix form as follows.

$$(\mathbf{F} - 2 \gamma \mathbf{D} - \gamma^2 \mathbf{I}) \mathbf{c} = 0 \tag{3}$$

If there exists a matrix $\mathbf{A}$ which satisfies the following equation

$$\mathbf{A} \mathbf{A} + 2 \mathbf{D} \mathbf{A} = \mathbf{F} , \tag{4}$$

then the following equation is equivalent to equation (3).

$$(\mathbf{A} + 2 \mathbf{D} + \gamma \mathbf{I}) (\mathbf{A} - \gamma \mathbf{I}) \mathbf{c} = 0 \tag{5}$$

If γ and $\mathbf{c}$ satisfy the following equation

$$\mathbf{A} \mathbf{c} = \gamma \mathbf{c} , \tag{6}$$

then γ and $\mathbf{c}$ satisfy equation (3). This means that the problem of dispersion equation (1) with boundary condition can be reduced exactly to the problem of eigen-system. From equation (4), following relations are established.

$$a_{hh} = - d_{hh} + \sqrt{ d_{hh}^2 + f_{hh} - \sum_{h' \neq h} a_{hh'} a_{h'h} } \tag{7-1}$$

$$a_{hh'} = (f_{hh'} - \sum_{h'' \neq h, h'} a_{hh''} a_{h''h'}) / (2 d_{hh} + a_{hh} + a_{h'h'}) \quad (h \neq h') \tag{7-2}$$

Matrix $\mathbf{A}$ can be evaluated through iterations of equation (7) with initial value of $\mathbf{A} = \mathbf{0}$.

Coupled differential equations[2,3], usually called the system of Howie and Whelan,

$$\varphi(z) / dz = 2\pi i z \mathbf{A} \, \varphi(z) \tag{8}$$

can be derived from equation (6). And Sturkey s expression[4]

$$\varphi(z) = \exp(2\pi iz\mathbf{A}) \varphi(0), \tag{9}$$

which is the solution of equation (8), can also be derived from equation (6). Therefore, equations (6), (8), and (9) are equivalent to each other. It was already pointed out that all the high energy electron diffraction formulations are in fact expansions or approximations of the Sturkey s expression.[5, 6] Considering what mentioned above, this statement is also true even when high energy approximation is not applied, and all of the dynamic theories are in fact various approaches to solve matrix equation (6). However, an approximate matrix of **A** has previously been used in many beam dynamic theories of electron diffraction. To obtain more exact solution, the high energy approximation should not be applied in the calculation.

References

1. H. A. Bethe, Ann. Phys., Lpz. 87(1928)55.
2. A. Howie and M. J. Whelan, Proc. Roy. Soc.(London) A263(1961)217.
3. M. Tournarie, Bull. Soc. Franc. Miner. Crist. 83(1960)179.
4. L. Sturkey, Proc. Phys. Soc. 80(1962)321.
5. D. Van Dyck, Phys. Stat. Sol.(b) 72(1975)321.
6. D. Van Dyck, Ph. D. Thesis UIA Antwrp(1977)
7. The authors gratefully acknowledge the helpful comments of Dr. Changmo Sung, University of Massachusetts.
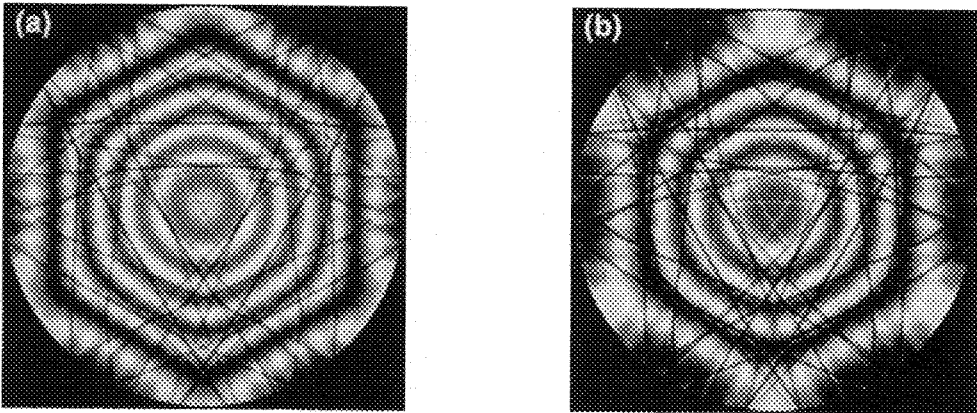
FIG. 1 Simulated [111] zone axis CBED pattern of Si. Acc. volt.: 120 KV, thickness : 250 nm, Debye parameter : 0.45. Inelastic scattering is not considered in the calculation. 7 lattices and 19 lattices in ZOLZ are included in the calculation of Fig. 1-a and Fig. 1-b, respectively. Not only the background but also the positions of HOLZ lines are certainly different. It shows that the strong interaction between the lattices in ZOLZ makes the positions of HOLZ lines different from the positions kinematically calculated.

CALCULATIONS OF ELECTRON INELASTIC MEAN FREE PATHS FOR CARBIDES

S. Tanuma, C. J. Powell* and D. R. Penn*

Japan Energy ARC. Co. Ltd., 3-17-35 Niizo-Minami, Toda, Saitama 335, Japan
* National Institute of Standards & Technology, Gaithersburg, MD 20899

Knowledge of the values of inelastic mean free paths (IMFPs) for low-energy electrons in solids is important for quantitative surface analysis by AES and XPS as well as for determining the surface sensitivity of other electron-spectroscopic methods of surface characterization. In previous papers, we have described the Penn algorithm for calculations of electron inelastic mean free paths in solids[1], and used this algorithm for calculations of IMFPs for 50 - 2000 eV electrons in a group of 27 elements[2], a group of 15 inorganic compounds[3], and a group of 14 organic compounds[4]. We fitted the calculated IMFPs for the groups of elements and organic compounds to a modified form of the Bethe equation4 for inelastic electron scattering in matter and found that the four parameters in this equation could be related empirically to several material parameters. The resulting general formula TPP-2M[4] for IMFPs in solids could be used to estimate IMFPs for other materials.

We report here IMFP calculations for 50 - 10,000 eV electrons in 8 carbides: $TiC_{1.0}$, $TiC_{0.95}$, $TiC_{0.7}$, $VC_{0.858}$, $VC_{0.758}$, $NbC_{0.93}$, $NbC_{0.844}$, $NbC_{0.712}$. These carbides were selected because the optical data needed for the IMFP calculations were available[5,6].

The accuracy of IMFPs calculated by the Penn algorithm depends on the energy loss functions of the compounds. We have evaluated the accuracy of these energy loss functions using two powerful sum rules. These sum rules are the oscillator strength rule (or f-sum rule)[3] and a limiting form of the Kramers-Kronig integral (or KK-sum rule)[3]. Evaluations of these sum rules are given in Table1. The results of the f-sum and KK-sum rule calculations for TiCx are excellent. We see that the errors from the f-sum rule for NbCx compounds are larger than 10%. These errors are, however, considered acceptably small for the IMFP calculations. On the other hand, the results of the KK-sum rule calculations are in good agreement with the theoretical values.

The calculated IMFPs of titanium carbides and vanadium carbides in the range 10 - 2000 eV are shown in Fig.1. From this figure, we find that the magnitude of the IMFPs for these compounds depends on the concentration of carbon. This result is due to the decrease in the number of valence electrons per molecule in the compounds with increase in carbon concentration.

We have analyzed the calculated IMFP data for each carbide in the same way as for the elements[2] and the compounds[3,4]. We fitted IMFP values for each material to a modified form of the Bethe equation in order to describe the energy and material dependence. This equation gave excellent fits to the calculated IMFPs. We have also compared the calculated IMFP data with those from our TPP-2M equation. The tendency of the IMFP to increase with increase of carbon concentration predicted by TPP-2M is in good agreement with that found from our calculated IMFPs.

130

References
1. S. Tanuma, C. J. Powell, D. R. Penn, Surf. Interface Anal. **11**, 577 (1988).
2. S. Tanuma, C. J. Powell, D. R. Penn, Surf. Interface Anal. **17**, 911 (1991).
3. S. Tanuma, C. J. Powell, D. R. Penn, Surf. Interface Anal. **17**, 927 (1991).
4. S. Tanuma, C. J. Powell, D. R. Penn, Surf. Interface Anal. **21**, 165 (1994).
5. T. Koide et al., Phys. Rev. B. 42, 4979 (1990); Private communication
6. J. Pfluger and J. Fink, " Handbook of Optical Constants of Solids II " ed. by E.D. Palik, Academic Press(1991).

Table 1. Calculated results of sum rules.

compounds	f-sum		KK-sum	
	Zeff	error(%)	Peff	error(%)
$TiC_{0.7}$	26.06	-0.5	1.004	0.4
$TiC_{0.95}$	27.47	-0.8	1.005	0.5
$TiC_{1.0}$	26.56	-5.2	1.073	7.3
$VC_{0.758}$	24.66	-10.5	1.010	1.0
$VC_{0.858}$	25.44	-9.6	1.009	0.9
$NbC_{0.712}$	40.30	-11	0.995	-0.5
$NbC_{0.844}$	40.81	-11.4	0.996	-0.4
$NbC_{0.93}$	41.13	-11.7	0.996	-0.4
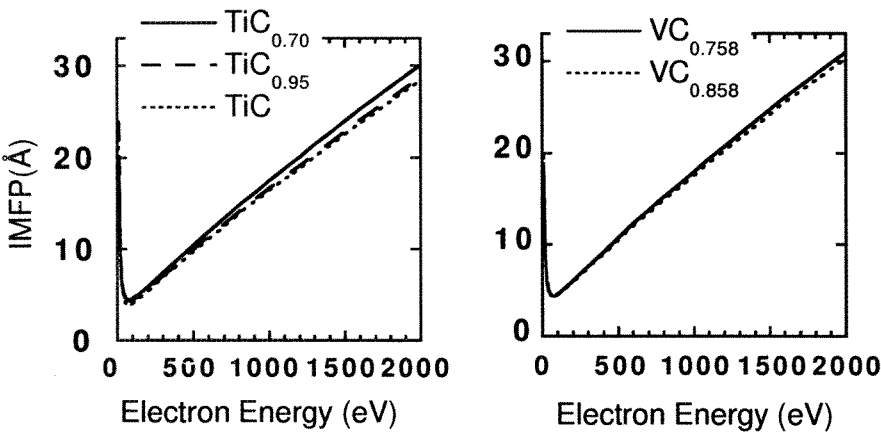
Figure 1. Calculated Inelastic Mean Free Paths for titanium carbides and vanadium carbides

ON INTERPRETING WEAK BEAM IMAGES OF MICROTWINS

H. S. Kim* and S. S. Sheinin**

* Department of Physics, Kyungsung University, Pusan 608-736, Korea
**Department of Physics, University of Alberta, Edmonton, AB, Canada T6G 2J1

The concept of a dynamically coupled set is of fundamental importance in carrying out theoretical calculations of image contrast of microtwins [1,2]. Up to the present, considerations based on the dynamical theory have indicated that the diffracted beams taken into account in a particular calculation of image contrast must always reside in the same dynamically coupled set [1,2]. The work presented in this paper indicates that for weak beam images this may not be the case. The reason for this can be seen from Fig.1b in which $\mathbf{g}$, $\mathbf{h}$ and (i), (j) are reciprocal lattice vectors and branches of the dispersion surfaces in the matrix and microtwin respectively. It can be seen that if the condition $(\mathbf{h} - \mathbf{g}) = \Delta\gamma\, n_f$ is obtained then the Bloch wave vectors in the matrix and twin, $\mathbf{k}_g^{(i)}$ and $\mathbf{k}_h^{(j)}$, are parallel. Under these circumstances $\mathbf{k}_h^{(j)}$ will make a coherent contribution to the intensity of diffracted beam $\mathbf{g}$, even though $\mathbf{h}$ does not reside in the same dynamically coupled set.

In order to determine if diffracted beams such as $\mathbf{h}$ have a significant effect on image contrast, calculations have been carried out for a microtwin in an FCC cobalt specimen of thickness 43.75 nm (see Fig. 1a). The thickness of the microtwin was taken to be 0.6138 nm (which is $3\,d_{111}$), and the directions of the beam and n_f were taken to be $[\bar{1}2\bar{3}]$ and $[1\bar{1}\bar{1}]$ respectively. Seven reflections in the systematic row containing $\mathbf{g} = (11\bar{1})$ were taken into account. The deviation parameter in Fig. 2b was taken to be $S_g = 0.265$ nm^{-1}, corresponding to weak beam diffraction conditions. Five low order twin reflections, such as $\mathbf{h}$ in Fig. 1b, were taken into account, while in Fig. 2a the effects of these reflections were neglected. Also, a translation, $\mathbf{R}$, of the lower matrix with respect to the upper matrix was taken into account ($\mathbf{R}$ satisfied the relation $\mathbf{g} \cdot \mathbf{R} = 1/3$). It can be seen in Fig. 2a that fairly strong fringe contrast is obtained while in Fig. 2b the fringe contrast is weak. The latter result is consistent with both experimental results presented elsewhere by the authors [3] and with a stacking fault calculation which considered the microtwin to be equivalent to 4 adjacent intrinsic faults. Finally it is worth noting that if the deviation parameters of the twin reflections are large, then it would be expected that their effects would be small. This should occur under strong beam diffraction conditions, as shown in Fig. 3 for $S_g = 0.0$. Again in Fig. 3b, the effects of the above twin reflections were taken into account, while in Fig. 3a they were not. It can be seen that, under these circumstances, no difference in fringe contrast is obtained, indicating that the effects of the twin reflections are negligible.

References

1. S. S. Sheinin and R. Perez, Phys Stat Sol (a) 79 (1983) 367
2. H. S. Kim and S. S. Sheinin, Phys Stat Sol (a) 115 (1989) 51
3. H. S. Kim and S. S. Sheinin, Proc. Microscopical Society America 53rd Annual Meeting (1995) 696
4. The authors are grateful to the Foundation of Kyungsung University and The Natural Sciences and Engineering Council of Canada for support.

(a)

(b)
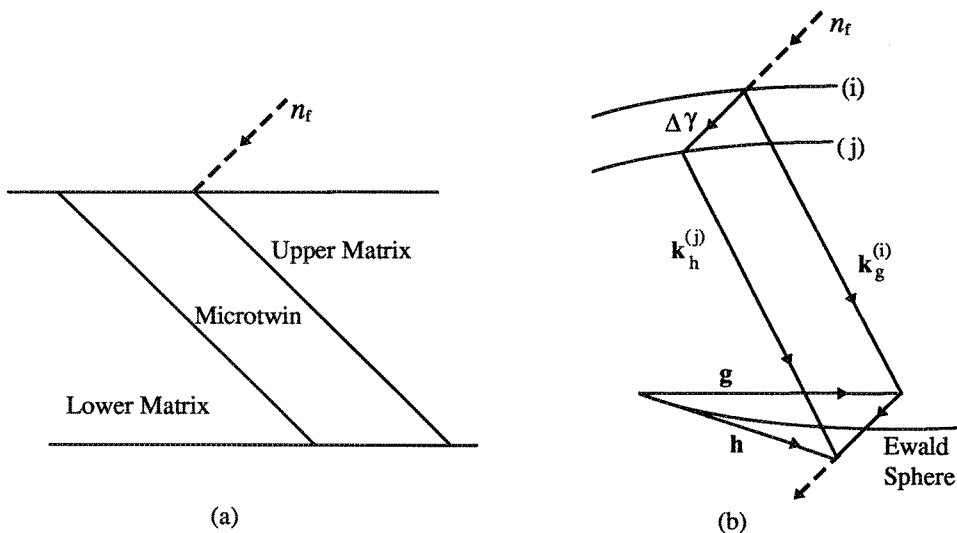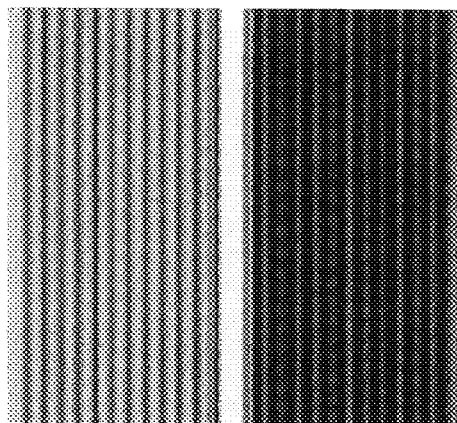
Fig. 1

(a)   (b)

Fig. 2
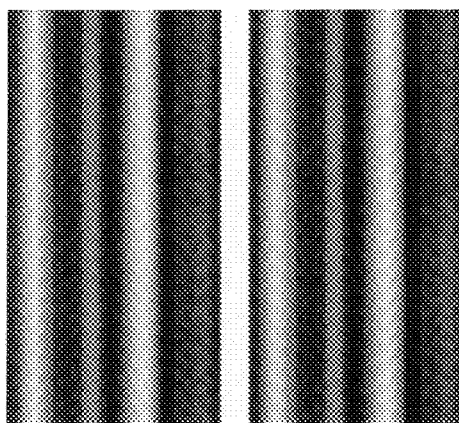
(a)   (b)

Fig. 3

FIG. 1 a) Schematic drawing in real space of a microtwin. n_f is a unit vector normal to the matrix-twin boundary. b) Schematic drawing in reciprocal space showing branches of the dispersion surface (i) in the matrix and (j) in the microtwin. **g** and **h** are reciprocal lattice vectors in the matrix and twin respectively.

FIG. 2 Shows theoretical weak beam image of a microtwin in FCC cobalt (see text for details). (a) does not take into account effects of reflections like **h** while (b) takes these reflections into account.

FIG. 3. Same as Fig. 2 except image is strong beam.

133

COMPUTER SIMULATIONS FOR THE TEM BEND CONTOUR TECHNIQUE

Vladimir Yu. Kolosov* and Anders R. Thölén
Physics Dept., Chalmers University of Technology, 412 96 Göteborg, Sweden

In this paper we give a short overview of two TEM applications utilizing the extinction bend contour technique (BC) giving the advantages and disadvantages; especially we consider two areas in which the BC technique remains unique. Special attention is given to an approach including computer simulations of TEM micrographs.

BC patterns are often observed in TEM studies but are rarely exploited in a serious way. However, this type of diffraction contrast was one of the first to be used for analysis of imperfections in crystalline foils, but since then only some groups have utilized the BC technique.[1-4] The most extensive studies were performed by Steeds, Eades and colleagues. They were the first to demonstrate the unique possibilities of the BC method and named it real space crystallography, which developed later into the somewhat similar but more powerful convergent beam method. Maybe, due to the difficulties in analysis, BCs have seldom been used in TEM, and then mainly to visualize different imperfections and transformations.

We here consider two situations where the BC technique still is the most useful method: bending and buckling of thin crystalline foils (in particular, resulting from thinning during specimen preparation or changes in structure due to ion beam thinning) and internal lattice bending (in particular, resulting from crystallization of amorphous films).

In the first approach it is assumed that everywhere in a bent region, **the whole crystal is bent**, the crystal surface can be specified in an explicit form. Using this geometry in direct space[5] a FORTRAN program can picture black and white or coloured (different colours for different extinction contours) BC patterns from arbitrarily chosen crystallographic planes, Fig. 1. This makes it possible to solve different problems using the theory of elasticity.

In the second approach **the lattice itself has an internal bending** (the surface of the crystal is supposed to be flat). The diffraction conditions are considered in reciprocal space using the Ewald construction.[6] Here we consider cylindrical lattice bending with parameters that can easily be adjusted to an arbitrarily chosen geometry. Two different cases encountered in practice, but usually ignored in TEM text books, are considered: a) the bending axis is not lying in the film plane, b) the zone axis [HKL] is not normal to the crystal surface (specimen plane). The present, third version of the program realized for PC has a simple menu-driven interface. One can change crystal structure, the content of the unit cell, the number and indices of zone-axis patterns, the maximum indices of reflecting planes, crystal thickness, accelerating voltage, etc. The program can plot BC patterns for cylindrical bending in different graphical modes which differ in the way of depicting BC intensities, widths and colours, Fig. 2; in a single mode it can handle an arbitrary geometry.
Experimental and simulated BC patterns can thus be compared using the two different approximations above.

*Permanent address: Ural State Economic University, 8 March St. 62, 620026 Ekaterinburg, Russia

References

1. V.N. Rozhanski and G.V. Berezhkova, *phys. stat. sol.*, 6(1964)185.
2. K.A. Jackson and R.S. Wagner, *J. Appl. Phys.*, 36, N 7(1965)2132.

3. J.W. Steeds, G.J. Tatlock and J. Hampson, *Nature*, 241(1973)435.
4. J.A. Eades, J.Riquelme, E.Silva and J.van Dun, *Phil. Mag.*, 30, N 4(1974) 945.
5. A.R. Thölén and J. Taftø, *Ultramicroscopy*, 48(1993) 27.
6. I. E. Bolotov and V. Yu. Kolosov, *phys. stat. sol.*, 69a(1982) 85.

Fig. 1 Simulated bend contour pattern around a hole. The pattern is a superposition of a pure and a sinusoidal bending.[5]
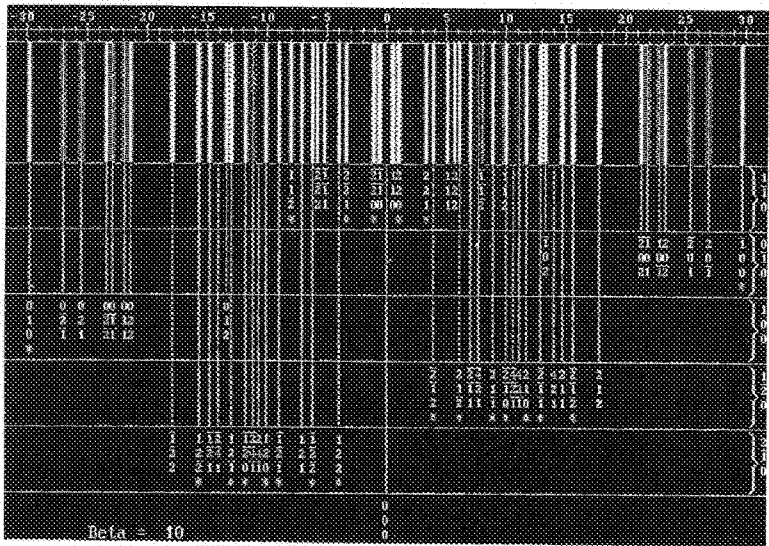
Fig. 2 One of the possible printouts of simulated BC pattern (Selenium crystal, internal lattice bending around [001], - β the angle between electron beam and central zone axis). The indices of BCs corresponding to 5 different zone axes are grouped separately.

LOW-VOLTAGE FESEM STUDY OF TiO$_2$ SURFACE STRUCTURE AND METALLIZATION

F. Cosandey*

* Ceramics Department, Rutgers University, Piscataway, NJ 08855-0909

Recent developments of Field Emission Scanning Electron Microscopes (FESEM) are now permitting material science studies of surfaces with nanometer scale resolution. For the study of oxide materials with low conductivity it is particularly important to image surfaces at low voltage in order to minimize both the electron range and charging. The unique electron optic design of the LEO (ex ZEISS) 982 GEMINI microscope combining retarding field and electrostatic lens concepts with Schottky field emission source is particularly well optimize for high resolution imaging of materials at low voltage.[1,2] In this study, we are presenting results on performance evaluation of the LEO 982 FESEM microscope with a study of TiO$_2$ surface structure and metallization.

The TiO$_2$ oxide is used extensively as metal supported catalyst and recent results have been reported which indicate that TiO$_2$/Au nanocomposites have high room temperature catalytic activity for CO.[3] This high resolution FESEM study was therefore designed to determine the effect of Ar bombardment on surface structures and the role of surface morphology on the stability and growth of Au clusters. The TiO$_2$ (110) single crystal surfaces used in this study were prepared in UHV using surface science tools and then transferred in air to the microscope.[4]

A typical TiO$_2$ (110) surface is shown in Fig.1a. The surface has a long range waviness in the range of 50 to 100 nm which is due in part to the surface cleaning by the 1 kV Ar$^+$ ion beam. After successive Ar bombardment and annealing at 900 °K giving rise to a reduced TiO$_x$ composition, the surface develop a ridge and valley configuration aligned along the [001] direction of TiO$_2$ with an average spacing of 35 nm. A smaller periodicity perpendicular to the ridges is also observable with a spacing in the range of 10 to 15 nm. These results indicate that surface damage caused by ion sputtering is highly anisotropic and occurs preferentially along the [001] direction which is parallel to the bridging oxygen rows on the TiO$_2$ (110) surface.

A low magnification image of a 0.15 nm thick Au deposited at room temperature is shown in Fig. 2a with in figure 2b a corresponding higher magnification image. Quantitative analysis using the PGT IMIX imaging system gives an average particle size of 8nm and a surface coverage of 3%. For a larger deposition thickness of 1.5 nm, the surface coverage increases to 35% but the average particle size remains essentially the same at 7nm but with a narrower size distribution (Fig.3a). At an even larger deposition thickness of 4.7 nm, the surface coverage increases to 65 % but with a bimodal particle size distribution (Fig.3b). The smaller particles have now coalesced to form a semi continuous network with an average width of 15nm and the larger particles have grown to an average size of 85 nm. In addition, most of the particles have a faceted morphology and are oriented along three specific directions. Their faceted edges are distributed with a 3-fold symmetry which is indicative of epitaxially grown Au particles with an orientation given by (111)$_{Au}$//(110)$_{TiO2}$. This orientation has been reported previously for other FCC metals (Cu, Pd) and corresponds to (111)$_{Au}$//(110)$_{TiO2}$ and [1-10]$_{Au}$//[001]$_{TiO2}$.[5]

References

1. I. Müllerová and M. Lenc, *Ultramicroscopy*, 41(1992)399.
2. J. Frosien, J. Vac. Sci. Technol., B7(6)(1989)1874
3. M. Haruta et al., *J. of Catalysis*, 144(1993)175.
4. L. Zhang, R. Persaud and T. E. Madey (To be Published)
5. P. Lu and F. Cosandey, *Interface Science*, 2(1994)169
6. Thanks to T. E. Madey and R. Persaud for numerous discussions and for providing the samples used in this study.
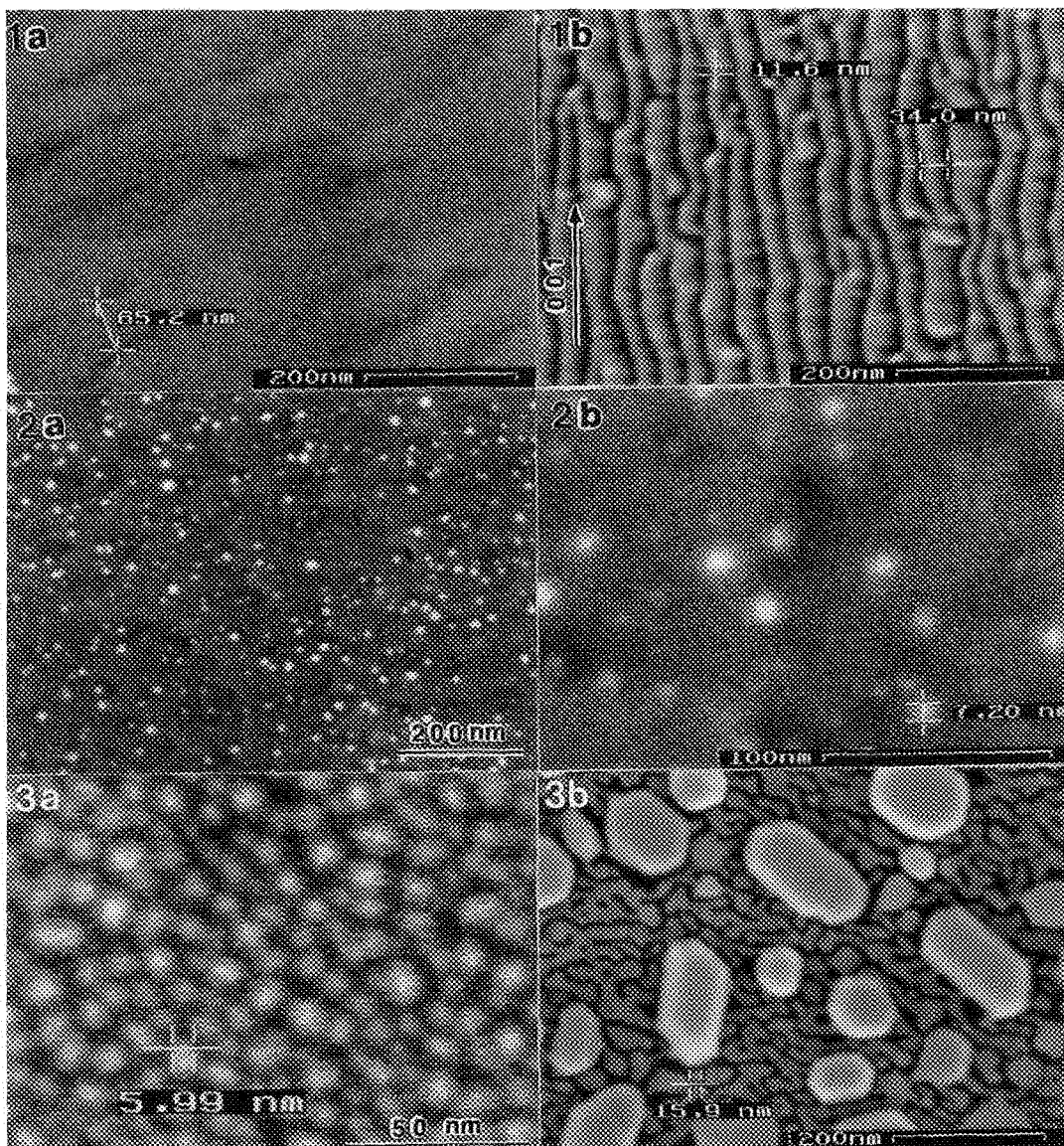
FIG. 1 Typical image of an as prepared TiO_2 (110) surface taken at 1 kV (a) and (b) image of a reduced
TiO_2 surface obtained after repeated Ar bombardment and annealing at 900 °K.

FIG. 2 Low magnification image taken at 3 kV of Au (0.15 nm in thickness) deposited on TiO_2 (110)
surface (a) and (b) respective higher magnification image.

FIG. 3 Images taken at 2 kV of Au deposited on TiO_2 (110) surface corresponding to average deposition
thicknesses of (a) 1.5 nm and (b) 4.7 nm.

APPLICATION OF LOW-VOLTAGE FIELD-EMISSION SEM TO THE STUDY OF INTERNAL PORE STRUCTURES OF ACTIVATED CARBON

J. Liu and R. L. Ornberg

Monsanto Corporate Research, Monsanto Company, 800 N. Lindbergh Blvd., St. Louis, MO 63167

Activated carbon has interesting and useful properties for industrial applications. It has been used extensively in purification, separation, chemical recovery and catalysis. To achieve a predictable performance of activated carbon materials, it is necessary to develop a comprehensive understanding of the pore structure including pore size, pore shape, and pore surface chemistry. Macropores (> 50 nm), mesopores (2-50 nm) and micropores (< 2 nm) generally coexist in activated carbon. It is thus desirable to synthesize activated carbon with controlled pore structures to optimize its performance. We previously reported the characterization of the **surface pore structure** of activated carbon by field emission SEM (FESEM) and the examination of the internal pore structure by HAADF/HRTEM techniques.[1] However, both HAADF and HRTEM techniques give only limited information about the carbon pore structure. We report here some preliminary observation of the **internal pore structure** of activated carbon by high resolution low voltage FESEM technique.

To study the internal pore structure of activated carbon we embedded carbon powders in an epoxy resin and ultramicrotomed them into thin sections (~ 60 nm) which were then supported on conducting Si substrates. The surface pore structure of these thin sections gives a good representation of the internal pore structure of activated carbon providing that the ultramicrotoming process does not significantly disturb the carbon pores. These thin sections were directly observed in a FESEM (Hitachi S-4500) without prior coating. The use of ultrathin sections was to provide conducting pathways for the embedded carbon particles to prevent excessive sample charging effect.

We previously identified that regions of porous and high density carbon coexist in the activated carbon.[1] Figure 1a shows a typical high resolution low voltage (1 kV) FESEM image of porous regions. The pores were elongated and were oriented randomly. Figure 1b shows a surface plot representation of the pore distribution. The sizes of the observable pores ranged from 5 to 50 nm in width and from 50 to 100 nm in length. Figures 2a and 2b show, respectively, typical high resolution low voltage (1 kV) FESEM image and surface plot representation of regions of high density carbon. No mesopores were observed. The micropores cannot be revealed in these SEM images due to poor image resolution and relatively low image contrast of micropores. In order to reliably observe micropores, an electron probe size < 0.5 nm in diameter and an image depth resolution < 0.8 nm has to be achieved. The resolution of SE images and the surface sensitivity of SE signals depend on the primary incident electron energy. At low beam energies the probe is broadened due to instrumental factors. The image resolution is deteriorated compared with that at high beam energies. The surface sensitivity of the collected SE signals is, however, determined by the spatial distribution of type I (generated by the primary beam only) and type II (generated by backscattered electrons) secondary electrons. At high incident beam energies the interaction volume of the primary electrons is large (for bulk samples). But the spatial distribution of type I and type II secondary electrons can be distinguished, thus making it possible to observe surface features on a nanometer scale. At low incident beam energies the interaction volume is reduced. But the type I and type II secondary electrons cannot be spatially separated. Therefore, the surface sensitivity and the spatial resolution of SE images is determined by both the type I and type II secondary electrons. Surface sensitivity can be optimized by either using very high or very low incident beam energies.[2] The contrast mechanism of carbon pores and its variations with incident beam energies will be discussed.

References

1. J. Liu et al., *Proc. Microscopy and Microanalysis 1995*, (1995) 418.
2. J. Liu and G. E. Spinnler, *Proc. 51st Annual Meeting of the MSA*, (1993)784.
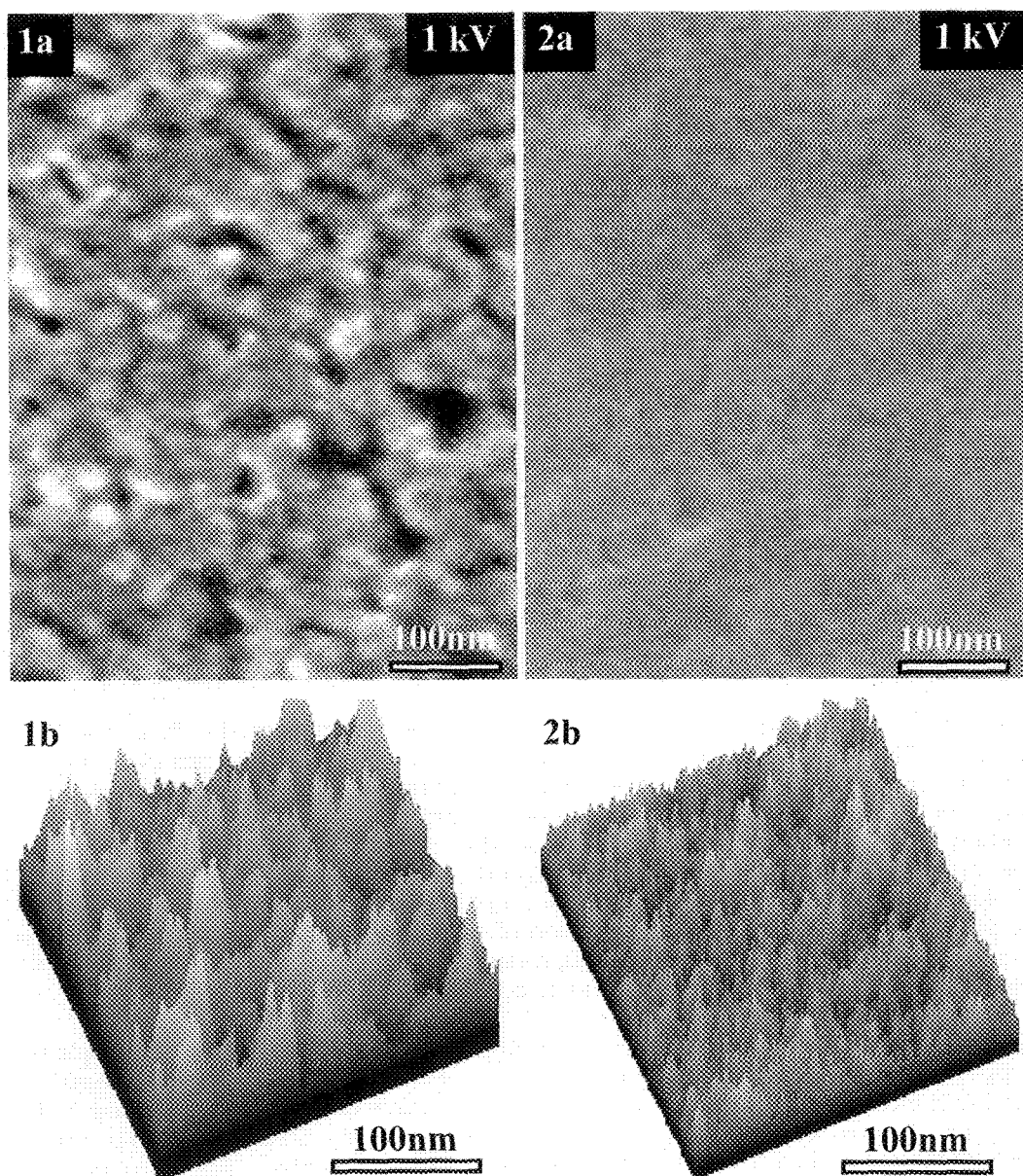
Fig. 1----High resolution low voltage FE-SEM image of regions of porous carbon (a) and
surface plot representation of pore distribution (b).

Fig. 2----High resolution low voltage FE-SEM image of regions of high density carbon (a) and
surface plot representation of pore distribution (b).

DISLOCATION DETECTION DEPTH MEASUREMENTS IN SILICON USING ELECTRON CHANNELLING CONTRAST IMAGING

B. A. Simkin,* M. A. Crimp*

*Department of Materials Science and Mechanics, Michigan State
  University, East Lansing, MI 48824

Electron Channelling Contrast Imaging (ECCI) employs local differences in backscatter yield due to local changes in the lattice orientation relative to the electron beam to provide imaging contrast. Due to the low contrast levels typically obtained for dislocations from this mechanism, efforts to enhance the signal to noise by tilting the specimen to high angles, signal averaging, or energy filtering are common.[1,2]

Determination of the depth to which individual dislocations can be imaged via ECCI in bulk samples has not previously been attempted by stereo imaging measurements due presumably to the common experimental setup of a high tilt angle. Previous measurements of dislocation detection depth[1] have relied upon sample geometry to approximate detection depths by estimating the dislocation diving angle based on the approximate line direction and surface normal, and were preformed using acceleration voltages not typical of most SEM work. In this investigation, dislocations were imaged employing stereo pairs at near normal sample inclination at an accelerating voltage of 25kV. The reduction in signal to noise at normal sample incidence is believed to be more than offset by the ease of sample manipulation due to the reduction of detector viewing geometry restrictions imposed by the high tilt configurations most commonly seen.

Single crystal semiconductor grade silicon samples were compressed ~2% at 700°C near the <123> direction to introduce dislocations, then cut near the principal slip bands, mechanically polished, and briefly etched (3 nitric:2 acetic:1 hydrofluoric) to prepare for imaging. SEM was preformed on a CamScan44FE equipped with a Schottkey field emission cathode and a selected area channelling module, using a probe current of 2.3nA, spot size of ~20nm, and convergence semi-angle of 4mrad. BSE signal detection employed a conventional polepiece mounted four quadrant solid state detector with a solid angle of detection of ~0.6π str. The (220) channelling band was used for imaging contrast, employing a negative deviation parameter. All photo frame times were kept to 25sec to minimize contamination accumulation.

Detection depths were determined from stereo pairs acquired by tilting the sample to approximately equal tilts to either side of the surface normal. Dislocations imaged using ECCI have the sharpest line width near the surface of the crystal (marked "e" in Figs. 1 and 2), with the image widening out at greater depth. Determination of the point at which visual contrast is lost is thus somewhat subjective. The parallax measured parallel to the channelling band between the point at which visual contrast was lost and the emergence point of the dislocation from the crystal was used to determine detection depth[3]. Using this method, an approximate depth of maximum

detection for the arrowed dislocation in Figs. 1 and 2 is calculated to be approximately 250nm. Repeatable determination of the point of contrast loss from one diffraction condition to the next is the principal source of error associated with this method.

References:

1. J.T. Czernuszka et al., Inst. Phys. Conf. Ser. No 117: section 10 (1991)
2. P. Morin et al., Phil. Mag. A, 40, 4 (1979) 511
3. A.W. Agar et al., Principles and Practice of Electron Microscope Operation, North-Holland, publisher (1974) p.178
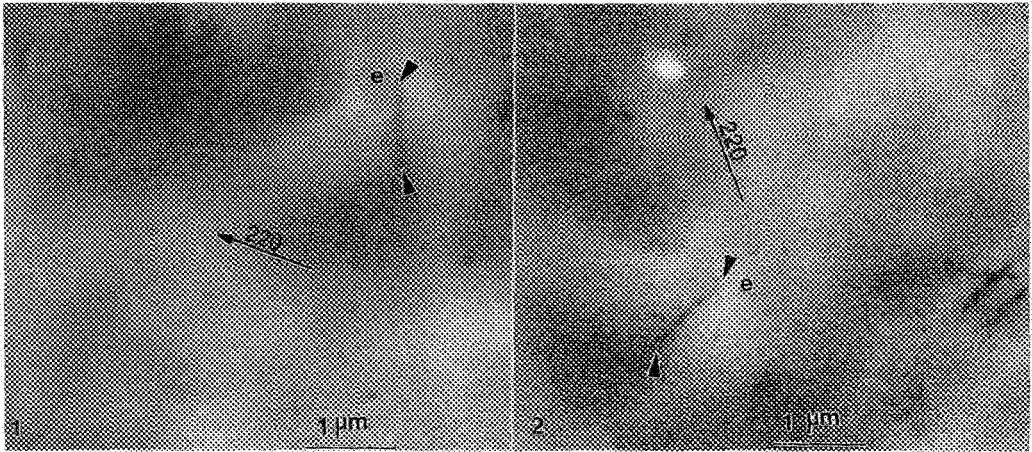
FIG. 1 Dislocation image at +8° tilt relative to sample normal. Note that by employing the (220) band for imaging contrast, the 220 g-vector becomes the tilt axis. Letter "e" marks the point of exit from the sample.

FIG. 2 Dislocation imaged at -10.5° from sample normal. Arrowed dislocation same as in Fig. 1.

SEM IMAGE SHARPNESS ANALYSIS[1]

M. T. Postek* and A. E. Vladar**

*National Institute of Standards and Technology, Gaithersburg, MD 20899
**ULSI Research Laboratories, Hewlett-Packard, Palo Alto, CA 94303

Fully automated or semi-automated scanning electron microscopes (SEM) are now commonly used in semiconductor production and other forms of manufacturing. The industry requires that an automated instrument must be routinely capable of 5 nm resolution (or better) at 1.0 kV accelerating voltage for the measurement of nominal 0.25-0.35 micrometer semiconductor critical dimensions. Testing and proving that the instrument is performing at this level on a day-by-day basis is an industry need and concern which has been the object of a study at NIST and the fundamentals and results are discussed in this paper.

In scanning electron microscopy, two of the most important instrument parameters are the size and shape of the primary electron beam and any image taken in a scanning electron microscope is the result of the sample and electron probe interaction. The low frequency changes in the video signal, collected from the sample, contains information about the larger features and the high frequency changes carry information of finer details. The sharper the image, the larger the number of high frequency components making up that image. Fast Fourier Transform (FFT) analysis of an SEM image can be employed to provide qualitiative and ultimately quantitative information regarding the SEM image quality.

Figure 1a is a micrograph of a heavily gold coated zinc oxide powder viewed at 1.5 keV. The image appears unsharp due to SEM performance and induced astigmatism. Figure 1b is a much sharper micrograph at 1.0 keV on that same sample. Figure 1c is a high accelerating voltage image. It is apparent that the sharpness of the image improves from Figure 1a through 1c. The FFT power spectra of the images are shown in Figures 1d, e and f, respectively. The high frequency information increases as the image gets sharper and the center part of the power spectra gets broader which is clearly shown in Figures 1d, e and f. This characteristic can be used in calculations to compute relative sharpness of an image series. Using ISAAC[2], with the use of a script containing the FFT routine, the frequency domain representation was computed in both x and y. With this sampling algorithm, the calculations occurred on the central two third of the images in order to minimize the effect of any possible distortions of the original image. The x and y sums were saved as text files. Further calculations were accomplished with spreadsheet software.

The technique described here, utilizing the sharpness concept, is facilitated by the use of the FFT techniques to analyze the electron micrograph to obtain the evaluation. This is not the first application of Fourier techniques to SEM images[3] but it is the first integrated approach considering the sample, computer analysis and measurement algorithm. This technique can be used to check and optimize two basic parameters of the primary electron beam, the focus and the astigmatism and it facilitates the periodic resolution determination of the SEM in an objective and quantitative form.

1. Contribution of the National Institute of Standards and Technology (NIST). This work was supported in part by the National Semiconductor Metrology Program at NIST; not subject to copyright.
2. M.T. Postek and A.E. Vladar. Scanning 18(1996)1-7 .
3. T.A. Dodson and D.C. Joy. Proc. XIIth Int. Cong.for EM. San Francisco Press. (1990)406-407.
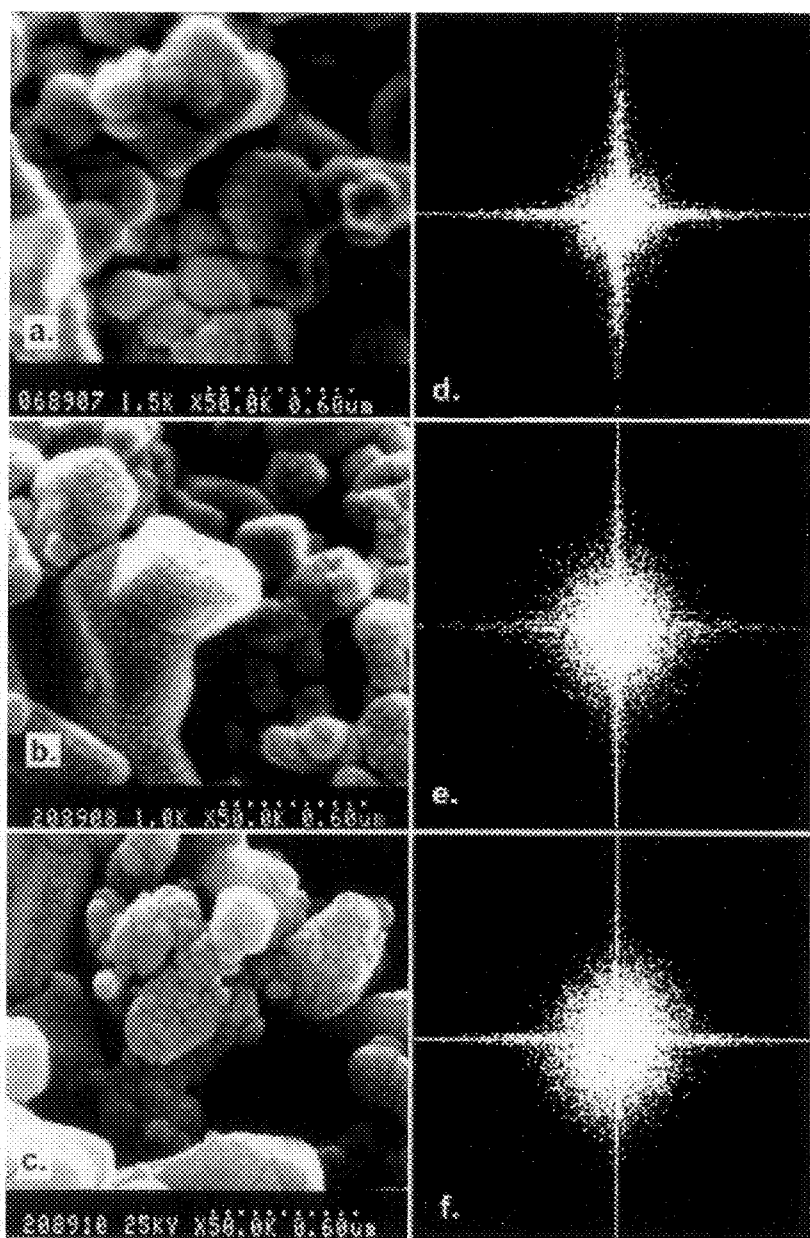
FIG. 1. Image sharpness evaluation. Displayed are three scanning electron micrographs of varying quality and the respective FFT analysis. Note how the high frequency components of the image increase as the image improves in sharpness.

ULTRA-LOW VOLTAGE SCANNING ELECTRON MICROSCOPY

David C Joy[+] and Carolyn S Joy
EM Facility, University of Tennessee, Knoxville, TN 37996-0810
[+] and Oak Ridge National Laboratory, Oak Ridge, TN 37831

Although the benefits of operating the scanning electron microscope at low beam energies have been evident since the earliest days of the instrument, the successful utilization of the SEM under these conditions has required the development of high brightness field emission electron source, advanced lenses, and clean vacuums. As these technologies became available the level at which imaging became regarded as "low energy" has fallen from 10keV, first to 5keV, and more recently to 1keV. At this energy state of the art instruments can now provide an excellent balance between resolution - which becomes worse with decreasing energy - and desirable goals such as the minimization of sample charging and the reduction of macroscopic radiation damage - which tend to become more challenging as the energy is increased.

An interesting new opportunity is to perform imaging in the ultra-low energy region between 1eV and 500eV. Over this energy range significant changes in the details of electron-solid interactions take place offering the chance of novel contrast modes, and the rapid fall in the electron beam range leads to the condition where the penetration of the incident beam into the sample is effectively limited to 1 or 2 nanometers. The practical problem is that of achieving useful levels of resolution and acceptable signal to noise ratios in the image. At energies below 1keV chromatic aberration dominates the probe formation in conventional instruments even when using an FEG source. However, the use of optimized retarding field optics essentially maintains chromatic aberration independent of landing energy down to very low values.[1,2] Figure (1) shows an example of the performance that can be achieved on a commercial instrument - an Hitachi S-4500 - modified to operate in this mode, in this case at 50eV landing energy. The resolution of the image is judged from edge sharpness and detail to be significantly better than 0.1μm and, from experimental observation, this performance is apparently limited by residual astigmatism caused by uncorrected sample charging rather than by fundamental aberrations in the probe forming optics. Comparable, if somewhat lower resolution, images have been achieved on this, and other FEG SEMs, at energies as low as 1eV.

At incident energies below 100eV it is necessary to describe the signal that is collected in terms that are rather different to those that are conventionally employed since the energy of both the backscattered and the secondary electrons are in the same range. Figure 2 shows a plot of the measured electron emission from tungsten in the incident energy range 1eV to 10keV where, for convenience, all of the emission in the low energy range is here referred to as secondary emission[3]. At high energies the SE signal shows the usual rapid rise as the incident energy falls, reaching a maximum at about 600eV. As the energy is further reduced the signal is seen to fall once more such that at an incident energy of 10eV the "secondary signal" once again has about the same magnitude as the SE yield at 10keV. In the energy range of interest, therefore, signal levels are comparable with those found at more usual accelerating voltages. It is interesting to compare this yield profile with the variation of electron stopping power in the material also plotted, in units of eV/Å, on figure (2).[3] Although the respective maxima of the two curves are displaced in energy it is evident that Bethe's hypothesis that electron yield is proportional to the stopping power is essentially correct. At incident energies above the stopping power maximum additional SE production (i.e SEII components) results from the backscattered signal. Although experimental data is limited it is probable that these levels of signal production are typical for most materials of interest. The form of image contrast is unlike that at higher energies since the beam penetration depth is less than the SE escape range. There is, thus, no

144
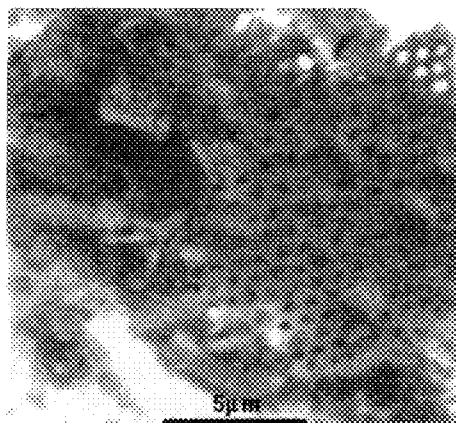
Figure 1. Image of diatom recorded at 50eV in modified Hitachi S-4500 FEGSEM.
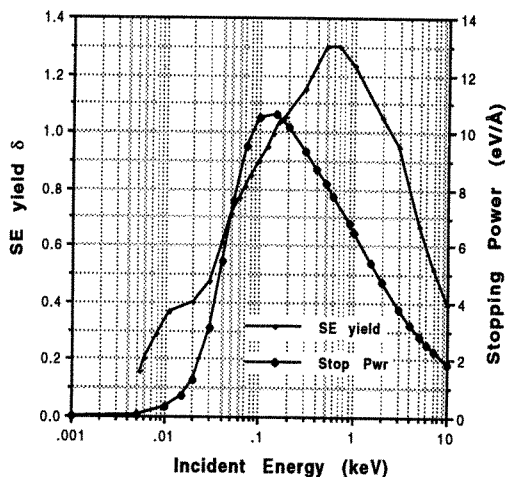
Figure 2. Variation with energy of SE yield and electron stopping power (in eV/Å) for tungsten.

topographic contrast, although shadowing can often be observed. The most common mode of contrast formation is associated with surface charging. The electron range is of the same order as native oxide film thicknesses on many metals and semiconductors, and the yield is <1. Hence negative charging occurs which may result in the formation of localized electron mirrors. At the lowest energies, below 30eV, interesting anomalous effects have been observed which may be associated with the increase of inelastic mean free path length in this regime.

Signal to noise limitations are important at these low energies as the gun brightness is much reduced compared to normal operation. An acceptable quality image is achieved by slow-speed scanning, but TV rate imaging is not presently possible. The efficiency of the detection system is clearly of importance in this case. The best arrangement uses the retarding field to accelerate the emitted 'secondaries' after they leave the specimen and before they enter the collection field of the detector. This ensures adequate quantum efficiency and guarantees symmetrical collection even if the detector is physically offset. Future development of instrumentation for ultra-low energy SEM would ideally include both improved detection systems and perhaps the use of nano-tip field emission sources which offer 100 to 1000x more brightness than conventional FEG sources.[4] Initial work is now proceeding in these directions.[5]

References

1.I Mullerova and L Frank, SCANNING **15**, (1993), 193
2. A D Brodie, J.Vac.Sci.Technol. **B12**, (1994), 3489
3. D C Joy, SCANNING **17**,(1995, 270. A complete copy of this data base is available from the author. The BS and SE data may also be accessed at http://www.nsctoronto.com/nissei-sangyo.
4. J C H Spence et al., J.Vac.Sci., **A12**, (1994), 542
5.Oak Ridge National Laboratory is operated by Lockheed Martin Energy Research Corp. for the U.S. Department of Energy under contract number DE-AC05-96OR22464

USE OF LOW-TEMPERATURE SCANNING ELECTRON MICROSCOPY TO OBSERVE ICICLES, ICE FABRIC, RIME AND FROST

William P. Wergin[1], Albert Rango[2] and Eric F. Erbe[1]

[1]Nematology Laboratory and [2]Hydrology Laboratory
Agricultural Research Service, USDA; Beltsville, MD 20705

Previous studies showed that low temperature scanning electron microscopy (SEM) can be used to record images of precipitated snow crystals, which collectively form structures that are commonly known as snowflakes[1,2]. Information about the structure of snow crystals can be used to improve models that estimate the water equivalent of the winter snowpack[3]. These models, which are based on satellite microwave data, have practical use in approximating the quantity of water that will be available for crop irrigation and hydroelectric power. Our previous success of using low temperature SEM to image snow crystals has encouraged us to utilize this technique for other types of frozen aqueous specimens.

Icicles were collected at Beltsville, MD; snow crystals, ice fabric and frost were collected from sites at Bearden Mountain, WV. Samples, which were obtained when air temperatures ranged from -12^0 C to -2^0 C, were collected on flat copper plates (15mm x 27mm) that contained a thin layer of methyl cellulose solution that was precooled to the ambient outdoor temperature and then rapidly plunged into LN_2. After a few minutes, the plates were inserted diagonally into 20 cm segments of square brass channelling and lowered into a LN_2 storage dewar where they remained until they were sputter coated for observation with low temperature SEM.

Small forming icicles, which were fractured and observed in cross section, revealed concentric rings of air bubbles that may be released and entrapped as successive layers of water freeze (Fig. 1). The weight of a ski was used to compress newly fallen snow. This process, which flattened the surface of the snowpack, caused fragmentation and compaction of crystals that could be readily characterized (Fig. 2). This type of surface is generally referred to as ice fabric. Rime, which could be imaged on the surfaces of precipitating crystals, probably formed as the crystals descended through clouds containing supercooled water droplets that condensed on their surfaces (Fig. 3). The frost consisted of needles that presumably formed from the condensation of water vapor (Fig. 4). These results suggest that low temperature SEM is useful for imaging frozen aqueous specimens that could also include ice core samples and particulate pollutants that become incorporated into snow and ice. In addition, this technique could be used to image such dynamic phenomenon as icing on the surface of aircraft wings.

1. W.P. Wergin, E.F. Erbe, *Proc. Royal Microsc. Soc* 29(1994)138.
2. W.P. Wergin et al., *Scanning*, 17(1995)41.
3. A. Rango et al., *IEEE Trans Geoscience and Remote Sensing*, 27(1989)740.

Figure 1. Cross fracture of a portion of an icicle illustrating concentric rings of small air bubbles.
Figure 2. Surface of ice fabric resulting from pressure, fracture and compaction of snow crystals by a snow ski.
Figure 3. Rime resulting from the atmospheric collision of a snow crystal (hexagonal plate) with super cooled water droplets.
Figure 4. Needles of frost formed by condensation or sublimation of water vapor.
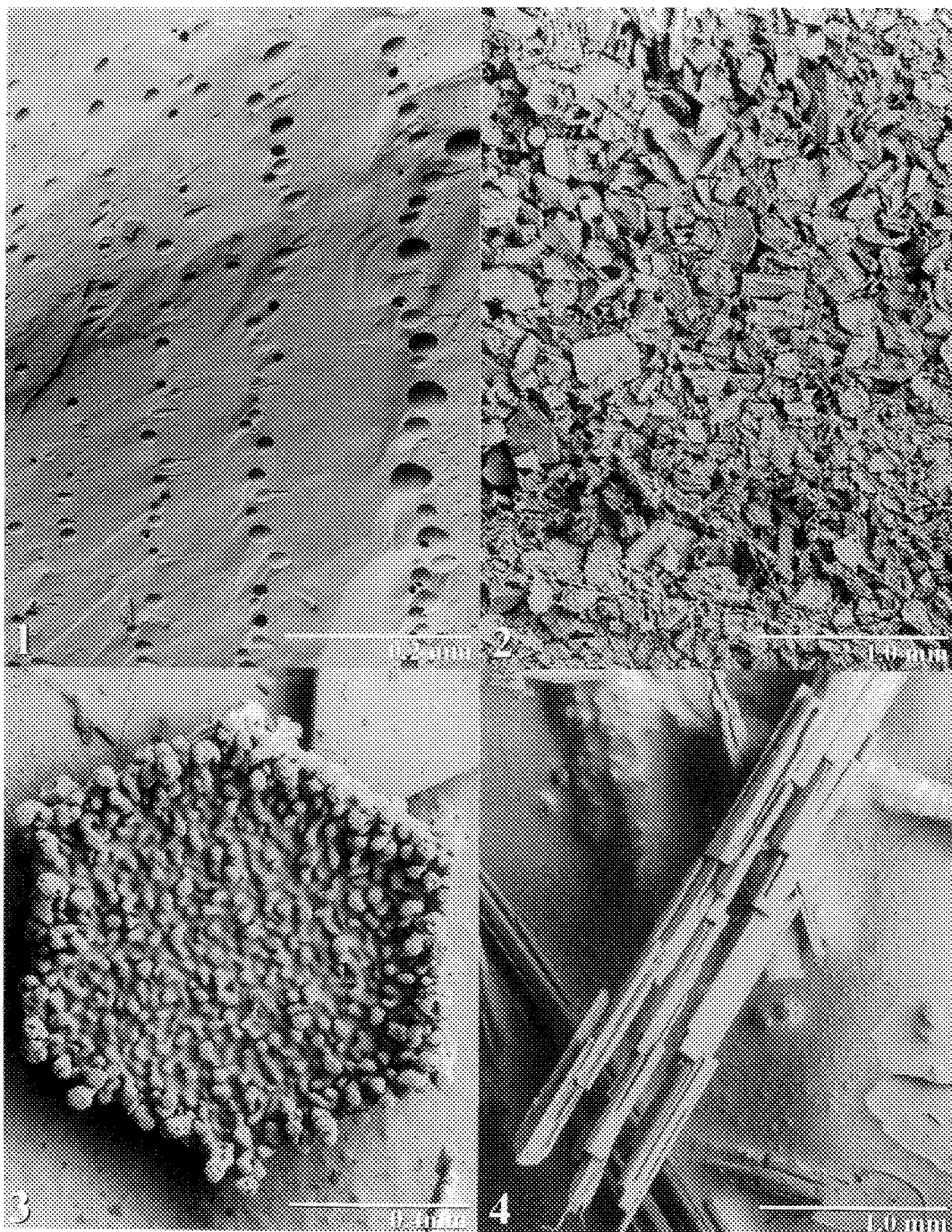
HOW TO GET THE MOST OF A SEM USING THE CASINO MONTE CARLO PROGRAM

D. Drouin, P. Hovington, R. Gauvin and J. Beauvais

*Département de génie mécanique, Université de Sherbrooke, Sherbrooke, Québec, CANADA, J1K 2R1

High resolution scanning electron microscopy (SEM) has become more and more popular for several reason. First, the new field emission (FE) source of electron is now able to produce a high current density electron probe even at very low energies. It is possible to perform analysis with spatial resolution comparable to one obtain in conventional transmission electron microscope (TEM). The major inconvenient of TEM analysis are related to sample preparation. Fabrication of electron transparency film is generally a complex and time consuming process.

To fully exploit a SEM, microscope users must have an accurate knowledge of the electron matter interaction. In order to help microscope users determine the appropriate microscope conditions, Monte Carlo simulation programs have been developed. Those programs, use random number sequences and complex models to accurately determine the signals recorded in a SEM (X-Ray and Backscattered electron). With the new generation of powerful personal computers, it is now possible to rapidly predict SEM outputs corresponding to the user's microscope conditions. The CASINO program is a shareware that can be used to fully exploit a SEM.

The CASINO acronym has been derived from the phrase "monte CArlo SImulation of electroN trajectory in sOlids". This Monte Carlo program is specially designed for low energy beam interactions in a bulk, thin foil, grain boundary and spherical inclusion. In a single scattering Monte Carlo program, all the electron trajectories are modeled as a series of collision. The distance and angle between each elastic collision is computed using the Mott cross section. The versions 1.0 of CASINO neglect inelastic collisions and all inelastic events are combined in a general expression, the stopping power. This expression determines the resulting energy at the next collision. The CASINO program can used either the Joy and Luo (1989) expression or the experimental stopping power of Hovington et al. (1996)[1].

Figure 1 shows some typical outputs that can be generated with CASINO. The sample investigated is a 10 nm Mg_2Si precipitated in 6061 aluminum alloy (center of figure 1). The incident electron beam was set to 5 kV with a probe size of 10nm, which corresponds to conditions used in a FESEM. To the left of figure 1, the corresponding backscattered electron profile is shown. The program can also generate an image with the simulated profile. An example of an X-Ray image is shown on the right of figure 1.

It is also possible to predict the current flowing through the specimen. This type of simulation is useful in the semiconductor industry. To investigate semiconductor devices, the electron beam induced current (EBIC) technique if often used. With this SEM mode, depletion zones are visible and thus can be characterized[2]. Figure 2 shows an example of an EBIC application. In this specimen, the main point is to determine the current that will flow in the Schottky diode formed by PtSi silicide and the Si substrate. In order to achieve this, the CASINO program was used to determined the amount of energy lost in each layer. Then dividing the amount of energy lost in the depletion zone (just below the PtSi) with the mean energy to create an electron-hole pair, it is possible to determine the diode current. In the case of 800 nm of Al, if the beam current is set to 1 nA, the diode current will be approximately 70 nA.

The Monte Carlo program CASINO is a powerful tool to fully understand the signals recorded with a SEM. This program is a shareware and is available at the following WEB site http://www.gme.usherb.ca/casino.

References
1   P. Hovington, D. Drouin and R. Gauvin, submitted to scanning.
2   D. Drouin, R. Gauvin, J. Beauvais, P. Hovington and D. C. Joy, to appear in this proceedings.

Backscattered electron profile

η_b

-60 -40 -20   0   20 40 60
Position (nm)

$E_0 = 5\ keV$

X - Ray images

Al $K\alpha$

Mg $K\alpha$

Si $K\alpha$

Figure 1

$E_0 = 10\ keV$
$I_b = 1\ nA$
$\eta = 15.5\ \%$

Al
Variable
thickness

SiO_2 50 nm

Si
Substrat

DVM

PtSi
10 nm

Diode current

200
180
160
140
120
100
80
60
40
20
0

650   700   750   800   850   900   950   1000
Aluminum thickness
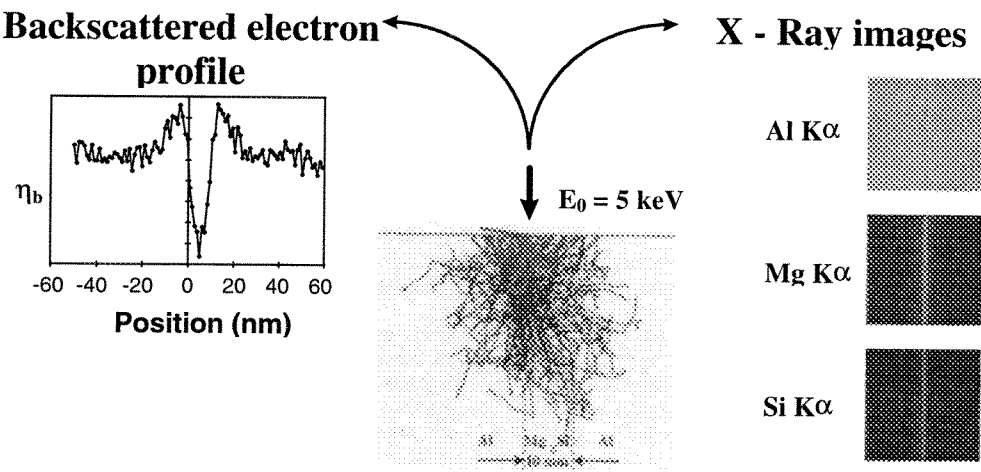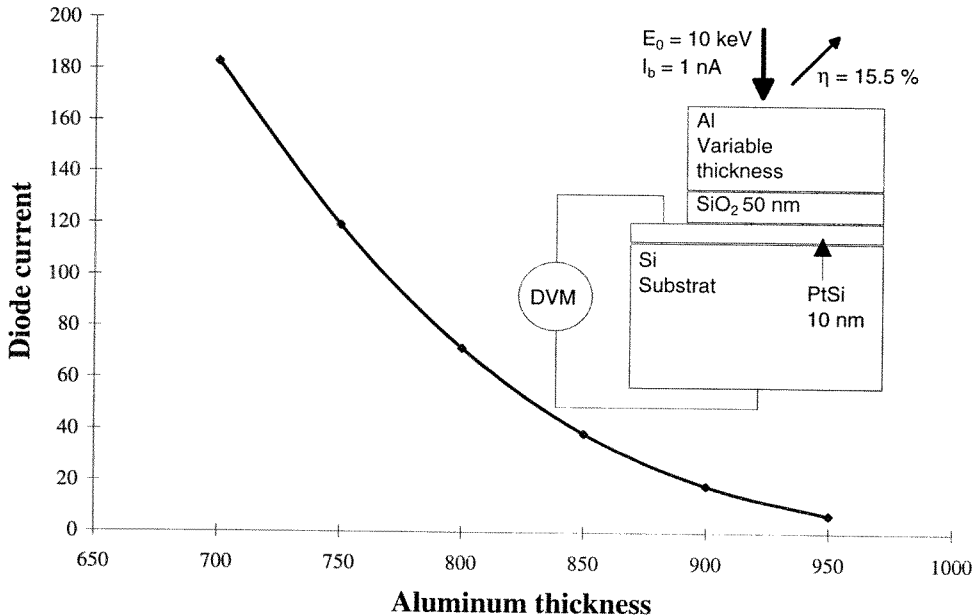
Figure 2

Fig. 1   Backscattered electron profile and X-Ray mapping of a 10 nm Mg_2Si precipitated in a 6061 Al alloy.

Fig. 2   Simulated diode current in function of the aluminum thickness. The beam current is 1 nA and the accelerating voltage 10 kV.

Energy Filtered Electron Backscattering Images of 10-nm NbC and AlN Precipitates   in Steels Computed by Monte Carlo Simulations

By Raynald Gauvin, Dominique Drouin and Pierre Hovington

Département de génie mécanique, Université de Sherbrooke, Sherbrooke, Québec, Canada, J1K 2R1

In modern materials science, it is important to improve the resolution of the Scanning Electron Microscope (SEM) because small phases play a crutial role in the properties of materials. The Transmission Electron Microscope (TEM) is the tool of choice for imaging small phases embedded in a given matrix. However, this technique is expensive and also is slow owing to specimen preparation. In this context, it is important to improve spatial resolution of the SEM.

In electron backscattering images, it is well know that the backscattered electrons have an energetic distribution when they escape the specimen.The electrons having loss less energy are those which have travelled less in the specimen and thus escape closer to the electron beam. So, in filtering the energy of the backscattering electron and keeping those which have loss only a small amount of energy to create the image, a significant improvement of the resolution of such images is expected. New detectors are now under development to take advantage of this technique of imaging[1].

In order to quantify the improvement of spatial resolution in energy filtered backscattering electron images, Monte Carlo simulations of electron trajectories in NbC and AlN semispherical precipitate of 10 nm of radius embedded in a Fe matrix have been performed with incident electron energy equals to 1 keV for NbC and 10 keV for AlN. The beam size have been set equals to 10 nm at 1 keV and to 1 nm at 10 keV, which correspond to the situation of a Field Emission Gun SEM. 1 000 000 electrons trajectories have been simulated for each beam position. The details of the Monte Carlo program (named CASINO) are given in the paper of Gauvin *et al.* (1995)[2]. Electron backscattering profiles have been computed with all the backscattered electrons (total curve) and with backscattered electrons having 80 to 100% , 90 to 100% and 98 to 100% of the incident electron energy. Figure [1] presents such profiles for the 10 nm NbC precipitate at 1 keV and figure [2] presents those of the AlN precipitate at 10 keV. Also shown is the contrast associated with each curves.In both cases, it is clear that imaging with backscattered electrons having loss only 2% or less of their initial energy significantly improve the spatial resolution and the contrast. The improvement is truly spectacular at 10 keV where the inclusion is almost invisible when all the backscattered electrons are used to create the image. This is because at 10 keV, the electron beam radius is one order smaller than at 1 keV. Therefore, to improve the resolution of using energy filtered electron backscattering images, it is advantageous to increase the beam energy.

REFERENCES

1 Rau, E. and Robinson, VNE, (1996), A Toroidal Backscattered Electron Energy Spectrometer for use in SEM, Proceeding of the IUMAS, pp. 153-4.
2 Gauvin, R., Hovington, P. and Drouin D. (1995), Quantification of Spherical Inclusions in the Scanning Electron Microscope Using Monte Carlo Simulations, SCANNING, Vol. 17, pp. 202-19.

List of figures

Fig. 1 Electron backscattering profile at 1 keV of NbC hemispherical precipitate in Fe matrix.
    See text for details
Fig. 2 Electron backscattering profile at 10 keV of AlN hemispherical precipitate in Fe matrix.
    See text for details

10 nm NbC inclusion in Fe matrix
$E_o = 1$ keV
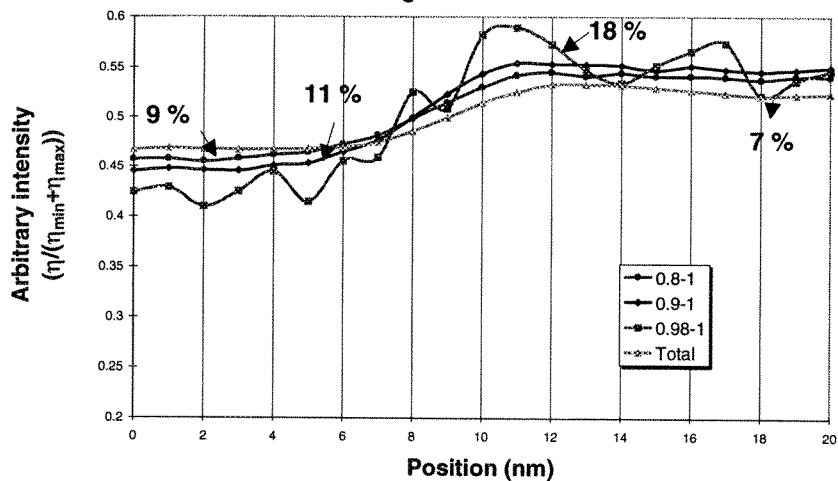
Fig. 1

10 nm AlN inclusion in Fe matrix
$E_o = 10$ keV
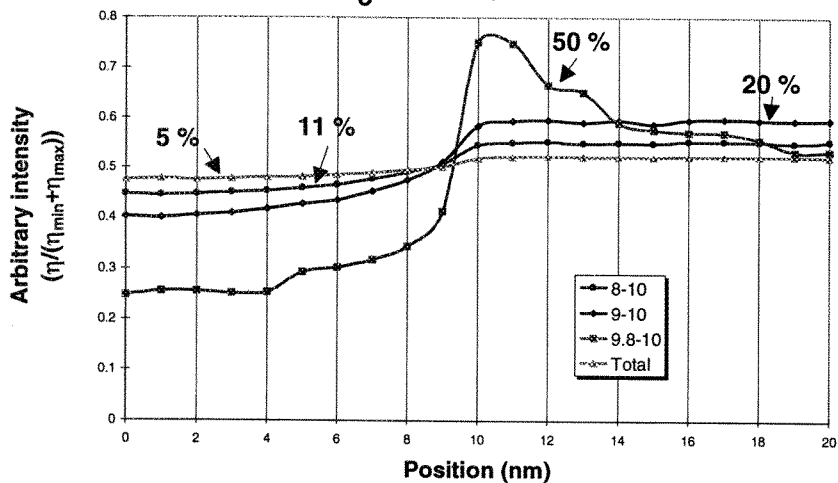
Fig. 2

CHARACTERIZATION OF SCHOTTKY DEPLETION ZONE USING EBIC IMAGING

D. Drouin*, R. Gauvin*, J. Beauvais**, P. Hovington* and D. C. Joy***

*Département de génie mécanique, Université de Sherbrooke, Sherbrooke, Québec, CANADA, J1K 2R1
**Centre de Recherche en Physique du Solide, Département de génie électrique et de génie électrique, Université de Sherbrooke, Sherbrooke, Québec, CANADA, J1K 2R1
***EM Facility, F241 Waltes Lifes Sciences Building, University of Tennessee, Knoxville, Tennessee, USA, 37996-0810

Scanning Electron Microscopy (SEM) has been widely used to characterize semiconductor materials. Approximately one half of all SEMs are used by the electronic industry[1]. The SEM can be used as a local current source that can be scanned over semiconductor device surfaces. This imaging mode is called Electron Beam Induced Current (EBIC).

A depletion zone formed by a Schottky diode is visualized using this technique. This Shottky diode is fabricated by placing a metal contact on a semiconductor surfaces. The work function of the metal and the semiconductor produce an equilibrium contact potential. This potential barrier occurs across a region free of charge carriers and thus an electric field is present. This region is called a depletion zone.

The Schottky barrier is formed by evaporating 10 nm of Pt through a diode mask on a clean 5000 Ω-cm <100> Si wafer. The diode mask consists of 1 mm holes in a thin metal sheet. A silicide (PtSi) is then produced by annealing the diode in a RTA (Rapid Thermal Annealer). A 200 nm layer of Cr is then deposited through a 0.5 mm mask on the surface of the sample to allow contact bonding. The ohmic-contact was completed by evaporating a Au-Sb alloy onto the backside of the sample. The sample was cut in the middle of the diode and the cross-section was polished. The sample is then placed with its cross-section facing upward from the sample holder, wire-bonded and held in place with silver paste. The electrically isolated sample holder was then placed in the microscope chamber. No external bias was applied to the diode. The diode current was amplified with an EBIC amplifier and monitored on a JEOL 6300 SEM using the auxiliary input.

Figure 1 shows a micrograph in secondary electron mode of the cross section of the Schottky diode. In this mode, no electrical contrast is visible and only topographical contrast is present. The wire is connected to the top of the diode and the silver paste connected the Au-Sb back contact to the sample holder.

Figure 2 is the EBIC image recorded at the same location. When the beam loses energy in a semiconductor, electron-hole pairs are created. For silicon the mean energy to create an electron hole pair is approximately 3.6 eV[1]. If the beam is not near the diode, the collected current is approximately constant because no electric field is present to sweep the generated charge carriers. Thus the carriers just diffuse until they recombine together or diffuses near an electric field. This diffusion can be observed below the diode. Just under the silicide a depletion zone of about 50 μm sweep all the electron-hole pairs generated in this region (the brighter region on figure 2). If the beam moves away from this zone the current decreases exponentially due to the diffusion of the carriers. This appears as a decrease in the intensity on the micrograph.

This technique of imaging combined with a Monte Carlo program can be use to characterize and quantify semiconductor devices. The CASINO[2] Monte Carlo program will be used to fully quantify and understand the contrast of EBIC images.

References
1. D. E. Newbury, D. C. Joy, P. Echlin, C. E. Fiori and J. I. Goldstein *Advanced Scanning Electron Microscopy and X-Ray Microanalysis*, Plenum Press, 1986.
2. P. Hovington, D. Drouin and R. Gauvin, submitted to Scanning, 1996.
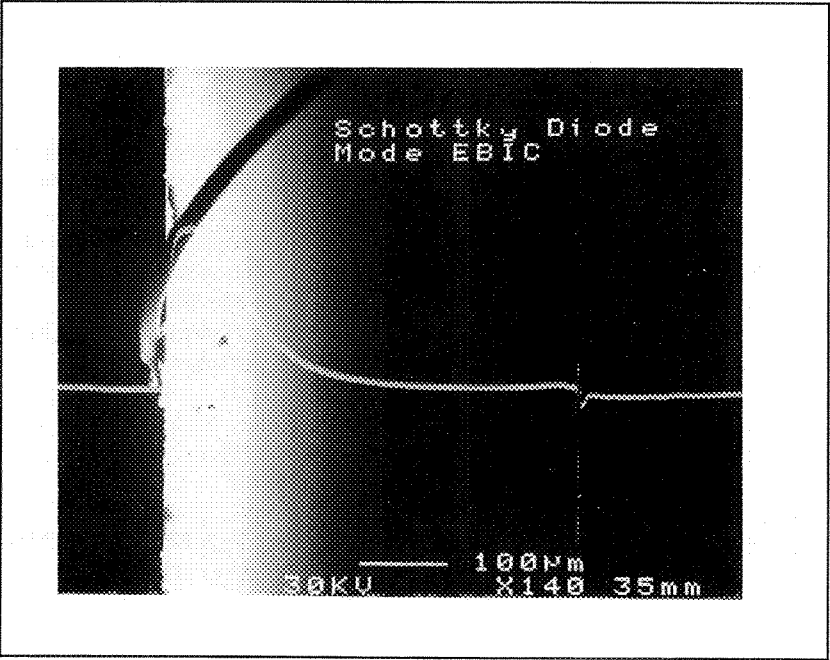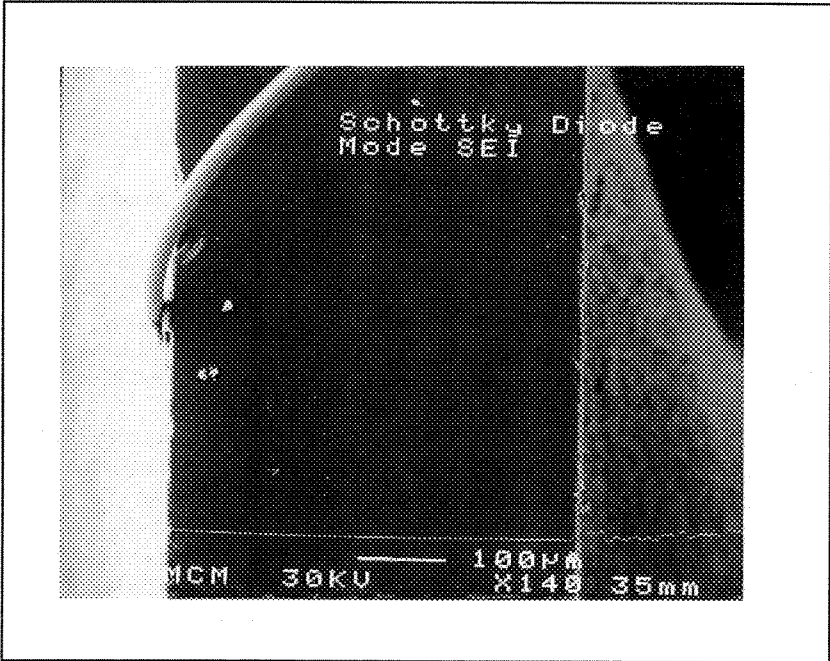
FIG. 1 SEM micrograph of the Schottky diode cross-section .
FIG. 2 EBIC micrograph of the Schottky diode cross-section.

153

INTEGRATION OF CORE-EDGE SPECTROSCOPY METHODS
FOR THE STUDY OF POLYMERS

E. G. Rightor, Dow Chemical, 2301 N. Brazosport Blvd. B-1225, Freeport, TX 77541

Core edge spectroscopy methods are versatile tools for investigating a wide variety of materials. They can be used to probe the electronic states of materials in bulk solids, on surfaces, or in the gas phase. This family of methods involves promoting an inner shell (core) electron to an excited state and recording either the primary excitation or secondary decay of the excited state. The techniques are complimentary and have different strengths and limitations for studying challenging aspects of materials. The need to identify components in polymers or polymer blends at high spatial resolution has driven development, application, and integration of results from several of these methods.

In a scanning transmission electron microscope (STEM), electron energy loss spectroscopy (EELS) can be used to determine the nature of polymer phases at very high spatial resolution based on chemical composition or spectroscopic differences. Although the core edge fingerprint of many polymers is characteristic, radiation damage, limited spectral resolution, and magnetic fields can severely limit confidence in the data. Parallel studies of polymer molecular analogues by inner shell electron energy loss spectroscopy (ISEELS) and molecular orbital calculations can help identify polymer transitions and push EELS capabilities in a TEM.[1,2] Near edge x-ray absorption spectroscopy (NEXAFS) experiments at a synchrotron are also quite useful for obtaining corroborating data of high spectral resolution and low radiation damage from polymer surfaces or "bulk" areas. Scanning transmission x-ray microscopy (STXM) adds to these capabilities a way to use characteristic core edge transitions in polymers for imaging and spectral analysis with high spatial resolution (~50nm) and the ability to look at solvated materials at ambient pressure.[3]

Figure 1 compares data from several core edge techniques for the carbon 1s edge of poly (ethylene terephthalate). Agreement between the techniques is very good, with differences mainly coming from different spectral resolution. Although the STEM-EELS data is of lower spectral resolution, this comparison demonstrates that at low dose it can give the correct fingerprint. Comparison with other techniques can confirm minimization of radiation damage, help push the spectral resolution for STEM-EELS experiments, verify the identity of useful transitions, examine effects of analysis environment (vacuum, air, wet, etc.), and help anticipate effects of molecular orientation. Integration of these techniques enables research on complicated polymers such as polyurethanes.[4]

1. E. G. Rightor et al., Microscopy: The Key Research Tool, 22(1992)67.
2. A. P. Hitchcock, S. G. Urquhart, E. Rightor, J. Phys. Chem., 96(1992)8736.
3. H. Ade, et al., Science, 258(1992)972.
4. S. G. Urquhart et al., J. Polym. Sci. B Polym. Phys. Ed., 33(1995)1593.
5. This work has benefited enormously from collaboration with A. Hitchcock, S. Urquhart (McMaster Univ.); H. Ade, A. Smith (N. C. State); R. Leapman, S. Sun (National Institutes of Health); G. Young, G. Mitchell , R. Priester, and W. Lidy (Dow). The author acknowledges those at the National Synchrotron Light Source, particularly D. Fischer, V. Zhuang, J. Kirz and C. Jacobson, and Advanced Light Source, especially T. Warwick, H. Shin, and B. Tonner, for use of synchrotron light.
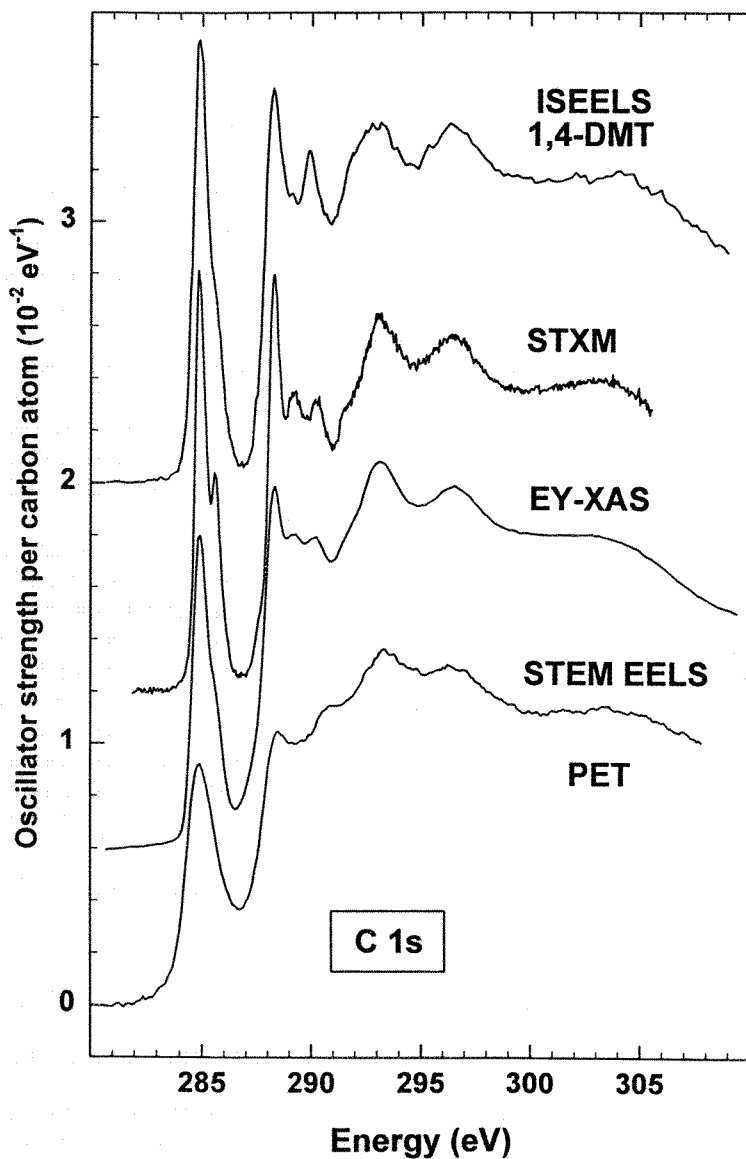
Fig. 1. Comparison of carbon 1s ISEELS core edge spectrum of (top to bottom) 1,4- dimethyl terephthalate (a molecular analogue of PET) and PET spectra recorded by STXM, NEXAFS, and STEM-EELS. ISEELS spectra were recorded with S. Urquhart and A. Hitchcock. The STXM and NEXAFS data were recorded at National Synchrotron Light Source with H. Ade, P. Smith, D. Fischer and G. Mitchell. STEM-EELS data were recorded at the National Institutes of Health with R. Leapman and S. Sun.

155

X-RAY MICROSCOPY: A NOVEL, LOW DAMAGE APPROACH TO CORE EXCITATION SPECTROSCOPY AT HIGH SPATIAL RESOLUTION

H. Ade

Dept. of Physics, North Carolina State University, Raleigh, NC 27695-8202

Only recently has transmission x-ray microscopy been utilized for chemical analysis from small spots and chemical mapping[1] via near edge x-ray absorption fine structure (NEXAFS) spectroscopy. NEXAFS microscopy is analogous to Electron Energy Loss Spectroscopy (EELS) in an electron microscope[2]. Particularly in imaging mode, NEXAFS microscopy requires a considerable lower dose than EELS microscopy[1-2] which makes it very suitable to studying radiation sensitive materials such as polymers. In addition, NEXAFS microscopy can exploit the dependence of x-ray absorption resonances on the bond orientation relative to the linearly polarized x rays (linear dichroism microscopy)[3] and determine the orientation of specific chemical bonds in (partially) orientated materials.

To date, most x-ray microscopy studies on polymers have been performed at the carbon K edge with the X1 Scanning Transmission X-ray Microscope (X1-STXM) located at the NSLS at BNL. The X1-STXM has a spatial resolution of 50 nm in imaging mode[4], and can acquire NEXAFS spectra from about $(0.1 \ \mu m)^2$. Significant progress in the quality of the acquired data regarding S/N and energy resolution has been made during the last two years. We show as examples recent spectra acquired with the X1-STXM of poly(ethylene terephthalate) (PET) and polyarylate (PAR) in Fig. 1.

Experiments performed and still under way include the study of the morphology of polymer blends[5,6], phase separated polymers, such as precipitates in polyurethanes[5] and liquid crystalline polyesters[7], layered polymers or polymer laminates, diffusion at interfaces, orientation in Kevlar fibers, studies of biological[8] and organic geochemical[9] samples, as well as a number of similar studies. As an example, Fig. 3 shows the morphology of a blend of poly(ethylene terephthalate), PET, low density polyethylene, LDPE, and Maleated Kraton. Careful inspection of the micrographs suggests that Kraton has a preference to be also distributed at the PET/LDPE interface, rather than just inside the LDPE domains. The features in the lower right hand corner make this particularly obvious: dark domains are touching each other (Kraton around the LPDE domain) in Fig. 3A, while by comparison the bright LDPE domains are sharply delineated and separated in Fig. 3B.

References
1. H. Ade, X. Zhang, S. Cameron, C. Costello, J. Kirz, and S. Williams, *Science* **258**, 972 (1992).
2. See for example E. Rightor, these proceedings.
3. H. Ade and B. Hsiao, *Science* **262**, 1427 (1993).
4. Jacobsen, et al., *Opt. Commun.* 86, 351 (1991).
5. Ade, et al., *Polymer* **36**, 1843-1848 (1995).
6. D.-J. Liu, et al., *1995 NSLS Activity Report* (1996).
7. H. Ade, in *Proc. 53rd Annual Meeting of the Microscopy Society of America*, G.W. Bailey and C.L. Rieder, Eds. (San Francisco Press, San Francisco, 1995)
8. X. Zhang, R. Balhorn, C. Jacobsen, J. Kirz, S. Williams, in *Proc. 52nd Annual Meeting of Microscopy Society of America* G. W. Bailey, A. J. Garratt-Reed, Eds. (San Francisco Press, San Francisco, 1994) pp. 50-51.
9. D. Cody, et al., *Energy & Fuels* **9**, 153 (1995).
10. Particular thanks is due to Profs. J. Kirz and C. Jacobsen from SUNY@Stony Brook and their groups for the maintenance and construction of the NSLS STXM, A.P. Smith and V. Zhang (NCSU) for help with some of the data acquisition, and D.-J. Liu, S.-C. Lui, A. Monisera, J. Marty, and J. Chung (AlliedSignal) for providing the samples and participating in the data acquisition.

1 PET Absorption Spectrum

PAR Absorption Spectrum

2

PET

PAR

3a

3b

5 μm

5 μm
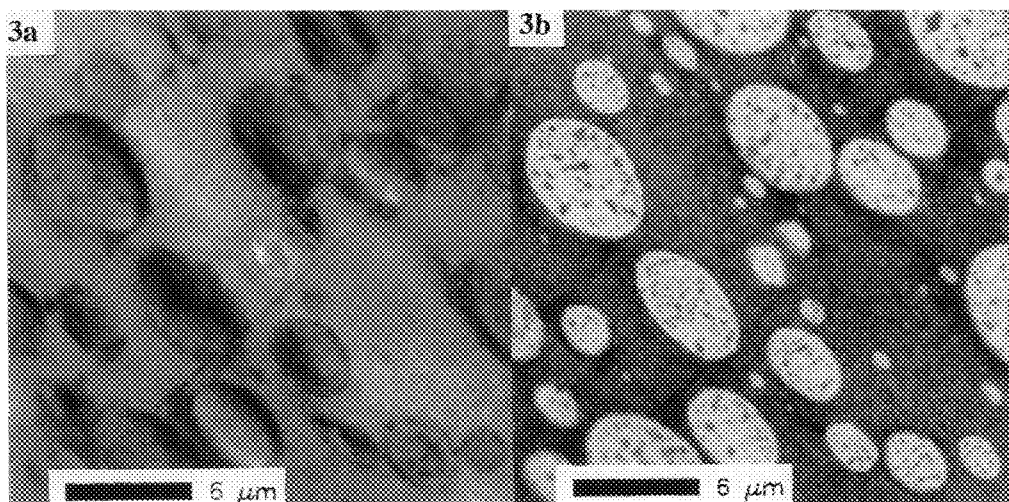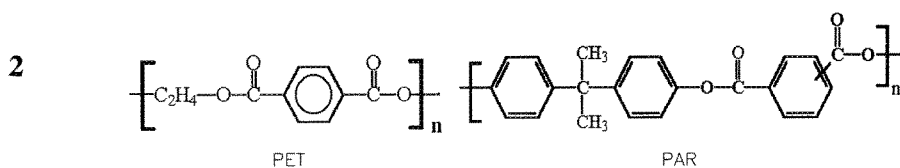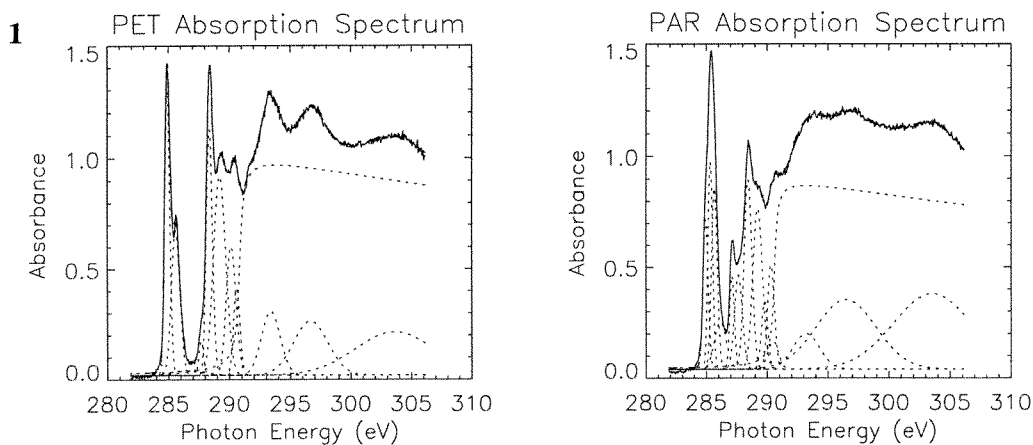
Fig. 1. Fitted NEXAFS spectra of PET and PAR.

Fig. 2. Chemical structure of PET and PAR.

Fig. 3. (a) Micrograph acquired at a photon energy of 299 eV. Both LDPE and Kraton appear dark while PET relatively transparent. (b) Micrograph acquired near 285 eV. LDPE is very transparent and appears bright while Kraton and PET are dark. Inspection of both micrographs shows that Kraton is also present at the LDPE/PET interface and not just in the LDPE domains (Taken from reference 6).

INVESTIGATION OF LOW-LOSS SPECTRA AND NEAR-EDGE FINE STRUCTURE OF POLYMERS BY PEELS

W. Heckmann

Kunststofflaboratorium der BASF AG, D-67056 Ludwigshafen, Germany

Transmission electron microscopy has changed from a purely imaging method to an analytical method. This has been facilitated particularly by equipping electron microscopes with energy filters and with parallel electron energy loss spectrometers (PEELS). Because of their relatively high energy resolution (1 to 2 eV) they provide information not only on the elements present but also on the type of bonds between the molecular groups. Polymers are radiation sensitive and the molecular bonds change as the spectrum is being recorded. This can be observed with PEEL spectrometers that are able to record spectra with high sensitivity and in rapid succession.

A PEEL spectrum can be divided into a low loss range and an inner shell loss range of higher energy. The low loss spectra of polymers always show a broad peak at about 22 eV and a further peak at 7 eV, if aromatic groups are present, as is the case with PS (Fig. 1). In the course of exposure, the intensity of this peak decreases, a sign that the benzene ring is destroyed by the radiation (Fig. 2).

The processes that take place during the exposure of the polymer can best be observed by recording short time-base spectra of the carbon K edge. When PE (Fig. 3) is exposed to the radiation, it releases H atoms, and the free radicals that form can recombine to give double bonds. With PS (Fig. 4) it can be seen from the decrease in the π^* resonance intensity that the benzene ring is destroyed. POM is a particularly radiation sensitive polymer where aldehyde groups are formed during spectra acquisition (Fig. 5).

A method that is closely related to electron energy loss spectroscopy is X-ray absorption spectroscopy (NEXAFS). Spectra obtained by NEXAFS are directly comparable with the EEL spectra[1]. As X-rays do not damage polymers as much as electrons, it is possible to obtain spectra from the almost undisturbed polymer molecules. Fig. 6 shows as an example the PEEL spectrum recorded with a low dose of radiation compared with a NEXAFS spectrum of poly(butylene terephthalate). All groups present in the molecule can be recognized in the spectrum. Thus, the EEL spectra of complex polymer molecules can be interpreted as the superimposed spectra of the diatomic basic building blocks. It has been found that this simple view, which has also been referred to as the „Building Block" Model [2], actually fits in many cases.

References

1.   H. Bethe, *Ann. Phys. (Leipzig)*, 5(1930)325.
2.   J. Stöhr, *NEXAFS Spectroscopy, Springer Series in Surface Sciences 25,* Springer Verlag Berlin, 1992
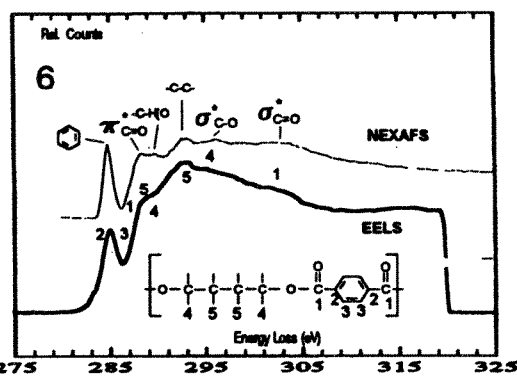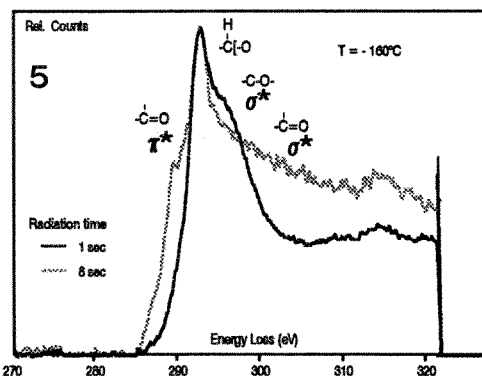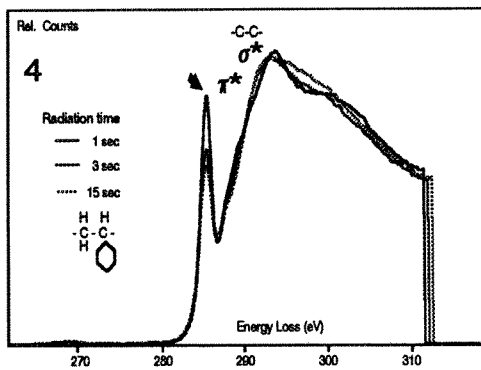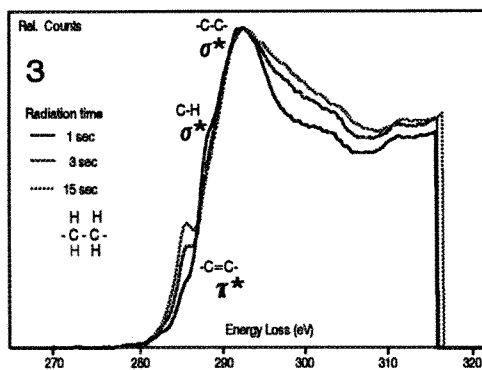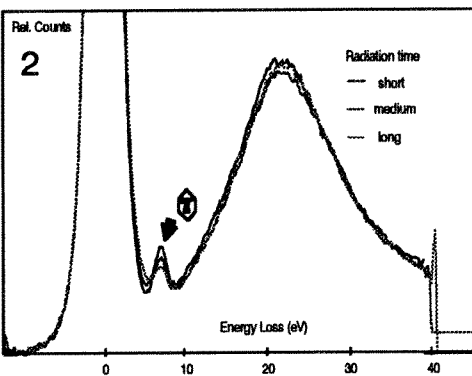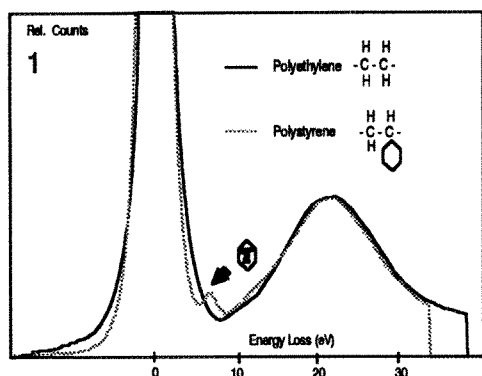
Fig. 1 Low Loss spectra of polyethylene (PE) and polystyrene (PS)
Fig. 2 Series of PS Low Loss spectra with increasing radiation time
Fig. 3 Series of carbon K-edge spectra of PE with increasing radiation time
Fig. 4 Series of carbon K-edge spectra of PS with increasing radiation time
Fig. 5 Carbon K-edge spectra of POM after 1 and 8 sec irradiation with 125 keV electrons at low temperature
Fig. 6 Comparison of NEXAF- and EEL-spectra of poly(butylene terephthalate)

ELECTRONIC STRUCTURE STUDIES OF CONDUCTING POLYMERS BY ELECTRON ENERGY-LOSS SPECTROSCOPY

J. Fink

IFW Dresden, Postfach 270016, D-01171 Dresden, Germany

Conducting polymers comprises a new class of materials achieving electrical conductivities which rival those of the best metals. The parent compounds (conjugated polymers) are quasi-one-dimensional semiconductors. These polymers can be doped by electron acceptors or electron donors. The prototype of these materials is polyacetylene (PA). There are various other conjugated polymers such as polyparaphenylene, polyphenylenevinylene, polypoyrrole or polythiophene. The doped systems, i.e. the conducting polymers, have intersting potential technological applications such as replacement of conventional metals in electronic shielding and antistatic equipment, rechargable batteries, and flexible light emitting diodes.

Although these systems have been investigated almost 20 years, the electronic structure of the doped metallic systems is not clear and even the reason for the gap in undoped semiconducting systems is under discussion.

Since it is very difficult to produce clean surfaces in these systems, it is extremely difficult to obtain reliable information on the electronic structure of these materials by photoemission. Therefore, less surface sensitive methods are required. Such a method is angle-resolved electron energy-loss spectroscopy (EELS). Using this technique we have studied the electronic structure of conducting polymers during the last 14 years. Valence band excitations measured by EELS yield information on the joint density of states of valence and conduction bands. Detailed information on the dispersion of bands is obtained. Core level excitations provide information on the density of unoccupied states as well as on the charge on C atoms and on counter ions.

In Fig. 1 we show EELS data[1] of highly oriented polyacetylene as a function of the angle θ between the chain axis and the momentum transfer. For $\theta = 0$, a well pronounced plasmon of the π electrons (which determine the transport properties) is observed at 4.9 eV while the plasmon of all valence electrons appears at 22.5 eV. For $\theta = 90^0$, the π-plasmon is strongly reduced indicating a low polarizability of these π-electrons perpendicular to the chains. Momentum dependent loss spectra[2] of polyacetylene for q parallel to the chain axis are shown in Fig. 2. The π-plasmon shows a strong dispersion from which the width of the π bands could be derived. Similar spectra on doped systems provided information on the energy of defect levels due to solitons, polarons and bipolarons as well as changes of the total π-electronic system. Typical C1s edges of p-type doped polymers such as polypyrrole (PPY), polythiophene and polyaniline (PANI) are shown in Fig. 3. The prepeak at about 284 eV is typical of p-type doped systems indicating occupied defect levels in the gap.

References

1. J. Fink and G. Leising, Phys. Rev. B 34 (1986) 5320
2. H. Fritzsche, N. Nücker, B. Scheerer, J. Fink, and G. Leising,
   Synth. Metals 28 (1989) D 237
3. J. Fink, Adv. *Elecr. Electron Phys.* 75 (1989) 121
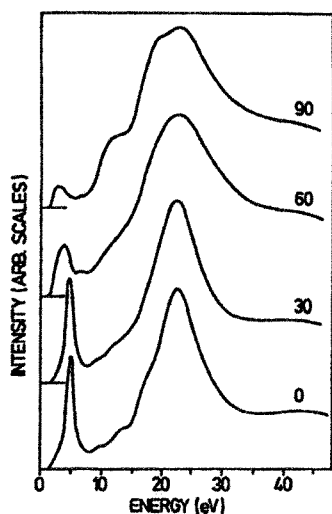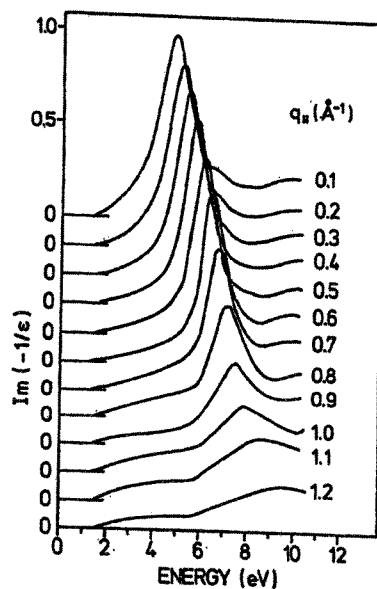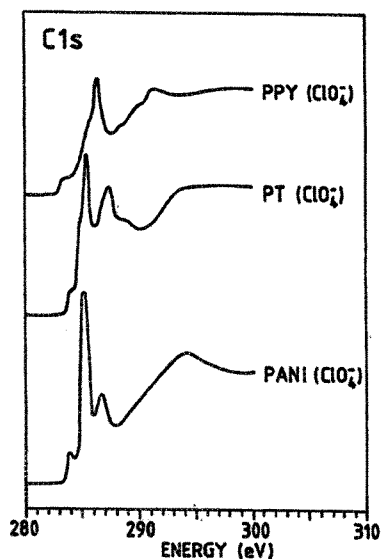
FIG. 1 Electron energy-loss spectra of highly oriented trans-polyacetylene as a function of the angle between the chain axis and momentum transfer

FIG. 2 Momentum dependent loss function of transpolyacetylene for q parallel to the chain axis

FIG. 3 Carbon 1s edges of p-type doped polymers such as polypyrrole (PPY), polythiophene (PT) and polyaniline (PANI)

161

ENERGY-FILTERED IMAGING OF POLYMER MICROSTRUCTURE

K. Siangchaew,* J. Bentley,** and M. Libera*

* Dept. MS&E, Stevens Institute of Technology, Hoboken, NJ 07030

** Metals & Ceramics Division, Oak Ridge National Laboratory, P.O. Box 2008, Oak Ridge, TN 37831-6376

Energy-filtered electron-spectroscopic TEM imaging provides a new way to study the microstructure of polymers without heavy-element stains. Since spectroscopic imaging exploits the signal generated directly by the electron-specimen interaction, it can produce richer and higher resolution data than possible with most staining methods. There are basically two ways to collect filtered images (fig. 1). Spectrum imaging (1) uses a focused probe that is digitally rastered across a specimen with an entire energy-loss spectrum collected at each x-y pixel to produce a 3-D data set. Alternatively, filtering schemes such as the Zeiss Omega filter and the Gatan Imaging Filter (GIF) acquire individual 2-D images with electrons of a defined range of energy loss (δE) that typically is 5-20 eV.

This paper presents results using spectrum imaging and a Gatan imaging filter (GIF) to study a melt-mixed polyethylene (PE)/polystyrene (PS) homopolymer blend (fig. 2). Spectroscopic differences in these purely hydrocarbon polymers are due to bonding differences rather than to the presence/absence of core-loss excitations from other elements such as O or N. Fig. 3 shows low-loss energy-loss spectra for PE and PS. PS displays a characteristic ~7eV $\pi-\pi^*$ peak (2-4) absent in PE. Spectrum images were collected at Stevens using a Philips CM20 FEG TEM/STEM with a Schottky source. The digital raster and coupling to a Gatan 666 PEELS spectrometer used an EMiSCAN acquisition system. Fig. 4 shows a filtered image from a 137x65 pixel spectrum image (200msec pixel dwell). The background was removed using a polynomial fit to both pre- and post-edge data, and the image was formed with a 5eV window centered at 7eV. Post-acquisition processing routines are currently being implemented for thickness corrections and Kramers-Kronig analysis of the dielectric properties. An analogous experiment at ORNL using a Philips CM30 LaB$_6$ TEM with a GIF was unable to show significantly improved contrast when filtering about the 7eV peak. This may in part be due to higher radiation damage or to the low signal-to-background ratio. It is certainly affected by the proximity to the rapidly falling zero-loss peak which prevents good background subtraction. When filtering about the zero-loss peak, fig. 5 shows that there is improved contrast relative to an unfiltered image.

Spectrum imaging appears better suited to polymer problems involving subtle variations in bonding and structure where good energy resolution and significant post-processing is required. There is already good evidence in the literature that filtering methods based on the Omega filter or GIF are quite effective at mapping differences due to the presence/absence of different elemental species using core-loss excitations in both organic (5) and inorganic systems (6).

1. C. Jeanguillaume and C. Colliex, Ultramicroscopy **28** (1989) 252-257.
2. N. Swanson and C. Powell, J. Chem. Phys. **39** (1963) 630-633.
3. J.J. Ritsko and R.W. Bigelow, J. Chem. Phys. **69** (1978) 4162.
4. J.A. Hunt et al., Ultramicroscopy **58** (1995) 55-64.
5. H.J. Cantow et al., Proc. 47th Ann. Mtg. EMSA (San Francisco Press, San Francisco, 1989) 348.

6. J.Bentley et al., Electron Microscopy and Analysis 1995 (Proc. EMAG 95), ed. D. Cherns, Institute of Physics Conference Ser. No. 147 (IOP Publishing, Bristol, 1995) 187-190.
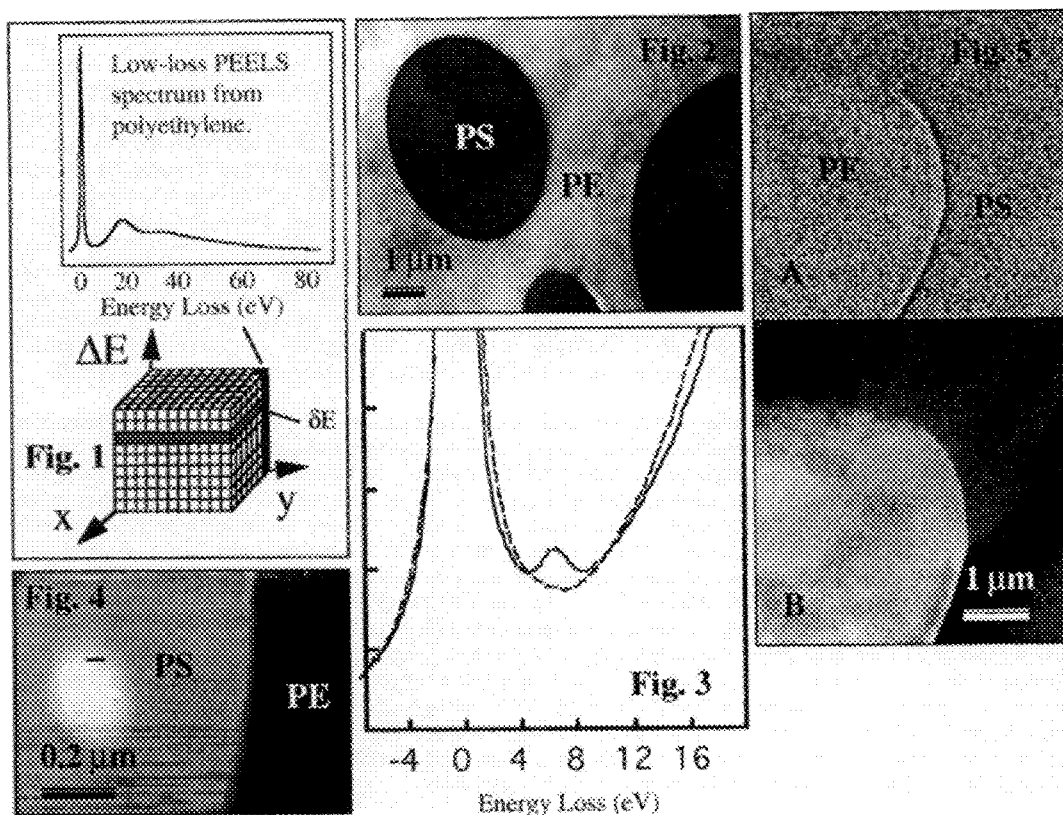
Fig. 1. Spectrum image records a 3-D data set of ΔE, x, and y by sequential acquisition of entire spectra. Energy-filtered imaging records a 2-D section from a 3-D data set about some energy window δE.

Fig. 2. RuO_4 stained PS/PE homopolymer blend.

Fig. 3. A magnified view of the energy-loss spectrum between the zero- and the plasmon loss region of PS (solid line) and PE (dash line).

Fig. 4. Energy-filtered spectrum image of a PS/PE blend using a 5 eV window (4 to 9 eV). An analytical background fit was performed in order to isolate the 7 eV $\pi-\pi^*$ peak.

Fig. 5. (A) Bright-field image of PE/PS. (B) Zero-loss filtered image of (A). Energy filtering was done with a GIF using a 10 eV energy window cetered at 0 eV energy loss.

163

ENERGY-FILTERED IMAGING OF CONSTITUENT PHASES IN POLYMER BLENDS

E. L. Hall and G. A. Hutchins

GE Corporate Research & Development, PO Box 8, Schenectady, NY 12301

Many engineering plastics consist of complex blends of chemically-distinct constituent polymers and other additives. These components are added in order to achieve desired performance in a variety of properties, including mechanical behavior, processability, color, fire retardency, and others. The distribution of the components, as well as the nature of the interfaces between constituents, are critically important to the performance of the engineering plastic. For many years, TEM has been the key tool in determining phase distribution. However, TEM studies are often limited by the need to stain the various constituents in order to achieve contrast, and also by the inability of TEM methods to unambiguously identify the chemical nature of the various constituents in the image. In the recent past, both electron energy loss spectroscopy (EELS) in the TEM[1] and x-ray absorption near-edge spectroscopy (XANES) using synchrotron sources[2] have demonstrated the ability to differentiate constituents based on characteristic carbon core loss edge structure. The EELS technique has the benefit of high spatial resolution, while the XANES method causes much less structural damage and mass loss. The advent of imaging energy filters has led to a third method for phase delineation for chemically distinct components, which combines the spatial resolution of EELS with the imaging capabilities of XANES.

Two model polymer blends were prepared for study in this investigation. The first of these consists of a blend of polycarbonate (PC), polymethylmethacrylate (PMMA), styrene-acrylonitrile (SAN), and carbon black. The second was a polypropylene oxide (PPO) - nylon - carbon black blend. The nominal elemental composition of each of these components is given in Table 1 in atomic percent. Samples were prepared for microscopy by conventional ultramicrotomy, yielding section thicknesses between 60 and 100 nm. In some cases RuO_4-stained sections were examined in a conventional TEM in order to ascertain general phase distribution, but only unstained sections were used for energy-filtered imaging. Elemental mapping was performed at 120kV (Fig. 1) and 200 kV (Fig. 2) with a Gatan Imaging Filter (GIF™) attached to a Philips AEM. Images were recorded with exposure times of up to 15 s and with 30eV windows before and after ionization edges of interest. Zero- and low-loss images were also recorded with 5, 30, and 60eV windows to aid in data interpretation and quantification. Core-loss and jump-ratio elemental maps were produced either by AE^{-r} background extrapolation from two pre-edge windows, or by simple division of the post-edge image by a pre-edge one, respectively. The samples were examined at room temperature with no special precautions to control electron dose, and therefore structural damage/mass loss during the experiments is very likely.

Figs. 1a,b,c show the zero loss (ZL), nitrogen, and oxygen maps for the PC/PMMA/SAN/C blend, respectively. Jump ratio maps were used to improve image contrast. The N map clearly delineates the SAN regions (bright), while the O map shows the PC/PMMA domains (bright). Contrast from the carbon black particles within the PC can also be seen. Figs. 2a,b,c show the same series of images (ZL, N, O) for the PPO/nylon/C blend. In this case the nitrogen map shows the nylon regions (bright), including some small entrapped nylon domains within the PPO particles. The carbon black is seen in the oxygen map as areas of dark contrast within the brighter PPO regions. In this case, the nominal O content of the nylon is similar to the PPO, leading to the possibility that preferential oxygen loss in the nylon due to electron irradiation has caused darker contrast of this phase in the oxygen image. The ZL image in Fig. 2a shows some non-uniformity in section thickness, and this can actually be quantified using a t/λ map (thickness/mean free path) produced using ZL and "total" intensity images.[3] The result shows a variation in t/λ from 0.4 in thin areas to 0.5 in thick. The t/λ map can also be used to convert the elemental maps in Figs. 1 and 2, where pixel intensity is a function of total number of atoms, to a true quantitative map where pixel intensity is a function of concentration.[3]

These preliminary results show that the energy-filtered imaging can be an important tool for phase

distribution assessment in complex polymer blends. Further work is in progress on extracting quantitative data from the images and on determining the nature of the interphase interfaces.

1. J. H. Blackson, D. W. Susnitsky, and D. R. Beaman, Proc. 52cd Ann MSA Meeting, (1994)946.
2. H. A. Ade et al., Science 258 (1992) 972.
3. J. Bentley, E. L. Hall, and E. A. Kenik, Proc. Microscopy and Microanalysis 1995 (1995)268.
4. The authors would like to acknowledge the assistance of Drs. S. Gubbins and C. Trevor of Gatan, Inc., Pleasanton, CA in obtaining the images in Figs. 1 and 2.

Table 1.   Elemental Composition of Polymers, at. pct. (ignoring H).

Element	PC	PMMA	SAN	PPO	Nylon
% C	84	71	96	89	70
% N	-	-	4	-	12.5
% O	16	29	-	11	12.5
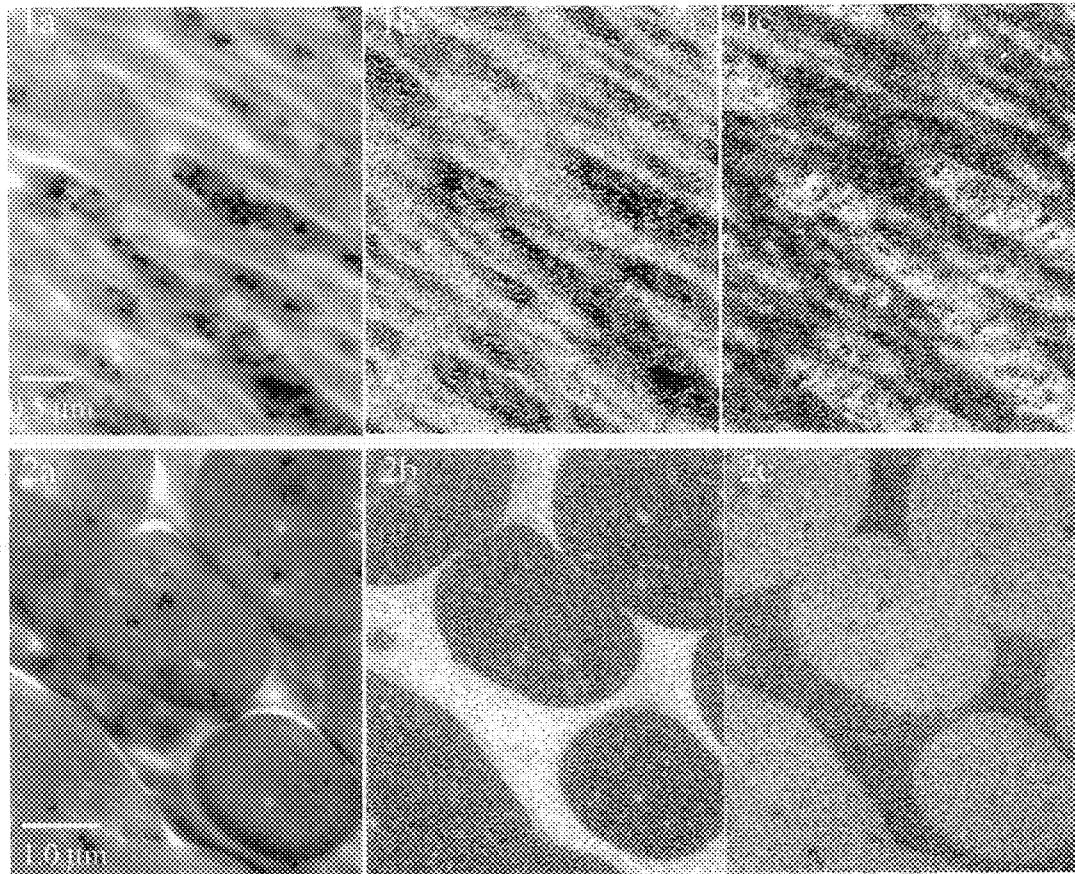
FIG. 1 - (a) Zero-loss image, (b) N jump ratio map, (c) O jump-ration map of PC/PMMA/SAN/C black blend.
FIG. 2 - (a) Zero-loss image, (b) N jump ratio map, (c) O jump-ration map of PPO/nylon/C black blend.

QUANTITATIVE HIGH-RESOLUTION ELECTRON MICROSCOPY (HREM) OF DEFECTS IN ORDERED POLYMERS

Patricia M. Wilson* and David C. Martin**

*Foster-Miller, Inc., Waltham, MA 02154-1196
**The University of Michigan, Ann Arbor, MI 48109-2136

Efforts in our laboratory[1] and elsewhere[2,3] have established the utility of low dose high resolution electron microscopy (HREM) for imaging the microstructure of crystalline and liquid crystalline polymers. In a number of polymer systems, direct imaging of the lattice spacings by HREM has provided information about the size, shape, and relative orientation of ordered domains in these materials. However, because of the extent of disorder typical in many polymer microstructures, and because of the sensitivity of most polymer materials to electron beam damage, there have been few studies where the contrast observed in HREM images has been analyzed in a quantitative fashion.

Here, we discuss two instances where quantitative information about HREM images has been used to provide new insight about the organization of crystalline polymers in the solid-state. In the first, we study the distortion of the polymer lattice planes near the core of an edge dislocation and compare these results to theories of dislocations in anisotropic and liquid crystalline solids. In the second, we investigate the variations in HREM contrast near the edge of wedge-shaped samples. The polymer used in this study was the diacetylene DCHD, which is stable to electron beam damage (Jc = 20 C/cm^2) and highly crystalline. The instrument used in this work was a JEOL 4000 EX HRTEM with a beam blanking device. More recently, the 4000 EX has been installed with instrumentation for dynamically recording scattered electron beam currents.

Studies of the distortion near dislocation cores in DCHD reveal both the nature and extent of disorder introduced by these defects on the crystalline polymer lattice. For dislocations perpendicular to the chain axis, the amount of distortion is highest in directions parallel to the Burger's vector of the dislocation. Measurements of the tilt induced in the crystal lattice as a function of azimuthal angle around the defect are compared with predictions of the distortion from elasticity theory, and provide information about the nature and extent of mechanical anisotropy.[4]

HREM images of wedge-shaped samples make it possible to evaluate the influence of thickness on the contrast observed. From information about the orientation of the crystal on the substrate, and estimates of the height variation obtained by atomic force microscopy. The variations in contrast anticipated for this crystal can be obtained from Pendellosung plots of the intensity of the (000) and (010) beams as a function of thickness predicted using the Multislice technique. Characteristic images are predicted to occur in certain orientations including half-spacings, extinctions, contrast reversals, and high contrast. These simulations provide the motivation to "tune" the operating voltage of an instrument in order to maximize this effect for a given sample orientation. Quantitative measurements of HREM image contrast are obtained by digital image analysis and compared with theory.[5]

References:
1. D. C. Martin and E. L. Thomas, *Polymer*, 36 (1995) 1743.
2. I. G. Voight-Martin, *Bull. Micros. Soc. America*, 24 (1994) 527.
3. M. Tsuji and S. Kohjiya, *Prog. Polymer Sci.*, 20 (1995) 259.
4. P. M. Wilson and D. C. Martin, *Macromolecules*
5. Wilson and Martin, *Ultramicroscopy*, in press.
6. Thanks are due to John Mansfield and Hal Estry of the University of Michigan Electron Microbeam Analysis Laboratory. Technical assistance was also provided by Jun Liao, Yu Shen, and Lebzy Gonzalez. Financial support was provided by the National Science Foundation and the Dow Chemical company.
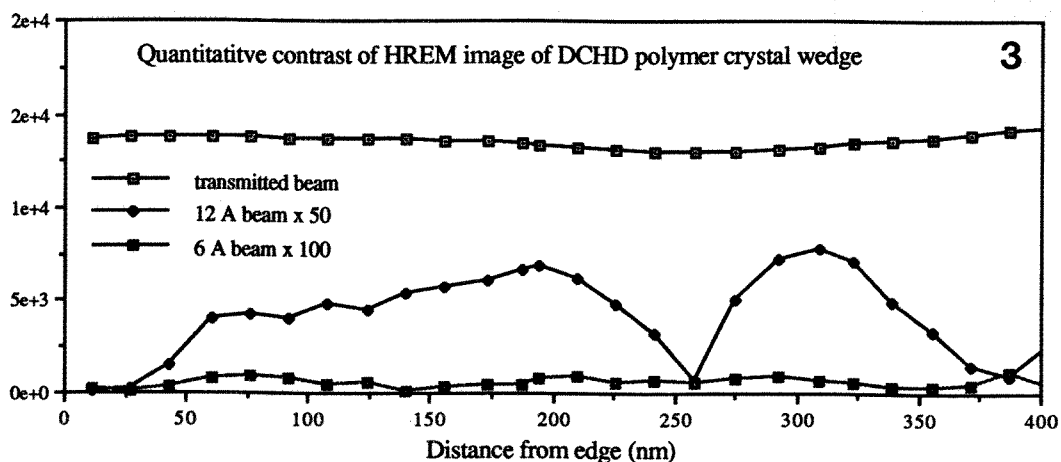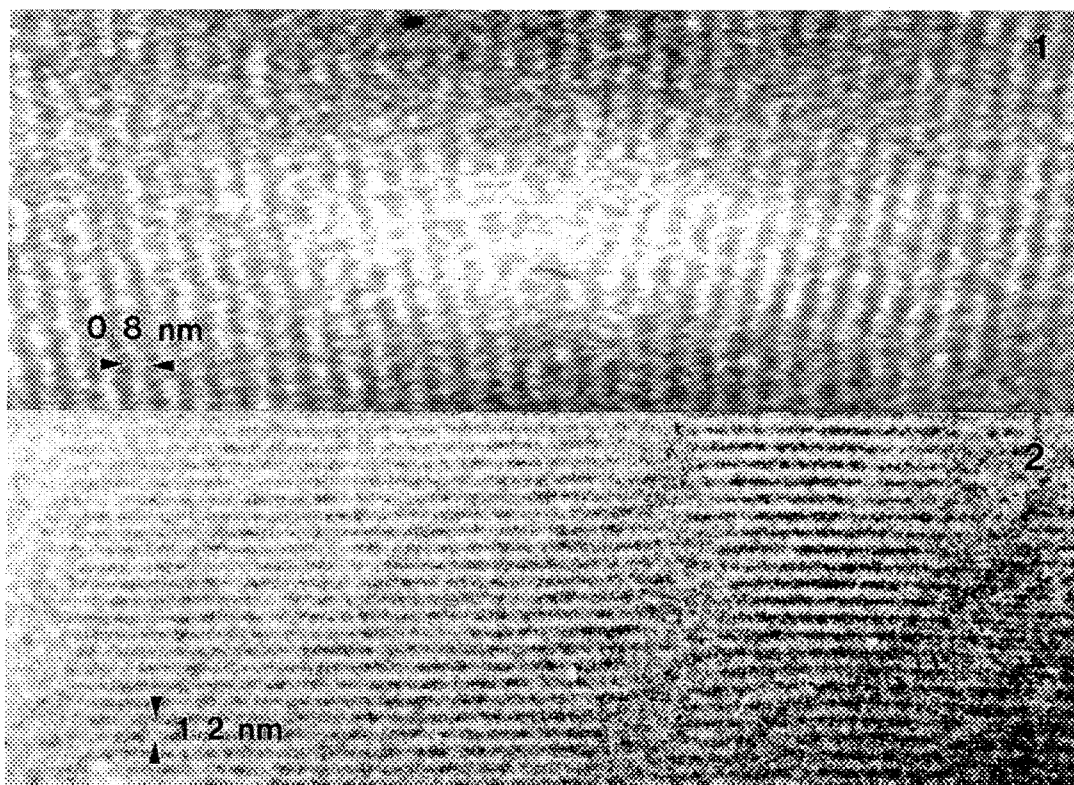
FIG. 1 Edge dislocation in DCHD 0.8 nm (200) lattice image (b=3a/2 [100] = 2.4 nm). Image compressed by 50% digitally along the y-axis.
FIG. 2 HREM image of DCHD polymer crystal wedge with (010) 1.2 nm fringes. Edge of crystal at left.
FIG. 3 Quantitative contrast measurements of FIG 2. as a function of distance from crystal edge.

167

MEAN INNER POTENTIAL MEASUREMENTS OF POLYMER LATEXES BY TRANSMISSION ELECTRON HOLOGRAPHY

Young-Chung Wang and Matthew Libera
Department of Materials Science and Engineering,
Stevens Institute of Technology, Hoboken, NJ 07030

Because polymeric materials consist primarily of light elements, weak contrast is often observed when imaging polymer microstructure in a transmission electron microscope. Preferential staining of microstructural features by heavy elements such as osmium, ruthenium, or uranium is commonly used to induce amplitude contrast. Because of its ability to recover the entire exit-face electron wavefunction, transmission electron holography raises the possibility of using phase contrast to measure polymer microstructure without the need for heavy-element stains.(1) Under kinematic scattering conditions, the phase shift, $\Delta\phi$, imposed on an incident high-energy electron wave is given by the product of the electron-optical refractive index, n_{eo}, and the specimen thickness, t: $\Delta\phi = (2\pi/\lambda)(n_{eo}-1)t$. The refractive index is related to the specimen's mean coulombic (inner) potential Φ_o: $n_{eo}-1 = (e \mid \Phi_0 \mid /E) [(E_0+E)/(2E_0+E)] = C_E\Phi_o$ where e is the electron charge, E is the kinetic energy of the incident electrons, E_0 is the rest energy, and C_E is an energy-dependent constant.(2) Quantitative measurements of Φ_o and n_{eo} can be made using holographic phase imaging to determine $\Delta\phi$ from specimens of known thickness.(3)

This research has measured the mean coulombic potential of polystyrene (PS) using ~30nm diameter spherical latex specimens. The spherical geometry enables the specimen thickness to be determined from two dimensional x-y coordinates. Digital holograms were collected at Oak Ridge National Laboratory (4) using a Gatan slow-scan ccd camera system mounted on a Hitachi HF-2000 FEG TEM. Specimens were prepared by dropping an aqueous emulsion of polystyrene latex particles on a holey carbon film.(5) Surfactant was removed by a warm water rinse. Holograms were collected from particles protruding over holes to avoid a contribution to the phase shift from the amorphous carbon as well as allow for a vacuum reference wave. A typical hologram is shown in figure 1. The fringe contrast is 0.14. This and other holograms were reconstructed using the HoloWorks package (6) within Gatan's Digital Micrograph software. The phase image reconstructed from figure 1 is shown in figure 2. In order to determine the specimen thickness as a function of position, the center and radius of the projected latex particle must be known. Since the entire particle is not contained within the holographic field of view, the center and radius were estimated using a least squares fit of a circle to the set of image pixels defining the edge of the particle. The edge was determined by thresholding the image intensity. The mean coulombic potential can then be extracted from a plot of phase shift against thickness. This procedure of determining Φ_o has been tested using simulated holograms. In these tests, the calculated value of Φ_o agreed with that assumed in the simulation to within 0.1%. Figure 3 shows a ten-pixel average of the phase shift versus position from the indicated box in figure 2. The plot of $\Delta\phi$ against thickness derived from the data of figure 3 is shown as figure 4. A straight line was fit to these data with the constraint that $\Delta\phi(t=0) = 0$. The slope of this line indicates that $\Phi_o=7.4$V. This is a typical value found in a number of similar measurements which average to about 8 V. Deviations from this average are attributed to variations in: (i) fringe contrast and (ii) definition of the particle edge in its 2-D projection. The experimental results are consistently higher than values of Φ_o calculated using neutral-atom atomic-scattering factors which range from 6.3-7.2 V depending on the assumed PS density.

1. M. Libera et al., *Electron Holography*, ed. by A. Tonomura et al. (North Holland, 1995) 231.
2. J. Spence, *Acta Cryst.* **A49** (1993) 231.

3. M. Gajdardziska-Josifovska, M. McCartney et al., *Ultramicroscopy* **50** (1993) 285.
4. We are grateful to Drs. L. Allard, D. Joy, E. Voelkl and B. Frost for their help at ORNL.
5. The latex was generously provided by the Emulsion Polymerization Institute at Lehigh University.
6. E. Voelkl, L. F. Allard, A. Datye, B. Frost, *Ultramicroscopy* **58** (1995) 97.
7. This research is supported by the Army Research Office under grant (DAAH04-93-G-0239) and the High Temperature Materials Laboratory User Program, DOE Office of Transportation Technologies, under contract DE-AC05-96OR22464 with Lockheed Martin Energy Research Corp.
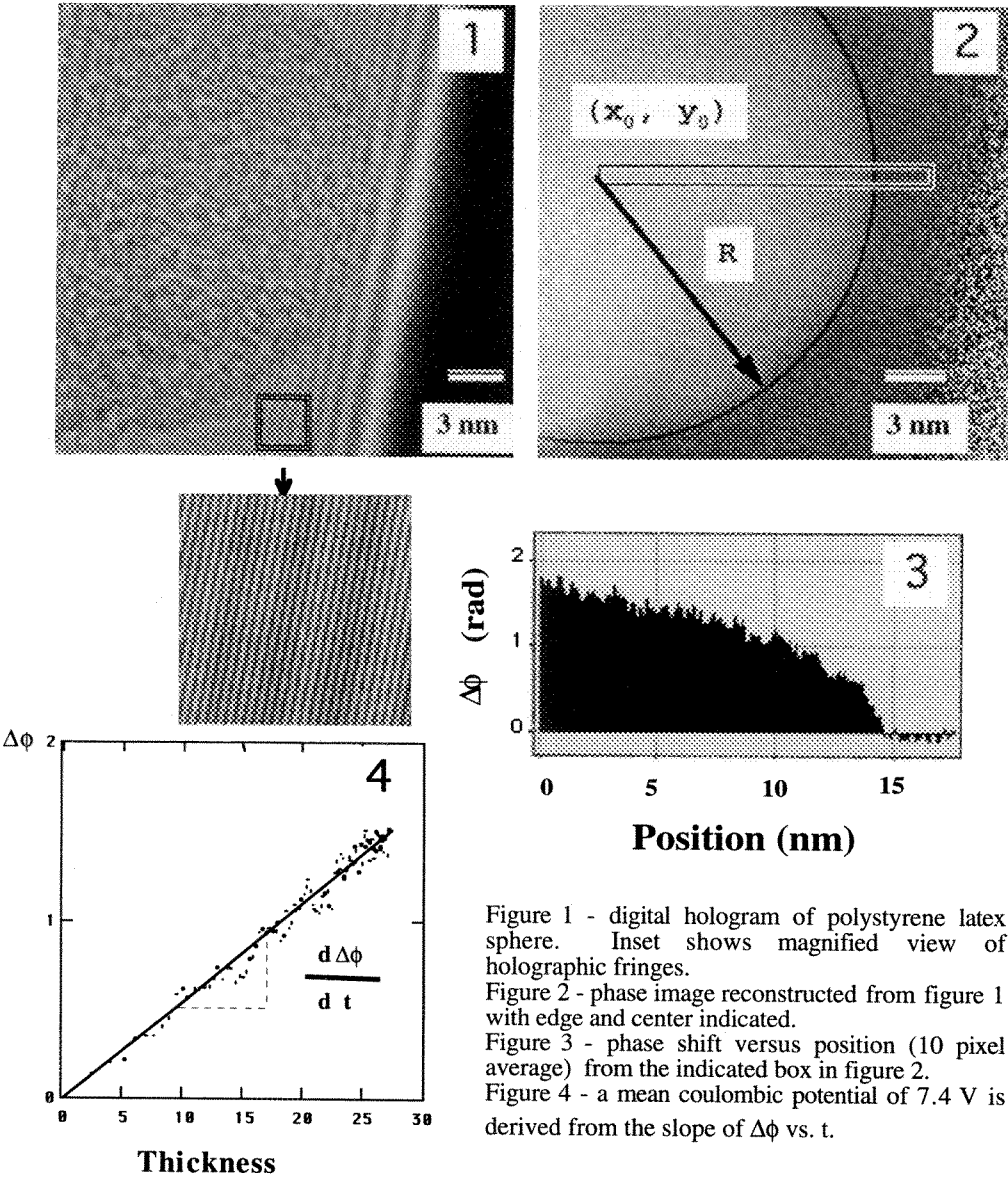
Figure 1 - digital hologram of polystyrene latex sphere. Inset shows magnified view of holographic fringes.

Figure 2 - phase image reconstructed from figure 1 with edge and center indicated.

Figure 3 - phase shift versus position (10 pixel average) from the indicated box in figure 2.

Figure 4 - a mean coulombic potential of 7.4 V is derived from the slope of $\Delta\phi$ vs. t.

169

Digital Imaging and Quantitative Image Analysis of Polymer Blends

Xiao Zhang

Technology Department, GE Plastics, Selkirk, NY 12158

Polymer microscopy involves multiple imaging techniques. Speed, simplicity, and productivity are key factors in running an industrial polymer microscopy lab. In polymer science, the morphology of a multi-phase blend is often the link between process and properties. The extent to which the researcher can quantify the morphology determines the strength of the link. To aid the polymer microscopist in these tasks, digital imaging systems are becoming more prevalent. Advances in computers, digital imaging hardware and software, and network technologies have made it possible to implement digital imaging systems in industrial microscopy labs.[1]

A digital imaging system often involves in four major operations: image acquisition, image storage, image processing and analysis, and data manipulation and presentation. Fig. 1 shows a schematic view of a globally networked digital imaging system that has been established in GE Plastics.[1] It consists of a local area network (LAN) which is connected globally with other site microscopy labs and customers via a wide area network (WAN). Most recently, an intranet Web page connection was also established, which provides even more flexibility to share wide-range information within corporate-wide microscopy labs and customers.[2]

The selection of an image acquisition device is dictated by the mode of imaging. TEM images are acquired by a Gatan CCD camera or directly captured with the scan generator in the STEM mode. Images capturing in SEM are done directly through the scan generator. LM images are collected using an Optronics CCD color camera.

Combinations of computer hard disk, optical disk, Zip disk, writable CD-ROM's, and VAX server are used as on-line/off-line storage media. The Window-based SEMICAPS software allows easy operation in both image acquisition and image archiving/retrieving. Pentium-based workstations are used for image processing and image analysis.

Image-Pro software is used for image processing and analysis.[3] Since no photographic film is used in the microscopy labs, the quality of the initial digital image plays a key role in the final success of image analysis. Care should be given in evaluating imaging criteria such as image resolution, capture speed, and the measurement resolution required. The most difficult and crucial step of image analysis is image processing/segmentation.[4] Since contrast in polymer blend morphologies is largely derived from chemical staining, and/or chemical, plasma or ion etching, low or varying feature contrast and varying background intensity are common problems that a polymer microscopist has to deal with. Feature measurement is the second step of the image analysis. Depending on the blend morphology, single or multiple parameters are needed for describing a feature in the morphology. Regular measurement includes particle size, size distribution, phase volume fraction, and particle spatial distribution.

Data manipulation and presentation are conducted using Origin software. Care should be applied for data statistical consistency. Although automation of image analysis is possible in a few cases, it is not

recommend in the image analysis of polymer blends due to the complexity of the image contrast formation.

The main advantages of such a digital imaging system in industrial polymer microscopy labs are (1) drastically reduced turnaround time by streamlining the operations; (2) reduced cost; (3) globally shared microscopy information; and (4) provided quantitative information of structure/property relationships. Overall, the system greatly improves microscopy lab capabilities in support of product development, manufacturing optimization, and customer satisfaction.

References

1. V. Berry and X. Zhang, *Proc. 52nd MSA Ann. Meeting*, (1994)454
2. X. Zhang, *in these proceedings*.
3. X. Zhang, *Proc. 51st MSA Ann. Meeting*, (1994)920
4. B.D. Newell, Proc. Microscopy and Microanalysis'95, (1995)678
5. The author is grateful to V. Berry and J. Scobbo for valuable discussion and to D. Clancy and O. Riccobono for excellent technical assistance.
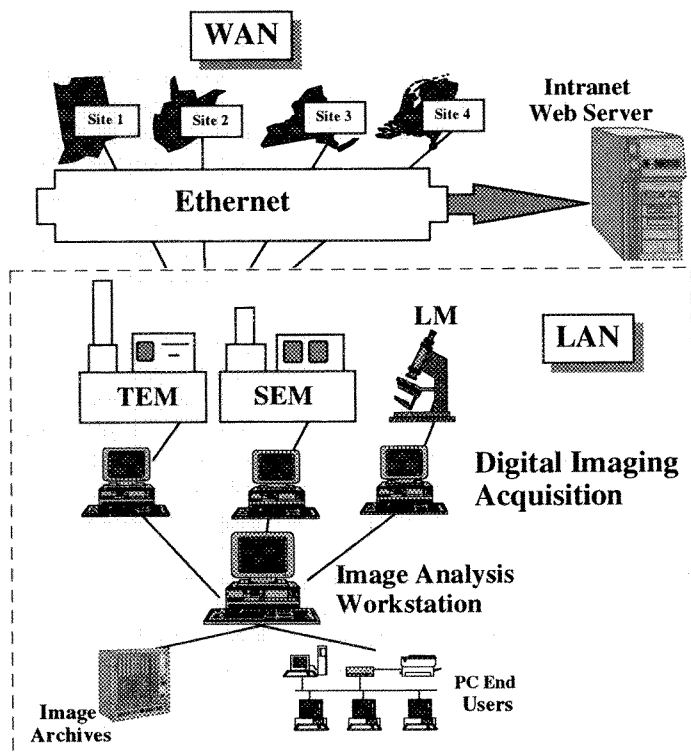
Fig. 1 Schematic view of a globally networked digital imaging system

CRYSTAL STRUCTURE AND MORPHOLOGY OF SYNDIOTACTIC POLYPROPYLENE SINGLE CRYSTALS

Jenny Z. Bu,* Stephen Z. D. Cheng**

*Technology Center, GE Plastics, Washington, WV 26181
**Department of Polymer Science, University of Akron, Akron, OH 44325

In the past several years there have been an increased interest in the crystal structure and morphology of s-PP due to the new development of homogeneous metallocene catalysts which can produce s-PP having a high stereoregularity. In this research, the crystal structure and morphology of s-PP single crystals grown from the melt were investigated. A series of ten fractions of s-PP was studied with different molecular weights ranging from 10,300 to 234,000 (g/mol). These fractions all possess narrow molecular weight distributions (around 1.1-1.2) and high syndiotacticities ([r]~95%).The main techniques employed including transmission electron microscopy (TEM), atomic force microscopy (AFM), wide-angle X-ray diffraction (WAXD), and small-angle X-ray scattering (SAXS).

Three alternative crystal structures have been proposed for s-PP in its high temperature orthorhombic form. In this study, we demonstrated through ED experiments that in our s-PP single crystals grown at high temperatures, the crystal structure is in agreement with the unit cell III: a= 1.450 nm, b= 1.120 nm (doubled b-axis), c= 0.740 nm and the space group is *Ibca*. Fully antichiral packing along both the a- and b-axes in the unit cell is formed. Such fully regular antichiral packing is obtained only at the highest crystallization temperatures (i.e., ≥130°C). Progressive incorporation of the isochiral packing defects causes the streaks along the (h10) plane in the ED pattern as the crystallization temperature was decreased. This gradual change of the crystal from an almost pure cell III to a mixture of cell I, II, and III is a kinetically controlled process, which is associated with the fast crystallization rate at lower T_cs and the slow crystal growth at high T_cs.

It has been found that the crystal morphology of s-PP is strongly supercooling dependent. At high crystallization temperatures (low supercooling), highly regular, faceted, and lath-shaped single crystals were observed. The long axis of the single lamellar crystal is the crystallographic b-axis. Decreasing the crystallization temperature leads to an axialitic morphology and eventually to spherulites. The crystal growth direction is always along the b-axis and no change of the crystal growth front plane is found. On the other hand, the molecular weight also affects the s-PP crystal morphology. Single crystals are more difficult to grow from the high molecular weight fractions.

Sectorization has also been clearly observed in single crystals grown at high temperatures (≥130°C). Sector lines are along the diagonal directions of the lath-shaped single lamellar crystals. More importantly, two neighboring sectors show a significant lamellar thickness difference, measured through both TEM and AFM. The sectored single crystal has the same crystal unit cell as the non-sectored single crystals based on the ED results. Polymer decoration and single crystal deformation techniques have been applied to investigate the chain folding in s-PP single crystals. For non-sectored single crystals, polymer decoration does not provide conclusive evidence since the orientation of the PE rod crystals is rather random. However for sectored single crystals, certain orientation of

the PE rods has been found along the long axis (*b*-axis) indicating that the chain folding direction is along the *b*-axis in the two thicker sectors. In single crystal deformation experiments on the non-sectored single crystals grown from high molecular weight fraction, microfibrillar structure has been observed along both the *a*- and *b*-axes after deformation along these two axes. This indicates that the chain folding direction in non-sectored single crystals may be along the (110) planes. The zigzag edge morphology along the *a*-axis of the single crystal after deformation is also supportive evidence for this chain folding mechanism.

Microcracks in the lamellar crystals have been found always perpendicular to the long axis of the crystal, when the crystal was quenched to room temperature after isothermal crystallization. This is due to the fact that the coefficient of thermal expansion along the unit cell *b*-axis is almost one order of magnitude higher than that along the a-axis, which has been measured by WAXD experiments.

References

1. B. Lotz, A. J. Lovinger, *et al.* , *Macromolecules* 1988, 21, 2375
2. A. J. Lovinger, B. Lotz, *et al.*, *Macromolecules* 1993, 26, 3494
3. J. Rodriguez-Arnold, Z. Z. Bu, S. Z. D. Cheng, *et al.*, *Polymer* 1994, 35, 24, 5194
4. J. Rodriguez-Arnold, Z. Z. Bu, S. Z. D. Cheng, *et al.*, Rev. *Macromol. Chem. Phys.* 1995, C35 (1), 117

EXTRACTION AND IDENTIFICATION OF FILLERS AND PIGMENTS FROM PYROLYZED RUBBER AND TIRE SAMPLES

P. Sadhukhan and J. B. Zimmerman

Bridgestone/Firestone Inc., Akron, Ohio 44317-0001

Rubber stocks, specially tires, are composed of natural rubber and synthetic polymers and also of several compounding ingredients, such as carbon black, silica, zinc oxide etc.[1] These are generally mixed and vulcanized with additional curing agents, mainly organic in nature, to achieve certain "designing properties" including wear, traction, rolling resistance and handling of tires.[2] Considerable importance is, therefore, attached both by the manufacturers and their competitors to be able to extract, identify and characterize various types of fillers and pigments. Several analytical procedures have been in use to extract, preferentially, these fillers and pigments and subsequently identify and characterize them under a transmission electron microscope.

Rubber stocks and tire sections are subjected to heat under nitrogen atmosphere to 550° C for one hour and then cooled under nitrogen to remove polymers, leaving behind carbon black, silica and zinc oxide and 650°C to eliminate carbon blacks, leaving only silica and zinc oxide. First pyrolyzed sample was then placed in platinum crucible which was then filled about 2/3 full with HF to remove silica, leaving only this time, carbon black and zinc oxide. Sample was heated until just dry. Pyrolyzed sample was also digested in 6N HCl to remove zinc oxide, leaving only carbon black and silica, then rinsed with water and dried. Same procedures were followed in steps to extract only carbon black, zinc oxide and silica each separately.

The representative photomicrographs are shown in Figures 1-8 and individual fillers and pigments are marked by arrows. It has thus been possible, to extract, identify and characterize the respective compounding ingredients in rubber stocks and from tire sections.

References

1. M. Morton, Introduction to Rubber Technology, Reinhold Publishing Corporation, New York, 1959.

2. G. G. Winspear, ed., The Vanderbilt Rubber Handbook, R. T. Vanderbilt Company, New York, 1968.
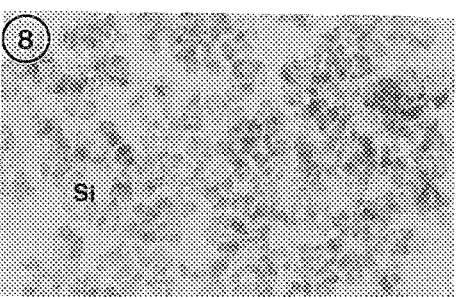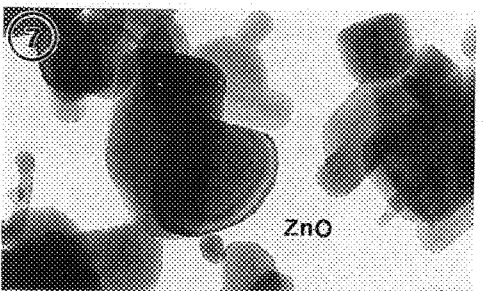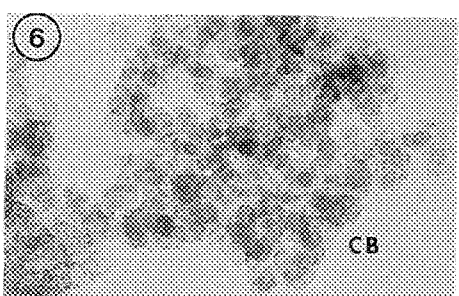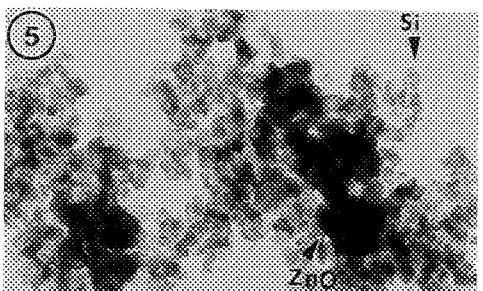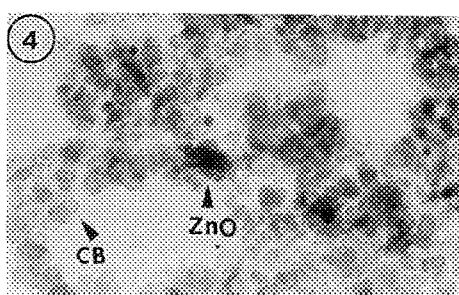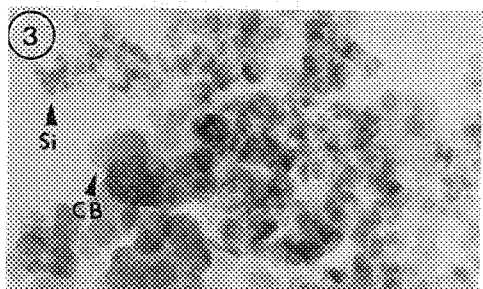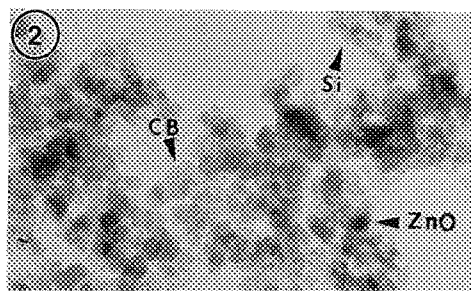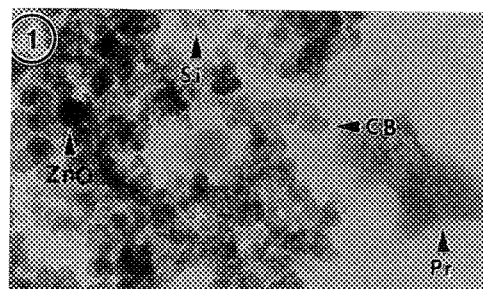
Fig. 1 : Pyrolyzed Tire Tread Part : Polymer remnant, Carbon Black, Silica, Zinc Oxide
Fig. 2 : Pyrolyzed Tread Part : Carbon Black, Silica, Zinc Oxide
Fig. 3 : Pyrolyzed + HCl Wash : Carbon Black, Silica
Fig. 4 : Pyrolyzed + HF Fume : Carbon Black, Zinc Oxide
Fig. 5 : Pyrolyzed (Ashed) : Silica, Zinc Oxide
Fig. 6 : Pyrolyzed + HF Fume + HCl Wash : Carbon Black
Fig. 7 : Pyrolyzed (Ashed) + HF Fume : Zinc Oxide
Fig. 8 : Pyrolyzed (Ashed) + HCl Wash : Silica

SEM ANALYSIS OF *IN SITU* POLYMERIZATION PRODUCTS FOR CHROMATOGRAPHIC SEPARATIONS

Bruce Cutler*, Joseph Algaier**, Frantisek Svec***

*Electron Microscopy Lab and Dept. of Entomology, University of Kansas, Lawrence, KS 66045
**Isco, Inc., 4700 Superior, Lincoln, NE 68504
***Department of Chemistry, Baker Laboratory, Cornell University, Ithaca, NY 14853

Two inherent problems associated with chromatographic separations are peak broadening and column efficiency. These are directly attributable to the interparticular porosity of the separation media in which limited utilization of column space results in column void volumes. In theory, a minimum of 26% void volume will occur if a column is packed using perfectly arranged monodispersed beads. Typically, with the best packed columns void volumes are 30 to 40%. Svec and Fréchet (1) have introduced an HPLC separation media with no discontinuity that are prepared in a single step by a free-radical polymerization within a column acting as a mold. The resulting rods consist of a continuous molded monolith of rigid, highly porous polymer. These columns proved to be very efficient and extremely fast for reverse-phase HPLC separation of proteins and for the separation of small and mid-size molecules (2). In this study, we continue to explore various reaction conditions with the resulting polymerization products examined by SEM, for internal morphology.

The continuous columns were prepared as previously reported (2) with 40:60 (v/v) mixture of monomers [glycidyl methacrylate (GMA) and ethylene dimethacrylate (EDMA) (60:40 v/v)] and porogenic diluents (cyclohexanol and dodecanol) with azobisisobutyronitrile as initiator. Two reaction parameters were varied; temperature and percentage of dodecanol. The resulting polymerization products were examined by SEM. Samples were prepared by fracturing in liquid nitrogen to provide a fresh surface, mounted on stubs and sputter coated with 10 nm of gold-platinum alloy. A variable accelerating voltage was used depending on the charging propensity of the individual sample.

The photomicrographs show the dramatic variation in particle sizes formed under different reaction conditions. In the presence of 85:15 (v/v) cyclohexanol:dodecanol (figures 2, 4, 6) the microglobule sizes appear to vary little with increasing reaction temperature. However, polymerization in the absence of dodecanol (figure 1, 3, 5) demonstrate that increased reaction temperature results in significantly smaller microglobular size, suggesting an increased formation of nucleation sites during the initial stages of polymerization. The microglobular sizes, which are presently being measured, will affect the chromatographic performance of the resulting column. Further work will evaluate peak shape and resolving power of columns formed under varying reaction conditions.

References

1.   F. Svec and J.M.J. Fréchet, Anal. Chem. 64 (1992)820.
2.   F. Svec and J.M.J. Fréchet, J. Chromatogr. A, 702 (1995)89.
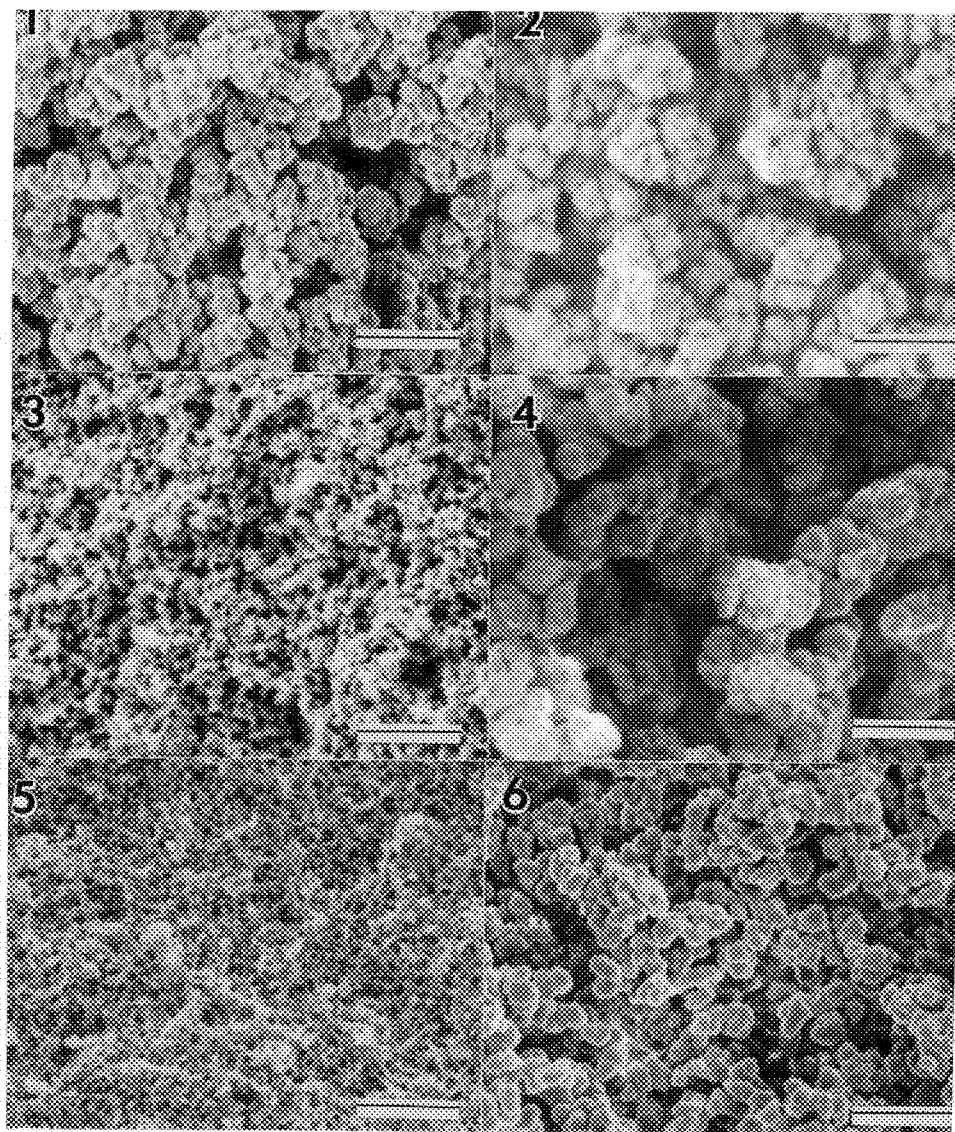
FIG. 1 55°C, 100% Cyclohexanol, 0% Dodecanol
FIG. 2 55°C, 85% Cyclohexanol, 15% Dodecanol
FIG. 3 70°C, 100% Cyclohexanol, 0% Dodecanol
FIG. 4 70°C, 85% Cyclohexanol, 15% Dodecanol
FIG. 5 80°C, 100% Cyclohexanol, 0% Dodecanol
FIG. 6 80°C, 85% Cyclohexanol, 15% Dodecanol

scale line = 5μm
for all figures

POSTMORTEM AND INSITU TEM METHODS TO STUDY THE MECHANISM OF FAILURE IN CONTROLLED-MORPHOLOGY HIGH-IMPACT POLYSTRENE RESIN

R. C. Cieslinski, M. T. Dineen, and J. L. Hahnfeld

The Dow Chemical Company, Midland, MI 48667

Advanced Styrenic resins are being developed throughout the industry to bridge the properties gap between traditional HIPS (High Impact Polystyrene) and ABS (Acrylonitrile-Butadiene-Styrene copolymers) resins. These new resins have an unprecedented balance of high gloss and high impact energies. Dow Chemical's contribution to this area is based on a unique combination of rubber morphologies including labyrinth, onion skin, and core-shell rubber particles. This new resin, referred as a controlled morphology resin (CMR), was investigated to determine the toughening mechanism of this unique rubber morphology. This poster will summarize the initial studies of these resins using the double-notch four-point bend test of Su and Yee (1), tensile stage electron microscopy (2,3), and Poisson Ratio analysis of the fracture mechanism.

An illustration of the double-notch four-point bend test is shown in Figure 1. After impact, the arrest crack was examined optically and by transmission electron microscopy. Figure 2 and 3 compare the deformation zones of the sub critical cracks of a CMR and conventional HIPS sample. Contrary to expectations, the deformation zone for the conventional HIPS appears larger then CMR HIPS. What cannot be determined from Figures 2 and 3 is the density of damage in the zones. By examining different areas of the deformation zones (Figures 4 and 5) in the TEM, the evolution of the failure process can be probe helping to understand the mechanism of rubber toughening. Using a TEM tensile stage (2) provided additional insight into the deformation process (Figure 6 and 7).

The microscopic methods presented in this poster suggest that the toughening mechanism of CMR HIPS is different from the accepted HIPS toughening mechanism in the literature (4). While the conventional HIPS resin relies on efficient damage initiation at low stress, the microscopic methods suggest CMR relies on the stabilization of damage and thereby permits extensive deformation before crack formation.

References

1. H.J. Sue, R.A. Pearson, D.S. Parker, J. Huang, and A.F. Yee, *Polymer Preprint* **29**, 147 (1988).
2. R.C. Cieslinski, *J. Mater. Sci. Lett.* **11**, 813, 1992.
3. R.C. Cieslinski, H.S. Silvis, and D.J. Murray, *Polymer* **36**, 1827 (1995).
4. C.B. Bucknall, "Toughen Plastics," Applied Science, Essex, England, 1977.
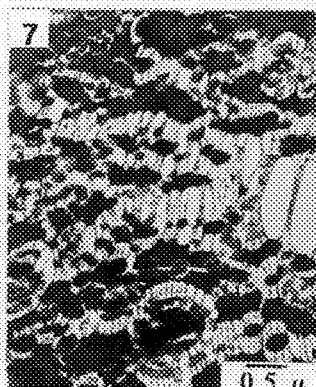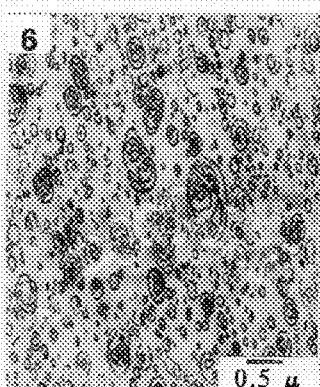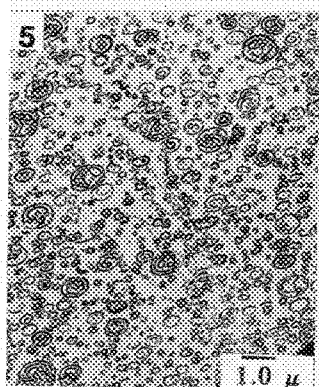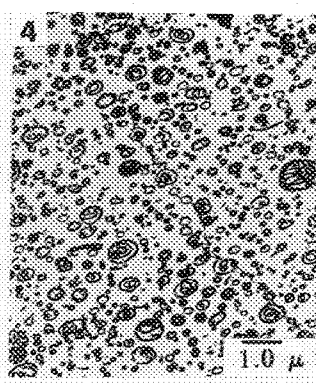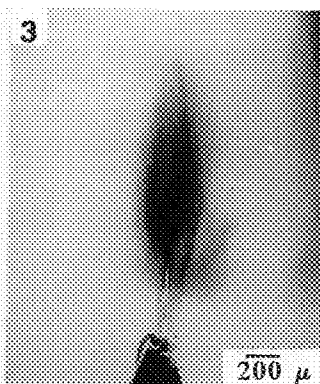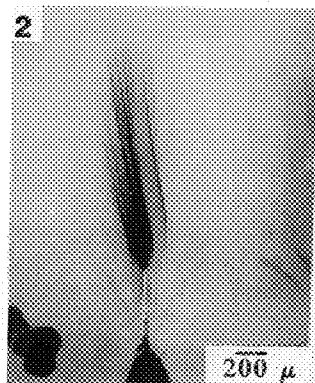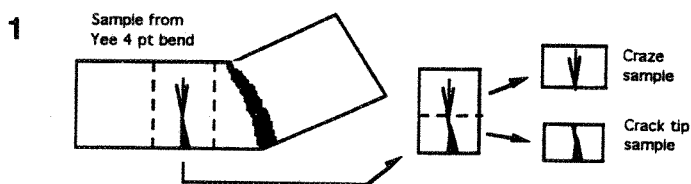
FIG. 1 Illustration of the double-notch 4 pt. bend deformation.
FIG. 2 Deformation zone following 4 pt. bend test in CMR HIPS.
FIG 3 Deformation zone following 4 pt. bend testin a conventional HIPS material.
FIG. 4 TEM micrograph of tip of damage zone in CMR HIPS.
FIG. 5 TEM migrograph of the damage midway betewwn crack tip and craze tip in CMR HIPS material.
FIG. 6 Early Tensile Stage damage in CMR HIPS.
FIG. 7 Late, High Strain Tensile Stage damage in CMR HIPS resin.

179

THE STUDY OF MULTIPHASE POLYMER-BLEND MORPHOLOGIES BY HVEM

T.J. Cavanaugh*, K. Buttle**, J.N. Turner**, and E.B. Nauman*

*The Isermann Department of Chemical Engineering, Rensselaer Polytechnic Institute, Troy, NY 12180-3590
**Wadsworth Center, New York State Department of Health, Albany, NY 12221

Multiphase polymer blends are important in the polymer industry. Most commercial blends consist of two main polymers combined with a third, compatibilizing polymer, typically a graft or block copolymer. The most common examples are those involving the impact modification of a brittle thermoplastic by the microdispersion of a rubber into the matrix. Recently, a model of ternary polymer blends has provided a wealth of morphologies for examination.[1] Even though this model can give an excellent basis for the design of a polymer blend, experimental verification is necessary. A correlation of blend properties such as impact strength with blend morphology must also be made. The focus is to confirm the predicted morphologies in binary and ternary blends using HVEM.

The polymer blends were produced by compositional quenching.[2] In this process, the polymers were dissolved in a solvent. The solution was pumped through a heat exchanger and then flashed across a needle valve to remove the solvent. The effluent polymer blend was then ground and dried in a vacuum oven. The blend was molded for various times in a compression molder. A sample of the blend was cut from the molded part and stained with 4wt% OsO_4 solution for 7 days. Sections, which were cut $0.75\mu m$ thick using a diamond knife, were placed on copper TEM grids and were imaged at 1.0MV using an AEI Mark IV HVEM.

In a blend of 23vol% polybutadiene (PB) in polystyrene (PS), the PB appears as spheres in the matrix (Figure 1). These spheres are large in size due to the fact that they were ripened in the mold at 200°C for 10 minutes. In a ternary blend of PS, PB, and PS-PB diblock, the spheres are much smaller, despite ripening in the mold for one hour (Figure 2). This occurs because the diblock hinders ripening. Another ternary blend that was examined includes PS, PB, and polypropylene (PP). In this case, the PB formed white rings around the dark spheres, which are PP (Figure 3). Using STERECON,[3] an image analysis program, quantitative analyses on variables such as particle size distribution and interparticle distance are currently being carried out.

High voltage electron microscopy along with STERECON will allow for a better understanding of the blend morphology and its relationship to blend properties.

References

1. E.B. Nauman and D.Q. He, *Polymer*, **35**(11), (1994), 2243.
2. E.B. Nauman et.al., *Chem. Eng. Comm.*, **66**, (1988), 29.
3. M. Marko and A. Zeith, in *Visualization in Biomedical Microscopes, 3-D Imaging and Computer Applications*, VCH, Weinheim, Germany, (1992), 45.
4. The figures were obtained from the equipment that is supported, in part, by Biotechnological Resource grant RR 01219, which supports the Wadsworth Center's Biological Microscopy and Image Reconstruction Facility as a National Resource.
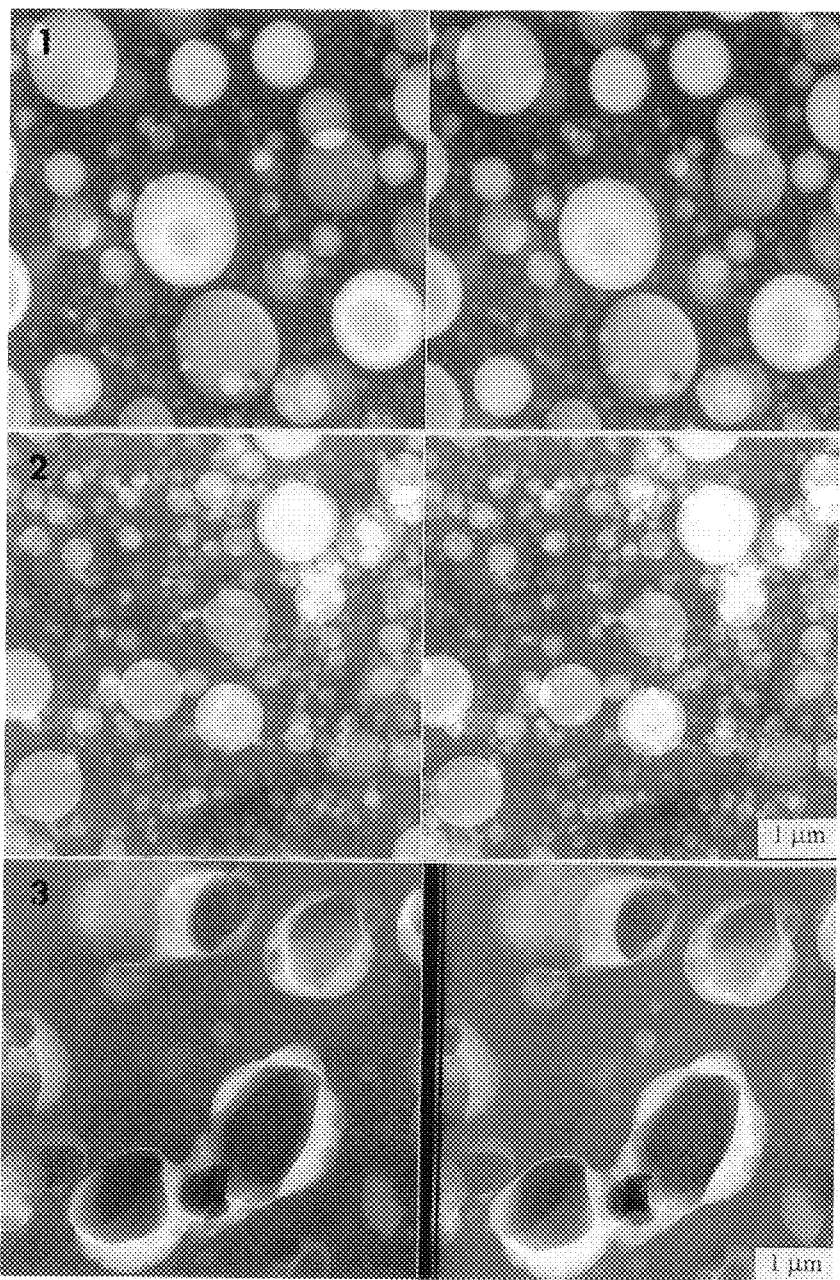
FIG. 1 Stereopair of a blend of polystyrene and polybutadiene taken at -4° and +4°
FIG. 2 Stereopair of a blend of PS, PB, and PS-PB diblock taken at -4° and +4°
FIG. 3 Stereopair of a blend of PS, PB, and Polypropylene taken at -4° and +4°

181

QUANTITATIVE EXAMINATION OF SEMICRYSTALLINE POLYMERS VIA ATOMIC-FORCE MICROSCOPY, TRANSMISSION ELECTRON MICROSCOPY, AND SMALL-ANGLE X-RAY SCATTERING

M. S. Bischel*, S. Balijepalli,** J. M. Schultz**

* Materials Science Program, University of Delaware, Newark, DE 19716
** Department of Chemical Engineering, University of Delaware, Newark, DE 19716

The Atomic Force Microscope (AFM) has been used to reliably measure lamellar thickness in semi-crystalline polymers, and to distinguish phases within blends of these polymers.

Traditionally, lamellar thicknesses of semi-crystalline polymers have been determined by (1) measuring structures directly from TEM micrographs or (2) using small angle X-ray scattering (SAXS) spectra. In the first case, the sample must either be etched and replicated, or stained with heavy metals or chlorosulfonic acid to reveal the lamellar structures. Good SAXS measurements require access to a synchrotron, or rotating anode diffractometer. In contrast, the AFM has been used to relaibly measure the lamellar structures in polymer specimens which have undergone minimal sample preparation.

The tapping mode of operation of a Digital Nanoprobe AFM has been used on the free surfaces of polyethylene oxide (PEO) specimens to determine lamellar thicknesses that are in excellent agreement with measurements obtained from both TEM and SAXS. Examples of such comparisons in the existing literature are few.[1,2,3,4]

The average lamellar thickness of PEO with a molecular weight of 270,000 was determined in three different ways: (1) SAXS spectra,‡ Fig. 1; (2) AFM, Fig. 2a; (3) TEM, Fig. 2b. The results from these complementary methods are given in Table 1.

By examining both unetched and etched samples of an 80/20 PEO blend of 5K and 270K molecular weight homopolymers, it was possible to distinguish phases within the structure: the etchant preferentially removes the low molecular weight component. The results, shown in Fig. 3, were confirmed by traditional melt studies performed in the optical microscope.

This method shows great promise for easily and quickly providing relaible measurements of lamellar thicknesses. Its use is currently being extended to other polymer blend systems to derive both lamellar measurements and phase information.

References:
1. N. H. Thomson, et al., *Ultramicroscopy*, **42-44**(1992) 1204.
2. M. E. Welland, et al., *Int. J. Biol. Macromolecule*, **11**(1989) 29.
3. K. D. Jandt, et al., *Polymer*, **35**(1994) 11.
4. B. K. Annis, et al., *J. Polymer Science: Part B*, **31**(1993) 93.

Table 1: Comparison of Average Lamellar Thicknesses for 270K PEO

Method	l_c, nm
SAXS‡	21 ± 1
AFM	21 ± 2
TEM	22 ± 2

‡ $l_c = x_c L$ where L is the long period derived from SAXS spectra, and x_c is the percent crystallinity.

$L = 2\pi/q = 31$ nm

y-axis: Iq^2

x-axis: q (nm^{-1})
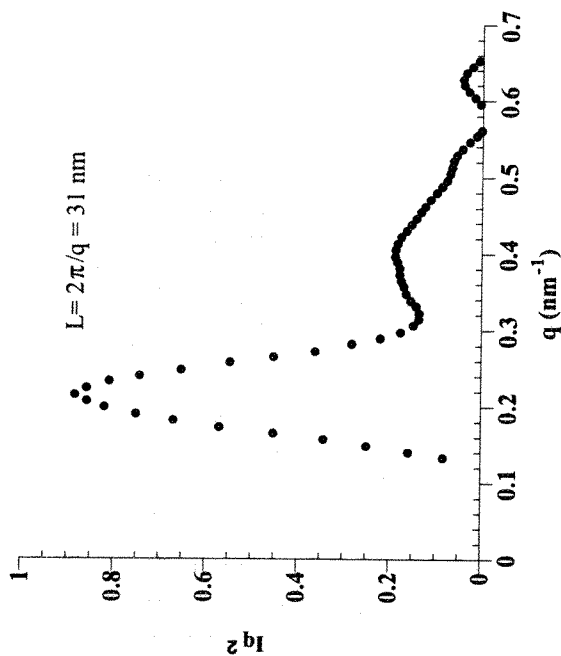
Figure 1: SAXS Spectra for 270K PEO, collected at Oak Ridge National Laboratory.

Figure 2a: AFM, 270K PEO free surface, tapping mode.
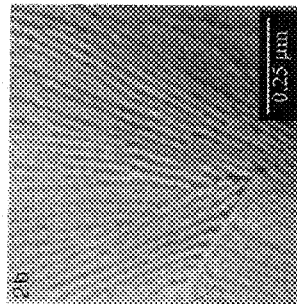
Figure 2b: TEM, 270K PEO free surface, 2 stage replica method.

Figure 3: AFM, etched 80/20 blend of 5K/270K MW PEO, tapping mode. Bundles are 270K polymer.

CHARACTERIZATION OF TRIBOLOGICAL SEALING SYSTEM COMPONENTS USING SCANNING ELECTRON MICROSCOPY (SEM) AND ENERGY-DISPERSIVE X-RAY SPECTROSCOPY (EDS)

Mark Shuster, Mick Deis
Dana Corporation, Advanced Technical Resource Group, Ottawa Lake MI 49267

A system approach to solving the tribological problems associated with sealing joints implies comprehensive investigation of all the components. To recognize the root cause of any problem and formulate the required performance for extended reliability we have to evaluate any changes in the system as quantitatively as possible. Any measurable parameters, including geometry, density (porosity), hardness distributions, microstructure and grain size changes observed during routine metallurgical analysis could provide evidence of the root cause of failure. In the head-gasket-block sealing system of the internal combustion engine, the EDS evaluation of the chlorine and sulfur distribution through the head gasket flange fracture in conjunction with analysis of the sludge between the head, block and gasket surfaces pointed to the corrosive nature of the gasket flange cracking *.

This approach is even more useful for the closed tribological system of telescopic hydraulic cylinders or rotary axle shaft oil seals. In these cases in addition to the routine metallurgical analysis of the metal shaft surface, we have to analyze the rubber or plastic sealing elements. The influence of oil contamination as a destructive mechanism must also be evaluated. Telescopic hydraulic seal damage could be a result of the wear of the seal lips. Figure 1 shows the typical texture of a failed polyurethane sealing element. The surface layer of polyurethane is stretched by shear forces probably the result of friction. Material displacements occurred from right to left and the channels produced are bridged by fibrils. When abrasive wear is the predominant influence on the seals we observe embedded particles of metal or sand in the working lips area (Fig. 2). EDS analysis provides proof of the abrasive nature of these particles. Analysis of contamination present in the hydraulic oil confirms the presence of abrasives in the cylinders.

The reliability of a rotary axle shaft sealing system depends on many factors. SEM and EDS analysis can determine the root cause of failure. Figure 3 shows an abrasive particle embedded in the seal lip. Excessive temperature can also lead to degradation of the rubber seal lip. In this case you can see the rough texture of the rubber (Fig. 4). Figure 5 shows the cross section of this lip. You can see the brittleness and cracking due to degradation from the heat.

Thus scanning electron microscopy and energy dispersive spectroscopy favor determining the root-cause of the problem for each tribological sealing system.

----

*M. Shuster and H. Willis Corrosion Fatigue Influence on Gasket Flange Cracking. SAE 932352
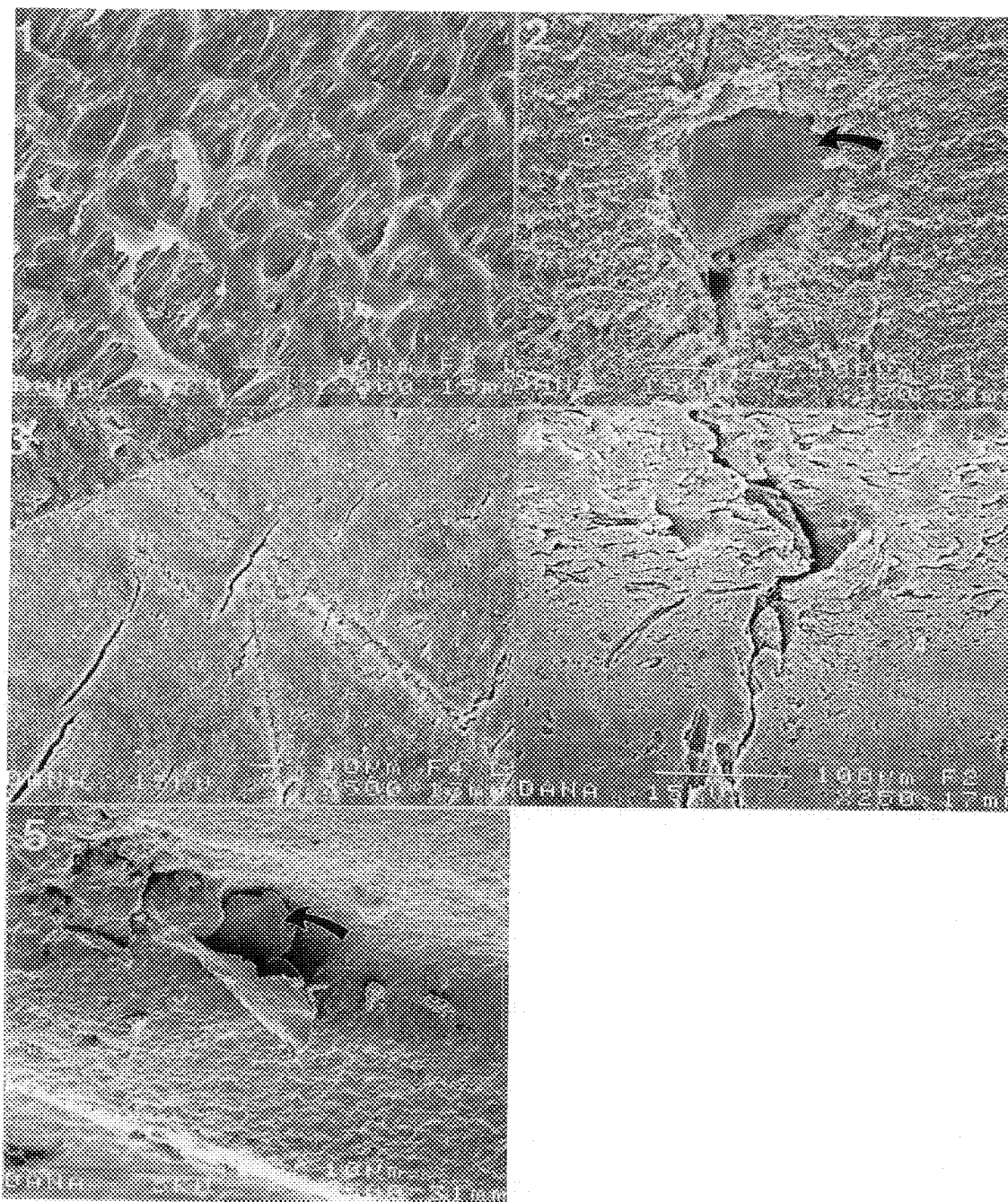
Fig. 1 Surface of a polyurethane seal following extended service in hydraulic cylinder.
Fig. 2 Metallic particle typical of those found embedded in polyurethane seal lips.
Fig. 3 Abrasive particle typical of those observed in the rotating shaft seal lips.
Fig. 4 Surface of a rubber seal which exhibits degradation due to heat and friction.
Fig. 5 Cross section through the working area of a rubber seal that exhibits cracking due to heat and friction.

CROSS-SECTIONAL TEM ANALYSIS OF SOLVENT-CAST SBS THIN FILMS

G. Kim and M. Libera
Dept. of MS&E, Stevens Institute of Technology, Hoboken, NJ 07030

Block copolymers can assume a range of microphase-separated
morphologies, and the dependence of morphology on temperature and
composition is an area of active research (1-3). Our work has been
studying the morphology of solvent-cast thin films of polystyrene-
polybutadiene-polystyrene (SBS) as a function of solvent
evaporation rate and post-specimen annealing (4). This paper
describes the analysis of thin film cross-sections to distinguish
between possible morphologies. ~50 nm-0.5 μm thick films were cast
from a 0.1 wt% solution of SBS (30 wt%, $M_w=10^5$) in toluene. GPC
analysis (5) indicates PS/PB diblock and PS homopolymer is present
(<5wt% total). 50 μl of solution was deposited on water-polished
salt. The solvent evaporation rate was roughly controlled between
200 nl/sec and 0.2 nl/sec. After evaporation, the film was cut,
floated from the salt, collected on grids, and exposed to OsO_4
vapor (20 min) to stain the PB. After plan view study, some
specimens were cross-sectioned. A carbon layer was evaporated on
both sides prior to embedding in epoxy and ultramicrotomy(-130°C).
Microscopy used a Philips CM30ST TEM.

Figs. 1a and 1b show plan-view images of the morphology resulting
from a 5 nl/sec evaporation rate. These display high contrast of
what appears to be PS cylinders with their axis perpendicular to
the film plane in a highly-ordered hexagonal array. The cross-
sectional view (fig. 1c) is from a film ~95 nm thick. It confirms
that the PS phase is present as vertical cylinders. Fig. 1c also
suggests that the PS phase extends to the free surface in contrast
to observations that a lower surface-energy PB layer forms there
(6,7). Figs. 2a and 2b show plan-view images of the morphology
resulting from the much slower 0.2 nl/sec evaporation rate. These
display lower contrast than the vertical cylinder structure. They
indicate a different morphology which might at first be interpreted
as alternating PS/PB lamellae. The cross-sectional views confirm,
however, that the morphology remains one of PS cylinders in a
continuous PB matrix. The cylinder axis now lies in the film plane
rather than perpendicular to it. Figs. 2c and 2d show cross-
sections of films ~95 nm and ~540 nm thick, respectively (the
latter would not being electron transparent in plan view). Both
show hexagonal arrays of in-plane cylinders. The surface of the
thicker film (2d) is covered with a PB layer, but the image from
the thinner film (2c) suggests again that the PS phase may extend
to the free surface. The transition from a vertical cylinder
structure to an in-plane cylinder structure is consistent with the
contrast differences observed in the plan-view images (figs. 1a,
1b, 2a, 2b) and can be understood by a simple kinematic scattering
model sketched in fig. 3.

1. S. Aggarwal, Polymer 17 (1976) 938-956.
2. S. Sakurai et. al., Macromolecules 26 (1993) 5796-5802.
3. D. Hajduk et. al., Macromolecules 27 (1994) 490-501.
4. G. Kim et. al., Proc. 5, Microscopy and Microanalysis 1995, (Jones and Begall, NY) 184-185.
5. Thanks to Dr. L. J. Fetters of Exxon Research for GPC analysis.
6. C. Henkee et. al., J. Materials Sci. 23 (1988) 1651-1694.
7. H. Hasegawa et. al., Macromolecules 20 (1987) 1651-1662.
8. Support from the Army Research Office and The New Jersey Commission on Science and Technology (through AIMS) is gratefully acknowledged.
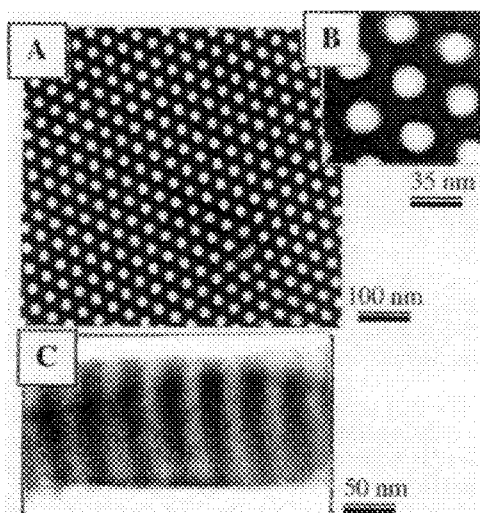
Figure 1. Plan (a,b) and cross-sectional (c) images of vertical-cylinder morphology resulting from 5 nl/sec evaporation
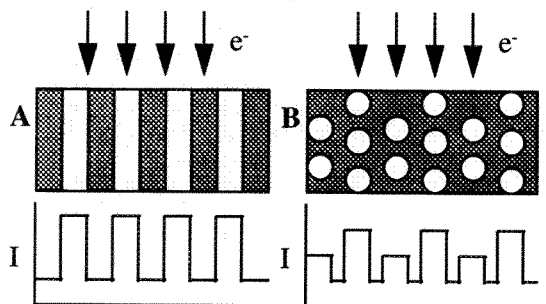
Figure 3. Schematic intensity profile resulting from vertical(a) and in-plane (b) cylinder morphologies
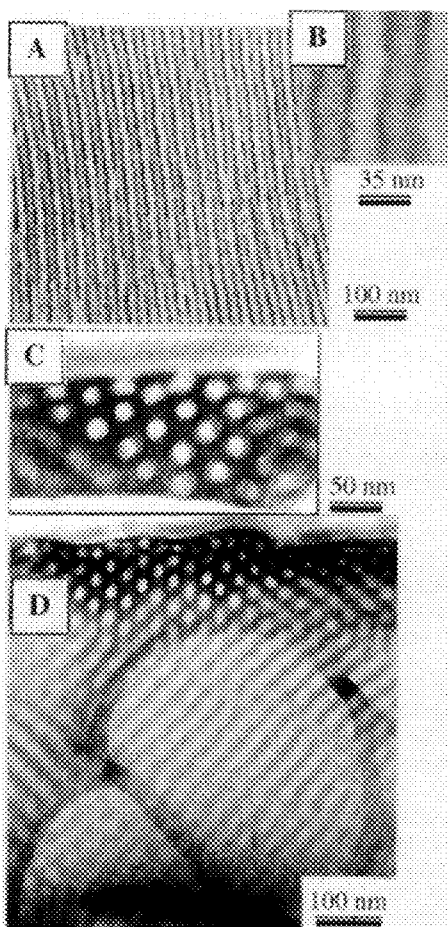
Figure 2. Plan (a, b) and cross-sectional (c, d) images of in-plane cylinder morphology resulting from 0.2 nl/sec evaporation

DIRECT IMAGING OF NON-CLASSICAL TRIBLOCK COPOLYMER BLEND AND GEL MORPHOLOGIES IN THE DILUTE REGIME

Jonathan H. Laurer,* Richard J. Spontak,* Steven D. Smith[†] and Rudy Bukovnik[‡]

*Department of Materials Science & Engineering, North Carolina State University, Raleigh, NC 27695
[†]Corporate Research Division, The Procter & Gamble Company, Cincinnati, OH 45239
[‡]Telecom Division, Raychem Corporation, Fuquay-Varina, NC 27526

Incorporation of a low-molecular-weight, midblock-selective homopolymer into the microstructure of a microphase-ordered triblock copolymer results in preferential midblock swelling or a morphological transition, depending on the blend concentration and the size of the homopolymer chain relative to that of the host block. Since the blend properties are strongly dependent on the existing microstructure, morphological changes induced by variation in blend composition have attracted considerable interest.[1] Recent efforts[2] have sought to discern the phase stability of both copolymer-rich (concentrated) blends, in which parent homopolymer molecules are contained within their preferred microphase, and homopolymer-rich (dilute) blends, in which the copolymer molecules micellize to reduce repulsive interactions in a parent homopolymer matrix.[3] Since dilute blends typically consist of spherical copolymer micelles, most morphological studies[4] have focused on concentrated copolymer/homopolymer blends in order to (i) tailor the blend microstructure, and properties, at the molecular level and (ii) examine macromolecular mixing in conformationally constrained nanoscale environments. In this work, we return to the dilute copolymer/homopolymer blend regime and examine the self-assembly of triblock copolymer molecules in the presence of low-molecular-weight parent and nonparent homopolymers and, in some cases, an oil.

Two families of copolymers were examined in this work. The first series consisted of poly[styrene-*b*-(styrene-*r*-isoprene)-*b*-isoprene] extended block copolymers (EBCs), in which the S/I midblock fraction (Φ) varied from 0.0 to 0.4 in 0.1 increments. These materials were synthesized via living anionic polymerization with *sec*-butyllithium and a potassium alkoxide (to control monomer sequencing). At 50/50 (w/w) S/I and the molecular weights (M) examined here (120-160 kDa), they all exhibited the lamellar morphology. Blends of the EBCs were prepared with a 20 kDa homopolystyrene (hPS) by solution casting from toluene. The second series of copolymers was comprised of poly[styrene-*b*-(ethylene-*co*-butylene)-*b*-styrene] (SEBS) triblock copolymers. The compositions of these materials were about 31-33 wt% styrene, and they ranged in M from 150 to 240 kDa. Blends were prepared with several homopolyisoprenes (hPIs) varying in M and a Witco 380 PD saturated aliphatic oil. Films were prepared by two routes: (i) solution casting from cyclohexane and (ii) mechanical mixing at 100°C. Resultant films and gels were sectioned at −100°C in a Reichert-Jung Ultracut-S ultramicrotome using a cryodiamond knife. Electron contrast was enhanced upon exposure to the vapor of OsO_4(aq) (to stain the isoprene in EBC blends) for 90 min or RuO_4(aq) (to stain the styrene in SEBS blends) for 5 min. Images were acquired with a Zeiss EM902 electron microscope at 80 kV and ΔE between 50 and 100eV.

The thermodynamic incompatibility, which governs microstructural ordering, is commonly regulated through temperature, which affects χ (the Flory-Huggins interaction parameter), and N, the copolymer chain length. In this work, χ is varied through Φ in the EBC/hPS blends. Shown in Fig. 1 is a series of TEM micrographs illustrating the effect of increasing Φ in blends composed of 90 wt% styrene. In Fig. 1a, the isoprene blocks of an EBC with Φ=0.2 organize into spherical micelles (the L_1 phase). As Φ is increased to 0.3 (Fig. 1b), the micelles coexist with large unilamellar vesicles, representative of the asymmetric L_3 ("sponge") phase. When Φ is increased, and χ is decreased, further (to 0.4, as in Fig. 1c), the micelles and vesicles seen in Fig. 1b transform into a randomly connected, bilayered membrane (the symmetric L_3 phase) coexisting with highly swollen lamellae (the L_α phase). The phases evident in Fig. 1 have been analyzed by electron microtomography and small-angle neutron scattering (SANS),[5] and are consistent with the theoretical[6] and experimental[7] behavior of the L_3 phase in surfactant systems. The blends displayed in Fig. 1 provide evidence for the symmetric and asymmetric "sponge" phases in

dilute triblock copolymer systems. Shown in Fig. 2 are images from two SEBS/oil thermoplastic elastomer gels, one at 30 wt% SEBS (Fig. 2a) and the other at 10 wt% SEBS (Fig. 2b). In Fig. 2a, the stained styrene blocks form a mesh structure, whereas those in Fig. 2b micellize. These micelles, responsible for physically crosslinking and stabilizing[3] the SEBS/oil gel, have been inferred from SANS data,[8] but have not been previously imaged. It is interesting that, unlike the micelles in Fig. 1a, the styrene micelles in Fig. 2b are not pure, but instead contain an EB/oil core (see the inset of Fig. 2b).

References
1. T. Pan, et al., *Macromolecules* 26(1993)2860.
2. Matsen, M.W., *Phys. Rev. Lett.* 74(1995)4225.
3. M. Nguyenmisra, W.L. Mattice, *Macromolecules* 28(1995)1444.
4. K.I. Winey, E.L. Thomas, L.J. Fetters, *Macromolecules* 25(1992)422, 2645.
5. J.H. Laurer, et al., *Nature* (submitted).
6. D. Roux, C. Coulon, M.E. Cates, *J. Phys. Chem.* 96(1992)4174.
7. H. Hoffmann, *Ber. Bunsenges. Phys. Chem.* 98(1994)1433.
8. N. Mischenko, et al., *Macromolecules* 28(1995)2054.
9. This work was supported by the Raychem Corp., the Shell Development Co. and, in part, by the National Science Foundation (CMS 941-2361).
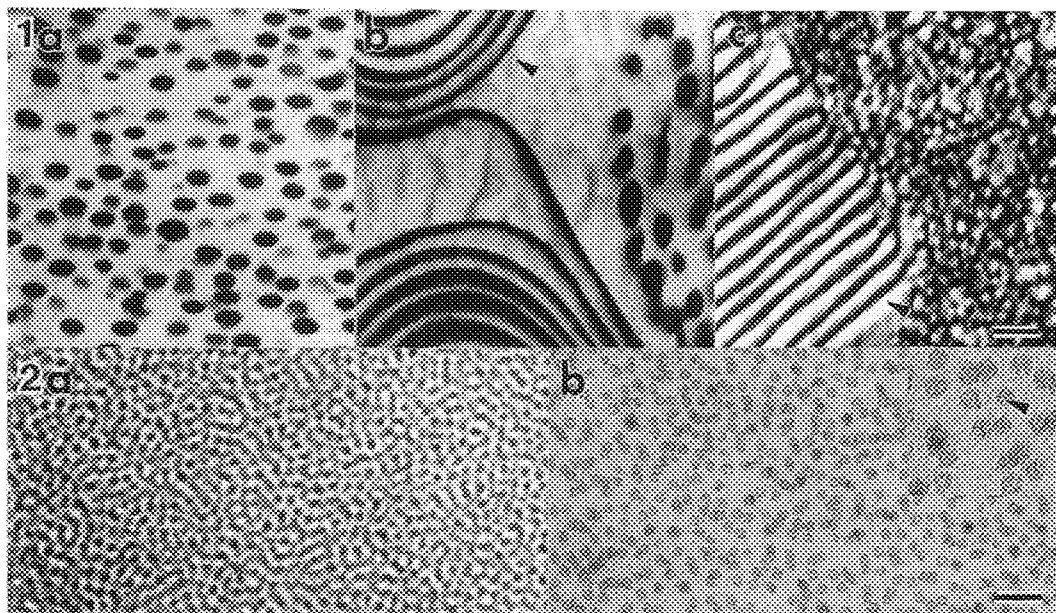
FIG. 1.—Micrographs of EBC/hPS blends at 90 wt% styrene illustrating effect of midblock fraction (Φ) on blend morphology in dilute copolymer regime. In (a), Φ=0.2 and OsO$_4$-stained isoprene micelles are evident. In (b), Φ=0.3 and micelles coexist with large unilamellar vesicles (asymmetric L$_3$ "sponge" phase, arrow). In (c), Φ=0.4 and swollen lamellae (arrow) coexist with randomly connected isoprene membrane, representative of symmetric L$_3$ phase and measuring about 50 nm across. Bar = 500 nm.

FIG. 2.—Pair of images from (mechanically mixed/solvent-cast) SEBS/oil gels composed of (a) 30 wt% and (b) 10 wt% copolymer with M=150 kDa. Irregular RuO$_4$-stained styrene mesh morphology is evident in (a), while spherical styrene micelles measuring *ca.* 26 nm in diameter are seen in (b). Note from inset in (b) that micelles are not pure, but instead contain unstained EB/oil (arrow). Bar = 100 nm.

A NEW METHOD FOR CHARACTERIZATION OF DOMAIN MORPHOLOGY OF POLYMER BLENDS USING RuO$_4$ STAINING AND LVSEM

G. M. Brown and J. H. Butler

Exxon Chemical Company, Baytown Polymers Center, PO Box 5200, Baytown, TX 77520, USA

Ruthenium tetroxide (RuO$_4$) staining for TEM is a well proven technique for the characterization of crystalline polyolefins.[1,2] Blend morphology has also been studied using RuO$_4$ staining and SEM and low voltage SEM.[3-6] A new method has been developed which uses RuO$_4$ staining and LVSEM in the characterization of polyolefin blend morphology, specifically blends of polypropylene modified by the addition of elastomers or plastics. This method is often preferred over TEM for the characterization of blends and is applicable to many problems encountered in commercial and industrial laboratories including the analysis of domain morphology in molded parts, extruded films and fibers, failure analysis, and the analysis of layer morphology in certain coextruded films.

Three sample preparation steps are required prior to the LVSEM analysis. (1) The sample face is cryogenically sectioned on a glass knife in the cryomicrotome. (2) This face is stained in RuO$_4$ vapors for 2.5 hours. The staining solution is prepared *in situ* by a modification of the method of Montezinos.[1] (3) 100nm thick sections are cut at ambient temperature to an optimal depth of approximately 0.5μm on a diamond knife equipped with a water floatation bath. During sectioning, the sections are floated onto the surface of the water in the boat and may be collected for analysis by TEM.[7] The stained and sectioned face is examined in the LVSEM. All samples were analyzed using the Hitachi S-900 Low Voltage Scanning Electron Microscope at 0.8-1.2KV accelerating voltage.

The contrast observed in LVSEM images of stained polymers is inverted relative to the TEM: heavily stained polymers appear light and poorly stained polymers appear dark.[8] Figure 1 illustrates the RuO$_4$ staining/LVSEM method for a blend of linear low density polyethylene/polypropylene (LLDPE/PP) in which the LLDPE domains are heavily stained compared to the polypropylene matrix. Figure 2 shows the domain morphology of an injection molded blend containing a plastomer (a semi-crystalline polyolefin with density <0.915g/cm^3), a polypropylene copolymer (RCP) and talc. The well stained plastomer domains (light) are easily differentiated from the poorly stained PP matrix (dark) and the talc particles (at arrows).

The keys to the success of this method are heavy staining of the sample with RuO$_4$ vapors and the superb imaging capabilities of the LVSEM. Heavy staining embrittles the polymer, allowing ultramicrotomy at ambient temperature without ductile deformation, and produces strong contrast between differently stained phases of the blend. The primary limitation of this method is the difficulty of differentiating similarly stained polymers since compositional information on the samples is based on stain uptake.

Low voltage-high resolution SEM's equipped with field emission guns offer dramatic improvements in image quality and resolution over conventional SEM's and minimized beam-induced sample damage at beam energies less than 2KV. Images of stained polymer blends with 3-4nm resolution are routinely made at 1.2KV over a range of magnification that encompasses both optical microscopy and TEM.[9,10]

Our observations suggest that staining of polymers with RuO$_4$ increases the secondary electron yield in the LVSEM and that the secondary electron yield is dependent on the RuO$_4$ concentration. The increase in secondary electron yield of a polymer following staining may result from the bonding environment of the ruthenium atoms and absorbance effects arising from ruthenium atoms that are embedded in the matrix of the unstained portions of polymer molecules.[8,11] Our observations also suggest that E2 of the stained polymer has shifted upward as a result of its increased secondary electron yield whereas E2 of the unstained portions of the molecules is unchanged. Thus staining broadens the useful range of accelerating voltages over which the sample can be analyzed.[12]
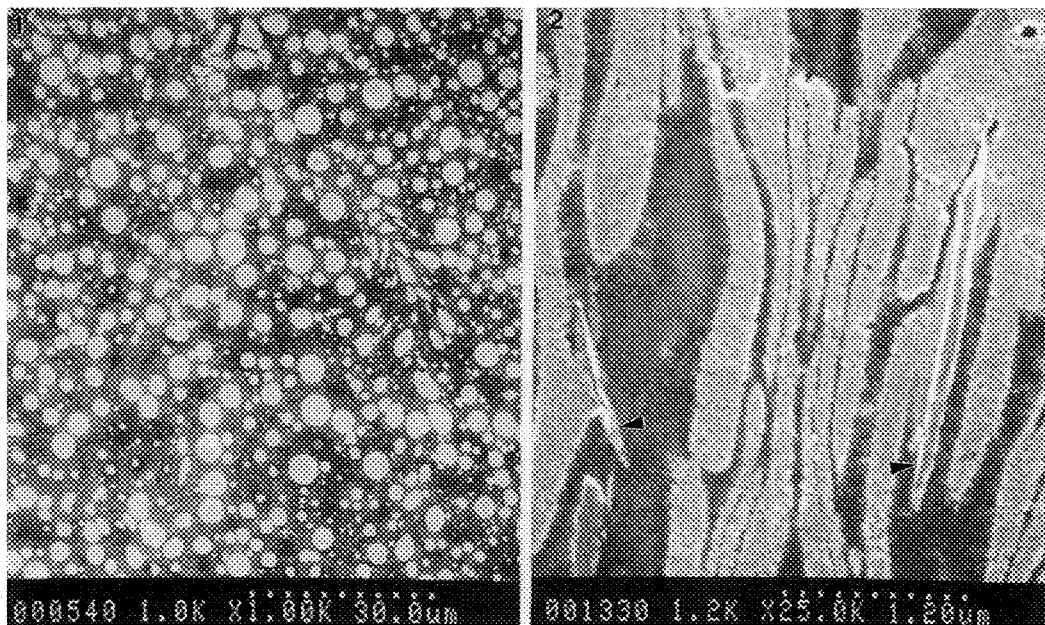
Figure 1 RuO$_4$ staining/LVSEM of LLDPE/PP blend (1KX, 1.0KV)
Figure 2 RuO$_4$ staining/LVSEM of a plastomer/RCP/talc blend (25KX, 1.2KV)

References

1. D. Montezinos, B. G. Wells and J. L. Burns, *J. Polym. Sci: Polym. Lett. Ed.* 23 (1985) 421.
2. H. Sano, T. Usami, and H. Nakagawa, *Polymer* 27 (1986) 1497.
3. G. Goizueta, T. Chiba, and T. Inoue, *Polymer* 33(4) (1992) 886.
4. G. Goizueta, T. Chiba, and T. Inoue, *Polymer* 34(2) (1993) 253.
5. V. K. Berry, *Scanning* 10 (1988) 19.
6. P. B. Himelfarb and K. B. Labat, *Scanning* 12 (1990) 148.
7. M. A. Hayat, *Principles and Techniques of Electron Microscopy, Biological Applications, Vol. 1,* Van Nostrand Reinhold, New York (1970).
8. J. I. Goldstein, D. E. Newbury, P. Echlin, D. C. Joy, C. Fiori and E. Lifshin, *Scanning Electron Microscopy and X-Ray Microanalysis,* Plenum Press, New York (1981).
9. J. H. Butler, D. C. Joy, G. F. Bradley, S. J. Krause, and G. M. Brown, *Microscopy: The Key Research Tool* (1992) 103.
10. J. H. Butler, D. C. Joy, G. F. Bradley, and S. J. Krause, *Polymer* 36(9) (1995) 1781.
11. D. C. Joy (ed.), *A Data-Base of Electron-Solid Interactions,* University of Tennessee (1995).
12. G. M. Brown and J. H. Butler, submitted for publication in *Polymer.*
13. The authors thank Dr. Hironari Sano of Mitsubishi Chemical Corporation for invaluable discussions and suggestions pertaining to the ruthenium tetroxide staining of polymers for TEM.

THE INFLUENCE OF SURFACE TOPOGRAPHY IN THE ADHESION OF POLYSTYRENE TO ALUMINUM

O. L. Shaffer,* S. Yankovskaya,**A. Namkanisorn,*** M. Chaudhury,*** and M. S. El-Aasser****

*Emulsion Polymers Institute, Polymer Interfaces Institute, Lehigh University, Bethlehem, PA 18015
**Polymer Interfaces Institute, Lehigh University, Bethlehem, PA 18015
***Polymer Interfaces Center, Department of Chemical Engineering, Lehigh University, Bethlehem PA, 18015
****Emulsion Polymers Institute, Polymer Interfaces Center, Department of Chemical Engineering, Bethlehem, PA 18015

Polymer/metal adhesion has been studied by scanning(SEM) and transmission electron microscopy(TEM). Now with atomic force microscopy(AFM) we can scan the metal's surface and correlate the roughness with adhesion energy. We have chosen aluminum as the metal substrate and polystyrene(PS) as the nonreactive polymer adhesive. A great deal of research has been done on primed metal surfaces which are used to improve adhesion between the metal and the polymer. Our interest is to study the mechanical interlocking of the polymer to the metal without a primer coupling agent.

Aluminum alloy 6061 was cut into plates 25x60x1mm, cleaned with an alkali cleaner, rinsed with water, etched and anodized. The plates were etched in a solution of $Na_2Cr_2O_7 \cdot 2H_2O$, H_2SO_4, and water in a 1:10:30 ratio by weight at 50-52°C for 12-20 min. After etching , they were rinsed, dried and anodized in 10% phosphoric acid solution with 15 V for 20 min, then were rinsed and dried again. A 1% PS solution in toluene was deposited on the prepared aluminum surface and air dried. A sandwich of aluminum/ polystyrene film (25x30x0.5mm)/ aluminum was prepared, clamped together and placed in a 150°C oven for two hours. The polymer metal adhesion energy was obtained by Instron (lap test), and the surface morphology by a Joel 6300F SEM and Park CP AFM. The aluminum surfaces were examined before and after the joint was fractured in the lap test. A joint was prepared with a silane primer for comparison.

The adhesive fracture energy showed the etched joint and the anodized joint to be very weak but the etched/anodized joint resulted in fracture energy of 380 J indicating mechanical interlocking is at work. For comparison, the fracture energy for the primed/etched/anodized joint was 1660 J. The XPS data show the alkaline cleaned aluminum to have O, C, Al, Si and Ca; cleaned/etched O, C, Al, Na, and Cl; cleaned/etched/anodized O,C Al and P. The fractured joint has O, C and Al indicating fracture through the interface. The silane primer treated joint shows only carbon indicating fracture through the polymer.

Figure 1a shows a FESEM image of the surface of etched/anodized aluminum at 5kV and 50,000x. Cellular structure due to etching can be seen. Figure 1b shows a 4.8 μm scan of the same surface imaging in the noncontact AFM mode; notice the granular surface and the 500 nm hole. The roughness was measured for all surface treatments and increased from 3.6 nm for an alkali cleaned surface, to 6.8 nm etched, 8.6 nm anodized and 9.7 nm for etched and anodized. The adhesion fracture energy increased as the roughness increased. The peak to valley data show 40 nm for etched and 90 nm for anodized aluminum which correlates with the reported oxide structures[1]. Figure 2a shows a FESEM of the fractured joint. Notice the large island of PS and the fibrils that have been pulled from "pores". Also, much shorter PS fibrils can also be seen covering the entire surface. Figure 2b shows a noncontact AFM image of the same fractured joint. Here we can see the PS being pulled, stretched and broken. This scan has no resemblance to figure 1B of the etched/anodized aluminum surface indicating coverage by the PS.

Reference

1. J.D. Venables et al., Applications of Surface Sci. 3 (1979) 88.
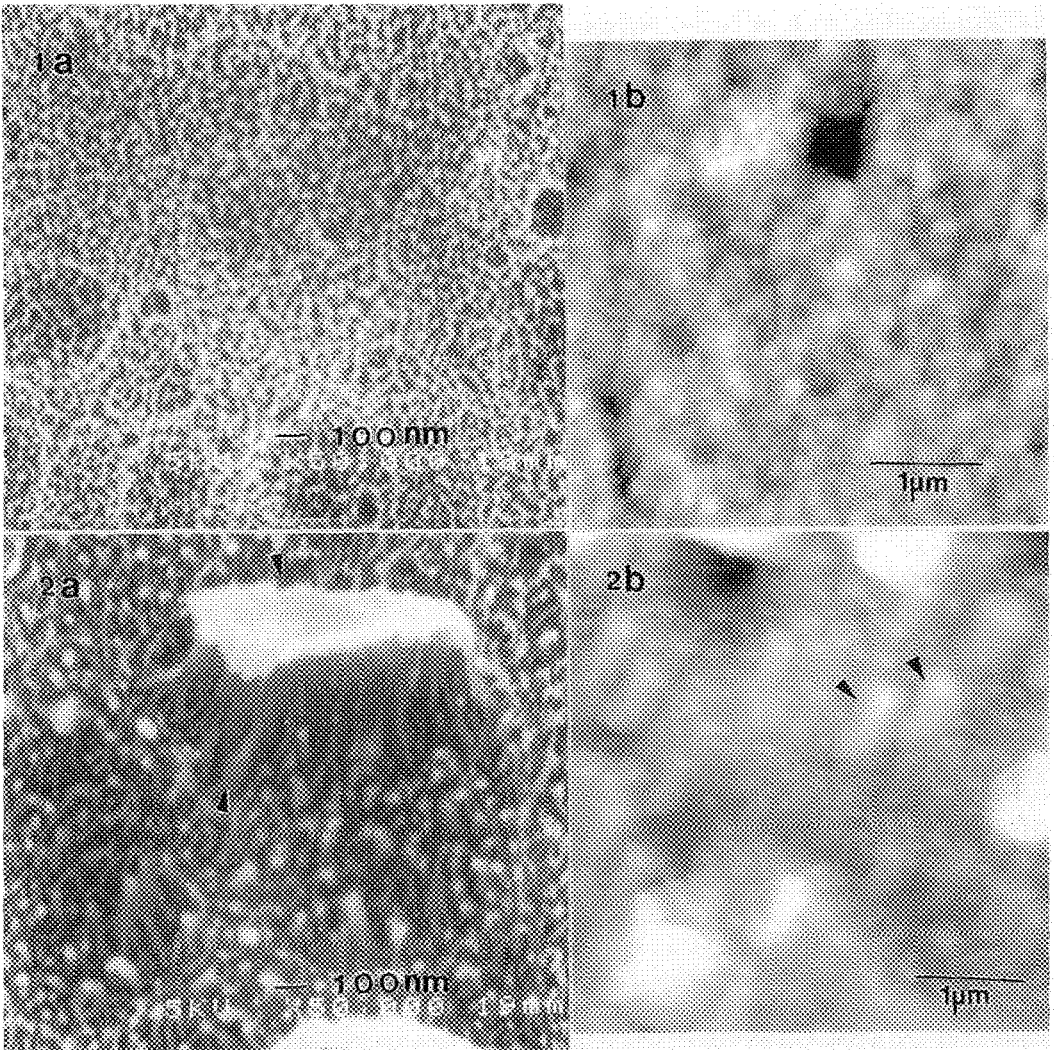
FIG. 1a - FESEM image of Al 6061 after etching and anodizing.
FIG. 1b - AFM of Al 6061 after etching and anodizing.
FIG. 2a - FESEM image of Al 6061 etched/anodized after fracture testing. Note the island of PS.
FIG. 2b - AFM of Al 6061 etched/anodized after fracture testing. Note PS fibrills.

A STANDARD METHOD FOR THE PREPARATION OF POLYMERS AND PLASTICS FOR MICROSTRUCTURAL EXAMINATION BY GRINDING AND POLISHING TECHNIQUES

M.E. CAVALERI* AND D.S. SEITZ**

*3M Corporate Research Laboratories, Analytical and Properties Research Laboratory, St. Paul, MN 55144
**Dacon Engineering and Service Company, Inc. 4915 W. 35th St. Minneapolis, MN 55416

One of the fundamental objectives of microstructural examination of manufactured materials is to gain a more complete understanding of the relationships between the manufacturing processes, the microstructure and texture of the material, and the product's performance. This objective, however, can only be achieved if the examination specimens are repeatably produced and are free of thermal, mechanical and chemical alterations, as well as artifacts, damage, or defects resulting from the specimen preparation process. It is also imperative that surface finish of the specimen be appropriate for the microscopical techniques to be used. The preparation process must provide specimens in a timely fashion, generally within a few tens of minutes or at most a few hours for typical industrial/manufacturing situations. Although designed for much harder more rigid materials, the general grinding and polishing techniques used in petrographic and metallographic specimen preparation can also be used for plastics and polymers.[1,2,3] ASTM Committee E-4 on Metallography has a task group (TG-E04.01.05) which is preparing a standard guide for the preparation of polymeric specimens based on the ASTM E3-95 standard.

The new standard guide will be based on the concept that there are methods, practices, and procedures that can be used to routinely produce acceptable quality plastic and polymeric specimens for microstructural studies. Also, like metallographic specimen preparation, there is a certain amount of artfulness and finesse that must be coupled with technical knowledge and technical skill in order to regularly produce high quality specimens. By considering the interactions between the specimen, the mounting medium, the abrasive medium, the coolant/lubricant, the applied forces, and the structure or texture of the grinding/polishing surface, specimen preparation times can be reduced from the several hours range for ordinary grinding and polishing schemes to a few tens of minutes. The approach is one that maximizes the removal of damage introduced during previous specimen preparation steps while minimizing the introduction of additional damage and minimizing the specimen preparation time. The preparation process is divided into three steps: 1) planarization, 2) exposure of the true microstructure, and 3) final polishing to enhance the contrast between the features of interest. Figures 1 and 2 are end results for typical preparation procedures for rigid plastics like PMMA and for semi-rigid plastics like polyethylene. In this case both materials under went three grinding steps using 120, 320, and 600 grit fixed abrasives. These steps were followed by polishing steps using 15μm and 6μm free abrasive on a low nap cloth and a final polish using 0.05μm free abrasive on a moderate to high nap cloth. The end result is acceptable for the PMMA although some rounding of the edges can be observed. However, the polyethylene sample exhibits extreme scratching and significant rounding of edges. Based on the proposed standard there is only one coarse grinding (planarization) step using a 320 grit fixed abrasive and a fine grinding (planarization) step using 30μm free abrasive on a perforated nappless pad. The exposure of the true microstructure is accomplished by using 9μm and 3μm free abrasive on perforated

nappless pads. The final surface is prepared by polishing with 0.05µm free abrasive on a low nap pad. Figures 3 and 4 are the end results for the PMMA and polyethylene samples, respectively. While there is little difference between the two approaches for the PMMA, there is a clear and dramatic improvement in the end PE when prepared according to the procedures being proposed here.

References

1. L.C.Sawyer and D.T. Grubb, *Polymer Microscopy*, Chapman and Hall, London (1987) 303.
2. T. G. Rochow, *Light-Microscopical Resinography*, McCrone Publications, Chicago, IL.(1983) 96.
3. W.U. Kopp and U. Linke, in *Microstructural Science*, Vol. 10 (1982)239-247.
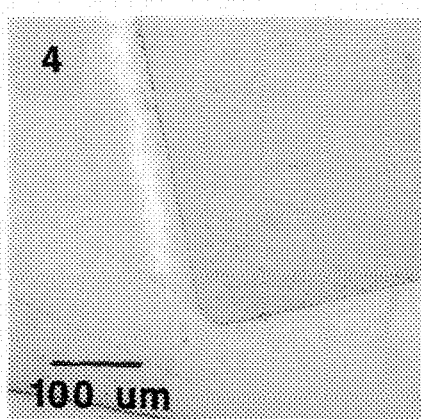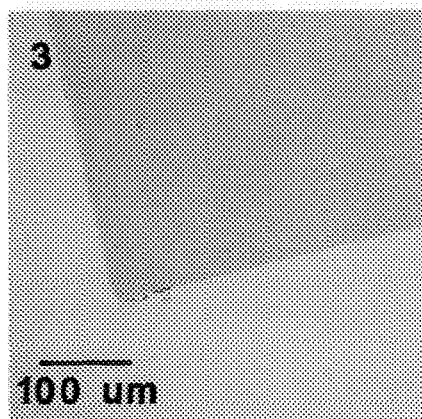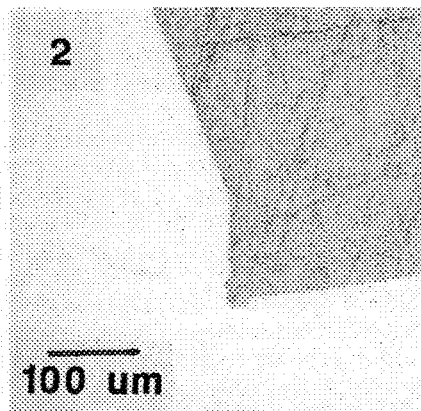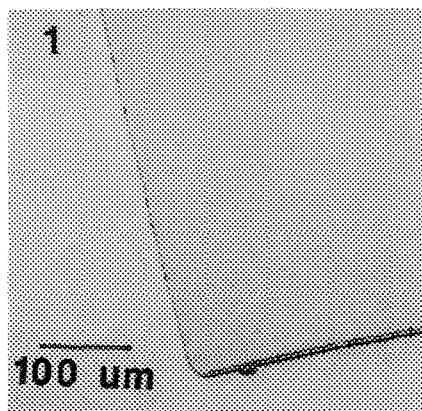
Fig. 1 Polished PMMA 'typical' preparation
Fig. 2 Polished Polyethylene 'typical' preparation
Fig. 3 Polished PMMA prepared according to ASTM TG-E04.01.05 guide
Fig. 4 Polished Polyethylene prepared according to ASTM TG-E04.01.05 guide

Application of Various Modes of Scanning-Probe Microscopies in Polymer Systems

Dale J. Meier

Michigan Molecular Institute, 1910 West St. Andrews Rd., Midland, MI 48640

The invention of the scanning tunneling microscope (STM) by Binnig and Rohrer[1] in 1982 demonstrated an unparalleled ability to image materials at the sub-nanometer scale. The invention rapidly lead to an explosion of applications of STM in a wide variety of fields. However, imaging by an STM is essentially limited to materials which are conductive, or could be made conductive, so many materials of interest could not be imaged by STM. This limitation was removed a few years later (1985) by the invention of the atomic force microscope (AFM) by Binnig, Quate and Gerber[2], in which imaging is based on the response of a soft cantilever beam to the contact forces between an ultra-fine probe tip and a sample. The cantilever/probe systems could be made sensitive enough to enable the AFM to easily resolve atomic or molecular level features.

The realization the cantilever beam could respond to forces other than contact forces quickly lead to a variety of other scanning microscopes in which images could be obtained based on other physical properties. These now include scanning probe microscopes which produce images based on friction, magnetism, electrostatics, chemical interactions, temperature, steric interactions, etc., and new techniques and applications appear regularly. In addition, a variety of new scanning modes have also been developed in recent years, e.g., non-contact, oscillatory, depth profiling, near-field optical, etc., which add new information or enable easier imaging. An example is the high-amplitude resonance or Tapping™ mode, in which the probe undergoes a high amplitude oscillatory motion, with the probe alternately in and out of contact with the sample. This mode avoids the lateral contact forces on the sample, and is particularly well suited in the scanning of soft or poorly anchored specimens. An example is shown in Figure 1, which shows images of an unconsolidated latex scanned in the normal contact mode and in the high-amplitude mode. The advantage of this mode for such imaging is obvious. In many cases, multiple images based on two or more physical properties can be obtained at the same time, e.g., topography/friction, topography/magnetism, etc. An example is shown in Figure 2, which shows images of a highly polished metal surface obtained in the contact mode and simultaneously in the lateral force (friction) mode. The metal surface is coated on the right-hand side with a very thin layer of a silicone mold release agent. The presence of the coating is not apparent in the contact-mode image, but is quite obvious in the lateral force image.

In this talk, the various scanning modes will be described and examples of images from the various modes will be shown. The virtues and limitations of each will be described, particularly as they pertain to polymeric systems.

References

G. Binnig, and H. Rohrer, *Helv. Physica Acta*, **55**, (1982) 726.
G. Binnig, C. F. Quate and Ch. Gerber, *Phys. Rev. Letters*, **56**, (1986) 930.

1a　　　　　　　　**1b**
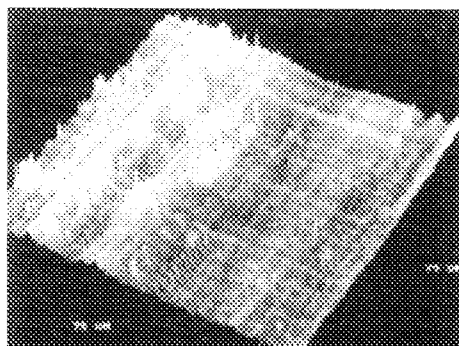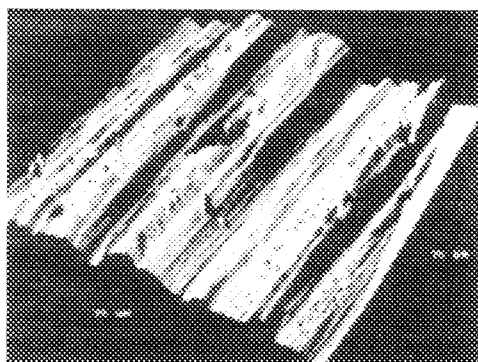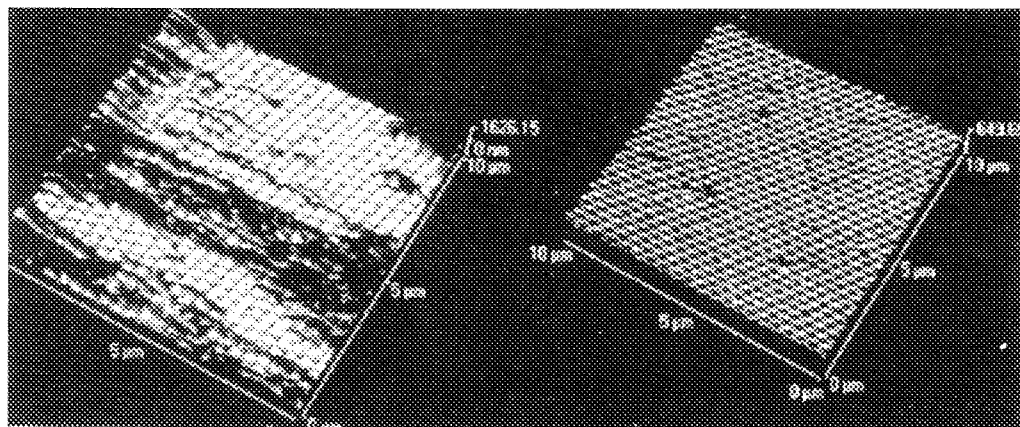
2a　　　　　　　　**2b**

FIG.1. Unconsolidated latex, scanned (a) contact mode (b) high-amplitude resonance mode

FIG. 2. Polished metal surface scanned (a) contact mode, (b) lateral force mode. Sample coated on right-hand side with film of silicone mold release agent

LENGTH-SCALE-DEPENDENT SURFACE ROUGHNESS MEASUREMENTS OF BIOACTIVE POLYMER THIN FILMS USING SCANNING PROBE MICROSCOPY

Christopher J. Buchko, Kenneth M. Kozloff, and David C. Martin

Department of Materials Science and Engineering
The University of Michigan, Ann Arbor, MI 48109-2136

The development of implantable biomedical devices requires active biological interfaces that minimize the body's immune response. We have identified candidate protein polymer coatings for biomedical applications and methods of processing these coatings that promote a favorable *in vitro* biological performance.[1] However, the chronic implantation of biomedical devices, specifically the neural prosthetic devices developed at the University of Michigan,[2] places additional requirements on the polymer coatings. Among these constraints are the efficient transport of neuronal signals from tissue to the device and the prevention of physical displacement of the device through tissue. To meet these potentially conflicting goals, we are developing discontinuous, porous polymer coatings that are rough at biologically-relevant length scales.

In order to quantify the surface morphology of these thin polymer films, which are typically 0.02 μm to 5.0 μm thick, we employ a number of complementary techniques, including scanning probe microscopy (SPM), scanning electron microscopy (SEM), light optical microscopy (LOM), and transmission electron microscopy (TEM). Among these techniques, SPM provides convenient information about the morphology of these polymer films at the biologically-relevant length scales of 1 μm to 100 μm. SPM can be used to determine characteristic length scales and identify related scaling regimes.[3] The instrument used for this work was a Digital Instruments NanoScope III with Multimode Head.

Polymer coatings are electrostatically deposited on substrates to produce discontinuous films that can have a variety of morphologies. Figures 1 and 2 show different types of a beaded coating morphology characteristic of electrostatic deposition from a dilute polymer solution.[1] The wide distribution of polymer bead sizes and the random nature of the surface coverage can be seen in both of these figures. The polymer coating in Figure 1 (Sample A) is discontinuous enough to reveal the silicon surface beneath it while the coating in Figure 2 (Sample B) is more continuous. The roughness of these coatings depends upon the length scale at which the roughness was measured. Power spectral density (PSD) measurements can be used to quantify the length-scale dependence of surface roughness.

The PSD of these surfaces (Figure 3) indicates that Sample A is rougher at length scales below 2 μm while Sample B is rougher at length scales above 2 μm. The change in slope that occurs in each of the samples describes characteristic dimensions of the polymer beads on the surface. The sharpness of the transition from one slope regime to another is related to the spread in sizes of the beads on the surface.

The PSD provides a quantitative means for determining characteristic morphological parameters such as discontinuity, porosity, and roughness. This information can be used to optimize the biological, electrical and mechanical properties of the polymer coatings.[4]

References:
1. C. J. Buchko et al., *Thin Films and Surface for Bioactivity and Biomedical Applications,* ed. C.M. Cotell, S.M. Gorbatkin, G. Grobe, and A.E. Meyer (Mater. Res. Soc. Proc. Pittsburgh, PA, 1995)
2. Center for Neural Communication Technology, http://www.engin.umich.edu/center/cnct/
3. G. Beaucage, D.W. Schaefer, *Journal of Non-Crystalline Solids,* 172-174, (1994) 797-805.
4. This work was supported by NIH Contract N01-NS-52322, the Whitaker Foundation, and Protein Polymer Technologies, Inc.
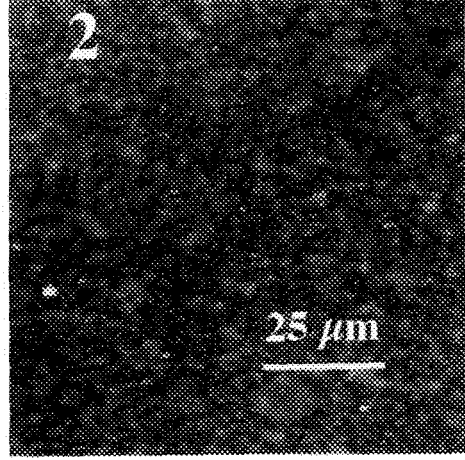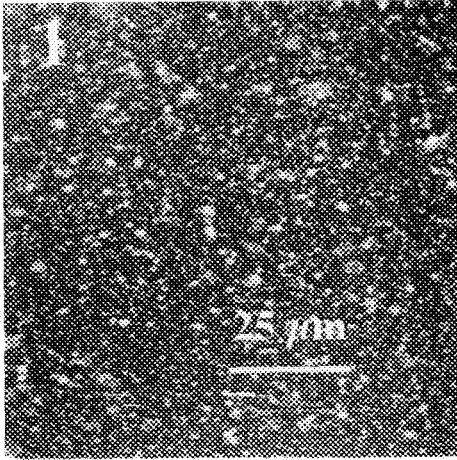
Power Spectral Density of AFM Data
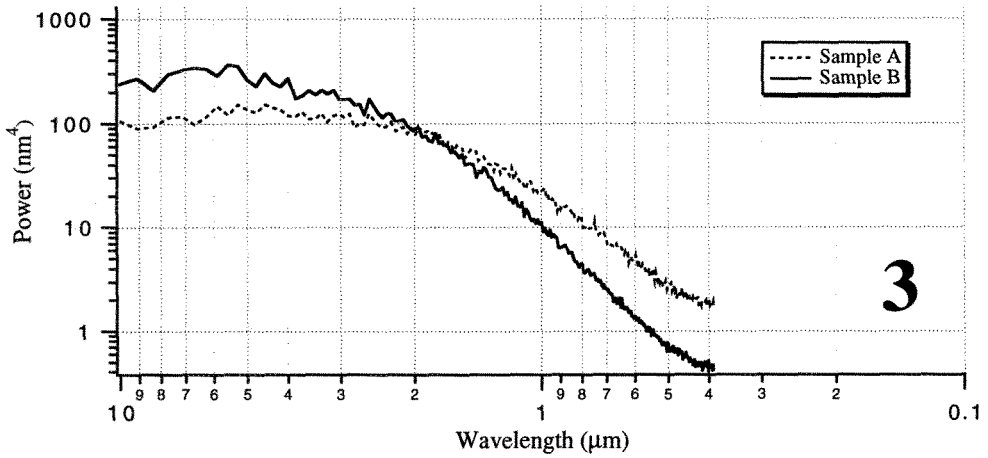
FIG. 1 Contact mode AFM scan of SLPF beads electrodeposited on a silicon surface to form a thin, discontinuous coating (Sample A).

FIG. 2 Contact mode AFM scan of SLPF beads electrodeposited on a silicon surface to form a thicker, more continuous coating (Sample B).

FIG. 3 Power spectral densities of Figures 1 and 2. Sample A is rougher at low wavelengths while Sample B is rougher at higher wavelengths.

ETCHING OF LLDPE AND LLDPE/HDPE BLENDS

M. S. Bischel* and J. M. Schultz**

* Materials Science Program, University of Delaware, Newark, DE 19716
** Department of Chemical Engineering, University of Delaware, Newark, DE 19716

Despite its rapidly growing use in commercial applications, the morphology of LLDPE and its blends has not been thoroughly studied by microscopy techniques. As part of a study to examine the morphology of a LLDPE narrow fraction and its blends with HDPE via SEM, TEM and AFM, an appropriate etchant is required. However, no satisfactory recipes could be found in the literature. Mirabella used n-heptane, a solvent for LLDPE, as an etchant to reveal certain morphological features in the SEM, including faint banding in spherulites.[1] A 1992 paper by Bassett included a TEM micrograph of an axialite of LLDPE, etched in a potassium permanganate solution, but no details were given.[2]

Attempts to use n-heptane, at 60°C, as an etchant were unsuccessful: depending upon thickness, samples swelled and increased in diameter by 5-10% or more within 15 minutes. Attempts to use the standard 3.5% potassium permanganate solution for HDPE[3] were also unsuccessful: the LLDPE was severely overetched. Weaker solutions were also too severe.

However, a version of the standard etchant for PEKK has proven to be highly successful in revealing both the banded spherulites and axialites seen in previous studies.[1,2] For the Exxon 3025 LLDPE being used in this study, the optimal conditions of 30 minutes with a 2% $KMnO_4$ solution were used to obtain the TEM results shown in Figs. 1a and 1b. All etching was performed in an ultrasonic bath.

LLDPE is overetched by the standard HDPE etchant, and HDPE is generally underetched by the PEKK etchant. Therefore, it should be possible to sequentially etch blends of LLDPE and HDPE in the two solutions to reveal first the LLDPE-related structures and then the HDPE-related ones. To prove this, a sample with side-by-side regions of the LLDPE and HDPE homopolymers was prepared. The entire sample was etched in the LLDPE etchant. Examination via SEM showed that the LLDPE portion etched very well (Fig. 2a), while the HDPE portion was underetched (Fig. 2b). The sample was then etched for 10 minutes in the standard HDPE etchant (less time than the usual to account for the earlier etching step). Examination via SEM showed that the LLDPE portion was severely overetched (Fig. 3a), while the HDPE portion was etched very well (Fig. 3b).

A 50/50 weight percent blend of the two homopolymers, crystallized near the melting temperature of the LLDPE, was then sequentially etched. Following the LLDPE etch step, SEM examination revealed large banded spherulites (Fig. 4a). After the HDPE etch step, small banded spherulites with even smaller axialites distributed throughout were revealed (Fig. 4b). These etched samples can also be used for TEM and AFM studies to examine the fine structures.

References:
1. F. M. Mirabella, Jr., et al., *J. Polymer Science: Part B*, **26**(1988) 1995.
2. D.C. Bassett in *Crystallization of Polymers*, M. Dosiere, ed., Kluwer Academic Publishers, Dordrecht, 1993, p. 110.
3. R.H. Olley, and D. C. Bassett, *Polymer*, **23**(1982) 1707.
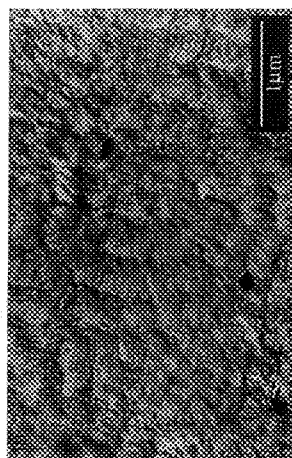
Figure 1a: Banded Spherulite of LLDPE
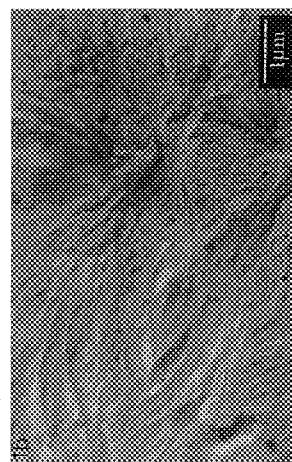
Figure 1b: Axialite of LLDPE
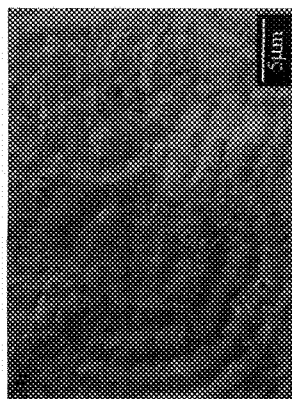
Figure 2a: LLDPE etch, LLDPE homopolymer

Figure 2b: LLDPE etch, HDPE homopolymer

Figure 3a: HDPE etch, LLDPE homopolymer

Figure 3b: HDPE etch, HDPE homopolymer
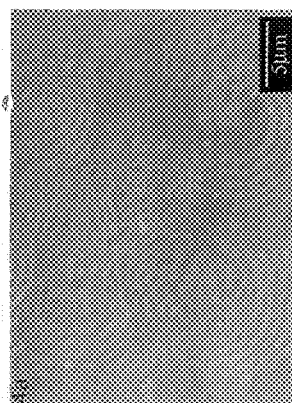
Figure 4a: LLDPE etch, LLDPE/HDPE blend
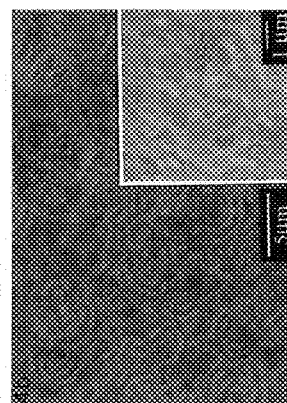
Figure 4b: HDPE etch, LLDPE/HDPE blend

A MOLECULAR YARN: NEAR-FIELD OPTICAL STUDIES OF SELF-ASSEMBLED, FLEXIBLE FLUORESCENT FIBERS

D. A. Higgins, J. Kerimo, D. A. Vanden Bout, and P. F. Barbara*

*Department of Chemistry, University of Minnesota, Minneapolis, MN 55455

The formation of flexible molecular fibers via the solution-phase self-assembly of the pseudoisocyanine dye (PIC) 1,1'-diethyl-2,2'-cyanine and poly(vinyl sulfate) (PVS) is reported. The physical and electronic properties of these fibers spin coated into thin films on fused-quartz substrates are studied by fluorescence and topographic imaging with near-field scanning optical microscopy (NSOM) and also by atomic force microscopy (AFM). The scanned-probe images demonstrate that fibers with lengths in the hundred micron range, widths of hundreds of nanometers, and thicknesses of a few tens of nanometers, are readily formed in aqueous mixtures of PVS and PIC. Unprecedented flexibility in these fibers is exemplified by the formation of numerous curved and looped structures in the spin-coated thin films. A sandwich-like composite structure of alternating anionic PVS and cationic PIC layers is proposed as a model for the assembly of the dye and polymer in these fibers. The alternating layers in this model are held tightly together via the cooperative "cross-linking" of the PVS and PIC layers by electrostatic dye/polymer interactions, and by hydrophobic van der Waals interactions between the PIC molecules. The intermolecular interactions in the PIC layer result in the formation of a liquid-crystalline-like, well-ordered layer of the PIC, which exhibits the spectral characteristics of J-aggregates. The proposed layered structure apparently possess "reactive" surfaces which link individual fibers into a yarn-like assembly. This cross-linking effect is supported by the presence of continuous circular fibers and by the gel-forming ability of the solutions from which these fibers are grown.
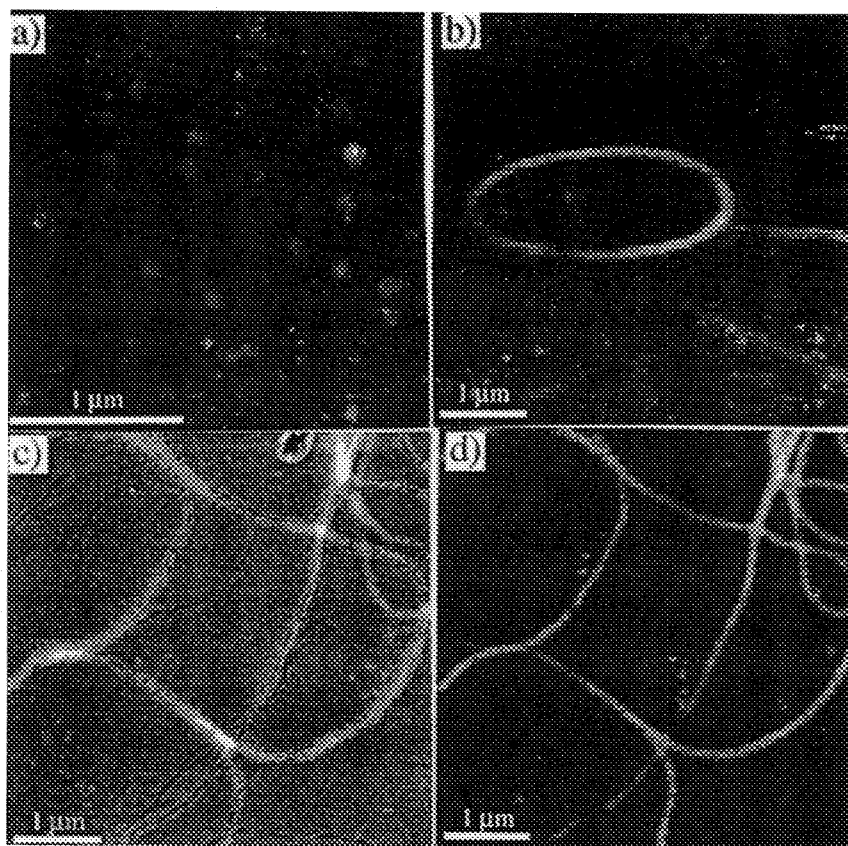
Figure 1. a) Fluorescence near-field image of a sample prepared by spin coating a 20 nM methanolic solution of DiI onto a thin film of poly(methyl methacrylate) which is supported on a fused-quartz coverslip. The fluorescent regions of the film result from excitation and detection of the fluorescence from single, isolated DiI molecules. b) A fluorescence NSOM image of a thin PVS film incorporating fluorescent fibers. The film was produced by spin coating a 10mg/mL PVS and 670 µM PIC solution onto a fused-quartz substrate. Important evidence for the flexibility of the observed fibers is given by the observation of highly curved fibers, such as the continuous loop shown here. c) A topographic image acquired with the NSOM instrument of a similar sample. The fibers are seen partially buried in the otherwise uniform PVS film of 45 nm thickness. An average height of 5nm is measured for the fiber topography in this image. d) The fluorescence NSOM image collected simultaneously with the topographic image in c).

Scanning thermal microscopy (SThM) of polymer blends: phase separation, localised calorimetric analysis

A. Hammiche,* H. M. Pollock,* J. N. Leckenby,** M. Song,* M. Reading*** and D. J. Hourston****

* School of Physics and Chemistry, Lancaster University, Lancaster, England LA1 4YB
** TopoMetrix Corporation, Saffron Walden, CB10 1JD
*** ICI Paints, Slough SL2 5DS   **** IPTME, Loughborough University, LE11 3TU

We are combining *thermal analysis* with the ability of thermal waves to give sub-surface imageing at sub-micron resolution.[1,2] Our aim is that the image contrast will be determined by the "modulated-temperature differential scanning calorimetry" peak (M-T DSC[3]) or feature chosen according to the particular component of the specimen that is of interest. As described elsewhere,[4] this will allow us to distinguish in the image between reversible processes such as amorphous-to-glass transitions, from recrystallisations, cure reactions and other irreversible processes within the polymer.

The SThM probe gives micron-resolution images whose contrast is determined by spatial variations in thermal properties. Either the temperature at any point is held constant, or we generate and detect evanescent thermal waves whose penetration depth depends on the frequency chosen. The evidence[1] is that a 1 μm-radius probe in air will give a lateral resolution of ca. 200 nm, with a depth detection of a few μm. We have a special interest in polymer blends that exhibit two-phase behaviour, and are able to study the behaviour of single polymer domains when heated, in real time. We present results for PVC/PB, PEO/PB and PMMA/CPE. For example, Fig. 1 shows that in this last system, PMMA, which has a higher thermal conductivity than CPE, segregates into island-like domains in a matrix of CPE. Precisely-defined regions of the sample may be raised through a temperature range of interest, the heat being supplied by the probe itself, and transitions detected in real time[2] through changes in heat flow or temperature.

We have recently shown[5] that the dC_p/dT signal given by modulated-temperature DSC may be used to characterise multi-component polymeric systems with high resolution of differences in T_g: even for multi-phase networks, we can determine weight fractions of less than than 7%. The formation of interpenetrating polymer networks (IPNs) is an example of micro-scale *phase separation*. SThM has been used to reveal binodal decomposition by nucleation and growth, as against spinodal processes. In PVME/PS (Fig. 2), a nucleation and growth process is clearly identifiable: PS nuclei are seen to form and grown within the matrix. Intermediate miscibility blends are also observed, but they disappear as decomposition proceeds towards complete separation of the phases.

Finally we review a novel thermal characterisation technique, based on the third harmonic detection principle, to achieve spatially localised calorimetry.[2] For a number of polymers, we have thereby recorded events such as glass transitions, meltings, recrystallisations and thermal decomposition within volumes of material estimated at a few cubic microns.

References
1. A. Hammiche et al., *Measurement Science and Technology* **7** (1996) 142.
2. A. Hammiche et al., *J Vac Sci Technol* **B14** (1996) accepted for publication.
3. M. Reading, *Trends in Polymer Science* **1** (1993) 248.
4. N. S. Lawson et al., *Physica Scripta* **T55** (1994) 199.
5. M. Song et al., *Polymer* **36** (1995) 3313.
6. The project is funded by EPSRC, MOD, T A Instruments and the TopoMetrix Corporation.

1

a   **b**

2

3a

Nylon 6/6

Tm= 240 to 265 degrees C

First Derivative of Phase

Melting

0   100   200   **300**   400   500   600

Temperature(^{o}C)

3b   Poly(ethyl methacrylate)

Tg= 60 to 90 degrees C

First Derivative of Phase

Glass Transition

0   50   100   150   200

Temperature(^{o}C)

3c   Poly(ethylene terephtalate)

First derivative of phase

decomposition

Heat Flow
(conventional DSC result)

melt

glass transition

recrystallisation

0   100   200   300   400

Temperature ($^{\circ}$C)

FIG. 1 Scanning thermal microscopy images of a PMMA (poly methyl methacrylate)/CPE (chlorinated polyethylene) blend. **a** is a constant temperature or "dc" image (40°C), and **b** is a modulated temperature or "ac" image (5 $^{\circ}$C amplitude, 10 kHz) taken simultaneously. Area: 115×115 μm.

FIG. 2 Succession of thermal images showing a binodal phase separation process of a PVME (poly vinyl methyl ether) / PS (polystyrene) blend at 105°C over a period of 6 hours. Area: 120×120 μm.

FIG. 3 Localised thermal analysis fingerprints of **a** nylon 6/6, **b** poly (ethyl methacrylate) and **c** quenched poly (ethyl terephthalate). In **a** and **b**, characteristic plots obtained at two different locations on each sample are shown, to illustrate reproduceability. In **c**, the inset shows the heat flow obtained for a bulk sample using conventional calorimetry.

205

POLARIZED MICROBEAM FT-IR ANALYSIS OF SINGLE FIBERS

Liling Cho and David L. Wetzel

Kansas State University, Microbeam Molecular Spectroscopy Laboratory, Shellenberger Hall, Manhattan, KS 66502

Polarized infrared microscopy has been used for forensic purposes to differentiate among polymer fibers. Dichroism can be used to compare and discriminate between different polyester fibers[1], including those composed of polyethylene terephthalate that are frequently encountered during criminal casework. In the fiber manufacturering process, fibers are drawn to develop molecular orientation and crystallinity. Macromolecular chains are oriented with respect to the long axis of the fiber. It is desirable to determine the relationship between the molecular orientation and stretching properties. This is particularly useful on a single fiber basis[2]. Polarized spectroscopic differences observed from a single fiber are proposed to reveal the extent of molecular orientation within that single fiber. In the work presented, we compared the dichroic ratio between unstretched and stretched polyester fibers, and the transition point between the two forms of the same fiber. These techniques were applied to different polyester fibers. A fiber stretching device was fabricated for use on the instrument (IRµs, Spectra-Tech) stage. Tension was applied with a micrometer screw until a "neck" was produced in the stretched fiber. Spectra were obtained from an area of 24x48 µm. A wire-grid polarizer was used between the source and the sample.

Polarized infrared spectra were obtained with the IR beam polarized both parallel and perpendicular to the z-axis (length) of each fiber. Fig. 1 shows spectra of different polarizations of a single polyester fiber. Replicate experiments provided microbeam infrared data from polyester fibers typically stretched to 140% of their original dimensions. Dichroic ratios ($A_\parallel/A_\perp$) were calculated for six fundamental bands (876, 973, 1376, 1455, 1505 and 1509 cm^{-1}) and two overtone bands (1960 and 3435 cm^{-1}). Partial dichroic spectra ($A_\perp$ - $A_\parallel$) show negligible difference for an unstretched fiber (A, Fig 2) and dichroic changes (B, Fig 2) in opposing directions at 876 and 973 cm^{-1} after stretching. This changes is indicative of the molecular orientation that has resulted from stretching. After the fiber was stretched (140%), the dichroic ratios for bands at 876, 1376, 1455, 1960, and 3435 cm^{-1} decreased 64.4, 13.7, 1, 13.9, and 14.1% respectively. The dichroic ratios at 973, 1505, and 1579 cm^{-1} increased 106, 66.4 and 106% respectively. An example of molecular orientation change is shown in Fig. 3. The intensity of the 973 cm^{-1} C-O stretch of the *trans* ethylene glycol units is an indication of the degree of crystallinity. The unstretched fiber data indicate a *gauche* configuration of the ethylene glycol units that during stretching are converted to *trans* form. The dichroic ratio increased 106%, when the fiber was stretched to 140% of its original dimension. The differences between drawn, neck and undrawn portions are shown in Fig. 4. At band 1579 cm^{-1}, the dichroic ratio increased 24% from the undrawn to the neck portion, and 98% from the undrawn to the drawn portion. Because the intensity of these bands change with orientation produced by stretching, it is anticipated that they would differ with the draw ratio. Spectra of polyester fibers from the same manufacturer, but differing in draw ratios demonstrate that fact (Fig. 5). More crystallinity (from dichroic ratio evidence) resulted from a higher draw ratio (Table I). The dichroic ratios calculated from the data shown in Fig. 5 increased 23% from a draw ratio of 2.72 to 3.19 at 973 cm^{-1}, and decreased 12% at 876 cm^{-1}.

206

References

1. M. W. Tungol et al., *J. Forensic Sci.*, 36(1991)1027.
2. D. L. Wetzel and L. Cho, *Mikrochimica Acta*, 1996, in press.

| Table I. Dichroic Ratio | | |
| Frequency | Draw Ratio | |
(cm⁻¹)	2.72	3.19
876	0.49	0.43
973	1.31	1.64
1376	0.23	0.56
1455	0.71	0.96
1505	1.30	1.49
1579	1.36	1.49
1960	1.04	0.86
3435	0.64	0.63
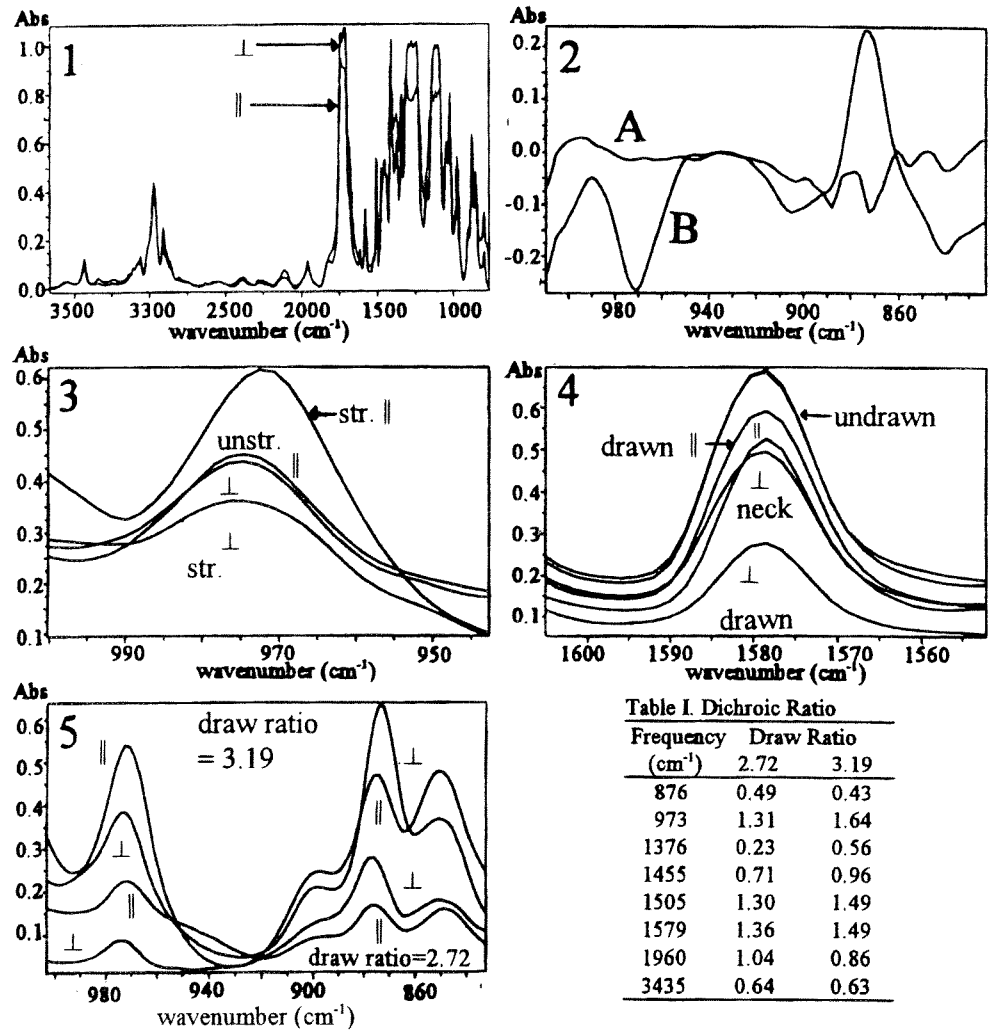
Figures 1-5 Spectra of single polyester fiber. FIG. 1 ⊥ and ∥, FIG. 2 partial dichroic spectra (unstretched A, stretched B), FIG. 3 ∥, ⊥, unstretched and stretched, FIG. 4 undrawn, neck and drawn parts of same fiber, FIG. 5 fiber with same composition but different draw ratios.

A SHEAR STABILIZED BIAXIAL TEXTURE IN A LAMELLAR BLOCK COPOLYMER

D. L. Polis,* B. S. Pinheiro,* R. E. Lakis,** and K.I. Winey*

*Department of Materials Science and Engineering, University of Pennsylvania, Philadelphia, PA 19104
**Laboratory for Research on the Structure of Matter, University of Pennsylvania, Philadelphia, PA 19104

Block copolymers spontaneously self-assemble into a variety of morphologies. Recent studies have produced a biaxial texture in poly(styrene-b-ethylene propylene), SEP, diblock copolymers by applying oscillatory shear.[1,2] This biaxial texture consists of "parallel" lamellae (normal to lamellae aligned perpendicular to shearing surfaces) and "transverse" lamellae (normal to lamellae aligned parallel to shearing direction) according to small-angle X-ray scattering, SAXS. The present study has determined how these two populations of lamellae are arranged and how they relax upon quiescent annealing by examining the superstructure via FE-SEM.

Sample preparation for the JEOL 6300 FE-SEM was designed to preserve a sample's orientation with respect to the shearing direction and provide a large viewing area (.1 - .3 mm^2) relative to what is typical with cryo-ultramicrotomed sections for TEM. Bulk samples were cut and mounted on a specimen stub with one of the 3 orthogonal directions of the shearing geometry oriented perpendicular to the stub surface. A smooth block face was created using cryo-ultramicrotomy. The block face was lightly coated with chromium and imaged in a FE-SEM at 2 kV. Ten to twenty adjacent images were taken digitally and combined using Adobe Photoshop 3.04 software, so that both the superstructure and microstructure of the lamellae could be investigated.

The nature of the biaxial texture is most evident in micrographs taken perpendicular to the shearing surfaces and parallel to the shearing direction (denoted as the 1 direction); see Figure 1. Samples having been sheared and then rapidly cooled show lamellae in the transverse orientation contained in bands. These bands are separated from the parallel lamellae by narrow tilt boundaries. A lower magnification composite image further indicates the banded superstructure of lamellae in either the parallel or transverse orientation as shown schematically in Figure 2. From this schematic it is apparent that the bands exist in two orientations which were characterized by the average angle of the bands relative to the parallel lamellae; ± 48° in this case.

Earlier SAXS studies indicate that the biaxial texture transforms into a predominantly parallel texture upon annealing.[2] FE-SEM images of samples annealed for 2 hrs following shearing indicate that the relaxation of the biaxial texture manifests itself as follows: The tilt boundaries widen as their curvature decreases. Furthermore, the previously transverse lamellae have apparently rotated so that their normals approach that of the parallel lamellae. Relaxation of the superstructure continues with further annealing, as evidenced by a sample annealed for 168 hrs after shearing (Figure 3), which shows focal conic type defects. Further analysis indicates that these relaxations occur primarily by the tilting of lamellae rather than twisting.

The morphology of the biaxial texture shows an astonishing resemblance to that of kink bands found in other layered systems:[3] rubber laminates, foliated rocks, card decks, oriented polymers. This suggests that the transverse lamellae may be the result of buckling in the parallel lamellae.

References
(1)   S. Okamoto et. al., *Macromolecules* **1994**, *27*, 5547.
(2)   B. S. Pinheiro et. al., *Macromolecules* **1996**, *29*, 1482.
(3)   E. Honea and A. M. Johnson, *Tectonophysics* **1976**, *30*, 197. N. C. Gay and L. E. Weiss, *Tectonophysics* **1974**, *21*, 287. R. E. Robertson, *Journal of Polymer Science: Part A-2* **1969**, *7*, 1315. S. J. DeTeresa et. al., *Journal of Materials Science* **1988**, *23*, 1886.
(4)   This research was funded by a University Fellowship (DLP), the NSF-MRSEC program, and the NSF-YIA program.
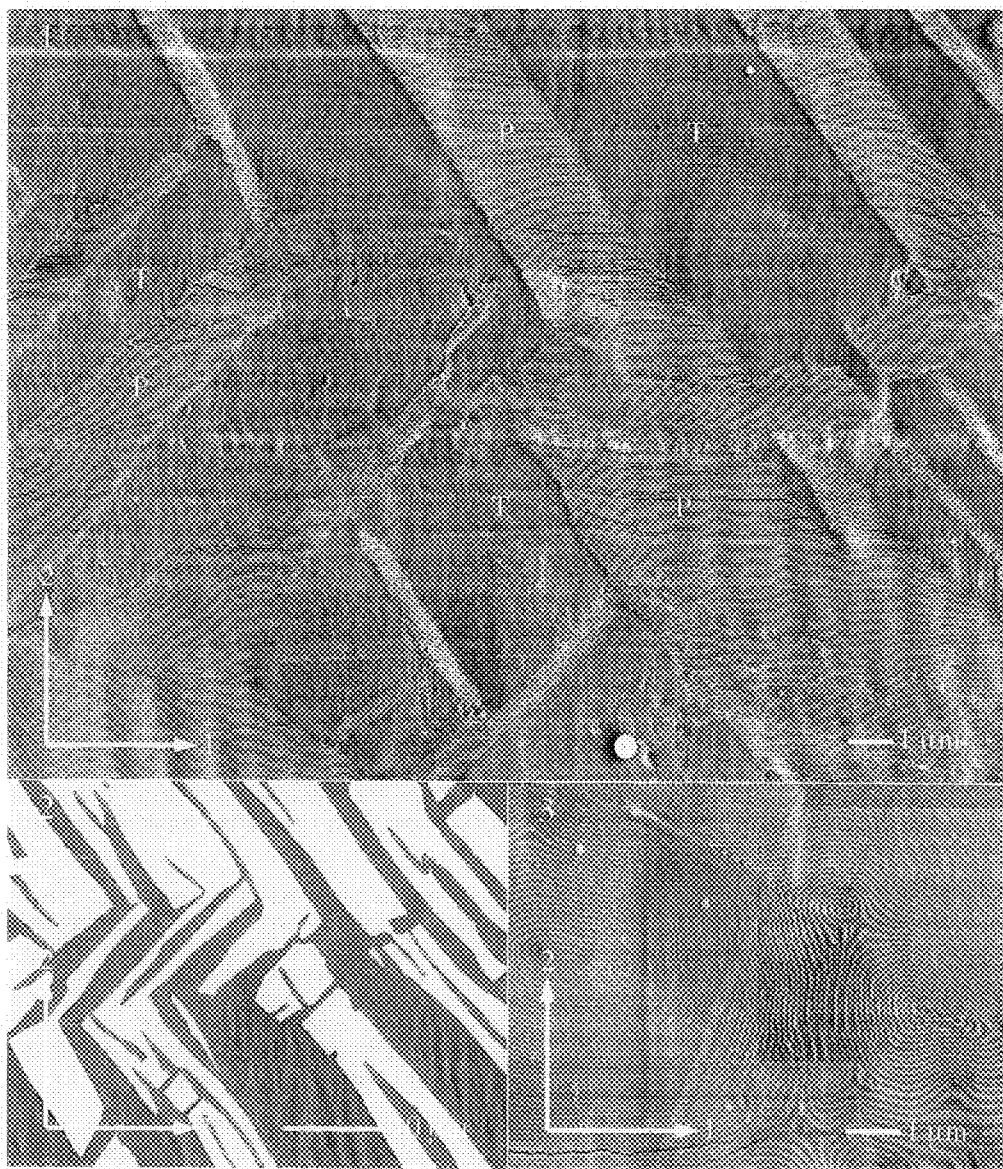
FIG. 1 FE-SEM micrograph of SEP as quenched after shearing shows both parallel (P) and transverse (T) lamellae coexisting to form a biaxial texture.

FIG. 2 Schematic based on a low magnification FE-SEM image of SEP as quenched after shearing. Dark and light areas represent parallel and transverse lamellae, respectively.

FIG. 3 FE-SEM micrograph of SEP after both shearing and a 168 hr anneal. Sample exhibits focal conic type defects.

ELECTRON MICROSCOPY OF Ni-Ti ALLOYS FOR MEDICAL DEVICES

Gary A. Smith[*] and Larry D. Hanke[**]

[*]Katz Analytical Services, Inc., Eden Prairie, MN 55344
[**]Materials Evaluation & Engineering, Inc., Plymouth, MN 55441

Nickel-titanium alloys (Ni-Ti) have many unique properties that make these alloys excellent prospects for a wide range of applications in medical devices.[1,2] However, these desirable mechanical properties cannot by utilized for many medical devices if the alloys cause undesirable reactions in the body or corrode from contact with body fluids or tissue.

The chemical inertness of Ni-Ti alloys is dependent on a passive film formed on the metal surface. Manufacturing processes, sterilization procedures, and general handling of the devices can have significant effects on the surface condition, and therefore, the corrosion and biocompatible behavior of Ni-Ti alloys.

An understanding of the passivation of Ni-Ti alloys, including the effects of mechanical processes, heat treating, and chemical surface alterations, is critical to ensure the benign presence medical devices in the human body. Two key factors in the understanding of passivation are surface morphology and surface chemical composition.

The material used in this study is a Ni-Ti alloy with a nominal composition of 50 at. % nickel and 50 at. % titanium. Coupons were annealed in an oxygen-rich atmosphere for variousannealing times. These annealed coupons were compared to samples of the same coupon before annealing.

Figure 1 shows an SEM micrograph of an as-received Ni-Ti coupon. The coupon surface shows many irregular shaped voids which may promote corrosion and other undesirable effects. Auger electron microscopy was also performed on this coupon and shows the presence of Ni and Ti as well as other impurities (see Fig. 2). After polishing most of these impurities are removed with the exception of small concentrations of Si, P, S, and Ca (see Figure 3).   The atomic concentrations of each of these coupons are shown in Table 1.

It is noted that the surface of both the as-received Ni-Ti coupon and the polished coupon show higher concentrations of Ti than found for Ni. This feature is also noted for the passivated coupons where the oxide layer appears to be mostly TiO_x with very little Ni present.

References

1. Y. Oshida and S. Miyazaki, *Corrosion Engineering*, 40(1991) 1009-1025.
2. D. E. Hodgson, et al., *ASM Metals Handbook*, 2(1990)897-902.
3. The authors gratefully acknowledge Shape Memory Applications, Inc., Santa Clara, CA for the Ni-Ti samples.
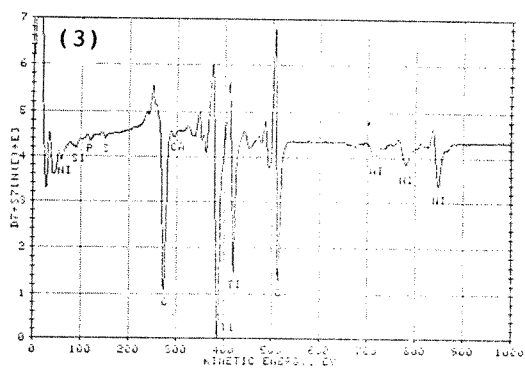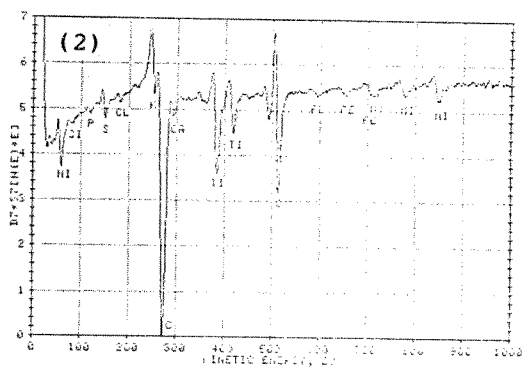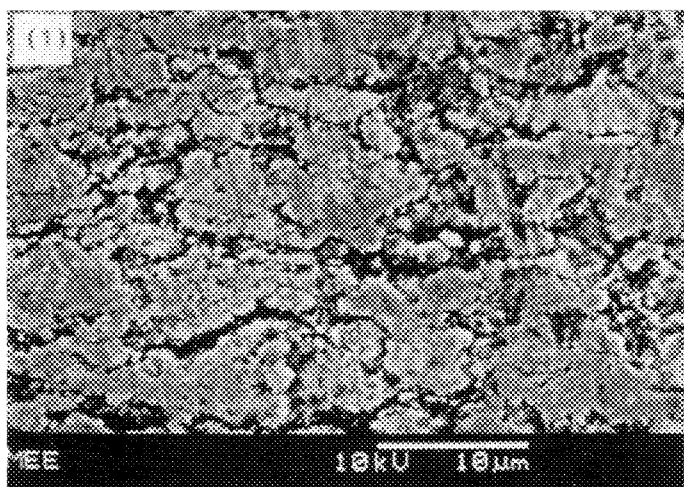
Table 1. Auger atomic concentrations of Ni-Ti coupons.

SAMPLE	C (at%)	O	Ti	Ni	Si	P	S	Cl	K	Ca
AS-RECEIVED	62.4	15.4	9.2	2.2	1.2	0.9	2.9	0.2	2.3	3.2
POLISHED	49.6	18.0	22.1	6.8	1.8	0.9	0.4	nd	nd	0.4

nd = not detected.

FIG. 1 SEM micrograph of as-received Ni-Ti alloy coupon.
FIG. 2 Auger survey scan of as-received Ni-Ti coupon.
FIG. 3 Auger survey scan of Ni-Ti coupon after polishing.

INVESTIGATION OF FILM FORMATION IN WATER-DISTRIBUTION SYSTEMS BY FIELD-EMISSION SEM AND SPECTROSCOPY TECHNIQUES

J. Liu*, R. M. Friedman*, E. Cortez*, F. Pacholec+ and S. M. Vesecky*

* Monsanto Corporate Research, Monsanto Company, 800 N. Lindbergh Blvd., St. Louis, MO 63167
+ Performance Materials, Monsanto Company, 800 N. Lindbergh Blvd., St. Louis, MO 63167

EPA has set limits on the concentration of heavy metals in drinking water supplies to protect the public health. Furthermore, the failure of pipes in the water distribution system from corrosion represents a massive investment in rebuilding its infrastructure. We have initiated a program to study the formation of corrosion-inhibition films formed in potable water delivery systems using various chemical phosphate treatments. In particular, blends of ortho- and polyphosphates have recently been used to reduce both lead and copper leaching.[1,2] Several factors are important to the successful implementation of the phosphate technologies, including film thickness and porosity, rate and stability of formation and water quality conditions. In an attempt to understand the performance of these phosphate blends, advanced analytical techniques have been employed to study the nucleation and growth mechanisms of the passivation films in a variety of water systems. We report here some preliminary results on the study of the film formation by field emission scanning electron microscopy (FESEM) technique.

Copper and lead test coupons were exposed to the flowing water stream in pipe loops at several different municipal water delivery systems. These test coupons were then dried under vacuum at ambient temperatures and were cut into 1 cm^2 pieces for analysis. The surface morphology of the Pb and Cu test coupons was directly observed in a high resolution FESEM (Hitachi S-4500) without prior coating. Low incident beam voltages (1 to 2 kV) were used to prevent sample charging effects since the passivation films were non-conducting. Chemical specification and compound identification of the films were accomplished by combining XPS and infrared spectroscopy techniques.

Test coupons subjected to different treatment times were investigated to extract information about the growth processes of the protective films. FESEM images clearly revealed only limited film growth at short time exposure. After two months there was still only a discontinuous film formed on either the copper or lead surfaces. The passivation phases also preferentially nucleated on certain sites on the test coupons and developed into a continuous porous film in later stages. Figure 1a shows a low magnification FESEM image of a copper coupon surface after approximately 7 months exposure. The rough surface morphology suggests that the growth of the passivation film was not uniform. Figure 1b shows a corresponding high resolution image revealing the high porosity of the passivation film. The surface morphology of the lead coupons was not significantly different from that of the copper coupons. XPS and infrared spectroscopy results suggested that the passivation films were composed, at least partially, of basic lead carbonate (PbCO$_3$·Pb(OH)$_2$) and basic copper carbonate (CuCO$_3$·Cu(OH)$_2$) for lead and copper coupons, respectively. Other cations which were present (e.g., Fe and Mn) also appeared to become incorporated in the passivation films with different effects on the final efficacy of the film towards corrosion inhibition. The corrosion of lead and copper depends on transport of dissolved reactants to the metal surface, reaction at the surface, and transport of dissolved products from the reaction sites. Therefore, the corrosion rate will reflect the diffusion of reactants and products through the protective film and their dissolution at the surface. A high density and thick passivation film may be more effective in reducing the corrosion rate. Figure 2 shows a cross-sectional view of the protective film on a copper coupon after approximately 7 months exposure. A thick, but highly porous, passivation film was formed on the copper surface. The protective qualities of these passivation films will be discussed.

References

1. C. A. Chen et al., *J. Environmental Science and Health*, A29(1994)1587
2. R. M. Friedman et al., *Proc. 1994 Water Quality Technology Conference*, Part I(1995)341.
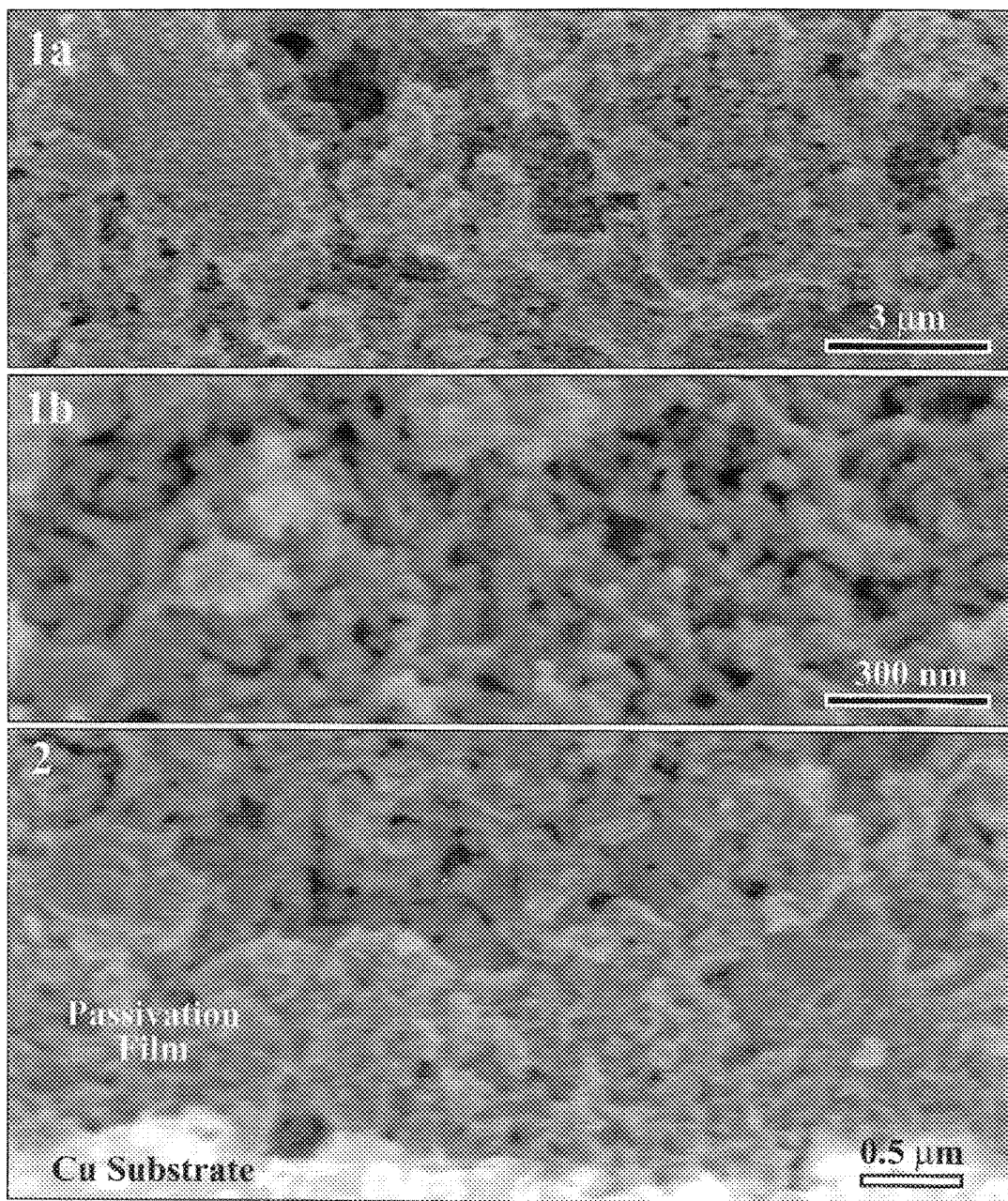
Fig. 1----Plan-view FESEM images of passivation film on copper coupon (7 months exposure).
Fig. 2----Cross-sectional FESEM image of copper coupon showing thick coating of passivation film.

213

MICROPROBE STUDY OF DIODE CORROSION[1]

Paul Hlava, Jeff Braithwaite, and Rob Sorensen

Materials and Processes Sciences Center, Sandia National Laboratories, Albuquerque, NM 87185

A few diodes from a production lot were discovered to have unacceptable current leak rates after about 5 years of storage. Inspection revealed the presence of copper sulfide deposits that bridged the external body of the diode and presumably provided a leakage path. Figure 1 shows the physical configuration of a diode. The function of this device is performed by a silicon-based semiconductor that is bonded between two cylinders of tungsten with copper headpins (Cu wire with a flat "nail-head" formed on one end) brazed to the opposite ends of the cylinders. A toroidal ring of glass protects the Si chip. All exposed metal parts are covered by an immersion plating of Ag. Then the entire assembly is coated with black epoxy and a band of green ink is applied to the cathode end. During storage, each diode was placed in a cardboard holder and secured in stacks of about ten with rubber bands.

Analytical and environmental exposure studies were performed at Allied Signal and Sandia to determine the cause and potential long-term significance of this corrosion-related degradation problem. The objective of the analytical work was to characterize the corrosion product and help identify the corrosion mechanism. Tools included optical microscopy, scanning electron microscopy, electron microprobe analysis, SIMS, and x-ray diffraction. Cu and Ag test samples were exposed to various environments to identify potential sulfur sources. Diodes were exposed to both mildly and highly accelerated environments (simulating 10 years of corrosion in 2 weeks) to determine the stability of the existing corrosion products and to duplicate the corrosion process under accelerated conditions.

Figure 2 shows SEM and back-scattered electron images of the Cu-Ag-P braze alloy used to attach the Cu headpins to the W cylinders. The braze alloy consists of bright grains of Ag, medium gray grains of pure Cu, and a matrix of slightly darker, P-bearing Cu. A thin Ag layer is visible on the outside surface of the braze material in direct contact with the Ag and the Cu+P but is apparently bridged across the corrosion pits in the pure Cu. Careful examination of SEM images and associated elemental maps revealed that there is a low density material partially filling the pits that contains Ag, Cu, P, C, and O. Overlying the metallic materials are two layers of organic materials that thin to less than 5 μm over the braze areas (see Figure 2b). The inner layer contains particles of Al+Si+O and Cu+Cr+O. The outer layer contains Cl, S, and Ti in addition to the C. This outside layer appears to be homogeneous; it does not show discrete particles at this scale. Many of the corroded grains are partially filled with the inner organic material. All three diodes that were examined (clean, moderately corroded and, heavily corroded) exhibited similar characteristics.

Existence of epoxy in Cu grain voids but over the Ag layer indicates that preferential corrosion occurred during the Ag-plating operation. Solution was trapped in the gaps, and probably under the Ag plate. After fabrication, hydrated Cu-bearing salts remained. Even so, the majority of the copper oxidation probably took place during the plating operation. During storage at AS, moisture condensed in the pores of the epoxy and served as a solvent and, potentially, as an electrolyte for even further corrosion. The dissolved Cu diffused to the surface and was subsequently sulfidized by the off-gas product from the rubber bands. Cu_2S is enough of an ionic and electronic conductor that it caused the diodes to leak.

The probable cause of the diode degradation is tied to a series of problems. First is the incompatibility of the P-bearing braze material with the Ag immersion plating solution (cyanide-based) which caused the preferential corrosion and the presence of trapped solution. Next is the lack of a significant barrier to prevent capillary condensation. Long storage-term in a environment containing sulfur-bearing species and sufficient humidity completed the conditions needed to compromise the diodes.

References

Figure 1. SEM image of the diode at 40x showing the basic construction
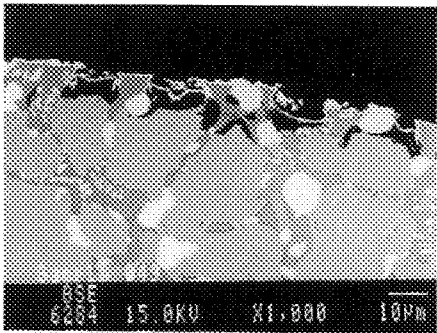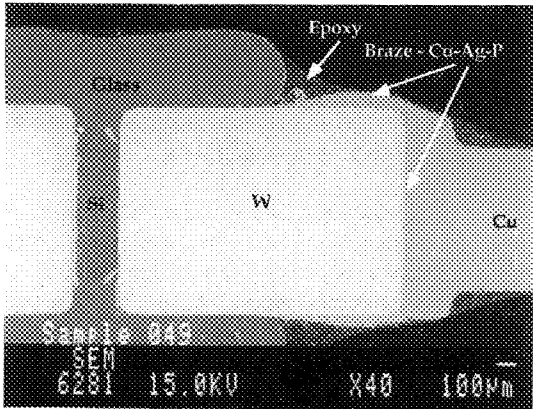
(a)
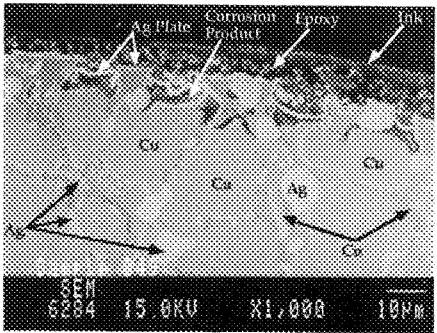
(b)

Figure 2. SEM (a) and BSE (b) images of the surface of the braze showing the three phases of the braze, the Ag-plating, the trapped Ag + Cu + P + C + O corrosion product, the epoxy, and the ink

CHARACTERIZATION OF ALUMINUM BONDING PAD CORROSION BY ELECTRON MICROSCOPY

J.E. Klein

Department of Materials Science and Engineering, University of Arizona, Tucson, AZ 85721

One leading factor of integrated circuit (IC) reliability today deals with the identification and prevention of aluminum bonding pad corrosion. Using three common IC industry conductors, namely aluminum (99.999%), aluminum-copper(0.5%) and aluminum-silicon(1.0%), samples were fabricated and analyzed by FE-SEM/EDS after various IC processing steps.

Samples consisted of boron doped (P type) <100> silicon wafers which were processed according to a standard fabrication procedure. Metal deposition was performed using a metal sputter system with an RF field and heated stage. To examine deposition temperature effects, stage temperature was varied from 200 to 300°C for each conductor type. Wafers were processed through normal fabrication with one wafer from each deposition temperature and metal type being examined after various processing steps. In addition, samples were also subjected to accelerated testing by exposure to a Pressure Cooker Test (PCT) at 120°C, 1.5 atm for 24 hours. In order to characterize the effects of oxide growth of the different metals, sputter deposited samples of each conductor as processed earlier but at one stage temperature, were microsectioned and examined by TEM.

Analysis of the samples indicate that through each parameter examined, both aluminum and aluminum-silicon (1.0%) contained large metal grains and some voiding or grain dislocations. These samples also exhibited some degree of intergrannular separation (Fig. 1-2). Conversely, it was found that the aluminum-copper (0.5%) metal displayed smaller metal grains with significantly less intergrannular separation as shown in Fig. 3. Additionally, only the copper doped metal failed to show significant $Al(OH)_3$ growth evident in aluminum corrosion[1] even after PCT. TEM microsections of the films revealed that aluminum oxide layers present all approached the same thickness of about 45 Å (Fig 4). DC Potentiodynamic polarization of the metals also showed that the aluminum-copper (0.5%) films had better resistance to corrosion than the other metals.

Although the addition of copper to aluminum metal has historically shown to increase corrosion due to copper migration and increased grain boundary area, the samples examined in this study contradict those findings. As observed by the FE-SEM micrographs, although the copper doped metal contained smaller grains yielding greater boundary areas, less intergrannular separation was observed. This characteristic prevented the entrapment of ionic contamination during processing leading to a greater resistance to corrosion than the other metals.

Reference
1. F. Neighbour, B.R. White, "Factors Governing Aluminum Interconnection Corrosion in Plastic Encapsulated Microelectronic Devices", *Microelectronics and Reliability*, vol 16, p161-164 (1977).
2. The author gratefully acknowledges the use and support of the facilities at Burr-Brown Corporation as well as the guidance and assistance of Dr. Supapan Seraphin.
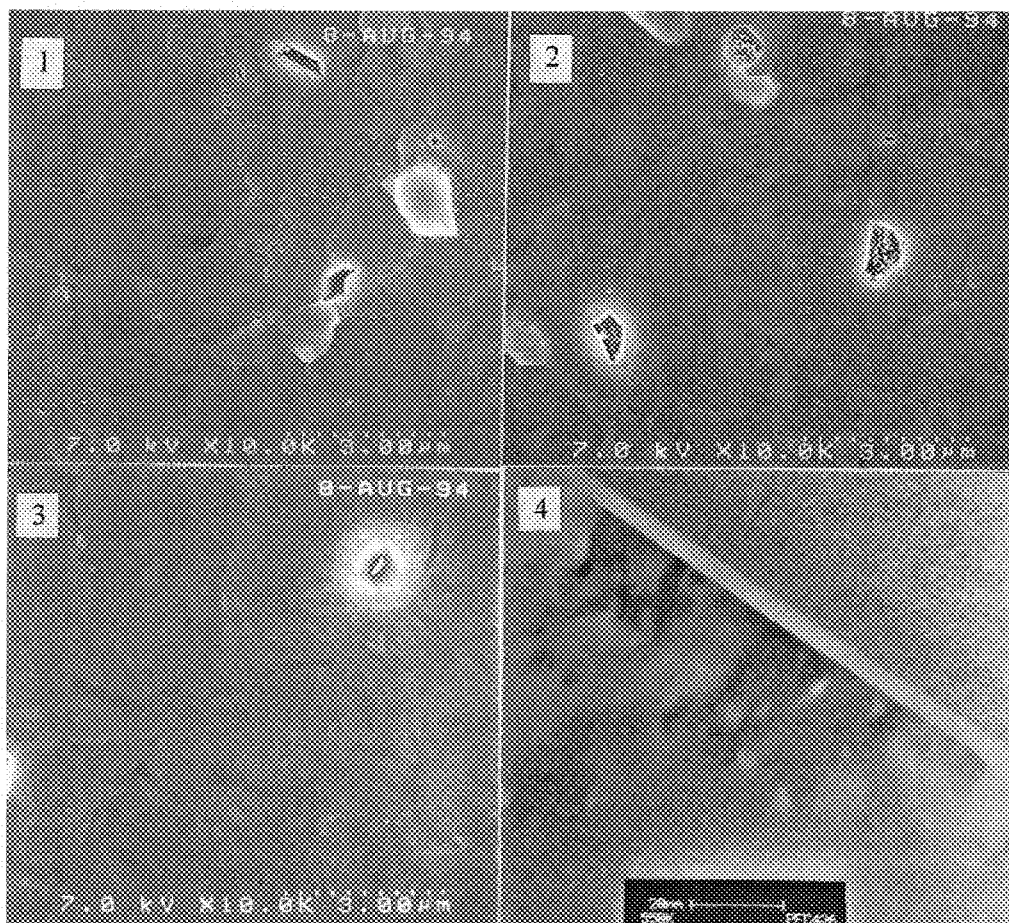
FIG. 1 Sputtered Aluminum (99.999%) bonding pad following fabrication.
FIG. 2 Sputtered Aluminum-Silicon (1.0%) bonding pad following fabrication.
FIG. 3 Sputtered Aluminum-Copper (0.5%) bonding pad following fabrication.
FIG. 4 Aluminum-Copper (0.5%) film microsection through aluminum oxide layer.

SELECTIVE CORROSION OF BRAZED JOINT BETWEEN BNi-2 FILLER METAL AND STAINLESS STEEL 316

H. S. Kim and R. U. Lee

LO-MSD-1, NASA, Kennedy Space Center, Florida 32899

A heating element/electrical conduit assembly used in the Orbiter Maneuvering System failed a leak test during a routine refurbishment inspection. The conduit, approximately 100 mm in length and 12 mm in diameter, was fabricated from two tubes and braze-joined with a sleeve. The tube on the high temperature side (heating element side) and the sleeve were made of Inconel 600 and the other tube was stainless steel (SS) 316. For the filler metal, a Ni-Cr-B brazing alloy per AWS BNi-2, was used. A Helium leak test spotted the leak located at the joint between the sleeve and SS 316 tubing. This joint was dissected, mounted in a plastic mold, polished, and examined with an optical microscope. Debonding of the brazed surfaces was noticed, more pronounced toward the sleeve end which was exposed to uncontrolled atmospheric conditions intermittently. Initially, lack of wetting was suspected, presumably caused by inadequate surface preparation or incomplete fusion of the filler metal. However, this postulation was later discarded based upon the following observations: (1) The angle of wetting between the fillet and tube was small, an indication of adequate wetting, (2) the fillet did not exhibit a globular microstructure which would be an indication of insufficient melting of the filler metal, and (3) debonding was intermittent toward the midsection of the sleeve.

The brazed joint was examined with SEM and WDS (Fig 1 through 4). Three different regions could be noticed from nickel and silicon x-ray line scans (Fig 1 and 2), and x-ray dot maps (Fig 2 and 4); SS 316 (containing 10% Ni), BNi-2 type filler metal (containing 82% Ni and 5% Si), and Inconel 600 (containing 73% Ni). The brazing alloy also contains about 3% boron, the presence of which was verified with WDS, but could not be quantitatively analyzed due to weakness of signal. Debonding occurred at the filler metal/SS 316 interface whereas the filler metal/Inconel 600 interface was unaffected. Literature reports a failure mechanism for boron-containing SS 304 based upon grain boundary precipitation of boride[1,2]. A discussion with a manufacturer of BNi-2 type filler metal confirmed that the same mechanism could cause debonding between the filler metal and SS 316 as boron would diffuse a short distance into SS 316 along the grain boundary, creating a pre-existing path of preferential corrosion[3]. It was therefore concluded that corrosion started and propagated along the BNi-2/SS 316 interface where corrosion resistance was lowered due to boride precipitation.

References

1. T. Gladman, Materials Performance, vol. 28, no. 2 (1989) 60
2. E. A. Loria, J. Metals, vol. 32, no. 12 (1980) 10
3. R. Peaslee, private communication
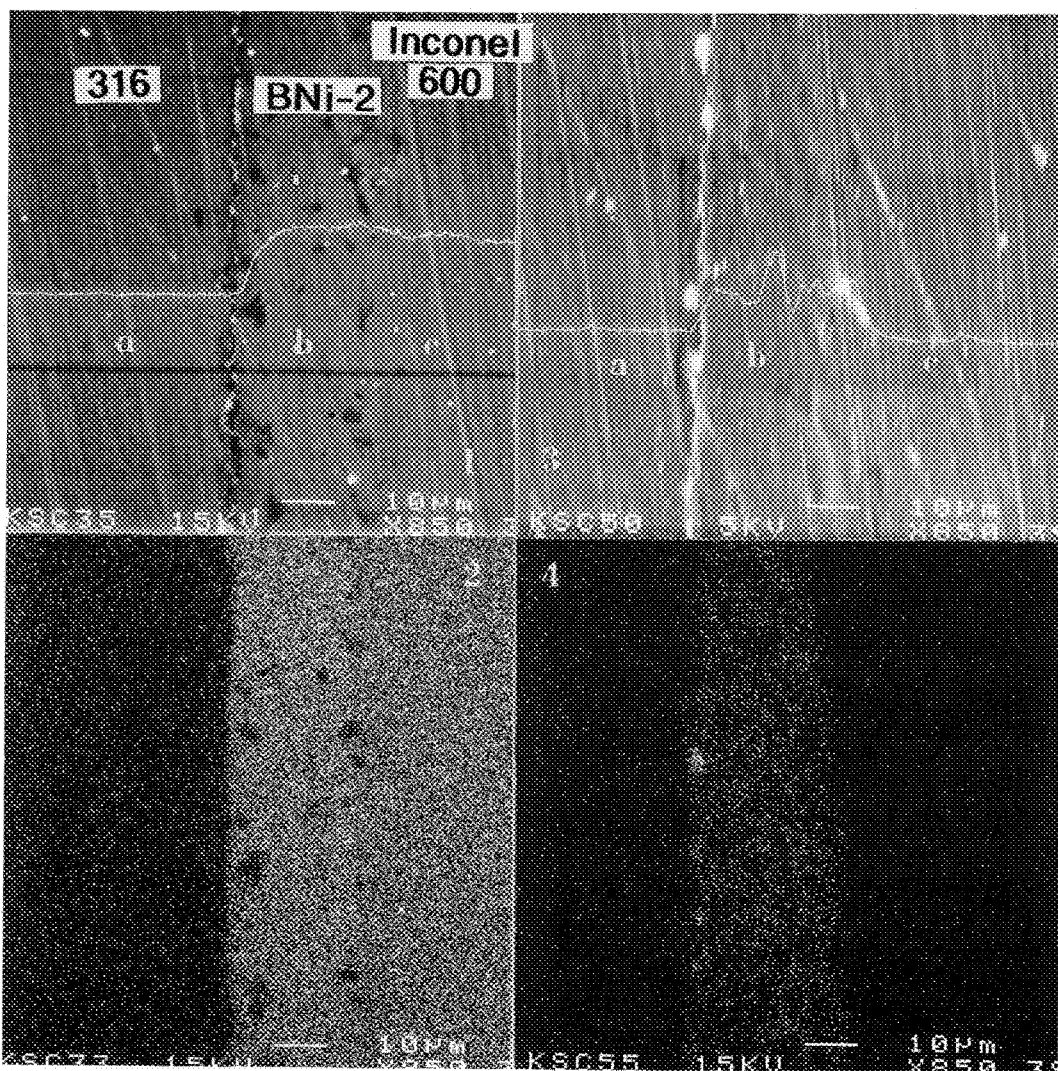
Fig. 1 SEM of stainless steel (a), filler metal (b), and inconel (c) with nickel x-ray line scan.
Fig. 2 Nickel x-ray dot map of Fig. 1.
Fig. 3 SEM of stainless steel (a), filler metal (b), and inconel (c) with silica x-ray line scan.
Fig. 4 Silica x-ray dot map of Fig. 3.

TEM STUDY OF A BIOFILM ON COPPER CORROSION

W. A. Chiou[1], N. Kohyama[2], B. Little[3], P. Wagner[3], and M. Meshii[1]
1. Department of Materials Science and Engineering, Northwestern university, Evanston, IL 60208
2. Department o f Occupational Diseases, National Institute of Health, Kawasaki 214, Japan
3. Naval Research Laboratory, Stennis Space Center, MS 39529

The corrosion of copper and copper alloys in a marine environment is of great concern because of their widespread use in heat exchangers and steam condensers in which natural seawater is the coolant. It has become increasingly evident that microorganisms play an important role in the corrosion of a number of metals and alloys under a variety of environments.[1,2] For the past 15 years the use of SEM has proven to be useful in studying biofilms and spatial relationships between bacteria and localized corrosion of metals.[3,4] Little information,[5] however, has been obtained using TEM capitalizing on its higher spacial resolution and the transmission observation of interfaces. The research presented herein is the first step of this new approach in studying the corrosion with biological influence in pure copper.

Commercially produced copper (Cu, 99%) foils of approximately 120 μm thick exposed to a copper-tolerant marine bacterium, *Oceanospirillum*, and an abiotic culture medium were subsampled (1 cm x 1 cm) for this study along with unexposed control samples. All samples were fixed in 3% glutaraldehyde at 4 °C for overnight, buffered at pH of 7.3 with 0.2 M cacodylate, and post fixed in 1% osmium tetroxide for 1-2 hrs. at room temperature. Subsamples were then dehydrated through a graded seawater/deionized water and deionized water/acetone series. Dehydrated samples were trimmed to a small triangular shape and put into a BEEM capsule filled with Spurr embedding medium. Ultrathin cross sections were cut with a diamond knife on a Sorvall MT-2 ultramicrotome, and stained with uranyl acetate for 20-30 minutes and lead citrate for 5 minutes to improve the contrast. To preserve the integrity of ultrathin sections, specimens were coated with a thin layer of carbon.

TEM micrographs have clearly demonstrated the effect of microorganism on copper foil. Results from unexposed and abiotic control copper foils were rather similar (Figs. 1 and 2), showing clean, uncorroded/undamaged surfaces without microorganisms and organic films. This "clean surface" is similar to those prepared by the ion milling technique (Fig. 3) which may destroy biofilms during the process of thinning. The surface of abiotic exposed Cu foils reveals that there is no observable change in microstructure and morphology. This may indicate that there is no detctable chemical and/or other reactions in the abiotic medium during the exposure period. In contrast, as shown in Figs. 4 and 5, ultrathin sections of Cu foil exposed to *Oceanospirillium* depicted many micropores near a ragged surface, bacteria and organic matter in a slime layer floating within 10 μm of the Cu foil, Cu particles detached from the Cu foil, and Cu particles suspended in Spurr epoxy. A montage of TEM image (Fig. 5) shows a typical slime film/layer consisting of microorganisms, presumably *Oceanospirillium*, and detached Cu particles on the surface of Cu foils. It also shows some cell walls bending and enclosing fine (1-2 μm) ultra dark and rounded particles while other cells contained even finer particles. The ultra dark and rounded particles were identified as Cu by electron diffraction and microchemical analyses (Fig. 6). The high amounts of Cu associated with cells may indicate that Cu uptake by bacteria or chemical bonding between the organism and copper. Nevertheless, further studies are required to know whether copper is directly absorbed or consumed by microorganisms and to understand the role of micoorganisms in copper corrosion.

1. G. C. Llewellyn and C. E. O'Rear, eds., Biodeterioration, the 6th International Biodeterioration Symposium: C.A.B. International Mycological Institute, The Biodeterioration Soc.,U.K. (1986)
2. B. Little et al., International Materials Review, 36: 253-272 (1991), and cited references.
3. V. K. Gouda et al., Corrosion Engineering, 49: 63-73 (1993)
4. S. P. Collins et al., Microscopy Res. & Tech., 25: 398-405 (1993)
5. G. Blunn, *in* reference 1.
6. This research was funded by the Naval Research Laboratory, and made use of MRL Central Facilities supported by the NSF, at the MRC of Northwestern University, under award No. DMR-9120521.
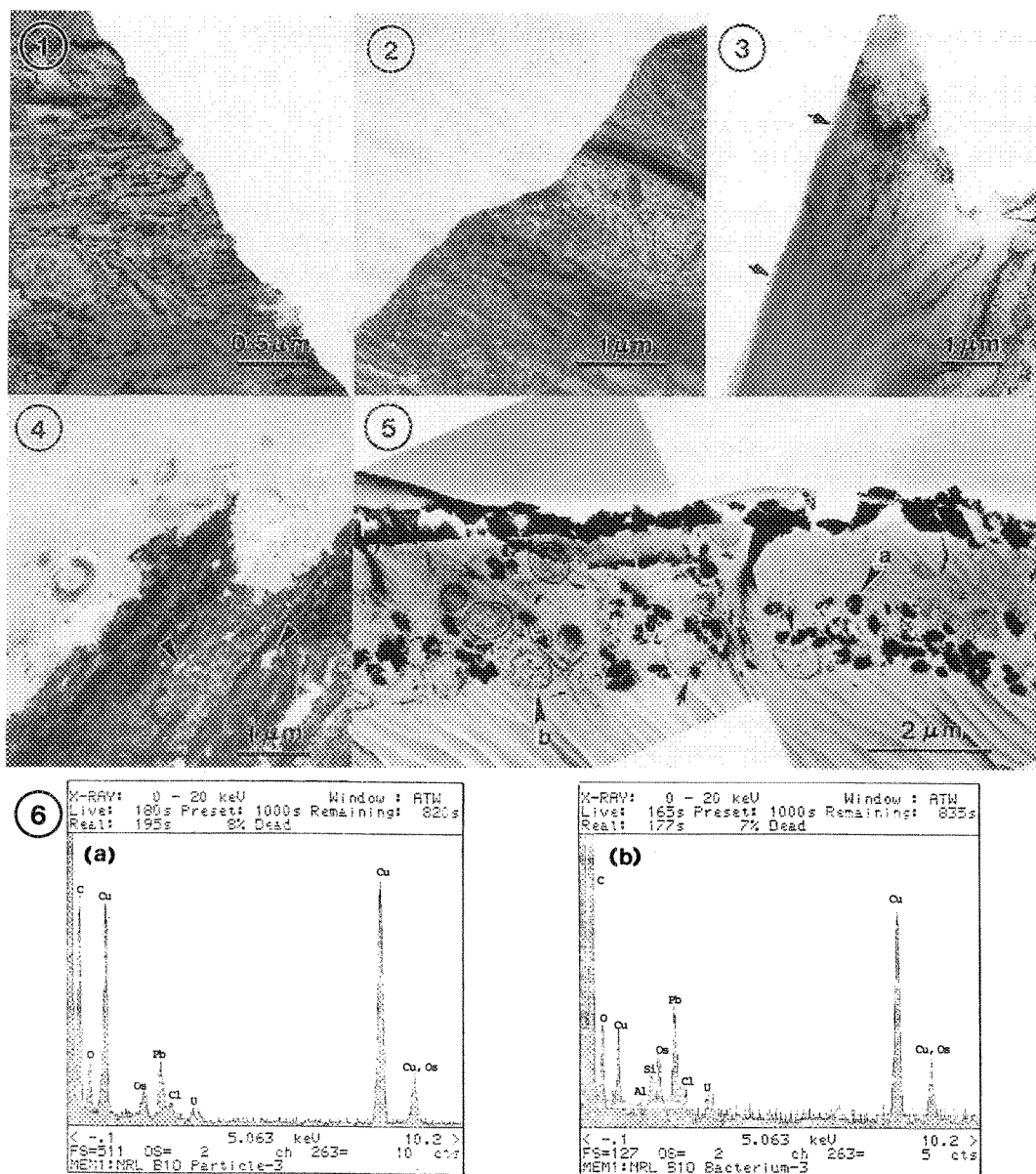
Fig. 1. TEM micrograph depicting the surface of an unexposed Cu foil.
Fig. 2. TEM micrograph revealing the clean surface of an abiotic control Cu foil .
Fig. 3. TEM micrograph of the surface (arrows) of an unexposed Cu foil thinned by ion milling.
Fig. 4. TEM image showing a ragged/corroded surface, micropores (arrows) in a biotic exposed Cu foil.
Fig. 5. TEM image showing a typical slime layer containing abundant bacteria remains and dispersed
   rounded particles. Note the bending of bacteria's cell wall and engulfing dark particles (arrows).
Fig. 6. EDS pattern of a dark particle (a), and of a bacterium remain (b) shown in Fig. 5.

Fracture Investigation of Fe-Zn Alloy Coating on Steel Sheets After Deformation

Yuli Lin And Wen-Shen Hou
Department of Mechanical Engineering
Chua-Hwa Polytechnic Institute, Hsinchu, Taiwan ROC

Steel coating technology has made great progress in recent years to meet the demand for corrosion-resistant steel. Fe-Zn coated steel sheet is one of those which has been developed with increasing production in response to the brisk demand in the automobile, construction and household electrical appliance industries[1].

The adhesion of coating to substrate is a critical property of any coating system for mechanical integrity and environmental protection of the substrate. The investigation of fracture on the coating layer and/or on any interfaces after deformation, specially the initiation of failure provides fundamental acknowledge to understand major factors contributing to the adhesion of coatings. This paper presents the results of fracture on Fe-Zn alloy coatings on steel sheets after deformation.

Samples of commercial produced hot-dipped galvanized coating were used. To investigate the fracture on the coating layer and/or any interfaces, thick coating layer specimens (about $50\mu m$ of thickness) which were utilized mainly on the construction industries. Several heating conditions were also applied to increase the thickness of particular phase layers (such as Γ or Γ_1 layers). The specimens were then tested in the pure shear mode[2]. Fig. 1 illustrates the sample mounting configuration used in the modified lap-shear test. It was found that the test must be terminated at the right moment in order to observe the crack initiation of the coated layer. The metallographically cross-section specimens were prepared to observe the structure and fracture of coating layer both before and after test.

Fig. 2 shows the cross-sectional microstructure of as-received specimen. It illustrates that ζ phase layer is dominant with η phase on the top of the coated layer and δ phase layer close to the steel substrate. Fig. 3 reveals the fracture of the coating layer on the as-received specimen. It clearly shows that failure (cracks) starts at the δ phase layer (as arrow indicated in the figure). Since the Γ or Γ_1 phase layer was not observed (or to thin to observe) on the as-received specimen, three heat-treated conditions was then applied (500°C, 550°C and 650°C for one hour) to increase the thickness of these two phase layers. Figs. 4 through 6 show the fracture of the coating layer with different heat-treated conditions. The results illustrate that the failure of all the specimens starts also at the δ phase layer without any influence of Γ or Γ_1 phase layers.

In summary, the investigation of fracture of coating layer shows that the failure of all the specimens after deformation starts at the δ phase layer despite the thickness of the Γ or Γ_1 phase layers. This result indicates that the δ phase layer is the most brittle area rather than any other phase layers or interfaces.

1. T. Hada, Nippon Steel Technical Report, No.63, Oct., 1994.
2. W.-S. Hou, Master Thesis, Chua-Hwa Polytechnic Institute, 1995.
3. This research is supported by NSC 84-2216-E216-001.
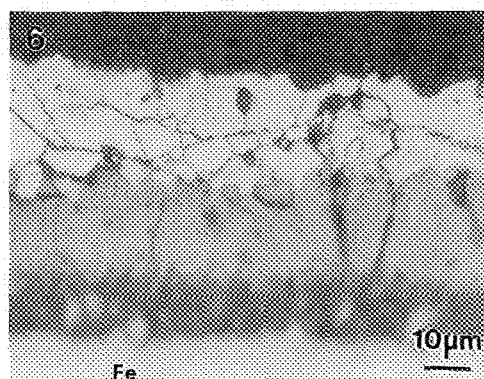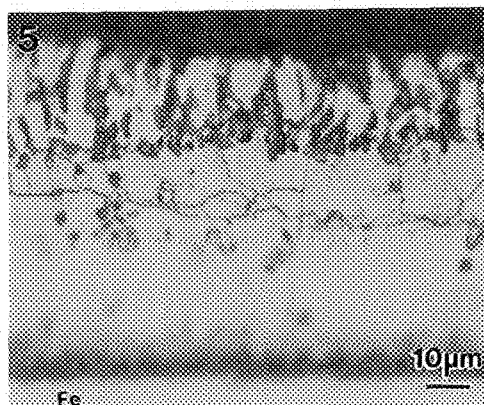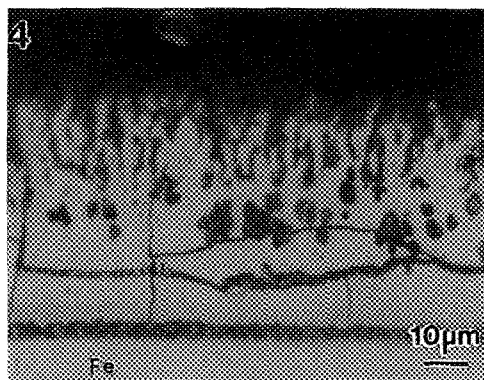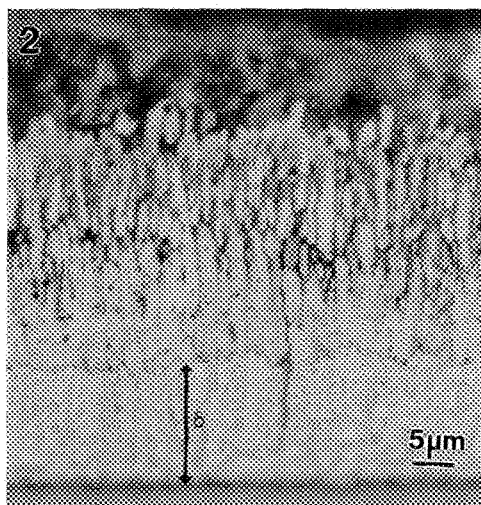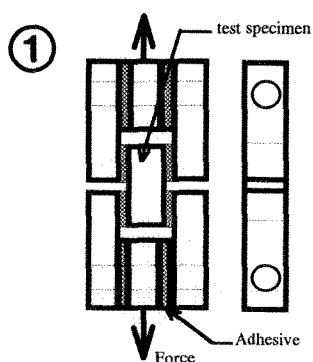
Fig.1 Mounting configuration used in the modified lap-shear test.
Fig.2 Cross-sectional microstructure of as-received specimen.
Fig.3 Fracture structure of as-received specimen (cracks as arrow indicated).
Fig.4 Fracture structure of specimen as heated at 500°C for 1 hour.
Fig.5 Fracture structure of specimen as heated at 550°C for 1 hour.
Fig.6 Fracture structure of specimen as heated at 650°C for 1 hour.

NANO-CHARACTERIZATION OF Rh-Sn BIMETALLIC CATALYSTS

P.A. Crozier and P. Claus*

Center for Solid State Science, Arizona State University, Tempe, AZ 85287-1704
*Institut für Angewandte Chemie, Berlin-Aldershof e. V., Abteilung Katalyse, Rudower Chausee 5, D-12489 Berlin, Germany

Bimetallic catalysts are of considerable importance because they possess both high activity and selectivity. Recently, there has been considerable interest in bimetallic catalysts produced by surface organometallic chemistry on metals[1,2]. A detailed description of the structure and composition at the nanometer level is critical to fully understand the behavior of such catalysts. We have undertaken a study of the microstructure of Rh-Sn/SiO$_2$ bimetallic hydrogenation catalysts.

A Rh-Sn precursor was prepared by reacting tetrabutyltin with a silica supported Rh parent catalyst (1%Rh/SiO$_2$). The bimetallic catalysts were produced by thermal decomposition of the precursor in flowing hydrogen at 623 K. Five different catalysts were produced with a range of different Sn loadings from Rh(1%)/SiO$_2$ to Rh(1%)-Sn(1.85%)/SiO$_2$. The resulting bimetallic catalysts were able to selectively hydrogenate isolated and conjugated C=O functional groups. In situ XPS showed that the Sn and Rh were in the fully reduced state. Mossbauer spectroscopy studies confirmed that Sn was present in the zerovalent state indicating that no oxidized Sn was present. Preliminary IR data suggests that most of the Rh atoms are isolated from their neighbors (presumably by Sn).

Samples were prepared for electron microscopy by grinding the catalysts and dispersing the fine powders over holey carbon films. A series of bright-field images were recorded from each catalyst using a Zeiss 912 energy-filtering electron microscope (EFEM). The contrast from the small metal particles was enhanced by filtering out the inelastic scattering. A typical image and size distribution from the Rh parent catalyst is shown in figure 1a and b. The image shows small Rh particles 10 - 30 Å in size dispersed on amorphous SiO$_2$ particles 200 - 300 Å size. The average particle size was about 20 Å. Figure 2a is recorded from the bimetallic catalyst with the heaviest Sn loading (Rh 1%, Sn 1.85%). The morphology is essentially identical to the parent catalyst and the particle size distribution (fig 2b) again had a mean particle size of about 20 Å. This suggests that no sintering occurs during the heating of the Rh-Sn complex and that differences in catalytic properties are related mainly to the effect of Sn. The dispersions calculated from the electron micrographs were 56 % for the parent catalysts and 66 % for the bimetallic catalyst. The difference in dispersion is attributed to the presence of some larger particles in the parent catalyst (around 500 Å in size) that were not detected in the bimetallic catalyst.

An energy dispersive x-ray spectrometer (EDX) on a VG HB501 scanning transmission electron microscope(STEM) was employed to measure the composition of the small particles in the bimetallic catalysts. The STEM is capable of forming small focused electron probes of about 5 Å in diameter. Preliminary EDX measurements showed that Sn mass loss occurred during irradiation and that the particles were rather mobile on the surface of the silica support. This effect was reduced by using a small virtual objective aperture to limit the beam current and limiting the EDX acquisition time to 60 -120 s. Typical EDX spectra from 20 Å particles are shown in fig 3a and b. The spectra, though noisy, show a variation in the Sn/Rh ratio of up to 50 % between different particles. This variation appears to be random and does not correlate with particle size[3].

References

1. J. P. Candy et al, *J. Catal.* 112(1988)210
2. P.Lesage et al, *J. Catal.* 155(1995)238
3. This work was supported by the HREM Industrial Associates Program of Arizona State University (ASU) and was performed in the Center for HREM at ASU.
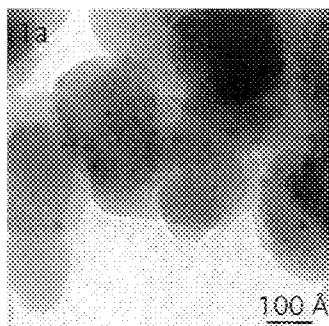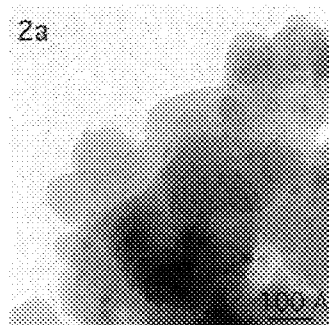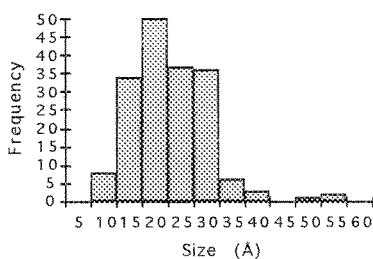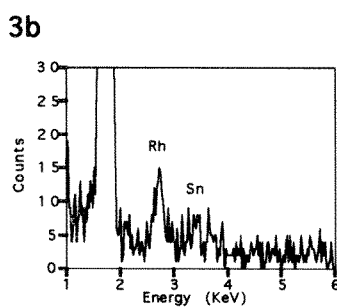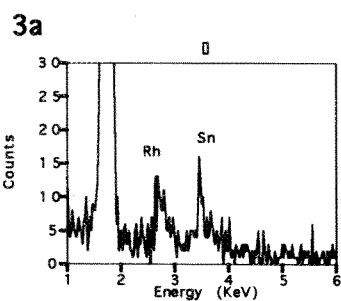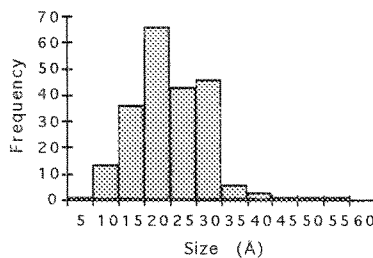
Figure 1: a) Energy-filtered bright field image of Rh parent catalyst and b) derived particle size distribution.
Figure 2: a) Energy-filtered bright field image of Sn(1.8%)Rh(1%) bimetallic catalyst and b) derived particle size distribution.
Figure 3: a) and b) EDX spectrum from two different particles 20 Å in size.

STABILIZING THE NANOSTRUCTURE IN BALL-MILLED IRON ALLOYS THROUGH THE ADDITION OF OXIDE PRECIPITATES

C.P Doğan[*] and J.C. Rawers[*]

[*]Albany Research Center, Albany, OR 97321

High-energy ball milling has proved to be an effective means of producing nanostructured metal alloys from elemental powders. Interest has focussed on this processing method because of its potential to form metastable compositions with a combination of properties not attainable by more conventional processing techniques. Consolidation of the resulting powders into commercially-viable solids has proven difficult, however. Because of the metastable nature of the compositions formed and the extremely high boundary area that makes up the nanostructure, these materials are very susceptible to exposure to elevated temperatures. Since most conventional consolidation techniques involve high temperatures, the nanostructure within the powders is typically lost during this processing step. Thus, a reliable means of enhancing the thermal stability of these materials, allowing economical consolidation, is clearly needed.

One possible method to enhance thermal stability is to introduce a homogeneous distribution of stable second phase particles that will pin the grain boundaries, allowing retention of the nanostructure at temperatures high enough for effective consolidation. In this study, elemental iron powders, with two atomic percent aluminum, were milled in an argon environment for 150 hours in an attritor mill. The resulting powders, which also contained ~3 weight percent oxygen (introduced during milling and subsequent handling) were then hot pressed at $900°C$ for 10 minutes under a pressure of 50 MPa. The microstructure of the consolidated material, illustrated in Fig. 1, consists of regions of retained nanostructure, interspersed by micron-sized grains of pure α-Fe. The nanostructured regions, illustrated at higher magnification in Fig. 2, are composed of α-Fe crystallites, with an average size of between 10 and 20 nm, and smaller (~ 10 nm) Fe_2AlO_4 spinel crystallites. The spinel crystallites are uniformly distributed throughout the nanostructured regions, and as is apparent in Fig. 2, are quite effective in pinning the α-Fe boundaries at this temperature. The larger grained regions are essentially free of spinel precipitates, giving the α-Fe grains freedom to grow during consolidation. This dual microstructure provides the material with an interesting combination of high hardness (imparted by the α-Fe + Fe_2AlO_4 nanostructure) and relatively good ductility (provided by the continuous network of larger α-Fe grains).

While the spinel particles have proved effective in stabilizing the nanostructure in iron alloys, not all second-phase particles are effective pinning agents. An iron alloy, processed and consolidated in an identical manner, and containing a less-uniform distribution of FeO precipitates, did not retain its nanostructure after consolidation. Similarly, a Fe-2C alloy containing both FeO and Fe_3C precipitates, had a post-consolidation grain size of several microns.
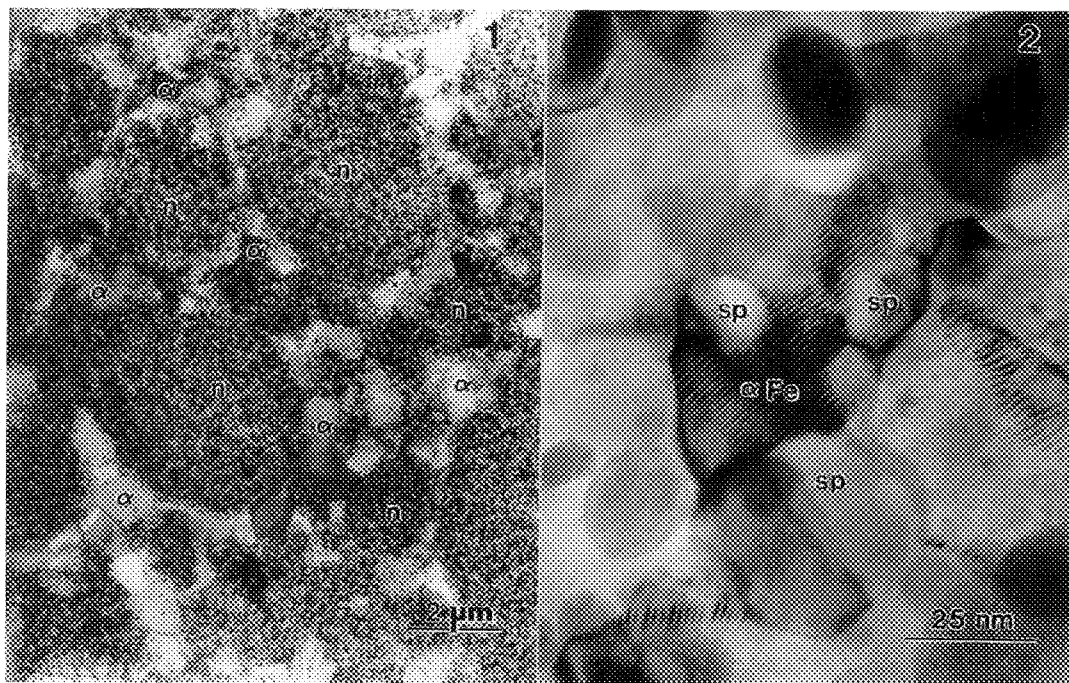
FIGURE 1. General microstructure of the consolidated Fe-2Al material. "α" marks the micron-sized ferrite grains, whereas "n" marks the retained regions of nanostructure.

FIGURE 2. Higher magnification look at the retained nanostructure. Spinel (sp) precipitates effectively pin the α-Fe grains in these regions.

THE STABILIZATION OF B.C.C. Cu IN Cu/Nb NANOLAYERED COMPOSITES

H. Kung, A.J. Griffin, Jr, Y.C. Lu, K.E. Sickafus, T.E. Mitchell, J.D. Embury, and M. Nastasi

Los Alamos National Laboratory, Materials Science and Technology Division, Los Alamos, NM 87545

Materials with compositionally modulated structures have gained much attention recently due to potential improvement in electrical, magnetic and mechanical properties. Specifically, Cu-Nb laminate systems have been extensively studied mainly due to the combination of high strength, and superior thermal and electrical conductivity that can be obtained and optimized for the different applications. The effect of layer thickness on the hardness, residual stress and electrical resistivity has been investigated [1]. In general, increases in hardness and electrical resistivity have been observed with decreasing layer thickness. In addition, reduction in structural scale has caused the formation of a metastable structure which exhibits uniquely different properties. In this study, we report the formation of b.c.c. Cu in highly textured Cu/Nb nanolayers. A series of Cu/Nb nanolayered films, with alternating Cu and Nb layers, were prepared by dc magnetron sputtering onto Si {100} wafers. The nominal total thickness of each layered film was 1 μm. The layer thickness was varied between 1 nm and 500 nm with the volume fraction of the two phases kept constant at 50%. The deposition rates and film densities were determined through a combination of profilometry and ion beam analysis techniques. Cross-sectional transmission electron microscopy (XTEM) was used to examine the structure, phase and grain size distribution of the as-sputtered films. A JEOL 3000F high resolution TEM was used to characterize the microstructure.

Fig. 1 (a) shows a typical XTEM image of a Cu/Nb nanolayer with a layer thickness of 25Å. The lattice fringes from the Cu and Nb grains can be seen extending from the layer interior to the interface. There is no evidence of interfacial mixing of the two elements which is consistent with the minimal mutual solubility of the two phases. Fig. 1(b) shows the corresponding selected area diffraction (SAD) pattern. A polycrystalline structure with a strong texture orientation relationship can be observed, which shows that Cu (f.c.c.) <110> {111} ∥ Nb (b.c.c.) <111> {110} ∥ Si <110> {001}. This orientation relationship corresponds to the Kurdjumov-Sachs relationship, rather than the symmetric Bain orientation relationship between the b.c.c. and f.c.c. structures. The geometrical constraints of the thin film growth which can limit the availability of certain sets of dislocations may have resulted in the realization of the Kurdjumov-Sachs orientation relationship. Fig. 2 (a) shows a XTEM image of a 11Å Cu / 11Å Nb nanolayer. No distinct difference in structure can be detected with the layer periodicity. A FFT pattern taken from ~ 5 bilayers (Fig. 2(b)) shows a slightly distorted <100> pattern of b.c.c. structure. The results suggest that the 11Å Cu has adopted the b.c.c. structure and exhibits a local epitaxial relationship with adjacent Nb layers. The slightly distorted square <100> pattern shows a slightly larger lattice spacing normal to the substrate plane than within the substrate plane. This may be a consequence of the lack of relaxation of in-plane strains within the film. A detailed characterization of the b.c.c. to f.c.c. transition in Cu nanolayers will be reported elsewhere.

In summary, b.c.c. Cu was observed in a Cu/Nb multilayer when the layer thickness was reduced to 11 Å. Cu with the metastable b.c.c. structure has been reported previously, either as fine precipitates in a b.c.c. matrix or as thin epitaxial layers grown on b.c.c. templates [2,3]. This is believed to be the first study to show that a large volume fraction (50%) of b.c.c. Cu can be preserved in a continuous polycrystalline microstructure. The nanolayered geometry has made it possible to investigate the various properties of the metastable phase, which is not readily available by other means.

References
1. A.J. Griffin, Jr., J.D. Embury, M.F. Hundley, T.R. Jervis, H. Kung, W.K. Scarborough, K.C. Walter, J. Wood and M. Nastasi, MRS Proc. Vol. 382, p. 309 (1995).
2. S.R. Goodman, S.S. Brenner, and J.T. Low, Met Trans., 4, 2363 (1964).
3. B. Heinrich, A.S. Arrott, J.F. Cochran, Z. Celinski, and K. Myrtle, in Science and Technology of Nanostructured Materials, edited by G.C. Hadjipanayis and G.A. Prinz, Plenum Press, New York, 1991.
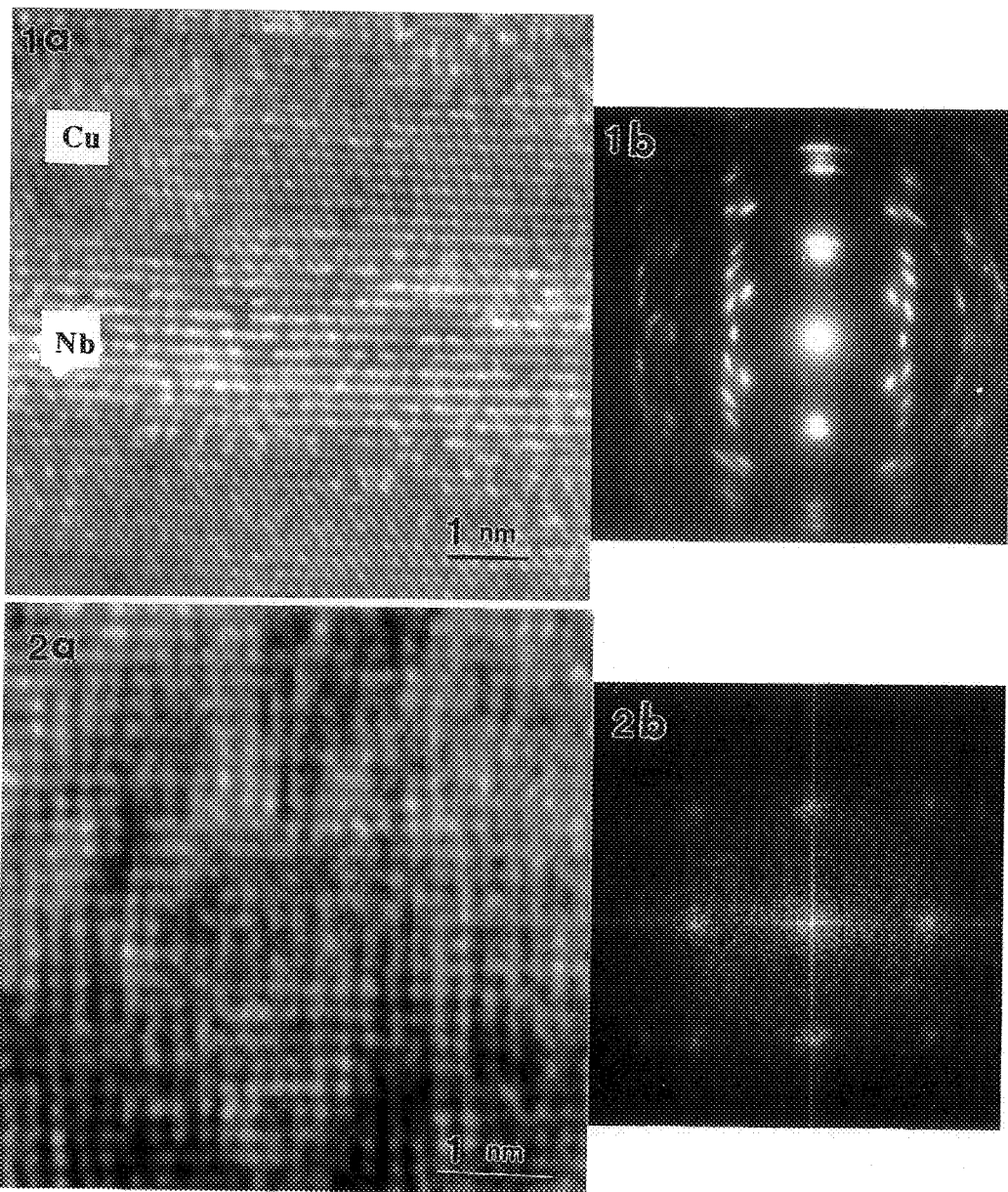
FIG. 1 (a) XTEM image of a 25Å Cu / 25Å Nb nanolayer. (b) Corresponding SAD pattern showing the texture orientation relationship.
FIG. 2 (a) XTEM image of a 11Å Cu / 11Å Nb nanolayer. (b) FFT pattern showing the epitaxial relationship between Cu and Nb.

HRTEM AND CHEMICAL ANALYSIS OF NiAl-5Ti

A. W. Wilson, J. M. Howe, A. Garg,* and R. D. Noebe*

Department of Materials Science and Engineering, University of Virginia, Charlottesville, VA 22903
* NASA Lewis Research Center, Cleveland, OH 44135

NiAl-based alloys are currently being studied to determine the effects of alloying additions on the mechanical and physical properties of NiAl.[1] Microstructural changes due to varying alloy composition have been determined and related to the mechanical properties, but high-resolution imaging and compositional profiles of the nanophases and interfaces in these alloys have not been performed.[2,3] The current study involves the use of a JEOL 2010F field-emission analytical TEM operating at 200 kV equipped with an ultra-thin window energy dispersive X-ray (EDX) detector to obtain high resolution images and compositional information from various nanophases. A single crystal of NiAl containing 5 at.% Ti was examined in this study. EDX spectroscopy of the specimen revealed the presence of low levels of impurities such as Si and P, as shown below. Bulk chemical analysis revealed that Si was present at 190 ppm while P was present at levels below detectability limits.

Figure 1 shows a dark-field TEM image of the NiAl-5 at% Ti alloy after a homogenization (1644K/32h) and aging (1255K/6h) followed by furnace cooling. The small bright particles in the image are β' (Ni_2AlTi) particles which appear to have nucleated homogeneously and coherently in the NiAl matrix. A higher magnification examination of the sample revealed that they are ~5 nm in width. In addition to these fine precipitates, a low density of somewhat coarser particles (~30nm) was also observed in the microstructure. A high resolution image of one of these particles, shown in Figure 2 revealed that it was in fact a two-phase particle. EDX spectra obtained from the locations labeled A, B, and C in the image are shown in Figures 3a, b, and c, respectively. The phase at A was P-rich (Figure 3(a)), whereas the phase at B was determined to be Ni_2AlTi by quantitative analysis of the spectrum in Figure 3b. The region in C was the NiAl matrix (Figure 3(c)). As shown in Figure 2, the β' phase appears to have nucleated heterogeneously at the P-rich particle and is larger than the homogeneously nucleated β' shown in Figure 1. A higher magnification image of the interface between the P-rich phase at A and β' phase at B in a similar two-phase particle, shown in Figure 4, reveals that the interface is semicoherent and contains misfit dislocations spaced about 7 {200} Ni_2AlTi planes apart. On the other hand, the coherent interface between the fine β' (Figure 1) and the NiAl matrix was essentially indistinguishable in the high-resolution image.[4]

References

1. W. S. Walston and R. Darolia, *Mater. Res. Soc. Symp. Proc.*, Vol. 288 (1993) 237.

2. A. Garg et al., *Micromechanics of Advanced Materials* (1995) 255.

3. I. E. Locci et al., submitted to *J. Mater. Res.* (1996).

4. The authors would like to thank Dr. V. Levit from the University of Florida for growing the NiAl-5Ti single crystal.
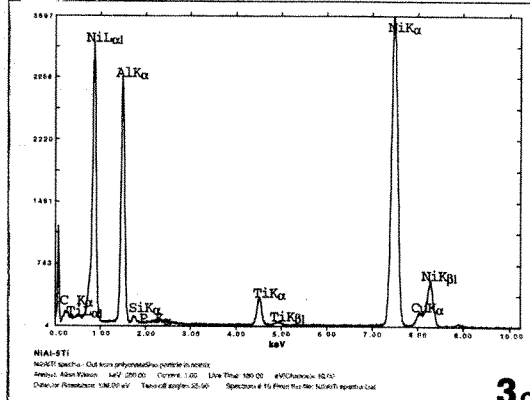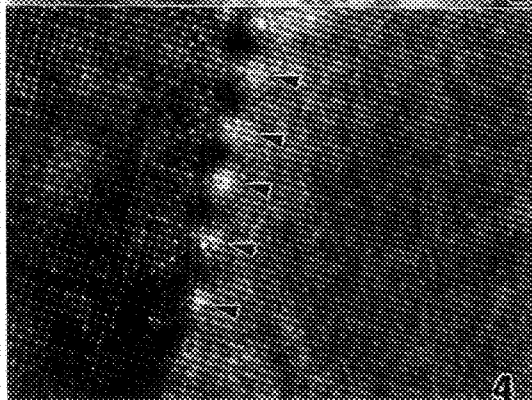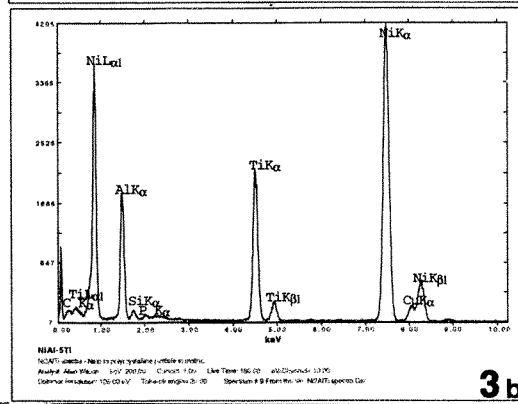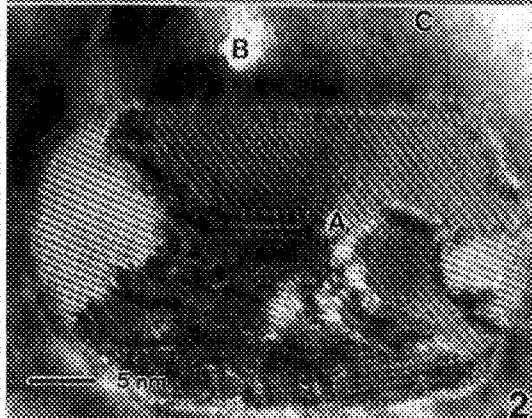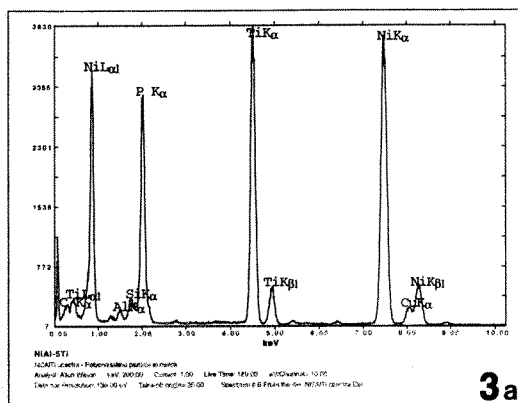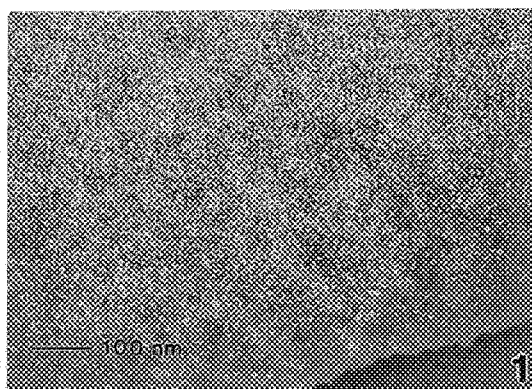
Figure 1 - Dark-field TEM image of Ni_2AlTi nanocrystals in NiAl matrix.

Figure 2 - High-resolution TEM image of precipitate with locations of EDX analysis labeled.

Figure 3 - EDX spectra from locations A, B, and C in Figure 2.

Figure 4 - High-resolution TEM image of interface between P-rich particle and β'.

MULLITE PHASE SEPARATION IN NANOCOMPOSITE POWDERS

Nan Yao,[*] Daniel M. Dabbs,[*,#] and Ilhan A. Aksay[*,#]
*Princeton Materials Institute, and
#Department of Chemical Engineering, Princeton University, Princeton, New Jersey 08540-5211

Mullite/alumina composite materials are of considerable interest in many applications because of their high-temperature properties, such as creep resistance, and thermal shock resistance.[1] Although mullite has relatively low fracture toughness and strength at low temperature (2.2 MPa·m$^{1/2}$ and 200-500 MPa, respectively), it retains the greater part of its physical strength up to 1500°C.[1] We seek to improve the mechanical properties of mullite monoliths by using nanosized (<100nm diameter) inclusions in the matrix, where the nanosized inclusions would act to strengthen the matrix in a manner akin to precipitation hardening in metals.[2] Our approach is to make nanocomposite powders and monoliths with controlled chemical composition and phase distribution on the nanometer length scale (1-10 nm).

We have recently formed nanocomposite powder using spray pyrolyzed precursors. The precursor was formed from a solution of TEOS and aluminum nitrate nonahydrate in ethanol, mixed in proportions equivalent to the stoichiometry of a mullite/alumina composite composed of 20 wt% alumina in a mullite matrix. The solution was sprayed onto a hot surface, resulting in immediate pyrolysis of the solvent and functional groups and forming white, weak agglomerates. The agglomerates were ground and heat treated to form an alumina/mullite composite powder. The high chemical homogeneity of the precursor powder was indicated by the low temperature of conversion to mullite (<1000°C). HREM studies were performed on the powder using a Philips-CM200 FEG transmission electron microscope operated at 200 keV under moderate vacuum conditions over the range from 10^{-6} to 10^{-7} Torr. Chemical analyses were performed using a nanosize electron probe on an EDAX MX-10 system. An ultrathin window Si(Li) detector was used to extend the range of element analysis to lighter elements such as B (Z=5). The elemental concentration was obtained by applying a standard quantitative thin film microanalysis to the X-ray spectra.

Figure 1(a) is a HREM image taken at 200 KeV near the Scherzer defocus with the electron beam coincident to the [001] direction on a very thin, pure mullite crystal (<100Å). The near perfect lattice image shows considerable local structural homogeneity in a 3:2 ($3Al_2O_3 \cdot 2SiO_2$) mullite matrix.

In contrast, precursor powder heat treated at 1500°C for one hour is found to be composed of nanometer size inclusions of 3:2 mullite ($3Al_2O_3 \cdot 2SiO_2$) and alumina (Al_2O_3) dispersed within a 2:1 mullite ($2Al_2O_3 \cdot SiO_2$) matrix (Figure 1(b)). It is unlikely that this is a stable phase composition (as alumina precipitates from the matrix, the 2:1 mullite will convert to 3:2) but with these results, we have demonstrated the proof of concept that a low temperature reaction pathway can be used to achieve exsolution within a matrix, without using a high temperature melt as an intermediate. However, several important issues remain: First, we do not expect a 3:2/2:1 mullite/mullite matrix to remain stable at high temperatures. If the 2:1 mullite reacts to form 3:2 mullite, alumina should precipitate or grow within the matrix. As seen in Figure 1(c), the alumina phase appears to be growing as fingers into the mullite matrix. The process by which this phase evolution occurs is under investigation.[3]

References:

1. I. A. Aksay, D. M. Dabbs, and M. Sarikaya, *J. Am. Ceram. Soc.*, **74**(1991)2343.
2. For example, see P. Haasen, *Physical Metallurgy*, Cambridge University Press, Cambridge, (1986).
3. This study used MRSEC Shared Facilities supported by the NSF under Award Number DMR-940032 and was supported by the U. S. Air Force Office of Scientific Research under grant AFOSR-F49620-93-1-0259.
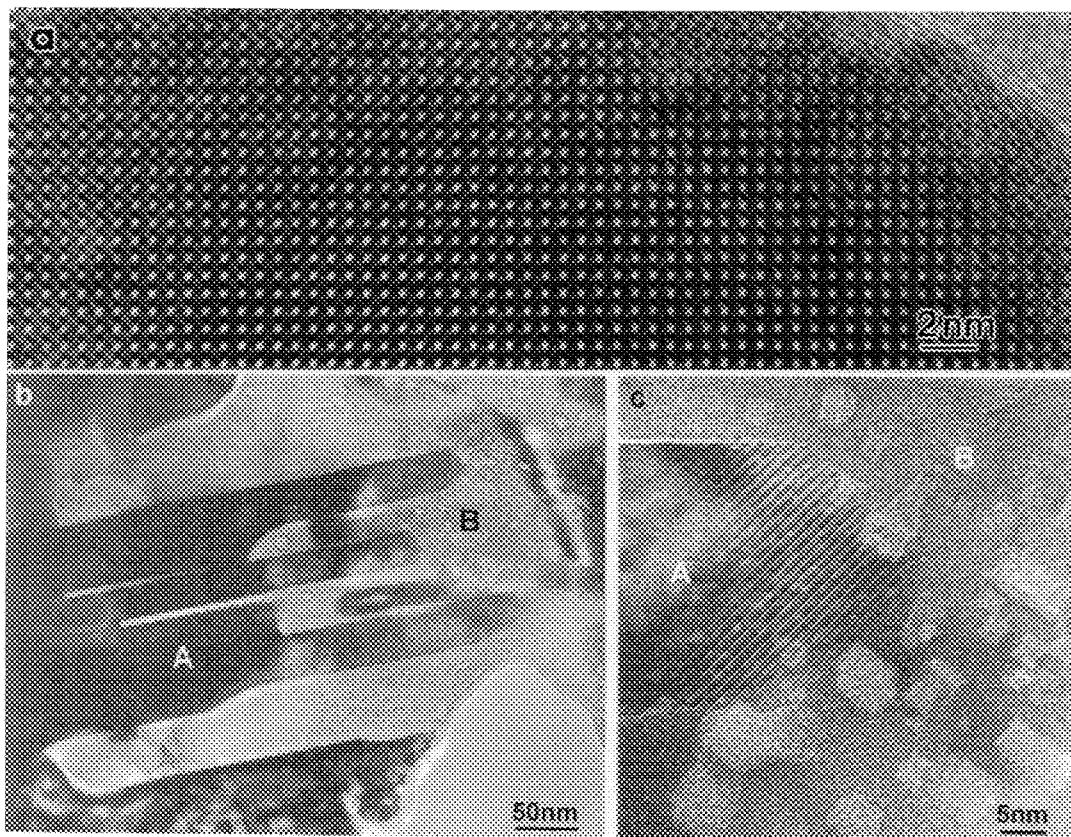
FIG. 1.—TEM images of alumina/mullite nanocomposite powder formed by exsolution of alumina from a mullite matrix. (a) HREM image of 3:2 mullite with electron beam incidence along the [001] direction at 200 KeV (the bright spots correspond to the column of Al atoms). (b) Region A consists of alumina (dark phase) containing mullite fingers (light phase). Region B consists of a 2:1 mullite matrix containing small dispersoids of 3:2 mullite. (c) A magnification of region B, more clearly showing the 3:2 inclusions in the 2:1 matrix. Alumina appears to be growing from the left edge of the image.

Nucleation and Growth of Si Quantum Nanocrystals in Silicon-Rich Oxide Films

S. C. Mehta, D. A. Smith, M. R. Libera[+], J. Ott[#], G. Tompa[*] and E. Forsythe[*], Department of Materials Science and Engineering, Lehigh University, Whitaker Lab, 5, E. Packer Avenue, Bethlehem, PA 18015, [+]Department of Materials Science and Engineering, Stevens Institute of Technology, Hoboken, NJ 07030, [#]IBM, T. J. Watson Research Center, P. O. Box 218, Yorktown Heights, NY 10598. [*]Structured Materials Industries, Inc., Piscataway, NJ 08854.

The observation of photoluminescence and electroluminescence in Si nanocrystals has generated renewed interest in these novel silicon based materials for their possible application as light emitters and detectors. Silicon Rich Oxide (SRO) films with a uniform dispersion of silicon nanocrystallites in a wider bandgap SiO_2 matrix manifest electroluminescence and photoluminescence in the infrared and visible portions of the spectrum. Understanding the nucleation and growth kinetics of these crystallites in amorphous matrix is of critical importance in the fabrication of future optoelectronic devices. One route to the fabrication of Si nanocrystals is by the crystallization of amorphous SiO_{2-x}. Consider the case when x=1. The reaction leading to the formation of Si crystallites can be written as;

$$SiO(amorphous) = 1/2\ Si\ (crystalline) + 1/2\ SiO_2\ (amorphous) \qquad .....(1)$$
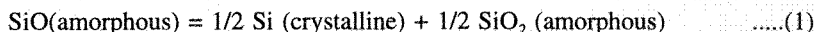
The nucleation, growth and coarsening processes of Si nanocrystals each require bulk diffusion of Si atoms through the amorphous matrix.

The SRO films, used in this study were deposited to a thickness of 1 μm on (100) oriented single crystal silicon using LPCVD; the reactor temperature was 600°C and the atmosphere was a mixture of N_2O and SiH_4. Microstructural studies of chemically thinned samples were performed on a Philips CM30 (at an operating voltage of 300keV) and on an EM400T (at an operating voltage of 120keV). The films in the as-deposited state were completely amorphous, (fig. 1). In-situ ramp heating experiments were first performed to quickly locate the temperature ranges where reaction rates are convenient for the isothermal experiments. The samples were heated in steps of 50°C up to a maximum temperature of 900°C with an intermediate hold for 10 minutes after each heating increment to allow image stabilization and facilitate monitoring of the microstructural changes accompanying the heating. Fig. 2 is a micrograph of an SRO film taken at 900°C. The micrograph shows a distribution of crystallite sizes, indicative of continuous nucleation and growth. The isothermal annealing experiments were performed in-situ in the TEM at 750°C and 850°C respectively. Fig. 3 is an HRTEM micrograph of an SRO film annealed at 750°C for 2 hours. The micrograph shows that the average crystallite (shown by an arrow) size is approximately 2 nm in diameter. The chemical driving force for nucleation at 750°C is large so that the nucleation density is very large (as is evident from the micrograph in fig. 3). On the other hand, isothermal annealing at 850°C clearly reveals a lower nucleation density. Fig. 4 is a micrograph of the SRO film isothermally annealed at 850°C up to 2 hours. The micrograph clearly shows a large crystallite (approximately 40 nm in diameter) surrounded by tiny crystallites, suggesting that the crystallite coarsening by Ostwald Ripening effect is operative at this temperature leading to a broadening of the crystallite size distribution.
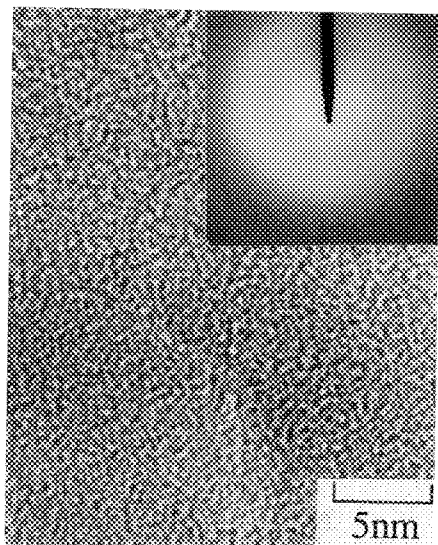
Fig. 1

Fig. 2
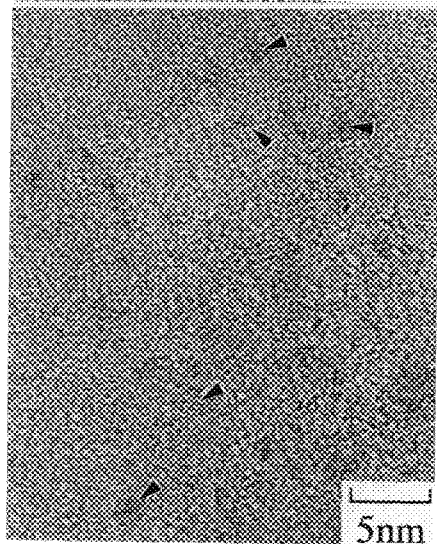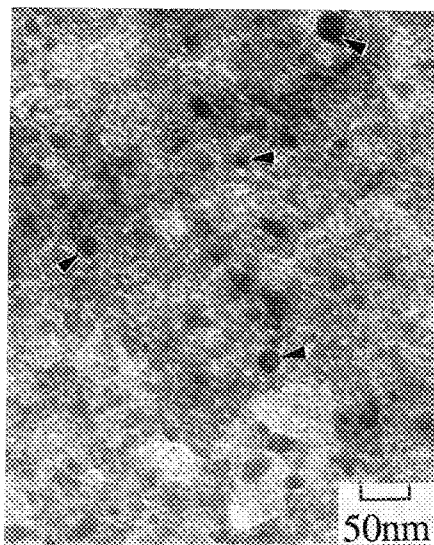
Fig. 3
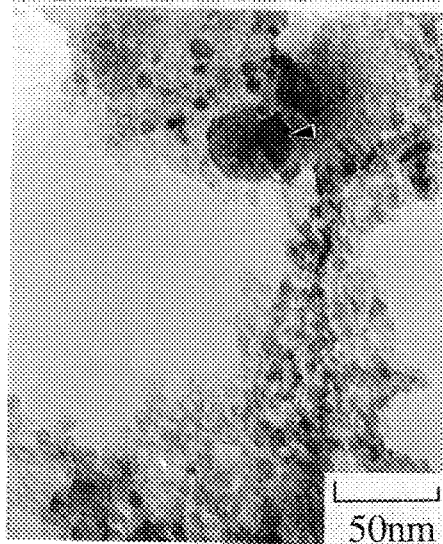
Fig. 4

Fig. 1 Micrograph of the as-deposited SRO film. Shown in the inset is a diffraction pattern of an as-deposited film.

Fig. 2 Micrograph showing the crystallite size distribution in the SRO film ramped in-situ up to 900°C.

Fig. 3 Micrograph of an SRO film isothermally annealed at 750°C for 2 hours.

Fig. 4 Micrograph of an SRO film isothermally annealed at 850°C for 2 hours.

235

TEM STUDY OF CdS NANOCRYSTALS FORMED IN SiO$_2$ BY ION IMPLANTATION

Jane G. Zhu, C. W. White, J. D. Budai, and S. P. Withrow

Oak Ridge National Laboratory, Solid State Division, Oak Ridge, TN 37831-6057

Quantum confinement effects and enhanced optical nonlinearity are expected from II-VI semiconductor nanocrystals, which are important for novel opto-electronic device applications.[1] The ion implantation method has been used in our study to form CdS nanocrystals inside amorphous SiO$_2$. The CdS nanocrystals were studied by transmission electron microscopy (TEM).

The samples were implanted (at room temperature) with equal doses (1×10^{17} ions/cm^2) of Cd and S into a SiO$_2$ layer on (100) silicon substrates and then annealed under Ar + 4%H$_2$ ambient at 800°C and 1000°C for 1 h. Implant energies were chosen to overlap the Cd and S ion profiles in the middle of the oxide layer. CdS precipitates are formed during the thermal annealing.

The effect of annealing temperatures on the nanocrystals size distributions are revealed in Figs. 1 and 2. The sizes of CdS nanocrystals are in the range of 2 - 11 nm for the sample annealed at 800°C, and in the range of a few to 16 nm for the sample annealed at 1000°C. The nanocrystals are randomly oriented in the amorphous SiO$_2$ matrix. While some of the CdS precipitates appear in near-spherical shape, some of them show elliptical shape. This differs from the nanocrystals of other semiconductor materials, where the nanocrystals inside SiO$_2$ are usually in near-spherical shape.[2]

The CdS crystals can be in cubic (ZnS) or hexagonal (wurtzite) structures. A high-resolution electron microscopy (HREM) image of two CdS particles is shown in Fig. 3. The ~3.4 Å lattice spacing in the particle on the left could be either the {111} planes in the cubic phase or the {0002} planes in the hexagonal phase. The two sets of lattice planes in the particle on the right closely match the {1$\bar{1}$01} and {01$\bar{1}$2} lattice planes in the hexagonal phase. Another CdS particle with two sets of lattice fringes is shown in Fig. 4(a). The Fourier transform of this HREM image is shown in Fig. 4(b), which is identified to be the <1$\bar{2}$1$\bar{3}$> axis of the hexagonal phase. To get two sets of lattice fringes to identify the crystal structure from HREM, the nanocrystals have to be aligned along low index orientations. The identification of some of the crystallites as having the hexagonal structure does not exclude the possibility that some of the crystallites may have the cubic structure.

References

1. L. Brus, Appl. Phys. A **53**, 465 (1991).
2. J. G. Zhu, et al., J. Appl. Phys. **78**, 4386 (1995).
3. This research was sponsored by the Division of Materials Sciences, U.S. Department of Energy, under contract DE-AC05-96OR22464 with Lockheed Martin Energy Research Corp., and supported in part by an appointment to Oak Ridge National Laboratory Postdoctoral Research Associate Program administered jointly by Oak Ridge National Laboratory and the Oak Ridge Institute for Science and Education.
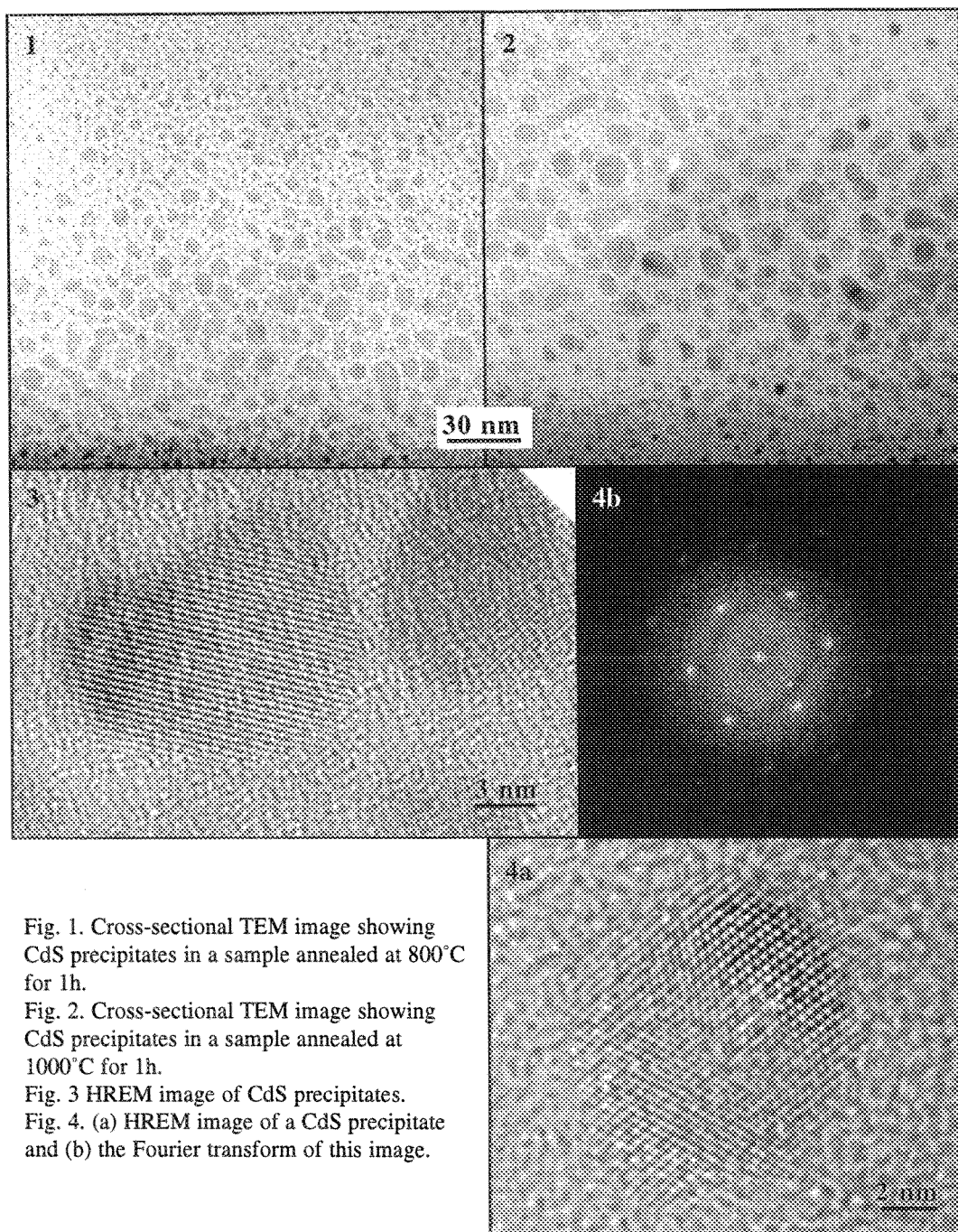
Fig. 1. Cross-sectional TEM image showing CdS precipitates in a sample annealed at 800°C for 1h.
Fig. 2. Cross-sectional TEM image showing CdS precipitates in a sample annealed at 1000°C for 1h.
Fig. 3 HREM image of CdS precipitates.
Fig. 4. (a) HREM image of a CdS precipitate and (b) the Fourier transform of this image.

PROTEIN CRYSTALLOGRAPHY USING CAPILLARY-FOCUSED X-RAYS

D. X. Balaic[a,b], Z. Barnea[a], K. A. Nugent[a], R. F. Garrett[c], J. N. Varghese[d] & S. W. Wilkins[b]

a) School of Physics, University of Melbourne, Parkville VIC 3052 Australia
b) CSIRO Division of Materials Science and Technology, Locked Bag 33, Rosebank MDS, VIC 3169, Australia
c) Australian Nuclear and Scientific Technology Organisation, Private Bag 1, Menai, NSW 2234, Australia
d) Biomolecular Research Institute, 343 Royal Parade, Parkville, VIC 3052, Australia

Tapered glass capillaries for X-ray beam concentration have been a topic of much interest for the synchrotron X-ray community in recent years[1,2,3]. These optics have long held the promise of high-intensity microbeam generation for the "hard" X-ray energies used in crystallography and fluorescence analysis.

X-ray concentration is achieved by exploiting the total external reflection property of glass surfaces for glancing angles of incidence[4]. X-rays directed into the entrance aperture of the capillary are reflected toward an exit aperture of smaller dimensions, resulting in an increased X-ray flux per unit area at the exit aperture. Capillary designs with a true geometrical focus beyond the capillary exit are also possible[5].

Our group has recently demonstrated a paraboloidally-tapered glass capillary optic which produced a focused X-ray beam using a monochromatised synchrotron source[6]. The optic was designed to produce a focal region for singly-reflected X-rays at a point 40 mm from the end of the capillary. Such a focal region was observed, with a FWHM intensity gain of two orders of magnitude over the incident X-ray intensity from the channel-cut monochromator. Moreover, this gain was achieved for X-ray energies from 5 to 20 keV. We subsequently used a similar optic to obtain X-ray diffraction patterns from a crystal of hen egg-white lysozyme on image plates[7]. The use of the capillary-focused beam yielded diffraction patterns 70 to 100 times faster than using an unfocused beam from the channel-cut monochromator alone. Placement of the crystal at different positions in the capillary-focused beam demonstrated the focusing of Bragg reflections and diffraction from a small volume of crystal.

The use of capillary optics with laboratory sources also holds great promise. Currently, the lower X-ray intensity available from these sources dictates long exposure times to obtain sufficient data to perform successful macromolecular crystallography. We expect that tapered capillaries can be used to reduce the exposure times required for macromolecular crystallography by a factor of more than 10, while still maintaining high resolution. Further, some small crystals may not be successfully analysed at all using existing laboratory X-ray installations. The use of focused beams may also permit the study of very small crystals with laboratory X-ray sources.

[1] Thiel, D. J., Bilderback, D. H. & Lewis, A. (1993). *Rev. Sci. Instrum.* **64**, 2872-2878.
[2] Engström, P., Larsson, S. & Rindby, A. (1991). *Nucl. Inst and Meth.* A **302**, 547-552.
[3] Hoffman, S. A., Thiel, D. J. & Bilderback, D. H. (1994). *Nucl. Inst. and Meth.* A **347**, 384-389.
[4] Stern, E. A., Kalman, Z., Lewis, A. & Lieberman, K. (1988). *Appl. Opt.* **27**, 5135-5139.
[5] Balaic, D. X. & Nugent, K. A., (1995). *Applied Optics* **34**. 7263-7272.
[6] Balaic, D. X., Nugent, K. A., Barnea, Z., Garrett, R. F. & Wilkins, S. W. (1995) *J. Synchrotron Rad.* **2**. 296-299.
[7] Balaic, D. X., Barnea, Z., Nugent, K. A., Garrett, R. F., Varghese, J. N. & Wilkins, S. W. (1996). Submitted to *J. Appl. Cryst.*
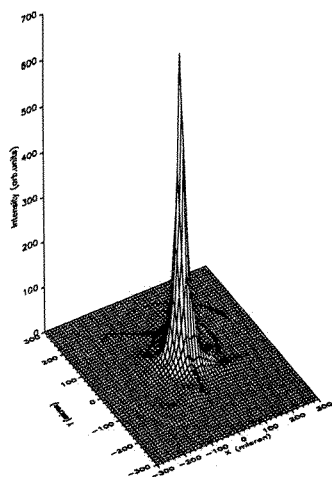
Figure 1: Focal plane x-ray intensity distribution 40mm from the exit of a 24 cm long paraboloidally-tapered glass capillary. Intensity axis is scaled to gain compared to unfocused synchrotron source intensity as unity. X-ray energy is 8 keV using a channel-cut monochromator before the capillary in the beam.
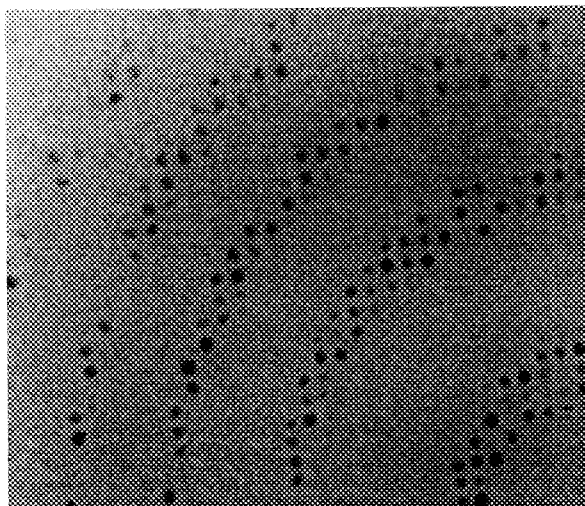
Figure 2: Hen egg-white lysozyme crystal diffraction pattern produced in a single 2 degree rotation of the crystal with 2 seconds per degree exposure with the crystal positioned at the capillary beam focus. The equivalent exposure required without focusing is 100 times greater. Detail of an image plate located 40 mm from the crystal.

Figure 3: Bragg reflections from lysozyme crystal 135 mm beyond capillary focal plane. Individual spots have diverged into diffuse annular rings (focal beam) with central spots (collimated beam through capillary). The crystal is located at the beam focus in this exposure (2 degree rotation, 5 sec/degree).

Figure 4: Geometry for producing focused Bragg reflections. A large (~0.3mm) crystal is placed at the exit of the capillary and the image plate or CCD is placed at the focal plane.
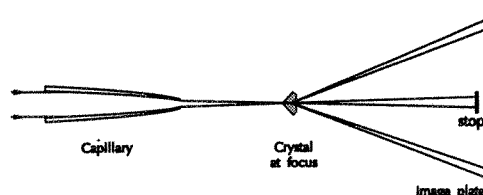
Figure 5: Geometry for small crystals (crystal at beam focus). In this geometry a 5 micron crystal would receive 700 times the intensity present in the unfocused beam using the capillary described by figure 1.

239

XRMF APPLICATIONS OF A MONOLITHIC, POLYCAPILLARY, FOCUSING X-RAY OPTIC

D. A. Carpenter*, Ning Gao**, and G. J. Havrilla ***

*Oak Ridge Centers for Manufacturing Technology, Oak Ridge, Tennessee 37831-8084
**X-Ray Optical Systems, Inc, 90 Fuller Road, Albany, New York 12205
***Los Alamos National Laboratory, Los Alamos, New Mexico 87545

A monolithic, polycapillary, x-ray optic was adapted to a laboratory-based x-ray microprobe to evaluate the potential of the optic for x-ray microfluorescence analysis. The polycapillary was capable of collecting x-rays over a 6 degree angle from a point source and focusing them to a spot approximately 40 μm diameter. The high intensities expected from this capillary should be useful for determining and mapping minor to trace elements in materials. Fig. 1 shows a sketch of the capillary with important dimensions.

The microprobe had previously been used with straight[1,2] and with tapered monocapillaries.[3] Alignment of the monocapillaries with the focal spot was accomplished by electromagnetically scanning the focal spot over the beveled anode. With the polycapillary it was also necessary to manually adjust the distance between the focal spot and the polycapillary.

The focal distance and focal spot diameter of the polycapillary were determined from a series of edge scans. Figure 2 shows the fwhm of the beam profile as a function of distance from the end of the capillary. At the focal point, the fwhm was 43 μm. The intensity of the Cu kα line from a copper anode was found to be 8.9 x 10^4c/s/μm^2 , by measuring the fluorescence count rates from the NIST SRM 1833 thin film standard. That intensity corresponded to a gain of 44, with respect to a straight 50-μm capillary.

When the polycapillary was used with different combinations of anodes and filters, it was a very effective tool for wide-area mapping of element distributions in materials. In Fig. 3, sulfur was mapped in the fracture surface of a failed pipe, using Cr radiation and a 12-μm Cr filter. The heterogeneous sulfur distribution had been difficult to detect with conventional aperture optics. Figure 4 illustrates the use of Cu radiation, filtered with 25-μm Ni, to reveal the heterogeneity of a micro-drop of NIST SRM 1643c on a thin membrane. Except for Ca, all elements in the dried micro-drop were present at levels less than 1 ng.[4]

References

1. D. A. Carpenter; *X-Ray Spectrometry, 18,*(1989)253.
2. D. A. Carpenter, et. al.; *J. Trace and Microprobe Techniques, 13(2),*(1995)141.
3. Ning Gao, et. al.; *Advances in X-Ray Analysis, 39*(1996)(to be published).
4. The Oak Ridge Centers for Manufacturing Technology at the Y-12 Site is managed by Lockheed Martin Energy Systems, Inc. for the Department of Energy under contract DE-AC05-84OR21400. LANL is operated by the University of California for the U.S. Department of Energy under contract W-7405-ENG-36.
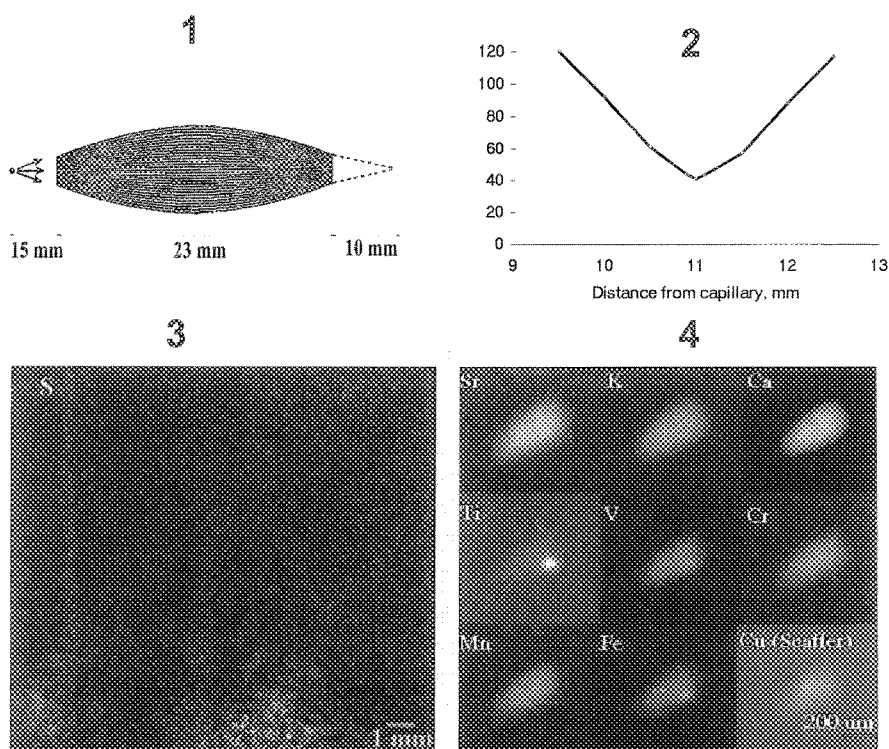
FIG. 1 Schematic of monolithic, polycapillary, x-ray optic.
FIG. 2 Profile width versus distance from the end of the capillary.
FIG. 3 Sulfur distribution in fracture surface of failed pipe
(Cr rad., 12 um Cr filter, 19 kV).
FIG. 4 Element distributions in dried micro-drop of SRM 1632c
(Cu rad., 25 um Ni filter, 30kv).

241

IN-SITU MEASUREMENTS OF PLANE SPACING DURING ELECTROMIGRATION IN A PASSIVATED Al LINE

P.-C. Wang, * I. C. Noyan, ** E. G. Liniger, ** C.-K. Hu, ** G. S. Cargill III *

* Columbia University, Dept. of Chemical Engineering, Materials Science and Mining Engineering, New York, NY 10027
** IBM Research Division, Thomas J. Watson Research Center, Yorktown Heights NY, 10598.

To determine the effect of confinement on the material transport that occurs during electromigration, in-situ x-ray strain measurements were conducted along the length of a passivated Al line that was first heated (in two steps) to 267°C and then subjected to current flow.

The specimen geometry used in the experiment is shown in Figure 1. Further details can be obtained from references 1,2. The Al in the line and the contact pads had a grain size of the order of the film thickness (0.5 μm) and exhibited strong 111 texture with a range of ±5 degrees. The W pads also exhibited strong 110 texture and had much finer grain size. The x-ray measurements were carried out on the NSLS X-26C beamline using a focussing tapered capillary for collimating the beam. The irradiated area on the line was a $10\mu m \times 10\mu m$ square. The Al 111 plane spacing (d_{111}) was measured using white beam (Laue) diffraction with a solid-state detector[1]. This plane spacing was measured at different locations along the line.

In Figure 2, the variation of the Al lattice parameter (calculated from the d_{111}) is plotted as a function temperature and position along the line. Since there is no change in the lattice parameter with position along the line and since the variation of the lattice parameter with temperature is constant at all positions, we can conclude that the boundary conditions at all points along the line are equivalent. This also indicates that a representative number of grains are being sampled by the x-ray beam at all locations.

Once the Al line was subjected to current flow, Al migrated from the cathode to the anode, causing voids and hillocks, respectively at these locations. The variation of the Al lattice parameter as a function of position and time during electromigration is shown in Figure 4. It can be seen that the change is plane spacing at a given point is not monotonic with time at all locations. The points closer to the anode exhibit a maximum during the early stages of electromigration, which may be interpreted as the stage of maximum (in-plane) constraint by the substrate. The points closer to the cathode show no such change. The results may be interpreted as being in qualitative agreement with the FEM analysis of wide lines[3]. However, complete strain tensor measurements are needed for verification. These studies are currently in progress.

References

1. P.-C. Wang, G. S. Cargill III, I. C. Noyan, E. Liniger, MRS Proceedings of 1995 Fall Meeting, Symposium I, In Print.
2. P.-C. Wang, G. S. Cargill III, I. C. Noyan, E. Liniger, C.-K. Hu, K. Y. Lee, MRS Proceedings of 1996 Spring Meeting, Symposium K, In Print.
3. D. Chidambarrao, K. P. Rodbell, M. D. Thouless, P. W. DeHaven, *Mat. Res. Soc. Symp. Proc.* vol. 338, (1994) 261.
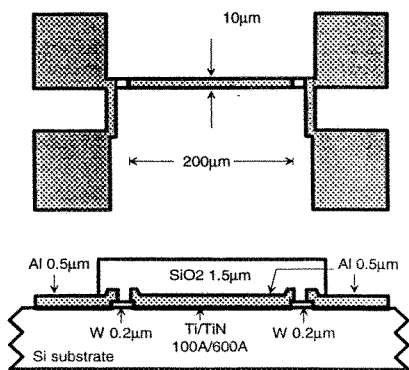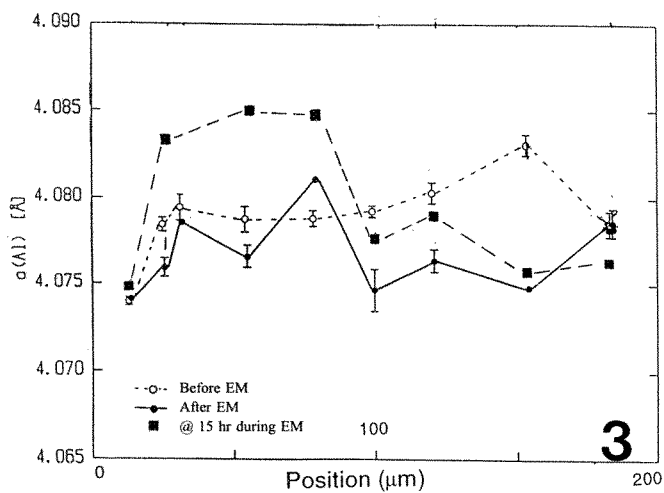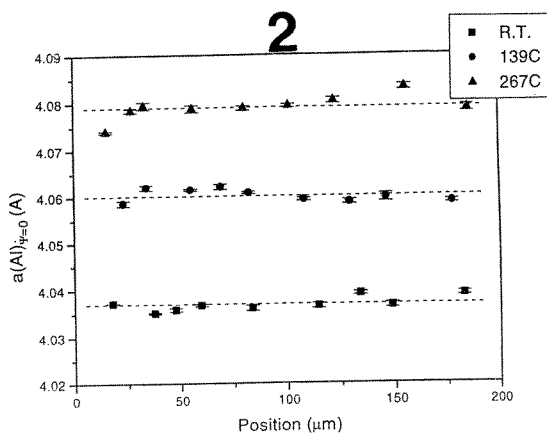
Fig. 1 Geometry of test samples.

Fig. 2 Variation of the Al lattice parameter along the line at various temperatures.

Fig 3 Variation of the Al lattice parameter along the line at different times during electromigration at T=267°C.

MICROANALYSIS OF FERROELECTRIC MEMORIES USING MICRO X-RAY DIFFRACTION

M. O. Eatough, M. A. Rodriguez, D. Dimos, and B. Tuttle

Sandia National Laboratories, Albuquerque NM 87185-1405

Since the advent of the microdiffractometer a new world of analysis possibilities have opened. In this paper we will discuss a novel use of microdifraction. We have developed a method for monitoring domain switching in ferroelectric thin films in situ using micro x-ray diffraction (μXRD). μXRD is a nontraditional x-ray diffraction technique which has recently attracted much attention [3]. The microdiffractometer is capable of obtaining a diffraction pattern from 0 - 150° 2θ simultaneously from regions as small as 30μm in diameter. The purpose of this study was to determine if ferroelectric switching of ferroelectric Pb(Zr,Ti)O$_3$ (PZT) thin films can be observed using μXRD. This method will be extremely valuable as we target the necessary processing parameters to achieve the desired switching behaviors and to monitor switching in micron-sized devices.

Ferroelectric thin films are being developed for the next generation of electronic devices, in particular nonvolatile RAM, optical memories, and microswitches. Understanding switching behavior is of paramoun concern because 90° domain switching is needed to obtain the field induced change in birefringence required for optoelectronic devices. Recent theories postulate that 90° domain formation and, therefore, 90° domain switching is severely limited in films when the grain size is less than about 1μm [2]. To study this behavior we investigated the 90° switching behavior of several films deposited on Si. These types of memories utilize the movement of beta site atoms in the perovskite structure to accomplish ferroelectric switching. If the beta site electron moves along the c-axis the switching behavior is refered to as 180° domain switching. If the beta site electron move 90° to it's original position the switching behavior is refered to as 90° domain switching. This latter type of switching in effect changes the orientation of the crystallite from, for example, having the a-axis normal to the plane of the film to having the c-axis normal to the plane of the film. Our study involved the use of a microdiffractometer to monitor the switching behavior in relatively small (0.7mm diameter) electroded areas on the surface of the thin films. Diffraction analyses were done while DC voltage were applied and removed, representing several places in the ferroelectric hysteresis loop. In particular, we were looking for relative intensity changes in the [h 00],[00l] diffraction peaks as a function of position in the hysteresis loop.

We have previously shown that processing conditions influence grain size and therefore domain formation [2]. Also the stresses that develop during cooling through the curie point greatly effects how the crystallites are oriented along their [h 00) and [00l] crystallographic directions normal to the plane of the film [1]. For example, if the in-plane stress is compressive during cooling through Curie point then the [00l] orientations will tend to develop normal to the plane of the film. This occurs because the slightly smaller a-axis will more easily develop in the plane of the film. It also has been shown that 90° domain formation does not readily occur in films with grain sizes less than about 1μm [4,5]. If 90° domain formation does not occur, despite the strong elastic forces generated by transformation strain, then 90° switching may be severely limited. In this study we showed that 90° domain switching was diminished in films where the grain size is smaller than one or two microns, but is possible in films with a much larger grain size and that we were able to monitor this behavior using t μXRD.[6]

References

1. P.W. DeHaven, C.C. Goldsmith, and T.L. Nunes, Rigaku J., **8,** No. 1, 1991.

2. B. A. Tuttle, T. J. Garino, J. A. Voigt, T. J. Headley, D. Dimos, and M. O. Eatough, , (Proc. NATO Advanced Workshop on Electroceramic Films, Villa del Mar, Italy, 1994.).

3. B. A. Tuttle, J. A. Voigt, T. J. Garino, D. C. Goodnow, R. W. Schwartz, D. L. Lamppa, T. J. Headley, and M. O. Eatough, (Proc. of IEEE 8th International Symposium on Applications of Ferroelectrics, Greenville, SC, 1992).

4. G. King and E. K. Goo, J. Am. Ceram. Soc. **6** 73 (1990).

5. B. G. Demczyk, R. S. Rai, J. Am. Ceram. Soc. **3** 73 (1990).

6. This work performed at Sandia National Laboratories, which is operated for the U. S. Department of Energy under contract number DE-AC04-94AL8500.
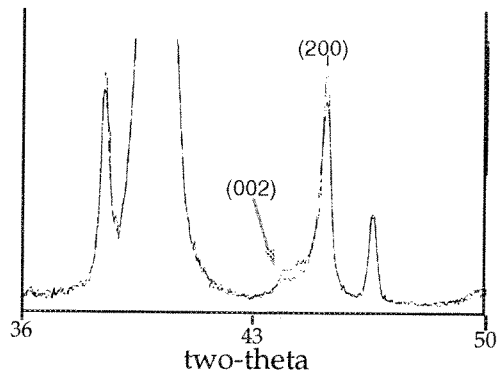
Figure 1
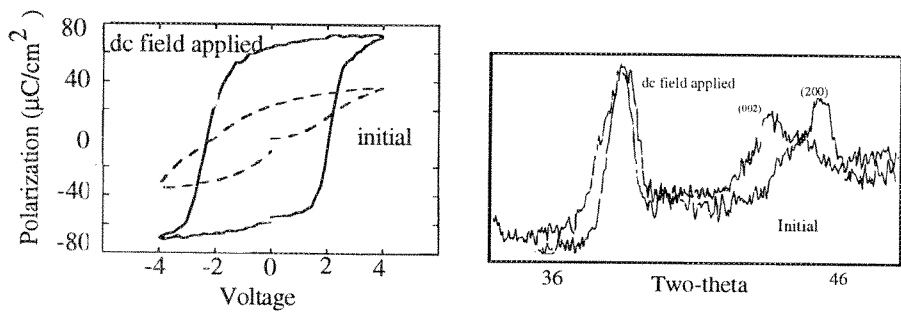
Figure 2.

Figure 1.   Superimposed diffraction patterns of 40/60 PZT taken with a microdiffractometer with no field applied and with a +12V DC field applied. Note the limited intensity of the (002) reflectio and the very slight increase when the field is applied.

Figure 2.   30/70 PZT on LaAlO$_3$ with a grain size exceeding 1µm. The hysteresis loop and diffraction patterns suggest that 90° domain switching has occurred

IMAGING FOCUSED X-RAYS FROM GLASS CAPILLARIES

Eric B. Steel and Terrence Jach
National Institute of Standards and Technology
Bldg. 222/Rm A113, Gaithersburg, MD 20899

Recent developments of glass capillaries allow x-ray probes to be focused down to micrometer sizes. These probes show promise for microanalysis applications, if they can reliably deliver high intensity, well formed x-ray beams to a specimen. We have developed an optical bench for viewing and evaluating the focused x-rays emitted from these capillaries. The optical bench allows pulse counting, direct viewing of the x-ray probe spatial distributions, and energy pass band by using exchangeable detectors. Our results are used to determine the probe forming capabilities of the lenses and to indicate problems and directions for improving the manufacturing of the x-ray optics.

The x-ray optical bench is shown in a schematic diagram in figure A. It consists of a conventional Cu Kα x-ray diffraction tube joined to an optical table. An optical rail extends across them. A shielded box with a hinged side covers the source and the optical rail. The x-ray optic and exchangeable detector system are located on computer controlled stages to allow fine adjustments in all necessary translation and tilt directions. This optical bench permits measurements to be devised, performed, and changed with a minimum of difficulty. The optical bench allows for maximum flexibility in sample positioning, detector positioning, source size, and source collimation. The quantities that we evaluate in each optical element include focal spot size, spot uniformity, total spot flux, spot aberrations, diffuse scattered radiation, and depth of field or convergence.

We have measured the optical properties of more than 40 elements such as that shown in figure B. The x-ray optical element categories measured include single-untapered capillaries, single-tapered capillaries, untapered-capillary bundles, and tapered-capillary bundles. The transmission of individual capillaries of different compositions, including pyrex, soda-lime, Pb-silicate, and H-Pb-silicate glass has been measured using the optical bench. We performed extensive imaging of the transmission of x-rays in sintered bundles of capillaries, and in compound bundles of large cross-sectional area (5 mm). Figure C shows an example of the imaging capability and utility of the x-ray optical bench in testing optics. The transmission at points and lines between the hexagonal bundles of capillaries, where the bundles did not completely fuse, is higher than down the center of the capillaries. This type of information is useful in the manufacture and understanding of the performance of the optical elements.

We are currently performing tests on optics to determine optimal properties of microprobes for x-ray fluorescence and diffraction. The complex and currently irreproducible nature of the x-ray optic production makes the optical test bench a very useful tool in the screening and characterization of individual optics.

A

2-D X-Ray CCD Array

Optical Element

X-Ray Source

Slits

Stepping-Motor Controlled
Two-Axis Rotation Stage

Stepping-Motor Controlled
XYZ Translation Stages

NIST

B

10 μm

C
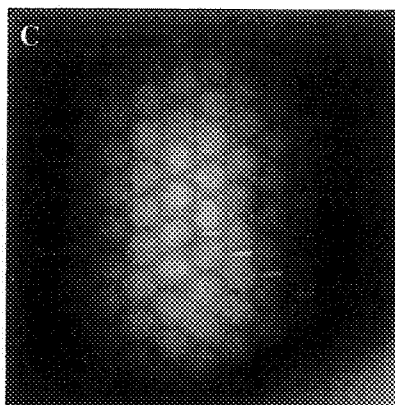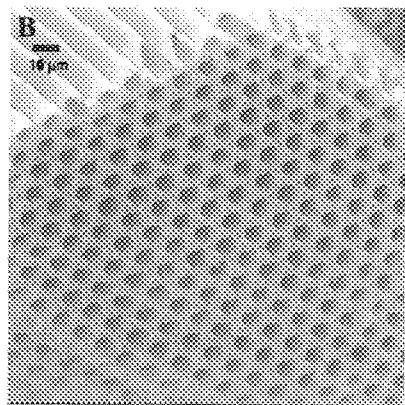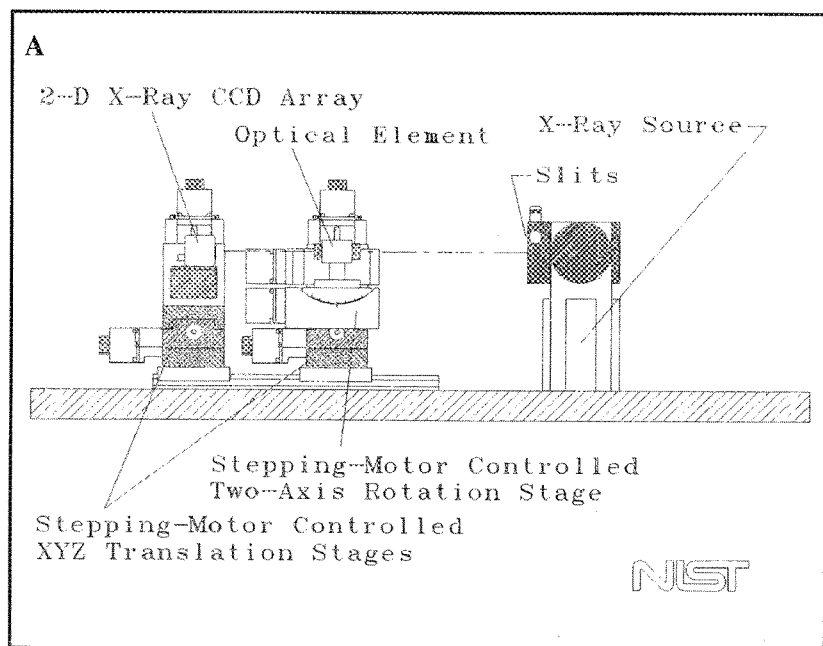
Figure A. Schematic of x-ray optical bench.

Figure B. Secondary electron micrograph of a single capillary bundle.

Figure C. Image of x-rays emitted from a bundle of capillary bundles.

247

MICROSCOPIC RADIOGRAPHY: A COMBINED TECHNIQUE FOR IMPROVED ANALYTICAL MICROSCOPIC ANALYSIS AND INTERPRETRATION

A. Angel and R.C. Moretz

Department of Analytical Sciences, Boehringer Ingelheim Pharmaceuticals, Inc., Ridgefield, CT 06877

Microscopic analysis of pharmaceutical devices and products relies primarily on destructive sample preparative methods, including sectioning, sawing, grinding and embedding. Reconstruction of images obtained from the prepared samples is often necessary to interpret the results. The preparative methods can introduce artifacts or distortion, which can affect the analysis, and the inability to visualize the intact object can also affect the interpretation. Radiography has been used to assist in the selection of preparative methods for microscopy, determine optimal orientation during preparation and analysis and to aid in the visualization and integration of the microscopic results in the final interpretation. The application of x-ray radiography to the examination of intact devices or manufactured drug products in conjunction with standard light and scanning electron microscopic evaluation presents a novel non-destructive technique to assess device structure and function as well as locate potential inclusions in manufactured drug products.

For this study, x-ray radiography has been carried out on intact commercially available inhalation aerosol canisters with mouthpieces to examine actuator-canister interaction in the "down" (actuacted or delivery) position and "up" (normal) position. Delivery of inhalation aerosols to the pulmonary system is critical to the treatment of chronic obstructive pulmonary disease, asthma and other respiratory diseases. Inhalation aerosol medications have traditionally been packaged under pressure in metal canisters. Components and dimensions critical to efficacious drug delivery are the mouthpiece, mouthpiece orifice, valve, valve stem, aperture, metering chamber (tank), spring and gaskets. Because penetration of x-rays varies with density and keV, the mouthpiece /stem interaction and the valve subcomponents could be studies by varying the keV.

Radiograms were obtained between 20 and 120keV to compare 4 Metered Dose Inhalers (2 glued in the actuation position and 2 in the normal position). Canisters examined in the "down" positions were prepared in the following way: the canister was shaken for ten seconds, inverted and actuated four times, shaken for ten seconds again then actuated and glued down the the drug delivery position.

Lower keV radiograms showed the actual seating of the mouthpiece to the valve stem (fig. 1). Radiographs obtained at higher keVs allowed visualization of the actual sub-components of the metering valve assembly (figs. 2 & 3). Valve stem/mouthpiece fit on actuation can be determined (fig. 1) as well as internal component alignment within the valve and the compression/position of the spring (fig. 3).

The information obtained through this technique provided information important in deciding which preparative methods were most appropriate for subsequent light and scanning electron microscopic studies. Knowledge about component interactions in intact devices was critical in interpretation of microscopic results and application to device analysis.
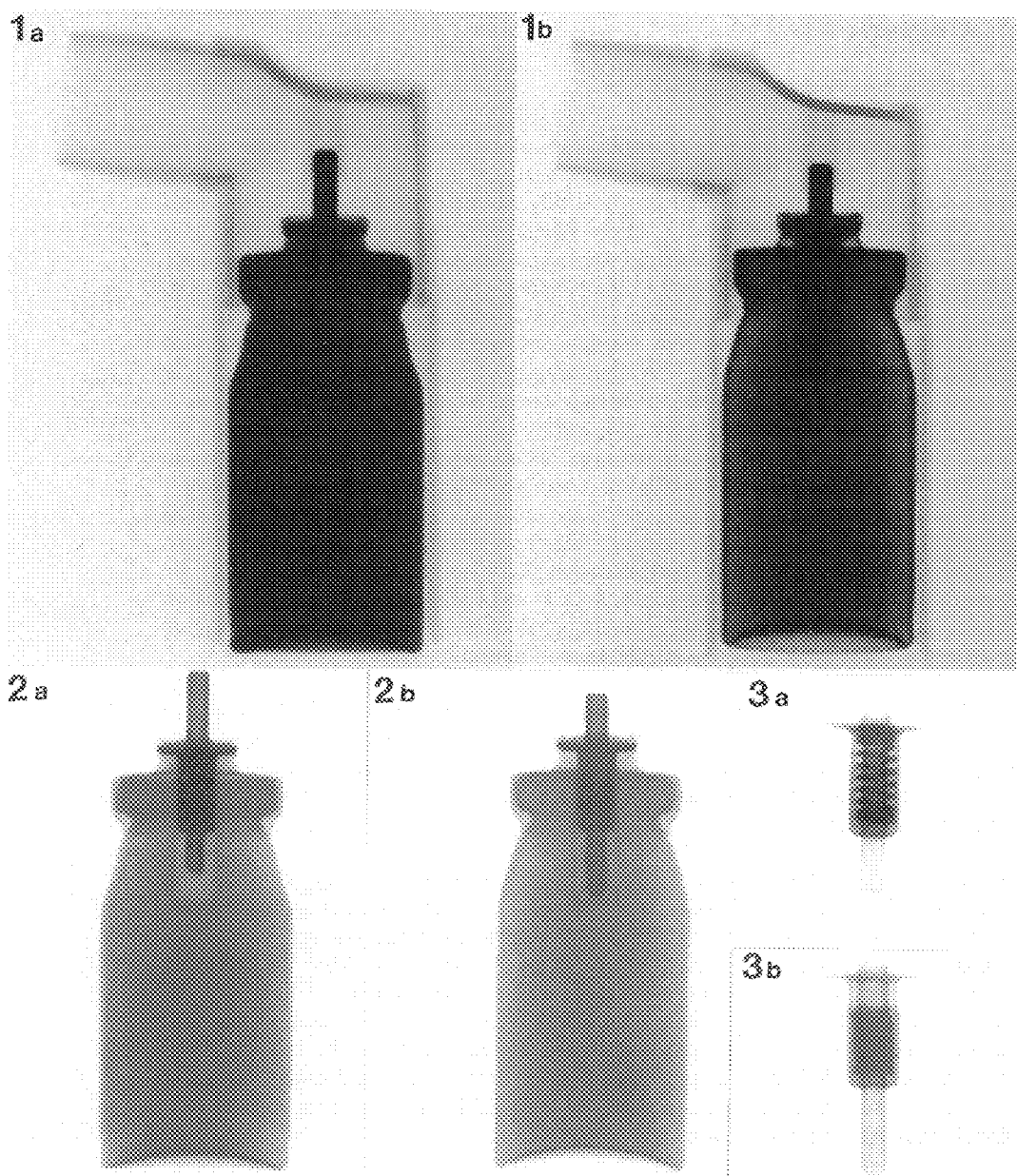
Figure 1. Radiographs taken at 55keV of intact canisters in the "up" (a) and "down" (b) positions.
Figure 2. Radiographs taken at 65keV of intact canisters in the "up" (a) and "down" (b) positions.
Figure 3. Englargements of the spring/stem assembly radiographs taken at 65keV in the "up" (a) and "down" (b) positions.

Molecular Microspectroscopy: Where are we and where are we going?

John A. Reffner

Spectra-Tech Inc. Shelton, CT 06484

Molecular microspectroscopy is the application of infrared or Raman spectroscopy, combined with light microscopy, for chemical analysis on the microscopic scale. For over a decade infrared microspectroscopy (IMS) has been an expanding technology both scientifically and commercially. Micro-Raman spectroscopy has a long history of scientific accomplishments with limited commercial success.[1] Both of these techniques give spectral data that can be related to the bonding, crystalline state, isotopic content and molecular orientation of a material, but not its elemental composition. In this regards, molecular microspectroscopy compliments the elemental analyses performed with electron microscopes using x-ray emission spectroscopy. Resolving molecular chemistry of microscopic domains is the essence of molecular microspectroscopy.[2]

Raman spectroscopy is experiencing renewed interest because of several advances in optics and photonics. Near-infrared lasers combined with Fourier transform spectro-meters greatly reduced fluorescence interference, making Raman spectroscopy practical for many samples.[3] The development of filters with high rejection of the Rayleigh scattered radiation simplifies the optical design of Raman systems.[4] These filters are playing an important role in micro-Raman. CCD and CID detector technology, lasers, acusto-optical tuned filters (AOTF), liquid-crystal tuned filters (LCTF) and imaging spectrometers are contributing to a proliferation of new micro-Raman systems.[5-6]

The advantages of micro-Raman spectroscopy are sub-micron spatial resolution, visible or near-infrared excitation and an extended spectral range for the analysis of both inorganic and organic molecules. Its disadvantages are that Raman scattering is very weak and many materials are naturally fluorescent, which interferes with Raman spectral measurement.

IMS has rapidly developed into a mature analytical discipline, achieving both scientific and commercial success.[7] Infrared spectroscopy is a fundamental instrumental method for chemical analysis with large data bases for qualitative analysis and established methods for quantitative analysis. IMS instrumentation is available as accessory microscopes for infrared spectrometers or as dedicated IMS systems. There are over five thousand IMS systems world wide, with sixty percent of these in the US. Chemicals, coatings, electronics, pharmaceuticals, plastics, rubber and textile industries are major users of IMS technology. Forensic laboratories have established IMS as an essential tool for trace evidence analysis. Clearly IMS has established itself as a valuable technique for molecular microanalysis.

The future holds the promise of spectral imaging. Spectral imaging is recording the infrared or Raman spectrum of an array of points simultaneously. With a spectral image it should be possible to point to any morphological feature within this image and

instantaneously display the infrared or Raman spectrum of that feature. In addition, by selecting certain spectral features, an image can be constructed wherein the contrast reflects the distribution of specific chemical components. With current technology chemical distributions are recorded by sequentially analyzing individual points. These methods are limited by the fact that the data collection time per point is several seconds to as much as a few minutes. If an array detector sensitive to the mid-infrared region were available that had 256 x 256 elements then, in theory, the data collection time for the array of 65,536 elements would be no longer than the data collection time for a single point. We look forward to seeing these detectors readily available at reasonable prices and the computational power expanded to rapidly process the large arrays of data. These chemical imaging IMS systems will then reach our goal of relating what we see to its composition.

An imaging Raman system (Renishaw[8]) is commercially available which uses filter technology combined with a CCD detector. This system combines filter technology for imaging with a point analysis system for high-resolution Raman spectroscopy. Other imaging Raman systems have been constructed from LCTF and AOTF. These systems are pointing the way to the future.

We are entering a new era of molecular microspectroscopy where relating chemistry to the micro-structure is of major importance. In the past decade, the users of molecular microspectroscopy have been primarily analytical chemists. Their major concern was chemical analysis; imaging was only a means to locate microscopic samples for spectral analysis. The era of spectral imaging is important to biologists and materials scientists who need to supplement their studies of micro-structure with detailed molecular analysis. The technology of combining imaging and chemistry has evolved over several decades with many major accomplishments. We are at the threshold of new advances, with new challenges and new opportunities.

References

1. G. Rosasco, E. S. Etz, and W. A. Cassatt, *Appl. Spectrosc.,* 29(1975), 396
2. C. D. Arvanitopolos and J. L. Koenig, Appl. Spectrosc., 50(1996), 1
3. *Fourier Transform Raman Spectroscopy fron Concept to Experiment*, D. B. Chase and J.F. Rabolt, Eds (Academic Press, New York, NY, 1994)
4. M. Futamata, *Appl. Spectrosc.,* 50(1996), 199
5. I. Kurtz, R. Dwelle and P. Katzka, *Rev. Sci. Instrum.* 58(1987), 11
6. P. J. Treado, I. W. Levin and E. N. Lewis, Appl. Spectrosc., 48(19940, 607
7. *Practical Guide to Infrared Microspectroscopy*, H. J. Humecki, Ed.,   (Marcel Dekker, Inc. New York, NY, 1995)
8. Renishaw Inc., Schamburg, IL.

SPECTRAL IMAGING THROUGH THE LIGHT MICROSCOPE: APPLICATION TO THE IMAGE ANALYSIS OF COLORED STRUCTURES IN HISTOLOGY

R. L. Ornberg

Monsanto Corporate Research, Monsanto Company, 800 N. Lindbergh Blvd., St. Louis, MO 63167

Color is an important factor in defining structures in both biological and materials microscopy. Indeed, the field of histology/pathology is founded on the use of special dyes and staining procedures which label features of interest with a defining color. Of particular interest is the use of colorigenic substrates in enzyme linked - immunochemistry on tissue sections and the subsequent measurement of the amount of labeling in a given tissue. Typically, colored image objects such as the red deposit produced by the reaction of AEC (aminoethylcarbazole) substrate with peroxidase enzyme can be detected in RGB (red, green, blue) images by a combination of RGB pixel intensities or by HSI (hue, saturation, intensity) pixel intensities. Using a new color imaging system with spectral image acquisition capabilities, we have develop an imaging algorithm based on the absorption spectra of the colored object and the counter stained surrounding space that provides optimal images of segmentation and morphological measurement.

The basic system consists of a low light level CCD coupled to a liquid crystal tunable filter (Cambridge Research Instruments). The filter is based on the Lyot-type birefringent filter and provides continuous wavelength selection from 400 - 720 nm with wavelength dependent resolution of about 10 nm at 500 nm. The system is controlled by a Silicon Graphic workstation and Isee software written by Inovision Corp. Spectral images, i.e., images at a given wavelength, can be obtained and the intensity of objects with in a given image can be sampled as a function of wavelength for microspectro -photometric or -fluorometric analysis.

We have used this system to acquire and process images of colored objects used in routine histological work. The example we describe below examines a tissue section that has been immunolabeled with a macrophage specific antibody, ED1, and detected with an AEC-peroxidase reaction product. The red in polymerized AEC has an absorption at 560 nm which is greater than at 630 nm while the counterstain has roughly the similar transmittance at these two wavelengths, Fig. 1. By collecting two flat field corrected images at these wavelengths and dividing them, red deposits in the resultant grey image appear as bright objects in a uniformly dark surround. In this form, these objects can be readily segmented by standard image threshold routines. Similar conditions can be obtained for other stained products such as diaminobenzidine-peroxidase reaction product and special stains such as Safranin O, trichrome stains and so on. Hence the number, area , and other size parameters of the objects can be easily measured with improved objectivity, accuracy and speed. Examples of immunostained biological tissue will be shown but these procedures work equally well for material specimens view in diascopic or episcopic imaging modes.

References:

1. The author would like to thank Dr. Doug Benson of the Inovision Corporation for his helpful discussion during the course of this work.
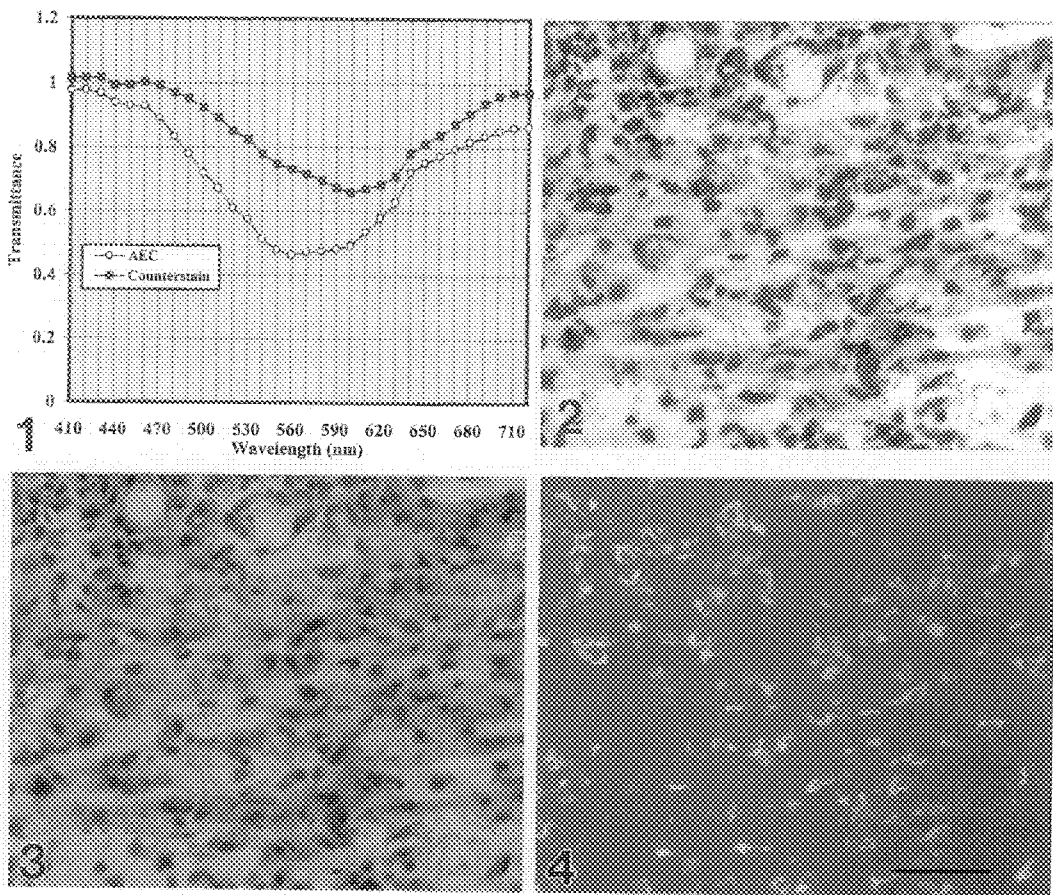
Figure 1. Transmittance spectrum of AEC deposit and hematoxylin counterstain.
Figure 2. Image of AEC stain immunolabeled section of tissue taken at 560 nm.
Figure 3. Image of AEC stain immunolabeled section of tissue taken at 630 nm.
Figure 4. Image obtained by dividing the image in Figure 3 by the image in Figure 2. The bright objects are the AEC reaction product which is identifying ED1 positive macrophages in the tissue. Bar = 50 um.

RAMAN IMAGING IN THE REAL WORLD

Michael D. Morris,* Kenneth A. Christensen,* and Nancy L. Bradley*

*Department of Chemistry, University of Michigan, Ann Arbor, MI 48109-1055

Recent technological advances including high spectral resolution liquid-crystal tunable filters and high-transmission well-corrected imaging spectrographs have made Raman microscopy a practical technique for study of real-world chemical systems.[1-3] With modern multivariate signal processing techniques, such as image reconstruction and principal components analysis (PCA) detailed information can be obtained from sets of relatively noisy images or spectra. In this talk we discuss techniques and results in two areas of materials chemistry: crystallization and freeze-drying mechanisms of alkali phosphates and strengthening mechanisms of glasses employed in dental restoration.

We employ Raman microspectroscopy to elucidate the structure of aqueous phosphates in solutions ranging in concentration from dilute to supersaturated. PCA of the concentration-dependent spectra of dihydrogen phosphate solutions unambiguously demonstrates the presence of at least three species, monomer, dimer and trimer or short polymer (Figure 1). PCA resolves long-standing disputes over the number and relative concentration of dihydrogen phosphate species PCA can to identify the spectrally unresolved solution species near the surface of a growing dihydrogen phosphate crystal.[4-6]

Similarly, phosphate buffer solutions are an important model system for study of freeze-drying mechanisms. As the temperature of the buffer is slowly lowered, pure ice crystallizes while the remaining solution is freeze-concentrated. This results in large changes in pH as the less soluble hydrogen phosphate salt precipitates or forms eutectic mixtures with ice and the dihydrogen phosphate, which easily forms supersaturated solutions, continues to be concentrated in the interstices. We use Raman microspectroscopy and imaging to identify and monitor the microenvironments present at different temperatures and starting concentrations. Figure 2 is the Raman image, perpendicular to the freeze-front, of freeze concentrated dihydrogen phosphate solution with ice microcrystals present. Figure 3 is a Raman image taken parallel to the freeze front showing inclusions of crystalline $Na_2HPO_4 \cdot 12\ H_2O$ in ice. From sets of similar images it is possible to develop a more complete picture of the dynamics of freezing and, ultimately, to extend the picture to industrially important freeze-drying systems.

High alkali silica glasses which fuse at low temperatures are emerging dental restorative materials. Glass offers many advantages over conventional materials, including durability, biocompatibility, and aesthetics, but most glasses are too weak to survive mastication forces. These glasses are strengthened either by refluxing in a weak acid solution or by autoclaving.[7,8] Neither technique has yet been proven superior. In both cases the chemical changes which cause strengthening remain uncertain. We use Raman imaging and depth-resolved Raman microspectroscopy to probe the glass chemistry. Because of small local composition differences and the presence of gaseous and solid inclusions, Raman imaging, rather than depth-resolved spectroscopy alone, is necessary. It has been proposed in both cases that the deplasticization of the surface layer through the addition of hydroxyl groups results in a strength increase. Analysis of depth-resolved images and spectra of acid-refluxed samples suggests the chemical reaction is conversion of the silicic acid species to silica, rather than the reverse. For example, Figure 2 shows the depth-dependence of the silicic acid (880 cm^{-1}) and silica (1090 cm^{-1}) Raman band intensities and their ratio, confirming our view of the chemistry. Essentially similar plots can be made at any region of the glass not containing inclusions or local concentration anomalies. The role of water in the conversion is still under investigation. Depth-resolved Raman imaging employing a dual Fabry-Perot filter maps the distribution of relevant species at planes perpendicular to the surface. From these images and from microprobe spectra, detailed composition profiles are constructed.

References

1. K.A. Christensen et.al.,*Appl. Spectrosc.*, 49(1995)1120.
2. H.R. Morris et.al., *Appl. Spectrosc.*, 48(1994)857.
3. D.E. Battey et.al., *Appl. Spectrosc.*, 47(1993)1913.
4. M.K. Cerreta and K.A. Berglund, *J. Cryst. Growth*, 84(1987) 577.
5. F. Rull et.al., *J. Raman Spectrosc.*, 20(1989)625.
6. G. Liu and G. Wu, *Spectrochim. Acta*, 44A(1988)1007.
7. R.F. Bartholomew, *J. Non-Cryst. Sol.*, 56(1983)331.
8. V.A. Bershtein et.al., *Sov. Phys. Dokl.*, 18(1974)730.
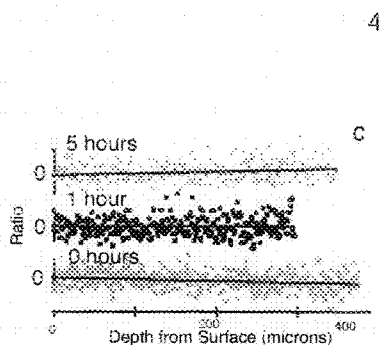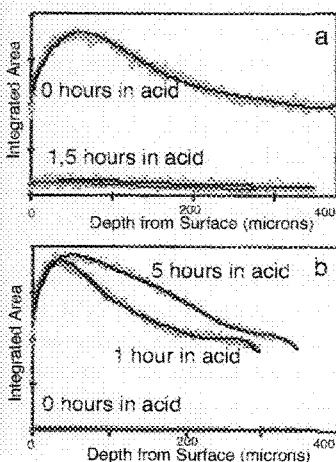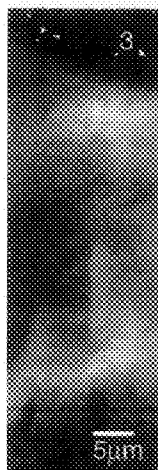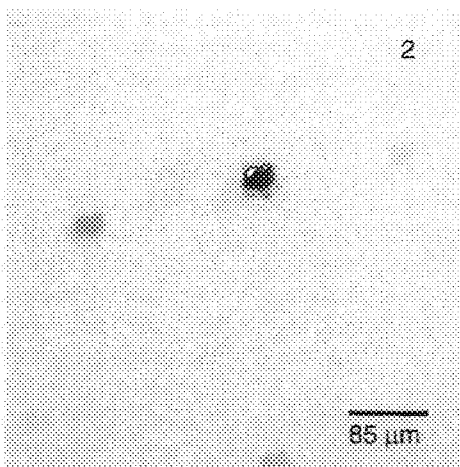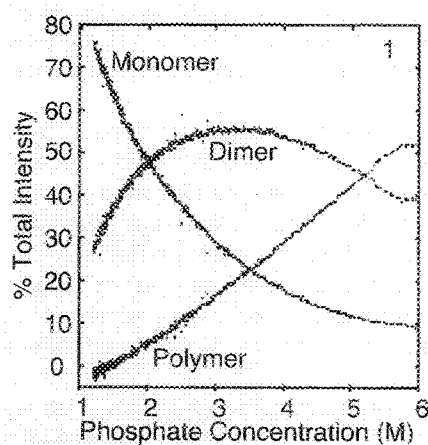
FIG. 1 Results of PCA from dilution experiments. Relative concentrations of each species.
FIG. 2 Raman image of $H_2PO_4^-$ solution showing ice microcrystals.
FIG. 3 Raman image of $Na_2HPO_4 \cdot 12\ H_2O$ crystals in ice.
FIG. 4 Effect of time in acid. a)Silicic acid band b)Silica band c)Silicic acid/Silica Ratio.

CRACK ANALYSIS OF UNFILLED NATURAL RUBBER USING INFRARED MICROSPECTROSCOPY

L. A. Neumeister and J. L. Koenig

Department of Macromolecular Science, Case Western Reserve University, Cleveland, Ohio 44106

Several spectroscopic methods are available for characterizing the crack tip region of natural rubber on the molecular scale to develop a material with fatigue resistant properties. Attenuated total reflectance or ATR-IR has been used to characterize the structure of many different polymers, including rubbers.[1,2,3] Transmission has also been well established as a viable technique for the molecular characterization of transparent materials including thin films of unfilled natural rubber.[3]

Unfilled natural rubber was stretched to 629% elongation until cracks appeared in the surface. A cross section of the sample containing a crack was then microtomed at -85°C into slices approximately 0.5 μm thick. Similarly, samples were cut with a razor and microtomed under the same conditions. The crack tip region was mapped using the IRμs™/SIRM Molecular Microanalysis System. The map consisted of ten spectra taken in the x and y directions as shown in Figure 1. The same region was analyzed for orientation of molecular structures. Points were selected along the crack tip, crack edges, and the bulk. Dichroic ratios of all prominent peaks were calculated. ATR was used to verify the results of the mapping experiments for both stressed and unstressed material.

Once the spectra were corrected for thickness variation, absorbance maps of the crack tip region were obtained. Figure 2 represents a map of the crack tip region for the =CH wag peak at 837 cm^{-1}. The crack itself has no material present and is represented by very low absorbances. Surrounding the tip and edges are areas of significantly higher absorbances which then gradually decrease to an overall average absorbance in the bulk. Another more visual representation of this result is shown by a 3-D contour map of the 837 cm^{-1} in Figure 3. This trend occurred for all prominent peaks mapped. The results of the ATR analysis are displayed as one dimensional line maps around the crack tip region. The absorbances of certain peaks are plotted against the distance the measurement was taken from the crack tip. Figure 4 shows this result for stressed material. The results for both techniques indicate that the material in the crack tip region is identical to the bulk in the case of a razor cut.

Molecular orientation was analyzed around the crack tip region for stressed and unstressed samples. Dichroic ratios for structures corresponding to prominent peaks are in Tables 1 and 2. The results indicate a high degree of orientation in the cracks created by stressing due to permanent set. Light crosslinking occurring at the crack tip region in the elongated state may cause molecular structures to maintain their high degree of orientation. This is reflected as high dichroic ratios upon relaxation.

References

1. D. H. Carey and G. S. Ferguson, *Macromolecules* **27**, 7254 (1994)
2. V. K. Kaushik and Y. N. Sharma, *Polymer Bulletin* **13**, 373 (1985)
3. R. C. Hirst, *Rubber Chem. & Tech.* **55**, 913 (1981)

FIG. 1. Procedure for mapping the crack tip region using transmission

1

240 μm

240 μm

Spectra obtained

91-100
81-90
71-80
61-70
51-60
41-50
31-40
21-30
11-20
1-10

40 μm x 40 μm square aperture

26.7 μm increments between spectra

2a

2b

High

Low

3

Crack

Table 1. Dichroic ratios for randomly selected locations around the crack tip region of the stressed unfilled natural rubber. Point c is at the tip and the others are along the crack edges. Errors are shown in parentheses after each dichroic ratio.

Location	3290 cm⁻¹	1742 cm⁻¹	1665 cm⁻¹	837 cm⁻¹
Structure	OH	C=O	C=C	=CH
a	1.45 (0.11)	2.18 (0.13)	1.39 (0.02)	2.46 (0.03)
b	1.29 (0.11)	2.24 (0.15)	1.44 (0.03)	2.61 (0.03)
c	3.68 (0.43)	4.24 (0.39)	1.76 (0.05)	2.37 (0.03)
d	1.55 (0.12)	2.00 (0.10)	1.45 (0.03)	2.80 (0.04)
e	1.24 (0.08)	2.28 (0.14)	1.40 (0.02)	2.36 (0.02)
bulk	1.55 (0.16)	1.53 (0.20)	1.20 (0.05)	1.04 (0.03)

Table 2. Dichroic ratios for randomly selected locations around the crack tip region of a crack made by a razor blade. Point c is at the tip and the others are along the crack edges. Errors are shown in parentheses after each dichroic ratio.

Location	3290 cm⁻¹	1742 cm⁻¹	1665 cm⁻¹	837 cm⁻¹
Structure	OH	C=O	C=C	=CH
a	1.24 (0.09)	1.37 (0.14)	1.28 (0.11)	1.04 (0.08)
b	1.21 (0.08)	1.31 (0.11)	1.24 (0.09)	1.03 (0.06)
c	1.20 (0.08)	1.31 (0.12)	1.22 (0.09)	1.05 (0.06)
d	1.47 (0.09)	1.63 (0.12)	1.51 (0.10)	1.27 (0.07)
e	1.23 (0.09)	1.38 (0.14)	1.30 (0.11)	1.03 (0.08)
bulk	1.15 (0.10)	1.34 (0.11)	1.26 (0.14)	1.07 (0.07)

4

Peak Height

Distance from crack (μm)

Peak 1536
Peak 1458
Peak 1397

FIG. 2. a) Actual picture of the crack tip region in unfilled natural rubber b) Map of the 837 cm⁻¹ peak in the crack tip region where the crack was created by stretching

FIG. 3. Three dimensional contour map of the 837 cm⁻¹ peak representing the =CH wag

FIG. 4. Peak height vs. distance from the crack tip in unfilled natural rubber where the crack was created by stretching the material. Data was obtained using attenuated total reflectance techniques.

257

FOURIER TRANSFORM INFRARED CHEMICAL IMAGING MICROSCOPY: APPLICATIONS IN NEUROTOXICITY AND PATHOLOGY

E. Neil Lewis[*], Linda H. Kidder[*], David S. Lester[**] Victor F. Kalasinsky[***] and Ira W. Levin[*]

[*]Laboratory of Chemical Physics, National Institute of Diabetes, Digestive and Kidney Diseases, National Institutes of Health Bethesda, Maryland 20892

[**]Center for Drug Evaluation and Research, Food and Drug Administration, Laurel, MD 20708

[***]Department of Environmental and Toxicologic Pathology, Armed Forces Institute of Pathology, Washington, D.C. 20306

We have developed a new Fourier transform infrared chemical imaging technique[1] which, when coupled with powerful multivariate data processing techniques, allows the visualization of complex intrinsic chemical distributions in biological materials with the potential for performing rapid histological examinations. Integrating spectroscopy with sample visualization and digital image processing is a potent combination of what have traditionally been two distinct methods for studying the chemistry and morphology of a sample. This synergy has been referred to as *chemical imaging* or *hyperspectral imaging* and has wide ranging applications in material characterization. In the infrared spectral region the technique relies on the use of infrared focal-plane array detectors, a newly developed commercial technology. These arrays are used in conjunction with standard Cassegrainian infrared microscopes and commercially available step-scan Michelson FTIR spectrometers to construct infrared imaging systems capable of collecting tens of thousands of spatially resolved infrared spectra ($3\mu m^2$) with less than 1 minute of data acquisition time.[2] The data sets contain both spatial and spectral information and typically consist of hundreds of images resolved in frequency space (wavenumbers, cm^{-1}), with each image containing many tens of thousands of pixels.

We have applied this chemical imaging approach to a common pathological problem, studying foreign inclusions in human tissue. Specifically, we have examined human breast tissue containing silicone and polyestyer found in subjects with a history of silicone implant breast reconstructive surgery. These samples were 5μm sections obtained from human biopsy, and layered onto calcium fluoride windows. Also, we have chemically imaged cerebellar tissue from Sprague Dawley rats that were treated with cytarabine. This antineoplastic drug induces neurotoxic responses in the rat, which are morphologically expressed as significant Purkinje cell death. Cerebellar slices prepared from rats exposed to either defined doses of cytarabine or control saline were cut 10 μm thick. These unstained slices were also layered onto calcium fluoride windows. Using a step-scan Fourier transform infrared spectrometer in conjunction with a high sensitivity infrared focal-plane array detector, spectra and images, containing 128x128 pixels, were collected from a series of samples at a spectral resolution of 16 cm^{-1} and a spatial resolution of approximately 6 μm.

Figure 1 shows a bright field and infrared chemical image obtained from a cytarabine treated rat cerebellum sample. Each data set contains hundreds of discrete images which can be analyzed in a variety of ways to provide contrast based on a particular cellular constituent. For example, image B in figure 1 has been processed so that the contrast is based solely on the lipid/protein ratio. Using this technique, the differences in each of the three layers is readily visualized and quantified. The image indicates that the lipid signature is particularly strong in the granular layer relative to the rest of the sample. In addition, in many of the treated samples, the individual Purkinje cell bodies could also be distinguished. Data will be presented showing detailed spectral and image analyses performed on these samples. Spectral differences observed between discrete regions within individual samples will be highlighted.

References

1. Lewis, E.N., Levin, I.W. and Treado P.J., US Patent number **5,377,003,** December 1994.
2. Lewis, E.N., Levin, I.W., Treado, P.J., Marcott, C., Story, G.M., Reeder, R.C., Dowrey, A.E., Analytical Chemistry **67**, 3377 (1995).
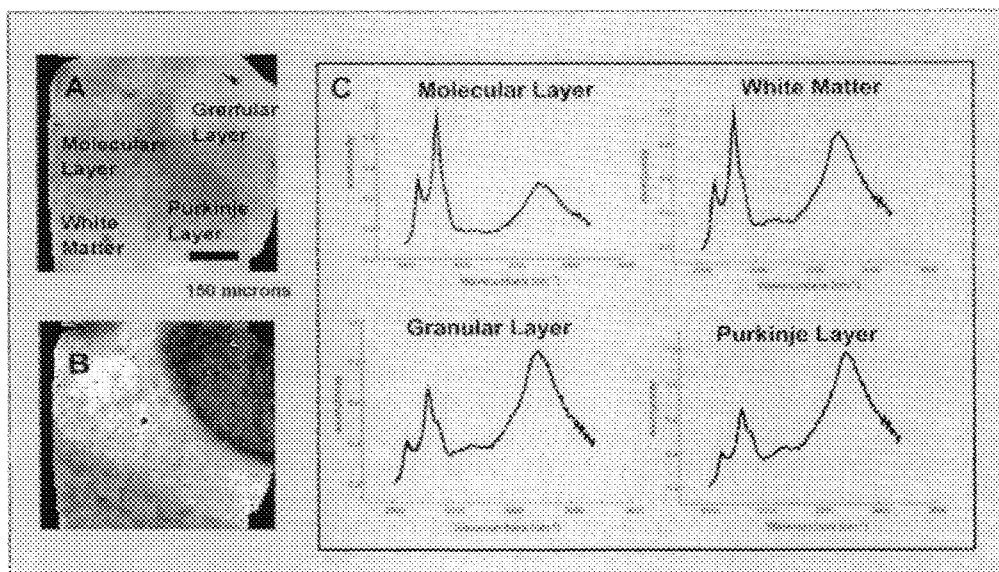
FIG. 1 Brightfield (A) and infrared image (B) of a 10 μm section of cytarabine treated rat cerebellum. Panel C shows individual spectra extracted from different morphological layers.

INFRARED SPECTROSCOPIC CHEMICAL IMAGING

Curtis Marcott and Robert C. Reeder

The Procter & Gamble Company, Miami Valley Laboratories, Cincinnati, OH 45253-8707

Infrared (IR) spectroscopy is a powerful, widely used technique for identifying materials or chemical compounds. An IR spectrum often provides a specific fingerprint for a given molecular component or species. IR frequencies, intensities, and line widths are also extremely sensitive to environmental perturbations and changes in molecular structure. Infrared spectroscopic images recorded through a Fourier transform infrared (FT-IR) microscope attachment have traditionally been constructed by translating a mapping stage a single pixel at a time through the sample area of interest; this is a very tedious and time-consuming procedure. Recently, a technique for rapidly performing high-fidelity FT-IR imaging spectroscopy using an indium antimonide (InSb) focal-plane array (FPA) detector coupled to an IR microscope and a step-scanning FT-IR spectrometer has been developed. These multichannel IR detectors were originally developed for thermal-imaging applications (mainly in the military), but they have tremendous potential as chemical imaging detectors when used as part of a spectrometer. The multiple detector elements enable images from all pixels to be collected simultaneously for each mirror retardation position of the interferometer. Use of an interferometer allows the entire IR spectrum over some wavelength range to be measured. The combination of a step-scanning FT-IR microscope and an InSb FPA detector provides unprecedented speed and image quality, limited only by the diffraction limit and/or the number of detector elements on the array.

A 25-μm-thick cross section of a commercial packaging material film (Paramount) was examined by FT-IR imaging microscopy. The sample consisted of a 12-μm-thick surface layer of poly(ethylene terephthalate) (PET), followed by a 7.5-μm-thick adhesive tie layer (possibly ethylene vinyl acetate copolymer), a 15-μm-thick layer of ethylene vinyl alcohol copolymer (EVOH), another 7.5-μm-thick adhesive tie layer, and a 75-μm-thick layer of low-density polyethylene (LDPE). The figure shows three image planes extracted from a complete spectroscopic image of the PET/EVOH/LDPE laminate cross section. A spectroscopic image can be thought of as a three-dimensional cube of absorbance values with x-y image planes for each wavenumber in the spectrum. A line drawn in the z direction through the same x,y coordinates in every image plane represents the infrared absorbance spectrum of that individual pixel in the x-y plane. The brighter areas on each image represent regions of higher IR absorbance at the corresponding wavenumber of the image. The three IR spectra shown are coadded averages of a 4-pixel x 4-pixel area near the arrow point in images A, B, and C. Spectrum A, taken from a bright area in the 2891-cm^{-1} image plane, is consistent with that of LDPE. Spectrum B from the bright stripe in the 3200-cm^{-1} image is due to EVOH. Image C highlights the PET portion of the film. IR absorbance spectrum C from the bright area of the 2972-cm^{-1} image plane is consistent with PET. These results illustrate the powerful ability of spectroscopic imaging to uniquely bring out information related to the chemical nature of a sample.

A - 2891 cm^{-1}

B - 3200 cm^{-1}

C - 2972 cm^{-1}
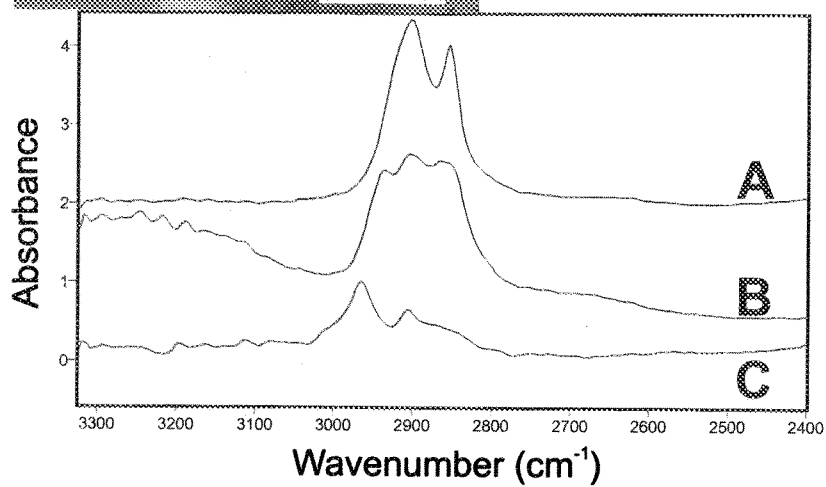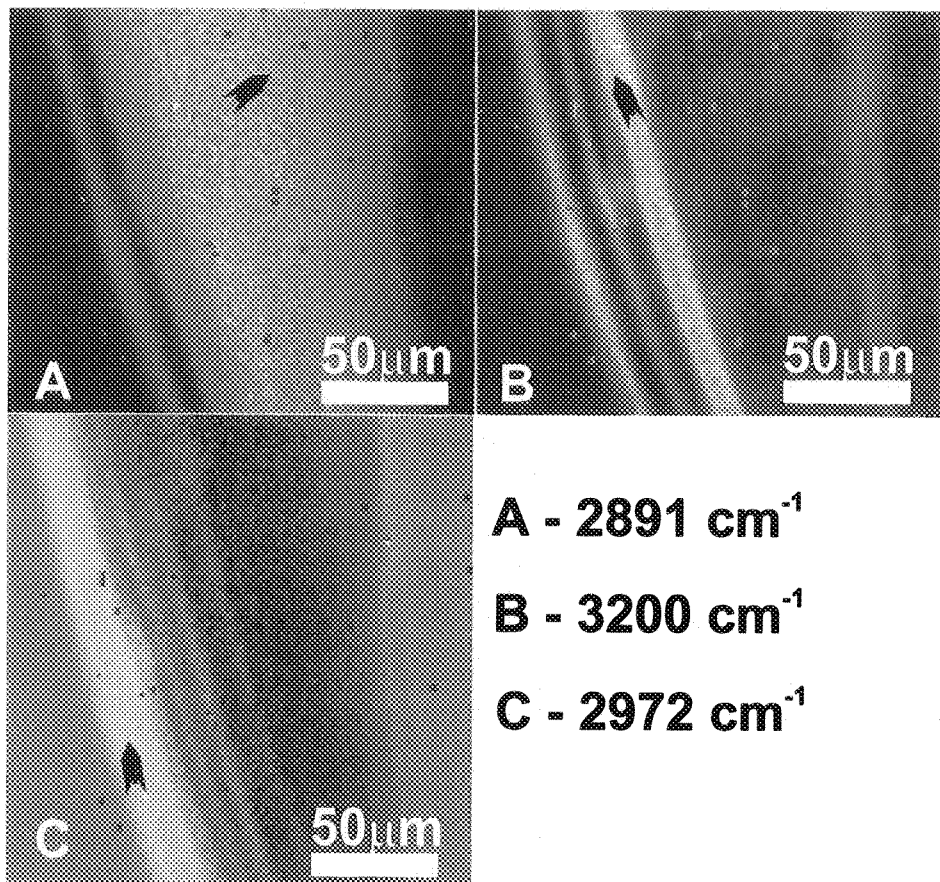
SYNCHROTRON INFRARED MICROSPECTROSCOPY CHALLENGES DIFFICULT ANALYTICAL PROBLEMS

David L. Wetzel*, John A. Reffner**, and Gwyn P. Williams***

*   Kansas State University, Microbeam Molecular Spectroscopy Laboratory, Shellenberger Hall, Manhattan, KS 66502
**   Spectra-Tech Inc., 2 Research Drive, Shelton, CT 06484
*** Brookhaven National Laboratory, NSLS, Bldg. 725B, Upton, NY 11973

Microspectroscopy of molecular species *in situ* takes advantage of biological concentration by nature of certain molecules within the bulk specimen. Localized hetergeniety is readily documented. Order or randomness may be established for substances that are present in a quantities below the detection limit in the bulk but that may be present in a measurable amount when acute probing is done in the correct region of the specimen. Spectral resolution with a microbeam directed at a relatively small spot from which spectroscopic data is obtained makes this task readily possible. Spectral resolution is achieved with optical efficiency of modern infrared microspectrometers in which signal is conserved and noise minimized. Improvement of S/N is routinely done by coadding multiple scans however reducing the aperture by half reduces the signal by at least four and doubling S/N requires taking data for four times as long. Thus even if a diffraction limiting situation does not arise one of these desirable goals of 1) good spectral separation (small aperture size), 2) high S/N (good low-noise spectra) and 3) short time of data accumulation must be compromised. This is true with even the most optically efficient instrument however substituting infrared radiation from the vacuum UV storage ring of the National Synchrotron Light Source (Brookhaven National Laboratory) for the conventional thermal (glowbar) instrument source makes it possible to achieve all three goals without the necessity of a severe compromise on at least one of them. The synchrotron beam is 2-3 orders of magnitude brighter, has no thermal noise, and has very low divergence. Aperturing the small concentrated beam results in a relatively small percentage loss in beam intensity.

Difficult analytical problems recently challenged with the synchrotron powered infrared microspectrometer include 1) localized differences (15µm apart) in finish on a single fiber by ATR, 2) probing 6µm thick longitudinal sections of human hair for street drug metabolites with a spot size equivalent to 22.4 minutes of hair growth in the life cycle of a drug user, 3) documentation (with incremental steps between scans) of the spectroscopic evidence of differences across a multiple sclerosis brain section through gray matter, white matter, peri-plaque and plaque, 4) sampling with cellular dimensions adjacent tissue or different cells for evidence of chemical difference, 5) detailed infrared mapping of tissue that visually appears homogeneous to reveal highly localized heterogeneities.

Fig. 1 shows carbonyl bands for a sequence of ATR spectra taken with a 10µm spot size at 15µm sampling intervals along the length of a single fiber. Irregularity in the ester bonded finish on the fiber surface is revealed. Fig. 2 shows an electronic photomicrograph of a 6µm thick human hair compressed between barium fluoride disks showing the 5µm spot that was sampled in transmission. The spectrum (Fig. 3) resulted from scanning the spot shown in the hair medulla.

The exceedingly small apertures gave a useful spectrum in the region shown but was diffraction limited below 1000 cm^{-1}. Other probing of this same hair that had been doped with a drug metabolite showed highly localized appearance of carbonyl absorption in the 1740 cm^{-1} region. Brain white matter spectroscopic characteristics[1] and changes upon demyelination or dismyelination have been previously reported[2,3]. Spectra for the plaque and adjacent relatively unaffected white matter from infrared mapping of MS brain tissue showed chemically-defined contrasted transitions between these adjacent tissues. Cell to cell differences were analyzed in wheat. One hundred percent mapping amide bandshape functions from small apertures suggested highly localized protein heterogeneities in both plant and mammalian tissues.

References

1. D. L. Wetzel and S. M. LeVine, *Spectroscopy*, 8(1993)40.
2. S. M. LeVine and D. L. Wetzel, *Am. J. Pathology*, 145(1994)1041.
3. S. M. LeVine et al., *Int. J. Neurosic.*, 12(1994)275.
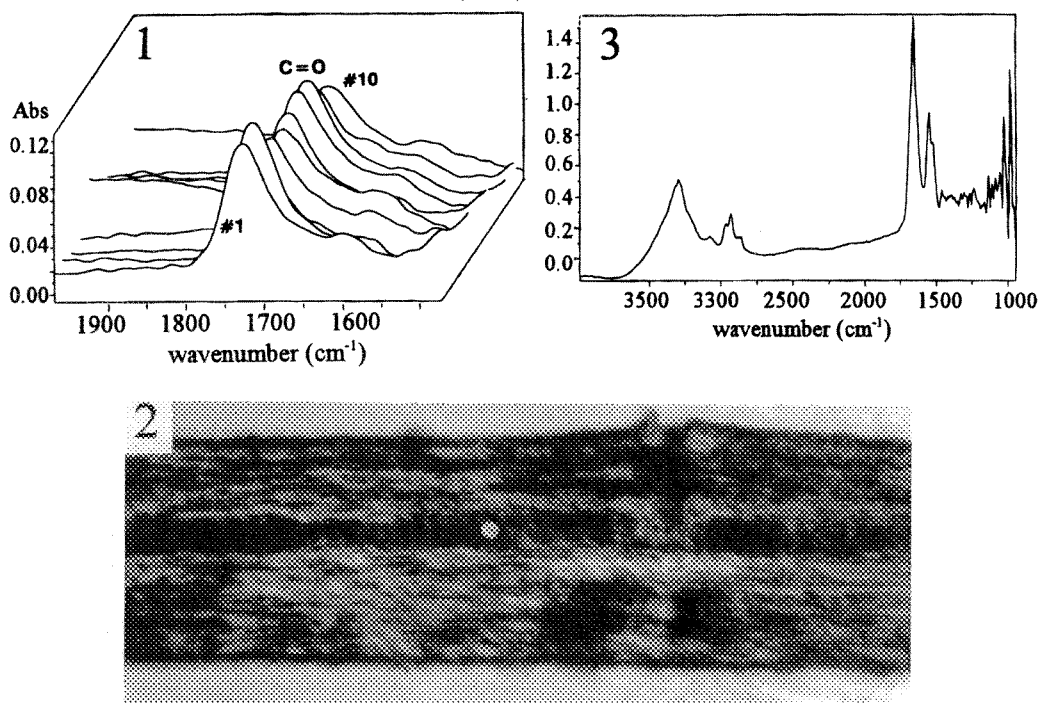
FIG. 1 Series of ATR Spectra from adjacent points 15μm apart along a single cotton fiber.
FIG. 2 6μm thick microtromed human hair showing 5μm projected aperture.
FIG. 3 Spectrum from spot shown in medulla of hair in Fig. 2

FTIR ANALYSIS OF PRINTED-CIRCUIT BOARD RESIDUE

Sharon A. Myers*, Troy D. Cognata** and Hugh Gotts***
*Component Engineering, Apple Computer, Cupertino, CA 95014
**Worldwide Operations Engineering, Apple Computer, Cupertino, CA 95014
***Materials Analysis Group, Philips Semiconductor, Sunnyvale, CA 94088

Logic boards were failing at Enhanced Mac Minus One (EMMO) test or Integrated Circuit Test (ICT) after printed circuit board (PCB) rework. The failure to boot was originally traced to a suspected bad microcontroller chip. Replacing this chip, or an oscillator tied to the microcontroller circuit, did not consistently solve the boot problem. With further testing, it was found the microcontroller circuit was very sensitive to resistance and was essentially shorted.

A resistor in the microcontroller circuit was identified on the flip side of the PCB. Several areas on the board, including the resistor R161, were seen to have a slight white haze/ low gloss appearance on the surface of the PCB. To test if the residue was electrically conductive, five boards were selected whose sole failure was R161. The resistance of the individual resistors was measured with a digital multimeter (DMM). The resistor was then cleaned with isopropyl alcohol and a cotton swab. Each board was retested at ICT and the individual resistors measured again with a DMM. Cleaning the area surrounding the resistor with isopropyl alcohol, corrected the failure four of the times.

Material was removed from the resistor and board surfaces by physically abrading the organic coating and transferring the abraded material to an infrared transparent substrate (single crystal silicon). FTIR spectra were collected in the transmittance mode using a Bio-Rad UMA 500 FTIR microscope using a circular aperture (40 micron diameter). Background spectra for the transmittance work were collected on clear areas of the infrared transparent substrate. Spectra generally consisted of 64 scans collected at 8 cm^{-1} that were co-added together before Fourier transformation.

The residue from the contaminant, Figure 1, exhibit FTIR spectra containing C-H stretching bands (2920 and 2851 cm^{-1}), C-H bending bands (1463 and 1378 cm^{-1}), C=O stretching band (1697 cm^{-1}) and C-O stretching bands (1281 and 1196 cm^{-1}). These residue spectra are consistent with the FTIR spectra of abietic acid.[1,2] The material does not match the flux after board processing, Figure 2 or the phenolic resin of the board spectra, Figure 3. Further FTIR analysis of flux used in the manufacturing process showed that the board residue is unreacted liquid flux.

During the rework process, liquid flux was entrapped under low clearance components, such as resistors. Flux in a liquid state is electrically conductive and will create a high impedance pathway. Flux residues that are completely dry are not conductive. Boards were no longer failing when solvents in the flux were volatilized. This occurred with the application of heat, such as when suspected IC's were replaced or with the use of isopropyl alcohol to clean the residue. The alcohol aided by displacing solvents trapped beneath components and aiding in the drying process.

References

1. L.J. Bellamy , *Infrared Spectra of Complex Molecules*, Chapman and Hall, 1975.
2. G. Socrates, *Infrared Characteristic Group Frequency,* John Wiley and Sons, 1980.
3. The authors gratefully acknowledge the use of facilities at the Materials Analysis Group,

Philips Semiconductor and Charlene Shebib for collection of some of the FTIR spectra. Frank Renfro and Mark Mercer of Apple Computer isolated the contamination problem and electrically characterized the pc boards before and after cleaning.
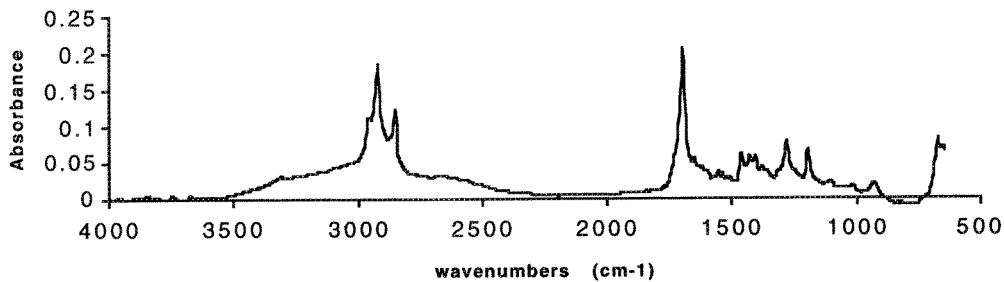
Figure 1
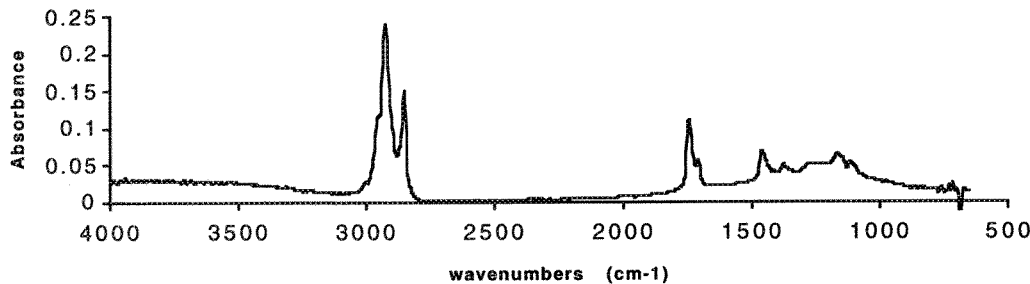
Figure 2
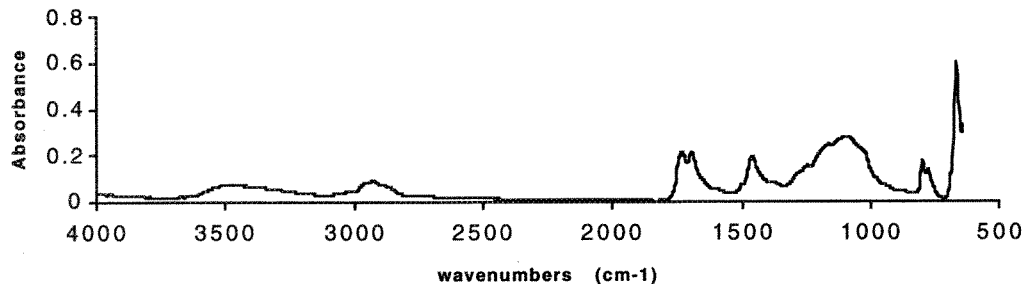
Figure 3

Figure 1 FTIR spectra of residue on printed circuit board.
Figure 2 FTIR spectra of activated flux.
Figure 3 FTIR spectra of printed circuit board phenolic resin.

<center>TUTORIAL</center>

ION-BEAM MILLING MATERIALS WITH APPLICATIONS TO TEM SPECIMEN PREPARATION

Ron Anderson

IBM Analytical Services, ZIP E-40, Hopewell Jct., NY 12533

For the last thirty years, ion milling has been an indispensable part of preparing TEM specimens in the physical sciences. While great improvements have been made in our ability to thin most materials to the point where ion milling may not be a requirement, there will still be a need to utilize ion milling to clean and polish specimens and to provide small amounts of incremental thinning as needed. Thanks mainly to the work of Barna[1] we now understand a great deal about the physics of ion milling. We also benefit from the works of a number of investigators who have studied the artifacts produced by ion milling (see Barber[2] for a review).

Ion milling is a subset of the topic "dry etching," which consists of two major categories: glow discharge methods and ion beam methods. Glow discharge methods include plasma etching, reactive ion etching, and glow discharge sputter etching. These techniques have little application in TEM specimen preparation aside from surface cleaning. The reactive ion etching literature is a source for suggesting gas/specimen combinations to perform chemically-assisted ion beam etching (CAIBE), to be discussed below. The other major dry etching category, ion beam methods, includes ion milling, reactive ion beam etching, and CAIBE. Ion milling involves utilizing inert, mostly neutral, ions directed at a rotating specimen, where thinning is accomplished by momentum transfer sputter etching. Argon ions are usually employed with accelerating voltages of 2 to 10 KeV. Reactive ion beam etching (RIBE) replaces the argon beam with a chemically active beam, like ionized iodine, and thinning proceeds via momentum transfer sputter etching and chemical dissolution of those portions of the specimen that chemically react with the reactive ion beam. Since the utilization of large amounts of strong reactive gases can have adverse consequences for most vacuum systems, the CAIBE method, where the ion guns emit a neutral gas, like argon, and small quantities of the reactive gas are directed at the point on the specimen surface where the ion beam is incident, has become a satisfactory compromise. RIBE and CAIBE have become important tools for the preparation of specimens that undergo chemical disproportionation of the specimen constituents, like the II-VI semiconductor InP, where the P volatilizes leaving In islands on the ion milled surface. Iodine introduced onto the surface during ion milling forms indium iodides that, in turn, volatilize in the mill vacuum, leaving a clean surface.

The thinning rate attained in conventional ion milling is a function of the relative mass ratio of the thinning ion and the specimen atom, the ion energy, the specimen crystal structure, and, most importantly, the angle of incidence of the ion beam relative to the specimen. From Barna's work we know that there are two regimes of milling phenomena as a function of ion beam angle of incidence. The high angle regime, from 15° angle of incidence relative to the surface and higher, where ion milling produces surface topography as a function of the atomic number and the relative hardness of the different components of a heterogeneous specimen. Short time milling at high angles can be useful in SEM studies where it is desired to produce compositional topography on the specimen surface. High angle milling, especially for times greater than 10 minutes, usually leads to large numbers of artifacts when preparing TEM specimens. It is easy to see how differential thinning rates of the components of a composite specimen is a problem for high angle milling, but even homogeneous specimens will develop hummocks and furrows as a result of differential thinning around specimen surface debris and wax residues. It can be shown that a 15° angle of incidence is the worst possible angle at which to mill if your intent is the production of a polished specimen.

<center>266</center>

The low angle milling regime, 5° and less, produces topographical thinning. This leads to a flat, polished surface as any topography, regardless of atomic number or hardness, is eliminated. Interestingly, the polishing operation involves the movement of certain types of surface topography across the surface of a rough specimen. The velocity of the movement of specimen features is a function of the angle of the feature relative to the flat surface and the angle of incidence of the ion beam relative to the surface. Incident ion beam angles of one or two degrees can result in surprisingly high surface velocities. Once all of the specimen asperities are knocked flat or pushed away and the specimen is polished, overall thinning proceeds at a slow rate. Several commercial ion mills have been introduced recently that provide for low-angle milling. These units are usually equipped with modern, high-power ion guns to make up for the slow thinning rates at low angles.

A side effect of ion milling is the introduction of radiation damage and, when applicable, various types of crystallographic defects into specimens. Ion milling has become such a routine part of TEM specimen preparation that many researchers may have never seen specimens without the salt-and-pepper radiation damage contrast or amorphised surface layers produced by ion milling. The amount and type of radiation damage produced is related to the sputtering yield of the specimen as a function of thinning ion angle of incidence. Sputtering yield for most materials and incident ion energies has a maximum around 15° angle of incidence relative to the surface. The reason that the angle 15° is frequently chosen for ion milling is that maximum sputtering yield occurring at that angle results in maximum specimen thinning rate—an important point when ion milling time is forecasted to be many hours. Reducing the angle of incidence of the ion beam to a few degrees greatly reduces the sputtering yield and associated radiation damage. Starting the ion milling operation with thinner specimens reduces ion milling time, which will also reduce the radiation damage seen in the TEM.

The deposition of the incident ion energy into the specimen during ion milling will make the specimen hot—especially in the final stages of thinning when the reduced mass of the specimen severely limits the amount of heat that can be conducted away from the very thin portions of the specimen exposed to the ion beam. Temperatures of 200 to 400°C or greater in the thinnest parts of the specimen are common. Lowering the angle of incidence of the ion beam will reduce the amount of energy deposited into the specimen and concomitantly the temperature rise. Reducing the ion milling time to one or two minutes at a time by starting with thin specimens will limit the temperature build-up in the specimen. If the increase in temperature experienced during ion milling is a concern, the use of an ion mill cold stage is recommended. Care should be taken when using a cold stage to make certain that the tool has returned to room temperature before opening the mill airlock, as water condensation on the specimen and subsequent ice formation will provide local masking to the following application of the ion beam—giving rise to the formation of artifactual surface topography and shadowing after further milling time.

A number of other effects, like electrical charging of insulator specimens by charged ions during ion milling, gas implantation from the ion beam, and surface reactivity of the specimen during milling all lead to the development of artifacts. These artifacts, like those discussed above, can be reduced by lowering the ion beam angle of incidence and reducing the milling time by pre-thinning the specimen to a point where only ion polishing and cleaning is needed in the ion mill. The result will be a smooth, ion *polished* specimen with minimal ion/specimen interactions. The new paradigm should be that ion milling shall be thought of as a tool for cleaning and polishing specimens, while doing the absolute minimum of thinning for the shortest possible time, instead of a tool used to remove bulk amounts of specimen material over tens of hours.

References

1. Barna, A., *MRS Symposium Proceedings,* Vol. 199, p.3
2. Barber, D.J., *Ultramicroscopy* 52 (1993), p.101.

FIVE-DIMENSIONAL MICROSCOPY USING WIDEFIELD-DECONVOLUTION: PRACTICAL CONSIDERATIONS AND BIOLOGICAL APPLICATIONS

W.F. Marshall, K. Oegema, J. Nunnari, A.F. Straight, D.A. Agard, and J.W. Sedat

Dept. Biochemistry and Biophysics, University of California, San Francisco, CA 94143

The ability to image cells in three dimensions has brought about a revolution in biological microscopy, enabling many questions to be asked which would be inaccessible without this capability. There are currently two major methods of three dimensional microscopy: laser-scanning confocal microscopy and widefield-deconvolution microscopy. The method of widefield-deconvolution uses a cooled CCD to acquire images from a standard widefield microscope, and then computationally removes out of focus blur. Using such a scheme, it is easy to acquire time-lapse 3D images of living cells without killing them, and to do so for multiple wavelengths (using computer-controlled filter wheels). Thus, it is now not only feasible, but routine, to perform five dimensional microscopy (three spatial dimensions, plus time, plus wavelength).

Widefield-deconvolution has several advantages over confocal microscopy. The two main advantages are high speed of acquisition (because there is no scanning, a single optical section is acquired at a time by using a cooled CCD camera) and the use of low excitation light levels Excitation intensity can be much lower than in a confocal microscope for three reasons: 1) longer exposures can be taken since the entire 512x512 image plane is acquired in parallel, so that dwell time is not an issue, 2) the higher quantum efficiently of a CCD detect over those typically used in confocal microscopy (although this is expected to change due to advances in confocal detector technology), and 3) because no pinhole is used to reject light, a much larger fraction of the emitted light is collected. Thus we can typically acquire images with thousands of photons per pixel using a mercury lamp, instead of a laser, for illumination. The use of low excitation light is critical for living samples, and also reduces bleaching. The high speed of widefield microscopy is also essential for time-lapse 3D microscopy, since one must acquire images quickly enough to resolve interesting events.

These advantages, of course, carry with them several disadvantages. The primary disadvantage is that the user must rely on a computational method to remove out of focus light, which requires a fairly detailed understanding

of the computation process, and may seem mysterious and difficult to users with less technical backgrounds. This has limited the popularity of this approach in the general biological community. Nevertheless, as these systems become commercially available and more user-friendly, this should be less of a problem. Another problem, often cited by opponents of this method, is the need for significant computer power. However, the continually declining costs of high-speed unix workstations has greatly alleviated this concern.

We will illustrate the utility of this method by several biological applications, including 1) measuring the rates of nuclear import and centrosomal accumulation of two centrosome proteins in living Drosophila embryos, 2) analysis of mitochondrial growth, fusion, and fission in living yeast cells, 3) measuring rates of anaphase motion in living yeast cells, and 4) mapping the positions of genes within the nucleus of Drosophila using fluorescence in situ hybridization.

Now, the question that remains is how best to make use of this data. The availability of low-cost high-speed graphics workstations has increased our visualization capability. Several approaches to visualizing 3D, 4D, and 5D images will be discussed. A further issue, though, is the sheer volume of data that is typically acquired. The ability to acquire large numbers of datasets at one sitting, using computer controlled automated microscopy coupled with the inherently high speed of widefield microscopy, means that the major time-consuming step is analysis of the data. Therefore, it is desirable to develop computational methods to automatically locate and analyze structures in the 3D images. Likewise, studies on motion and flow rates in living cells (as discussed in the applications above) requires the ability of make quantitative measurements on moving objects over tens or even hundreds of 3D datasets in one 4D time-series. In both cases, recent developments in computer vision techniques may hold the key, and exploitation of such techniques is currently a major focus of our research.

3D MICROSCOPY USING CONFOCAL MICROSCOPY

Ernst H. K. Stelzer * and Steffen Lindek **

*Light Microscopy Group, European Molecular Biology Laboratory (EMBL), Postfach 10 22 09, D-69012 Heidelberg, Germany

**Institut für Angewandte Physik, Ruprecht-Karls-Universität, Albert-Überle-Str. 3-5, D-69120 Heidelberg, Germany.

The importance of confocal fluorescence microscopy in modern biological research results from its optical sectioning capability, which allows the three-dimensional analysis of thick specimens. This property is due to the combination of a point-like light source and a point-like detector, which restrict the illumination and detection volumes, respectively. Only the volume that is illuminated *and* detected is relevant to the confocal observation volume. The smaller it is, the better is the resolution. The performance of a confocal microscope is thus primarily specified by the spatial extent of the confocal point spread function (PSF). The extent can be estimated, e.g., by the volume enclosed by the isosurface at half maximum of the PSF (VHM – volume at half maximum).

The relationship of the parameters that determine the lateral resolution of a microscope has been described by Ernst Abbé. The diameter of a light spot in the focal plane Δx is proportional to the wavelength λ of the incident light and inversely proportional to the numerical aperture of the optical system ($N.A. = n \cdot \sin\alpha$).

$$\Delta x \propto \frac{\lambda}{N.A.} \quad \Rightarrow \quad \Delta x = K \cdot \frac{\lambda}{N.A.} = \frac{\lambda}{n} \cdot \frac{1}{\sin\alpha}$$

The diameter of the light spot can be made smaller and hence the lateral resolution can be improved by decreasing the wavelength of the incident light λ, by increasing the refractive index of the medium n and by increasing the opening angle of the optical system α. During the past few years a number of groups have systematically worked on all parameters: Confocal fluorescence microscopy[1] and two-photon absorption[2,3] both decrease the factor K by $\sqrt{2}$. Theta[4,5] and 4Pi[6,7,8] arrangements increase the opening angle and hence the numerical aperture. A 3D probe microscope[9] replaces the light source and directly modifies Δx. Many papers have also evaluated the influences of aperture shapes[10] as well as combinations of different methods[11].

Even with a high numerical aperture (NA) objective lens, illumination and detection are performed over only about a third of the total solid angle. This gives rise to a PSF that is elongated along the optical axis, which means that the lateral resolution of any conventional or confocal microscope is better than its axial resolution[1]. Therefore, especially during the past few years, a lot of work has been devoted to the improvement of the axial resolution[6,7,10,12].

Recently, the development of multi-objective-lens microscopes has revealed new prospects[6,12]. The confocal theta microscope[4] uses two orthogonal placed lenses to illuminate the sample and to detect the fluorescence light, thereby removing the elongation of the PSF. This particular

mechanical arrangement requires the use of objective lenses with a long working distance and a small field of view. Water-immersion objective lenses with a moderate NA and a low magnification can be used. Such optical elements have the advantage not to induce any aberrations by a refractive index mismatch[13]. Confocal theta microscopy is therefore suited for work with large biological specimens in an aqueous medium[14].

An important but not very well addressed problem in the literature on fluorescence microscopy of biological samples is the resolution that can be achieved under more or less well defined circumstances. The formula by Abbé is often misunderstood as describing the resolution of a microscope. In fact, it describes the resolution under optimal conditions. One of those optimal conditions is an infinite signal to noise ratio. An idea of the specific problems in fluorescence light microscopy can be grasped when one realises that the ratio of the number of photons emitted by a dye over the number of photons required for its excitation is in the range of millions. Another hint is that the human eye can discern objects much better under **bright** conditions. Resolution is defined as the distance between two point objects when their image has a certain contrast. Contrast, however, must take the ratio of signal to noise into account and therefore contrast is ultimately limited by the number of detected photons. Since the number of photons is especially small in fluorescence microscopy the full resolution offered by the diffraction limit is never achieved when observing biological objects.

The most obvious consequence is that the number of photons has to be maximised by optimising each and every element in an instrument. However, assuming that this has been achieved we arrive at two very important questions: 1) Can one estimate the resolution once an image has been recorded? 2) Can one estimate the circumstances that are required to achieve a certain resolution?

References

1. T. Wilson and C.J.R. Sheppard, *Scanning Microscopy*, Academic Press, 1984.
2. W. Denk et al., *Science*, 248 (1990) 73.
3. E.H.K. Stelzer, Opt. Commun., 104 (1994) 223.
4. S. Lindek et al., *Rev. Sci. Instr.*, 65 (1994) 3367.
5. S. Lindek et al., *Appl. Opt.*, 35 (1996) 126.
6. S.W. Hell et al., *J. Opt. Soc. Am. A*, 9 (1992) 2159.
7. C.J.R. Sheppard et al., Optik, 87 (1991) 129.
8. E.-L. Florin et al., *Appl. Phys. Lett.*, in press.
9. C.J.R. Sheppard et al., Opt. Commun., 84 (1991) 7.
10. S. Lindek et al., Appl. Opt., 35 (1996) 126.
11. B. Bailey et al., *Nature*, 366 (1993) 44.
12. E.H.K. Stelzer, Opt. Commun., 111 (1994) 536.
13. S.W. Hell et al., J. Microsc.,169 (1993) 391.
14. E.H.K. Stelzer, J. Microsc., 179 (1995) 1.

BLIND DECONVOLUTION TO AID MORPHOMETRICS OF 3D LIGHT MICROGRAPHS

T.J. Holmes,* ** N.J. O'Connor,* ** D. Szarowski,*** S. Bhattacharyya,** H. Ancin,** M. Holmes,* M. Marko,*** B. Roysam,* ** and J.N. Turner** ***

*AutoQuant Imaging Inc., Troy NY 12180. **Rensselaer Polytechnic Institute, Troy NY 12180. ***Wadsworth Laboratories, NYS Health Dept., Albany NY

We are developing novel deconvolution algorithms for 3D light microscopy that include the widefield fluorescence, transmitted light brightfield and confocal fluorescence modalities.[1,2,3] The main novelties that we have introduced are (1), the usage of maximum likelihood estimation as a mathematical optimization criterion and (2), incorporation of blind deconvolution such that the optical point spread function does not need to be measured (see references in 1,2).

Our recent research has included evaluations of performance. This includes validating the images, using artificial test objects of (reasonably) "known" geometry and evaluating the accuracy of morphometrics that are aided by deconvolution. Test objects include microspheres and specially drawn, fluorescent filled micropipette tips. The performance measures are comparisons of various morphometrics against chosen benchmarks. Rat hippocampal neurons filled with lucifer yellow were used in evaluating performance with a biological sample. Morphometrics obtained from nondeblurred and deblurred data sets, by way of automatic segmentation, were compared against benchmark measurements. The benchmarks, in these cases, were measurements obtained by way of the Stereocon software.[4] The Stereocon software uses operator judgement to segment the object, and, in our case, uses the assumption that the dendrites have circular cross sections. This assumption provides a realistic benchmark measurement because it ensures that the thickness of the dendrites, on average, is isotropic. Some of these benchmark comparisons, with confocal fluorescence, are summarized in Table 1. Fig. 1 shows projectional images of the data sets from which some of these measurements were obtained. These data imply that incorporation of deconvolution methods will improve the accuracy of absolute morphometric measurements whenever automated segmentation schemes are embedded within the measurement process.

References

1. T.J. Holmes et al, "Recent Developments with Blind Deconvolution for 3D Light Microscopy," MSA 53rd Annual Mtg., JMSA Proceedings, Aug. 1995.
2. T.J. Holmes et al, "Light Microscopic Images Reconstructed by Maximum Likelihood Deconvolution," The Handbook of Biological Confocal Microscopy, 2nd Ed., J. Pawley, Ed., Plenum, 1995.
3. Research funding provided by the NIH (1R43MH53691-01, 1R43MH53692-01; AutoQuant) (RR01219; Wadsworth), the NSF (BES9413037; Rensselaer), and Proctor & Gamble, Inc. (Rensselaer). Computing resources were partly provided by the Cornell National Supercomputer Facility (NSF, IBM, NY State; Rensselaer).
4. Marko, M. and Leith, A., "Stereocon - Three Dimensional Reconstructions from Stereoscopic Contouring," J. of Structural Biology, 116: 93-98, 1996.

top projections

side projections

(a) (b) (c)

|— 60.4 microns —|
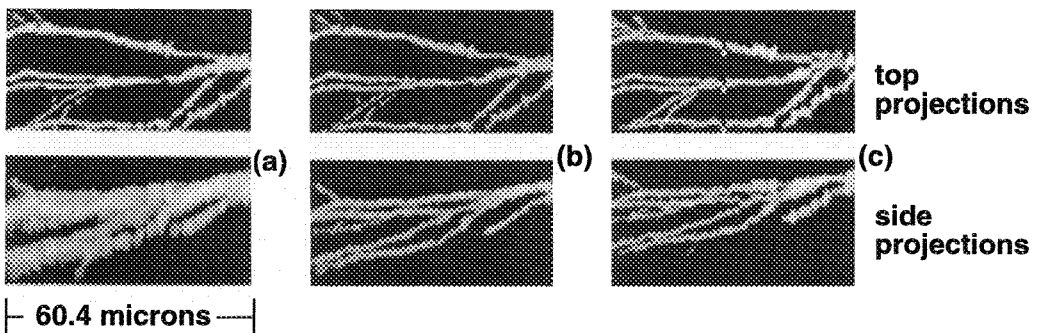
Fig. 1. Projections of segmented volumes. The segmentation thresholds of (a) and (b) were determined automatically (see references in 1,2). Morphometrics were then calculated from these segmented volumes. Sample: rat hippocampus pyramidal neuron, lucifer yellow, confocal fluorescence, NA=0.8 oil, sample spacing 0.944 (xy) 1.0 (z) micrometers. Subfield shown is a 64x128x64 section taken from a 384x512x180 data set. Biorad MRC 600.(a) Automatic segmentation of raw data. (b) Automatic segmentation of deblurred data. (c) Benchmark: Stereocon user–interactive segmentation of raw data, under the assumption that the dendrite thicknesses (axial) are the same as their widths (along x,y). Note that the deblurring improves the isotropy of the dendrite thickness such that it better compares to the benchmark segmentation.

Table 1. Examples of morphometrics and their benchmarks. (*) The micropipette and microsphere benchmarks were calculated by assuming perfect conical and spherical geometries, and inserting the measured in–plane thicknesses into the formulae for these geometries. The Dendrite benchmarks were calculated directly from the data shown in (c) above.

Sample		Ratio of axial vs. in–plane thickness	Volume	Surface area
Micropipette tip (pt4z2x)	Raw data	2.00 (μm; averaged over 20 points)	112.1 (μm^3)	168.18 (μm^2)
	Deblurred	1.12	56.3	100.08
	Benchmark	1.0	57.1	88.28
Microsphere (fb410z5)	Raw data	1.38	150.9	147.6
	Deblurred	1.14	120.0	113.4
	Benchmark	1.0	92.0	98.5
Dendrite data of Fig. 1	Raw data	2.96 (averaged over 25 points)	2111.5	2224.5
	Deblurred	1.06	852.6	1164.5
	Benchmark	1.0	997.7	1340.6

3D MICROSCOPY: CONFOCAL, DECONVOLUTION OR BOTH?

J. B. Pawley and K. Czymmek*

Department of Zoology, University of Wisconsin-Madison, WI 53706
*Noran Instruments, Middleton WI, 53562

Over the past 20 years great improvements have been made in the techniques available for doing 3D fluorescent microscopy on living cells. The first approach, generally referred to as image deconvolution, treats the stack of 2D widefield (WF) image data as merely the sum of a number of discrete point-spread functions (PSF) and uses the computer to find the array of emitters that, when blurred by the PSF, best fits the stored data. If the PSF is known, only presence of statistical and electronic noise in the data, prevents this best-fit set of emitters from being a perfect image of the dye distribution in the specimen.[1] The crucial role played by noise can be appreciated by comparing images from the Hubbell space telescope in its original condition, even after deconvolution, with images taken after the optics had been repaired.

The second approach to 3D microscopy requires the introduction of a confocal aperture in front of the photodetector of a scanning laser microscope so that only the fluorescent signal emitted from the plane-of-focus is recorded. As a result the image formed represents an "optical section" and a stack of such sections can be recorded at different focus heights to produce a 3D data set.[2]

The purpose of this paper is to list the differences between these two techniques with the idea of defining the types of studies best suited to each method. In these contexts, the word "best" is usually defined as that method which provides the largest amount of structural information (considering both resolution and contrast) from a given dose of light to the specimen. Even assuming that all methods employ the most appropriate optical components and use optimal sampling methods in all 3 dimensions, WF/deconvolution still differs from the confocal approach in a number of important respects:

- **Excitation Intensity:** The photon flux is $\sim 10^5$-10^7x higher in a laser confocal than in WF.
- **Detector Quantum efficiency:** Depending on wavelength, the CCD sensors used for WF have 3-10x more quantum efficiency (QE) than the photomultiplier tubes (PMT) used in confocal.
- **Signal levels:** In fluorescent confocal images, the signal from bright areas often represents only 20-100 detected photons/pixel (dpp), while even in "low-dose" WF images, bright areas represent 5,000 dpp and 30x this number is not uncommon. Although some of this increase results from the greater detector QE and the presence of out-of-focus light in the WF signal, it still seems that those using the WF method start with a signal representing 5-20x more light from the specimen.
- **Read-out noise:** Although, at ±5 e- RMS/pixel, the CCD has more readout noise than the PMT, even this level becomes less than the Poisson or "shot" noise for signals above 25 electrons/pixel.
- **"Real-time" imaging:** To date no deconvolution method has approached confocal for obtaining optical-section data at a high frame rate, especially where only a single plane is viewed over time.

The Intensity Problem

Can we assume that fluorescence efficiency and bleaching rate are the same for both confocal and WF image capture? Is it possible that the intensity of the confocal spot is high enough to drive a large fraction of the dye molecules in the focused spot into a triplet state during the first $\sim 10\%$ of a 1 μs pixel, thereby significantly reducing the "effective" dye concentration (and hence the signal level averaged over the 1μs)? As triplet-state lifetimes are much longer (msec) than the μsec pixel times of confocal but shorter than CCD exposure times, such a mechanism would provide less signal/excitation-photon in the confocal case. It would also prevent the signal level from increasing linearly with laser intensity, an effect that should be less evident if the probe illuminates a given area for only a short time. To investigate this possibility we have collected quantitative fluorescence data using a wide variety of laser intensities (0.01-1.0 mW), zoom settings and scan rates (0.33 - 2 sec/frame) to vary spot intensities and pixel times over several decades. Although no large departure from linearity was noted, measurements have been limited to fluorescent plastics and liquids. Possibly the effect may still be important on aqueous or embedded specimens.

Although the light flux in the confocal microscope can be intense enough to cause singlet-state saturation of the fluorophor[2], we generally assume that it is insufficient to produce many 2-photon events

unless fast, pulsed lasers are employed[3]. However, it is possible that, near singlet -state saturation, the absorption of a second photon by a molecule already in the excited state may occur. Though such events are probably too rare to effect the fluorescence efficiency significantly, they may be a cause bleaching of the fluorophor and thereby become another mechanism to explain the disparity in total light dose that the specimen evidently finds tolerable under the two types of observation.

The   Detector   QE   vs.   Out-of-focus-Signal-Noise   Problem

Any comparison of the two methods depends on the extent to which the higher detector QE of the CCD used in WF provides enough extra signal to offset the effects of the Poisson noise associated with the presence of the photons from out-of-focus planes[4]. Does the detection of photons from out-of-focus planes provide "information": something that you wanted to know about the structure of the specimen, or simply "signal": that which comes from the detector? If light originating from planes more than, say 2 μm, above or below the plane of focus, is found to contribute only slightly to the final processed image, but adds significantly Poisson noise to the signal from the CCD, can it still be thought of as providing information? As a lot of time and money is being spent in this field of research, it would be good to know if one method is clearly superior, or even clearly-superior-for-some-subset-of-specimens. Clearly the answer to this question depends on how much out-of-focus light actually reaches the detector as well as how far out of focus it is: the Poisson noise associated with a small signal from a nearby plane, may add more information than noise but the converse is also true. Clearly, the analysis depends on the geometry of the stain distribution but unfortunately there are as yet few direct quantitative comparisons of the two techniques on a single specimen, perhaps because even viewing a fluorescent specimen once causes bleaching and other damage. If we could make this measurement for a number of actual specimens, we might be able to find where those "missing" photons are going and, if we add S/N calculations, including Poisson noise in "real-photons", we might be able to define a "stain-density-thickness" product threshold above which mechanically excluding photons from out-of-focus planes would produce better data.

On the other hand, even using a confocal aperture diameter equal to the radius of the first Airy dark ring, only ~50% of light emerging from the plane of focus ever reaches the detector. It is hard to see this as an advantage, especially when combined with low detector QE. To address this latter point, I have been working with others to develop a device called the CCDiode. It is a single-channel silicon detector that is read out like a CCD but using 16x parallel readout channels to keep the noise level at +/- 3e- RMS even at a 1 MHz readout rate.[5] A QE of a rear-illuminated detector of this type is the same as that of a CCD and using a more advanced version designed to readout from a 5x5 CCD-array at each pixel of the scanned raster, data could be effectively collected at several pinhole settings separately and simultaneously.

Is a   compromise   possible?

Although each method has been used to produce results of great interest and worth, aside for readout speed, no clear-cut rules to indicate the usefulness of either for a given study have yet emerged and it is certainly possible that two-photon fluorescence microscopy, in which the dye is not even excited unless it is near the plane of focus, may eventually be the best method of all.[3] Some have suggested that the best plan might be to do confocal[6] with a pinhole somewhat larger than the Airy disk and then deconvolving the results. Such an approach would make best use of data collected using the 5x5 CCDiode confocal detector mentioned above. However, this would require the development of new methods of deconvolution.

[1]Agard, DA, *et al.* Fluorescence Microscopy in Three Dimensions, Methods in Cell Biology, **30**:353-377

[2] Pawley, J.B. , (ed.) Handbook of Biological Confocal Microscopy, Plenum, NY, 1995

[3]Denk,W. *et al.*, Two-photon laser scanning fluorescence microscopy, Science, **248**:73, 1990

[4]Pawley, J.B. The sources of noise in three-dimensional microscopical data sets, in Three Dimensional Confocal Microscopy: Volume Investigation of Biological Specimens, ed. J. Stevens, Academic Press. NY. 47-94, 1994

[5]Pawley, JB, Blouke, M and Janesick J. The CCDiode: An optimal detector for laser confocal microscopes. Proc. SPEI, **2655**:41, 1996

[6]Shaw, P. in #2 (above), chapter 23 and also, van der Voort HTM, and Strasters, KC, Restoration of confocal images for quantitative image analysis, J. Microsc. **178**:165-181, 1995

TWO-PHOTON EXCITATION MICROSCOPY IN CELLULAR BIOPHYSICS

David W. Piston

Department of Molecular Physiology and Biophysics, Vanderbilt University, Nashville, TN 37232.

Two-photon excitation microscopy (TPEM) provides attractive advantages over confocal microscopy for three-dimensionally resolved fluorescence imaging and photochemistry.[1,2] Two-photon excitation arises from the simultaneous absorption of two photons in a single quantitized event whose probability is proportional to the square of the instantaneous intensity.[3] For example, two red photons can cause the transition to an excited electronic state normally reached by absorption in the ultraviolet. In practice, two-photon excitation is made possible by the very high local instantaneous intensity provided by a combination of diffraction-limited focusing of a single laser beam in the microscope and the temporal concentration of 100 femtosecond pulses generated by a mode-locked laser. Resultant peak excitation intensities are 10^6 times greater than the CW intensities used in confocal microscopy, but the pulse duty cycle of 10^{-5} limits the average input power to less than 10 mW, only slightly greater than the power normally used in confocal microscopy.

Three properties TPEM give this method a tremendous advantage over conventional optical sectioning microscopies for the study of thick samples: **1)** The excitation is limited to the focal volume because of the intensity-squared dependence of the two-photon absorption. This inherent localization provides three-dimensional resolution and eliminates background *equivalent to an ideal confocal microscope* without requiring a confocal spatial filter, whose absence enhances fluorescence collection efficiency. Confinement of excitation to the focal volume also *minimizes photobleaching and photodamage* - the ultimate limiting factors in fluorescence microscopy of living cells and tissues. **2)** The two-photon technique allows imaging of UV fluorophores with conventional visible light optics in both the scanning and imaging systems, because both the red excitation light (~700 nm) and the blue fluorescence (>400 nm) are within the visible spectrum. **3)** Red or infrared light is far less damaging to most living cells and tissues than bluer light because fewer biological molecules absorb at the higher wavelengths. Longer wavelength excitation also reduces scattering of the incident light by the specimen, thus allowing more of the input power to reach the focal plane. This relative transparency of biological specimens to 700 nm light *permits deeper sectioning*, since both absorbance and scattering are reduced.

One of the most powerful applications of TPEM is imaging fluorescence from the naturally occuring reduced pyridine nucleotides (NAD(P)H). NAD(P)H is a useful indicator of cellular respiration, but it is not a "good" fluorophore (it has a small absorption cross-section and a low quantum yield). Thus, previous examinations of cellular dynamics by NAD(P)H autofluorescence have been limited by severe photobleaching and photodamage problems. Since two-photon excitation of NAD(P)H yields minimal photodamage, it allows time-resolved three-dimensional metabolic mapping of cellular redox state.[4,5] Figure 1 shows an optical section of NAD(P)H autofluorescence through the middle of a pancreatic islet (approximately 40 μm into the islet from the cover slip). The outlines of single cells are clearly visible as are the nuclei, which appear dark. Imaging of the temporal and spatial pattern of NAD(P)H has revealed that individual β cells within the islet form a much more uniform population than was expected from studies of dissociated β cells.[6] Since glucokinase has been postulated as the rate-limiting step in glucose transduction by β cells, we are currently investigating the connection between glucokinase distributions and those of NAD(P)H.

Another powerful application of TPEM is its use in photoactivation of caged compounds. Caged compounds have an attached chemical cage that inactivates them. When certain light (such as the two-photon excitation laser) is shined upon the compound, the caging group dissociates, which activates the compound. We have used two-photon photorelease of a caged fluorophore to visualize cell lineage patterns in sea urchin embryos.[7] The pinpoint control of excitation in TPEM can be utilized to photorelease specifically within a single cell or group of cells. The caged fluorophore becomes active and "lights up" this single cell. The dye is coupled to 10,000 MW dextran, so it does not travel between cells. Thus, only descendants of the original marked cell will be marked with visible dye. The exact locations of the marked descendent cells can be tracked and correlated with the morphology of the developing larva. A single optical slice of an embryo in which a small group of cells within the early gut has been marked is shown in figure 2. The fluorescence is overlayed upon a Nomarski DIC image to correlate the resulting lineage with the embryo structure.

[1] Denk W., J.H. Strickler and W.W. Webb *Science* **248**:73-76 (1990).
[2] Williams, R.M., D.W. Piston, W.W. Webb. *FASEB J.* **8**:804-813 (1994).
[3] Goppert-Mayer, M. *Ann. Phys.* **9**:273-294 (1931).
[4] Piston, D.W., B.D. Bennett, G. Ying. *J. Micro. Soc. Amer.* **1**:25-34 (1995).
[5] Piston, D.W., B.R. Masters, W.W. Webb. *J. Microscopy* **178**:20-27 (1995).
[6] Bennett, B.D., T.L. Jetton, G. Ying, M.A. Magnuson, D.W. Piston. *J. Biol Chem.* **271**:3647-3651. (1996).
[7] Summers, R.G., D.W. Piston, K.M. Harris, J.B. Morrill. *Dev. Biol.* **In Press.** (1996).
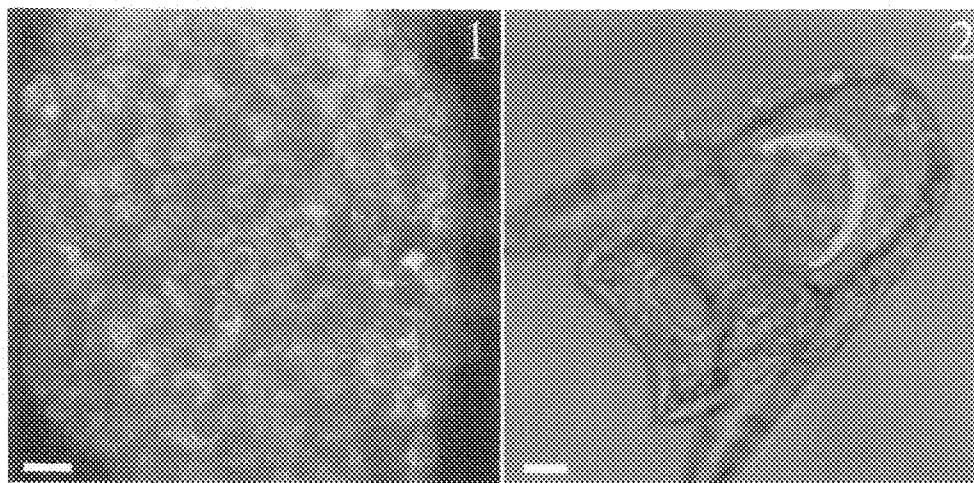
FIG 1. NAD(P)H Autofluorescence from an isolated islet (8 sec exposure, bar = 10 μm).
FIG 2. Single confocal microscopic optical slice of a sea urchin pluteus larva where a small group of cells was "uncaged" at the end of gastrulation. As can be seen in the overlaid Nomarski DIC image, the marked cells have formed the back half of the stomach (bar = 25 μm).

TIME-RESOLVED STIMULATED-EMISSION FLUORESCENCE MICROSCOPE

P. T. C. So, C. Y. Dong, C. Buhler and E. Gratton

Laboratory for Fluorescence Dynamics, Department of Physics, University of Illinios at Urbana-Champaign, IL 61801

Time-resolved stimulated-emission fluorescence microscopy is a novel technique for obtaining super-diffraction limited spatial resolution and sub-nanosecond time resolution using a multi-photon process[1]. This technique is inspired by traditional asynchronous stimulated-emission pump-probe spectroscopy.[2] Fluorescence sample is first excited by a pump laser pulse, tuned to the molecular absorption band of the molecule. Within the chromophore lifetime, a second probe pulse, tuned to the emission band, stimulates fluorescence emission.

The spatial resolution enhancement originates from the bilinear dependence of the stimulated emission efficiency on both the pump and probe beam intensities. At the objective focal point, the stimulated emission point spread function is the product of the point spread functions of the pump and probe beams. This situation is mathematically equivalent to both the confocal and the two-photon methods[3,4]. 3-D depth discrimination and superior spatial resolution is expected.

The stimulated emission efficiency also depends on the excited state population at the arrival of the probe pulse. The excited state decay kinetics can be monitored by measuring the stimulated emission amplitude as a function of pump and probe pulse temporal separation. Frequency domain heterodyning technique greatly simplifies this data acquisition process and eliminates the use of mechanical delay line. In the heterodyning scheme, the repetition rate of the pump and probe pulse train are slightly offset. The beating of the two pulse trains translates the high frequency information to the low frequency offset signal which can be accurately measured by digital method. Heterodyning is equivalent to periodically vary the timing between the pump and probe pulses.

We have characterized the spatial point spread function of this microscope by imaging 0.28 μm latex spheres. A comparison of the theoretical point spread function with the experimental data is presented in Fig. 1 a, b. The superior resolution of this microscope is demonstrated in two biological systems: erythrocytes and fibroblasts labeled with membrane probe DHPE. Fig. 2 a, b and 3 a, b. The time-resolve capability of this microscope is demonstrated in Fig. 4 a, b. A mouse fibroblast cell is double labeled with ethidium bromide (24 ns lifetime; bound to nucleic acid) and DHPE (3 ns lifetime). While the intensity picture provide no functional information, the time-resolved image show sharp distinction between the nucleus and cytoplasm regions.

References

1. C. Y. Dong et. al., Biophys. J., (1995) 2234.
2. P. A. Elzinger et. al., Applied Optics, (1983) 4303.
3. T. Wilson and C. Sheppard, "Theory and Practice of Scanning Optical Microscopy", (1984).
4. W. Denk et. al., Science (1990) 73.
5. This work was supported by NIH grant R30155.
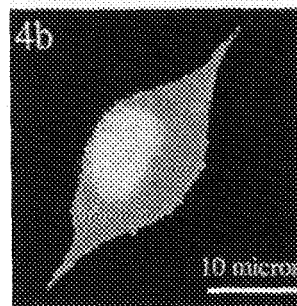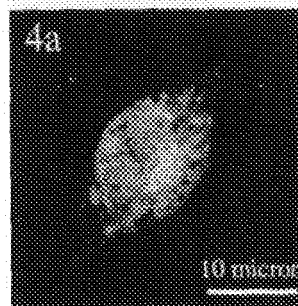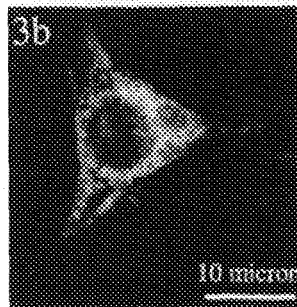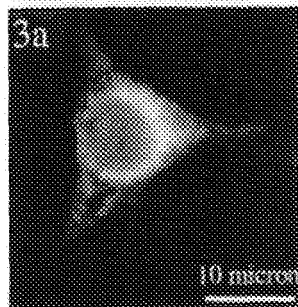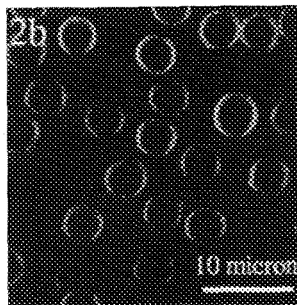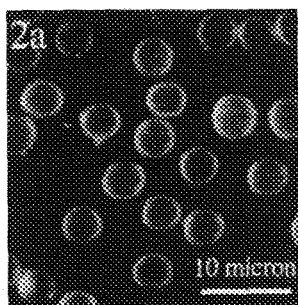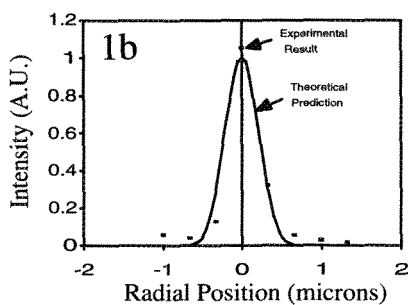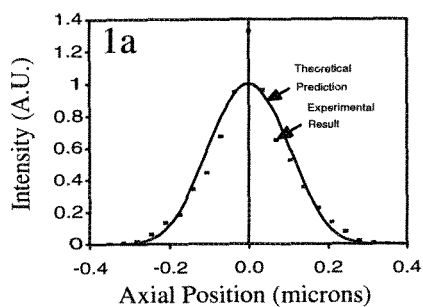
FIG. 1 Characterization of (a) radial and (b) axial psf of 0.28 micron sphere
FIG. 2 (a) One-photon scanning and (b) stimulated-emission microscopes images of erythrocytes
FIG. 3 (a) One-photon scanning and (b) stimulated-emission microscope images of a fibroblast
FIG. 4 (a) Stimulated-emission and (b) time-resolved images of a double labeled fibroblast

IMAGING DEEP OPTICAL SECTIONS WITH TWO-PHOTON EXCITATION FLUORESCENCE MICROSCOPY

J.G. White, V.F. Centonze, and D.L. Wokosin

Integrated Microscopy Resource, University of Wisconsin.

The technique of optical sectioning allows the visualization of a succession of images of parallel planes within a thick specimen with little or no out-of-focus interference. Ultimately, a limit is reached on the depth to which optical sections can be obtained from a given sample. This limit, up to the working distance of the objective, is largely determined by the degree of light scattering encountered by the incident excitation beam as well as the returning emission signal.

Confocal imaging was one of the first optical sectioning techniques applied to fluorescence imaging. Two-photon excitation imaging[1] is a recently developed alternative optical sectioning technique for fluorescence imaging where an excitation wavelength of around twice the excitation peak of the fluorophore is used in a laser-scanning microscope. This excitation wavelength produces very little fluorophore excitation in the bulk of the sample, but when the incident photons are confined in space and time sufficient two-photon absorption events can take place to obtain rapid imaging of fluorophores. With high peak powers--obtained with a sub-picosecond pulsed laser source focused by a lens--sufficient photon density can be obtained for easily detectable two-photon events. Thus fluorophore excitation occurs as two photons are absorbed essentially simultaneously, which act effectively as a single photon of twice the energy (half the wavelength). Two-photon events have a quadratic dependence on intensity, and, therefore, decrease rapidly away from the focal volume of the lens. In a raster scanning system, fluorophore excitation is confined to the optical section being viewed as fluorophore away from the lens focal volume is not excited by the long-wavelength illumination.

One potential advantage of two-photon excitation fluorescence imaging over confocal imaging is the reduction in light scattering, thereby allowing deeper optical sections inside highly scattering samples. There are three potential reasons for this increase in sectioning depth: there is very little absorption of the excitation beam by fluorophore above the plane of focus, the longer excitation wavelength suffers less Raleigh scattering, and the emission signal does not have to be imaged so all collected photons can be used--there is no need for a pinhole.

We have developed a two-photon excitation fluorescence imaging system with a compact, solid-state, mode-locked laser as an excitation source. This laser is a prototype designed for two-photon excitation imaging and was built by Microlase, Ltd. (Scotland). It uses two, four-watt laser diodes to pump a Nd:YLF gain medium. An additive pulse mode-locking scheme is used to provide 1.8 ps pulses at 1047nm wavelength[2]; these pulses are then reduced to 300 femtoseconds by an external grating pulse compressor. The laser produces a mean power of around 300 mw and has a repetition rate of 120Mhz. The laser is used in conjunction with a relatively standard Bio-Rad MRC 600 laser-scanning microscope. The original argon ion laser of the confocal microscope was retained and the system was set up so it could be rapidly changed from two-photon to confocal imaging modes; this has enabled us to compare the relative performance of these two imaging modes on the same sample.

We used whole-mount zebrafish embryos stained with safranine as a test sample (kindly supplied to us by Dr. Brad Amos). The embryos were fairly heavily stained. We obtained reasonable images to a depth of around 40μm with confocal imaging with 488nm excitation, (Fig. 1A). In contrast, we obtained images to a depth of 80μm with two-photon imaging with 1047nm excitation, (Fig. 1B). We have found similar increases in the depth at which good images may be obtained from a variety of other specimens (unpublished observations). Figure 1C shows a confocal XY image 36 μm into the embryo, while the same plan obtained with two-photon excitation fluorescence is shown in Fig. 1D. These observations suggest that two-photon excitation fluorescence imaging offers a considerable improvement over confocal imaging for obtaining information from deep within a specimen. This is especially important

for live cell and fixed sample studies using fluorescence microscopy.

References

1   W. Denk et al. *Science*, **248**:73 (1990)
2   G.P.A. Malcolm et al. *Optics Letters*, **15**:1303 (1990)
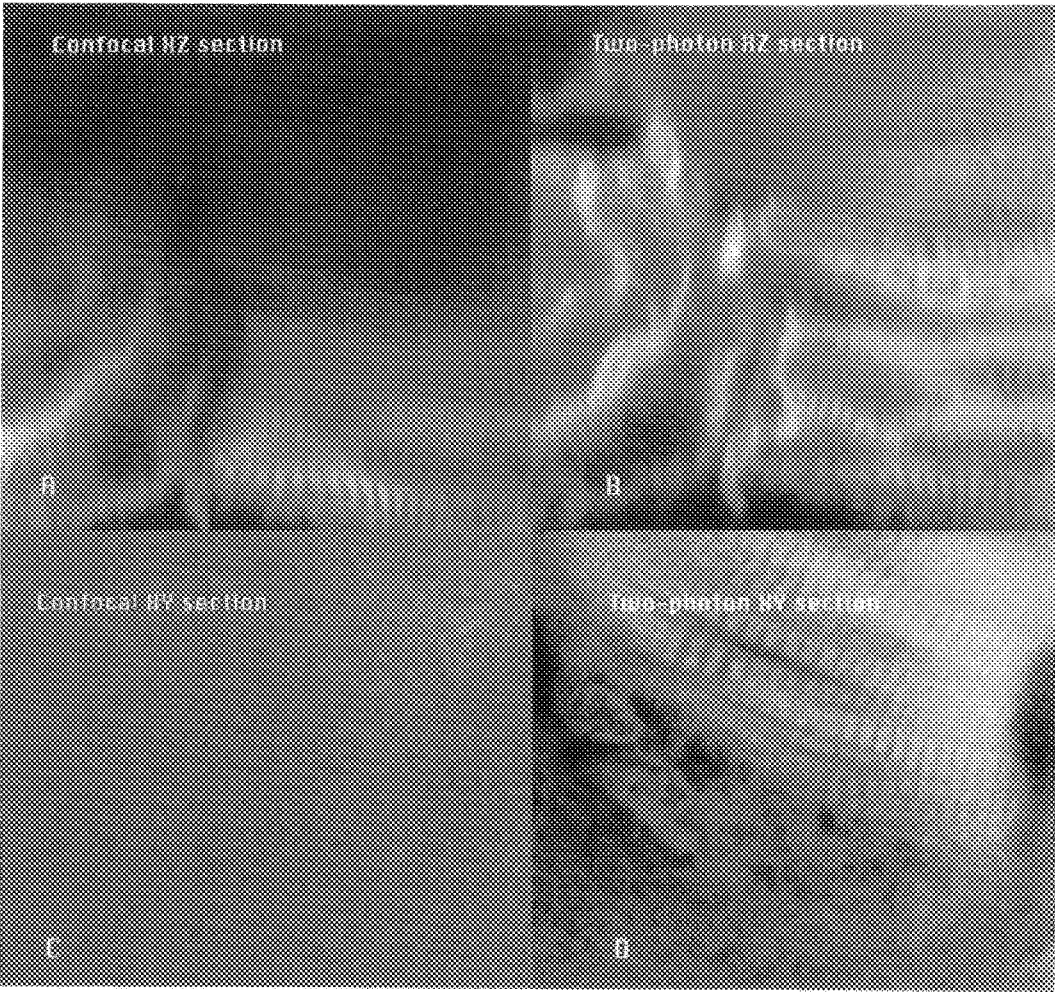
Figure 1. Images of a zebrafish embryo that is heavily stained with safranine to visualize muscle sarcomeres. Figure 1A is the confocal (488nm) XZ image. Depth into sample increases going up, useable information was obtained to 40 μm depth. Figure 1B is the same section of embryo XZ imaged with two-photon excitation (1047nm); useable information was obtained to 80 μm. Figure 1C is a confocal XY optical section 36 μm into an embryo and Figure 1D is the same section with two-photon excitation. All images were taken with a Nikon X60 (1. 4 NA) objective.

GOING BEYOND 3-D IMAGING: AUTOMATED 3-D MONTAGED IMAGE ANALYSIS OF CYTOLOGICAL SPECIMENS

Badrinath Roysam*, Hakan Ancin*, Douglas E. Becker*, Robert W. Mackin*, Matthew M. Chestnut**, Gregg M. Ridder**, Thomas E. Dufresne**, Donald H. Szarowski***, and James N. Turner***

ECSE Department, Rensselaer Polytechnic Institute, Troy, New York 12180-3590, USA
Procter and Gamble Co., Miami Valley Laboratories, Cincinnati, Ohio 45239-8707
Wadsworth Center for Laboratories and Research, NYDOH, Albany, New York 12201-0509

This paper summarizes recent advances made by this group in the automated three-dimensional (3-D) image analysis of cytological specimens that are much thicker than the depth of field, and much wider than the field of view of the microscope. The imaging of thick samples is motivated by the need to sample large volumes of tissue rapidly, make more accurate measurements than possible with 2-D sampling, and also to perform analysis in a manner that preserves the relative locations and 3-D structures of the cells. The motivation to study specimens much wider than the field of view arises when measurements and insights at the tissue, rather than the cell level are needed.

The term "analysis" indicates a activities ranging from cell counting, neuron tracing, cell morphometry, measurement of tracers, through characterization of large populations of cells with regard to higher-level tissue organization by detecting patterns such as 3-D spatial clustering, the presence of subpopulations, and their relationships to each other. Of even more interest are *changes* in these parameters as a function of development, and as a reaction to external stimuli. There is a widespread need to measure structural changes in tissue caused by toxins, physiologic states, biochemicals, aging, development, and electro-chemical or physical stimuli. These agents could affect the number of cells per unit volume of tissue, cell volume and shape, and cause structural changes in individual cells, inter-connections, or subtle changes in higher-level tissue architecture. It is important to process large intact volumes of tissue to achieve adequate sampling and sensitivity to subtle changes. It is desirable to perform such studies rapidly, with utmost automation, and at minimal cost. Automated 3-D image analysis methods offer unique advantages and opportunities, without making simplifying assumptions of tissue uniformity, unlike random sampling methods such as stereology.[1,2] Although stereological methods are known to be statistically unbiased, they may not be statistically efficient. Another disadvantage of sampling methods is the lack of full visual confirmation - an attractive feature of image analysis based methods.

This group is producing core 3-D image analysis and database tools that are making such large-scale studies routinely possible. Fig. 1 illustrates the scope of this work. Starting from 3-D microscopy images of cytological specimens, we are able to perform automated cell counting (Fig. 2) and population analysis, automated tracing and analysis of neurons, and store the results in the form of tables and spreadsheet databases.[3-6] A variety of quantitative analyses can be performed on this data. We have also been able to produce large-scale montages of images, and the results of 3-D image analysis on overlapping series of 3-D images of extended regions (Fig.3). Recently, we have investigated the possibility of quantitating and counting neuronal spines using some reflection-mode confocal images of Golgi preparation data provided by Dr. Clayton Wiley at Pittsburgh. Fig. 4 presents a sample result from this preliminary study.

References:
1. Dehoff R. T., J. Microsc. (Oxford), 131:259-263, 1983.
2. Gundersen H. J. G., J. Microsc. (Oxford) 143:3-45, 1986.
3. Cohen, A. et al., J. Micros. (Oxford), Vol. 173, Pt. 2, 1994.
4. Roysam et al., J. Micros. (Oxford), Vol. 173, Pt. 2, 1994.
5. Ancin H. etal., Cytometry, (accepted, to appear), 1996.
6. Becker D. E., et al., Cytometry, (accepted, to appear), 1996.
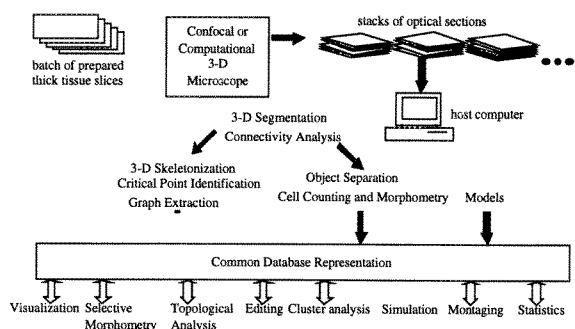
Fig.1: Showing the scope and organization of our current studies on automated 3-D image analysis.
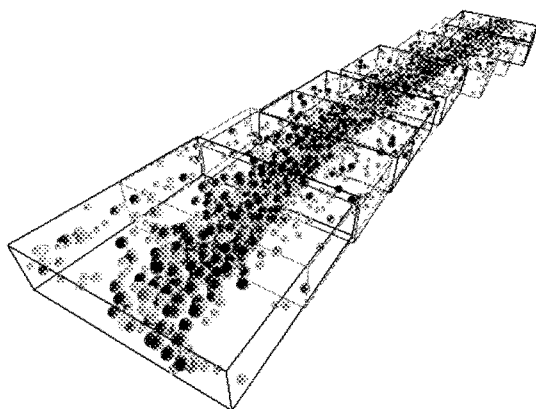
Fig.2 (up): Shows the results of automated 3-D cell counting on a rat hippocampus image (shown inverted). The numbers indicate detected nuclei. This example illustrates the ability of our method to analyze extremely dense connected clusters of cells.

Fig.3 (left): Showing a sample montage generated by stitching together the results of performing cell counting and population analysis on 10 overlapping fields such as Fig. 2, of an acriflavine-stained rat hippocampus preparation. The individual fields, indicated by the boxes, are at different depths within the specimen. Each sphere indicates a detected cell. The size of a sphere is proportional to the measured cell volume. In the original color image, colors are assigned by measured average cell brightness. There are 2,204 cells in this montage. All the measurements are available as tables that can be imported into spreadsheets/databases.
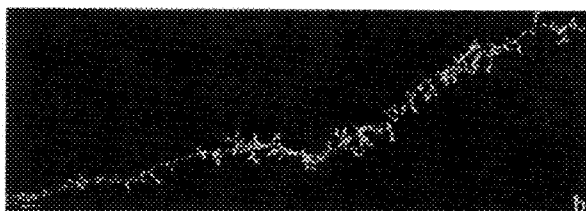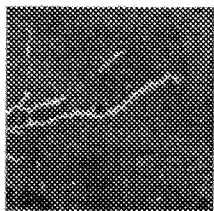
Fig.4: Sample results showing analysis of dendritic spines. (left) Showing a reflection-mode confocal image of a Golgi preparation. (Right) Showing the spines detected on the longest dendritic fiber in the image on the left. The program produces tables that can be imported into a database or spreadsheet program for further analysis.

283

COMPUTER-ASSISTED ANALYSIS OF MULTI-COLOR CONFOCAL MICROSCOPIC DATASETS: AUTOMATED LIGHT MICROSCOPIC DISCRIMINATION OF SYNAPTIC RELATIONSHIPS

M Wessendorf*, A Beuning*, D Cameron[†], J Williams[§], and C Knox[#]
*Dept Cell Biology and Neuroanatomy, Univesity of Minnesota, Minneapolis, MN
[†]Dept Anatomy, Flinders University, Adelaide, Australia
[§]Vollum Institute, Oregon Health Sciences University, Portland, OR
[#]Minnesota Datametrics Corp, Shoreview, MN

Multi-color confocal scanning-laser microscopy (CSLM) allows examination of the relationships between neuronal somata and the nerve fibers surrounding them at sub-micron resolution in x,y, and z. Given these properties, it should be possible to use multi-color CSLM to identify relationships that might be synapses and eliminate those that are clearly too distant to be synapses. In previous studies of this type, pairs of images (e.g., red and green images for tissue stained with rhodamine and fluorescein) have been merged and examined for nerve terminals that appose a stained cell (see, for instance, Mason et al.[1]). The above method suffers from two disadvantages, though. First, although it is possible to recognize appositions in which the varicosity abuts the cell in the x or y axes, it is more difficult to recognize them if the apposition is oriented at all in the z-axis--e.g., if the varicosity lies above or below the neuron rather than next to it. Second, using this method to identify potential appositions over an entire cell is time-consuming and tedious.

We attempted to address this problem by devising a computer program ("DField") capable of identifying the axon varicosities in contact with, or within a defined distance from, the cell surface. Briefly, an existing program (ImageVolumes, Minnesota Datametrics) was used to define the surfaces of the cell soma and of the varicosities in its vicinity. Next, a modification of the distance-field algorithm of Payne and Toga[2] was used to calculate the distance of closest approach to the surface of the soma from every voxel (within a maximum range set by the user) in the dataset. Finally, the distance-field values were intersected with the positions in space of the axon varicosities. Any axon or varicosity that fell within the criterion distance was identified and counted (Figure 1), and the statistical results were saved to a text file.

As a control, distances calculated by the Dfield program were compared to distances measured manually. A glass bead with a diameter of about 30 μm was placed in a solution of rhodamine B in 60% sucrose and imaged on a Bio-Rad MRC1000 (zoom = 4.8; 60x, 1.4 NA objective; z-steps = 0.2 μm). The bead was then moved to different positions in the x-y plane and imaged again. Minimum projections were made of the datasets and pairs of projections were merged. Distances between the pairs were measured directly using a Bio-Rad utility. These values were then compared to the values derived using the Dfield program (Figure 2). It was found that the x-intercept of the regression line was 270 nm, i.e. close to the resolution of the instrument in x-y. Moreover, the slope of the regression line was not significantly different from 1 ($p > .05$). These finding suggest that the Dfield program is capable of measuring the proximity of two structures with sub-micron accuracy. Although it is not possible to state that the appositions identified by Dfield are synapses, the program appears capable of providing a reliable means of identifying potential synapses at the light microscopic level.

References:
1. Mason P et al. (1992) J Neuroscience 12: 4023-4036
2. Payne AP and Toga AW(1992) IEEE Comp Graphics & Appl 12: 65-71
3. The authors gratefully acknowledge support from NIH grants DA 04523 and NS 33815.
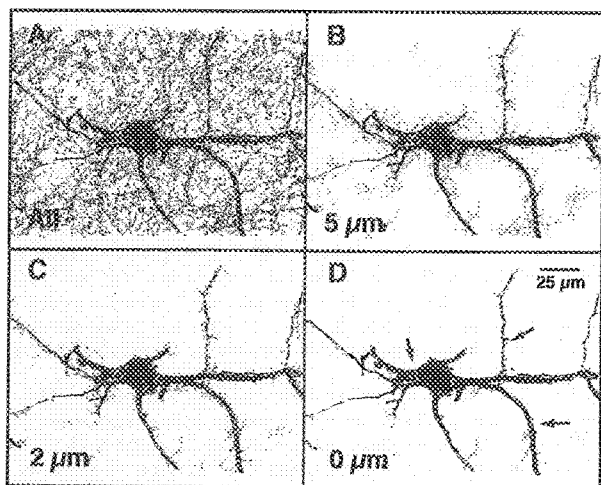
Figure 1: Surface reconstructions of a section from ventral tegmental area containing a cell filled with biocytin and staining for serotonergic axons and varicosites. Cell = black; varicosities = gray. A: Filled cell plus all stained varicosities. B: Cell with only those varicosities identified by DField as being within 5 μm of the cell. C: Cell with varicosities within 2 μm. D: Cell with only those varicosities that appeared to be in contact with the cell surface. Arrows point at some examples of putative contacts.
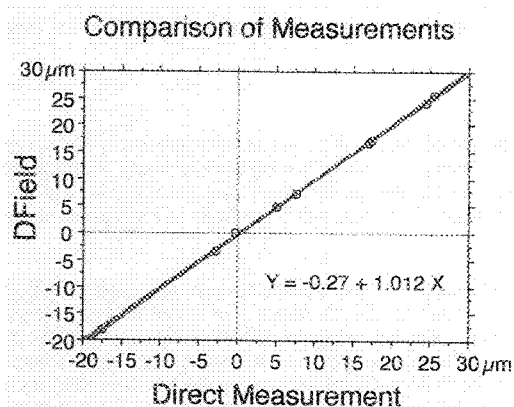
Figure 2: Linear regression comparing measurements performed manually to those obtained using DField. The thin shaded region around the line represents the 95% confidence limits. Values obtained by DField corresponded very closely to manual measurements. The small amount of difference may be due to the difficulty of manually determining the point of closest approach between two objects.

285

APPLICATIONS OF WIDE-FIELD FLUORESCENCE AND CONFOCAL REFLECTANCE MICROSCOPY TO BONE AND CARTILAGE STUDIES

M.H. Chestnut, K.J. Ibbotson, Y.O. Taiwo, T.E. Dufresne, J.S. Amburgey, F.H. Ebetino, J.L. Finch

The Procter & Gamble Company, P. O. Box 538707, Cincinnati, OH 45253

Bisphosphonate Uptake by Living Cells

Bisphosphonates are drugs which inhibit bone resorption and are being pursued as therapies for osteoporosis. The molecular mechanisms by which bisphosphonates exert their biological effects are still unclear. It is generally assumed that uptake of these highly polar molecules by cells is very limited.[1] In order to determine whether bisphosphonates are internalized and therefore may act intracellularly, we have examined the extent of their cellular uptake using a fluorescent naphthalene-dicarboxaldehyde (NDA) derivative of alendronate (ALN).

The distribution of NDA-ALN was examined in Ros 17/2.8 osteoblast-like osteosarcoma cells and freshly isolated neonatal rat osteoclasts by fluorescence microscopy following 0.5-24 hours of treatment *in vitro*. Data were collected using a Nikon Diaphot 300 equipped with a 60x planapochromat objective and high N.A. DIC optics. Images captured using a Photometrics PXL camera were processed using UIC Metamorph software.

Uptake of the bisphosphonate into the cells was rapid and could be detected after 30 minutes of treatment in cells exposed to an external concentration of 10^{-5}M NDA-ALN. Bisphosphonate appeared to accumulate over time within vacuolar, often perinuclear structures similar in appearance to secondary lysosomes (Figure 1). NDA-ALN was retained within cells after washing. These observations are consistent with the uptake of NDA-ALN proceeding via fluid-phase endocytosis. Uptake was greatly reduced when cells were incubated with the bisphosphonate at 20°C rather than 37°C. Freshly isolated osteoclasts also exhibited a noticeable amount of diffuse cytoplasmic staining (Figure 1), possibly indicating the presence of a second path of entry into the cell.

These observations indicate that key bone cell types that are affected by bisphosphonates appear to internalize bisphosphonates initially via fluid-phase endocytosis. Since the cellular effects of bisphosphonates also appear to require endocytic uptake, the present studies support the view that bisphosphonates have an intracellular mechanism of action.

Articular Cartilage Lesion Measurements

The formation of lesions in the femoral articular cartilage of rabbits after partial meniscectomy has promise as a model of osteoarthritis in humans. Grading lesion severity is usually a subjective process with the attendant imprecision and error. Here we present the development of a method for measuring the volume of intact lesions (Figure 2A) and for closely examining their morphology. The approach used here is analogous to that taken previously for smaller surface structures[2].

Reflectance confocal microscopy with a Molecular Dynamics Sarastro 2000 system was used to collect image data that defined the surface of the cartilage by points of maximum reflectance. For specimens with lesions from 1 to 4 millimeters in diameter, multiple sets of images collected using a 4X Nikon Planapochromat objective were used to produce a map of the cartilage surface. The mapmaking and measurements were accomplished with modules custom written using Iris Explorer for the Silicon Graphics computing environment. By fitting a curved surface plane to the map and manually defining the perimeter of the lesion, direct measurement of lesion volume, depth and area in real units is achieved (Figure 2B). Curved surface fitting reduces error when working with naturally curved structures. The cartilage surface maps have spatial resolution in X and Y of 2 μm and Z resolution of roughly 15-20 μm, making them an excellent way of examining lesions for fine morphological features when compared with macrophotography. Direct measurement of lesions may exhibit less statistical variation than does subjective grading.

References

1.   R. Felix et al. *Calcif Tissue Int 36(1984)108.*
2.   A. Boyde and S. J. Jones *Handbook of Biol. Confocal Microscopy* Pawley: Plenum Publishing, New York *(1995)255.*
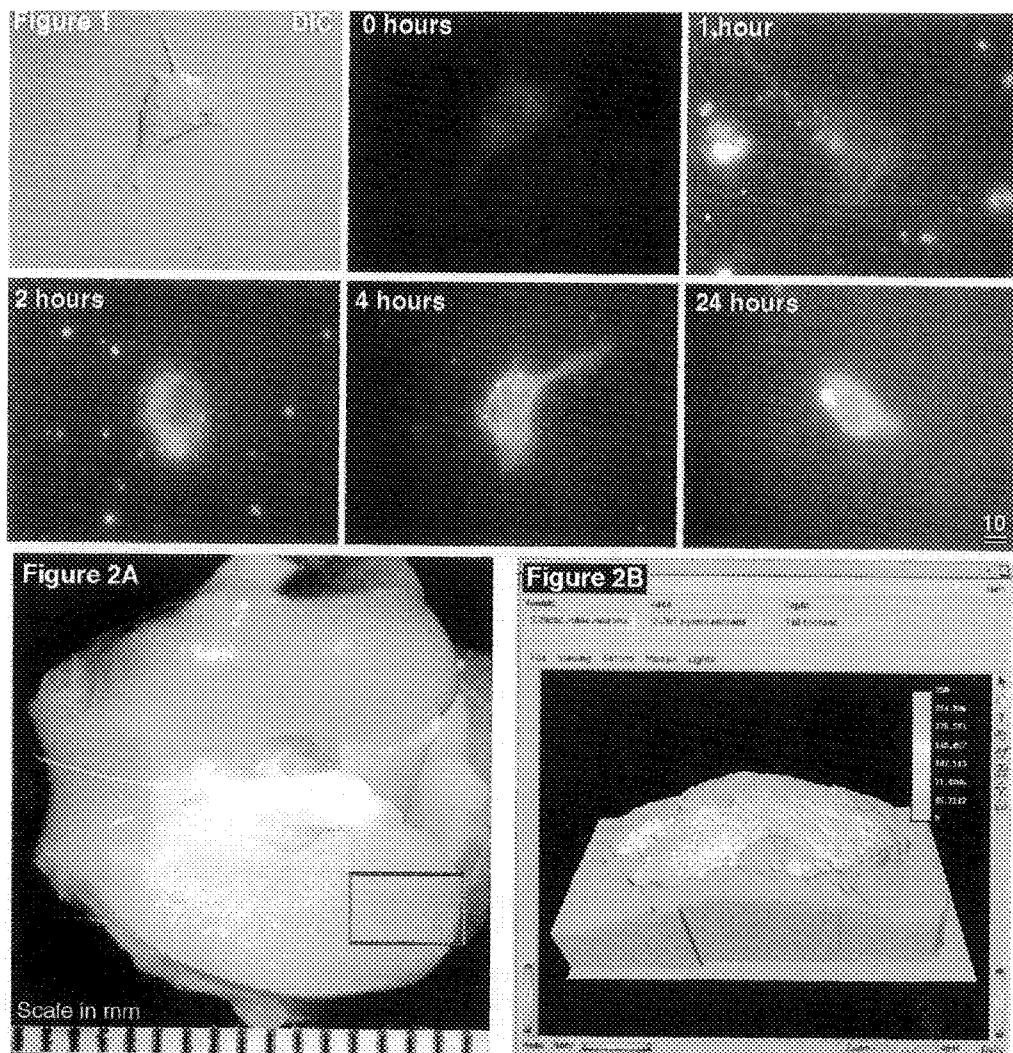
FIGURE 1   Time course of NDA-ALN uptake by rat osteoclasts. DIC = differential interference contrast
            image for comparison with the fluorescence images. Bar is 10 μm.
FIGURE 2   Measurement of rabbit articular cartilage lesion volume. Image 2A shows freshly excised
            articular surface with lesion area boxed. Image 2B shows a 3-D rendering of the cartilage
            surface and lesion after confocal imaging and 3-D measurement. Scale in mm.

287

THREE-DIMENSIONAL SUBCELLULAR ORGANIZATION OF HEPATOCYTES IN INTACT LIVER: SIMULTANEOUS VISUALIZATION OF CYTOSKELETAL AND MEMBRANE MARKERS BY CONFOCAL MICROSCOPY

Greg V. Martin and Ann L. Hubbard

Dept of Cell Biology and Anatomy, Johns Hopkins School of Medicine, Baltimore, Maryland, USA

The microtubule (MT) cytoskeleton is necessary for many of the polarized functions of hepatocytes. Among the functions dependent on the MT-based cytoskeleton are polarized secretion of proteins, delivery of endocytosed material to lysosomes, and transcytosis of integral plasma membrane (PM) proteins.[1] Although microtubules have been shown to be crucial to the establishment and maintenance of functional and structural polarization in the hepatocyte, little is known about the architecture of the hepatocyte MT cytoskeleton *in vivo*, particularly with regard to its relationship to PM domains and membranous organelles. Using an *in situ* extraction technique that preserves both microtubules and cellular membranes, we have developed a protocol for immunofluorescent co-localization of cytoskeletal elements and integral membrane proteins within 20 μm cryosections of fixed rat liver. Computer-aided 3D reconstruction of multi-spectral confocal microscope images was used to visualize the spatial relationships among the MT cytoskeleton, PM domains and intracellular organelles.

The livers of anesthetized rats were extracted by *in situ* perfusion via the portal vein with a microtubule stabilizing buffer (MSB) containing 0.025% saponin for 5 min. at room temperature.[2] The livers were then excised, cut into thin strips and rinsed in a 8% sucrose solution in MSB. Following fixation in Nakane fix[3] for 4 hr. at room temperature, the specimens were cut into 2 mm cubes, infiltrated with cryoprotectant and frozen in liquid nitrogen. Co-localizations were performed on 20 μm thick cryosections using antibodies to the following proteins: α-tubulin; HA4, an apical PM marker; sialyltransferase, a marker of the trans-Golgi and TGN; and albumin, which is highly concentrated in the Golgi of rat hepatocytes. Antibody incubations were performed on free-floating sections for 2-3 days in the presence of 0.1% saponin to facilitate labeling through the depth of the sections.

Results from these studies indicate that MTs radiate from what may be multiple microtubule-organizing centers (MTOCs) within individual hepatocytes. Putative MTOCs were observed as areas of intense tubulin labeling in close association with the apical PM and in perinuclear regions of the cells (Figs. 1&2). Co-localization studies demonstrate that Golgi cluster near both the apical and perinuclear regions of intense tubulin labeling (Fig. 3). Because Golgi position is established by migration towards the negative ends of MTs anchored in the MTOC, both regions probably contain negative ends of MTs and are likely to be MTOCs. Triple-localization of the Golgi, apical PM, and nuclei in sections of non-extracted liver confirms that Golgi are strongly associated with both the apical and perinuclear regions of hepatocytes (Fig. 4).

Both apical and perinuclear MTOCs exhibit extensive arrays of MTs extending to both the basal (facing the blood stream) and lateral (facing an adjacent hepatocyte) PM domains, thus forming a complex network of multiple, interwoven, MT arrays (Fig. 5). The MT array associated with the perinuclear MTOC appears to be the more extensive, radiating throughout the cell in three dimensions. The apical array appears somewhat flattened, its MTs generally occupying a peripheral location within the cell. No correlation was observed between the location of the apical MTOC and placement of the perinuclear MTOC. The observed MT arrangements are consistent with the strongly basolateral-oriented movement of Golgi-derived transport vesicles being anterograde (plus-end directed) and basolateral-to-apical transcytosis being retrograde (minus-end directed).[4]

1. A.L. Hubbard and G. Ihrke. 1995. *In*: Progress in Liver Diseases. J.L. Boyer, ed. pp.63-99.
2. N. Araki et. al. 1993. J. Electron Microsc. 42: 51-54.
3. I.W. McLean and P.K. Nakane. 1974. J. Histochem. Cytochem. 12: 1077-1083.
4. This research was supported by NIH grant DK44375.
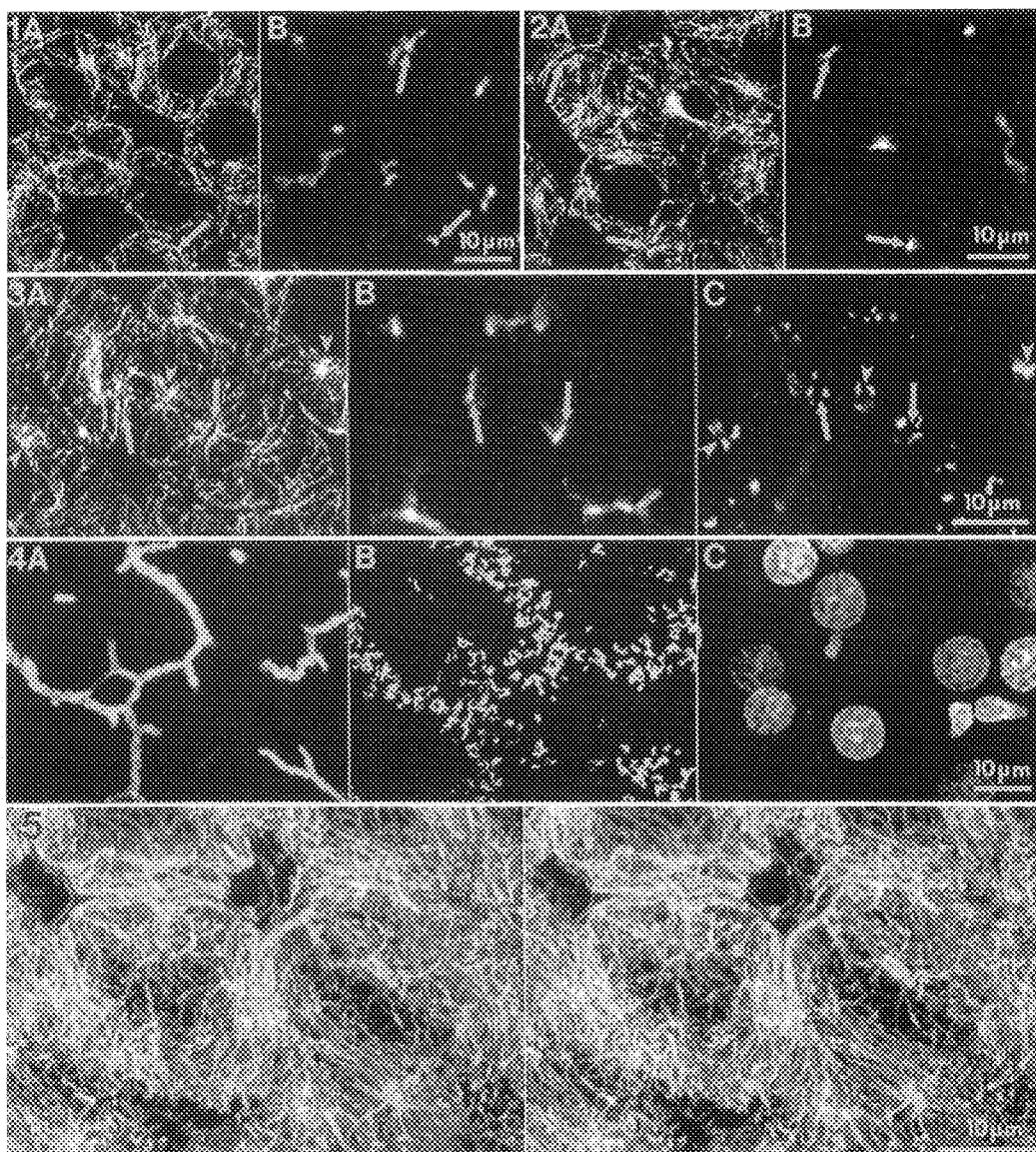
Figs. 1 & 2. Co-localization of MTs (A) and the apical PM (B). Arrows indicate corresponding apical regions in the paired fields. Each image is a single confocal optical section.

Fig. 3. Co-localization of MTs (A), apical PM (B), and Golgi (C). Arrows indicate corresponding apical regions; arrowheads indicate corresponding perinuclear MTOC regions. Each image is a single confocal optical section.

Fig. 4. Co-localization of the apical PM (A), Golgi (B), and nuclei (C) in non-extracted liver. Each image is a projection of confocal optical sections collected over a depth of 10 μm.

Fig. 5. Stereo pair of MT distribution in rat hepatocytes.

ANALYSIS OF CELLULAR ORGANELLES AND MACROMOLECULAR ASSEMBLIES BY ELECTRON ENERGY LOSS SPECTROSCOPY

R.D. Leapman* and S.B. Andrews**

*Biomedical Engineering & Instrumentation Program, NCRR; **Laboratory of Neurobiology, NINDS, National Institutes of Health, Bethesda, MD 20892

Recent advances in electron energy loss spectroscopy (EELS) have significantly extended the range of applications for biological microanalysis.[1-6] For example, EELS can now detect physiological concentrations of the important element calcium in rapidly frozen cells with a sensitivity greater than that achievable by energy-dispersive x-ray spectroscopy (EDXS).[7] It can also detect small numbers of phosphorus atoms bound to macromolecular assemblies,[8] and measure water distributions in frozen hydrated tissue.[9] Here we discuss some of these developments in the context of detection limits and mapping techniques in the scanning transmission electron microscope (STEM) and energy-filtering transmission electron microscope (EFTEM).

The useful information about elemental composition in EELS of biological specimens generally resides in weak core-edge signals corresponding to atomic concentrations in the 10^{-5}–10^{-3} (1–100 mmol/kg dry weight) range. For example, the Ca $L_{2,3}$ signal/background ratio is typically only 10^{-3} and it is necessary to measure differences in signal that are only 10^{-4} of the background. Changes in low-loss fine structure corresponding to varying chemical composition are also very subtle; for example, detection of a 3% change in water content requires reliable measurement of a 0.1 eV shift in the low-loss intensity maximum. To extract such information requires efficient parallel detection of the energy loss spectrum and a high-brightness source to provide a sufficient number of incident electrons. The dedicated STEM is particularly well-suited for analyzing low concentrations of biological elements. If desired, the probe current can be reduced into the picoampere range for low-dose, high-resolution imaging prior to elemental analysis. The STEM's field-emission source can then be used to deliver a current approaching 10 nA into a ~10 nm diameter probe. High electron flux conditions are ideal for spectrum-imaging applications where adequate counting statistics must be achieved within a limited pixel dwell time. The cold field-emission source of the STEM has the additional advantage of providing electrons with a narrow energy spread of <0.5 eV which is important in fine structure studies.

In processing energy loss spectra from biological specimens it is necessary to remove the pattern-noise caused by detector channel-to-channel gain variations. This can be achieved either by gain normalization or by applying difference-acquisition techniques where spectra are shifted electrically across the detector and subtracted. Although the read-out noise of photodiode arrays limits detective quantum efficiency at low dose, in analytical applications at high dose these detectors can be operated near saturation so that statistics are limited mainly by shot-noise.[2,10] To measure successfully the weak core-edge signal methods must be devised for modeling the EELS background intensity as accurately as possible, allowing for plural scattering effects in thicker samples. Finally, the spectra can be quantified by fitting appropriate reference spectra. It is often useful to determine elemental ratios relative to carbon, which can then be converted into values in units of mmol/kg.

When local elemental concentrations are relatively high (e.g., phosphorus in DNA or sulfur in certain proteins), the EFTEM can offer some advantages over the STEM. Efficient, cooled slow-scan CCD cameras used in conjunction with a variety of EFTEM systems provide quantitative images with low detector noise.[11,12] It is possible to record sequences of energy-selected images containing 1024x1024-pixels in short acquisition times of a few minutes or less, from which elemental maps can be computed by extrapolating and then subtracting the background under the core edges. However, because the inelastic scattering can only be sampled at a few energy losses in the EFTEM, it is not feasible to image low concentrations of elements like calcium.

The collection of energy loss spectra at each pixel in a scanned image (spectrum-imaging)[13] provides a powerful means of mapping elements present at lower concentrations.[3,4] After acquisition the spectra can be processed to provide elemental maps of major elements by fitting an inverse power law to the pre-edge background. To analyze minor elements, the data set can be segmented into regions of interest and selected spectra summed to give $>10^7$ scattered electrons per channel in the integrated spectrum. We have used this approach to measure Ca with a sensitivity <1 mmol/kg dry weight in cerebellar neurons. Calcium concentrations of 5±1 mmol/kg dry weight were found in cisterns of endoplasmic reticulum in neuronal dendrites, corresponding to fewer than 100 atoms of this element in each analyzed cistern.[7]

Spectrum-imaging can also be used to map subcellular water content in hydrated cryosections of rapidly frozen tissue.[9] The valence excitation spectrum of a hydrated specimen can be modeled as the sum of spectra from vitreous ice and protein which exhibit significant differences in shape over the energy range 5-25 eV. Several processing steps are required to extract this chemical information, including deconvolution by the detector point-spread function, correction for plural scattering, correction for the support film, energy alignment of the single scattering distributions at each pixel, and finally multiple least squares fitting of reference spectra. This technique has recently yielded subcellular water distributions in liver and brain with a precision of about ±2% at a spatial resolution of ~100 nm as limited by radiation damage.[9]

It has been realized for some twenty years that EELS offers the potential for near single atom detectability.[14] Using EELS we have been able to measure small numbers of phosphorus atoms bound to squid axonal neurofilaments, and hence to determine the phosphorylation state of this cytoskeletal protein. In these experiments, dark-field STEM mass maps recorded at low electron dose reveal the number of protein subunits per filament length. Subsequent EELS analysis at high dose (~10^9 electrons/nm^2) then provides the number of phosphorus atoms in 10-nm length segments of the filament with a sensitivity of 5 atoms, even though the spatial information is degraded by beam damage to the dimensions of the filament diameter, i.e., ~10 nm. The measurements gave 5.1±0.5 P atoms/nm along the neurofilament indicating that more than half of the potential phosphorylation sites (from sequence data) are in fact phosphorylated.

In principle, it should be possible to detect single atoms of calcium and phosphorus in 10 nm diameter analytical volumes. In practice, the main obstacle to achieving this goal is radiation damage. The required dose of ~10^{10} e/nm^2 for single atom detection is about an order of magnitude greater than the observed dose for complete loss of light elements from organic material. In the future it may be possible to circumvent this limitation by utilizing the spectrum-imaging technique to average EELS spectra from many similar regions of the specimen.

References

1. H. Shuman and P. Kruit, *Rev. Sci. Instrum.* 56 (1985) 231.
2. O.L. Krivanek et al., *Ultramicroscopy* 22 (1987) 103.
3. J.A. Hunt and D.B. Williams, *Ultramicroscopy* 38 (1991) 47.
4. G. Ballosier et al., *Microsc. Microanal. Microstruct.* 2 (1991) 531.
5. Z. Tang et al., *J. Microsc.* 175 (1994) 100.
6. R.D. Leapman and J.A. Hunt, *J. Elect. Microsc. Soc. Am.* 1 (1995) 93.
7. R.D. Leapman et al., *Ultramicroscopy* 49 (1993) 225.
8. R.D. Leapman and S.B. Andrews, *J. Microsc.* 165 (1992) 225.
9. S.Q. Sun et al., *J. Microsc.* 177 (1995) 18.
10. R.F. Egerton et al., *Ultramicroscopy* 48 (1993) 239.
11. W. Probst and V.E. Bayer, *Proc. 53rd Ann. MSA Meeting*, (1995) 668.
12. O.L. Krivanek et al., *Ultramicroscopy* 59 (1995) 267.
13. C. Jeanguillaume and C. Colliex, *Ultramicroscopy* 28 (1989) 252.
14. M. Isaacson and D. Johnson, *Ultramicroscopy* 1 (1975) 33.

HIGH-RESOLUTION MEASUREMENTS OF SUBSARCOMERE CALCIUM-BINDING DISTRIBUTIONS FROM EPXMA IMAGES

M. E. Cantino and J. G. Eichen

Department of Physiology and Neurobiology, University of Connecticut, Storrs, CT 06269

The distribution of calcium binding to thin filaments in vertebrate striated muscle provides clues about the role of calcium in regulation of contraction. A number of studies have suggested that the extent of Ca binding to the thin filament regulatory protein, troponin, is enhanced by the attachment of crossbridges.[1] Electron probe X-ray microanalysis (EPXMA) has provided direct evidence of this enhancement by showing that more Ca is found in the overlap than in the nonoverlap region of sarcomeres in skinned rabbit psoas muscle in rigor.[2] In that study, characterization of the spatial extent of this enhancement was limited by the pixel width of bands (4 pixels) within which Ca counts were averaged at each position across the sarcomere. In order to improve the resolution with which data are extracted from the image we have developed an automated routine for averaging calcium counts from successive columns of pixels across each half sarcomere in the image.

Samples were prepared as described previously.[2] Briefly, bundles of approximately 10 glycerinated rabbit psoas muscle fibers were rapidly frozen in rigor solutions containing specified levels of free Ca^{2+}, cryosectioned and freeze dried. Total [Ca] in the final solution was around 50 μM to ensure that only bound Ca would be detectable. Digital X-ray images were collected for approximately 24 hours using a Zeiss EM910 STEM and an Oxford ExL2 microanalysis system. Images were then analyzed on an Apple Power Mac 7100/80. An example of an image used for analysis is shown in Figure 1. An automated routine for extraction of data from the images was constructed using subroutines available in the IPLAB data analysis suite (Signal Analytics Corp.). First, a line of pixels was selected which followed the vertical outline of the A-I junction in a particular half sarcomere in the STEM image (Figure 2). This contour line (mask) was then overlaid on the corresponding Z line and translated pixel by pixel laterally across the Ca image, and the sum, mean and s.d. of counts at each location were computed. Pixels associated with remnants of the sarcoplasmic reticulum (identified from the P image), were subtracted from the mask. Often alignment of the mask with the underlying structure was good across the entire sarcomere, however, in some cases, each half sarcomere was analyzed using a separate mask.

In order to improve counting statistics, Ca profiles from several comparable half sarcomeres in the same section were averaged. The field shown in Figure 2 was mapped twice, results were averaged, then the data from the four half sarcomeres were combined to generate the Ca distribution shown in Figure 3. The data from the pixel position corresponding to the A-I junction in each half sarcomere were aligned at the same horizontal coordinate (see arrow). This procedure ensured optimal resolution of the Ca profile at the A-I junction, which shows a steep drop-off in Ca outside the overlap region. Slight variations in thin filament and sarcomere lengths within and between half sarcomeres probably contribute to the more gradual decline of Ca in the H zone. Using these techniques we hope to determine to what degree cooperativity between thin filament functional units extends Ca binding enhancement into the I band.

References

1. R. D. Bremel and A. Weber (1972) *Nature* 238:97-101
2. M.E. Cantino, T. StC. Allen, and A. M. Gordon (1993) *Biophys J.* 64:211-222
3. The authors gratefully acknowledge Ms. Shellee Cunnington, Mr. James Romanow, Dr. Lamia Khairallah and Dr. Albert Gordon for their help and advice. This work is funded by the National Institutes of Health (NIH HL49443, HL02142)
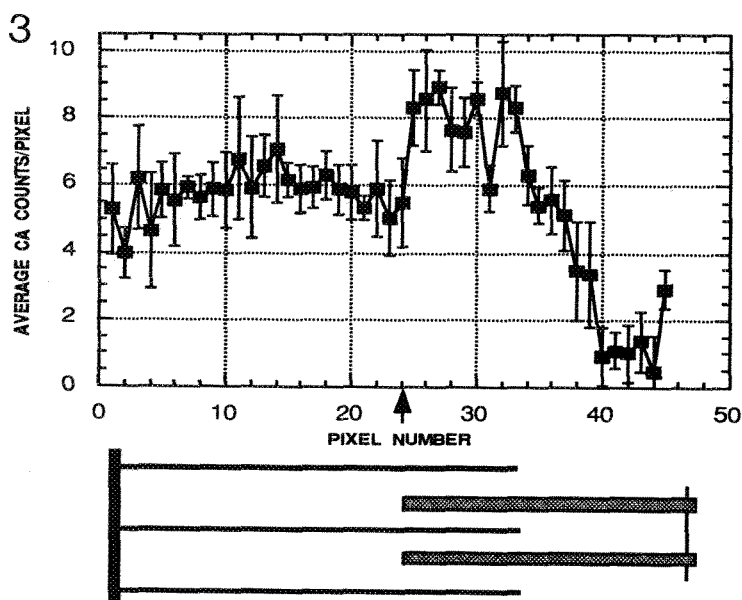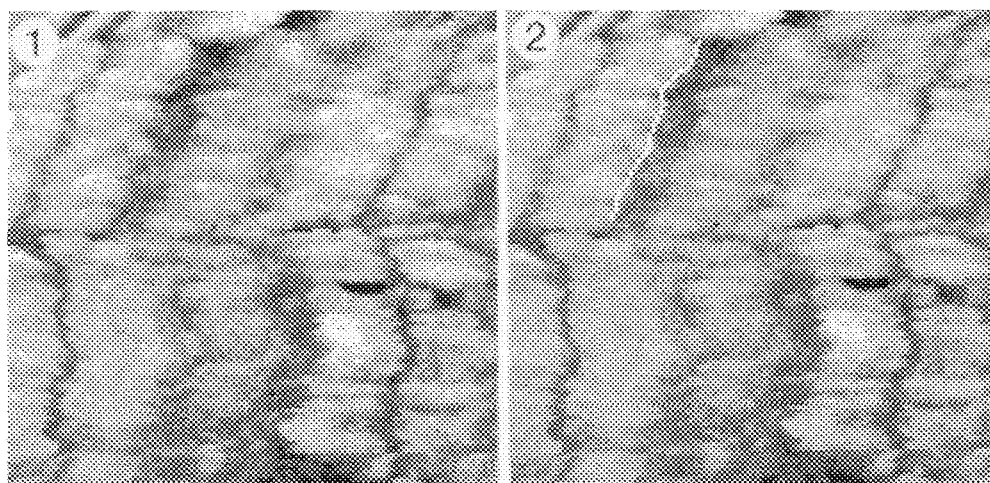
FIG 1. Digital STEM image of sarcomeres in a freeze dried cryosection of glycerinated rabbit psoas muscle.

FIG 2. STEM image with overlaid mask of A-I junction used to select pixels at each successive position across the sarcomere.

FIG 3. Plot of the Ca counts/pixel (mean ± SEM) in the four half sarcomeres in FIG 1 versus relative pixel position. The coordinate corresponding to the A-I junction is identified by the arrow. A schematic diagram showing corresponding sarcomere components is shown directly below the graph.

ION GRADIENTS ACROSS CONTRACTILE VACUOLE MEMBRANES OF AMOEBAE GROWN UNDER DIFFERENT OSMOTIC CONDITIONS

S.-L. Shi*, B. Bowers** and R.D. Leapman*

*Biomedical Engineering and Instrumentation Program, NCRR; **Laboratory of Cell Biology, NHLBI, National Institutes of Health, Bethesda, MD 20892.

The contractile vacuole (CV) regulates internal osmolality of free-living protozoa such as amoebae. The CV membrane is known to contain a V-H+ ATPase but the other ion transporters involved in the water pumping mechanism are not yet established.[1,2] Here we continue our earlier investigation by analytical electron microscopy to measure vacuolar and cytoplasmic ion concentrations in *Acanthamoeba castellanii*.[3] The present aim is to determine concentrations of ions transported across the CV membrane of amoebae grown under different osmotic conditions.

Subcellular ion concentrations in freeze-dried cryosections can generally be determined from x-ray microanalysis using the Hall method.[4] However, this approach is not suitable for measuring ion concentrations in the CV, which contains mainly inorganic salts and little, if any, organic compounds. A new method based on electron scattering measurements was therefore devised to deal with this highly aqueous compartment. This method involves: (i) measuring the volume of water in the hydrated cryosectioned vacuole with parallel electron energy loss spectroscopy (PEELS); (ii) measuring the mass of vacuolar salt in the freeze-dried cryosection by dark-field scanning transmission electron microscopy (STEM); and (iii) measuring the ratios of ions by energy-dispersive x-ray spectroscopy (EDXS).

Acanthamoeba was incubated for 1.5–2 hours in 100% growth medium (210 mosmol) and 25% growth medium (60 mosmol) each containing 5% polyvinyl pyrrolidone (PVP). The cells were centrifuged at low speed and drops of the suspensions were rapidly frozen on wooden sticks by plunging into liquid nitrogen-cooled ethane. Frozen blocks were cryosectioned to a thickness of 100 nm at -160°C using a diamond knife and were placed on Formvar/carbon coated grids as described previously.[5] Sections were cryotransferred at -180°C into a 100 keV HB501 STEM (VG Microscopes) equipped with a Gatan 666 PEELS and a Noran Micro-ZHV EDXS detector. EELS spectra were recorded at low electron-dose (<100 e/nm^2) from 1-µm diameter regions of the frozen hydrated cells. The cryosections were then dehydrated by warming slowly to -100°C and were imaged in dark-field STEM to determine the mass per unit area of the dried salts relative to the support film. EDXS spectra were recorded from regions of cytoplasm and dried vacuolar salts; these were quantified with a SIMPLEX fitting procedure using the NIH DTSA program.[6] The EDXS measurements were made at sufficiently low electron dose (~10^4 e/nm^2) to avoid loss of chlorine. For the cytoplasm, dry weight ion concentrations were determined using the Hall method, whereas for the dried vacuolar salts, only cation ratios were computed.

The calculated mean Na+ and K+ concentrations for cytoplasm and contractile vacuoles in 10 cells and the growth medium are shown as bar graphs in Fig. 1 (100% growth medium) and in Fig. 2 (25% growth medium). To convert the dry weight concentrations to molar concentrations, the cytoplasmic water content was taken to be 85% as determined from previous measurements on hydrated cells.[7] The water content of the 100% and 25% growth media were known from their preparation as 92% and 94.3% respectively.

Our measurements indicate that Na+ is pumped into the CV of *Acanthamoeba* cultured in normal growth medium, and that the CV fluid is approximately isosmotic with the cytoplasm if the equal number of counter anions are included. When cells are cultured in hypotonic 25% growth medium significant amounts of K+ are found to enter the CV. The major vacuolar counter anion does not appear to be Cl-, which is consistent with generation of HCO$_3$- by carbonic anhydrase known to be present in amoeba

cytoplasm. The CV fluid remains approximately isosmotic with the cytoplasm in both high and low osmotic strength media as expected.

The results suggest that an antiporter operates in conjunction with the vacuolar H^+ pump to remove protons from the vacuole in exchange for Na^+ ions. This ion transport mechanism appears to be in competition with movement of K^+ ions into the vacuole when the cytoplasm is depleted of Na^+ which occurs in the hypotonic growth medium.

References

1. T. Zeuthen, *Biochim. Biophys. Acta* (1992) 1113, 229.
2. J. Heuser et al., *J. Cell Biol.* (1993) 121, 1311.
3. B. Bowers et al., *Proc. 53rd Ann. MSA Meeting* (1995) 880.
4. T.A. Hall and B.L. Gupta, *J. Microsc. 126* (1982) 333.
5. S. Shi et al., *Microsc. Res. Tech.* (1996) 33, 241.
6. C.E. Fiori and C.R. Swyt, *Microbeam Analysis*, R. Linton, Ed., San Francisco Press, San Francisco (1989) 236.
7. S.Q. Sun et al., *J. Microsc.* 177 (1995) 18.
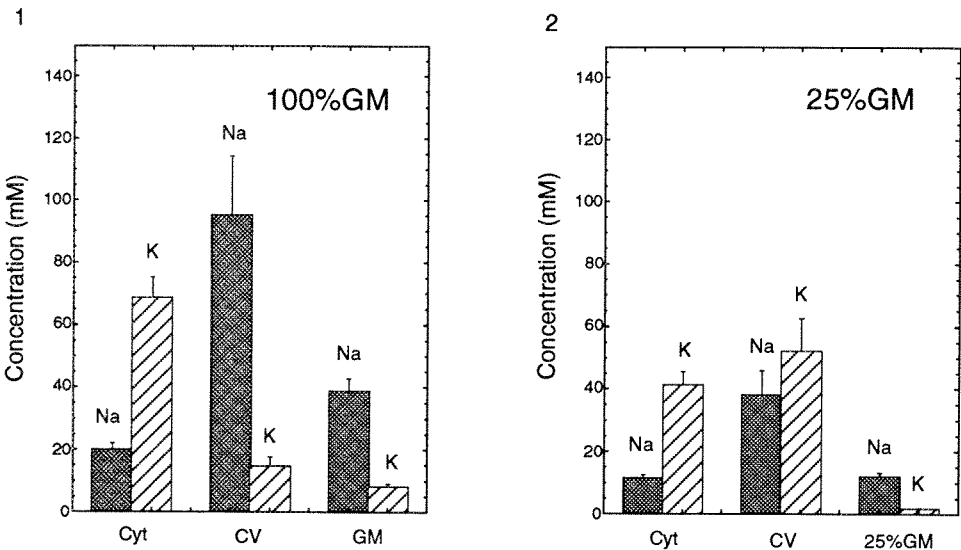
FIG.1 Estimated Na^+ and K^+ concentrations in cytoplasm and contractile vacuoles of *Acanthamoeba* cultured in 100% growth medium. Ion concentrations in the growth medium are also indicated.
FIG.2. Estimated Na^+ and K^+ concentrations in cytoplasm and contractile vacuoles of *Acanthamoeba* cultured in 25% growth medium. Ion concentrations in the growth medium are also indicated.

CALCIUM QUANTITATION WITH A PARALLEL EELS/COOLED CCD SYSTEM

Ruoya Ho, Zhifeng Shao and Andrew P. Somlyo

Dept. of Molecular Physiology & Biological Physics, Univ. of Virginia, Medical Center, Box 449 Charlottesville, VA 22908

The value of electron energy loss spectroscopy (EELS) for analyzing low concentrations of phosphorus and calcium, in biological cryo-sections, has been well documented[1-5]. With currently available techniques, the sensitivies of EELS for phosphorus and calcium can be three to ten fold higher than those of electron probe microanalysis (EPMA).

Our experiments were performed with an EELS system including a Philips CM200 electron microscope equipped with a field emission gun and a STEM unit, and a GATAN 666 PEELS. We replaced the original fiber optically coupled photodiode array on the PEELS with a cooled CCD camera with lens coupling[6] for better performance. The microscope is operated at 200 keV, allowing us to use relatively thick cryo-sections ($\lambda_i = 1700$ Å for carbon at 200 keV). We also used the shortest camera length in the STEM unit for achieving higher collection angle. According to our experience, the 2 mm aperture on the PEELS provides the best compromise of energy resolution and collection angle. Under these conditions, the collection semi-angle of this system is about 7 mrad and the energy resolution (full width at half maximum without specimen) is about 2.2~2.4 eV. The main limitations on using a larger collection angle are the 90 mm column between the viewing screen of the microscope and the entrance aperture of the PEELS and the poor energy resolution obtained with larger PEELS aperture.

In the above system, one primary 200 keV electron will generate 2 digital counts on the CCD that is cooled to -25°C to reduce dark current. The readout speed of the CCD is adjusted to 250 kHz with 12 bits A/D readout. The frame readout time is about 0.94 s. After dark current subtraction and gain normalization, the residual dark current is less than 5 counts per pixel per readout and the residual gain variation is about 0.1%.

To simulate biological matrix, we used standard specimens made by mixing different concentrations of $Ca(NO_3)_2$ into a buffer containing 3% of PVP-40 (polyvinylpyrrolidone), 10 mmol EGTA and 40 mmol Tris. The dried PVP film was covered with a thin layer of carbon to increase conductivity and reduce radiation damage. The thickness of the standard specimen was about 0.46 λ_i (~ 780Å), measured by both the conventional and fitting method[7]. The Ca concentration of the specimen was also calibrated by a calibrated EPMA system mounted on a Philips CM12 microscope. The X-ray spectra were collected at 120 keV beam voltage and 2.2 nA beam current for 1000 s with a Si(Li) detector extending an approximately 0.13 steradian solid angle. First difference EELS spectra were collected at 200 keV beam voltage, 3.8 nA beam current for 94 s (100 frames/spectrum) with a 10 eV energy shift. The specimens were cooled to -100°C when collecting both the EELS and X-ray spectra to reduce radiation damage. The results for EELS and X-ray spectra are listed in Table 1.

Our results show that with our system, the uncertainty of quantitating Ca with EELS is about four times less than with EPMA at the same total dose, indicating that we can achieve with EELS, equivalent sensitivity in only 1/16 of the time required for EPMA. At the 99% confidence level, the minimum Ca concentration detected with EELS, using a total dose of 353 nA·s, from a 780Å thick specimens, is about 5.1 mmol/Kg dry weight. Under the same conditions, but reducing the total dose by a factor of ten, we can detect about 16 mmol/Kg Ca in 10 s, and without additional processing

overhead time, a 60x60 pixels EELS map will be collected in about 10 hours. For the same sensitivity, collection of an equivalent x-ray map would require 160 hours. Therefore, even with our current "imperfect" system, the advantage of EELS quantitation is already apparent.

References

1. M. Isaacson and D. Johnson, Ultramicroscopy, 1 (1975), 33.
2. A. P. Somlyo and H. Shuman, Ultramicroscopy, 8 (1982), 219.
3. R. D. Leapman and J. A. Hunt, Microsc. Microanal. Microstruct., 2 (1991) 231.
4. S. Shuman and A. P. Somlyo, Ultramicroscopy, 21 (1987), 23.
5. C. Colliex et al., Ultramicroscopy, 29 (1989), 31.
6. Tang et al., J. of Microscopy, 175 (1994), 100.
7. L. Zhao et al., Ultramicroscopy, 48 (1993), 290.
8. This work is supported by NIH grant P01-HL48807.

Table 1. - EELS and EPMA analysis results.

spectra type	total dose (nA·s)	fitting uncertainty (mmol/Kg)	standard deviation (mmol/Kg)	EELS uncertainty dose normalized to X-ray spectra (mmol/Kg)
EELS	353	1.7	1.1~2.5	0.68
X-ray	2200	2.9	2.7	

VALENCE ELECTRON ENERGY LOSS SPECTROSCOPY OF LIPIDS

S.Q. Sun*, J.A. Hunt*, S.-L. Shi** and R.D. Leapman**
*Gatan R&D, 6678 Owens Drive, Pleasanton, CA 94588
**Biomedical Engineering and Instrumentation Program, NCRR, NIH, Bethesda, MD 20892

We have recently demonstrated that chemical mapping by valence electron energy loss spectroscopy (EELS) can provide water distributions in frozen hydrated biological specimens.[1] That investigation also considered the EELS spectra from proteins, nucleic acids and lipids. Next to proteins, lipids are the second most abundant component of eukaryotic cells in terms of their mass fraction, but since lipids usually contain a high fraction of saturated carbon bonds they are particularly sensitive to radiation damage in the electron microscope. Here we characterize in further detail the valence EELS spectra of various lipids (arachidic acid, carotene, cholesterol and phosphatidylethanolamine) to determine what information is available about the ratio of saturated and unsaturated bonds and how the EELS fine structure changes as a function of dose.

The dedicated STEM is a very convenient technique for acquiring valence EELS spectra from beam-sensitive specimens for two main reasons. First, a cold field-emission source provides electrons with an energy spread <0.5 eV and therefore gives high energy resolution.[2-4] Second, the individual spectra recorded in a two-dimensional array of pixels (spectrum-imaging technique)[5] can be aligned in order to descan the energy shift produced in the image plane of the spectrometer by the extended object size at low magnifications.[1,6] In addition, the single scattering distribution can be derived separately at each pixel so specimen thickness need not be uniform. The results obtained in this way are highly reproducible. Care must be taken, however, to defocus the electron probe to a diameter greater than the pixel separation in order to avoid undersampling and radiation damage.

The lipids were dissolved in chloroform; bare 600-mesh grids were then dipped into this solution, blotted, and allowed to dry slowly in chloroform vapor. Spectrum-images were acquired with a system described previously using a Gatan 666 PEELS coupled to a VG Microscopes HB501 STEM.[5,7] Data were obtained under low dose conditions (<2 e/Å^2) from 10 μm-diameter areas of the lipid specimens which were cooled to -160 °C. Fig. 1 shows the resulting integrated spectra in the energy range <15 eV. These data can be interpreted in the following way. Carotene is a terpene containing 11 conjugated carbon-carbon double bonds which produce a strong resonance at 3.4 eV. This peak corresponds to a strong absorption band in the optical spectrum of carotene that gives carrots their orange color. In contrast to carotene, all 19 carbon-carbon bonds in arachidic acid are saturated and this explains the lack of structure below 8 eV in the spectrum from this compound. Cholesterol contains 27 carbon atoms but only one double bond which gives rise to a weak but definite maximum at 6.7 eV. Phosphatidylethanolamine contains 37 carbon-carbon bonds, which are all saturated except for one; a weak intensity might therefore be expected near 7 eV but none is detected.

Fine structure in the spectra from all four compounds was very beam-sensitive as illustrated in Fig. 2. The spectrum from arachidic acid exhibits significant changes in fine structure after an exposure of only 10 e/Å^2. The 10 eV peak is lost at this dose and the main plasmon-like maximum shifts up in energy by about 1 eV; these changes are probably due to loss of hydrogen. Carotene and cholesterol are somewhat less sensitive to beam damage although significant damage effects are observed at exposures of 100 e/Å^2; carotene is probably stabilized by its conjugated double bonds.

In conclusion, the fraction of the EELS signal in the energy range 3-7 eV reflects the ratio of unsaturated to saturated carbon-carbon bonds in lipid compounds. Application of chemical mapping to lipid systems is limited by radiation damage but a spatial resolution of ~200 nm might be achievable in the future.

References

1. S.Q. Sun et al., *J. Microsc.* 177 (1995) 18.
2. M. Isaacson, *J. Chem. Phys.* 56 (1972) 1813.
3. M. Isaacson et al., *Rad. Res.* 55 (1973) 205.
4. D.E. Johnson, *Rad. Res.* 49 (1972) 63.
5. J.A. Hunt and D.B. Williams, *Ultramicroscopy* 52 (1991) 47.
6. J.A. Hunt et al., *Ultramicroscopy* 58 (1995) 55.
7. O.L. Krivanek et al., *Ultramicroscopy* 22 (1987) 103.
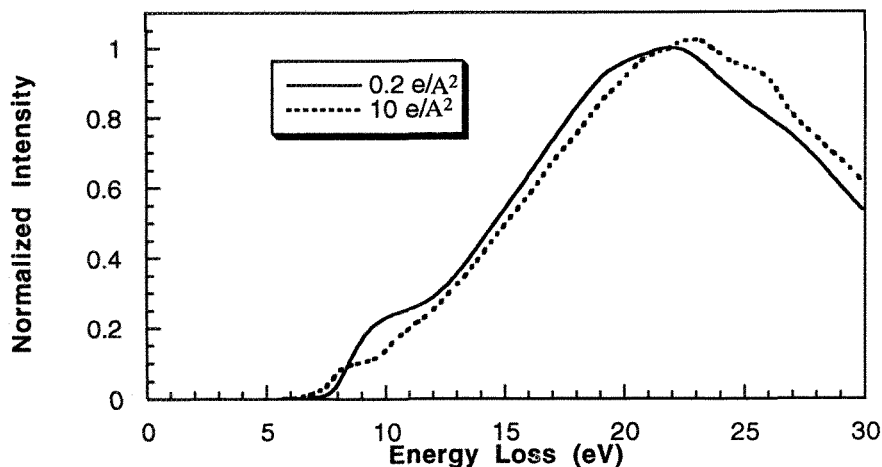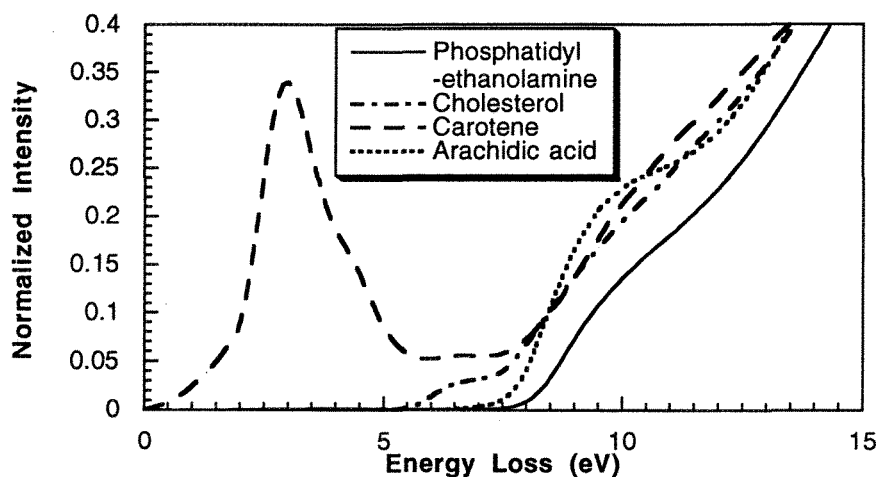
FIG. 1.   Valence EELS of arachidic acid, carotene, cholesterol and phosphatidylethanolamine recorded at a dose $< 2e/Å^2$. Structure in the energy range 3-7 eV is attributed to unsaturated carbon-carbon bonds.
FIG. 2.   Radiation damage in arachidic acid as dose is increased from $0.2e/Å^2$ to $10\ e/Å^2$; peak at 10 eV is lost and maximum at ~21 eV shifts up in energy by ~1 eV at the higher dose.

COMPARISON OF TECHNIQUES FOR EELS MAPPING IN BIOLOGY

R.D. Leapman[*], and S.B. Andrews[**]

[*]Biomedical Engineering and Instrumentation Program, NCRR; and [**]Laboratory of Neurobiology, NINDS, National Institutes of Health, Bethesda, MD 20892-4062, USA

Elemental mapping of biological specimens by electron energy loss spectroscopy (EELS) can be carried out both in the scanning transmission electron microscope (STEM),[1-4] and in the energy-filtering transmission electron microscope (EFTEM).[5-7] Choosing between these two approaches is complicated by the variety of specimens that are encountered (e.g., cells or macromolecules; cryosections, plastic sections or thin films) and by the range of elemental concentrations that occur (from a few percent down to a few parts per million). Our aim here is to consider the strengths of each technique for determining elemental distributions in these different types of specimen.

On one hand, it is desirable to collect a parallel EELS spectrum at each point in the specimen using the 'spectrum-imaging' technique in the STEM.[1-4] This minimizes the electron dose and retains as much quantitative information as possible about the inelastic scattering processes in the specimen. On the other hand, collection times in the STEM are often limited by the detector read-out and by available probe current. For example, a 256 x 256 pixel image in the STEM takes at least 30 minutes to acquire with a read-out time of 25 ms. The EFTEM is able to collect parallel image data using slow-scan CCD array detectors from as many as 1024 x 1024 pixels with integration times of a few seconds.[7] Furthermore, the EFTEM has an available beam current in the μA range compared with just a few nA in the STEM. Indeed, for some applications this can result in a factor of ~100 shorter acquisition time for the EFTEM relative to the STEM. However, the EFTEM provides much less spectral information, so that the technique of choice ultimately depends on requirements for processing the spectrum at each pixel (viz., isolated edges vs. overlapping edges, uniform thickness vs. non-uniform thickness, molar vs. millimolar concentrations).

The most straightforward experiment (Fig. 1A) involves mapping an element that has an 'isolated' edge in its energy loss spectrum, i.e., where no other feature is present within a 50–100 eV energy range below the edge so that the pre-edge background can be modeled to good approximation by an inverse power law.[8] Examples include imaging nucleic acid distributions using the phosphorus $L_{2,3}$ edge (at 132 eV) in unstained plastic-embedded thin sections or in preparations of isolated macromolecules adsorbed onto thin carbon films.[9] Sulfur ($L_{2,3}$ edge at 162 eV) which reflects the distribution of certain cysteine-rich proteins can also be mapped in this way but only in the absence of phosphorus. In practice, it is found that the signal/background is typically a few percent in which case a 'three-window' mapping method (two pre-edge images and one post-edge image) may be used satisfactorily in the EFTEM. Unless the specimen is very thin or has uniform mass-thickness, the net core-loss image should be divided by the corresponding low-loss image to correct for mixed elastic-inelastic scattering.

It is sometimes feasible to apply a simpler 'two-window' or 'ratio' technique (Fig. 1B) where a post-edge image is divided by the corresponding pre-edge image.[7] This approach is only valid when the sample mass-thickness is uniform and when the local elemental concentrations are relatively high. If applicable, ratio imaging in the EFTEM provides less noisy data than the three-window method because statistical uncertainty from the background extrapolation is reduced. It also has the advantage of canceling out contrast due to mixed elastic-inelastic scattering. However, ratio images cannot be easily quantified and are prone to artifacts from systematic variations in background shape.[8]

Use of CCD detectors with near single-electron sensitivity provides a quantitative assessment of statistical and systematic errors in background fitting that affect accuracy and precision in elemental maps. In this assessment it is often useful to obtain 'control' maps of elements not present in the specimen.

The STEM approach is particularly powerful when edges overlap (e.g, mapping sulfur in the presence of phosphorus) or when plural inelastic scattering strongly affects the pre-edge spectral shape (e.g., carbon K-edge + plasmon below the calcium $L_{2,3}$ edge), so that the inverse power law becomes invalid. Parallel detection in the STEM (Fig. 1C) provides excellent counting statistics as well as high energy resolution and therefore allows precise modeling of overlapping edges using procedures such as multiple least squares fitting.[3] For some applications, e.g., mapping high levels of calcium in mineralized tissue, similar results can be obtained in the EFTEM by collecting multiple image sequences at different energy losses, a technique known as 'imaging-spectrum' by analogy to 'spectrum-imaging' in the STEM.[10] Spectrum-imaging in the STEM (Fig. 1D) is presently the only workable approach to map low concentrations of elements such as calcium (typically present at only 10–100 atomic ppm).[11] In this case the signal is typically ~0.1% of the background and it is impossible to achieve sufficient precision or accuracy for background extrapolation in the EFTEM.

In summary, both the EFTEM and STEM are useful for elemental mapping by EELS but the two techniques should not generally be applied to the same types of specimen. Instead they should be considered as complementary—the EFTEM is particularly useful for characterizing large fields containing relatively high concentrations of elements such as P and S, whereas the STEM can map low concentrations of Ca and other elements in well-defined structures.
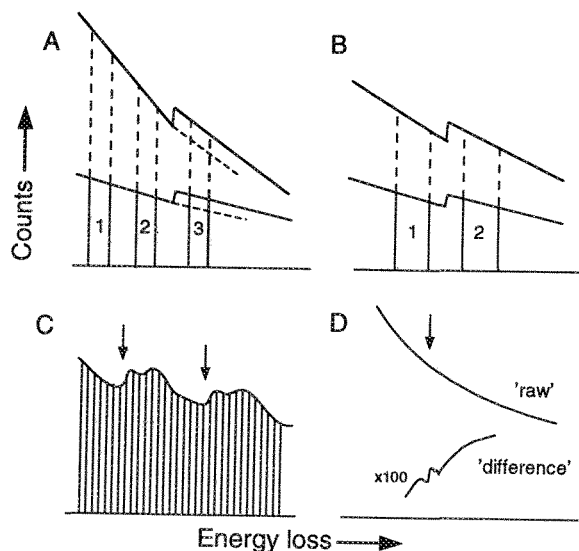
FIG. 1 Schematic diagram showing different situations that arise in EELS mapping of biological specimens: (A) 3-window method in EFTEM for extrapolating background of form $I_b = AE^{-r}$ under an isolated edge; (B) 2-window method in EFTEM where background below an isolated edge is assumed to have constant shape; (C) spectrum-imaging in STEM (or EFTEM) can be used to model background under overlapping edges (arrows); (D) spectrum-imaging in STEM can detect edges with very small signal/background, e.g., by using 'difference' techniques.

References

1. H. Shuman et al., *Ann. NY Acad. Sci.* 483 (1986) 295.
2. C. Jeanguillaume and C. Colliex, *Ultramicroscopy* 28 (1989) 252.
3. J.A. Hunt and D.B. Williams, *Ultramicroscopy* 38 (1991) 47.
4. R.D. Leapman and J.A. Hunt, *J. Elect. Microsc. Soc. Am.* 1 (1995) 93.
5. F.P. Ottensmeyer, *J. Ultrastruct. Res.* 88 (1984) 121.
6. W. Probst and V.E. Bayer, *Proc. 53rd Ann. MSA Meeting,* (1995) 668.
7. O.L. Krivanek et al., *Ultramicroscopy* 59 (1995) 267.
8. R.D. Leapman, *Ann. NY Acad. Sci.* 483 (1986) 326.
9. D.P. Bazett-Jones et al., *Science* 264 (1994) 1134.
10. J.L. Lavergne et al., *Microsc. Microanal. Microstruct.* 3 (1992) 517.
11. R.D. Leapman et al., *Ultramicroscopy* 49 (1993) 225.

ELECTRON SPECTROSCOPIC IMAGING AND ANALYSIS IN THE TEM: HAVE THE LIMITS BEEN REACHED

F.P. Ottensmeyer

Ontario Cancer Institute and Department of Medical Biophysics, University of Toronto, Toronto, Ontario, M5G 2M9, Canada

Electron energy filtering in the transmission electron microscope has had two major applications: 1) contrast enhancement in the image by elimination of chromatic aberrations, and 2) microanalysis by utilization of the information carried in the electron energy loss spectrum.

The first application is unique to the fixed beam electron microscope, in which the image suffers from the interaction of the imaging lens with a broad spectrum of electron energies. Since the modal energy loss in the spectrum of 100 kV electrons traversing a carbonaceous light-atom material is about 25 eV per mean-free-path length in the specimen[1], a lens even with a chromatic aberration constant as good as 1 mm will blur the corresponding image to about 25 Å. In the STEM in which no imaging lenses are used after the electron beam has interacted with the specimen, chromatic aberrations do not occur; at most an effect due to the non-localization of the electron-specimen interaction may be detected as a blurring due to low-loss electrons. Even in the TEM, the effect of energy filtering to use only elastic electrons is small for bright field images of thin specimens stained with heavy atoms, since contrast and visibility is achieved primarily from the predominant elastic scatter from the heavy atoms. However, for dark field microscopy of unstained specimens the effect of filtering is dramatic[2], since for carbon atoms inelastic scattering dominates elastic scattering by a ratio of 3 to 1[3].

As specimen thickness increases to the level of one inelastic mean free path (about 1500 Å in sections) or more, fewer and fewer elastic scattering events contribute to the image, even for stained specimens. In this case filtering can achieve huge increases in contrast by selecting the few elastic electrons that still penetrate the specimen. In addition, however, by selection of a small energy band in the energy loss spectrum around 25 eV or somewhat higher, one can take advantage of the mix of electrons that have undergone multiple and mixed elastic and inelastic collisions to obtain useful structural information by the so-called "contrast-tuning"[4], information that would otherwise be lost for such thick specimens. Quantitative analysis in terms of mass density is too complex in such approaches; however, since staining in general is used to delineate rather than to quantify, the gain in information, coupled with judicious care in interpretation, is well worth the approach.

For both qualitative and quantitative microanalysis, electron energy loss spectroscopy and imaging are now widely applied. Even in biological applications the techniques have reached limits that in different conditions approach the spatial resolution limitations of the microscope on the one hand, and near-atom detection and identification on the other. Such successes must be understood in context in order to translate the potential from those results to new applications.

Qualitatively, every aspect of the electron energy loss spectrum is being exploited, from analysis and imaging using inner-shell losses of all atoms in the periodic table[5], to the use of the electron-optical

equivalent of molecular chromophores in the low-loss region[6]. Quantitatively, spatial resolutions of 3-5 Å for phosphorus core-loss electrons have been observed for membrane bi-layers imaged edge-on[7], equivalent to a about a 10 M phosphorus concentration; spatial resolution limitations at lower energy losses, using plasmon and valence shell excitations, are still being explored theoretically and experimentally[8]. In imaging with a TEM, 30 phosphorus atoms were the limit of detection at a signal to noise ratio (S/N) of 5[9]; this limit was observed in nucleosomal DNA, in tRNA and 5S RNA[10], all nucleic acids with a high intrinsic phosphorus concentration. In spectra a similar S/N resulted in a detection of 3 calcium atoms[11].

The differential cross-section for phosphorus of about $3 \times 10^{-20} cm^2/atom$ [12] requires and electron exposure of close to 10,000 $e/Å^2$ to obtain a signal of about 150 electrons for the 30 P-atoms detected above at such an S/N in the presence of carbonaceous atoms from the support and from the biological structures themselves. Utilization of a STEM for phosphorus imaging would be of but marginal advantage, since in bothe the TEM and the STEM virtually all of the inelastic electrons are forward scattered into the acceptance angle of the respective spectrometers. The steep decay of the energy loss intensity with increasing energy loss confers a small advantage to parallel spectral recording in the STEM, but even this is lost unless single-electron counting capabilities exist in the electronic signal detection cascade.

Are the above results generally achievable? Can they be extended? The answer in many instances is now calculable. It depends on the radiation dose, on the specimen stability, the elemental concentration in the beam direction, the ionization cross-section of the atom to be analysed, the background signal from all other atoms subtending and surrounding the target atoms, the permissible or acceptable S/N, the electron counting efficiency, and in many instances, including comparisons of TEM and STEM, on the magnitude of the current of the electron beam. In the above examples these factors conspired to achieve success. Moreover, none of the examples made use of low temperature to achieve greater radiation resistance, or included elements of structural symmetry to permit averaging for a greater S/N or for a lower electron dose. Thus in some instances the present limits will be exceeded, in others they will not be reached.

1.   A.M. Rauth and J.A. Simpson (1964) Rad. Res. 22, 643-61.
2.   R.M. Henkelman and F.P. Ottensmeyer (1974) J. Microscopy 102, 79-94.
3.   R.F. Egerton (1986) Electron energy-loss spectroscopy in the electron microscope. Plenum Press New York, p. 143.
5.   C.C. Ahn and O.L. Krivanek (1983) EELS Atlas. GATAN Inc., Warrendale, PA.
6.   M. Barfels and F.P. Ottensmeyer (1996) These Proceedings
7.   K.M. Adamson-Sharpe and F.P. Ottensmeyer (1981) J Microscopy 122, 309-314.
8.   H. Kohl and H. Rose (1985) Adv. Electron. Electron Physics 65, 173-85.
9.   G. Harauz and F.P. Ottensmeyer (1984) Science 226, 936-940.
10.   D.W. Andrews (1985) High dose electron microscopy of macromolecules. Ph.D. Thesis. University of Toronto.
11.   H. Shuman and A.P. Somlyo (1987) Ultramicroscopy 21, 23-32.
12.   Y.M. Heng, G.T. Simon, M. Boublik and F.P. Ottensmeyer (1990) J. Microscopy 160, 161-71.

PRINCIPAL COMPONENT ANALYSIS AS A STRATEGY FOR MULTISPECTRAL ACQUISITION OF IMAGES

P. Ingram,* D. A. Kopf** and A. LeFurgey**#+

*Research Triangle Institute, Research Triangle Park, NC 27709
**Division of Physiology, Department of Cell Biology, Box 3709, Duke University Medical Center, Durham NC 27710
#School of the Environment, Duke University, Durham NC 27706
+Veterans Affairs Medical Center, Durham NC 27705

Principal Component Analysis (PCA) has been used by many authors to improve the statistical accuracy and interpretation of multispectral images in a variety of settings from the analysis of satellite radar images[1] to mapping of biological cells and tissues[2]. In this work we describe a strategy to characterize analytical data from biological cryosections by objectively using a scatterplot routine from PCA images to generate masks on the original STEM image; in this way control of the acquisition of spectral data can be performed in a statistically optimal manner.

If a set of images are obtained, the corresponding set of Principal Component (PC) images are easily generated. Mathematically, the PC images are the projection of the original images onto a set of orthogonal, complete axes that are the eigenvectors of the symmetric variance-covariance matrix obtained by summing the product of corresponding pixels in each element pair across the entire image (or selected region thereof). The corresponding eigenvalues are the variance contribution of each eigenimage to the total variance of the original set of images. When sorted into order of decreasing variance, the first PC axis represents the greatest covariance that can be found among all the elements; the second represents the largest remaining covariance orthogonal to the first axis and so on. The computation time required for such a calculation is about 10 seconds for eight 128x128 images for a 35 MHz 68040 processor.

PCA images are a complete set of images that contain the same information as the original set of images, but organized in a form which reveals *independent* sources of information and are displayed in decreasing order of variance.

In energy dispersive x-ray (EDX) microanalysis data, for example, each elemental image pixel can be considered as a point in a space whose axes are orthogonal. Principal Component (PC) space has another set of coordinate axes which are also orthogonal, and are linear combinations of the original axes. These axes are determined by removing any covariance among the coordinates in original image space, when computed over all pixels in the image. Thus in PC space the covariance of any pair of coordinates, when summed over all pixels in the generating region, is zero. Put another way, the transformation detects covariance in the original set and converts it into variance in the PC set. The resulting images are (usually) ordered in decreasing variance so that PC1 contains the greatest variance, and hence greatest covariance in original space. For example, Na and Cl elemental images obtained from a table salt specimen would transform into a PC1 image representation of NaCl, and a PC2 image containing any stoichiometric discrepancies. In a biological cryosection the transformation results in seven or eight PC images corresponding to the statistical preponderance and distribution of physiological elements present (Na, Mg, P, S, Cl, K, Ca, etc.). A drawback of using elemental images in this manner is the requirement that all elements that are potentially present must be included in the original set. The analyst typically does not collect images of exotic elements that are "known" not to be present. This subjective limitation can be overcome by saving the complete spectrum at each pixel and performing PCA directly in these spectra.

In our multispectral imaging software ImagNSpect,[3] a plugin module allows a spectral file to be subject to PCA. For a 1024 channel spectrum, this would be the equivalent of PCA of 1024 output

images. Such a calculation requires careful attention to precision and overflow during the eigenvalue calculation, as well as several hours of computing time. The use of a smaller subset of the spectra would ease this requirement, such as in a "routine" biological cryosection with only seven physiological elements. Normally PCA of the spectra gives a set of eigenvectors as before, upon which the input spectra can be projected. The number of distinct eigenvectors corresponds to the number of distinct spectral patterns, and an examination of the eigenvectors indicates which elemental peaks are present and need to be quantitated. Since the eigenvectors are orthogonal to the preceding ones, small peaks that otherwise would be lost in noise or a sidelobe of a larger peak are readily identified, and can be physically located on the corresponding image.

There are several useful ramifications of this approach. For example a feature which appears, disappears, or is displaced in successive images will stand out in PC space. Note that even though the entire image is projected onto the PC axes, the PC calculation can be done on a selected region of the image and spectrum which can be chosen to enhance the desired differences. This also makes possible the identification of underlying instabilities, e.g. beam current variations, peak jitter, energy drift correlated with count rate, improper deadtime correction, secondary fluorescence, amplifier overloading, etc. The original spectra can be recovered to any desired accuracy by including enough PC spectra and transforming back to original coordinates. It may happen that only a few PC spectra need be saved to recover the original data to the needed accuracy. Another application that may have utility is in the reduction of noise from spectra and the deconvolution of overlapping peaks, such as the potassium K beta and calcium K alpha peaks.

PC images obtained through either of the above methods can be used, after an initial low-statistics pass, to form individual masks in image space to optimize the acquisition of data. This is accomplished through the use of scatterplots (2-D histograms);[4,5] regions which require more or less dwell times (for optimum x-ray counting statistics) are identified through the PC scatterplots and indexed back to the original STEM while the specimen is still in the microscope REF. Scatterplots in PC space tend to be better separated than in original image space, since diffuse lines that might overlap are converted to diffuse blobs that are more easily discriminated.

The end result of implementation of this interactive scheme is a net savings of time of acquisition together with optimized counting statistics. Previously an experiment to detect and measure the localized elemental distribution in a typical cryosection of mammalian cells required about 26 hours of acquisition time for a 128x 128 pixel image set with 4 sec dwell time per pixel; this can now be accomplished in about 8 hours using a programmed beam acquisition protocol based on the above strategy.

References

1. R. C. Gonzalez and P. Wintz, *Digital Image Processing*, Addison-Wesley Publ. Co., Reading MA (1987)pp. 322 -329
2. C. Quintana and N. Bonnet, *Scanning Microscopy*, 8(1994)563
3. D. A. Kopf et al, *Microbeam Analysis Proceedings*, (1995)317
4. D. S. Bright and R. Marinenko, *MSA Bulletin*, 22(1992) 21
5. P. Ingram et al, *Microbeam Analysis Proceedings*, (1994)111
6. This work was supported by the Office of Naval Research grants #N00014-93-0067, s40095FEL102, and NSF DIR9106607.

APPLICATIONS OF CONFOCAL MICROSCOPY AND SCANNING ELECTRON MICROSCOPY TO THE LOCALIZATION OF IMMUNOREAGENTS USED IN MEDICAL DIAGNOSTIC SYSTEMS

J.P. Neilly, G.D. Gagne, J. Bryant, B. Daanen and K. Schuette

Abbott Laboratories, 200 Abbott Park Road, Abbott Park, IL 60064

Medical diagnostic assays often are based on the immobilization of immunolabeling reagents on solid substrates such as polystyrene beads, microparticles, or membranes. The distribution of immuno-reagents on or within these substrates has a significant effect on product performance. Confocal laser scanning microscopy (CLSM) and scanning electron microscopy (SEM) can be used to localize immunological reagents on beads and other surfaces.[1,2] In this paper we describe examples in which CLSM and SEM were used to assist in the design and troubleshooting of three diagnostic systems.

A protective overcoat is used on HIV antibody-coated 0.25" polystyrene beads in an HIV screening assay. To visualize topographical detail of the antibody distribution on beads with and without the overcoat, beads were labeled with a fluorescent secondary antibody and examined by CLSM. On overcoated beads, the distribution of HIV antibody was relatively uniform; but on non-overcoated beads, HIV antibody distribution was patchy and located mostly in low areas of the bead surface (Fig. 1), evidence that the overcoat provided protection for the HIV antibody. In the same assay system, performance was enhanced by using beads coated with a mixture of HIV antibodies from two IgG subclasses. The relative distribution of the two primary antibodies on the bead surface was demonstrated using isotype-specific secondary antibodies and CLSM.

Immunogold labeling and imaging with a field emission SEM were used to compare the distribution of HIV antibody coated onto 0.25" polystyrene beads and 1µm microparticles. On the beads the greatest antibody density was localized in grooves and low areas (Fig. 2a). The microparticles, however, were uniformly coated, and the antibody density was similar to that seen in low areas of the beads (Fig. 2b).

Using CLSM to analyze a membrane-based assay system, vertical distribution of assay components in nitrocellulose membranes was compared before and after the assay was performed. With the optical sectioning capabilities of CLSM, it was possible to evaluate the membranes non-destructively and to show that, before the assay, sprayed fluorescent antibody had penetrated 60 µm into the 150 µm thick membrane (Fig.3a). After the assay was performed, the antibody had diffused into surrounding areas of the membrane. Using the reflectance mode of CLSM, selenium microparticles were visualized throughout antibody-sprayed areas, to a depth of 100 µm (Fig. 3b).

Using CLSM and SEM to localize components of diagnostic assay systems can provide insight into how the assays perform at the microscopic level. This information has proven to be useful for troubleshooting problems with these systems and may be useful in the design of future assays.

References
1. M.C. Pinto and P. Marcias, Biotechnology Techniques, 9 (1995) 481-486.
2. G.M. Hodges et al., Immunolabelling for Electron Microscopy (1984) 189-233.
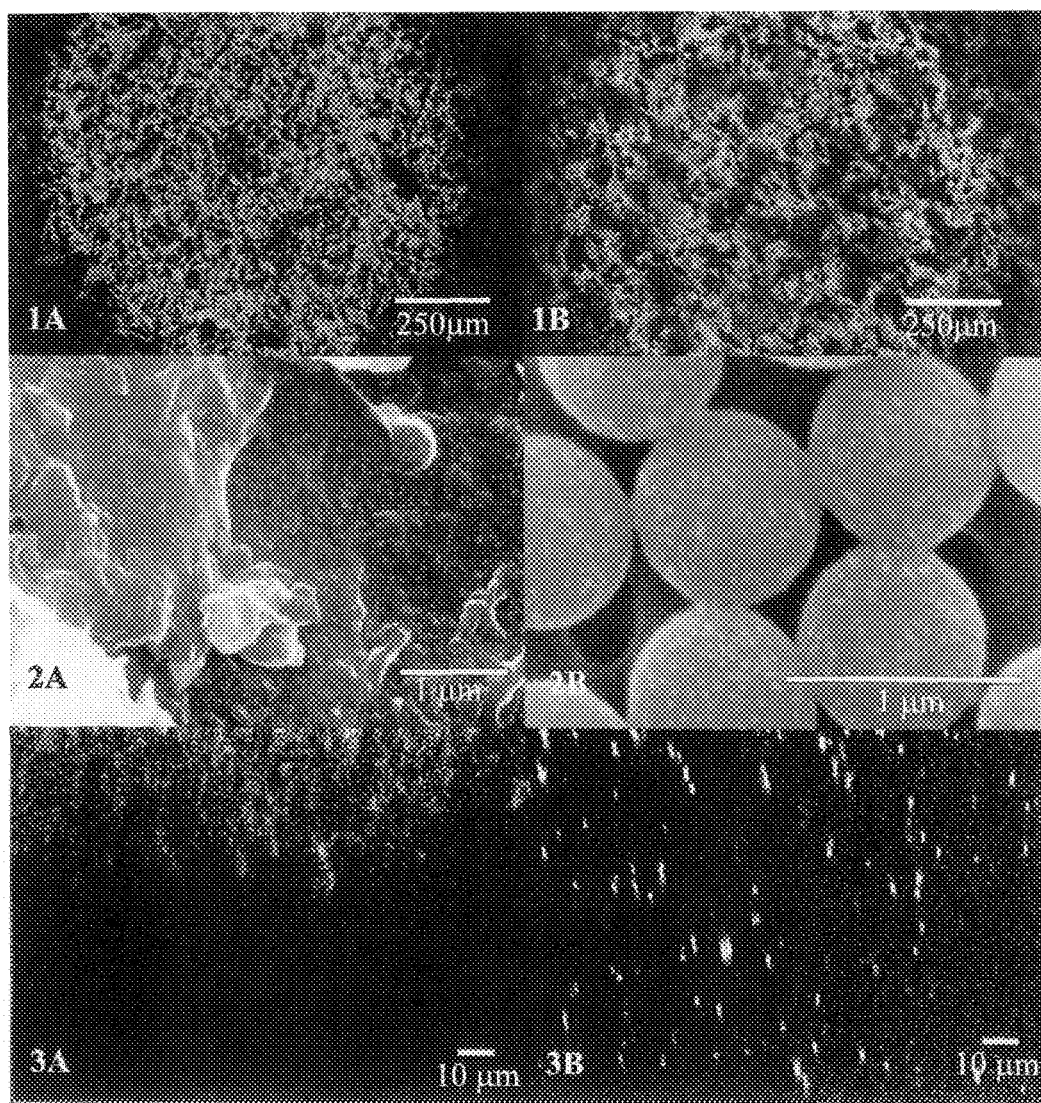
FIG. 1 - Extended-focus CSLM images of antibody distribution on 0.25" polystyrene beads (A) with overcoat and (B) without overcoat.

FIG. 2 - SEM image of gold-conjugate antibody on (A) 0.25" polystyrene bead and (B) microparticles from HIV assay.

FIG. 3 - Optical cross-section of nitrocellulose filter sprayed with (A) fluorescent antibody and (B) exposed to selenium microparticles.

A SIMPLE CORRELATIVE TECHNIQUE FOR MORPHOLOGIC AND ENERGY-DISPERSIVE ANALYSIS OF GLASS-MOUNTED PARAFFIN SECTIONS

K. W. Baker*, L. King*, R. Walker*, I. Piscopo** and A. Smith***

*Parke-Davis Research Institute, Miss. Ont. Canada, L5K-1B4
**Philips Electronics, Mahwah, N. J., U. S. A, 07430
***Univ. Of Guelph, Guelph, Ont., Canada, N1G-2W1

Tissue sections, smears, and many other varied types of specimen are often mounted on glass slides for light microscopic (LM) evaluation and analysis. These same preparations, using gold/palladium-coated glass slides as specimen mounts, are also well suited to correlative scanning electron microscopy (SEM) and, energy dispersive X-ray analysis (SEM/EDX). The following short note describes a procedure for glass-mounted specimens that provides slides suitable for combined LM, SEM and SEM/EDX characterization. In addition, the method establishes a specimen-based reference point for the empirical determination of optimum electron probe depth and accelerating voltage for SEM/EDX analysis.

For illustrative purposes we used sections of mammalian kidney cortex known to be heavily laden with crystalline deposits of unknown structure and composition.

In each sample, birefringent crystalline material was initially observed in hematoxylin and eosin-stained paraffin sections using bright field polarized light microscopy (Fig. 1).

All glass slides were sputter-coated with 60/40 gold/palladium(Au/Pd), both as an elemental reference background and, as an adhesive for the sections. Sections were then cut at thicknesses ranging from 2 -12 µm, mounted on Au/Pd-coated glass slides, deparaffinized with xylene (2 mins;2 changes), cleared with 100% ethanol (1 min;3 changes) and finally, air-dried from 100% ethanol. Critical point drying was not pursued in the interests of speed and simplicity. These sections were left uncoated for SEM/EDX analysis and epifluorescent/brightfield light microscopy. Sections were additionally sputter-coated with Au/Pd for routine secondary electron imaging of crystal morphology. Glass slides, with adherent sections, were mounted directly in the specimen chamber of the scanning electron microscope. These were examined and analyzed using a HITACHI S-570 scanning electron microscope equipped with a Noran Voyageur II Quantitative X-ray microanalysis system, including a 408F-3GSS Explorer high purity germanium detector with a Norvar thin window (Noran Instruments, Middletown, WI, Noran software version 2.6). Peaks were identified and characterized using "standardless analysis".[1] For analytical SEM/EDX, the electron probe was rapidly scanned over a rectangular "reduced area". All X-ray spectra were collected over a fixed time of 60 seconds with deadtime to livetime ratios at levels below 30%. X-ray microanalysis was performed from 3 kV to 20 kV in order to encompass elements from the entire periodic table and in order to determine the optimum penetration depth. The same experiment was performed on sections cut at thicknesses from 2-12 µm. If Au or Pd appeared in the spectrum, it was assumed that at that kV and on that area of sample, the beam's teardrop had exceeded the specimen's thickness and had begun to elicit X-rays from the underlying support film. If Ca appeared, it was assumed that the glass slide had been reached. These subtle diffrences were shown to occur within 1-2 kV (Figs 3a-c).

For fluorescence and brightfield light microscopy all sections and crystalline deposits were examined using a Zeiss Axiophot microscope fitted with incident light fluorescence illumination.

Crystalline deposits were pleomorphic and birefringent (Fig. 1) and, were fluorescent under all wavelengths tested. In the SEM, these same crystals were prominent and easily observed as "brighter" structures within the clearly recognizable matrix of the sectioned renal cortex (Fig. 2). The prominence of crystals was exaggerated by the airdrying-induced artifactual shrinkage of the surrounding renal tissue as embedded crystals remained relatively unaffected by such processing artifacts (Fig. 2).

Mounting paraffin sections on Au/Pd-coated glass slides greatly facilitated the correlation of LM/SEM morphology and SEM/EDX analysis. Sections easily adhered to the coated slides and were accessible for both LM and SEM (including fluorescence light microscopy and SEM/EDX analysis). The conductive Au/Pd undersurface also eliminated the need for conductive heavy element surface coatings

while simultaneously providing an empirical reference point for the depth of EDX microprobe penetration. Once a working, optimum configuration had been established (ie.12 kV, 5 μm), the appearance of Au/Pd peaks served as a useful indicator for excessive probe depth within the tissue section (Figs. 3a-c). This in turn allowed the qualitative comparison of (Au/Pd-free) spectra from separate samples of the same elemental composition and matrix material with assurance that probe depth (and therefore the source of X-ray signals) was comparable. Based on this experiment, we were then able to determine the optimum accelerating voltage for various sample thicknesses and elemental composition even when mounted on a non optimum substrate. This method has proven well suited to evaluations of stained or unstained paraffin sections mounted on glass microscope slides and many varied specimen types should also be accommodated by this technique.

References

1. J.I. Goldstein, D.E. Newbury, P. Echlin, D.C., Joy, A.D. Romig Jr., C.E. Lyman, C. Fiori, and E. Lifshin: *Scanning Electron Microscopy and X-Ray Microanalysis. A Text for Biologists, Materials Scientists, and Geologists.* Plenum Press, New York, 1992.
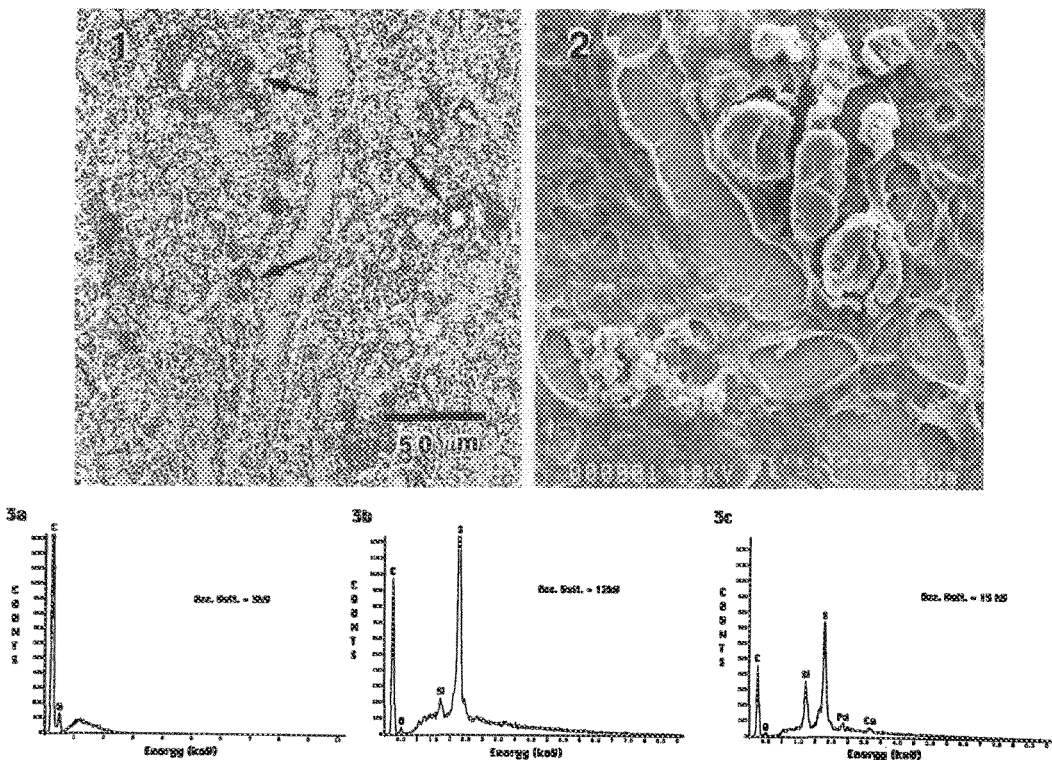
Fig. 1 Polarized, bright field light micrograph showing 5 μm paraffin section of renal cortex mounted on Au/Pd coated glass slide. Crystals (arrows) are abundant and easily observed.

Fig. 2 Scanning electron micrograph showing the same specimen. Note the higher elevation of crystals due to artifactual drying-down of the surrounding epithelial cells.

Fig. 3 Spectra from a crystal similar to those shown above and acquired using selected accelerating voltages (a) 3 kV; (b) 12 kV, and;(c) 15 kV. For this particular section thickness of of approximately 5 μm the 12 kV probe was optimum.

SECRETORY PITS IN BACKSWIMMERS (HETEROPTERA: NOTONECTIDAE).

R. J. Williams*, N. R. Dollahon*, E. Larsen**, S. O'Neill**, and R. Chapman***

*Electron Microscopy Facility, Villanova University, Villanova, PA 19085
**Department of Biology, Villanova University, Villanova, PA 19085
***Department of Entomology, University of Arizona, Tucson, AZ 85721

In studies of several families of aquatic heteropterans we have found exoskeletal pits not described in the literature. These structures are associated with the lateral margins of the pronotum and/or the dorsal surface, posterior to the scutellum in notonectids, nepids, and corixids. The function of these pits is unknown, but we presumed that they might be either sensory or secretory in nature. We undertook this study of the microscopy of pits in the notonectid, *Buenoa margaritacea* to learn if either of these functions is consistent with the fine structure.

For TEM, adult insects were submerged in 1.0% paraformaldeyde and 2.0% glutaraldehyde in 0.02M sodium cacodylate buffer with 0.01% calcium chloride at a pH of 7.2, then dissected with a razor blade cleaned with acetone. Tissues were fixed overnight at 4oC in paraformaldehyde and glutaraldehyde, then fixed in 1% osmium tetroxide in cacodylate buffer, dehydrated in a graded series of acetone, embedded in Spurr resin and polymerized at 70oC for 21 hours. Blocks were thin sectioned with a diamond knife, and sections were stained with uranyl acetate and lead citrate. Whole specimens for SEM were similarly fixed, dehydrated in an ethanol series and critical point dried. SEM micrographs of internal pit anatomy were produced by adhering 500nm sections to a glass coverslip, then removing the embedding resin by incubation for 5 minutes in a saturated solution of potassium hydroxide in absolute ethanol, followed by three 20 minute rinses in absolute ethanol and air drying.[1] Cover slips were attached to an aluminum specimen stub and sputter coated for 60 seconds with gold/palladium as were whole insects .

The location of pits on the pronotum and their appearance are shown in Figs. 1-3. Fig. 4 is an SEM micrograph showing a thick section through a pit. A large duct can be seen extending from the base of the pit into the exoskeleton. Fingerlike projections are part of the exoskeleton and provide a large surface area for staging a product. Fig. 5 is a thin section of a similar area showing the presence of a large duct extending from below the exoskeleton up into the base of the pit. Cellular infoldings (arrow) can be seen in a large cell which may be involved in secretion. Fig. 6 is a higher magnification view of a portion of the duct and cell.

The structures observed are not sensory, but appear to be secretory. They are not chloride cells because they are different in fine structure and distribution.[2] We have never found the pits in larval forms, whereas the chloride cells are found in all stages.

1. A.W. Robards & A.J. Wilson (eds.) *Procedures in Electron Microscopy*, Wiley &Sons, New York (1995) Update 4, 10:2.79-80.
2. H. Komnick & W. Wichard, *Int. J. Insect. Morphol. & Embryol.*, 4 (1975) 89-105.
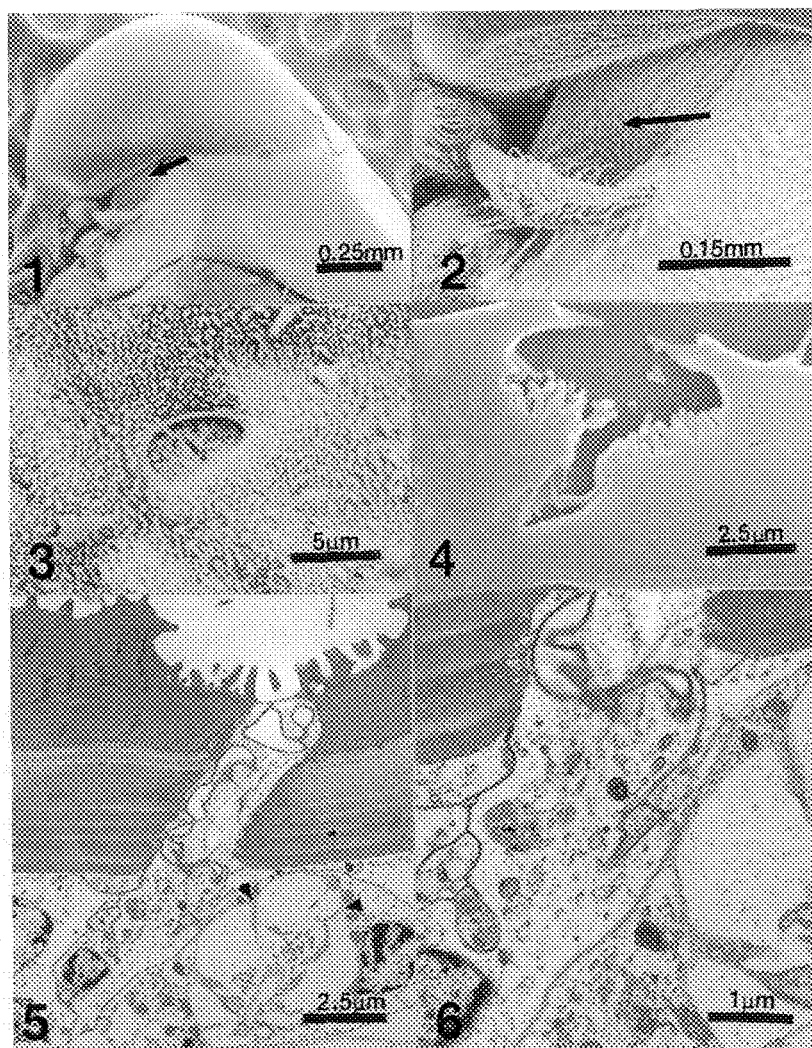
Fig. 1. Lateral view of head of *B. margaritacea*, arrow indicates pronotum.
Fig. 2. Higher magnification of pronotum, arrow indicates pits.
Fig. 3. Pit showing fingerlike projections and rim.
Fig. 4. SEM of longitudinal thick section of pit showing rim, fingerlike projections and duct.
Fig. 5. TEM of pit illustrating the duct and possible secretory cell, arrow indicates cellular infoldings.
Fig. 6. Higher magnification of base of duct and portion of cell with infoldings.

SMOKE-DERIVED CUES FOR SEED GERMINATION IN THE POST-FIRE RECRUITER *EMMENANTHE PENDULIFLORA*

L.M. Egerton-Warburton, K.A. Platt and W.W. Thomson

Botany and Plant Sciences, University of California, Riverside, CA 92521-0124

Wildfires are typically associated with the destruction of vegetation. However, in the chaparral of southern California, fires are responsible for the persistence of many species. In these communities, vegetative regrowth is accompanied by a striking post-burn recruitment of species from a flush of seed germination. Typically, the flora is dominated by 'fire annuals' or those species in which occur primarily in the first year after fire and persist thereafter as deeply dormant seeds held in the seedbank until the next fire. *Emmenanthe penduliflora* (Hydrophyllaceae) is a prominent fire annual and possesses dormant seeds which germinate in response to smoke, extract of charred wood or nitrate-N. The underlying mechanism for these responses is unknown. Consequently, we initiated a systematic assessment of the ultrastructure of dormant (8% germination) *versus* smoke-treated seeds (79%) to identify changes which may be associated with the germination of *E. penduliflora* seeds.

Scanning electron microscopy indicated that externally, the testa (seed coat) was characterized by a series of tightly adjoining hexagonal plates which formed well defined ridges at the abutting edges. In dormant seeds, both the plates and ridges were sealed by a layer of smooth wax. In smoke-treated seeds, these surface waxes characteristically coalesced into spheres to expose open sites along the ridges, while hair-line cracks occurred in the centre of many plates.

Internal barriers to water uptake were detected using the apoplastic dye, Lucifer yellow CH (LYCH)[1]. In dormant seeds, LYCH accumulated in an area bounded by the testa (external) and endosperm (internal); this region corresponds with the site of an internal cuticle. When smoke-treated seeds were incubated in the same manner, LYCH infiltrated all tissues. Transmission electron microscope studies coupled with freeze-fracture replica studies[2] confirmed the presence of a well developed cuticle immediately below the testa (Fig. 1), and cuticular pegs between endosperm cells (Fig. 2). The cuticle proper was composed of a clear cutin layer covering a cutinized layer which consisted of a cellulose skeleton embedded with cutin and wax (Fig. 3). At the ultrastructure level, the passage of water was evaluated using the electron-dense tracer, lanthanum nitrate[3]. In dormant seeds, lanthanum was deposited at the testa-cutin interface thereby confirming the cuticle as being the impermeable barrier to water (Fig. 3). Smoke-treated seeds incubated in the same manner showed lanthanum deposits along channels within the cutin layer (Figs. 4a,b). Channels originated at discrete points at the testa-cutin interface and travelled horizontally before entering the cutinized layer. Once inside the cutinized layer, the passage of water was widespread and readily detected through to the endosperm.

From these studies, we concluded that dormancy in *E. penduliflora* may be enforced by surface waxes and an internal cuticle. Exposure to smoke altered the seed dormancy via external chemical scarification and/or modification of the surface waxes, and changes within the internal cuticle thus allowing the passage of water from the seed surface to the endosperm. Since both wax and cutin were affected, these findings suggest that the active component of smoke may function analogous to a detergent or saponifying agent.

References
1. T.P. Owen et al., *Protoplasma* (1991) 115.
2. K.A. Platt-Aloia and W.W. Thomson, *Stain Technology* (1982) 327.
3. R.T. Leonard et al., *Plant Physiology* (1975) 542.
4. We thank David Scharf for the scanning electron microscopy, and Jon Keeley for the seeds. This research was undertaken while LEW was a Fulbright Post-Doctoral Fellow at UC (Riverside), and supported by the Australian Society for Electron Microscopy.
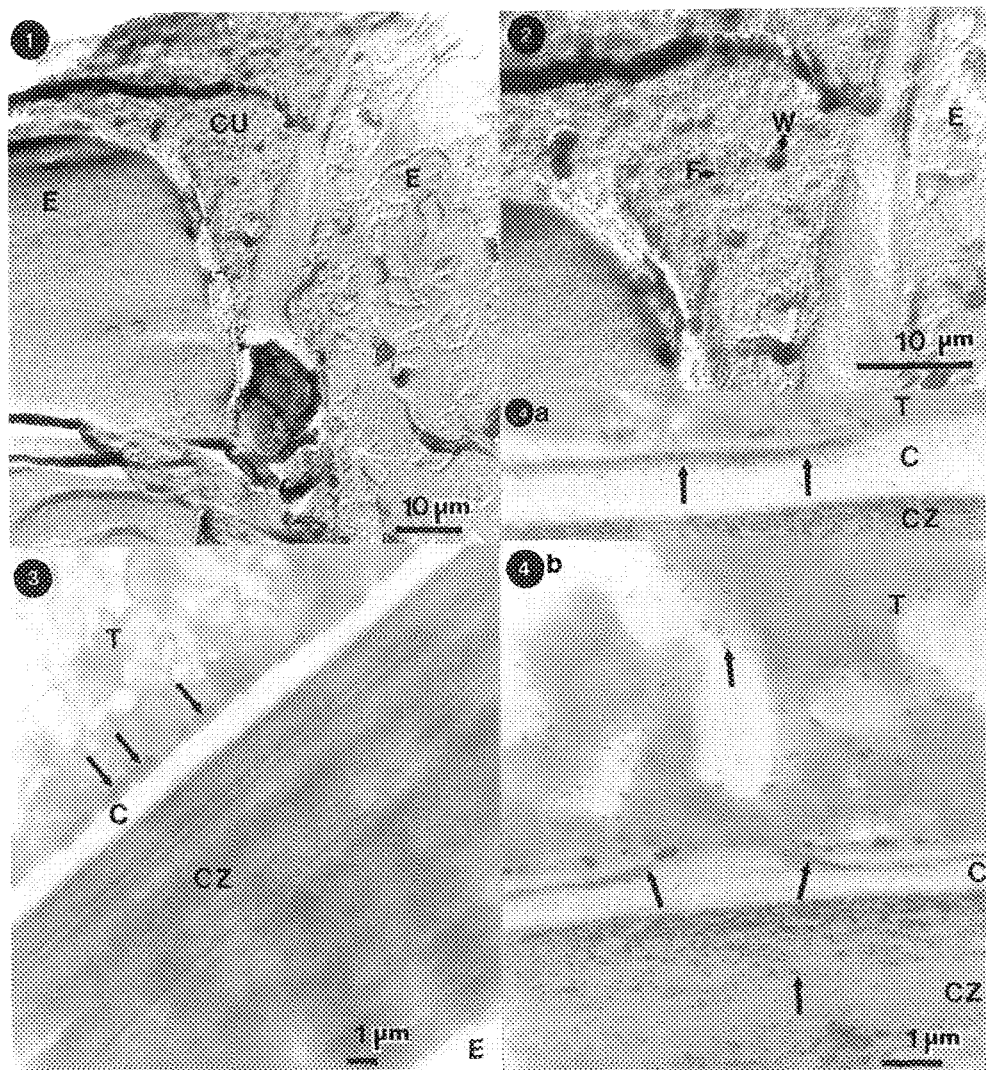
FIG. 1 Freeze-fracture replica of cuticle region in dormant seeds.
FIG. 2 Freeze-fracture replica of cuticular peg between endosperm cells.
FIG. 3 Dormant seed incubated with lanthanum nitrate. Arrows denote lanthanum deposits.
FIGS. 4a,b Smoke-treated seed incubated with lanthanum nitrate. Arrows denote lanthanum deposits.
FOR FIGS. 1-4 T, testa; CU, cuticle; C, cutin layer; CZ, cutinized layer; F, cellulose fibres; W, embedded wax; E, endosperm cells.

THE SURFACE STRUCTURE OF BIOMOLECULES USING CORRELATIVE MICROSCOPY: TEM, SEM, STM AND AFM

H. Gross, P. Tittmann, R. Wepf, K.H. Fuchs

Institute for Cell Biology
ETH-Hoenggerberg 8093 Zürich, Switzerland

Freeze-drying followed by heavy metal shadowing is a long established and straight-forward TEM-approach to routinely study the structure of dehydrated macromolecular structures. Very thin specimens, such as isolated membranes or single macromolecules, can directly be adsorbed on Carbon-coated support grids. To attain the highest possible resolution, efforts were made to improve dehydration[1], metal shadowing[1] and to mini-mize post-deposition changes in the metal film. Using our MIDILAB high vacuum cryo-transfer system the freeze-dried and shadowed specimens are transferred into the microscope under high vacuum and cryo conditions.[2] At no stage are the specimens exposed to air or warmed to ambient temperature. As a consequence, the stabilizing carbon film used in the conventional shadowing approach can be omitted and thereby images containing higher resolution structural features are recorded.

After careful freeze-drying (i.e. preservation of the "structural water"), shadowing with 0.3 - 0.5 nm Ta/W ("optimal granularity"), vacuum cryotransfer, imaging at -175 °C under low dose-conditions ($<500e^-/nm^2$), image averaging (reduction of the noise being induced by the metal film granularity) and surface relief reconstruction, object surfaces details in 3-D at a spatial resolution of <1.5 nm laterally and <0.5 nm vertically are routinely attained with 2-D crystalline objects. The surface reconstruction is a procedure which derives the 3-D surface information from a two-dimensional, projectional TEM image of a unidirectionally metal-shadowed object.[3] By evaporating a metal layer onto the object at an angle which differs from the observation angle in the TEM, distinct surface gradients of the object yield different grey levels in the image which can then be reconstructed to the height information by computational analysis. In the case of a symmetric structure with minimally P3-symmetry the complete surface structure can be reconstructed from one single, unidirectionally shadowed micrograph. If a structure without symmetry has to be reconstructed, minimally, three recordings with distinct different shadowing azimuth are necessary.

The TEM-surface data obtained from several 2-D protein crystals (Polyhead, actin sheets, purple membrane, chip 28) will be quantitatively compared with the surface information obtained with high resolution in-lens SEM and scanning probe microscopy (STM[4] and AFM). Advantages and disadvantages of the different imaging modes will be discussed and several examples will be given to support the rationale for using the combination of different microscopies ("correlative microscopiy") to elucidate the structure and function of biomacromelecules.

1. H. Gross, *Cryotechniques in Biol. Electron Microscopy*, Springer Verlag, (1987) 205
2. H. Gross et al., *Proc. XIIth Internat. Congress for Electron Microscopy*, (1990) 510
3. K.H. Fuchs et al., *Bioimaging 3* (1995) 12
4. M. Amrein et al., *Journal of Ultra- and Molecular Structure Research*, 102 (1989) 170
5. Supported by the Swiss National Science Foundation (grant 31-36324.92)
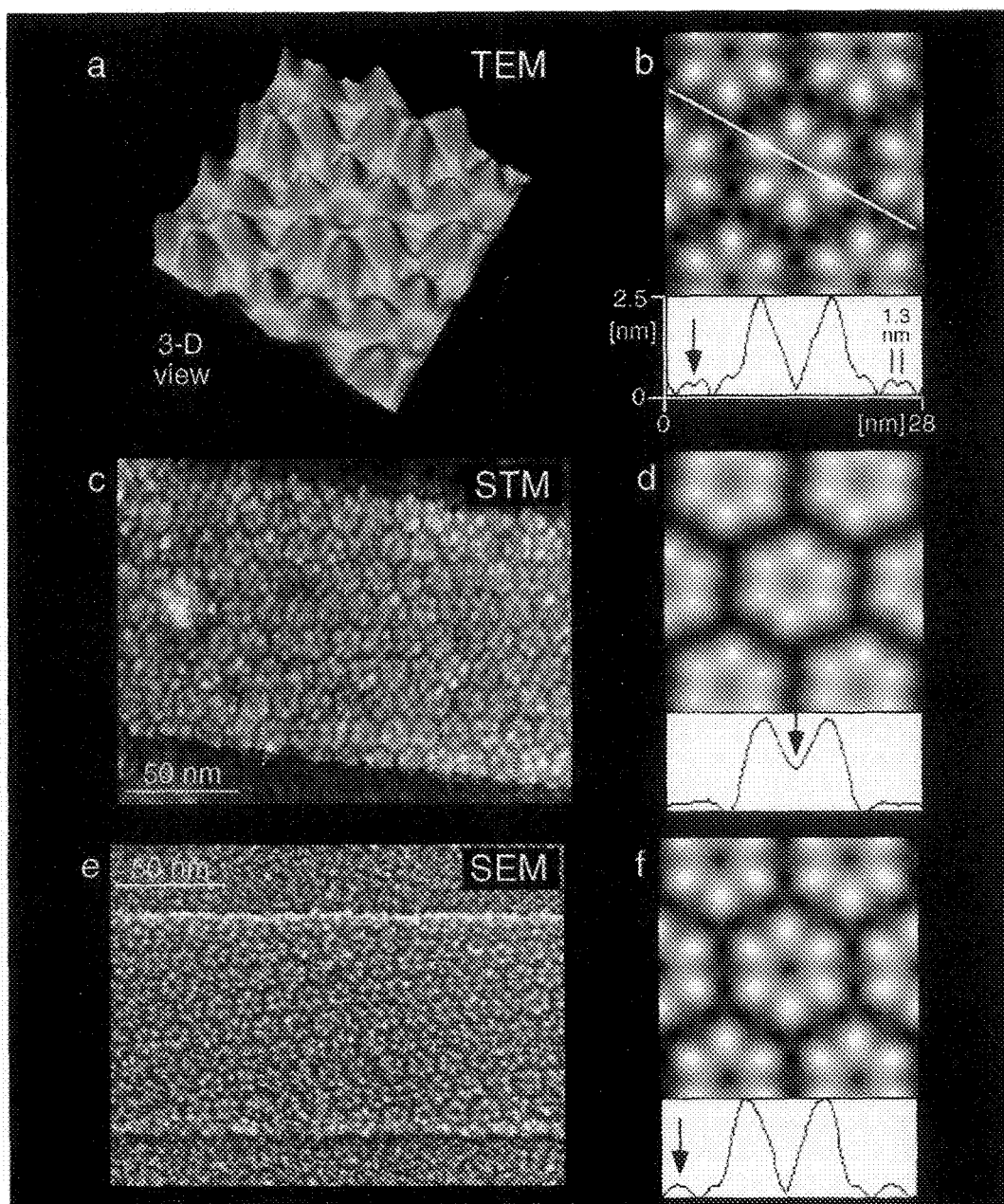
Surface structure of the bacteriophage T4-polyhead after freeze-drying and metal contrasting a,b) TEM after TaW-shadowing, averaging and relief reconstruction. c, d) STM after electron beam evaporation of Pt/Ir/C at high elevation angle. c) micrograph, d) average. e,f) cryo SEM after planar magnetron sputter-coating of W. e) micrograph, f) average.

315

LOW-VOLTAGE, HIGH-RESOLUTION, SCANNING ELECTRON MICROSCOPY OF PLATELET-BOUND FIBRINOGEN

S.R. Simmons and R.M. Albrecht

Animal Health and Biomedical Sciences, University of Wisconsin, Madison, WI 53508

An essential element in blood clot formation is fibrinogen-mediated platelet aggregation. Fibrinogen is an adhesive plasma protein which binds to the $\alpha IIb\beta 3$ integrin on activated platelet surfaces. Platelets do not aggregate in the absence of fibrinogen binding, and fibrinogen bound to surfaces of platelets in aggregates is localized to regions of platelet-platelet contact. The fibrinogen molecule is symmetrical and bifunctional and may directly bridge the gap between platelets to bind to receptors on two adjacent platelets. However, the precise mechanism by which fibrinogen links platelets is unclear.

Previously we have utilized colloidal gold labeling with correlative light and electron microscopy to investigate the binding of fibrinogen to receptors on surfaces of spread, substrate adherent platelets.[1] The initial binding of gold-conjugated fibrinogen (FgnAu) and subsequent ligand-triggered receptor movement was followed on living platelets by video-enhanced light microscopy. Fibrinogen receptors initially are dispersed over much of the platelet surface and move centripetally upon fibrinogen binding, ultimately forming a band of bound fibrinogen on the platelet surface overlying a densely woven band of actin filaments surrounding the central granulomere. After preparation for electron microscopy, the same platelets as were followed in the light microscope were located in the high voltage TEM and the low voltage, high resolution, SEM (Hitachi S-900) and the final locations of the gold labeled receptor/ligand complexes were determined relative to internal or surface ultrastructure, respectively.

More recently, we have utilized the SEM operated at low (1-2 kV) beam voltage to examine in detail the binding of unlabeled fibrinogen to platelets.[2] With appropriate specimen preparation, individual cell surface macromolecules can be resolved *in situ* by low voltage SEM. In addition to the centripetal receptor redistribution seen with FgnAu, unlabeled fibrinogen appeared to undergo self-adhesive interactions following binding to platelet fibrinogen receptors, forming small, branched and globular protein aggregates during translocation across the platelet surface.(Fig.1)

The identity of the fibrinogen aggregates was confirmed by colloidal gold labeling and imaging by SEM in BEI mode at 5-10 kV for clear detection of gold labels, or at 2-3 kV beam voltage in SEI mode for images in which gold labels and protein structures could both be seen. Fibrinogen added in soluble form was subsequently labeled with 3 nm gold conjugated to Fab fragments of anti-fibrinogen. The 3 nm gold/Fab provides a specific probe which is smaller than the fibrinogen molecule, permitting positive identification of the protein without obscuring the structure of the fibrinogen aggregates.(Fig.2)

Fibrinogen was also conjugated directly to 5 nm colloidal gold. Five nm diameter gold particles are much smaller than the fibrinogen molecule and produce a conjugate in which single fibrinogen molecules are each adsorbed to 1-3 gold particles (in contrast to larger 10-30 nm gold, where a number of molecules adsorb to each gold particle). Five nm FgnAu bound to the platelet surface and triggered typical receptor/ligand redistribution. Clusters of 5 nm gold labels formed on the platelet surface, increasing in size as the FgnAu centralized.(Fig.3) Examination of the centralized 5 nm FgnAu with the SEM at 1-2 kV beam voltage revealed that the 5 nm FgnAu had formed aggregates of protein identical in appearance to that of unlabeled fibrinogen on the platelet surface.(Fig.4)

Fibrinogen aggregate formation subsequent to platelet receptor binding may be attributed in part to active clustering of ligand-bound receptors, or to exposure of potentially self-adhesive epitopes by the conformational change of the fibrinogen molecule which takes place upon receptor binding.[3] The effect

of such increased self-adhesiveness in fibrinogen when it is bound to a platelet surface would be to increase the effectiveness of the protein in bridging the space between platelets and binding platelets together in thrombus formation. By using the SEM at low voltage to image unlabeled proteins directly on the platelet surface, and at slightly higher beam voltage to identify specific gold labels on the fibrinogen aggregate structures, we are able to elucidate a mechanism of protein activity at the cell surface.

1. Olorundare, O.E. et al. 1993. Eur J Cell Biol 60:131.
2. Simmons, S.R. ,Albrecht, R.M. 1996. J Lab Clin Med, In press.
3. Mosesson, M.W., et al. 1995. J Structural Biol 155:88.
4. Electron microscopy performed at the Integrated Microscopy Resource, Univ. of Wisconsin, Madison.
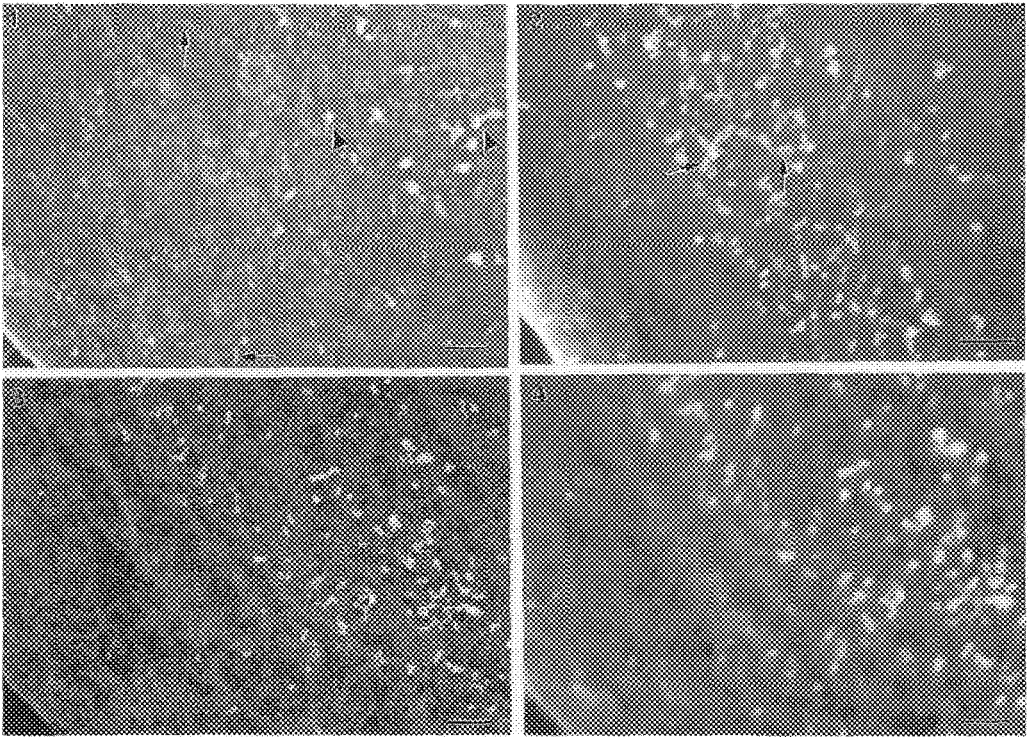
Fig.1 SEM image of unlabeled fibrinogen on platelet surface. SEI, 1 kV. Arrow indicates structure of appropriate size and shape for individual fibrinogen molecule, for scale. Most of the bound fibrinogen is incorporated into branched and globular aggregates (arrowheads). Bar=0.1 μm.
Fig.2 Three nm gold/Fab anti-fibrinogen provides positive identification of centralized, platelet-bound fibrinogen aggregates. Both structure of fibrinogen aggregates and gold labels (arrows) can be seen at this intermediate voltage. Bar=0.1 μm.
Fig.3 Five nm gold/fibrinogen centralized on platelet surface. BEI, 5 kV. Bar=0.1 μm.
Fig.4 Same area as shown in Fig.3. SEI, 1 kV. 5 nm gold fibrinogen forms aggregates identical in structure to those seen with unlabeled fibrinogen in Fig,1. Bar=0.1 μm.

CORRELATIVE MICROSCOPY ON THE MECHANISM OF ATTACHMENT OF THE INTESTINAL PROTOZOAN, *GIARDIA*: OBSERVATIONS USING IMMUNOFLUORESCENCE, INTERFERENCE REFLECTION, PHASE, AND VIDEO MICROSCOPY TOGETHER WITH TEM AND HIGH-RESOLUTION SEM.

S.L. Erlandsen*, P.T. Macechko*, and D.E. Feely**

*Department of Cell Biology and Neuroanatomy, University of Minnesota Medical School, Minneapolis, MN 55455; **Department of Oral Biology and Basic Science, University of Nebraska School of Dentistry, Lincoln, NB

The intestinal protozoan *Giardia* has evolved a mechanism for adherence of trophozoites to the intestinal epithelium by means of a holdfast or attachment organelle called the ventral adhesion disc. The ventral adhesion disc is formed by a monolayer of microtubules bound to one another and to the ventral plasmalemma by cross links, and each microtubule has a dorsal ribbon-like extension, composed of giardin. These dorsal ribbons are cross-linked with one another, and project from each microtubule into the overlying cytoplasm (1, 2). The peripheral margin of the ventral disc is named the lateral crest. SEM and TEM studies have shown that the monolayer of microtubules forms an overlapping spiral, which externally is visible as a spiral ridge resembling the figure six. Using immunofluorescence, the ventral adhesion disc has been shown to contain contractile proteins distributed in the lateral crest which composes the peripheral margin of the disc (3). The presence of microtubules/contractile proteins and evidence for the adhesion disc attaching to the microvillous border of epithelial cells suggests a contractile mechanism for trophozoite attachment (4, 5).

To study the mechanism of attachment of *Giardia* trophozoites to both artificial or natural substrates, we utilized interference reflection light microscopy to visualize the distance between the trophozoite and substratum to determine the presence of focal, close, and absence of direct contact. Video microscopy was used in conjunction with phase, Nomarski interference, and interference reflection microscopy (IMR) to observe adherence of both fixed and living trophozoites to artificial surfaces and to isolated intestinal villi. Investigation of the cytoskeleton of trophozoites was performed with TEM and SEM. The cytoskeleton in trophozoites was studied by field emission SEM after using hypotonic swelling and detergents to remove membranes and cytosolic proteins.

In earlier studies on IMR of fixed trophozoites, focal contacts were observed between the lateral crest of the trophozoite and the glass substratum, while the central region of the adhesive disc showed either close contact or lack of contact to the

substratum (5). Videomicroscopy with IMR revealed that the adhesion pattern of living *Giardia* trophozoites to a glass substratum was consistent with that seen in fixed cells since focal contacts were present between the lateral crest of the ventral disc and the substratum, but that the rest of the disc was capable of dynamic changes. The central region of the adhesive disc displayed patterns of contact that rapidly varied in time, with changes occurring from close contact to absence of contact within fractions of a second. In addition to the rapid oscillations of the ventral disc, the presence of focal contact between the lateral crest and substratum did not prevent gliding motions of the trophozoite on the surface. Videomicroscopy with phase optics of trophozoites attached to the microvillous border of isolated intestinal villi revealed a rapid oscillation of the body of the trophozoite over the adhesive disc and also revealed a "pumping" action of the tail, suggesting that the ventral disc was undergoing motions similar to that observed by IRM on artificial substrata.

Collectively, these observations suggest that the attachment organelle of *Giardia* may not be a simple holdfast device to anchor the trophozoite to the microvillous border of epithelial cells, but instead may play an active role in the traumatization of the microvillous border of epithelial cells, thus playing a major role in the production of malabsorption seen in giardiasis. (Supported in part by U.S.E.P.A. grant R82140401 and the Minnesota Medical Foundation).

References:

1. D.E. Feely et al., in *Giardia and Giardiasis*, Plenum Press, New York (1984)3.
2. D.E. Feely et al., in Giardiasis, Elsevier, New York (1990)11.
3. D.E. Feely et al, Exp. Parasitol. **53**:145-154.
4. S.L. Erlandsen and D.G. Chase, Am. J. Clin. Nutr. **27**:1277-1286.
5. S.L. Erlandsen and D.E. Feely, in *Giardia and Giardiasis*, Plenum Press, New York (1984)33.

CORRELATIVE MICROSCOPY IN PATHOLOGY

D. N. Howell[1,4], S. E. Miller[1,2], E.A. LeFurgey[3,4], P. Ingram[1,5], J.D. Shelburne[1,4]

Departments of Pathology[1], Microbiology[2] and Cell Biology[3], Duke University Medical Center, Durham, N.C. 27710; Pathology and Laboratory Medicine Service[4], V.A. Medical Center, Durham, NC 27705; Research Triangle Institute[5], Research Triangle Park, NC 27709

Microscopy has always provided important anatomical and structural information for biologists and clinicians. The amount of information available has increased exponentially as a result of recent advances in light microscopy, immunohistochemistry, in situ hybridization, electron microscopy, and microprobe analysis. These techniques provide important insights regarding the anatomic distribution, biochemistry, and physiology of a wide range of analytes, including ions and elements, genes and their products, molecular fragments, whole molecules, and macromolecular complexes such as ribosomes and viruses.

Proper interpretation of this vast array of new information requires a correlative approach with regard to both different types of data (e.g., biochemical and structural observations) and different levels of resolution (e.g., gross, light microscopic, and electron microscopic observations). This principle is of particular importance to the pathologist, whose ultimate goal is to apply studies of tissues and body fluids to the understanding of disease as it affects the whole organism. Correlative information is particularly important in the interpretation of ultrastructural studies, where high resolution is often obtained at the expense of context. Accordingly, our laboratories have always emphasized the importance of correlative microscopy. In the case of electron microprobe analysis, we have published different regimens that allow the precise correlation of the chemical data obtained with an x-ray spectrometer with structural data seen by transmitted light microscopy (1,2).

Correlative microscopy is also of critical importance in viral pathology. The advent of confocal imaging provides new approaches to the sampling problems which are common in conventional transmission electron microscopy (CTEM) studies. For example, viral inclusions are often widely scattered in tissues such as liver even in cases of fulminant hepatitis. Finding the affected cells at CTEM magnifications can be a daunting, if not impossible, task.

320

To address this problem we have developed the procedures illustrated below (3,4). Areas of necrosis, inflammation or other cytopathology can be identified by confocal imaging, and then the affected foci can be embedded for CTEM. This approach permits precise identification and correct diagnosis of viral infections.

In the case of microprobe analysis, using correlative microscopy the chemical content of a single particle can be understood in the context of that particle's relationship to anatomic structures as seen in conventional H&E sections. In the case of viral infections, specific virions can be imaged and thus identified. In both types of studies, the histologic findings can then be related to the clinical problem.

References:

1. D. Baker et al., Scanning Electron Microscopy, (1985) II, 659.
2. P. Ingram, J.D. Shelburne, and V.L. Roggli, Eds., in Microprobe Analysis in Medicine. Washington, D.C.: Hemisphere Publishing Corporation (1989).
3. S.E. Miller et al., Identification of focal viral infections by confocal and electron microscopy: A study in correlative microscopy. Proc. Southeastern Micros. Soc. 17 (1995) 32.
4. S.E. Miller et al., Identification of focal viral infections by confocal microscopy for subsequent ultrastructural analysis. In preparation (1996).

Figures: (Left) Confocal scanning laser micrograph of sample human renal pelvis stained with propidium iodide. Enlarged urothelial cells are visible (250x). (Right) Light photomicrograph of the identical field following epoxy embedment, microtomy and toluidine blue staining (250x).
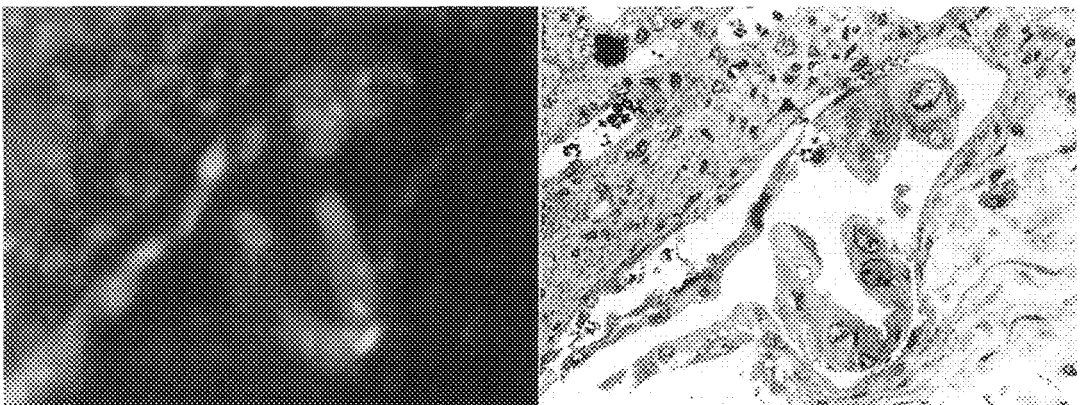
MONOLAYER MORPHOLOGY AND COLLAPSE INDUCED BY LUNG SURFACTANT PROTEIN: OBSERVATION VIA FLUORESCENCE AND ATOMIC FORCE MICROSCOPY

Michael M. Lipp

Department of Chemical Engineering, University of California at Santa Barbara, Santa Barbara, CA

Understanding the role of lung surfactant specific proteins in lipid monolayers is essential for improved treatments for Respiratory Distress Syndrome, which is a leading cause of death in premature infants. Fluorescence (FM) and Atomic Force (AFM) microscopies reveal that the amino-terminal peptide of lung surfactant protein SP-B alters the behavior of palmitic acid (PA) monolayers, enhancing their *in vivo* performance[1]. The combination of these techniques provides an excellent correlation between the protein-lipid interactions on the molecular level with the macroscopic properties of the monolayer.

SP-B protein incorporates into monolayers of PA, an important component of natural and synthetic lung surfactants monolayers[2]. The effect of the protein on the monolayer is evidenced in the isotherm data shown in Fig 1, in which the area per PA molecule, compressibility, and surface pressure at collapse all increase as a function of increasing protein concentration. The protein accomplishes this by inhibiting the formation of ordered phases of PA. This is seen via FM as a transition from a homogeneous, dark ordered phase without protein (Fig 2a) to a network of a disordered, bright phase (the fluorescent lipid probes used in this study prefer to partition into disordered phases, making them appear as bright regions in FM images) that separates ordered phase domains at coexistence (Fig. 2b). The network is stabilized by the low line tension between the bright phase and other lipid phases as confirmed by the formation of extended linear domains of bright phase in a dark background, or "stripe" phases (Fig. 3a) under certain subphase conditions. Similar stripe phases also occur in single component fluorescein-labeled SP-B monolayers (Fig 3b), implying that the protein is responsible for the reduction in line tension. The formation of the fluid phase network is responsible for the increased collapse resistance of these mixed monolayers. The mechanism of collapse shifts from a heterogeneous process of nucleation and growth of large rigid crystalline collapse phases (Fig. 4a) to a more homogeneous process with nucleation and growth of smaller domains distributed uniformly across the film (Fig. 4b). This is due to the protein-induced network breaking up and isolating the domains of ordered phase, effectively lowering the probability of finding a heterogeneous nucleation site within each domain (analogous to the classic experiments of Turnbull on supercooled microemulsions of metallic liquids[3]). The partitioning of the protein into the bright phase network was confirmed through the use of a dual-probe system. Fluorescein-labeled SP-B was added to a PA monolayer incorporating a fluorescent lipid analogue that emits at a higher wavelength. Upon imaging the same region of a monolayer at the different wavelengths (Fig. 5a and 5b), the protein is seen to be located in the bright phase network regions as expected.

To probe the molecular mechanisms of collapse in the presence of protein, monolayers of mixed PA/SP-B films were deposited on mica employing a novel deposition system in which the entire monolayer is simultaneously lowered onto a mica substrate. The deposition is viewed by FM to ensure that the transfer process does not influence or change the morphology of the film. An AFM image of a collapsed PA/SP-B film shows the separation of the ordered phase domains in the monolayer by the protein-rich network and the homogeneous nucleation of collapse phase domains on the sub-micron level on top of the ordered domains (Fig. 6). The height difference between these collapse nuclei and the original monolayer are on the order of a bilayer thickness (4-5 nm).

References

1. D. Shapiro et al., Surfactant Replacement Therapy, New York: Liss (1989)
2. M. Longo et al., Science **261**, 453 (1993).
3. D. Turnbull, J. Chem. Phys. **20**, 411 (1952).
4. The author wishes to thank K. Y. C. Lee, A. Waring, and J. A. Zasadzinski for their assistance
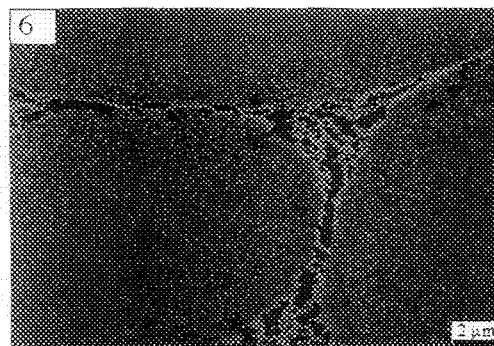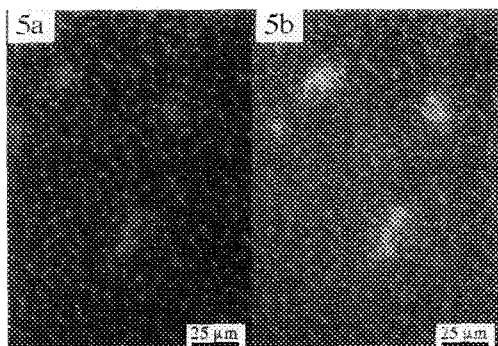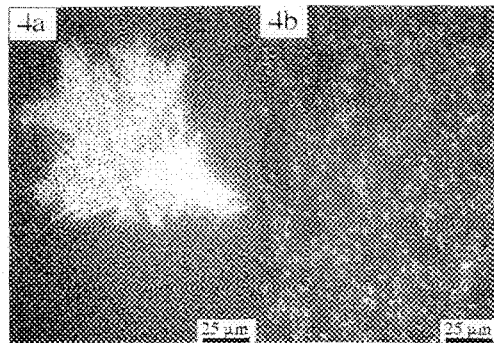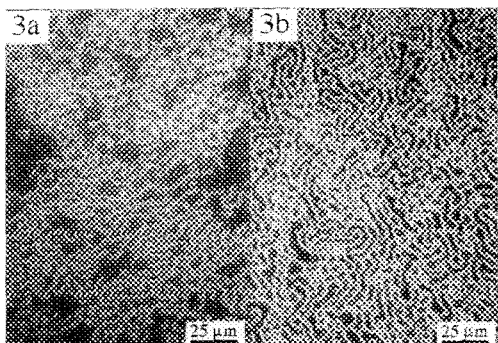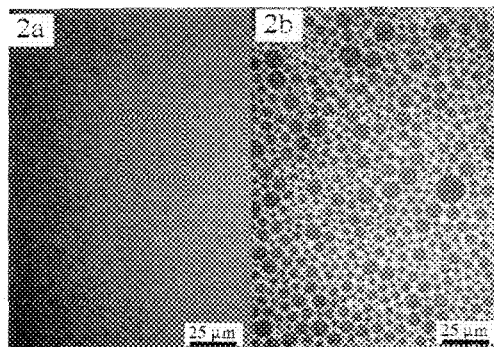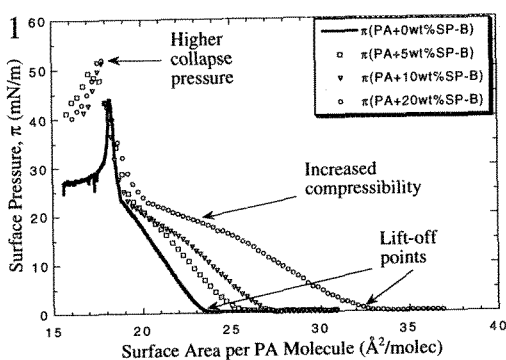
Fig. 1. Surface pressure vs. area isotherms of PA monolayers as a function of weight % SP-B.

Fig. 2. FM images of monolayers of (a) PA and (b) PA/20 wt. % SP-B containing 0.5 % of the fluorescent probe NBD-hexadecylamine at their lift-off points (shown in Fig. 1).

Fig. 3. FM images of stripe phases of (a) PA/20 wt. % SP-B and (b) fluorescein-SP-B.

Fig. 4. FM images of collapse domains of (a) PA and (b) PA/20 wt. % SP-B.

Fig. 5. FM images of a monolayer of PA/20 wt. % fluorescein-SP-B/0.1 % Texas Red lipid post-collapse showing the detected fluorescence from the (a) Texas Red and (b) fluorescein fluorophores.

Fig. 6. AFM image of a monolayer of PA/20 wt. % fluorescein-SP-B post-collapse.

THE ROLE OF HEPATOCYTES AS THE BODY'S "GLUCOSTAT": CORRELATION OF DATA FROM STUDIES RANGING FROM A (ANALYSIS OF BIOCHEMICAL AND MORPHOLOGICAL OBSERVATIONS)TO Z (ZIPPING UP cDNA PROBES AND mRNA)

E.L. Cardell, J.K. Gao, B.F. Giffin and R.R. Cardell, Jr.

Department of Cell Biology, Neurobiology and Anatomy, University of Cincinnati College of Medicine, Cincinnati, OH 45267-0521

The maintenance and regulation of blood glucose levels is a vitally important liver function, among more than 500 metabolic functions ascribed to hepatocytes. Brain cells cannot function properly if blood glucose levels vary greatly from the normal range of 90-100 mg/100 ml; coma results from extremes of hypo- or hyper-glycemia, and death occurs when the status is not corrected. Because glucose is the primary energy source for brain cells, other cell types throughout the body utilize lipids and amino acids as energy sources in a "glucose-sparing" mechanism to reserve relatively low levels of blood glucose for use by the brain. Acting collectively as the body's "glucostat," hepatocytes convert glucose to insoluble glycogen by the process of glycogenesis when blood glucose levels are high (post-prandial, absorptive state), and convert glycogen, fats, and/or protein-derivatives to glucose when blood glucose levels are low (post-adsorptive, fasting state). Various other cell types in the body form glycogen and utilize it for their own energy needs, but only hepatocytes, certain kidney tubule cells, and enterocytes have glucose-6-phosphatase (G-6-Pase), the enzyme needed to convert glycogen back to glucose for release to the blood. Hepatocytes specialize and excel in this process called glycogenolysis; the G-6-Pase is found in the smooth endoplasmic reticulum that can be abundant in these cells and varies according to changes in the individual's nutritional and physiological status. In addition, hepatocytes have the enzyme phosphoenylpyruvate carboxykinase (PEPCK) that allows gluconeogenesis, the conversion of amino acids ultimately to glucose when carbohydrate sources are not available.

We have evaluated the role of hepatocytes as the body's glucostat by correlating biochemical data from several analytical approaches in a variety of normal and experimental conditions. Our methods for studying hepatic glycogen metabolism, the primary mechanism through which the hepatocyte glucostat function is accomplished, have included biochemical analysis, cell fractionation, hormonal manipulation, immunogold cytochemistry, in situ hybridization histochemistry, and light and electron microscopy. Our animal models have included fetal mouse, rat, and chick; however, adult mice and rats have been used primarily. We have also evaluated primary cultures of developing chick hepatocytes and a sustained-perfused animal model; these two models allowed sequential samples to be obtained for evaluation of changes occurring during the course of experimental manipulation.

LEGEND

Regions within the hepatocyte cytosome include organelles involved in numerous activities, including glycogen metabolism. Magnification, 37,000x.
FIGURE 1 shows a portion of the nucleus (N), rough and smooth endoplasmic reticulum (RER, SER), and mitochondria (M). Glycogen is absent, a condition observed in 30 hour fasted normal rats and overnight fasted adrenalectomized rats.
FIGURE 2 includes compact glycogen (G) with SER (arrows) peripheral to the mass, typical of normal periportal hepatocytes and most hepatocytes when higher than usual hepatic glycogen levels occur (control fed normal animals and high insulin replacement in diabetic animals).
FIGURE 3 shows glycogen dispersed among SER, (arrows) a distribution typical of centrilobular hepatocytes in normal liver and all hepatocytes from diabetic animals without insulin treatment.

324
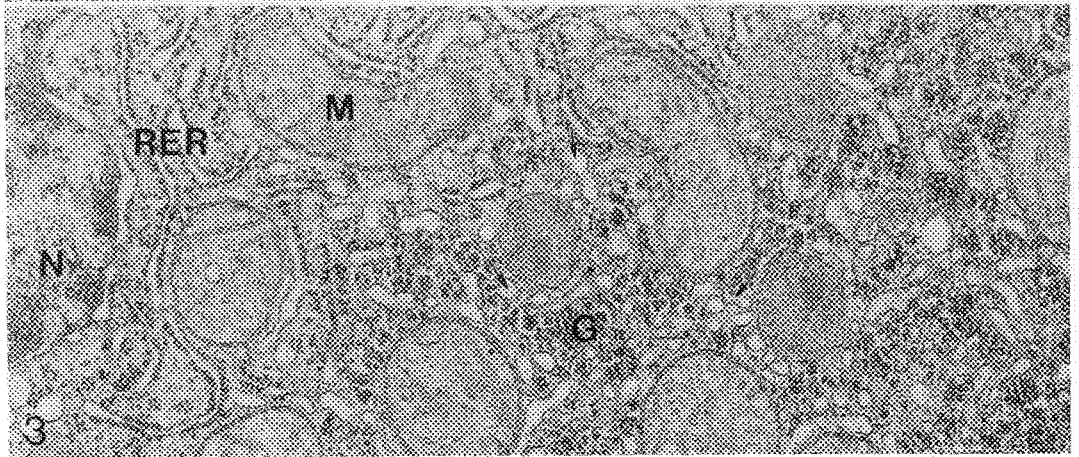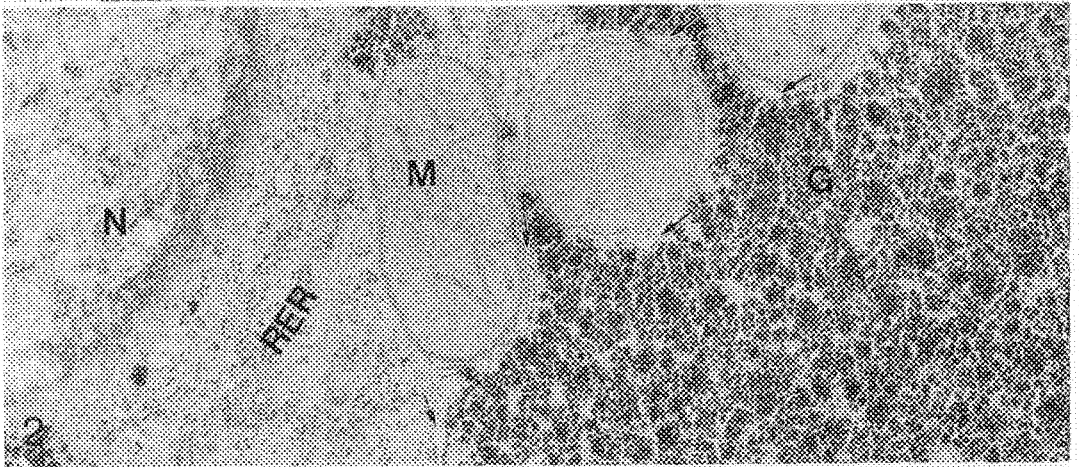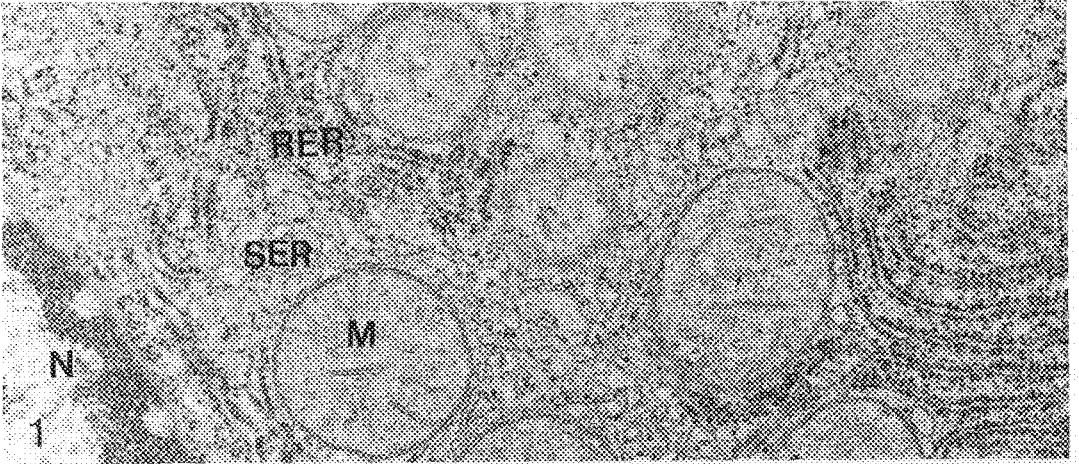
ANALYSIS OF GRAIN-BOUNDARY STRUCTURES BY QUANTITATIVE HRTEM

K. Nadarzinski, O. Kienzle, and F. Ernst

Max-Planck-Institut für Metallforschung, Institut für Werkstoffwissenschaft, Seestraße 92, D-70174 Stuttgart, Germany

HRTEM (high-resolution transmission electron microscopy) constitutes a powerful technique to investigate the atomistic structure of grain boundaries. However, interpreting HRTEM images of grain boundaries in terms of „projected structure" may lead to errors: Near a boundary, the contrast patterns of atom columns may differ from the corresponding patterns in regions of unfaulted crystal. Even worse, dynamic diffraction and lens aberrations may *displace* the contrast patterns against the actual (projected) positions of the columns. Nevertheless, it is possible to interpret such images safely by *comparing* them with simulated images of structure models. This method becomes powerful if one compares experimental and simulated images not merely by visual inspection but *quantitatively*, by means of digital image processing. [1]

For a given HRTEM image of a grain boundary we *iterate* such quantitative image comparisons to perform an automatic *structure refinement*, which determines the structure that yields the best-matching simulated image to the experimental image (Fig. 1). While we can refine the positions of atom columns to any numerical precision, the coordinates only have a limited *reliability*. This arises because it is impossible to simulate HRTEM images perfectly – even if one *knew* the structure of the specimen. To quantify error limits for the column coordinates we explore how the simulated image of the refined structure changes with small displacements of the columns. It turns out that our method delivers the coordinates of atom columns with a precision in the order of 0.01 nm. The method also accounts for the damage that electron beam irradiation introduces in the specimen. By means of „beam damaging experiments" we estimate the maximum duration of irradiation to be allowed before damaging interferes with determining the structure at a given precision. [2, 3]

We have applied our method of „quantitative" HRTEM to analyze the structures of highly symmetric grain boundaries in materials with different types of interatomic bonding.[3-5] For example, Fig. 2 presents a HRTEM image of a $\Sigma3(111)$ grain boundary in NiAl (CsCl structure), recorded with the Stuttgart Atomic Resolution Microscope JEM-ARM 1250 at a point resolution of 0.105 nm. [6] Quantitative image analysis yields the structure of Fig. 3 (top) with a precision of 0.015 nm for the column positions. In contrast with a „geometrical" model (bottom of Fig. 3) the real structure exhibits an excess volume and broken mirror symmetry. [3] The „holes" in the atom arrangement at the boundary indicate mechanical weakness, which may contribute to the brittleness of polycrystalline NiAl at room temperature.

References

1. D. Hofmann and F. Ernst, *Ultramicroscopy, 53* (1994) 205.
2. G. Dehm, K. Nadarzinski, F. Ernst, and M. Rühle, *Ultramicroscopy,* in press.
3. K. Nadarzinski and F. Ernst, *Philosophical Magazine A,* to be published.
4. D. Hofmann and F. Ernst, *Interface Science, 2* (1994) 201.
5. O. Kienzle and F. Ernst, unpublished.
6. F. Phillipp, G. Möbus, and M. Rühle, *Ultramicroscopy, 56* (1994) 1.
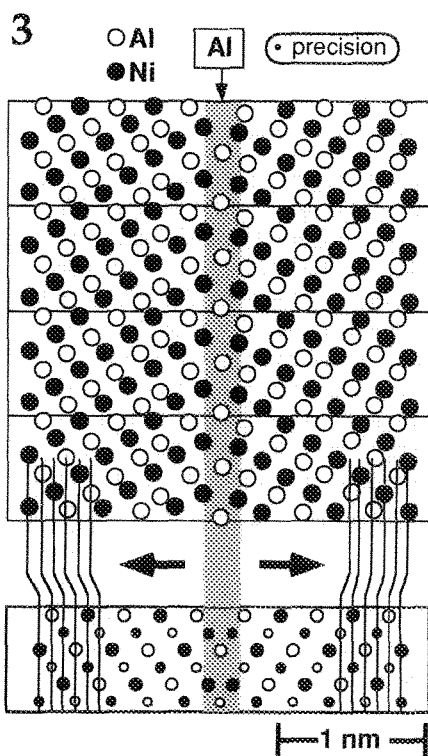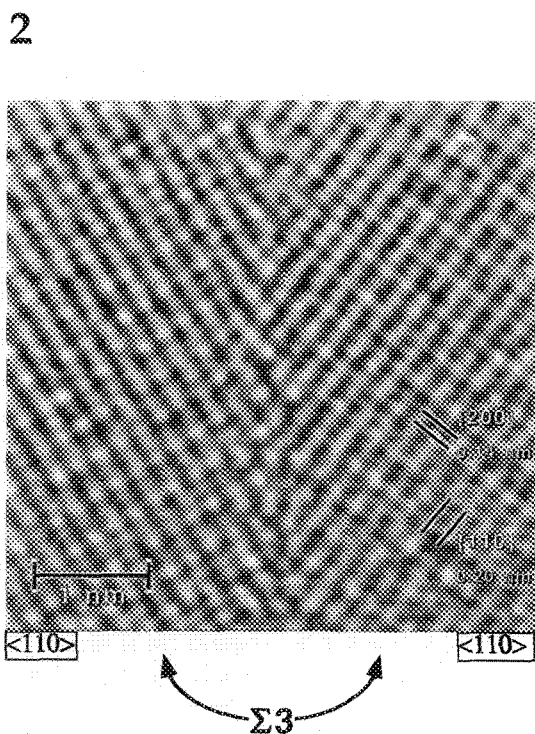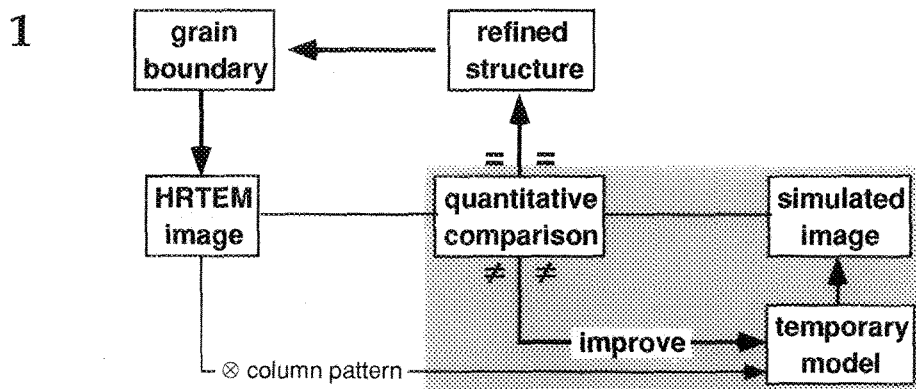
FIG. 1 Flow diagram of strucuture refinement through quantitative analysis of HRTEM images.

FIG. 2 Experimental HRTEM image of a $\Sigma 3$ (111) grain boundary in NiAl in <110> projection.

FIG. 3 Structure of the grain boundary (top) compared to a geometrical model (bottom).

GRAIN BOUNDARY DISLOCATION STRUCTURE AND MOTION IN AN ALUMINUM Σ=3 BICRYSTAL

D.L. Medlin, S.M. Foiles, and C.Barry Carter*

Sandia National Laboratories, Livermore, CA 94551
*Department of Chemical Engineering and Materials Science, Amundson Hall, University of Minnesota, Minneapolis, MN 55455.

A lattice dislocation may interact with a grain boundary leaving either a residual dislocation or a step or both. These products may then contribute to further deformation by themselves moving along the interfaces. For instance, Pond[1] observed the dissociation of a perfect lattice dislocation in an aluminum Σ=3 $(2\bar{1}\bar{1})$ incoherent twin boundary by a reaction of the type:

$$a/2 [011] \rightarrow a/3[111] + a/6[\bar{2}11]$$
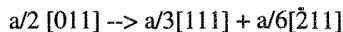
Furthermore, the a/3[111] dislocation was observed to dissociate into two partial grain boundary dislocations (GBD), with Burgers vectors of approximately 2a/9[111] and a/9[111], separating structurally degenerate regions of opposite rigid body displacement[1].

We are investigating the structure and migration mechanisms of such defects using a combination of high resolution electron microscopy (HRTEM) and atomistic simulation methods. Figures 1 and 2 show a calculated structure and HRTEM observations of the 2a/9 [111] component of an a/3[111] GBD which has dissociated on the Σ=3 $(\bar{2}11)$ boundary in aluminum. The structure in Figure 1 was calculated using the Embedded Atom Method[2] and is similar to calculations presented earlier by Vitek and coworkers[3]. As can be identified from the lines drawn though the (111) planes on either side of the boundary, the partial GBD separates two regions of opposite rigid body [111] displacement . At the top of the figures, the (111) planes/fringes bend down across the boundary (looking from left to right) whereas at the bottom they bend up. Additionally, in the middle of the figures is a region of anti-symmetry in which the (111) planes/fringes are offset by 1/2 d_{111}. In contrast, calculations and observations of the a/9[111] component show a region of mirror symmetry.

As was noted by Pond[1], the dissociated a/3[111] grain boundary dislocations are extremely mobile and can translate by glide. Our HRTEM observations show a sequence of such dislocations gliding on the Σ=3 $(2\bar{1}\bar{1})$ boundary. Upon meeting a coherent twin facet, the dislocations are blocked and constrict in order to climb past the barrier. This results in a periodic array of steps forming on a growing coherent twin lamella. An example of an a/3[111] grain boundary dislocation that has climbed out of the $(2\bar{1}\bar{1})$ boundary (labelled ICT) and along a coherent twin boundary (CT) is shown in Figure 3. By such a climb process, the thickness of the coherent twin increases by one (111) plane. The interactions and HRTEM contrast features of these defect configurations will be discussed and compared with theoretical predictions.

References:
1. R.C. Pond, Proc. Roy. Soc. Lond. A **357**, (1977) 471.
2. *e.g.*, M.S. Daw, S.M. Foiles, and M.I. Baskes, *Mat. Sci. Rep.* **9** (1993) 251.
3. V. Vitek, A.P. Sutton, D.A. Smith, R.C. Pond, in Grain Boundary Structure and Kinetics, ed. R.W. Baluffi, (ASM, Metals Park OH, 1979) (1979) 115-148.
4. This research is supported by the U.S. Department of Energy, Office of Basic Energy Sciences, under contract number DE-AC04-94-AL85000.

$[111]$

$[\bar{1}11]$

$[0\bar{1}1]$ $[\bar{2}11]$
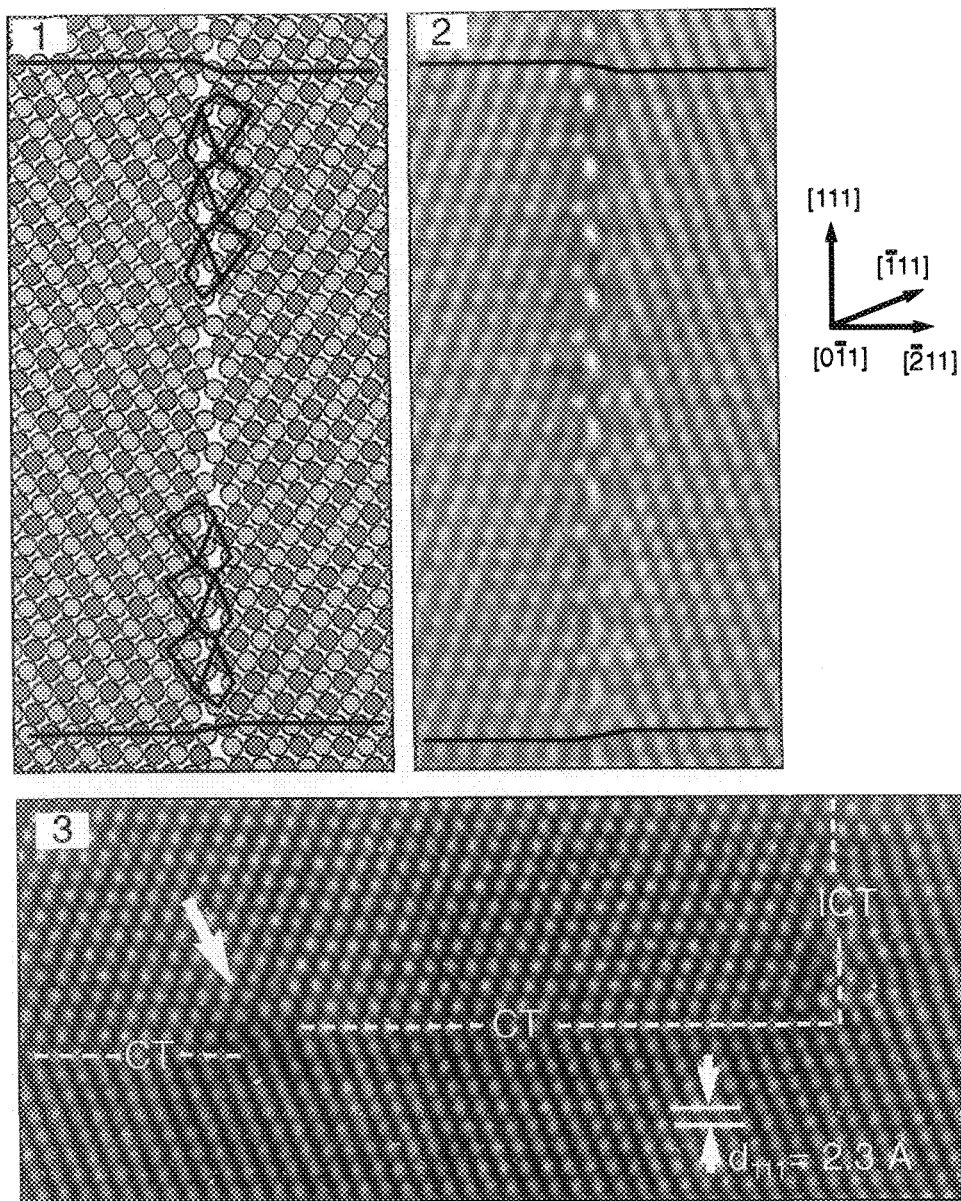
FIG. 1   Calculated structure for the 2a/9 [111] component of a dissociated a/3[111] GBD on the $\Sigma=3$ $(\bar{2}11)$ boundary in aluminum. Note the change in rigid body displacement and reversal of the structural motifs between the top and bottom of the figure.

FIG. 2   HRTEM image showing reversal of rigid body displacement in the $\Sigma=3$ $(\bar{2}11)$ boundary.

FIG. 3   Junction of the $(\bar{2}11)$ (labelled ICT) and (111) (labelled CT) boundaries. Arrow indicates position of climbing a/3[111] dislocation which produces a step in the coherent twin boundary.

329

ATOMIC STRUCTURE OF THE (310) SYMMETRICAL TILT GRAIN BOUNDARY IN STRONTIUM TITANATE - A COMPARISON AMONG EXPERIMENTAL METHODS AND ATOMISTIC SIMULATIONS

V. Ravikumar*, Vinayak. P. Dravid,** and D. Wolf***

* GE Corporate Research and Development, K1-1C36, 1 Research Circle, Schenectady, NY 12309.
** Department of Materials Science and Engineering, Northwestern University, Evanston, IL 60208.
*** Materials Science Division, Bldg. 212, Argonne National Laboratory, Argonne, IL.

Strontium Titanate is a prototypical perovskite oxide whose macroscopic electroceramic properties, like varistor and grain boundary barrier layer capacitor (GBBLC) behavior, are controlled by grain boundary (GB) phenomena. In this paper, we present a comparative analysis of the results of both experimental and theoretical investigations of the atomic structure of a (310) symmetrical tilt GB (a Σ=5 (310) [001] GB in the CSL notation) in $SrTiO_3$. Bicrystals of $SrTiO_3$ were procured from Shinkosha Ltd., and electron backscatter kikuchi pattern analysis as well as transmission electron diffraction studies confirm that the GB conforms to the Σ =5 misorientation. The atomic structure of this GB has been investigated using high resolution transmission electron microscopy (HRTEM) and associated image simulations,[1] as well as by atomistic simulations using static iterative energy minimization schemes ("lattice-statics").[2]

Fig. 1 shows an HRTEM micrograph of a typical region of the Σ =5 GB which indicates a symmetrical tilt GB on a (310) plane. There are occasional steps along the GB, but in between the steps, the GB is flat and has a compact core with a periodically repeating structural unit. There was negligible volume expansion associated with this GB; however, an in-plane rigid body translation (RBT) of (1/2)d310 was identified. An empirical model of the repeating structural unit of the GB core was determined from image analysis, and Fig. 2 shows a comparison between the experimental and simulated images. An investigation of the core structure of this GB using Z-contrast imaging by our collaborators identified the presence of point defects at the GB core; they deduced that columns of cations are only half filled at the GB core, with every other site vacant.

Lattice-statics simulations were performed first on completely dense GB configurations (Fig. 3). There are two types of (310) planes in $SrTiO_3$ - a cation rich SrTiO +4 charged plane, or a -4 charged oxygen plane, and both GB terminations were considered. The results indicated that both configurations yielded very similar structures, with practically identical relaxed energies. As a first refinement, Schottky vacancy defects were introduced to the GB core in the form of completely missing atomic columns, and the simulation results indicated that vacancies were very strongly preferred at the GB core. The GB configurations were further refined to incorporate the vacancies as half-filled cation and anion columns of atoms (Fig. 4); the results indicate that while there is a further decrease in GB energy for the half-column structures, the GB energy is only slightly lower than the structures where the vacancies were incorporated as completely missing columns.

A comparative evaluation of the results of HRTEM, Z-contrast, and Lattice-statics investigations will be presented, which provides a consistent picture of the GB core structure.[4]

References:

1) V. Ravikumar and V. P. Dravid, Ultramicroscopy, **52** (1993) 557. 2) V. Ravikumar, D. Wolf and V. P. Dravid, J. Am. Ceram. Soc., submitted. 3) N. B. Browning et al., Interface Science, **2** [**24**] (1994) 397. 4) Research supported by U. S. DOE-BES, Grant Number DE-FG02-92ER45475.
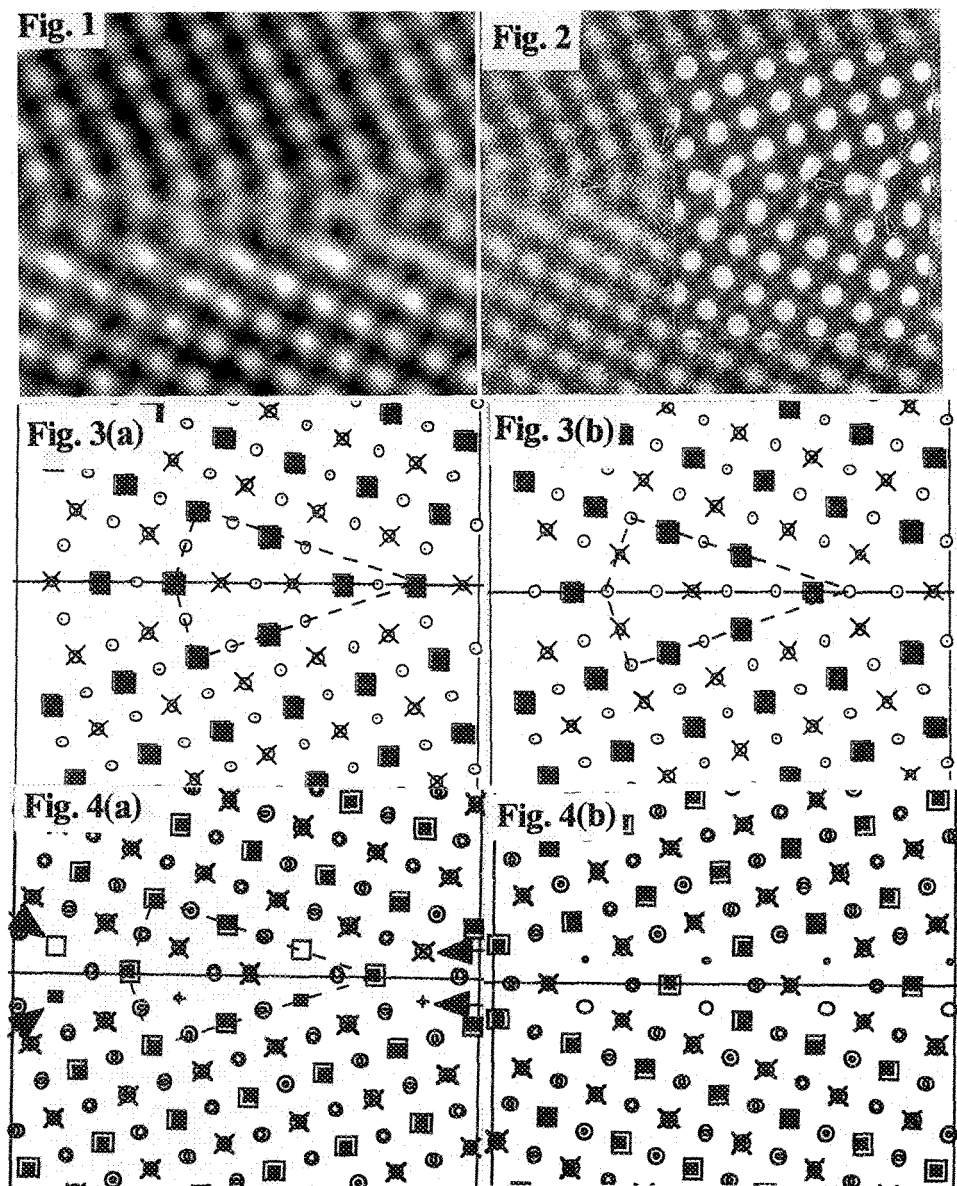
FIG. 1 HRTEM of the (310) symmetrical tilt GB in SrTiO$_3$. FIG. 2 Comparison between the simulated image (inset) and experimental image. FIG. 3 Two configurations of the fully dense GB, with either (a) the cation-rich plane or (b) the oxygen plane as the GB plane. FIG. 4 Two of the 18 distinct unrelaxed starting configurations of the GBs with half-filled cation and anion columns at the GB core, respectively.

Z-CONTRAST IMAGING OF GRAIN BOUNDARIES IN SEMICONDUCTORS

M. F. Chisholm and S. J. Pennycook

Oak Ridge National Laboratory, Solid State Division, Oak Ridge, TN 37831-6030

Interest in grain boundaries in semiconductors is linked to the application of polycrystalline semiconductors as photovoltaic and interconnect materials. In real devices such as solar cells and MOS structures as well as future devices such as flat-panel displays, the intergranular regions of the polycrystalline solid have a significant effect on the flow of electronic current. These grain boundary barriers exist because the chemical potential of the boundary atoms are shifted from the bulk value by the change in local symmetry. The chemical potential is also changed by impurities, other structural defects, and other phases in the boundary. The lack of knowledge on the atomic structure of grain boundaries is, at present, the greatest barrier to advancements in the understanding of the electrical properties of these defects.

The advances of the last few years have provided the tools with which to probe these interfaces at the true atomic scale. One such tool is the high-resolution scanning transmission electron microscope installed at Oak Ridge National Laboratory (VG Microscopes HB603) that can form a 1.27Å electron probe. Images are formed by scanning the probe across a thin sample and using an annular detector to collect electrons scattered to high angles. Because the annular detector collects electrons scattered over a wide range of angles, phase correlations and dynamical diffraction effects are averaged by this annular integration. Thus, an image with incoherent characteristics is produced and retained to relatively large specimen thickness.[1] The key advantage of incoherent imaging is that when the microscope is focused to produce maximum image contrast, the bright image features directly correspond to the positions of the atomic columns. As long as the probe is smaller than the projected atomic column spacing and the inner detector angle is larger than the beam convergence, the observed atomic columns can be treated as independent incoherent scatterers. This column-by-column imaging is crucial when investigating interfaces and other unknown structures. Additionally, as the inner detector angle is increased beyond this minimum setting for incoherent imaging, the contribution of nuclear scattering increases, leading to increased compositional sensitivity of the images.

Atomic resolution of the grain boundary cores in silicon represents a severe test and remarkable demonstration of the technique. Figure 1 is a Z-contrast image of a section of a 39° <110> symmetric tilt boundary in silicon (Σ=9 {221}<110>) as viewed along the [110] direction. The boundary is seen to consist of a periodic array of perfect edge dislocation with their line direction parallel to the <110> tilt axis. While this grain boundary core structure had been previously identified to be the stable atomic configuration by both experiment[2] and theory[3], the unprecedented resolution of the image clearly reveals the 5- and 7-atom rings of the distinct boundary dislocations.

The capabilities and advantages of the technique are more fully displayed in images from a 23° <001> symmetric tilt boundary in silicon (Σ=13 {310}<001>). As revealed in Figure 2, this boundary contains a more complex arrangement of boundary dislocations. Six distinct dislocation cores are present in each 13.84Å periodic repeat of the boundary.[4] This structure had not been proposed previously as the preferred atomic configuration for this tilt boundary. The directly interpretable incoherent image removes the need for preconceived model structures.

The compositional sensitivity of the technique should allow the nature and distribution of impurities segregated to these structures to be obtained column-by-column. It is believed that the

combination of the detailed atomic structure data from the microscope along with theoretical modeling will improve our understanding of the physical processes that occur at grain boundaries.[5]

References

1. D. J. Jesson and S. J. Pennycook, *Proc, R. Soc. Lond. A* **441** (1993) 261; *Proc, R. Soc. Lond. A* **449** (1995) 273.
2. O. L. Krivanek et al., *Phil. Mag.* **36** (1977) 931.
3. D. P. DiVincenzo et al., *Phys. Rev. Lett.* **56** (1986) 1925.
4. M. F. Chisholm et al., *Phil Mag.* in press.
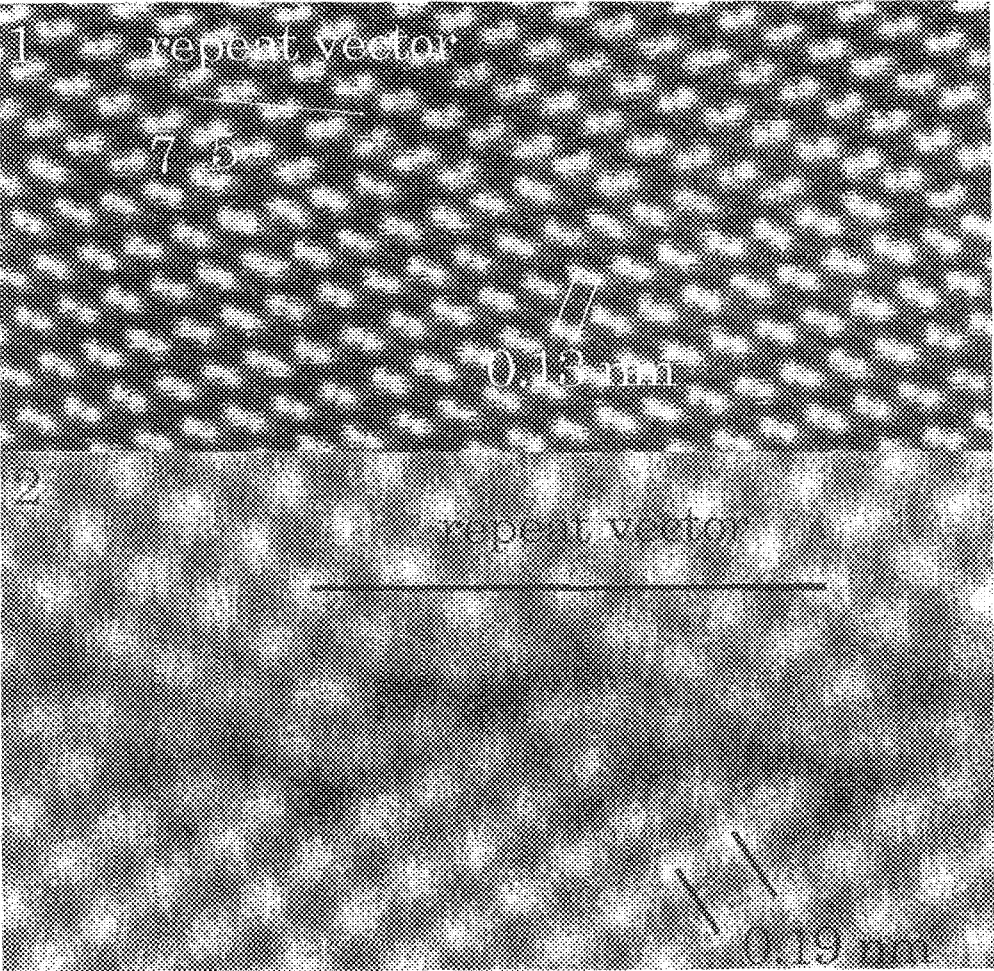
Fig. 1 [110] Z-contrast image of a 39° <110> symmetric tilt boundary in silicon.
Fig. 2 [001] Z-contrast image of a 23° <001> symmetric tilt boundary in silicon.

DETERMINING ATOMIC STRUCTURE-PROPERTY RELATIONSHIPS AT GRAIN BOUNDARIES

N. D. Browning*, D. J. Wallis*, P. D. Nellist** and S. J. Pennycook**

*Dept. Physics (M/C 273), U. Illinois-Chicago, 845 W. Taylor St., Chicago, IL 60607-7059. USA
**Solid State Division, Oak Ridge National Laboratory, P. O. Box 2008, Oak Ridge, TN 37831. USA

Atomic scale effects at grain boundaries are known to play a dominant role in controlling the bulk properties of many materials. However, a detailed understanding of this role is complicated by the tendency for boundaries to behave in a "non-ideal" manner, i.e. the boundary plane can change on the scale of a few nanometers, altering the number of vacancies and impurities and the presence of second phases. The crucial first step to engineering boundary properties is therefore the ability to observe these changes experimentally with both atomic resolution and sensitivity. Such a capability is provided by the combination of Z-contrast imaging and electron energy loss spectroscopy (EELS) in the scanning transmission electron microscope (STEM) [1,2].

The Z-contrast technique generates an incoherent, atomic resolution structural image of a grain boundary which can be used to position the electron probe with atomic precision for spectroscopy. As the spectrum has nearly the same resolution as the image for core-losses >100eV, this arrangement has the unique advantage of allowing compositional fluctuations to be correlated directly with structural features in the boundary plane. Furthermore, multiple-scattering (MS) analysis can be utilized to extract 3-dimensional structural information from the spectrum [3]. MS techniques consider the fine-structure of the spectrum to arise from interference effects occurring when a photoelectron created during the energy loss process is reflected from neighboring atoms. The real-space clusters used in this methodology allow the flexibility to determine whether the contributions to the spectrum arise from single or multiple scattering paths and from which atomic neighbors they originate. This allows the different structural relaxations that occur at boundaries, i.e. vacancies or structural disorder, to be distinguished from the spectrum.

These correlated techniques have been used to analyze a range of [001] tilt boundary structures in $SrTiO_3$ [4]. Shown in figure 1 is the Z-contrast image and structure schematic for the 45° asymmetric boundary. Titanium L-edge and oxygen K-edge spectra from the bulk and the boundary (figure 2), indicate that the titanium valence remains bulk-like in the boundary (no change in L_2/L_3 intensity ratio or edge onset position) and the linear titanium-oxygen coordination is preserved. However, noticeable in the structure are positions where two Ti-O columns are seperated by distances much shorter than in the bulk material. Since the Z-contrast technique provides an incoherent image, both of these columns must exist, and one explanation is partial occupancy. Testing this partial occupancy hypothesis by MS-analysis (figure 3) reveals the only realistic fit to experiment does indeed occur for a half-column structure.

This partial occupancy is seen to be a ubiquitous feature of [001] tilt boundaries in $SrTiO_3$ [4]. However, partial occupancy can occur on different sub-lattice sites, i.e. Sr or Ti-O, depending on whether the boundaries are symmetric or asymmetric and the misorientation angle. This strongly suggests that the doping of grain boundaries in these materials to tailor electronic properties will be a function of the grain boundary plane. The different "structural units" that occur in each boundary can potentially accomodate differently sized and charged dopant atoms leading to vastly different properties. Furthermore, controlling the grain boundary plane itself can have a dramatic effect on the properties of the grain boundary. This boundary plane effect is observed for the structurally similar high-temperature superconductor $YBa_2Cu_3O_{7-\delta}$ (YBCO). In recent studies [5], the grain boundary critical current as a function of misorientation angle has been accurately modelled by considering the prevalence of partial occupancy on the copper sites. These results indicate that in addition to striving to reduce high-angle boundaries in YBCO wires, significant advances in transport properties could be induced by engineering predominantly symmetric boundary structures, where partial occupancy occurs on the Y/Ba sites [6].

References

1. S. J. Pennycook and D. E. Jesson, *Phys.Rev.Lett* 64 (1990) 938
2. N. D. Browning et al, *Nature* 366 (1993) 146
3. D. J. Wallis and N. D. Browning submitted *Phys. Rev. Lett*
4. N. D. Browning and S. J. Pennycook, in press *J. Phys. D*
5. N. D. Browning et al, submitted *Nature*
6. Research sponsored by NSF under grant DMR-9503877, by DOE-DMS under contract DE-AC05-84OR21400 with Martin Marietta Energy systems Inc and in part by an appointment to the ORNL postdoctoral program administered by ORISE.
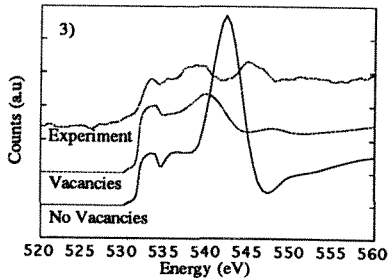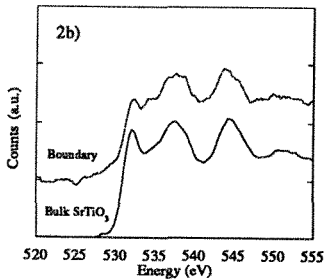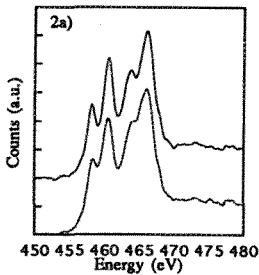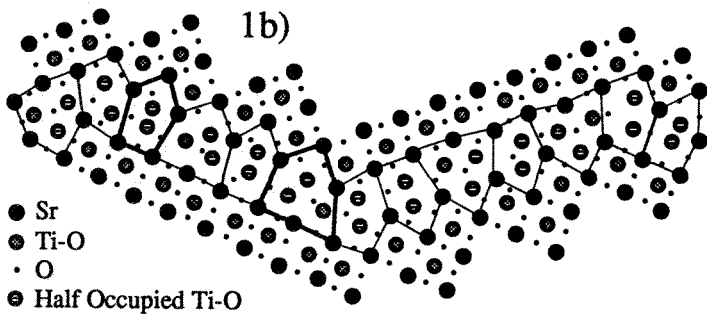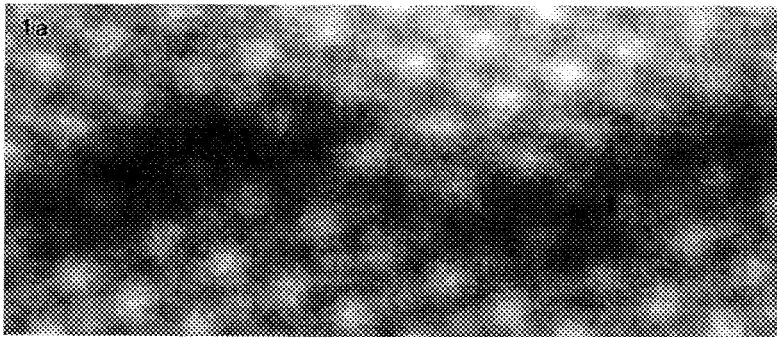
Figure 1:(a) Z-contrast image and (b) model of an asymmetric 45° [001] tilt boundary in SrTiO$_3$
Figure 2:(a) Titanium L-edges (b) Oxygen K-edges from the bulk and 45° [001] tilt boundary in SrTiO$_3$
Figure 3:Comparison of multiple scattering calculations and experimental spectra for the bulk and 45° [001] tilt boundary in SrTiO$_3$

IN SITU ELECTRICAL AND MICROSTRUCTURAL CHARACTERIZATION OF INDIVIDUAL BOUNDARIES

J.Y. Laval*, M.H. Berger*[+] and C. Cabanel*

*Laboratoire de Physique du Solide UPR5, CNRS ESPCI 10, rue Vauquelin, Paris France
[+] Centre des Matériaux de l'Ecole des Mines de Paris, Evry, France

In order to get direct information on the relationships between the structural and electrical properties of interfaces, we developed in situ experiments in TEM-STEM and SEM for the characterization of the local behaviour of majority and minority carriers. In particular, we described here our new technique for local determination of interfacial potential barriers in electronic ceramics. This information is completed by voltage contrast imaging in SEM at 1 kV which enables a full map of the distribution of these interfacial barriers to be obtained.

The TEM experiment is schematized in fig. 1. A tungsten microelectrode (100 nm diameter) can be micromanipulated in situ and gently set down on the TEM sample. The contact between the microelectrode and the sample is shown sharply by the modification of extinction contours in each adjacent grain (Fig. 2ab). The sensitivity of the contact detection minimizes the fracture hazard. When a dc voltage $\cong$ 9 volts is applied along the sample, the voltage drop across the boundary is measured directly. This methodology was applied to Mn-Zn soft ferrites where eddy current losses must be greatly reduced by developing high potential barriers at boundaries for high frequency applications. General boundaries display voltage drops ΔV in the range $20 < \Delta V < 50$ mV whereas for glassy film coated boundaries a $\Delta V \cong 10$ mV is found. Special boundaries exhibit $\Delta V < 10$ mV and even down to a few mvolts. The specific behaviour of these different boundaries is well explained by local analysis of the oxidation state of Fe by EELS spectroscopy in STEM. It was found that the Fe^{2+}/Fe^{3+} ratio is not modified at Σ boundaries whereas it is reduced on general boundaries on a 10 nm width. Consequently, these boundaries are highly resistive since hopping conduction by electron jumps between Fe^{2+} and Fe^{3+} in octahedral sites is almost entirely suppressed.

A complementary potential mapping was carried out by voltage contrast in SEM. In order to get a semi-quantitative contrast related to the potential barrier of individual boundaries, samples were thinned down to a thickness of 10 µm, ie smaller than the average grain size (10-20 µm). A secondary SEM image of the sample is shown on Fig. 4a. When a dc voltage of 2 volts is applied between the silver contacts a voltage contrast map is obtained (Fig. 4b). It confirms that potential barriers are always located at grain boundaries. Furthermore, it is seen on some triple junctions that one of the abutting boundaries is not visible which corresponds to the low barriers ≤ 10 mV previously found in TEM. On the example given it is found that the 2D rate of low ΔV boundaries is < 10 %, in good agreement with the TEM results. From the percolation theory (1) it can be inferred that the corresponding size of 3D clusters of grains is < 5. Thus the eddy currents will be much reduced through the sample and will not impede high frequency applications. This process enables the simultaneous execution of electrical, microstructural and crystallographical characterization of individual boundaries and to infer the bulk properties via potential mapping in SEM.

1. V.K.S. Shante, S. Kirkpatrick, An introduction to percolation theory, *Adv. Phys.*, **20**, 325 (1971)
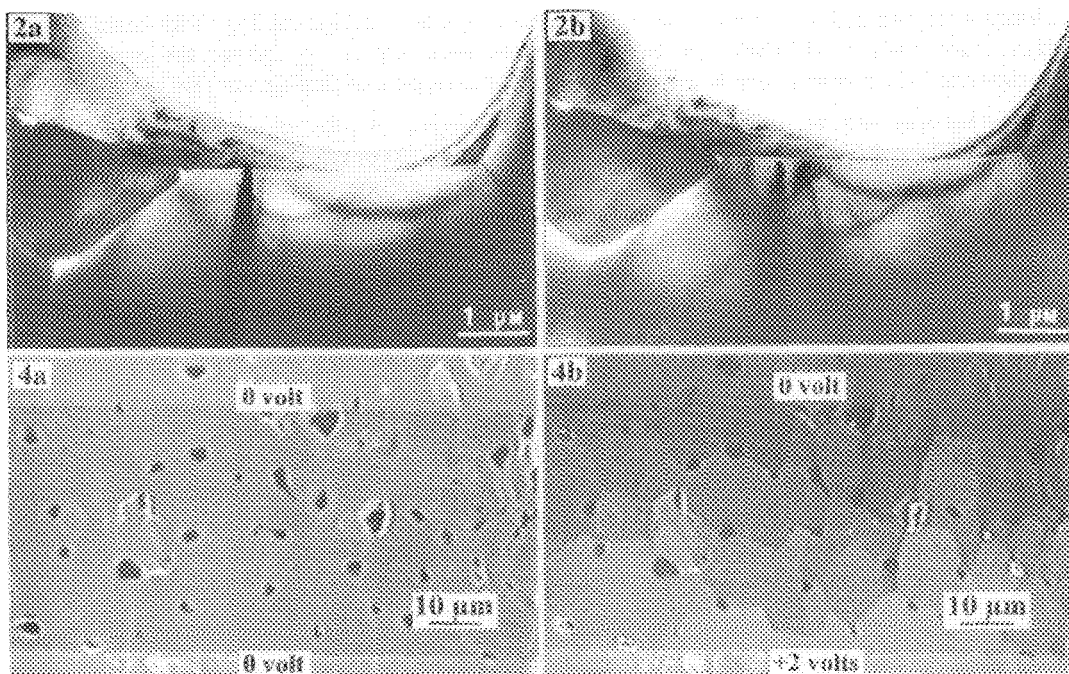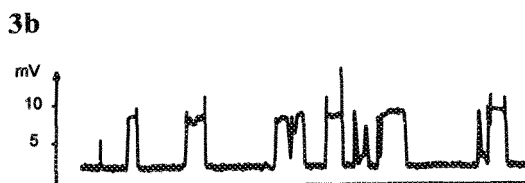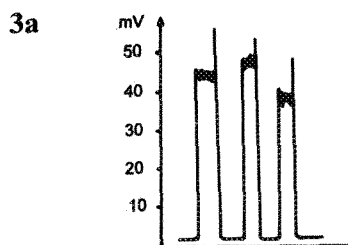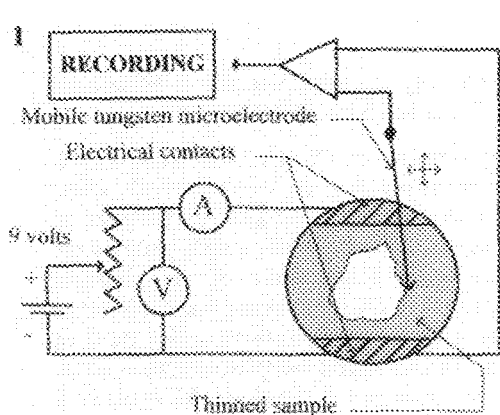
Fig. 1 : Schematic of the in situ voltage drop experiment in TEM

Fig. 2 : Transmission electron micrographs showing the two successive positions (a and b) of the microelectrode on each side of the boundary

Fig. 3 : Voltage drop signal measured on : a) a general boundary b) a special boundary (Σ boundary)

Fig. 4 : Voltage contrast in SEM   a) SEM image of the sample with the silver contacts

  b) Voltage contrast mapping of the grain boundaries

FACET TOPOGRAPHY AND DISLOCATION STRUCTURE AS A POSSIBLE SOURCE FOR ELECTRICAL HETEROGENEITY IN [001] TILT BICRYSTALS OF YBa$_2$Cu$_3$O$_{7-\delta}$

I-Fei Tsu*, D.L. Kaiser**, and S.E. Babcock*

*Materials Science & Engineering and Applied Superconductivity Center, University of Wisconsin-Madison, Madison, WI 53706; **Ceramics Division, NIST, Gaithersburg, MD 20899.

A current theme in the study of the critical current density behavior of YBa$_2$Cu$_3$O$_{7-\delta}$ (YBCO) grain boundaries is that their electromagnetic properties are heterogeneous on various length scales ranging from 10s of microns to ~ 1 Å.[1] Recently, combined electromagnetic and TEM studies on four flux-grown bicrystals have demonstrated a direct correlation between the length scale of the boundaries' saw-tooth facet configurations and the apparent length scale of the electrical heterogeneity.[2] In that work, enhanced critical current densities are observed at applied fields where the facet period is commensurate with the spacing of the Abrikosov flux vortices which must be pinned if higher critical current density values are recorded. To understand the microstructural origin of the flux pinning, the grain boundary topography and grain boundary dislocation (GBD) network structure of [001] tilt YBCO bicrystals were studied by TEM and HRTEM.

Bicrystals of YBCO (~ 500×200×20 μm) were produced by the flux-growth method.[3] TEM specimens were prepared by a combination of laser cutting, grinding, and ion-milling. Two-beam **g·b** analysis, trace analysis, HRTEM, and Frank's formula were applied to analyze the boundary microstructure. The results shown here from a 6° bicrystal are typical of flux-grown YBCO samples.

Structural heterogeneity on various length scales was observed. A most obvious feature of the boundaries is their strongly faceted topography on the scales of 10s of nm, shown in Figs. 1(a)-(c). Less striking, but still clearly visible is the repeated, but non-uniform grain boundary dislocation (GBD) configuration in the individual facets. For example, in the (130) facet the spacing between the **b**=[110] GBDs (the darker ones) is ~ 11.4 nm near the facet centers and ~ 3.8 nm near the facet junctions. In (22$\bar{1}$) facet, the GBD spacing in the center is only half that near the junctions (2.8 vs. 5.6 nm) due to the dissociation of lattice dislocations into pairs of partial dislocations. A lattice image (Fig. 2) shows (1) nano-scale subfaceting of the (130) that appears to be flat in Fig. 1 into (010) and (110) facets with lengths of ~ 15 and 4 nm, respectively and (2) a direct connection between the GBD configuration and the facets, as illustrated in Fig. 3. A third pronounced feature is the strong, extended strain contrast at the facet junctions that is most clear in Fig. 1(a). An estimate of the elastic strain field that would be produced by a finite set of GBDs, as would exist in a facet, was in reasonable agreement with the observed strain contrast.[4] The size and magnitude of the strain were estimated to be sufficient to cause flux pinning. More recently, STEM-EDX studies have indicated excess copper at the facets junctions.[5] It thus appears that the facet topography, and the facet junctions in particular, are a significant cause of heterogeneity in YBCO grain boundaries.

References
1. O.M. Froehlich et al., Appl. Phys. Lett. 66(1995), 2289.
2. X.Y. Cai, I-Fei Tsu, S.E. Babcock, A. Gurevich, and D.C. Larbalestier., work in progress.
3. D.L. Kaiser et al., Appl. Phys. Lett. 51(1987), 1040.
4. I-Fei Tsu, S.E. Babcock, and D.L. Kaiser, to appear in J. Mater. Res., June(1996).
5. J.Vargas, N. Zhang, D.L. Kaiser, and S.E. Babcock, work in progress.
6. This work was supported by the NSF-MRG program under contract DMR-9214707.
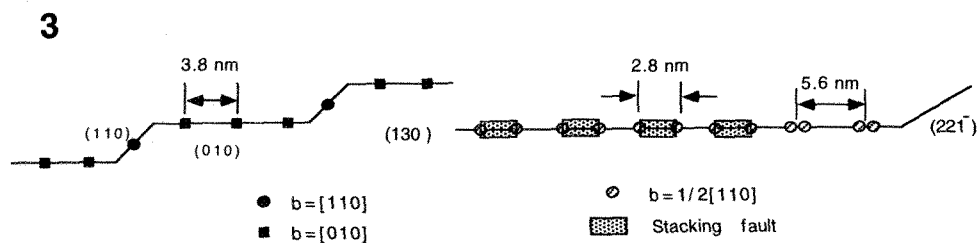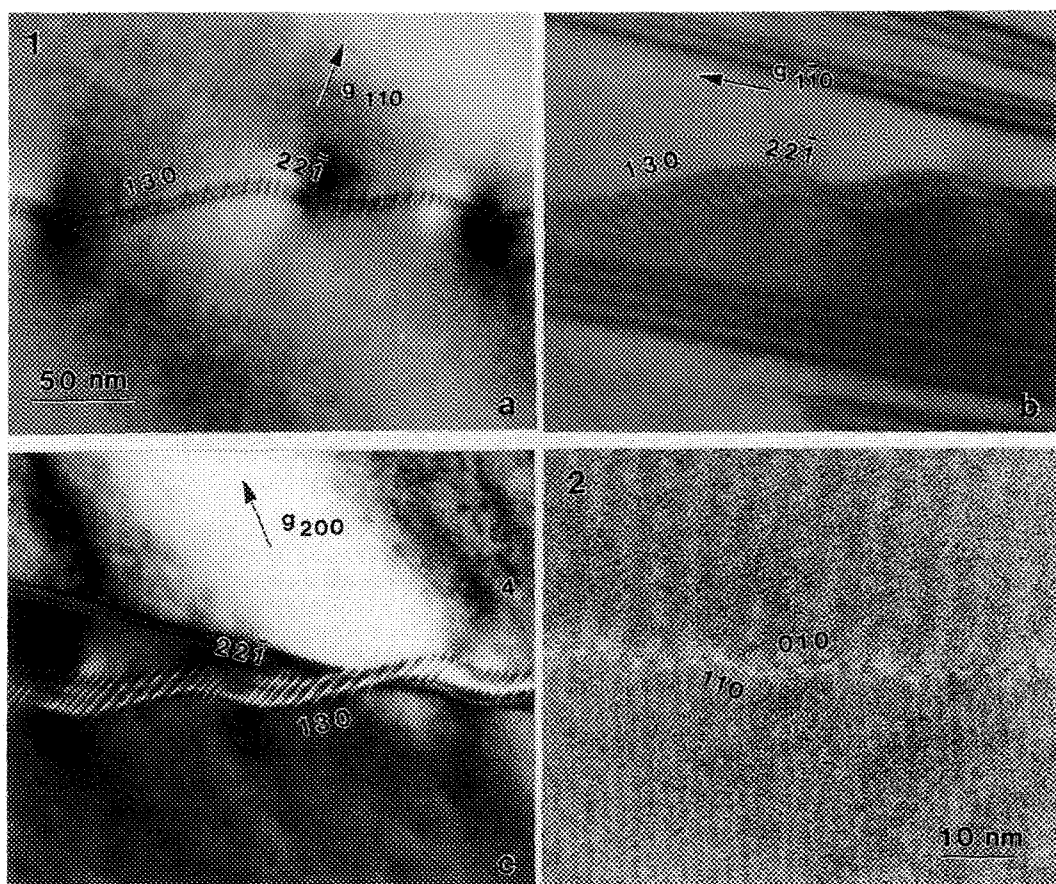
Figure 1. Diffraction-contrast TEM images of the boundary under different two-beam conditions: (a) **g** = [110], bright field; (b) **g** = [1 $\bar{1}$ 0], bright field; (c) **g** = [200], dark field.

Figure 2. HRTEM lattice image of the (130) facet with the beam aligned along [001].

Figure 3. Schematic diagram of the GBD configurations in different facets.

CHEMISTRY, BONDING AND MECHANICAL PROPERTIES OF GRAIN BOUNDARIES IN INTERMETALLIC COMPOUNDS

Shanthi Subramanian[+], David A. Muller[*], John Silcox[*] and Stephen L. Sass[+]

+ Department of Materials Science and Engineering, Cornell University, Ithaca, NY., 14853
* Department of Applied and Engineering Physics, Cornell University, Ithaca, NY., 14853

Grain boundaries in ordered intermetallic compounds have a great influence on their mechanical properties. Considerable progress has been made on characterizing the chemistry at grain boundaries experimentally and understanding their electronic structure theoretically. The approach in the present study is to experimentally examine the bonding changes at grain boundaries, in the presence and absence of dopants, using Electron Energy Loss Spectroscopy (EELS), and interpret these changes in terms of the observed mechanical properties.

EELS of transmitted electrons probes excitations which occur at unique energy losses. In the present study, the Ni $L_{2,3}$ edges were examined which select excitations from the Ni 2p orbitals to states above the Fermi level. For single electron excitations, it can be shown that the area under the sharp peaks at the onset of the $L_{2,3}$ edges is proportional to the number of holes in the Ni d band for the 3 d transition metals.[1,2] Fig. 1 shows the EELS spectra from bulk Ni, Ni_3Al and Ni_3Si. The edge intensity (historically called a white line) is reduced in Ni_3Si and Ni_3Al with respect to Ni.

EELS and Energy Dispersive X-ray spectroscopy (EDX) in a UHV STEM were used to examine the chemistry at grain boundaries in Ni-24 at % Al with and without B, and relate the changes in chemistry and bonding to cohesive strength. Fig.2. shows an Annular Dark Field (ADF) image of a large angle grain boundary in Ni_3Al with boron where the boundary appears as a bright line consistent with Ni-enrichment in a ~ 0.8 nm thick layer. The boron concentration is high in positions 'a' of the boundary and is low at positions 'b'.[3] Our observations in the inset show that segregation of B results in bulk-like bonding (and hence cohesive strength) at grain boundaries, whereas in the absence of boron the bonding at grain boundaries was similar to that of pure Ni with a narrower Ni d band.[3] This is consistent with the observed change in fracture mode from intergranular to transgranular in Ni_3Al containing B.

To obtain further insight into the effect of dopants on grain boundary properties, we extended our work to other intermetallic compounds, such as Ni_3Si. Recent work on B-doped Ni-23 at % Si has shown that B prevents environmental embrittlement but does not change the fracture mode in Ni-23 at% Si, unlike its effect on Ni_3Al.[4] Large angle grain boundaries in Ni-23 at % Si with and without B were examined using EDX with a probe size of ~1 nm. Ni-enrichment between 6 to 9 at % is seen to occur at grain boundaries in Ni-23 at % Si, both in absence and presence of B. The magnitude of Ni-enrichment is similar in both cases. From the ADF images it was seen that the width of Ni-enrichment is quite narrow (~1 to 1.5 nm) with no second phase present. Ni-enrichment at grain boundaries was also seen using Auger spectroscopy in work done by Baker et al.[5] B was not detected at any of the boundaries examined in the present work. The same alloys were examined by Auger electron spectroscopy at Oak Ridge by C.T. Liu and co-workers .[4] Their results showed that ~4 at % B is present at grain boundaries in the B-doped alloy. Since the detection limit for EELS is ~1/10th of a monolayer, it is likely that the amount of B at the grain boundary was below the detection limit .

Figs. 3 and 4 show the Ni L_3 edge recorded at large angle grain boundaries in undoped and doped Ni-23 at % Si, respectively. The EELS observations show that the bonding at Ni-rich boundaries in Ni-23 at % Si is Ni-like, i.e., the Ni d band at the grain boundary is narrower than in the bulk. This effect is seen both in the absence and presence of B. It is clear, therefore, that the bonding at Ni-rich grain boundaries is similar both in the absence and presence of B. Since B segregation was observed using Auger spectroscopy in the same alloy, we can conclude that B segregation is most likely present at the boundaries in the present study, but in an amount insufficient to have a significant effect on the bonding.
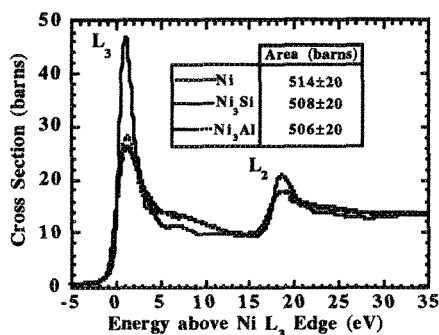
FIG. 1. Ni $L_{2,3}$ edge for bulk Ni, Ni_3Al and Ni_3Si showing the decrease in the white line intensity in the intermetallic compounds as compared to Ni.
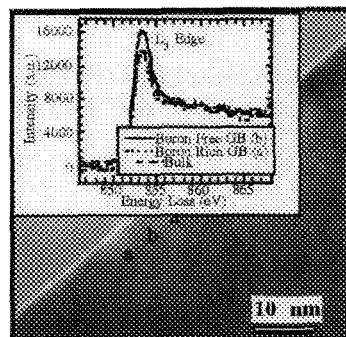
FIG. 2. ADF image of a large angle boundary in Ni_3Al with B. Inset shows the Ni L_3 edge recorded at position a and b of the boundary
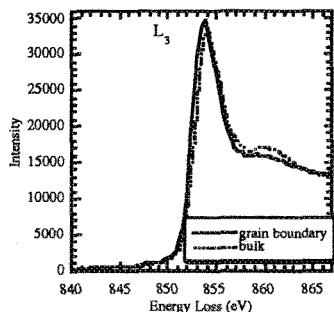
FIG. 3. EELS Ni L_3 edge at a Ni-rich large angle grain boundary in undoped Ni-23 at %Si
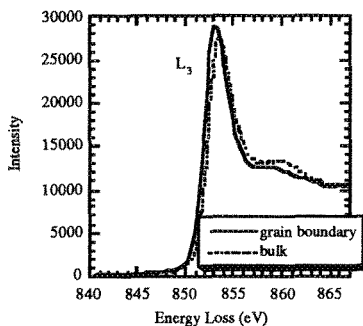
FIG. 4. EELS Ni L_3 edge at a large angle grain boundary in Ni-23 at %Si doped with 150 wppm B

Our previous work on Ni_3Al showed that a loss of hybridization (reflected in an increased white line intensity) at the boundary resulted in a high boundary energy, while B segregation made the bonding at the boundary similar to that of the bulk, i.e., lowered the boundary energy as compared to that of an undoped boundary.[6] Thus it was seen that B segregation increased the cohesive strength of boundaries in Ni_3Al. Using a similar argument, based on our observations in Figs. 3 and 4, we would expect the boundary energy to be high both in the presence and absence of B in Ni-23 at % Si. Therefore, we expect the cohesive strength of these grain boundaries to be low both in the doped and undoped material. This is consistent with the fact that the fracture mode of these alloys was intergranular even when doped with B.

References

1. L. F. Matheiss and R. E. Dietz, Phys. Rev., B22 (1980) 1663
2. D.H. Pearson, C.C. Ahn and B. Fultz, Phys. Rev.,B47 (1993) 8471
3. D. A. Muller et al., to be published in Acta Met.
4. C.T. Liu, E.P. George and W.C. Oliver, to be published in J. Intermetallics
5. I. Baker, J. Yuan and E.M. Schulson, Metallurgical Trans. A., 24A (1993) 283
6. D. A. Muller et al., Physical Review Letters, 75 (1995) 4744; D.A. Muller, in these proceedings

EELS MEASUREMENT OF THE LOCAL ELECTRONIC STRUCTURE OF COPPER ATOMS SEGREGATED TO ALUMINUM GRAIN BOUNDARIES

S.J. Splinter[a], J. Bruley[a], P.E. Batson[b], D.A. Smith[a] and R. Rosenberg[b]

[a]Department of Materials Science and Engineering, Lehigh University, Bethlehem, PA 18017
[b]IBM T.J. Watson Research Center, Yorktown Hts., NY 10598

It has long been known that the addition of Cu to Al interconnects improves the resistance to electromigration failure[1]. It is generally accepted that this improvement is the result of Cu segregation to Al grain boundaries. The exact mechanism by which segregated Cu increases service lifetime is not understood, although it has been suggested that the formation of thin layers of θ-CuAl$_2$ (or some metastable substoichiometric precursor, θ' or θ'') at the boundaries may be necessary[2,3]. This paper reports measurements of the local electronic structure of Cu atoms segregated to Al grain boundaries using spatially resolved EELS in a UHV STEM. It is shown that segregated Cu exists in a chemical environment similar to that of Cu atoms in bulk θ-phase precipitates.

Films of 100 nm thickness and nominal composition Al-2.5wt%Cu were deposited by sputtering from alloy targets onto NaCl substrates. The samples were solution heat treated at 748K for 30 min and aged at 523K for 4 h to promote equilibrium grain boundary segregation. EELS measurements were made using a Gatan 666 PEELS spectrometer interfaced to a VG HB501 STEM operating at 100 keV. The probe size was estimated to be 1 nm FWHM. Grain boundaries with the narrowest projected width were chosen for analysis. EDX measurements of Cu segregation were made using a VG HB603 STEM.

Fig. 1 shows the Cu L$_{2,3}$ energy loss spectrum obtained from a θ-CuAl$_2$ particle in the Cu-2.5Al alloy matrix after background subtraction and deconvolution of multiple scattering. The spectrum obtained from pure Cu is included for comparison. The Cu L$_2$ and L$_3$ edges at 931 eV and 951 eV energy loss respectively correspond to excitations from inner shell Cu 2p orbitals to vacant states with s-like or d-like symmetry above the Fermi level on the same Cu site. Because absorption to s-like final states is usually negligible, the area under the sharp peaks at the onset of the L$_2$ and L$_3$ edges (the so-called "white lines") can be regarded as being proportional to the number of holes in the Cu d-band[4]. Fig. 1 shows, therefore, that the white line intensity is enhanced for the θ-phase compared to pure Cu (filled d-shell), indicating that some electrons have left Cu 3d states upon compound formation. The absence of a core-level shift between CuAl$_2$ and Cu suggests that little net charge is transferred from the Cu site; instead, the enhanced white line intensity for θ-phase may be attributed to a redistribution of Cu 3d to Cu 4s states.

Fig. 2 shows an EDX line scan across a high-angle grain boundary in Al-2.5wt%Cu, clearly indicating that Cu is concentrated close to the boundary plane. The associated Cu L$_{23}$ energy loss spectrum from the grain-boundary region is shown in Fig. 3 and that from a nearby triple point is shown in Fig. 4. It is noteworthy that we were unable to detect Cu in the Al matrix by EELS, likely due to the very low solid solubility limit. Plural scattering effects have not been removed from Figs. 3 or 4 because of the relatively poor statistics obtained from the very weak signal. Nevertheless, both Fig. 3 and Fig. 4 show clear white line intensity, suggesting that the local symmetry and nearest-neighbour coordination of Cu segregated to Al grain boundaries and triple points is similar to that of Cu in θ-phase precipitates or one of its substoichiometric precursors.

References

1. R. Rosenberg, J. Vac. Sci. Tech. 9 (1971) 263.
2. D.R. Frear et. al., Met. Trans. 21A (1990) 2449.
3. D.R. Frear et. al., Mat. Res. Soc. Symp. 229 (1991) 303.
4. D.H. Pearson, C.C. Ahn, B. Fultz, Phys. Rev. B50 (1994) 12969.
5. This research was supported in part by NSF grant number DMR 93-06253.
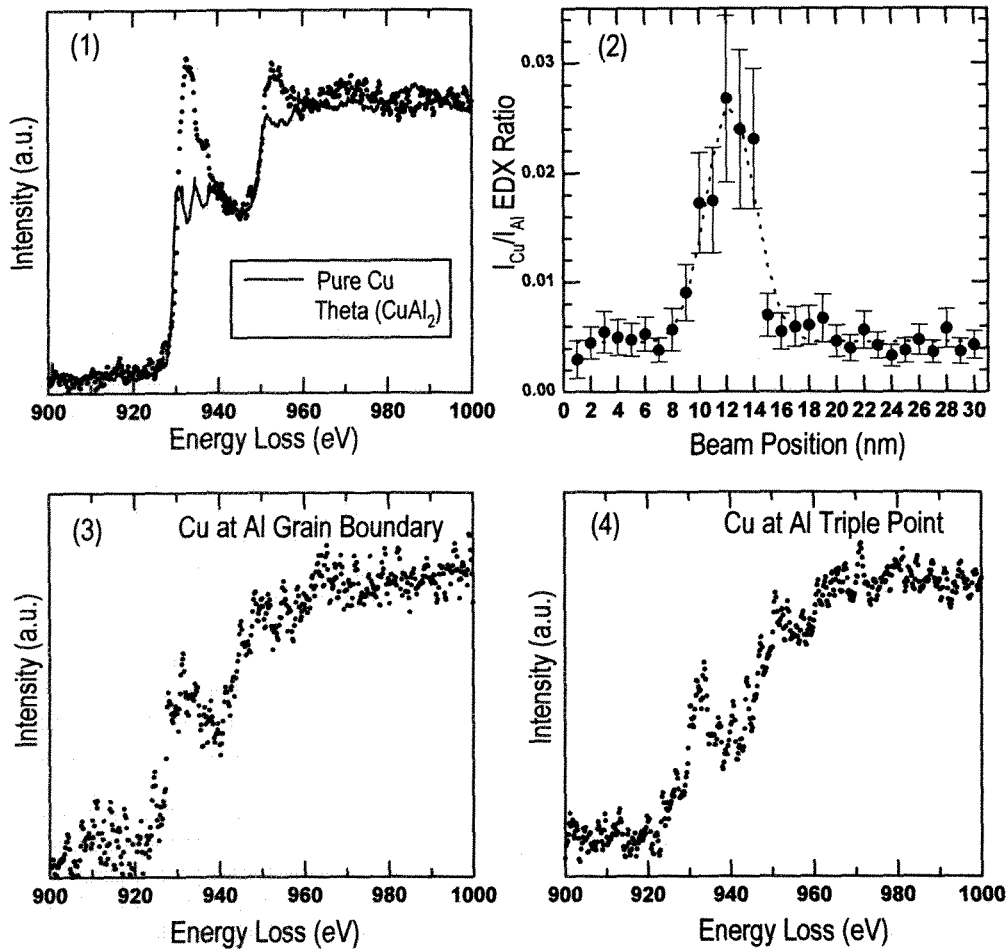
Fig. 1: Cu $L_{2,3}$ core-level energy loss spectrum of θ-CuAl$_2$ and pure Cu.

Fig. 2: EDX line scan across a high-angle grain boundary in Al-2.5Cu.

Fig. 3: Cu $L_{2,3}$ energy loss spectrum from high-angle grain boundary in Al-2.5Cu.

Fig. 4: Cu $L_{2,3}$ energy loss spectrum from triple point in Al-2.5Cu.

GRAIN-BOUNDARY CHARACTERISTICS IN AUSTENITIC STEEL

M.D.Caul and V.Randle

Department of Materials Engineering, University of Wales Swansea, Swansea SA2 8PP, U.K.

Grain boundaries are an active area of research interest due to their effect on material property and structure relationships. In order to discuss material properties with regard to grain boundaries it is necessary to know the boundary type. The optimum technique for performing this task is Electron Backscatter Diffraction (EBSD) in concert with the Scanning Electron Microscope (SEM).[1] By collecting texture measurements in the form of individual orientations from grains it is possible to obtain misorientation measurements from grain boundaries. These measurements are three of the five degrees of freedom necessary to geometrically describe a grain boundary. The other two can be obtained by a serial sectioning technique.[2]

Grain boundaries in austenitic steel specimens, isothermally aged at either 700°C or 800°C, have been evaluated with the aim of relating boundary geometry to Cr_2N precipitate formation. Samples were analysed using SEM and EBSD in order to obtain orientation measurements of individual grains to misorientations at grain boundaries and to Cr_2N precipitates. These precipitates are detrimental to room temperature properties of high nitrogen stainless steels,[3] so a reduction in their formation at grain boundaries would be advantageous. The steel is therefore an ideal candidate material for relating boundaries to material properties. The 700°C isothermally aged sample induces precipitate formation at grain boundaries whereas precipitation by cellular decomposition of austenite occurs in the 800°C sample. The 700°C sample was used to categorise boundary types using the CSL model and relate this to Cr_2N formation. The 800°C sample was used to examine the effect of aging temperature on boundary inclination. Therefore all five degrees of freedom in grain boundary geometry were obtained.

Figure 1 represents the microstructure of an austenitic stainless steel and depicts random boundaries, incoherent twins and coherent twin boundaries. The misorientations between neighbouring grains have been calculated and are shown in figure 2 for both samples using the CSL model and demonstrate that they have a similar proportion of boundary types. Figure 3 shows the percentage of boundaries with precipitate formation for each of the boundary types.[4] It is clear that random boundaries are more prone to precipitate formation than low angle boundaries and Σ type boundaries. The free volume associated with boundaries would explain this phenomena as the disordered structure in random boundaries has more free volume than low angle boundaries. Figure 3 also shows that $\Sigma=3$ or twin boundaries will exhibit precipitate formation in low numbers. On closer inspection of the microstructure (see figure 1) it can be seen that these precipitates form on *incoherent* twins rather than *coherent* twins. This can be attributed to the degree of fit at these boundaries such that the coherent twins have higher energies than incoherent twins.

Figure 4 depicts the inclination angles found in both sample types and demonstrates that the higher aging temperature results in an increase in the amount of boundaries at small angles to the sample surface. These boundaries abutted the specimen surface such that partial rotational freedom was available to reduce their specific areas. The driving force for this process is that grain boundary area correlates directly with energy. Further data manipulation is in progress to evaluate the boundaries in terms of their nearest Miller indices and enable further classification according to the interface-plane scheme.[5]

References.

1.   Randle, V., *Microtexture determination and its applications*, The Institute of Materials, London, Book 510, (1992).
2.   Caul, M.D., *A study of grain boundary geometry by use of EBSD*, MPhil Thesis, University College of Swansea, U.K., 1994.
3.   Simmons, J.W., Atteridge D.G., Micro. Sci., 20, (1993), 311.
4.   Mehta, S.C., Smith, D.A., *Grain Boundary Engineering*, A Symposium held in conjunction with the 5th Canadian Materials Science Conference, (1993), 3. Ed: Urb, U., Palumbo, G.
5.   Caul, M., Fielder, J., Randle, V., submitted to Scripta.Met. Mat.
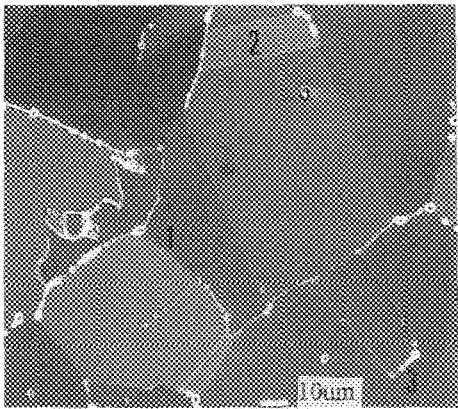
Figure 1.   Microstructure of austenitic steel showing (1) random boundaries, (2) coherent twins (3) incoherent twins.
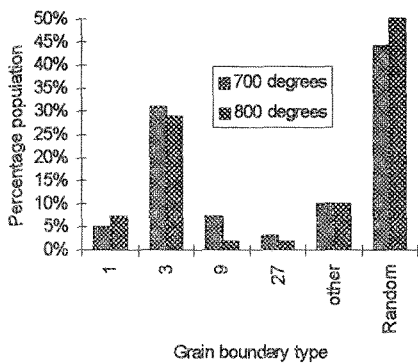
Figure 2.   Population of boundary types in austenitic steel samples.
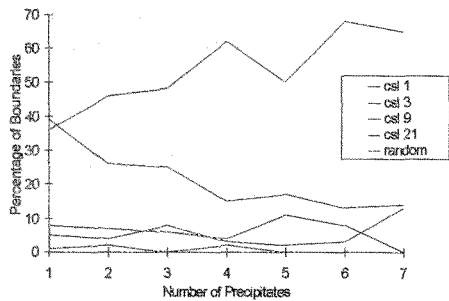
Figure 3.   The percentage of boundaries associated with precipitate formation.
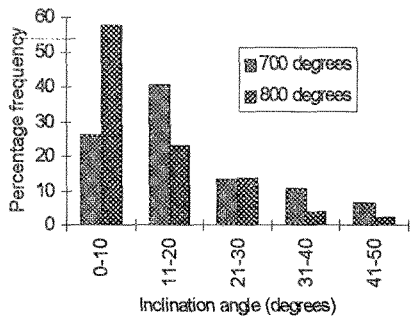
Figure 4. Inclination angles with respect to specimen surface of austenitic steel boundaries.

345

ON THE RELATIONSHIP BETWEEN GRAIN-BOUNDARY CHARACTER DISTRIBUTION AND INTERGRANULAR CORROSION

E.M. Lehockey, G. Palumbo, P. Lin, and A. Brennenstuhl

Ontario Hydro Technologies, Toronto, Ontario, Canada, M8Z 5S4

Intergranular corrosion can under severe conditions lead to "grain-dropping" which results in significant material loss. It has been demonstrated that grain boundaries described by low-Σ CSL misorientations are more resistant to corrosion, cracking (SCC), and sliding (creep) than "general" boundaries, and that the frequency of these "special" boundaries can be enhanced offering the possibility of producing materials with improved bulk corrosion and creep properties.[1,2] This contribution presents a model for predicting the effect of "special" boundaries on the extent of gross wastage from grain-dropping.

For any grain to be ejected from the matrix, *all* of its bounding interfaces must be fully compromised. Assuming "special" grain boundaries are immune to corrosion and considering a material containing hexagonal prism grains with a diameter and length, d, it can be shown that the probability, X, of observing grain-dropping at a depth, L, through the material thickness is related to the "special" boundary fraction, F_{sp}, by:

$$X = [(1 - F_{sp})^3 \, (1 - F_{sp}^3)]^{\frac{2L}{d}} \qquad \ldots Eqn \; (1)$$

Use of hexagonal prism grains slightly over-estimates in the probability of grain-dropping at depths below 1 grain diameter. Probabilities for grain-dropping at depths extending from one to four grain diameters through the material thickness are plotted as a function of "special" boundary frequency in Figure 2. Grain-dropping is predicted to decrease rapidly as F_{sp} approaches 50%; beyond which virtual immunity to grain-dropping is predicted (L<1d). Figure 3 compares the depth of a "damage layer" as a function of "special" boundary frequency predicted from corrosion by grain-dropping vs. intergranular cracking; the latter calculated from a model proposed by Palumbo et. al.[3] The depth of grain-dropping decreases more abruptly than intergranular crack penetration as "special" boundary fractions increase.

Figure 4 tabulates corrosion rates (in mm/yr) for sensitized Inconel 600 during a 24 hour immersion in a ferric sulphate-50% H_2SO_4 solution at 100°C.[4] Experimental reductions in corrosion rate with "special" boundary frequency are compared with those estimated from Equation (1). Within the limits of experimental error, the model accurately predicts the impact of increasing the "special" boundary population on the intergranular corrosion rate. Predicted reductions in grain-dropping with elevated "special" boundary frequencies, advocates considerable promise in applying a "grain boundary engineering" approach for designing corrosion resistant materials.

References

1. G. Palumbo et al., Materials Interfaces (eds. D. Wolf and S. Yip), Chapman & Hall, 190, 1992.
2. T. Watanabe, Res. Mechanica, 11, 47, 1984.
3. G. Palumbo, C. Cheung, and U. Erb, Materials Science and Engineering "A", 185, 93, 1994.
4. P. Lin, G. Palumbo, U. Erb, and K.T. Aust, Scripta. Met., 33, 1387, 1995.
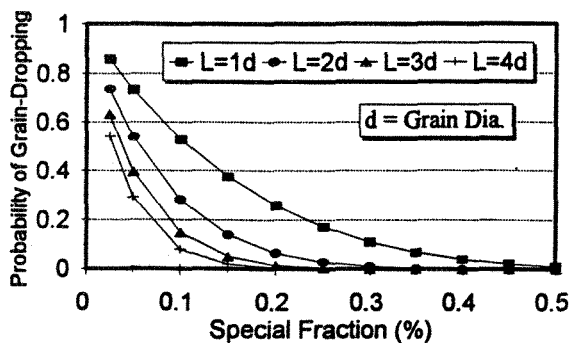
Figure 1:   Probability of grain-dropping predicted by Eqn (1) at depths between one and four grain diameters as a function of "special" boundary fraction.
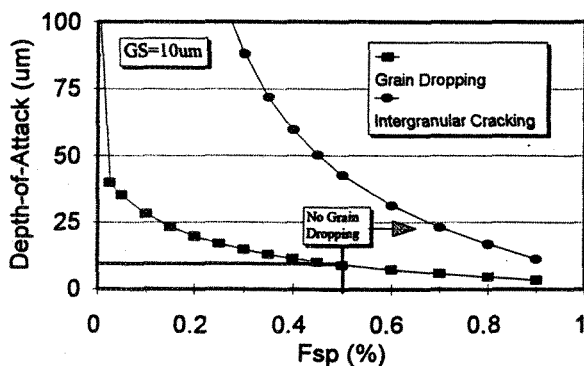
Figure 2:   Comparison in depth-of-attack calculated for grain-dropping versus intergranular cracking as a function of "special" boundary frequency.

Sample	F_{sp} (%)	Corrosion Rate (mm/yr)	Decrease in Corrosion Rate[†] (%)	
			Experimental	Predicted
Conventional	37	5.1 ± 0.4	reference	**reference**
Sample (1)	63	3.55 ± 1.1	30.4 ± 14.9	**44.6**
Sample (2)	71	2.17 ± 1.1	57.5 ± 16.9	**53.9**

[†]Decrease in corrosion rate with respect to conventionally processed material (ie F_{sp}=37%). Note: All samples contain similar grain sizes of 10μm.

Figure 3:   Decrease in the corrosion rate of sensitized I600 as a function of "special" boundary fraction observed experimentally [ref. 4] and predicted from the grain-dropping model.

347

SPATIAL RESOLUTION OF ELECTRON BACKSCATTER DIFFRACTION IN A FEG-SEM

Edward A. Kenik[*]

[*]Metals and Ceramics Division, Oak Ridge National Laboratory, Oak Ridge, TN 37831-6376

Crystallographic information can be determined for bulk specimens in a SEM by utilizing electron backscatter diffraction (EBSD), which is also referred to as backscatter electron Kikuchi diffraction. This technique provides similar information to that provided by selected area electron channeling (SAEC). However, the spatial resolutions of the two techniques are limited by different processes. In SAEC patterns, the spatial resolution is limited to ~2 μm by the motion of the beam on the specimen, which results from the angular rocking of the beam and the aberration of the probe forming lens. Therefore, smaller incident probe sizes provide no improvement in spatial resolution of SAEC patterns. In contrast, the spatial resolution for EBSD, which uses a stationary beam and an area detector, is determined by 1) the incident probe size and 2) the size of the interaction volume from which significant backscattered electrons are produced in the direction of the EBSD detector. The second factor is influenced by the accelerating voltage, the specimen tilt, and the relative orientation of scattering direction and the specimen tilt axis.

This study was performed on a Philips XL30/FEG SEM equipped with a TexSEM Orientation Imaging Microscopy (OIM) system. The signal from the EBSD detector (SIT camera) is flat-fielded and enhanced in a MTI frame storage/image processor. The Schottky FEG source provides the fine probe sizes (~10 nm) desired with sufficient probe current (~1 nA) needed for image processing with the low signal/noise EBSD signal. The EBSD detector is at ~110° to the incident beam direction (i.e.; the forward-scattered direction) and the specimen is tilted 60-80° toward the EBSD detector, in order to increase the number of forward scattered high energy electrons. For a specimen-to-screen distance of ~12 mm, the EBSD patterns subtend an angular range of ~65° by 55°. A disk specimen was cut from a directionally-solidified copper tri-crystal perpendicular to the long columnar grains of the crystal and subsequently electropolished.

Figure 1 shows the image of the grain boundary under the electron optic conditions for EBSP (20 kV, intermediate spot size, 30 μm condenser aperture) with the specimen tilted to 70.4°. The faceted nature of the boundary is evident. However, the roughness of the boundary is exaggerated by the foreshortening (~3x) in the vertical direction of the micrograph, which results from the high specimen tilt. The true included angle between the facets is ~173°. Though similar faceting of the boundary perpendicular to the plane of the specimen is possible, the boundary should be very close to the edge-on orientation. Figures 2a, b are EBSD patterns from the left and right grain at ~1 μm from the grain boundary. From these patterns the misorientation (axis, angle pair) across the boundary is [-0.61 0.64 -0.46], 56.5° and corresponds to a boundary ~8.5° from a Σ = 3 twin boundary. Figures 2c, d show EBSD patterns from ~50 nm on either side of the boundary and both exhibit only single patterns similar to Figures 2a, b, respectively. When the beam straddles the boundary, both patterns are observed at reduced intensity. The grain boundary image width for secondary electron imaging was ~80 nm, possibly indicating some preferential relief at the boundary. This effect made it difficult to reproducibly position the beam much closer to the boundary.

Similar measurements were made with the specimen rotated 90° around its surface normal. Under these conditions, the spatial resolution for EBSD should be poorer due to forward scattering of electrons from the uppermost grain into the neighboring grain. In addition, as the grain boundary is inclined ~70° from edge-on, there is a contribution from the underlying grain when the beam is located near the boundary in the uppermost grain. Initial results are consistent with this discussion. For the lower grain, single crystal patterns were observed within 100 nm of the boundary, whereas the beam had to be at least 200 nm from the boundary in the uppermost grain to observe a single crystal pattern. The dependence of spatial resolution on accelerating voltage and the constrained combination of spot size and aperture will also be discussed.[1]
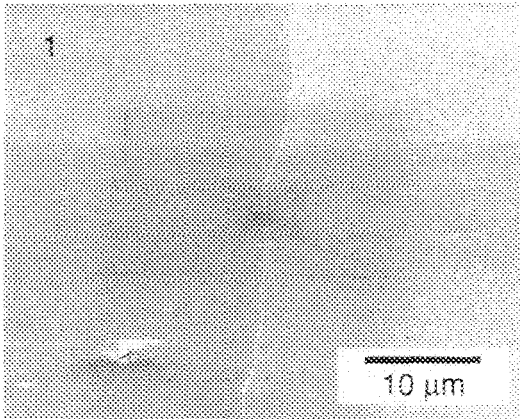
FIG. 1. SE image of faceted grain boundary aligned edge-on at a specimen tilt of 70°.

FIG. 2. EBSD patterns as a function of distance from the grain boundary. Patterns (2a, 2c) in left grain ~1 µm and ~50 nm from boundary; (2b, 2d) in right grain ~1 µm and ~50 nm from boundary.
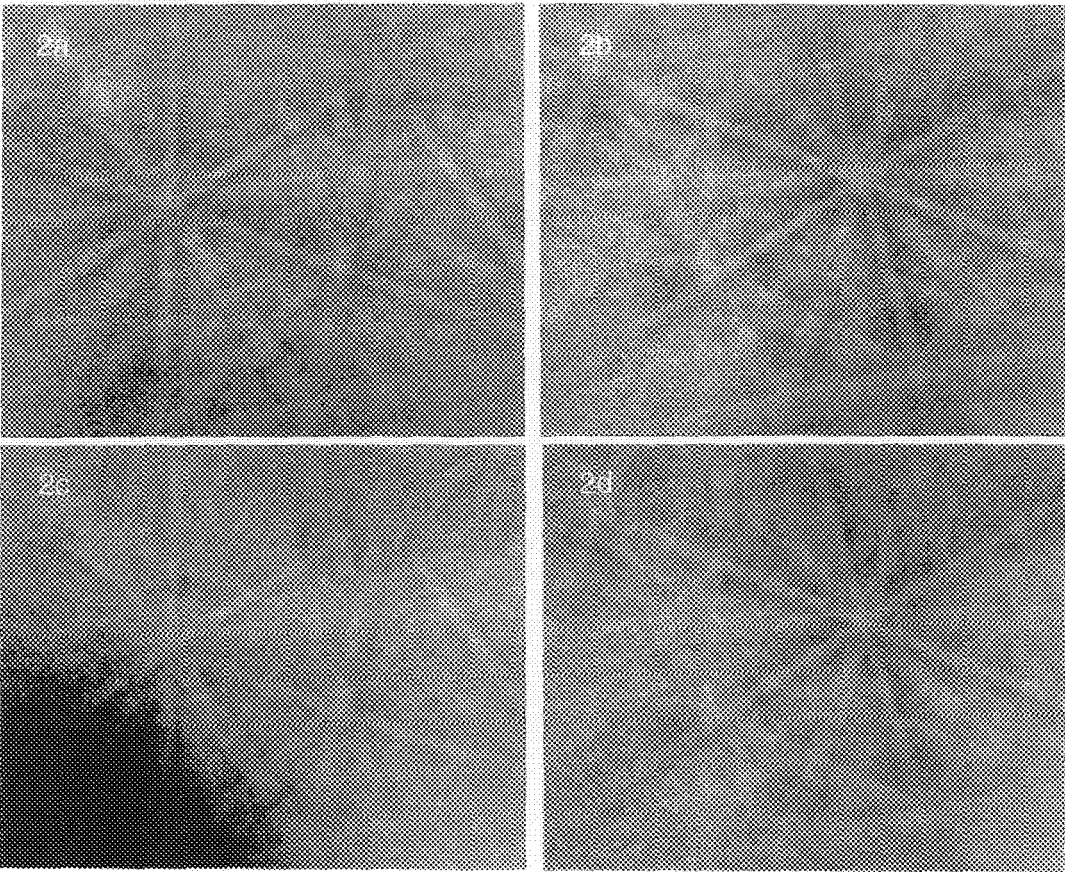
ORIENTATION IMAGING OF A Nb-Ti-Si DIRECTIONALLY SOLIDIFIED IN-SITU COMPOSITE

J. A. Sutliff and B. P. Bewlay

GE Corporate R&D, P.O. Box 8, Schenectady, NY 12301

In this paper we report on the microstructural characterization of a directionally solidified (DS) Nb-Ti-Si alloy. The solidified ingot had a nominal composition of Nb-33 at%Ti- 16 at% Si and was grown using the Czochralski technique with growth rate of 5 mm/min. The as-solidified ingot was approximately 50 mm long with a 10 mm diameter. The microstructure was examined using backscatter electron imaging and the microtexture of each of the phases was determined using the Electron BackScattering Pattern (EBSP) technique for electron diffraction in the scanning electron microscope.[1] The details of the experiments are similar to those we have reported previously.[2] Automated EBSP scans were acquired in order to map the local texture (microtexture) over most of a transverse cross-section through the ingot.

Figure 1 is a backscattered electron image (BEI) of a transverse section of the as-solidified microstructure. In this image, the bcc-Nb phase is the lighter gray phase and has a dendritic structure. The dark gray phase is $(Nb,Ti)_3Si$ having a Ti_3P crystal structure. The silicide phase appears as both multiply-faceted dendrites and irregularly bounded grains. A pattern of shading, due to Ti segregation, can be seen in figure 1 and suggests a cellular solidification structure. Figure 2 is a BEI taken at higher magnification to show a region that was analyzed by automated-EBSP. Figure 3 contains orientation images generated from the automated-EBSP data set. In Figure 3a, the color black signifies positions for which no Nb diffraction patterns could be indexed and other shades of gray signify specific Nb orientations, as described by a set of Euler angles. A similarly generated orientation image for the silicide phase is shown in Figure 3b. The greyscale image presented here is actually a rendering of a truecolor image based on a RGB triplet using the Euler angles.

From the automated-EBSP data, we draw two principle conclusions. First, the orientation images show distinct regions in which the silicide and metallic grains have a single orientation. These regions correspond to the solidification cells that were anticipated by the BEIs. Second, both phases in this composite exhibit strong texture. The silicide phase has a very strong alignment of [001] with the growth direction and significant orientation clustering in a radial direction, giving an appearance more like a single crystal than a fiber texture oriented polycrystal. This is true for additional measurements extending over many cells. The metallic phase has a less intense, broader alignment of [113] with the growth direction and has more evenly distributed fiber texture. Further analysis of the automated-EBSP data to determine additional information, such as intra- and inter-cellular misorientation distributions, will be made. These results are significant with respect to the anisotropic mehanical properties of this material.[3]

References

[1] J.A. Venables and C.J. Harland, *Philosophical Magazine*, **27** (1973) 1193
[2] J.A. Sutliff and B.P. Bewlay, Proc. 53rd Ann. MSA Meeting, (1995) 123.
[3] Funding form the Air Force Office of Scientific Research is gratefully acknowledged
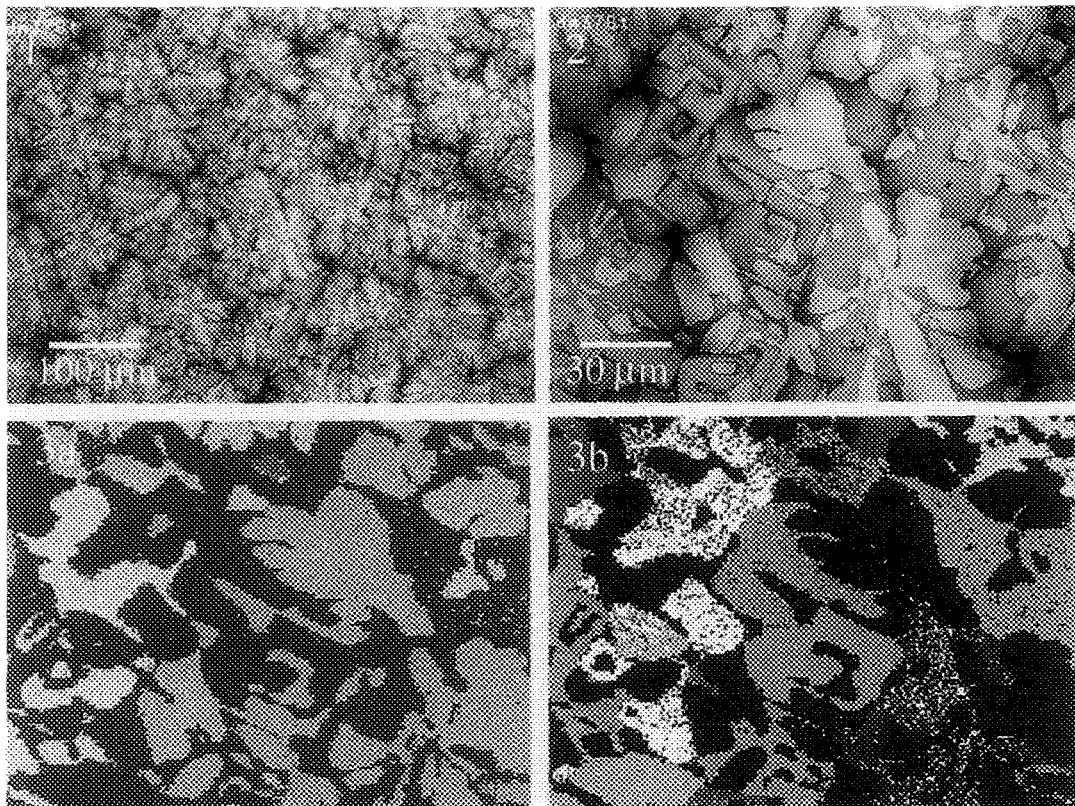
FIG. 1 - Backscattered electron image (BEI) of DS Nb-Ti-Si alloy.
FIG. 2 - A sub-region analyzed by automated-EBSP-(BEI).
FIG. 3 - Orientation images of sub-region for (a) the (Nb,Ti) phase and (b) the (Nb,Ti)$_3$Si phase.

DETERMINING DEFORMATION, RECOVERY AND RECRYSTALLIZATION FRACTIONS FROM ORIENTATION IMAGING MICROSCOPY (OIM) DATA

S. I. Wright, D. J. Dingley, D. P. Field

TexSEM Laboratories, 226 West 2230 North, Provo, UT 84604

While orientation imaging microscopy (OIM) via automatic analysis of electron backscatter diffraction patterns (EBSPs) has become routine[1,2], methods for analyzing results obtained by OIM are still maturing. Interrogating the OIM data to distinguish between deformed, recovered and recrystallized material in a polycrystalline sample is one example. An advantage for using OIM data in such a case is that the corresponding textures can also be determined providing more information regarding these processes. This work reports on two different approaches for distinguishing between these structures from OIM data on a sample of partially recrystallized low-alloy steel.

The first approach is, in a sense, patterned after that used in optical microscopy; where, deformed material can be identified because it is more deeply etched than recrystallized material. A similar approach can be used in OIM by considering the quality of EBSPs[3]. EBSPs from deformed material are more diffuse than patterns obtained from recovered or recrystallized material. At each measurement point in an OIM scan an image quality (IQ) parameter is determined for the corresponding EBSP. The IQ is mapped onto a gray scale and an image is formed from the OIM data as shown in Fig. 1. In this image the measurement points are shaded so that points with associated EBSPs of high IQ receive a lighter shade of gray than points with a lower IQ. The deformed regions can then be identified by the darker regions in the OIM map. However, this method has some drawbacks. The first is that the IQ parameter is not sensitive enough to distinguish recovered material from recrystallized material. The second is that measurement points near grain boundaries generally have lower IQ values than measurement points in the grain interiors due to the superposition of EBSPs from the two neighboring grains. This can lead to higher fractions of deformed material. This problem can be solved by only using measurement points in the grain interiors.

The second approach can be compared to that used in transmission electron microscopy (TEM) where deformed material can be identified by the tangles of dislocations present, recovered material by the ordered dislocation cells and the recrystallized material by the absence of dislocations. In an OIM scan these same features are distinguishable[4] if the scan is done on a fine enough grid by considering the misorientations between neighboring measurement points. An example is shown in Fig. 2. In this figure, the thick lines represent boundaries between pairs of measurement points with misorientations exceeding 15° whereas the thin lines represent misorientations exceeding 1°. The deformed regions are then distinguishable by the many small angle misorientations contained within the grains. While the resolution in the scan shown in Fig. 2 is not quite fine enough to see a well defined cell structure, it is sufficient to distinguish recovered and recrystallized material. In OIM scan, "grains" can be identified by collecting similarly oriented and connected points together. If 1° misorientations are used to define "similarly oriented" the deformed material would correspond to a single measurement point with no connected points oriented within 1° of it, the recovered material would have a size corresponding to several so connected points, and the recrystallized material would have a size corresponding to the grain size. In such an approach the user must then make an appropriate choice of misorientation angle for defining the structures and the choice of the number of connected points for distinguishing between dislocation cells and recrystallized grains. The spatial resolution of the OIM scan must also be fine enough to resolve the cell structures.

References

1. S.I. Wright, *Journal of Computer-Assisted Microscopy*, 5 (1993) 207.
2. B.L. Adams, *Metallurgical Transactions*, 24A (1993) 819.
3. N.-C. Krieger-Lassen, *Materials Science Forum*, 157-162 (1994) 449.
4. D.P. Field, *Materials Science and Engineering*, A190 (1995) 241.

FIG. 1. OIM map formed by mapping the IQ parameter associated with each measurement point on to a gray scale. Thick lines are drawn between neighboring measurement points with misorientations exceeding 15°.

350μm = 70 steps

350μm = 70 steps
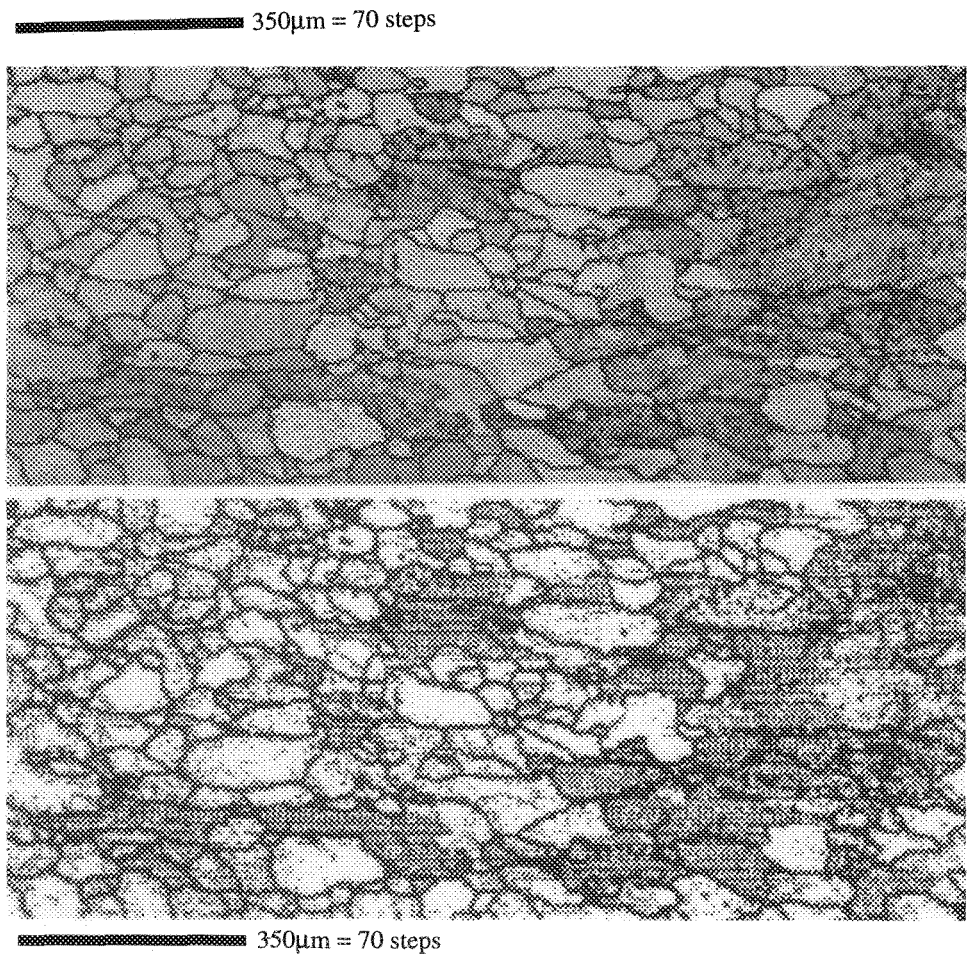
FIG. 2. OIM map formed by drawing thin lines between neighboring measurement points with misorientation exceeding 1° and thick lines between measurement pairs exceeding 15°.

SEM-ECP ANALYSIS OF GRAIN-BOUNDARY CHARACTER DISTRIBUTION IN POLYCRYSTALLINE MATERIALS

Tadao Watanabe

Laboratory of Materials Design and Interface Engineering, Department of Machine Intelligence and Systems Engineering, Faculty of Engineering, Tohoku University, Sendai, 980-77, Japan.

As demonstrated early 1980's (1), the scanning electron microcopy-electron channelling pattern (SEM-ECP) technique is very powerful in determination of orientation of individual grains and the character of grain boundaries in polycrystalline materials. Figure 1(a) and (b) show SEM and ECP images of a grain boundary in polycrystalline iron-6.5mass%silicon ribbon produced by rapid solidification and subsequent annealing. We can intuitively recognize from the SEM-ECP image that the character of the boundary is of <100> tilt type with about 7° misorientation angle. This kind of direct observation is very useful for a study of grain boundary migration and grain growth.

This paper discusses advantages of the SEM-ECP technique for the precise determination of the character of grain boundary and for statistical analysis of grain boundaries to bridge roles of individual grain boundaries and bulk properties in a polycrystal. The new microstructural parameter associated with grin boundary termed "grain boundary character distribution (GBCD)" which was introduced by the present author (2, 3) and has been utilized in designing and engineering grain boundaries in order to produce desirable and/or high bulk performance in polycrystalline materials (4, 5). GBCD describes the type and the frequency of different types of grain boundaries, ie. random general boundaries and special boundaries like low-angle boundaries and low Σ coincidence boundaries.

It has been found that the GBCD is closely related to the grain size and the frequency of special boundaries tends to decrease with increasing grain size for bulk samples of metallic materials produced thermomechanically (3). Moreover a close relationship between GBCD and the type and sharpness of texture has been recently found experimentally and theoretically (6).

Sharply {100} or {110} -textured iron-6.5mass %silicon ribbons (indicated in Fig.2(a)) can have high frequency of coincidence boundaries with specific Σ values predicted from possible coincidence orientations for <100> or <110> rotation, as indicated in Fig.2(b) and 2(c). These findings on GBCD are important clues to grain boundary microengineering aiming at designing and producing high performance and desirable properties in advanced materials. Quite recently it has been shown that "intrinsic brittleness" of polycrystalline Ni_3Al without boron can be completely controlled by introducing a high frequency of low Σ coincidence boundaries which are resistant to intergranular fracture (5).

References

1. T. Watanabe, Philosophical Magazine, A47(1983), 141.
2. T. Watanabe, Res Mechanica, 11(1984), 47.
3. T. Watanabe, Scripta METALLURGICA et MATERIALIA, 27(1992), 1497.
4. T. Watanabe, Materials Science and Engineering, A166(1993), 11.
5. T. Watanabe, Materials Science and Engineering, A176(1994), 39.
6. T. Watanabe, Textures and Microstructures, 20(1993), 195.

Fig. 1
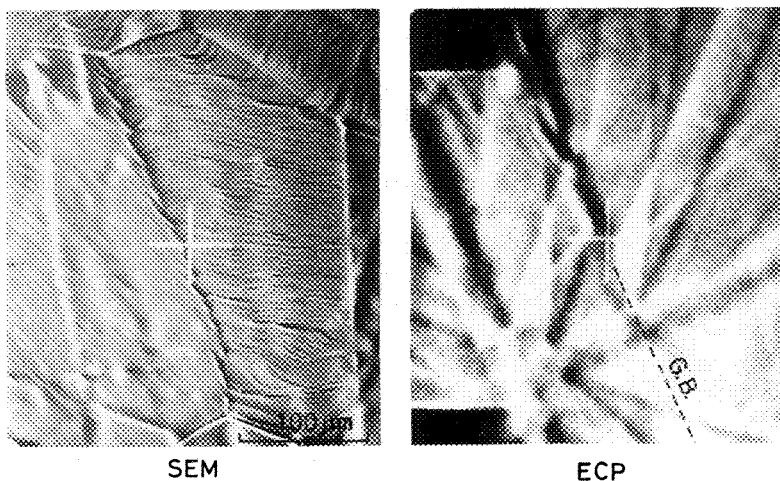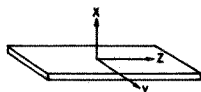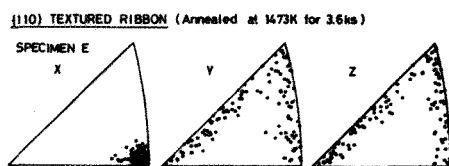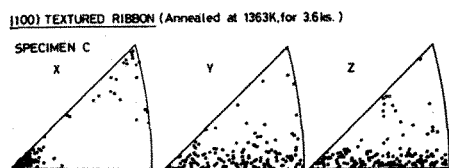
SEM   ECP

Fig. 2
(a)

(b)
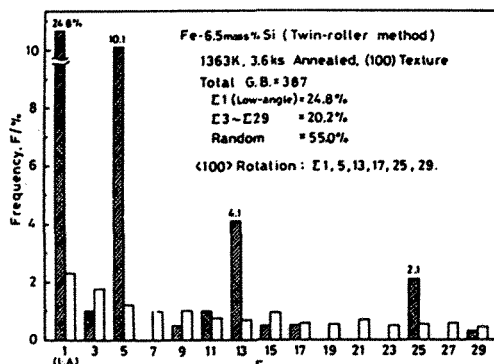
(c)
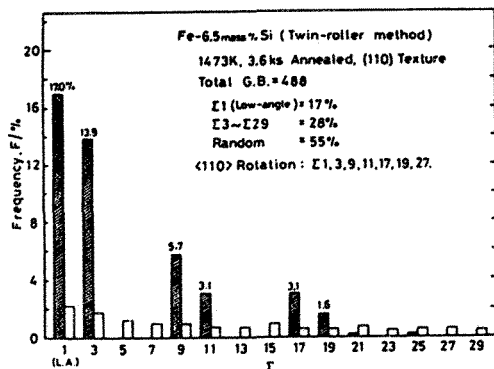
Fig. 1 (a), (b) SEM-ECP images of a grain boundary in a polycrystalline Fe-6.5mass% Si ribbon.
Fig. 2 (a), (b), (c) Grain orientation distributions and grain boundary character distributions (GBCD)
in sharply {100} or {110} -textured Fe-6.5mass % Si ribbons.

TOWARDS OPTIMIZATION OF GRAIN-BOUNDARY STRUCTURES IN ANNEALED NICKEL

C.B.Thomson and V.Randle

Department of Materials Engineering, University of Wales Swansea, Swansea SA2 8PP, U.K.

Many properties of materials are influenced by intergranular structure. Increasing the number of grain boundaries with favourable properties, or 'special' boundaries, can enhance the performance of a material in service. However, the criteria that must be satisfied for a boundary to be classified as special are not widely understood. For example, it has been shown that $\Sigma3$ coincidence site lattice (CSL) boundaries alone present a resistance to corrosion greater than for other boundary types in nickel (fcc).[1] In contrast, Rolim Lopes *et al.* observed no statistical preference for $\Sigma3$s in the grain boundary network of FeAl (bcc),[2] and Bouchet and Priester discovered that in nickel there was a weak propensity for segregation to several boundary types, including $\Sigma3$, $\Sigma11$ and $\Sigma19a$ CSLs.[3]

Commercially pure and superpure nickel specimens have been subjected to the strain annealing treatments detailed in the Table. Fig. 1 shows the results from an electron backscatter diffraction study of the commercial purity specimens (C1 to C4). It is clear that the only boundary types that increase in frequency with increased thermal processing are $\Sigma3^n$ (n=1,2,3) CSLs. An abundance of annealing twins was observed for sample C4, and is unique to this sample, and this accounts for the very high proportions of $\Sigma3$s. Samples C1 to C3 were annealed under vacuum, whereas C4 was treated in air, and it is proposed that the dominant energy minimization mechanism has changed from grain/grain boundary rotation for samples C1 to C3, to annealing twin formation for sample C4. If the structure of a grain boundary evolves towards the exact misorientation of what is considered a special CSL type, the special properties of that boundary will, in general, become more marked. $\Sigma3$s have been shown to possess special properties.[1,4] Fig. 2 shows the average deviation from exact misorientation for the $\Sigma3$s in each sample, normalised by the Brandon criterion for maximum permitted deviation.[5] This clearly indicates that the $\Sigma3$s created by annealing twin formation can be considered more special than those produced via grain/grain boundary rotations.

Fig. 3 and Fig. 4 show the results from a similar study on superpure nickel (samples S1 to S4, see Table). Despite all the annealing treatments being conducted in air, lower $\Sigma3^n$ levels than for sample C4 were observed, and analysis of the grain boundary morphologies revealed annealing twin densities similar to those in samples C1 to C3. This suggests that the dominant active energy minimization mechanism is grain/grain boundary rotation. An optimized CSL distribution seems to have been achieved for samples S3 and S4. On studying the deviations from exact $\Sigma3$ misorientation, however, a quite dramatic average reduction is observed with increased annealing time. It is proposed that this effect is a consequence of 'fine-tuning' the original grain boundary network, making use of any extrinsic grain boundary dislocations retained after attaining the optimum CSL distribution.[6] This is a potentially important result because, whereas the formation of new annealing twins improves the proportion of special boundaries in a grain boundary network, it also increases the total number of boundaries. It is therefore possible that the absolute number of 'weak' boundaries does not decrease. However, if the proportion of special boundaries is enhanced without a commensurate increase in the total number of grain boundaries, a reduction in the number of weak boundaries must occur. Such a result needs to be verified in more detail, and currently experiments utilizing more direct, structure sensitive methods, including micro/nanohardness and corrosion studies of grain boundaries, are in progress.

References

1. G.Palumbo and K.T.Aust, *Scripta Metall.* 22 (1988) 847.
2. L.C.Rolim Lopes et al., submitted to Scripta Metall.Mater.
3. D.Bouchet and L.Priester, *Scripta Metall.* 21 (1987) 475.
4. L.C.Lim and R.Raj, *Acta Metall.* 32 (1984) 1183.
5. D.G.Brandon, *Acta Metall.* 14 (1966) 1479.
6. C.B.Thomson and V.Randle, *Scripta Metall.Mater.*, in press.
7. CBT acknowledges the financial contribution of the EPSRC.

TABLE - Details of the strain annealing treatments.

Sample ID	C1	C2	C3	C4	S1	S2	S3	S4
Strain (%)	NONE	-6	-6	-6	NONE	-6	-6	-6
Heat Treatment (v=vacuum; a=air)	NONE	12H/750°C (v)	24H/750°C (v)	9H/500°C (a) + 12H/750°C (a)	NONE	9H/500°C (a) + 8H/850°C (a)	9H/500°C (a) + 48H/850°C (a)	9H/500°C (a) + 168H/850°C (a)
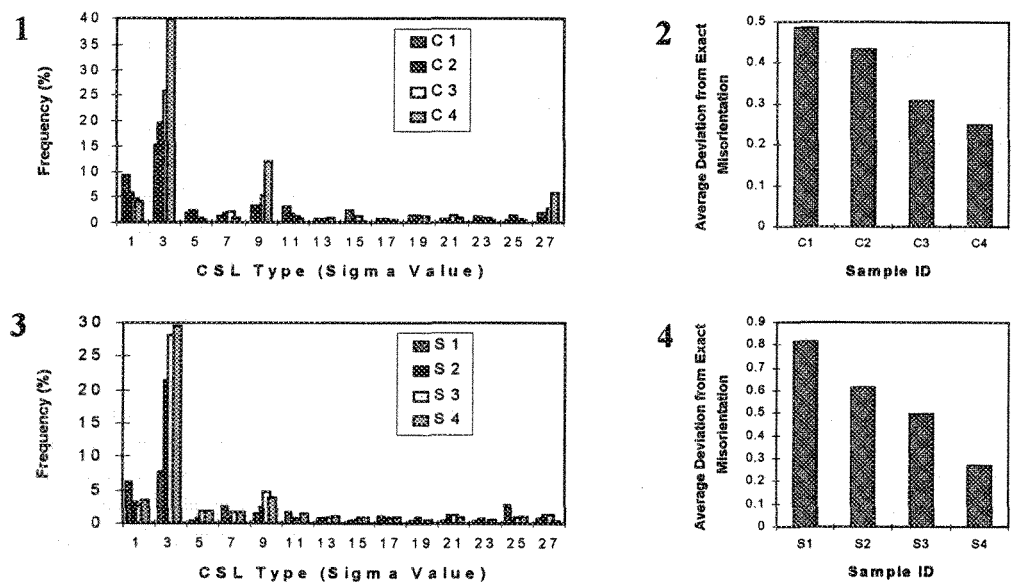
FIG. 1 CSL distribution for the strain annealed commercially pure nickel samples C1 to C4.
FIG. 2 The average deviation of $\Sigma 3$s from the ideal 60°/111 misorientation for samples C1 to C4.
FIG. 3 CSL distribution for the strain annealed superpure nickel samples S1 to S4.
FIG. 4 The average deviation of $\Sigma 3$s from the ideal 60°/111 misorientation for samples S1 to S4.

METAL MICROSTRUCTURES IN ADVANCED CMOS DEVICES

L. M. Gignac and K. P. Rodbell

IBM T.J. Watson Research Center, Yorktown Heights, NY 10598

As advanced semiconductor device features shrink, grain boundaries and interfaces become increasingly more important to the properties of thin metal films. With film thicknesses decreasing to the range of 10 nm and the corresponding features also decreasing to sub-micrometer sizes, interface and grain boundary properties become dominant. In this regime the details of the surfaces and grain boundaries dictate the interactions between film layers and the subsequent electrical properties. Therefore it is necessary to accurately characterize these materials on the proper length scale in order to first understand and then to improve the device effectiveness. In this talk we will examine the importance of microstructural characterization of thin metal films used in semiconductor devices and show how microstructure can influence the electrical performance. Specifically, we will review Co and Ti silicides for silicon contact and gate conductor applications, Ti/TiN liner films used for adhesion and diffusion barriers in chemical vapor deposited (CVD) tungsten vertical wiring (vias) and Ti/AlCu/Ti-TiN films used as planar interconnect metal lines.

A transmission electron (TEM) micrograph of the interconnection metallurgy of a typical semiconductor device is shown in Fig. 1. Here, three layers of Ti/Al-0.5%Cu/Ti-TiN metal lines are built on top of a doped epitaxial Si layer with W vias used to both join the AlCu lines together and to contact the Si substrate. Fig. 2 shows a TEM micrograph of a W contact via. The W vias contain Ti/TiN liner films and contact the Si through $TiSi_2$. A gate conductor consisting of $TiSi_2$ on polycrystalline Si is also shown in Fig. 2.

Both titanium and cobalt disilicides are used in silicon based devices. Titanium disilicide exists in two crystallographic phases: a high resistivity $C49-TiSi_2$ and a low resistivity $C54-TiSi_2$. The low resistivity phase $C54-TiSi_2$ is desirable in devices but it can be difficult to form in narrow lines (< 500 nm wide).[1] Recent x-ray diffraction (XRD) pole figures show that patterned 190 nm wide $C54-TiSi_2$ lines have a strong preferred (040) orientation.[2] In contrast, cobalt disilicide does not have a line width dependence, however its formation is very sensitive to the cleanliness of the Si surface.[3]

Although CVD tungsten via technology has significantly aided in shrinking device dimensions, sputtered Ti/TiN liner films are still required to promote adhesion and prevent interdiffusion. For small diameter, high aspect ratio vias, the step coverage of the liner films can be poor. Exposed Ti in the via during W deposition can reduce the WF_6 carrier gas and cause incomplete via filling which leads to large contact resistances. Ti/TiN liner films produced under various processing conditions have been characterized by XRD and TEM to understand how the microstructure of these films can influence the electrical performance and via reliability.

In Al interconnect lines, the microstructure is known to affect the electromigration reliability.[4] Crystallographic texture has been shown to be an important factor in determining electromigration lifetimes for films with identical grain sizes and grain size distributions.[5] Texture influences mass

transport by defining the grain / grain misorientations along a line, which determines the rate of grain boundary diffusion. In bamboo lines (one grain per linewidth) the role of surface diffusion is also important. Crystallographic texture determines both the grain to grain misorientaion at the grain boundary and the grain surface orientation. The effect of the oxide (SiO_2) surface roughness[6] on texture in Ti/Al-Cu films and local texture effects on reliability[7] will be discussed.

References

1. J.B. Lasky, et al., IEEE Trans. Electron. Devices, **ED-38**, 262 (1991).
2. V. Svilan, et al, in press, Adv. Metallization for Future ULSI, MRS Proc., Spring (1996).
3. K. Maex, Mat. Sci. Eng., **R11**, 53 (1993).
4. S. Vaidya and A. K. Sinha, Thin Solid Films, **75**, 252 (1981).
5. D.B. Knorr, et al., Appl. Phys. Lett., **59**, 3241 (1991).
6. H. Onoda, et al., Jpn. J. Appl. Phys., **34**, L1037 (1995).
7. K. P. Rodbell, et al., in press, Polycrystalline Thin Films II, MRS Proc., Fall (1995).
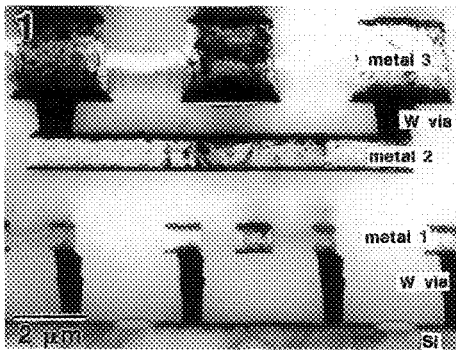
Fig. 1. TEM cross-section of typical CMOS semiconductor device.
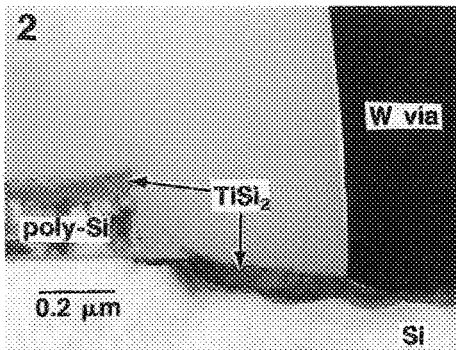
Fig. 2. TEM cross-section of a W via contacting $TiSi_2$. Also shown is a $TiSi_2$-polysilicon gate.

RESOLUTION AND SENSITIVITY OF ELECTRON BACKSCATTERED DIFFRACTION IN A COLD-FIELD EMISSION SEM

T.C. Isabell and V.P.Dravid

Department of Materials Science and Engineering, Northwestern University, Evanston, IL 60208

With the advent and development of automated beam control and pattern identification software, the use of electron backscattered diffraction (EBSD) as an analytical tool has increased in recent years. EBSD has been used to determine local crystallography and identification of phases[1], texturing of polyscrytalline materials[2], ion implantation damage[3] and the extent of crystal deformation[4]. X-ray diffraction yields crystallographic information, but with lateral resolution on the order of a millimeter. TEM provides local information with resolution of a few angstroms, but this is only over a small lateral region of electron transparency and with poor statistics. EBSD provides a true link between the local crystallographic data and real space information.

The tradeoff between sensitivity and spatial resolution is inherent in all analytical techniques. EBSD is no exception, and determining this tradeoff for this technique is the focus of our work. In a specimen with minimal interfacial strains, as the electron beam is brought near a crystal boundary, the interaction volume of scattered electrons will straddle both crystals, resulting in an overlapped Kikuchi pattern on the imaging phosphor. By aligning such a boundary parallel to the incident electron beam, the "best case" lateral resolution of EBSD can be determined by taking patterns as the probe is stepped in known increments across the boundary. Likewise, the "worst case" resolution can be determined by orienting the boundary perpendicular to the electron beam and stepping the probe. These two cases are shown schematically in Figure 1.

A specimen of well annealed (grain size of a few mm) polycrystalline nickel was used to carry out such experiments. The specimen was mechanically polished followed by a chemical polish to ensure the removal of any surface damage. A straight, long grain boundary was then oriented parallel to the incident electron beam for EBSD and a stationary probe of 20nm diameter was stepped across the boundary. Figure 2 is a typical backscattered diffraction pattern from a bulk area away from the boundary. Figures 3a and b show patterns taken with a beam voltage of 30kV, 3a with the probe at the interface and 3b at the distance where pattern overlap first disappears. The Ni specimen was then removed from the microscope and reoriented so the same boundary was perpendicular to the beam. Figures 4a and b show patterns taken across the boundary in this manner.

Similar experiments were conducted for accelerating voltages of 20kV and 10kV. With the boundary oriented parallel to the electron beam, the distance at which no pattern overlap was detected did not vary with decreasing voltage. This can be explained by the elongation of the interaction volume in a direction parallel to the incident beam. For instances with the boundary perpendicular to the beam direction, the extent of pattern overlap decreased with decreasing voltage, indicating improved lateral resolution in this direction as the interaction volume decreases. All experimental results will be presented and compared to Monte Carlo simulations of the interaction volume. In all, our experiments conducted here show an orientation dependence on the spatial resolution of the technique, showing that any orientation imaging microscopy (OIM) conducted should be interpreted appropriately.

1. Dingley, D.J., Alabaster, C. and Coville, R., *Inst. Phys. Conf. Ser* **98** 451-454 (1989)
2. Dingley, D.J., Randle, V., *J. Mater. Sci.,* **27** 4545-4566 (1992)
3. Troost, K.Z., *Appl. Phys. Lett.* , **63** [7] 958-960 (1993)
4. Wilkinson, A.J., and Dingley, D.J., *Acta Metall* , **39**[12] 3047-3055 (1991)
5. Research supported by the National Science Foundation, grant no. DMR-9203722 and NSF Materials Research Center, grant no. MRL-9120521.
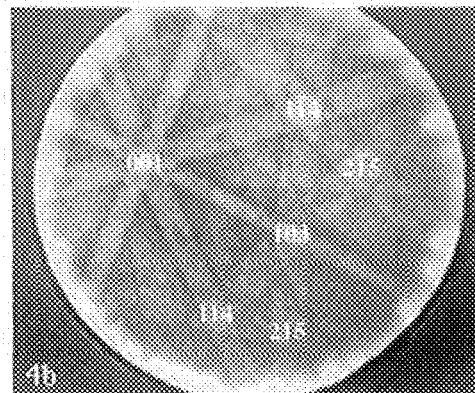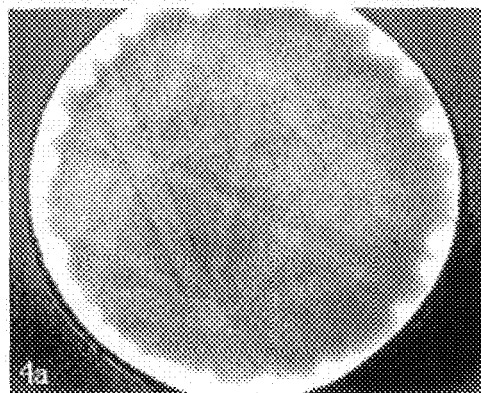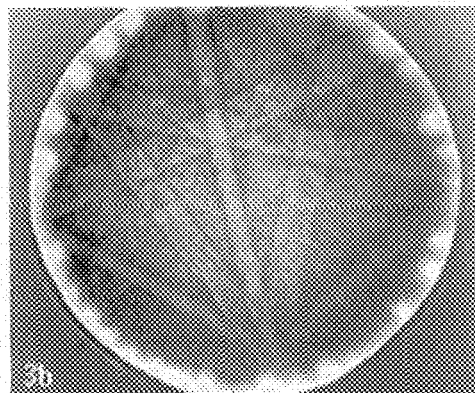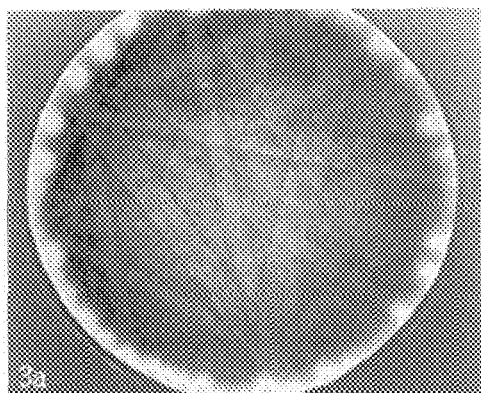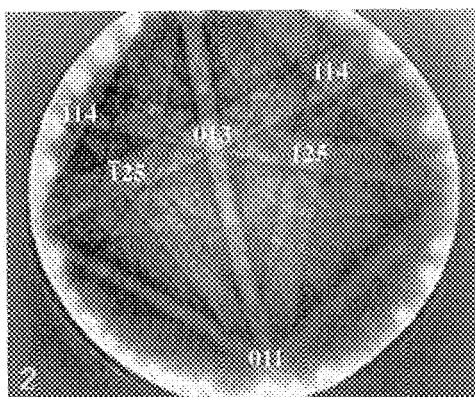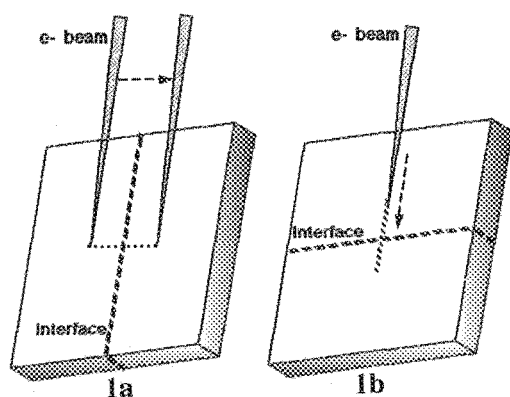
Figure 1. Schematic of experimental procedure
Figure 2. Bulk Ni EBSP
Figure 3. EBSP from a) interface and b) distance where overlap of patterns no longer occurs for boundary parallel to electron beam.
Figure 4. EBSP from a) interface and b) distance where overlap of patterns no longer occurs for boundary perpendicular to electron beam.

361

GRAIN BOUNDARY ENGINEERING FOR INTERGRANULAR FRACTURE AND CREEP RESISTANCE

G. Palumbo*, E.M.Lehockey* P. Lin*, U. Erb** and K.T. Aust***

*   Ontario Hydro Technologies, 800 Kipling Avenue, Toronto, Canada, M8Z 5S4
**   Dept. of Materials and Metallurgical Engineering, Queen's University, Kingston, Canada K7L 3N6
***   Dept. of Metallurgy and Materials Science, University of Toronto, Toronto, Canada M5S 1A4

Previous studies (see review[1]) have shown that grain boundaries crystallographically described by low Σ Coincidence Site Lattice (CSL) relationships can often display a high resistance to intergranular sliding, cavitation, and fracture; these boundaries satisfying Brandon's criterion [2] ($\Delta\theta \leq 15^o \Sigma^{-1/2}$), for $\Sigma \leq 29$. Figure 1 summarizes the grain boundary structure-dependence of intergranular cracking on stressed C-rings (0.5% strain) of Alloy 600 (75Ni-15Cr-10Fe) following autoclave exposure to 10% NaOH at 350°C for 3000 hours.[3] Grain boundaries connected to intergranular crack paths were characterized using electron backscattered diffraction (EBSD) in a SEM. As shown in Fig. 1, general grain boundaries ($\Sigma > 29$) are the preferred paths for intergranular cracking; 'special' grain boundaries ($\Sigma \leq 29$) show a high resistance to intergranular attack.

In quantifying the effect of 'special' grain boundary frequency on bulk intergranular cracking susceptibility, a geometric model has been formulated [4] which considers that a propagating crack can arrest at a triple junction when both of the available intergranular paths for crack continuation are inaccessible owing to either (1) intrinsic resistance to cracking (e.g., low Σ CSL grain boundary) or (2) unfavourable orientation to the applied stress axis. Figure 2 summarizes the effect of 'special' grain boundary frequency on the probability of intergranular crack propagation as predicted by this model. Increasing the fraction of 'special' grain boundaries by only moderate amounts can considerably reduce the maximum attainable intergranular crack length in a material. For example, the probability of a crack propagating beyond 5 grain diameters is approximately 35% in a material having 15% special grain boundaries; the probability is reduced to approximately 1% in a material containing 45% 'special' grain boundaries, and to less than 0.001% in a material containing 75% special grain boundaries. These concepts have been recently applied in developing a proprietary thermomechanical processing methodology [5] which serves to increase the frequency of special grain boundaries in austenitic stainless alloys to values in excess of 60%; such a treatment having been demonstrated to render Alloy 600 (see Fig.1) immune to intergranular cracking.

The effect of special grain boundary frequency on the bulk creep performance of 99.99% Ni at 84MPa and 450°C (grain boundary sliding regime) is shown in Fig.3.[6] Increasing the frequency of 'special' grain boundaries (by thermomechanical processing) from 13% to 66% results in a 16-fold reduction in steady state creep rate and a 6-fold reduction in primary creep strain. Consistent with the previous intergranular fracture analysis, a moderate increase in special boundary frequency from 13% to 45% yields the greatest reduction in the creep strain parameters. Microstructural evaluation of the specimens following testing to 1.8% total strain showed that (1) cavitation had occurred exclusively at general grain boundaries (i.e., $\Sigma > 29$) and (2) no cavities were formed in the material containing 66% special grain boundaries.

The results of this study provide considerable promise for a 'grain boundary engineering' approach towards the mitigation of intergranular -creep and -fracture in practical engineering materials.

References

1. G. Palumbo, and K.T. Aust, in Materials Interfaces (D. Wolf and S. Yip eds.), Chapman and Hall, London, 1992, p. 190.
2. D.G. Brandon, Acta Metall., 14(1966), 1479.

3. R. Langer, G. Palumbo and U. Erb, to be published.
4. G. Palumbo et al., Scripta Metall., 25(1991), 1775.
5. G. Palumbo, US Patent Pending.
6. E.M. Lehockey and G. Palumbo, Mater. Sci. Eng. A (submitted for publication).
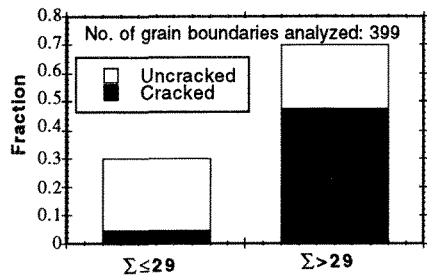
FIG. 1. Grain boundary character distribution along crack paths in Alloy 600 C-rings.[3]
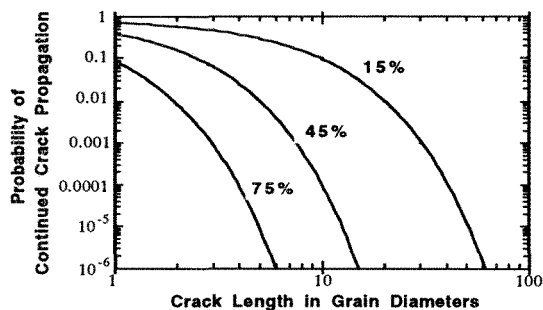
FIG. 2. Probability of continued intergranular crack propagation as a function of crack length and 'special' boundary frequency.
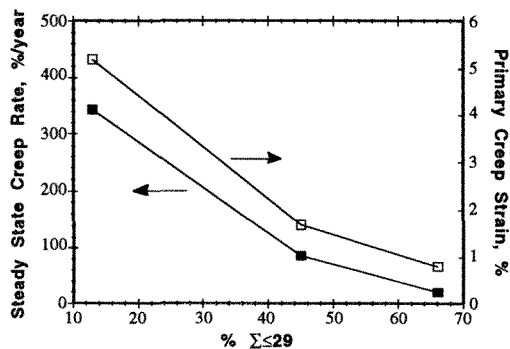
FIG. 3. Effect of special grain boundary frequency on creep strain parameters for 99.99% Ni stressed to 84MPa at 450°C. [6]

EQUILIBRIUM SHAPES OF Pb INCLUSIONS AT 90° TILT GRAIN BOUNDARIES IN Al

E. Johnson[1,2], U. Dahmen[1], S.-Q. Xiao[1], A. Johansen[2]

[1]Niels Bohr Institute, Ørsted Laboratory, University of Copenhagen, Denmark.
[2]National Center for Electron Microscopy, LBNL B72, Berkeley CA 94720.

Ion implantation of lead in aluminum leads to spontaneous phase separation and formation of dense distributions of nanosized lead inclusions[1]. The inclusions have fcc structure, and despite the large lattice mismatch (a_{Al} = 0.4048 nm and a_{Pb} = 0.495 nm) they grow in parallel-cube topotaxy with the matrix. Their shape is cuboctahedral with larger {111} facets and smaller {100} facets which is the minimum-energy shape for an fcc crystal in equilibrium with its vapor, as calculated by considering only nearest neighbor bonds. Implantation of polycrystalline aluminum films is accompanied by preferential nucleation and enhanced growth of inclusions in the grain boundaries. In adapting their equilibrium shape, grain boundary inclusions will be subject to a larger number of constraints than inclusions in the bulk matrix. This may result in a variety of morphologies characteristic for different types of grain boundaries.

In the present study we have used a well-defined bicrystal geometry to study the morphology and structure of lead grain boundary inclusions in mazed bicrystal aluminum films containing mainly 90° <110> tilt boundaries with fixed misorientation but variable inclination[2]. It was found that the shape, size and orientation of the inclusions in the grain boundaries depend on the inclination, i.e. the orientation of the grain boundary plane. Inclusions were all single crystalline and invariably faceted toward one aluminum grain and more rounded toward the other grain (fig.1). Independent of grain boundary inclination, the faceted side was a section of the cuboctahedral equilibrium shape of inclusions in parallel topotaxy with the bulk aluminum matrix. The rounded side, where the inclusions were rotated by 90° with respect to the aluminum lattice, approximated a spherical cap consisting partly of somewhat flatter segments with complex faceting, illustrating the lack of distinctly flat low-energy facets.

The equilibrium shape of a grain boundary inclusion can be determined by a generalized Wulff construction (see inset schematics). The two equilibrium Wulff shapes (a sphere and a cuboctahedron) are superimposed on the grain boundary and then translated into the opposite grain until the distance between the Wulff centers corresponds to the grain boundary energy of the aluminum matrix. The two equilibrium shapes truncate each other across the grain boundary such that only the part of each equilibrium shape which remains in its own grain, survives. The final morphology is a composite of the two equilibrium shapes, and depends on the relative magnitude of the energy of the grain boundary (the distance between the Wulff centers), the energy of the 90° Pb/Al interface (the radius of the sphere), and the energy of the topotaxial Pb/Al interface (the distance between opposite facets of the cuboctahedron).

Figure 1 illustrates the dependence of the inclusion shape on the boundary inclination: (a) and (b) show symmetrical (557/55$\bar{7}$) boundaries with inclusions in two approximately mirror-related shapes, whereas (c) and (d) show asymmetrical (110)/(001) boundaries where inclusions can take different shapes depending on the grain with which they maintain a parallel-cube orientation relationship. The generation of the equilibrium shape from mutual truncation of two intersecting equilibrium shapes across the boundary is illustrated in the inset schematics. Efforts to use these observations to measure relative interface energies as a function of inclination are currently underway.

References
1. S.-Q. Xiao, E. Johnson, S. Hinderberger, A. Johansen, K.K. Bourdelle and U. Dahmen, J. Microscopy, **180** (1995) 61.
2. E. Johnson, S. Hinderberger, S.-Q. Xiao, U. Dahmen and A. Johansen, Interface Sci., in press.
3. J.W. Cahn and D.W. Hoffman, Acta Metall. **22** (1974) 1205.
4. C. Rottman, Scripta Metall. **19** (1985) 43.
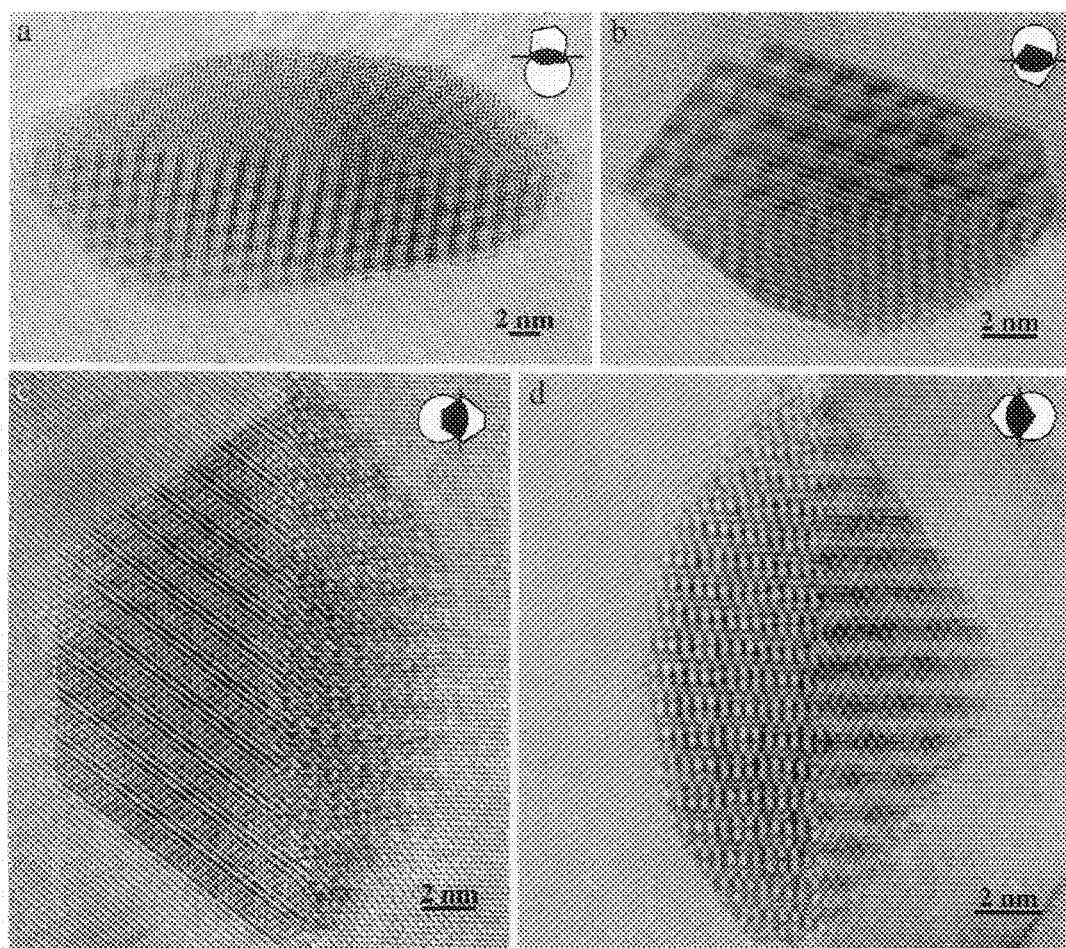
Fig. 1: High resolution micrographs of typical Pb grain boundary inclusions in Al showing the effect of boundary inclination on the inclusion shape. All four images show 90° <110> tilt boundaries. For the symmetrical inclination (557/55$\bar{7}$) in (a) and (b) the inclusion can take two equivalent mirror-related orientations. For the asymmetrical inclination (110)/(001), there are two different equilibrium shapes (c) and (d), depending on the orientation of the faceted segment.

365

ON THE FACETING OF POLAR CERAMIC SURFACES: MICROSCOPY AND HOLOGRAPHY STUDIES OF MGO(111) SURFACES

M. Gajdardziska-Josifovska[*], B. G. Frost[**], E. Völkl[**] and L. F. Allard[**]

[*]   Department of Physics and Laboratory for Surface Studies, University of Wisconsin Milwaukee, P.O. Box 413, Milwaukee WI 53201
[**] High Temperature Materials Laboratory, Oak Ridge National Laboratory, Bethel Valley Road 1, Oak Ridge, TN 37831-6064

Polar surfaces are those crystallographic faces of ionically bonded solids which, when bulk terminated, have excess surface charge and a non-zero dipole moment perpendicular to the surface.[1] In the case of crystals with a rock salt structure, {111} faces are the exemplary polar surfaces. It is commonly believed that such polar surfaces facet into neutral crystallographic planes to minimize their surface energy.[1] This assumption is based on the seminal work of Henrich which has shown faceting of the MgO(111) surface into {100} planes giving rise to three sided pyramids that have been observed by scanning electron microscopy.[2] These surfaces had been prepared by mechanical polishing and phosphoric acid etching, followed by Ar^{+} sputtering and 1400 K annealing in ultra-high vacuum (UHV). More recent reflection electron microscopy studies of MgO(111) surfaces, annealed in the presence of oxygen at higher temperatures, have revealed relatively flat surfaces stabilized by an oxygen rich ($\sqrt{3}$x$\sqrt{3}$)R30° reconstruction.[3] In this work we employ a combination of optical microscopy, transmission electron microscopy, and electron holography to further study the issue of surface faceting.

Single crystals of MgO were oriented with the use of X-ray Laue backscattering and cut with a diamond saw parallel to a {111} crystallographic plane. After mechanical polishing with a sequence of diamond, alumina and sytone abrasives, some samples were etched in boiling phosphoric acid to investigate the effect of this chemical reaction on the surface topography. The acid removes the layers damaged by mechanical polishing, and gives a smooth shiny surface on visual inspection. However, a closer look under an optical microscope revealed a (111) surface made of pyramids with {100} faces, as illustrated in Fig. 1. Previously it was believed that the faceting occurs during annealing in UHV, as the clean polar surface rearranges itself into a collection of neutral facets,[2] but our results indicate that such faceting must have been present on the surface as a consequence of the chemical polishing.

The effects of annealing on the polar surface was examined with the use of plan view electron-transparent samples which were prepared by dimpling followed by eighter a phosphoric acid etch, or by 5KeV Ar^{+} ion milling. The perforated samples were annealed in alumina muffle tube furnaces under a steady flow of research grade oxygen. A temperature of 1500°C was maintained for 24 hours, with a heating and cooling rate of 100°C/hour. Optical microscopy of all annealed samples did not show visible surface faceting. Bright field TEM confirmed the absence of triangular facets, both for samples prepared by chemical etching (Fig. 2a) and by ion-milling (Fig. 2b). Therefore, even when the surface starts faceted, as in the case of the acid perforated samples, oxygen annealing at high temperatures removes the {100} facets.

Electron holography experiments were undertaken to obtain a quantitative view of the projected surface topography. A Hitachi HF-2000 field emission electron microscope was used, equipped with a Möllensted type biprism and with a slow-scan CCD camera. The microscope was operated in a free lens mode to enable recording of holograms with a large width of the interference pattern.[4] Fig. 3 shows the phase (a) and amplitude (b) images reconstructed from a representative hologram of an ion-milled and annealed sample. This sample was tilted away from the [1$\bar{1}$1] zone to a weekly diffracting orientation, resulting in a phase image which is linearly proportional to the projected specimen thickness. The phase image is more sensitive to surface topography than the amplitude image, though both confirm the absence of {100} surface faceting. In conclusion, we show that faceting of the polar MgO(111) surface into neutral planes is a result of acid etching, rather than a basic surface property. We also show that this faceting is removed by annealing in oxygen at atmospheric pressure. Further studies are planned to explore if these conclusions would be altered by annealing in UHV.[5]

References:

1. V. E. Henrich and P. A. Cox, *The Surface Science of Metal Oxides*, Cambridge Univ. Press (1994)
2. V. E. Henrich, *Surf. Sci.* 57 (1976) 385.
3. M. Gajdardziska-Josifovska at al., *Surf. Sci. Lett.* 284(1991)L259; P. A. Crozier at al., *Microscopy Research and Technique* 20 (1992) 426.
4. B. G. Frost et al., in *Electron Holography*, Eds. A. Tonomura et al., Elsevier (1995) 169.
5. Help by M. H. Malay, M. A. Schofield and D. V. Josifovski with parts of sample preparation are acknowledged. Work at UWM was supported under grants NSF/DMR-9553148 and NSF/BIR-9413762. Microscopy studies at Arizona State University were sponsored under NSF/DMR-9115680. Holography studies were sponsored by the Assistant Secretary for Energy Efficiency and Renewable Energy, Office of Transportation Technologies, as part of the High Temperature Materials Laboratory Fellowship Program, Oak Ridge National Laboratory, managed by Lockheed Martin Energy Research Corp. for the U.S. Department of Energy under contract number DE-AC05-96OR22464
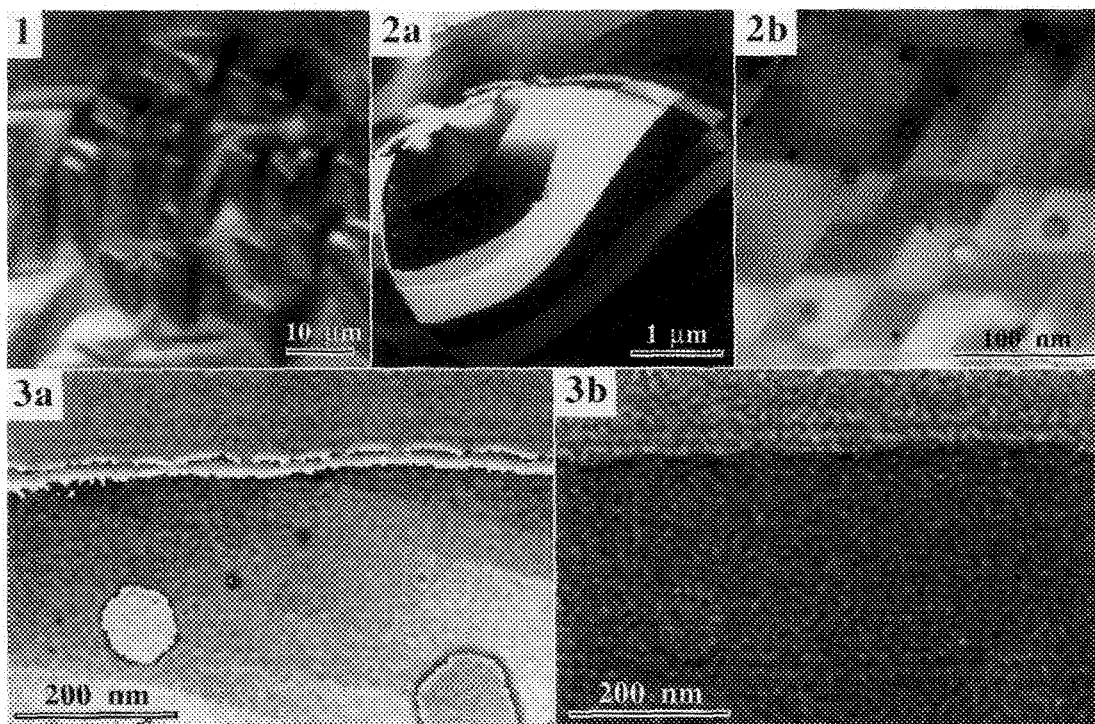
Fig. 1 Optical micrograph of MgO(111) surface after etching by boiling phosphoric acid for 2 minutes. Note pronounced surface faceting into three sided pyramids with {100} faces.

Fig. 2 Bright field images of MgO(111) samples annealed in oxygen at 1500°C. Note the absence of {100} faceting both in samples prepared by: a) phosphoric acid etching, and b) ion milling.

Fig. 3 Phase (a) and amplitude (b) images reconstructed from an electron hologram showing absence of surface faceting on annealed MgO(111) sample.

AFM AS A TOOL FOR STUDYING CERAMIC SURFACES

Jason R. Heffelfinger, Michael W. Bench, Matthew T. Johnson and C. Barry Carter

Department of Chemical Engineering and Materials Science, University of Minnesota,
421 Washington Ave. S.E., Minneapolis, MN 55455

Atomic-force microscopy (AFM), which is a relatively new technique, has found an invaluable niche in the imaging of insulating surfaces.[1-2] AFM allows for analysis of topographical details at the atomic level with minimum sample preparation.[3] Unlike scanning electron microscopy (SEM), AFM sample preparation requires no conductive coatings that may cover small surface features. The real power of the AFM lies in its ability to directly measure the heights of various surface features such as surface steps and particulates that measure as small as a few tenths of a nanometer in size. This technique does have limitations, and image artifacts, such as broadening of surface structures and ghost images of the tip, arise from the finite size and shape of the contacting probe.[4] In the present investigation, AFM is used to characterize ceramic surfaces in a variety of experiments which range from surface faceting to solid-state reaction studies.

AFM studies were performed on a multi-mode, Nanoscope III (Digital Instruments, Santa Barbara, CA) using microfabricated Si_3N_4 cantilevers. The cantilevers were Cr coated to avoid charging effects between the tip and specimen. All images were recorded in air with a nominal applied force of 10-15 nN. AFM samples which were used to study the effect of surface faceting were prepared from polished single crystals. To remove surface damage and create a faceted surface, these sample were annealed at 1400°C for different amounts of time in air. Special precautions were taken to minimize the exposure of the surfaces to any contamination from the furnace environment during annealing. Solid-state reactions experiments were performed by reacting a cleaved {001} MgO surface with a Fe_2O_3 powder for 6 hours at 1450°C in air.

The flat surfaces of polished and annealed ceramic single crystals are ideal candidates for analysis by AFM. Features on these surfaces tend to measure a few nanometers in height and are often not seen in the SEM. Figure 1 shows an AFM line plot profile of the $\{10\bar{1}0\}$ α-alumina surface that has been annealed for 2 hours at 1400°C. Exaggerated in the vertical direction, this image shows an individual facet that is ~5 nm in height and several microns in length. Faceting of this surface was found to start with the nucleation and growth of individual facets. Further annealing leads to the formation of a hill-and valley surface morphology, as discussed elsewhere.[5] Figure 2 is an AFM image of an (0001) α-alumina surface that has been annealed for 5 minutes at 1400°C. In this image regions of greater brightness correspond to areas of greater height. Smaller steps that measure only ~0.2 nm in height have bunched together to form a larger step which measures ~ 1.3 nm in height. Steps of 0.2 nm in height are approximately one sixth the unit cell height of alumina along the [0001] direction. This image demonstrates the vertical resolution of the AFM by being able to measure 0.2 nm high steps and the horizontal resolution by showing steps which are spaced some 20 nm apart. Horizontal resolution is greatly dependant on the sharpness of the AFM tip. Figure 3 is an AFM image of an {001} $LaAlO_3$ surface which has been annealed for 6 hours at 1400°C. Single crystals of $LaAlO_3$ inherently contain twin boundaries which are associated with a phase transformation during cooling.[6] Since the crystals are polished at room temperature (i.e. when the twins are present), there is a slight difference in misorientation of the surface on either side of the twin. Figure 3 shows the effect of this misorientation and the different surface morphologies that occur on either side of the twin boundary. Figure 4 is an AFM line plot profile of an Fe_2O_3 powder that was reacted with a cleaved {001} MgO surface. This image shows a step on the MgO surface and particles of spinel, $MgFe_2O_4$, the reaction product between the powder and substrate. Regions of spinel are seen both on the terraces and along the MgO step. The abundance of spinel along the MgO step suggests that the step may be a favorable location for the reaction to occur. This work demonstrates the many useful applications of AFM to the analysis of ceramic materials.[7]

References:
1. H. G. Hansma, et al., Science, **256** 1180-1184 (1992).
2. D. Rugar and P. K. Hansma, Physics Today, **43** 23 (1990).
3. G. Binnig, C. Gerber, E. Stoll, T. R. Albrecht and C. F. Quate, Surface Science, **189/190** 1-6 (1987).
4. T. Thundat, et al., Scanning Microscopy, **6** [4] 903-910 (1992).
5. G. W. Berkstresser, A. J. Valentino and C. D. Brandle, Journal of Crystal Growth, **109** 467 (1991).
6. J. R. Heffelfinger, M. W. Bench and C. B. Cartrer, Surface Science, **343** L1161-L1166 (1995).
7. Research is supported by the U. S. DoE under Grant No. DE-FG02-92ER45465. JRH and MTJ are supported by the Center for Interfacial Engineering, which is a National Science Foundation Engineering Research Center. The AFM is part of this research center. The authors thank Dr. Susie Yang for technical assistance on the AFM.
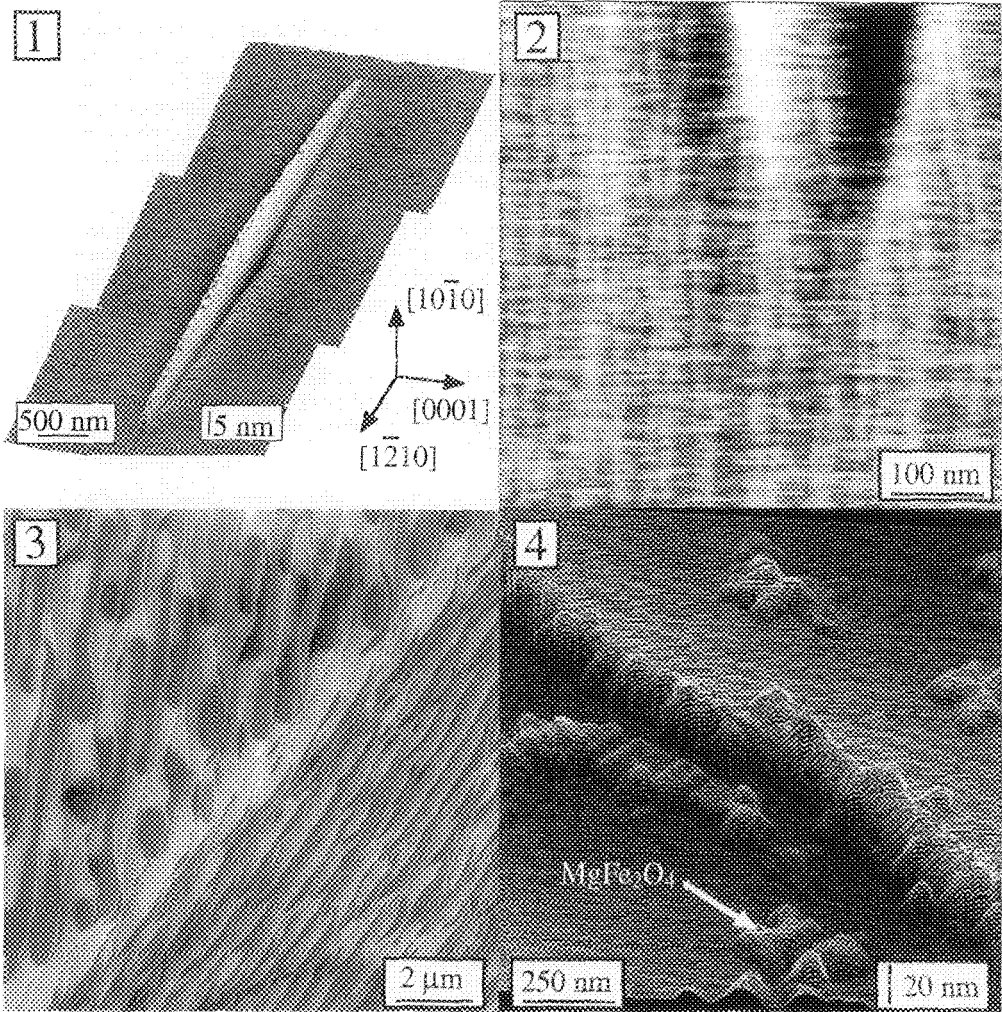
Fig. 1 is a line-plot AFM image showing an individual facet on the {10$\bar{1}$0} alumina surface. Fig 2. is an AFM image showing step bunching on the (0001) alumina surface. Fig. 3 is an AFM image of the {001} LaAlO$_3$ surface showing a region which contains a twin boundary. Figure 4 is an line-plot AFM image of the {001} MgO surface which has been reacted with Fe$_2$O$_3$ powder.

369

THE VARIATION OF (1 0-1 0) SURFACES OF SAPPHIRE BETWEEN DIFFERENT ANNEALING TIME AND TEMPERATURES[1] USING REFLECTION ELECTRON MICROSCOPY (REM) [1]

Tung HSU, Guo Hung SU, and Yootaek Kim*

Materials Science Center, National Tsinghua University, Hsinchu, TAIWAN 30043, R.O.C.
*Department of Materials Engineering, College of Engineering, Kyonggi University, Yiui-dong, Jangan-ku, Suwon, Kyonggi-do, REP. OF KOREA

The (1 0 -1 0) surface of sapphire (α-Al_2O_3), one of the prismatic surfaces, is a high energy surface [2,3]. Therefore, upon annealing, this surface breaks down into two sets of facets of lower energies. The two facets have been indexed and have been found to start developing along defects of the polished (1 0 -1 0) surfaces [4, 5]. The goal of this study was to observe the very beginning of the development of these facets under various temperatures. The technique employed was reflection electron microscopy (REM) [6, 7] which is very sensitive to irregularity on crystal surfaces and has been successfully applied to the study of other low index surfaces of sapphire [8-10].

The sapphire specimens used in this experimental were manufactured with the edge-defined film -fed growth (EFG) method by Saphikon, Inc., Milford, NH. Specimen orientation was confirmed with the reflection Laue camera. The specimens were polished by hand to 0.1 μm. Annealing was done in a Lindberg tube furnace, with a heating rate of 200°C/hr and maximum temperatures of 1000°C to 1400°C maintained for 0.1 hr to 40 hr.

The REM observations were made in a commercial JEM-200CX electron microscope operated at 100 kV. All specimens are inspected in the [1 1 -2 0] azimuth since the surface corrugation is along this direction. Foreshortened REM images recorded in this azimuth clearly show the two major facets. A perspective view of the experimental condition is shown in Fig. 1.

Facetting appeared to reach a stable configuration, as shown in Fig. 2, after a very short period of annealing at 1400°C. Holding the temperature for 0.1 or 20 hours did not make a significant difference. When the maximum temperature was 1000°C and held for 10 to 40 hours, facetting was barely detectable under REM (Fig. 3). The non-uniformity of the facet distribution was due to polishing marks (clearly visible in Fig. 3), crystalline defects, etc.

It was found that the well developed and atomically flat facets are {1 -1 0 1}[4, 5]. The other set of facets are not atomically smooth and not exactly of the same index. They are curved and have the same zone axis of <-1 1 0 1> [4].

Further study is in progress, with attempts to image the facetting at an even earlier stage than that in Fig. 3. This will push the sensitivity of REM to its limit and will provide a better picture of the facetting processing of sapphire.

REFERENCES

1. Supported by NSC 83-0208-M-007-058, 84-2112-M-007-047, and 85-2112-M-007-024, R.O.C.
2. M. Causa, R. Docvesi, C. Pisani, C. Roettti, Surface. Sci., 215 (1989) 259-271.
3. S. Blonski and S.H. Garofalini, Surface. Sci., 295 (1993) 263-274.
4. Yootaek Kim, Ph.D. dissertation, University of Utah, 1991.
5. Michael W. Bench, Jason R, Heffelfinger, and C. Barry Carter, in Proceedings of Microscopy and Microanalysis 1995, 334-335.
6. Microscopy Research and Technique, Vol. 20, No. 4, (1992) a special issue featuring current research on REM, guest ed. T. Hsu.

7. Ultramicroscopy Vol. 48, No. 4 (1993) pp. 365-496, a special issue featuring invited papers for
  an REM symposium at the 5th Asian Pacific Electron Microscopy Conference, Beijing, China, 1-6
  August, 1992, guest eds. L.-M. Peng and K.H. Kuo.
8. Y.T. Kim and T. Hsu, Surface Sci., 275 (1992) 339-350.
9. Y.T. Kim and T. Hsu, Surface Sci., 258 (1991) 119-130.
10. Y.T. Kim and T.Hsu, Surface Sci., 258 (1991) 131-146.
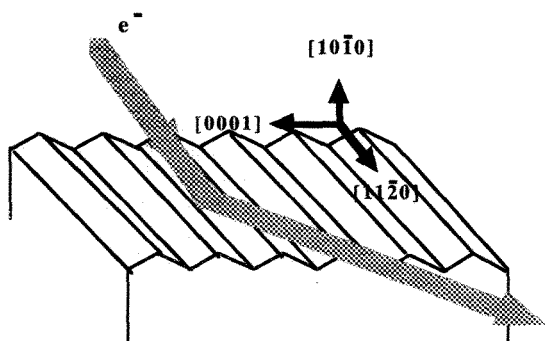
Fig 1. The perspective view of exprimental conditons.
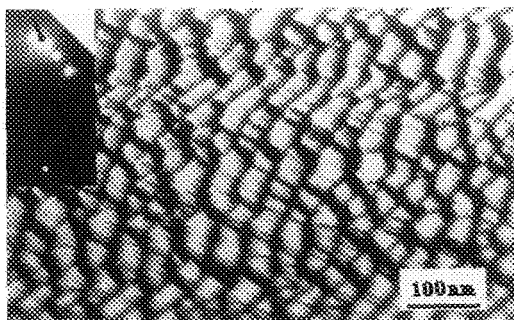
Fig 2. The REM image and its RHEED pattern of ($\bar{1}$ 0 -1 0) after annealing at 1400°C for 16 hours. The RHEED spot indicated with the beam stop was used for forming the image.
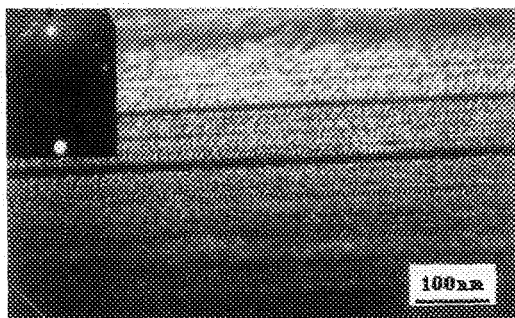
Fig 3. The REM image and RHEED pattern of ($\bar{1}$ 0 -1 0) after annealing at 1000°C for 40 hours. The RHEED spot indicated with the beam stop was used for forming the image.

371

Microstructure of artificial 45° [001] tilt grain boundaries in YBCO films grown on (001) MgO

Y. Huang[a], B.V.Vuchic[a], D.B.Buchholz[b], K.L.Merkle[a] and R.P.H.Chang[b]

[a] Material Science Division, Argonne National Laboratory
[b] Dept. of Materials Science and Engineering, Northwestern University

It is well known that high-angle grain boundaries in $YBa_2Cu_3O_{7-x}$ (YBCO) show weak-link effects and behave as Josephson junctions. This kind of grain boundary junction (GBJ) has potential applications in magnetic field measurement and electronic devices. This work studies the microstructure of artificially made GBJs in YBCO films on (001) MgO and the mechanism of the boundary formation, with the goal to improve the GBJ quality and obtain a better understanding of the junctions' transport properties.

Ion-sputter-induced epitaxy[1] is used to form YBCO films with isolated 45° [001] tilt grain boundaries. Prior to YBCO film growth the (001) MgO substrate is selectively sputtered by a low energy Ar ion beam. A portion of the substrate remains non-sputtered by protecting the surface with a patterned photoresist mask. After removing the mask, a YBCO film is grown on the substrate using pulsed organometallic molecular beam epitaxy (POMBE)[2]. Under suitable conditions single crystal YBCO c-axis films can be reproducibly obtained in both the sputtered and non-sputtered regions. The orientation between the films and the substrate has been examined by both x-ray diffraction and electron diffraction. The in-plane orientation relation is $[1\bar{1}0]_{YBCO}//[100]_{MgO}$ on the non-sputtered epitaxially polished MgO and $[100]_{YBCO}//[100]_{MgO}$ on the sputtered MgO. Thus, 45° tilt boundaries are formed in the film at the boundary between the sputtered and non-sputtered substrate regions.

TEM samples are prepared by mechanical polishing and Ar ion milling. Care is taken to keep them from exposure to moisture and elevated temperature. The samples are examined in a JEOL-4000EXII and a Hitachi HF2000. Fig.1-2 are plan-view images of the boundary. There is no second phase on the boundary except for a few Y_2O_3 particles often observed in YBCO films. One of the most obvious feature of the boundary is that it meanders across the straight line defined by the photoresist. It is easy to see in dark field TEM image (fig.1) that the interpenetration between the two sides can be over 100 nm. Another important feature is the preference for asymmetric facets at which the (100) plane on one side is parallel to the (110) plane of the other side. About 70% of the boundary is formed by this kind of facet. A cross-section view of a typical boundary is shown in fig.3. At the edge of the sputtered region there is a small step formed by the ion sputtering(indicated by an arrow). The 45° boundary, indicated by the curved black line, starts about 40 nm from the edge of the sputtered region. The boundary is initially inclined but becomes practically pure tilt at a distance of 20 nm from the substrate. The vertical features at the boundary are Moiré fringes which is believed to be caused by the crystal overlap in the beam direction due to the meandering of the boundary. The fact that the GBs are free of secondary phases and formed by well connected asymmetric facets explains the relatively high critical current supported by the sputter-induced GBJs. The boundary meandering and inclination may in part be responsible for the complex behavior in the magnetic field dependence of the junction critical current[3].

The microstructural difference of the YBCO/MgO interfaces in the sputtered and non-sputtered regions is shown in fig. 4 and 5 . The interface in the non-sputtered region is flat, sharp and free of precipitates. The periodical features indicated by arrows are caused by interfacial dislocations. Except in the immediate vicinity of the interface no distortions are observed in either sides of the interface, presumably because most of the strain caused by the lattice mismatch is relieved by the interfacial dislocations. The interface in the sputtered region, however, is relatively rough. Between YBCO film and MgO substrate there is an intermediate layer of 2-5 nm thick. Rutherford backscattering spectroscopy of the as-sputtered MgO surface indicates that the ion sputter process implants an amount of W and Ar corresponding to 0.8 and 1 monolayer, respectively, into the top 3 nm of the surface. The source of the W is the hot W filament in the Ar ion gun. High-resolution EDX confirms that W is present in the interface layer of the sputtered region. The detection of W in the interface region is significant in that it may plays an important role in the mechanism of the sputter-induced rotation discussed by Buchholz et al[4]. The initial growth of the film may be affected by the W present in the surface layer of the MgO substrate. This is still being investegated.[5]

References:
1. B.V.Vuchic, K.L.Merkle, K.A.Dean, D.B.Buchholz, R.P.H.Chang and L.D.Marks, J. Appl. Phys. 77 (1995) 2591
2. D.B.Buchholz, S.J.Duray, D.L.Schulz, T.J.Marks, J.B.Ketterson and R.P.H.Chang, Mater.Chem.Phy. 36 (1994) 377
3. B.V.Vuchic, K.L.Merkle, K.A.Dean, D.B.Buchholz, R.P.H.Chang and L.D.Marks, to be published on Physica C.
4. D.B.Buchholz et al, to be published on Appl. Phys. Lett.
5. Work supported by the NSF grant #DMR 91-20000 (YH) and DOE grant #W-31-109-ENG-38 (KLM).
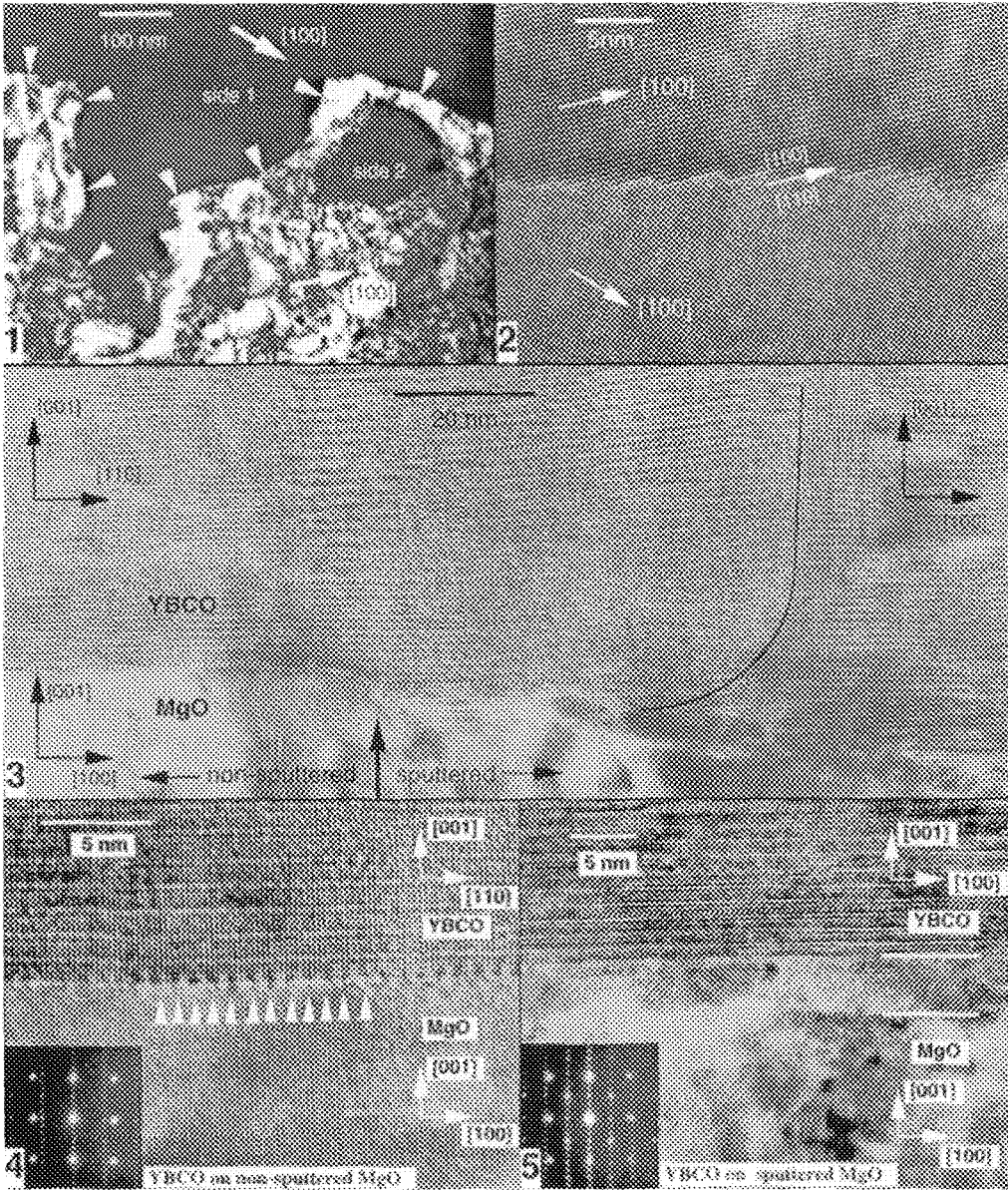
High-Temperature Instability Of A Cr_2Nb-Nb(Cr) Microlaminate Composite

M. Larsen, R.G. Rowe and D.W. Skelly

General Electric Corporate Research and Development
P.O. Box 8, Schenectady, NY 12301

Microlaminate composites consisting of alternating layers of a high temperature intermetallic compound for elevated temperature strength and a ductile refractory metal for toughening may have uses in aircraft engine turbines. Microstructural stability at elevated temperatures is a crucial requirement for these composites. A microlaminate composite consisting of alternating layers of Cr_2Nb and Nb(Cr) was produced by vapor phase deposition. The stability of the layers at elevated temperatures was investigated by cross-sectional TEM.

The as-deposited composite consists of layers of a Nb(Cr) solid solution with a composition in atomic percent of 91% Nb and 9% Cr. It has a bcc structure with highly elongated grains. Alternating with this Nb(Cr) layer is the Cr_2Nb layer. However, this layer has deposited as a fine grain Cr(Nb) solid solution with a metastable bcc structure and a lattice parameter about half way between that of pure Nb and pure Cr.[1] The atomic composition of this layer is 60% Cr and 40% Nb. The interface between the layers in the as-deposited condition appears very flat (figure 1). After a two hour, 1200 °C heat treatment, the metastable Cr(Nb) layer transforms to the Cr_2Nb phase with the C15 cubic structure.[1] Grain coarsening occurs in the Nb(Cr) layer and the interface between the layers roughen. The roughening of the interface is a prelude to an instability of the interface at higher heat treatment temperatures with perturbations of the Cr_2Nb grains penetrating into the Nb(Cr) layer.

The interfacial instability is apparent when the 1200 °C, two hour heat treated sample is given an additional heat treatment at 1300 °C for eight hours. Grains of the Cr_2Nb phase are seen to protrude into the Nb(Cr) layer (figure 2). This is readily seen in figure 3 which is an x-ray map using CrKα x-rays. The Cr_2Nb phase, which is bright in this image, is seen to penetrate deep into the Nb(Cr) layer. There are regions where near complete bridging of the ductile Nb(Cr) layer by the brittle intermetallic layer is occurring.

Closer examination of the penetrating Cr_2Nb grains reveal that they are growing into the Nb(Cr) layer along the Nb(Cr) columnar grain boundaries. The Nb(Cr) grain boundary ahead of the penetrating Cr_2Nb grains are depleted in Cr with respect to the surrounding Nb(Cr) matrix region (figure 4). Transportation of Cr along these grain boundaries is assisting the growth of the Cr_2Nb grains into the Nb(Cr) layers. Examination of the Cr-Nb phase diagram suggests that a chemical driving force resulting from a Nb(Cr) layer supersaturated in Cr and a Cr_2Nb layer high in Nb could be the explanation for this interfacial instability.

References

1. M. Larsen, et al., Proceeding of the 52nd Annual Meeting of MSA, 1994, p. 706-707.
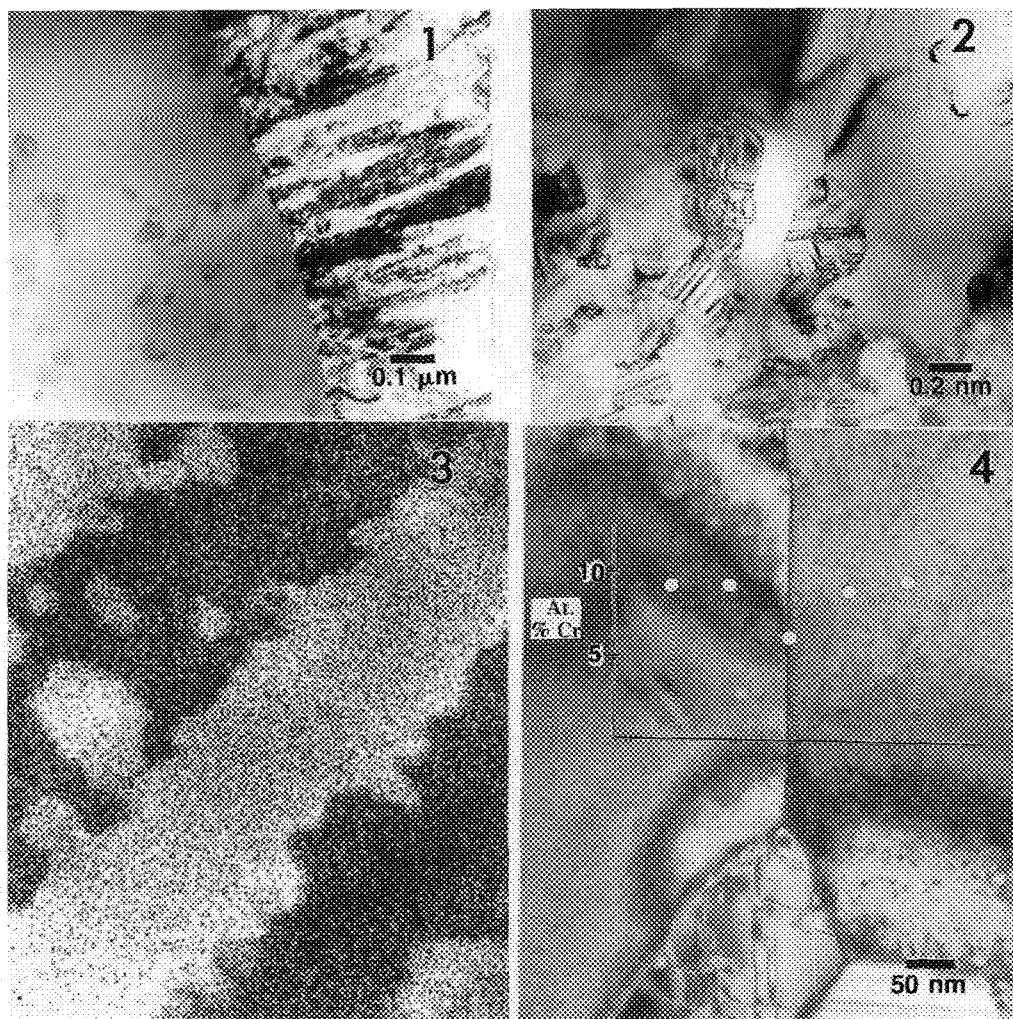
Fig. 1-- Cross-sectional TEM image of the interface of an as-deposited $Cr_2Nb-Nb(Cr)$ microlaminate composite.

Fig. 2-- Cross-sectional TEM image of the interface of a $Cr_2Nb-Nb(Cr)$ microlaminate composite heat treated at 1200°C for two hours and 1300°C for eight hours.

Fig. 3-- X-ray map of the heat treated sample using $CrK\alpha$ x-rays. The Cr_2Nb layer is bright in this image.

Fig. 4-- Cross-sectional TEM image of the heat treated sample showing Cr depletion at the grain boundary ahead of the penetrating Cr_2Nb grains.

ELECTRON MICROSCOPY ANALYSIS OF GRAIN BOUNDARY STRUCTURE AND COMPOSITION IN SUPERPLASTICALLY DEFORMED Al-Mg ALLOYS

J. S. Vetrano and S. M. Bruemmer

Pacific Northwest National Laboratory, P.O. Box 999, Richland, WA 99352

Evaluation of grain boundary composition and structure in superplastically deformed AA5083-based alloys (Al-4.5Mg-1.6Mn-0.2Zr) was carried out in a field-emission gun transmission electron microscope (FEG-TEM). During superplastic deformation at high homologous temperatures materials undergo extensive grain boundary sliding (GBS) which creates a flow of defects in the near-boundary region. Recent literature has shown that the grain-boundary composition in Al-Mg alloys is not necessarily the same as the matrix, and that these differences can have an effect on GBS.[1-3]

Two alloy conditions were tested, with slightly different particulate content and superplastic deformability. Samples were tested at temperatures of 400°C and 450°C and a strain rate of $1 \times 10^{-3} s^{-1}$ to vary the degree of grain boundary sliding, then quenched under load to preserve as much of the high-temperature structure as possible. TEM samples were prepared by carefully punching disks from the gage section of the deformed sample and electropolishing. Additionally, one sample was brought up to temperature and quenched but not deformed.

Analytical microscopy using energy-dispersive x-ray spectroscopy and a 0.7 nm electron probe was performed in the boundary and near-boundary regions. A depletion of Mg at the grain boundary was observed in samples that underwent GBS. The amount of depletion scaled with the degree of GBS, which is related to the measured strain-rate sensitivity (higher strain rate sensitivity corresponds to more GBS). Figure 1 is a plot of grain-boundary Mg concentration versus strain-rate sensitivity and shows this correlation.

Microstructural analysis of the deformed samples showed few dislocations when GBS was prevalent, but nano-scale cavities were present along many of the grain boundaries. In an attempt to understand their origin, one sample was placed in a TEM heating stage and heated *in situ*. The micrographs of Figure 2a-c show a sequence of the cavities at room temperature, their coarsening at 170°C, and their disappearance at 225°C, respectively. Dissolution at this temperature indicates that they formed during quenching, not at the deformation temperature. Their absence in the undeformed sample indicates that they formed by a condensation of excess boundary vacancies created during GBS.[4]

References

1. J.S. Vetrano et al., *Materials Science Forum*, 170-172 (1994)225.
2. J.S. Vetrano et al., *Superplasticity and Superplastic Forming 1995*, ed. by A.K. Ghosh and T.R. Bieler, TMS, Pennsylvania (1995) 49.
3. J. Koike et al., *J. Mater. Res.*, 10 (1995) 133.
4. This work was supported by the Materials Division, Office of Basic Energy Sciences, U.S. Department of Energy under Contract DE-AC06-76RLO 1830.
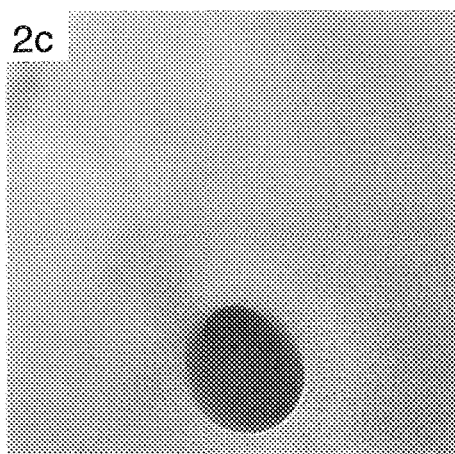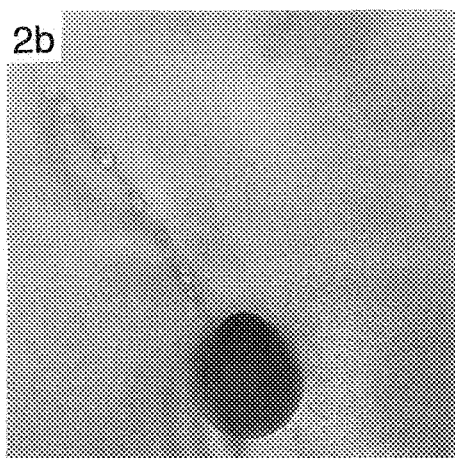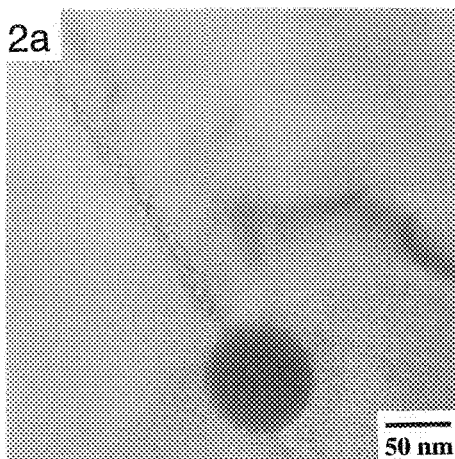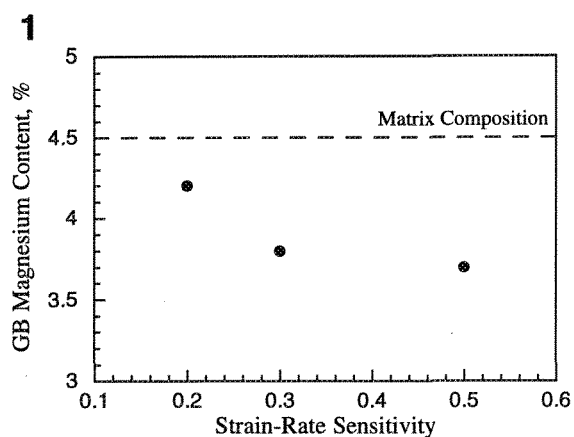
Figure 1. Plot of grain boundary Mg concentration versus strain-rate sensitivity in a deformed Al-Mg-Mn alloy. Matrix concentration is shown.

Figure 2. Changes in grain boundary cavities during in-situ heating. a) room temperature, b) coarsening after 10 minutes at 170°C and c) disappearance at 225°C. The dark circle is a contamination spot generated to mark the area.

INHOMOGENEOUS REACTION BETWEEN EPITAXIAL Al AND Si(111) REVEALED BY SCANNING INTERNAL PHOTOEMISSION MICROSCOPY (IPEM)

S. Miyazaki*, T. Okumura*, Y. Miura** and K. Hirose**

*Department of Electronics & Information Eng. Faculty of Eng., Tokyo Metropolitan University 1.1, Minami-ohsawa, Hachiohji, Tokyo 192-03, Japan
**Microelectronics Research Laboratories, NEC Co.,34, Miyukigaoka, Tsukuba, Ibaraki 305, Japan

Aluminum is one of the most important materials for the Si LSI metallization. An epitaxial growth of Al films on Si can be achieved since the lattice constant ratio between Al and Si is approximately given by 3 to 4.[1] It is expected that epitaxial Al films are highly stable against thermal annealing. However, epitaxial-Al/Si contacts have sometimes shown a significant change in Schottky barrier height (SBH) and interface structure upon annealing.[2] The objective of this paper is to clarify the relation between the SBH inhomogeneity and the thermally induced reaction between Al and Si through grain boundaries. The microscopic SBH distribution was measured by using scanning internal-photoemission microscopy (IPEM).[3]

Epitaxial Al layers were deposited on n-Si(111) by electron beam evaporation at substrate temperatures of 220 °C and 250 °C. In the as-deposited state, the Al film fabricated at 220 °C consisted mainly of "type-A"- and partially of "type-B"-orientated interfaces (referred to as a mixed phase: MP-AS), while that deposited at 250 °C consisted only of "type-B" (referred to as a single phase: SP-AS). The samples were annealed for 1 hour at temperatures between 450-550 °C and then quenched.

In IPEM measurements, a light from a 1.3 μm laser diode is focused at the Al-Si interface through Si substrates. When a metal layer is illuminated by photons with energy greater than the SBH, internal photoemission current is generated, and its wavelength dependence reflects the SBH. Thus, imaging of the SBH is realized by raster scanning of the laser beam in the interface (see Fig. 1).

Figure 2 shows the variation of the SBHs determined by I-V and C-V methods as a function of annealing temperature. For the interfaces with mixed-phases (MP), the SBH (I-V) and the SBH (C-V) decreased by about 15 meV and increased by about 50 meV after annealing at 500 °C, respectively. On the other hand, both SBHs (I-V and C-V) for the single-phase sample (SP) decreased by about 40 meV. Figures 3a, 3b and 3c show typical SBH images taken by IPEM for MP-AS, MP-500 and SP-500, respectively. Although the SBH seems to be homogeneous in case of the single-phase interface even after annealing at 500 °C (SP-500), the mixed-phase interface became inhomogeneous after annealing at 500 °C (MP-500). The formation of low and high SBH regions is a prime cause of large discrepancy between two "macroscopic" SBH values determined by I-V and C-V methods.

It is expected that Si atoms diffuse outward much faster at grain boundaries than in the other regions. We suppose that Si atoms dissolved into Al films mainly through grain boundaries upon annealing and formed the recrystallized p^+-Si layer between Al and Si on cooling. Hence, inhomogeneous formation of recrystallized Si-layers through grain boundaries induced the nonuniform distribution of SBH.

References

1. I. Yamada et al., IEEE Trans. Electron Devices. **ED-34**, 1018 (1987)
2. Y. Miura et al., Appl. Phys. Lett. **61**, 1057 (1992)
3. K. Shiojima et al., Jpn. J. Appl. Phys. **30**, 2127 (1991)

a) present address: Institute of Space and Astronautical Science, 3.1.1, Yoshinodai, Sagamihara, Kanagawa 229, Japan

1

LD temp. controller | LD modulator

LD $\lambda = 1.3\,\mu m$

Single-mode fiber

I.R. objective lens

Ref.

Lock-in amplifier

Sig.

I-V converter

Sample

X-Y stage controller

Computer

3a MP-AS

20 µm

3b MP-500

20 µm

3c SP-500

20 µm

Low ← S B H → High

2

SBH (eV)

0.78

0.70

0.66

C-V (MP)

I-V (MP)

I-V (SP)

C-V (SP)

As-depo. 450 °C **500 °C** 550 °C
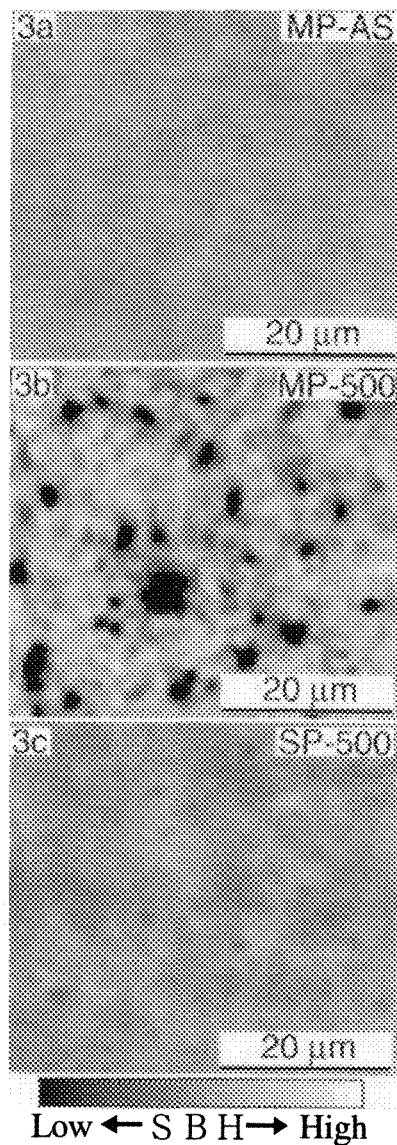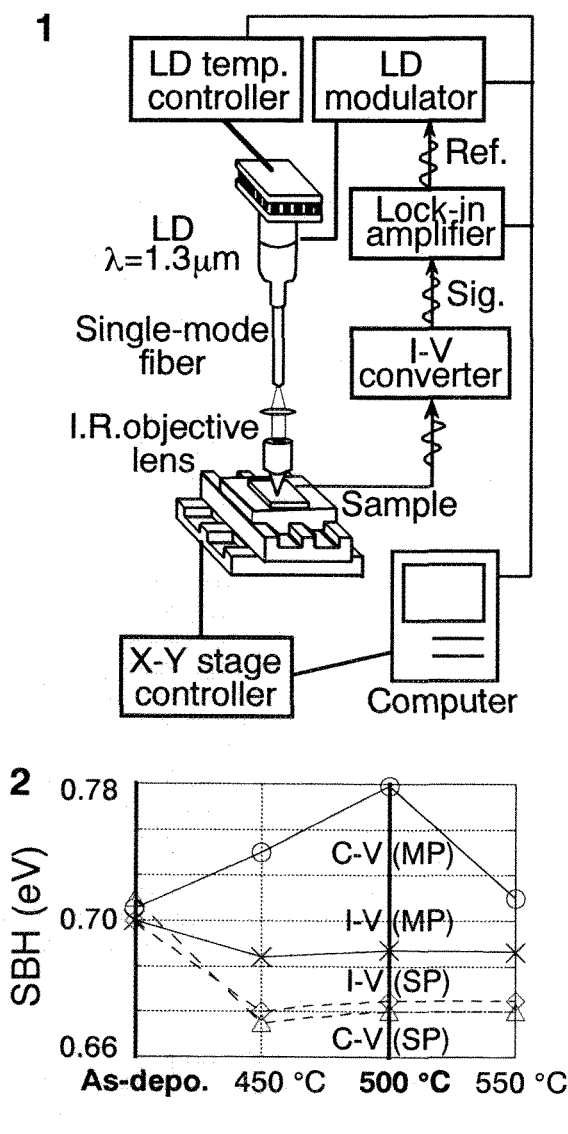
FIG. 1 A schematic diagram of scanning internal-photoemission microscopy.

FIG. 2 Summary of the SBHs determined by *I-V* and *C-V* methods for Al/(111)Si deposited at 220 °C (MP) and 250 °C (SP).

FIG. 3 Typical images of internal photoemission current for MP-AS (220°Cdepo. As-depo.), MP-500 (220°Cdepo. 500°C annealed) and SP-500 (250°Cdepo. 500°C annealed).

1/60 SEC TIME-RESOLVED HIGH-RESOLUTION ELECTRON MICROSCOPY OF STEP-DIFFUSION OF TUNGSTEN ATOMS ON MgO (001) SURFACES

N. Tanaka, H. Kimata and T. Kizuka

Department of Applied Physics, School of Engineering, Nagoya University, Furō-chō, Chikusa-ku, Nagoya, 464-01, Japan

Surface-diffusion process of atoms is one of the important factors for understanding various types of surface-related phenomena such as thin-film growth and catalysis reaction[1]. Development of field ion microscope (FIM) was a great breakthrough for the study of the process in atomic level. The diffusion process of Rh and Re atoms on tungsten surfaces was quantitatively studied, and the barrier potential (Ed) and the pre-exponential factor (D_0) were successfully determined[2]. Recent development of scanning tunneling microscope (STM) has also enabled us to measure directly the moving of Pb and Sb-atoms on Ge and Si (111) surfaces[3,4]. The time-resolution of these methods is, however, not sufficient to trace the diffusion process in detail.

In previous papers, we reported the first experiment of tracing the diffusion process of tungsten(W)-atoms on terrace-regions of MgO (001) surfaces in the time-resolution of 1/60 s using dynamic high-resolution electron microscopy[5,6]. The values Ed=0.18 eV and Do = 1.5×10^{-14} cm^2/s were successfully determined from the video-tape images. In the present study, we have observed diffusing atoms along the surface-steps and studied the phenomena quantitatively.

Tungsten (W) atoms and clusters adsorbed on (001) magnesium oxide (MgO) films were prepared from tungsten tri-oxide (WO$_3$)/MgO or tungsten (W)/MgO samples by the following method. A single crystalline MgO thin film was prepared on a NaCl substrate heated at 300°C by vacuum deposition in a UHV chamber. The mean thickness was controlled to be an optimum value. The MgO film supported on a molybdenum- microgrid was placed on a heating holder in a UHV sample-transfer chamber attached to an electron microscope[7]. WO$_3$ or W was then deposited on the MgO film heated at 300°C, which was cleaned by heating at 800°C. The WO$_3$/MgO or W/MgO samples were transferred into the electron microscope without exposure in air and observed in a few minutes. For the WO$_3$/MgO samples, W-clusters were prepared by a heavy electron irradiation of more than 100 A/cm^2 for 20-30 min.[6].

Observation of the samples was performed with a 200 kV electron microscope (JEM-2010) equipped with the transfer-chamber, a high-sensitivity TV camera with a fluorescent screen and a digital video recording system[5,6]. The video recording system ensured the analysis of one "field image" with the time-resolution of 1/60 s. Each of the "field images" was displayed through an image processing device (Japan Avionics, Image-sigma) on a TV monitor (Sony, PVM-122J), and photographed by a camera.

Figs. 1, 2 and 3 show a time-sequential series of electron microscope images recorded in the time-resolution of 1/60 s. Black dots indicated by arrows (w) correspond to a W-atom diffusing at a step on the MgO (001) surface at 218°C as illustrated in Fig. 4. The image contrast and size agree with those of simulated images of single W-atoms adsorbed on MgO (001) crystals of the optimum thickness[8]. The clear observation of the atoms is possible only in the suitable MgO thickness and under off-Bragg conditions which weaken MgO 200 lattice fringes[9]. Fig. 5 shows a comparison of distribution of jump-length between the step-diffusion and terrace-diffusion, showing that the step-diffusion has more long-jump processes. The diffusion constant along the steps is one-fifth of that of the terrace-diffusion. Also we measured the dwelling time, which was longer than that of the terrace diffusion. The high-resolution electron micrographs showed that the adsorbed atoms were located at down-sites of the steps. The present results suggest that in the beginning of the growth, atoms impinging on the surfaces are firstly adsorbed at the down-steps, and the next atoms are also located there and make one-dimensional diffusion as illustrated in Fig. 6. Probability of collision is higher than that of the terrace-diffusion. The critical nucleus

should be produced more frequently. This conclusion was supported also for W/MgO samples[8]. By using the time-resolved HREM, we have observed the initial stage of nucleation process at the step edges of MgO (001) surfaces, such as adsorption and one-dimensional diffusion processes. The present study shows a new possibility of HREM to study surface related dynamic processes in the single atom level.

References
1. A. Zangwill , *Physics at Surfaces* , Cambridge University Press, Cambridge (1988), Chap. 14.
2. G. Ayrault   and G. Ehrlich , *Phys. Rev. Lett.*, **3 1**(1973), 1407.
3. E. Ganz, S.K. Theiss, I-S. Hwang and J. Golovchenko, *Phys. Rev. Lett.*, **6 8** (1992), 1567.
4. Y.M. Mo, *Phys. Rev. Lett.*, **7 1**(1993), 2423 .
5. N. Tanaka , H. Kimata and T. Kizuka, *Proc. MRS'95 Fall-Meeting, "Session J"* in print. (1996).
6. N. Tanaka, H. Kimata and T. Kizuka: *J. Electron Microsc.*, **4 5**(1996), 113 .
7. N. Tanaka , T. Kizuka, M. Naruse and T. Yanagisawa , *Proc. 13th Int. Cong. E.M. (Paris),* Vol. **2 A**, (1994), 381 .
8. N. Tanaka, H. Kimata and T. Kizuka, *Thin Solid Films*, (1996), in print .
9. K. Kimoto, N. Tanaka and K. Mihama, *J. Electron Microsc.*, **3 8**(1989), 165 .
10. The present study is partly supported by Sumitomo, Gokiya and Izumi Scienece Foundations, Amada Technology Development Foundation, and Grant-In-Aid in Ministry of Education, Japan, Priority-area Research (#05214208).
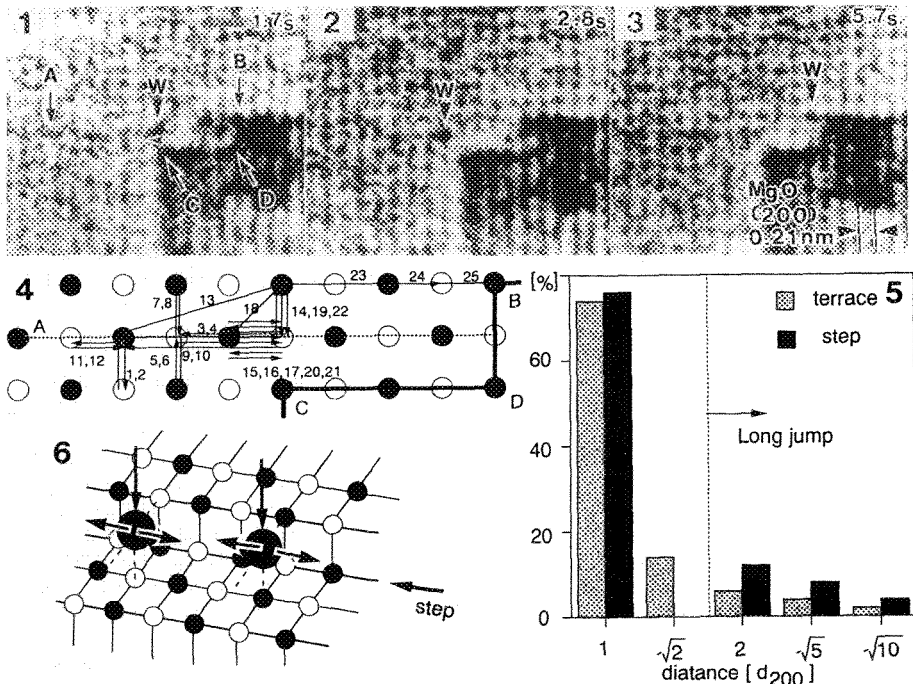
Figs.1,2,3: Time-sequential series of high-resolution images of a W-atom diffusing along a step on a MgO (001) film at 218°C, reproduced from digital-framed video tape images.
Fig. 4:   Illustration of the path of the step-diffusion in Figs. 1,2,3.
Fig. 5:   Comparison of jump-length for the step-diffusion and terrace-diffusion.
Fig. 6:   Illustration of adsorbed atoms with one-dimensional diffusion at a step.

TELE-PRESENCE MICROSCOPY/LABSPACE: AN INTERACTIVE COLLABORATORY FOR USE IN EDUCATION AND RESEARCH

Nestor J. Zaluzec

Materials Science Division, Kinetics & Irradiation Effects Group
Argonne National Laboratory, Argonne, Illinois 60439 , USA

Computerized control of scientific instrumentation has been successfully implemented in recent years to facilitate the indirect operation or remote observation of a wide variety of equipment including the full range of electron microscopes[1-4]. The concept is, however, usually applied in it's simplest sense, namely-the direct one-to-one functional replacement of "local operation" of equipment by a remote workstation. While the microscope is clearly central to the our research, real collaboration will not be achieved simply by creating a networked interface to a microscope for remote scientists. This is merely a simple exercise in computer programming and digital control. For true distributed collaboration (either in research and/or teaching) to be successful, all of the aspects of the research/teaching environment must be considered. For example, the investigators must be able to talk to and see each other while running an instrument, and they should be able to do everything else they would normally do if they were in the same laboratory. This includes sharing experimental data, review previous experiments, write papers, talk over coffee and even visiting each other in their office to plan current and/or future work. The TelePresence Microscopy (TPM) /LabSpace[1] project attempts to bridge the gap between simple "remote microscopy" and true collaboration, by integrating protocols, tools, and interactive links to instrumentation, data (real-time as well as archived), and audio-visual communications. The initial goal of this project has been to create a virtual space, accessible via the Internet, where microscopists and their colleagues, who are distributed across the nation or the world, can meet, talk, plan their research, and also run their experiments.

After the first year of development, we have interfaced the control functions of the ANL Advanced Analytical Electron Microscope to TelePresence operation. Figure 1 illustrates the various data streams which include: instrument control, data archiving, and teleconferencing which have been implemented on the AAEM. The remote collaborator has control of all lenses, specimen position (shift/tilt), and imaging modes and can control these functions using secure (password protected) remote login using either direct command entry (text) or via a GUI. Figure 2 shows examples of typical data fields which correspond to laboratory views, instrument / experimental data and multicast teleconferencing windows. Choice of fast frame low resolution or slow frame high resolution windows for image transfer is an option for imaging. This allows optimal configuration of the telepresence interface, particularly over slow network lines. The generic TPM system is composed of both software and hardware, which operate in a client/server relationship and is based upon customized software, with a minimum of commercial products. This was chosen to provide maximum versatility, and minimum cost to the user. All source code and platform independent Internet browsers will be distributed free of charge as it is completed. While it may be argued that this creates one-of-a- kind software tool, the interface is generic enough that it may be applied to a wide range of instruments and includes the possibility of plug-in modules which can be customized for different equipment. In addition, to enhance the concept of collaboration, an interaction space is being experimented with which attempts to add video and audio support to a MOO server, which is usually a simple text based communications medium. When fully implemented this will allow a researcher to walk into a virtual electronic laboratory and be able to see and hear their colleagues who are present in the eLab. The current status of the TPM project can be checked by accessing the Microscopy and Microanalysis WWW Site (URL= *http://www.amc.anl.gov*). This site provides a demonstration of some of the capabilities of a passive link using conventional WWW browsing tools and provides update on the project.

References:
1.) R. Stevens,etal Lab Space and The National Electronic Laboratory Infrastructure : Documentation available via WWW at http://www.amc.anl.gov and http://www.ccs.neu.edu/research/labspace/
2.) N.J. Zaluzec 53rd. Ann Proc. MSA, Kansas City, Mo (1995) 14-15
3.) B. Parvin etal 53rd Ann. Proc. MSA, Kansas City, Mo (1995) 82-83
4.) L.S. Chumbley etal. 53rd Ann. Proc. MSA, Kansas City, Mo (1995) 654-655
5.) M. Ellisman 53rd Ann. Proc. MSA, Kansas City, Mo (1995) 66-67
6) Supported by US. DoE under contracts BES-MS W-31-109-Eng-38, and DE-AC03-76SF00098.

Figure 1. TPM/LabSpace Data Streams on the ANL AAEM

Figure 2. Typical Lab (a), Instrument Data (b), TeleConference(c)
and Experimental Image (d) Information Screens

REMOTE ON-LINE CONTROL OF A HIGH-VOLTAGE *IN SITU* TRANSMISSION ELECTRON MICROSCOPE WITH A RATIONAL USER INTERFACE

M.A. O'Keefe, J. Taylor✧, D. Owen, B. Crowley✧, K.H. Westmacott, W. Johnston✧ and U. Dahmen

National Center for Electron Microscopy, University of California, LBNL B72, Berkeley, CA 94720
✧Information and Computing Sciences, University of California, LBNL B50B Berkeley, CA 94720

Remote on-line electron microscopy is rapidly becoming more available as improvements continue to be developed in the software and hardware of interfaces and networks. Scanning electron microscopes have been driven remotely across both wide[1] and local[2] area networks. Initial implementations with transmission electron microscopes have targeted unique facilities like an advanced analytical electron microscope,[1] a biological 3-D IVEM[3-5] and a HVEM capable of *in situ* materials science applications.[6-8] As implementations of on-line transmission electron microscopy become more widespread, it is essential that suitable standards be developed and followed. Two such standards have been proposed for a high-level protocol language for on-line access,[1,9] and we have proposed a rational graphical user interface.[7] The user interface we present here is based on experience gained with a full-function materials science application providing users of the National Center for Electron Microscopy with remote on-line access to a 1.5MeV Kratos EM-1500 *in situ* high-voltage transmission electron microscope via existing wide area networks. We have developed and implemented, and are continuing to refine, a set of tools, protocols, and interfaces to run the Kratos EM-1500 on-line for collaborative research. Computer tools for capturing and manipulating real-time video signals are integrated into a standardized user interface that may be used for remote access to any transmission electron microscope equipped with a suitable control computer.

In general, *in situ* experiments require dynamic adjustment of microscope controls as the specimen under observation is subjected to external stimuli such as heating, cooling, straining, or gaseous environment. Operation requires adjustments of external stimuli, adjustment of specimen position and orientation, and manipulation of microscope controls such as illumination, magnification, and focus. Usually, a local operator makes these adjustments in response to the microscope image; but, in remote mode, current wide area networks cannot offer the real-time response required. We have minimized real-time lag by using advanced computer vision algorithms locally. We have implemented drift correction (often severe during rapid heating and cooling) by controlling stage movement with optical flow fields, automatic compensation of specimen movement during tilting, and automatic focus using summed wavelet coefficients with Daubechies kernels. Wavelet transforms have also been used for image compression; a remote user operating from Washington D.C. observed 640x480 images at a rate of 0.6fps over a T1 line.

The standardized user interface (fig.1a) displays the frequently-used controls for magnification, apertures, objective focus and specimen tilt, with a 640x480 window for standard NTSC video. Microscope magnification can be stepped up and down through the full set available. Objective focus control is continuous with four decades (corresponding to coarse, medium, fine, and vernier) and auto-focus. Tilt rate is set and then stepped in the desired direction. The specimen stage is moved by dragging the image. Subsidiary windows are opened as required, e.g. for adjustments of apertures (fig.1b), using the plate camera (fig.1c), and positioning the beam and beam stop (figs.1d,e). In the implementation of our standardized remote user interface used on the Berkeley Kratos, a Sun workstation accepts signals from the remote user and passes commands to a PC to control the microscope (fig.2).[6] We have found that driving the microscope with the standardized remote user interface greatly eases the user's tasks, leaving him/her free to concentrate on the science rather than the mechanics of running the microscope.[10]

1. Nestor J. Zaluzec, *53rd Ann. Proc. MSA,* Kansas City, Missouri (1995) 14-15.
2. L.S. Chumbley et al., *53rd Ann. Proc. MSA,* Kansas City, Missouri (1995) 654-655.
3. G.Y. Fan, P.J. Mercurio, S.J. Young and Mark H. Ellisman, *Ultramicroscopy* **52** (1993) 499-503.
4. Mark H. Ellisman et al., *52nd Ann. Proc. MSA,* New Orleans, Louisiana (1994) 10-11.
5. Mark H. Ellisman, *53rd Ann. Proc. MSA,* Kansas City, Missouri (1995) 66-67.
6. B. Parvin et al., *53rd Ann. Proc. MSA,* Kansas City, Missouri (1995) 82-83.
7. B. Parvin et al., Proc. *IEEE Int. Conf. on Multimedia Systems and Computing* (1996) -- to be published.
8. B. Parvin et al., *Proc. 15th Pfefferkorn Conf. on Electron Imge & Signl Processing,* Silver Bay, NY (1996).
9. T.A. Dodson et al., *53rd Ann. Proc. MSA,* Kansas City, Missouri (1995) 16-17.
10. Work supported by the Director, Office of Energy Research, Office of Basic Energy Sciences, Material Sciences Division of the U.S. Department of Energy, under contract No. DE-AC03-76SF00098.
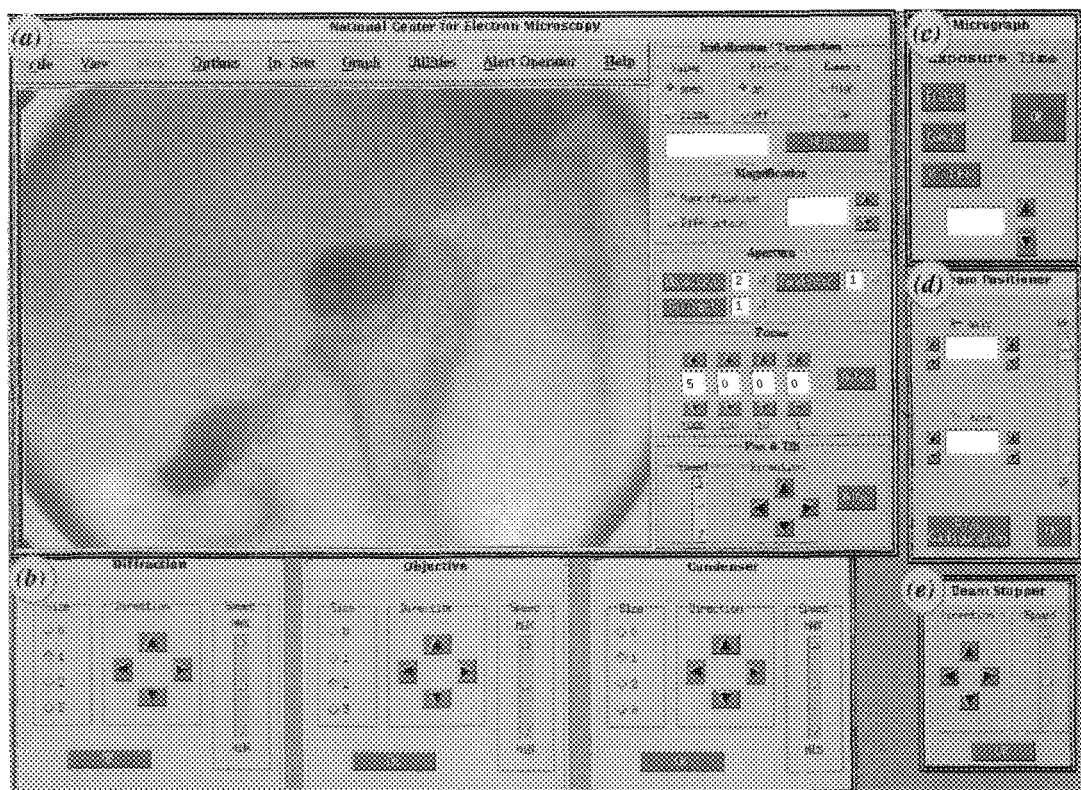
Fig. 1. Remote operator interface. The main interface window (a) contains the live 640x480 image and controls for magnification, focus and specimen tilt. Other pop-up windows control apertures (b), plate camera (c), beam position (d) and beam-stop position (e).
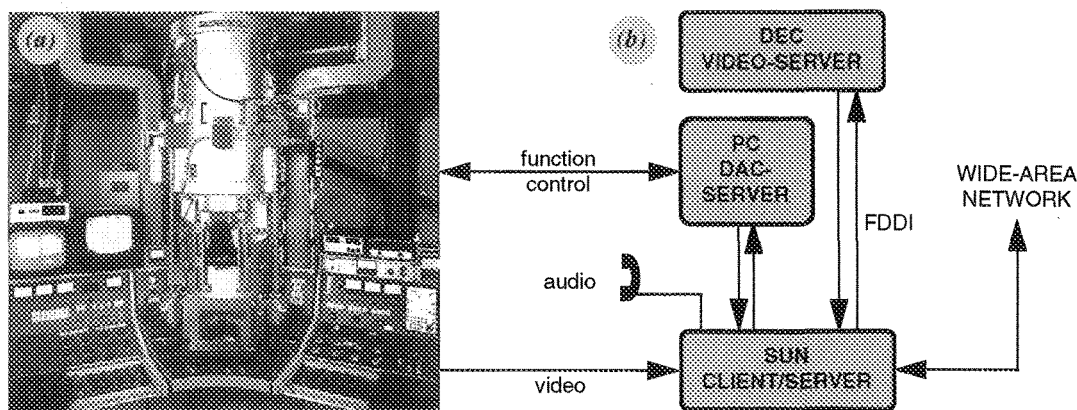
Fig. 2. (a) The operator area of the 1.5MeV Kratos HVEM. (b) System architecture for handling video and servo loops. Video is digitized in the Sun and transmitted to the remote user and to the DEC for processing for auto control. Commands from the DEC or the remote user are received by the Sun and passed to the PC, where DACs pass control signals to, and receive status signals from, the microscope.

A SIMPLE AND INEXPENSIVE ROUTE TO REMOTE ELECTRON MICROSCOPY

E. Völkl,* L.F. Allard,* T.A. Nolan,* D. Hill,* and M. Lehmann*

*High Temperature Materials Laboratory, Oak Ridge National Laboratory, Oak Ridge, TN 37831-6064
**Institute for Applied Physics, University of Tübingen, Germany

Due to the availability of fast computer networks such as Ethernet, FDDI and ATM, the idea of Telemicroscopy, including running electron microscopes from remote locations has gained momentum. Fan, Ellisman, Zaluzec and Parvin, have discussed aspects of systems which support such capabilities.[1, 2, 3, 4] In each of these reports the authors describe new stand-alone software packages that are required to run their systems. In order to make remote microscopy more universally available, we have chosen to expand de facto standard commercial software to provide for computerized microscope control and remote control.[5, 6]

All of the major instruments in our user facility have been converted to digital operation and the darkroom has been abandoned completely.[7] It is a logical extension of digital imaging to provide for computer control of the instrument operation, since the instrument parameters can be adjusted using feedback from analysis of the digital image. Digital image recording and display typically uses commercial software such as DigitalMicrograph© (which controls e.g. the CCD camera on the HF-2000).[8] This program provides the four capabilities necessary to implement instrument control. It allows camera control, provides image processing tools, incorporates a scripting language and also allows C-code to be implemented.

Presently, the Hitachi HF-2000 (TEM) and the Hitachi S4500 (SEM) are both being adapted for computer control. The first task was to write a plug-in module for DigitalMicrograph© which adds additional SET and GET commands to the scripting language. Using this expanded scripting language, we then designed menu items to facilitate the basic controls of an electron microscope. On the HF-2000, these initially include, but are not limited to: change of magnification, focus, translation of specimen and illumination control. All of the digitally controllable microscope functions are accessible in the same way.

The capability to conveniently control the microscope from the local computer then leads to the possibility for microscope control from a remotely located computer. We found that the commercially available software package `Timbuktu® Pro' (v2.0) provides a simple and straightforward solution.[9] With Timbuktu® Pro, the remote user has the capability to display the screen of the microscope computer on his own computer, and to access the microscope computer's mouse and keyboard by using his own mouse and keyboard. Visual and audio communication between the remote site and the local site is provided using a `QuickCam' camera together with the software CU-SeeMe on both ends.[10,11]

A screen snap-shot from a remote computer running the HF-2000 is displayed in Figure 1. In the center, the TEM image acquired with the CCD-camera is shown. Image resolution is 128 by 128 pixels and a binning factor of 8 was used in this case. These settings allow the microscope to be run through a 128 Kbps standard ISDN-line with a refresh rate of about 0.5 frames per second. If the remote user has access to a T1 link (1.5 Mbps) or better, improved resolution can be provided at faster refresh rates. On the right hand side of Figure 1, CU-SeeMe provides a live image of the HF-2000 and one of our operators.

In order to access one of our instruments at Oak Ridge National Laboratory from your own office or lab, simply send a request via email to: `remoteEM@ornl.gov'. We will then be able to contact you and set up a time so you can run these microscopes from your site.[12]

References

1. G.Y. Fan et al., *Ultramicroscopy,* **52** (1993) 499-503
2. M.H. Ellisman, *Proc. 53rd Ann. Meet. MSA,* Kansas City, MI, 1995, J&B Publishing, NY, 66-67
3. N.J. Zaluzec, *Proc. 53rd Ann. Meet. MSA,* Kansas City, MI, 1995, J&B Publishing, NY, 14-15
4. B. Parvin et al., *Proc. 53rd Ann. Meet. MSA,* Kansas City, MI, 1995, J&B Publishing, NY, 82-83
5. E. Voelkl et al., *Proc. 53rd Ann. Meet. MSA,* Kansas City, MI, 1995, J&B Publishing, NY, 22-23
6. T.A. Dodson et al., *Proc. 53rd Ann. Meet. MSA,* Kansas City, MI, 1995, J&B Publishing, NY, 32-33
7. E. Voelkl et al., *Hitachi Instrument News, Electron Microscopy Edition,* 29th Edition, 1996, 5-11
8. Gatan Inc., Owens Drive, Pleasanton CA 27822, USA
9. Farallon Computing Inc., Alameda, CA 94501-1010, USA
10. Connectix, 2600 Campus Drive, San Mateo, CA 94403.
11. CU-SeeMe (v0.83b3) available via FTP from: `cu-seeme.cornell.edu/pub/cu-seeme`.
12. Research sponsored by the Laboratory Directed Research and Development Program of Oak Ridge National Laboratory, managed for the Department of Energy by Lockheed Martin Energy Research Corp., under contract DE-AC05-96OR22464.
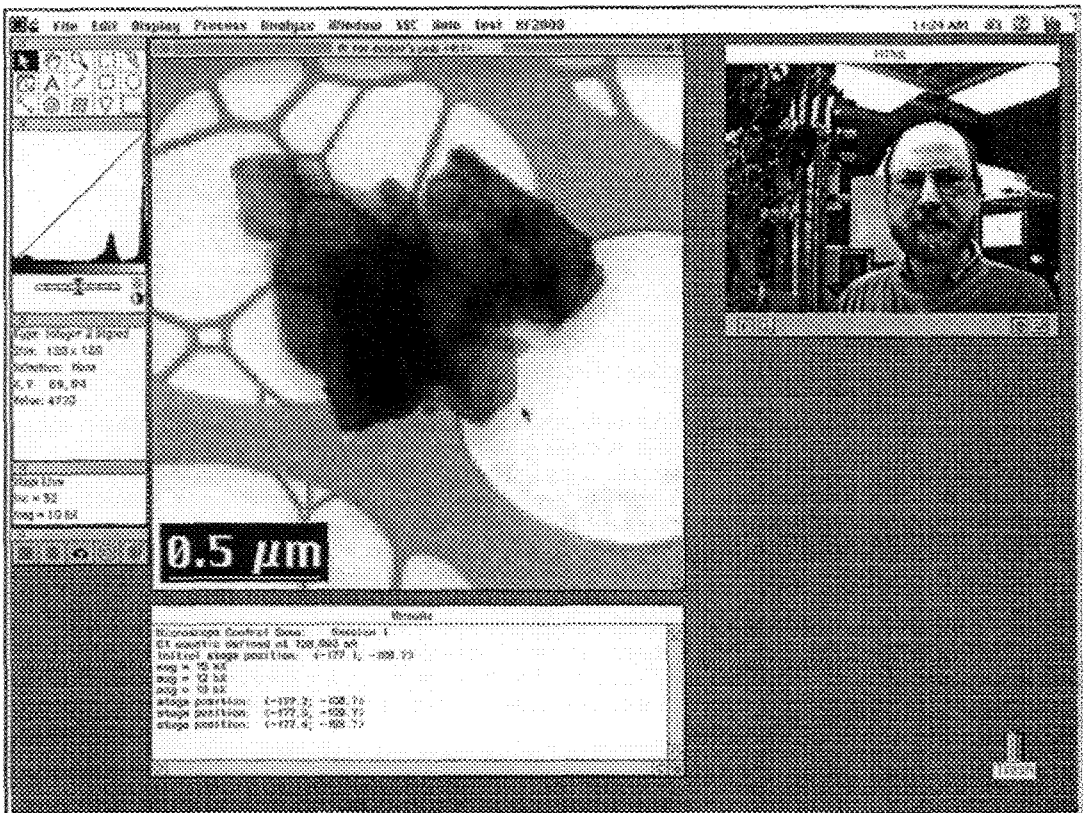
FIG. 1. – Screen snap-shot of remote computer connected through an ISDN line (128 Kbps) to the computer which controls the HF-2000. A 128 by 128 pixel `preview' image is displayed with zoom factor 4. Scale marks are inset automatically. `QuickCam' camera and CU-SeeMe provide `TelePresence' (top right). `Results' window displays most recent remote microscope activities.[10, 11]

A Scalable Approach to Teleoperation

J. Taylor and B. Parvin
Imaging and Distributed Computing Group
Information and Computing Science Division
Lawrence Berkeley National Laboratory, Berkeley, CA 94720
E-mail: jrtaylor@george.lbl.gov

Due to the fast pace of computer instrumentation and technology, we are quickly approaching an age where on-line use of expensive research facilities will become commonplace. The consequences of this trend will be multifaceted. It will allow scientist and researchers to perform experiments and access data with greater ease without the burdensome overhead associated with working onsite. It will allow for the on-line storage and analysis of data. And lastly, an ideal testbed will be provided for integrating intelligent man-machine interfaces in order to reduce labor intensive tasks. This will simplify the control of complicated instruments via automation of the controls whose human control is not essential. Unfortunately, attempts at building a common platform for remote operation will face several problems. First of all, a successful general purpose architecture will frequently need to be extended in order to perform new functions as well as utilize new hardware. Similarly, the continued development of new microscopes, stage controls, etc. will undoubtedly create incompatible interfaces which will break presently working systems. Lastly, the environment that such a system will operate will likely be characterized by heterogeneous hardware and software. Based on the experience of building on-line systems for use of optical and electron microscopes, we propose a scalable system architecture based on the principles of object oriented design and analysis, a machine independent user-interface based on Java, and a software bus that supports distributed objects over the network.

Object oriented design is a technique that focuses design on the data and on the interfaces to it. This a powerful concept because it facilitates the clean definition of interfaces and makes is possible to provide reusable "software ICs". The requirements for teleoperation can be divided into several basic groups including: user interface, network communication, system control and automation, instrument drivers, and auxiliary system services such as databases, on-line analysis and teleconferencing. In conformance to our paradigm, these can be elegantly modeled as objects. Besides those components which are elementary, it is sometimes the case that a particular system requires additional functionality. During in-situ microscopy, for example, an on-line system must satisfy an additional set of real-time constraints. In this case, the specimen under observation is subjected to complex buffers and EM field variation requiring dynamic adjustment of the microscope controls (Fig. 1). This becomes a problem when coupled with insufficient network bandwidth over the WAN. An effective multimedia system for this type of application must integrate automated capabilities to eliminate the real-time delivery requirement. Object technology will ease any integration effort.

The user interface to an on-line system must provide all the necessary functionality to the user in a simple, intuitive and platform independent fashion. A central goal in the design will be to hide the complexity of the instrument as much as possible without sacrificing functionality. This will ease the acceptance of the system for users without a high level of computer experience. Platform independence is an important criteria due to the heterogenous nature of current computer environments. We have chosen to build the graphical user interface for our system using X-windows and the Motif toolkit (Fig. 2) This allows for easy porting of the interface module to various unix platforms as well as providing the user with an standard "look and feel". Additionally, we have begun migration towards a Web based approach. Rather than rely on the use of an expensive workstation to access the instrument, we are developing a Java version which can be run from within a Java enabled Web browser on either a Mac or PC. This will provide a low cost and completely platform independent solution. In addition to allowing easy access to the instrument, Java provides features that are essential to distributed computing. Java has support for object oriented programming, internet protocols, security, and multimedia. Java is extendable, supports multi-platforms, and has built in version control.

Beyond the requirement of operating an instrument, a teleoperation system must provide additional features necessary for a distributed computing environment. The need for a standard in high level application interworking across multiple platforms and network architectures has been recognized by the computer industry and is addressed by the Object Management Group (OMG) and in particular the Common Object Request Broker Architecture (CORBA) specification. The OMG is the chief industrial body for the promotion of standardization and adoption of object technology. In this architecture, communication between objects is handled via an Object Request Broker (ORB). An

ORB is a fundamental service to enable messaging between objects in a distributed system and may be viewed as a "software bus". The CORBA specification consists of two main parts: an Interface Definition Language, and a Dynamic Invocation Interface. Essentially, CORBA provides a set of object oriented interfaces that support the construction and integration of object-oriented software components in heterogenous environments.

The communication subsystem for an on-line system will be responsible for providing images, video and instrument readouts to the user as well as relay user commands to the control subsystem. The main issues incurred in the evaluation of the communication subsystem will be reliability, speed, cost, and platform independence and will ultimately be effected by both network hardware (FDDI and Ethernet) and software protocols (TCP/IP and ATM). By identifying this component as an object we may design the rest of the system with respect to the interfaces this object provides. Conformance to the CORBA specification will greatly simplify the transition to new networking technology. A scalable system will also provide auxiliary object services including database and online quantitative analysis. It is necessary for the remote user to be able to easily and efficiently store the image and video data that has been gathered during a remote session. This will allow the remote scientist to review the experiment and distribute copies of the session to fellow users as well as perform additional image processing. Web browsers such as Netscape or HotJava will provide a low cost and platform independent method for viewing and downloading images captured during microscope operation. Important criteria for evaluating a database system include ease of integration into the on-line system, ability to store large datasets including high resolution images, query capabilities, and browser interface. Additional services for collaborative computing including teleconferencing and shared notebook will be necessary to allow communication between scientist and technicians working onsite.

An on-line system for remote microscopy is a complicated software system entailing the use of a modern software engineering approach. This is particularly the case for a rapidly emerging field such as remote microscopy. In this case the system architect will be faced with the problem of keeping up with the latest computer technology as well differing user needs. We propose that a CORBA compliant object oriented architecture will provide the modular framework necessary for successful implementation of remote control systems as well as facilitate the further integration and extension of new components.
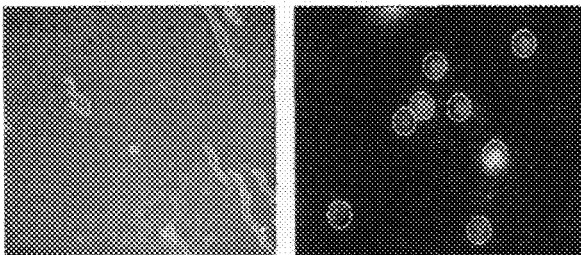
Fig. 1 -- Automated extraction of DNA molecules stretched under an E-field and cells that are excited with mitogen injection. Our system can track shape changes and record the molecule's motion.
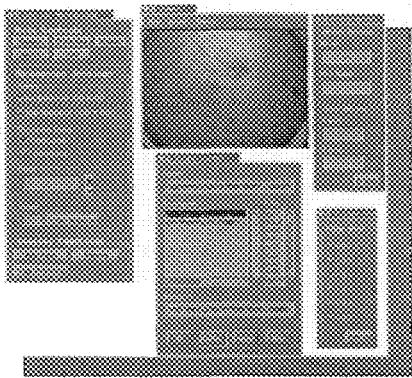
Fig. 2 -- Graphical User Interface

References:
1) B. Parvin et al., *Telepresence for In-situ Microscopy* , Proc. IEEE Int. Conf. on Multimedia Systems and Computing, June 1996.
2) Nestor J. Zaluzec, *Tele-Presence Microscopy: An Interactive Multi-User Environment for Collaborative Research using High Speed Networks and the Internet* 53rd Ann. Proc. MSA, Kansas City, Missouri (1995) 14-15.
3) Thomas J. Mowbray, Ron Zahavi, *The Essential Corba*, John WIley & Sons, Inc. 1995.
4) Hirano Satoshi, *The Magic Carpet for Network Computing: HORB Flyer's Guide* http://jefferson.village.virginia.edu/courses/ensp482-S96/java.summary.html 1996.

WEBSCOPE.TEM: A MODULAR SYSTEM FOR DISTRIBUTED TEM

N.J. Kisseberth, C.S. Potter**, G.E. Brauer, J.A. Lindquist, M.K. Jatko, B. Carragher*
Beckman Institute for Advanced Science and Technology, *Department of Cell and Structural Biology, **National Center for Supercomputing Applications, University of Illinois at Urbana-Champaign, Urbana, IL 61801.

We will describe our implementation of a system for controlling and acquiring images from a transmission electron microscope (TEM) over a distributed network. Over the past few years several groups have begun to develop systems for remote microscopy and there are now a number of prototypes and working examples that demonstrate the feasibility of this goal.[1,2] The system we are developing is part of a larger project which we refer to as the World Wide Laboratory (WWL).[3] This is a collaborative effort between the Beckman Institute, the Biomedical Magnetic Resonance Laboratory, and the National Center for Supercomputing Applications at the University of Illinois. The goal of the WWL project is to provide a set of specifications for developing instrument control servers and image processing tools which can be accessed over the Internet through a variety of user interfaces. We are currently developing servers and control applications for TEM, a magnetic resonance imaging system[4], a scanning tunneling microscope and a laser scanning confocal microscope.

The first of these instrument control applications, *webScope.TEM*, has been developed for a Philips CM200 equipped with a Gatan slow scan digital camera. Two WWL instrument servers have been developed for this system. One server runs on an IBM RS/6000 Unix workstation and controls the Philips CM200 via a serial port. The other server runs on a PowerMac and controls the Gatan slow scan camera via a plug-in module to Gatan's Digital Micrograph software. Each server accepts non-instrument specific commands over the Internet and translates them into appropriate instructions for the instrument. Examples of commands include instructions to change magnification, tilt the beam, change the defocus or acquire an image. Applications built with these "generic" commands will be able to communicate with any compatible WWL instrument server. The distributed organization of the software allows these control and acquisition applications to be located on any machine on the Internet, not necessarily the machine which is physically connected to the instrument. Thus all that is required to port an application to a new instrument is to write a WWL compliant control server for that instrument. In the case of the CM200 and Gatan camera servers this task was accomplished in less than two months.

One of the overall design strategies of the WWL project has been to develop applications which are compatible with several different user interfaces. We are developing an image processing library which can be accessed by applications either directly, or indirectly through an extensions package to the TCL scripting language. A core instrument control and image processing package can then be developed such that several different user interfaces may be placed on top of it. We have currently developed prototypes[4,5] for two very different user interfaces, viz. a room sized immersive virtual reality environment (NCSA CAVE[6]), and a web browser running Java applets (see Fig. 1). The same application software could be accessed using user interfaces developed using native operating

system interfaces such as X-Windows/Motif, Windows API, or MacOS API. These interfaces can be run on any computer which can access the required WWL instrument servers over the Internet.

References
1. G.Y. Fan et al. *Ultramicroscopy* 52 (1993) 499.
2. N.J. Zaluzec, *Proc. Microscopy and Microanalysis* (1995) 14.
3. http://bvf.beckman.uiuc.edu/WWL.
4. C.D. Gregory, et al., *Proc. 4th Annual Meeting, International Society for Magnetic Resonance in Medicine*, in press.
5. Potter et al., submitted to *IEEE CGA*.
6. C. Cruz-Neira, et al., *Siggraph Conference Proceedings*, (1993) 135.
7. The authors thank Anna Klintsova for providing the micrograph shown in Fig. 1. B.C. is partially supported by NIH grants RR0450 (to M.H. Ellisman) and GM-44932 and AR-39155 (to R.A. Milligan).
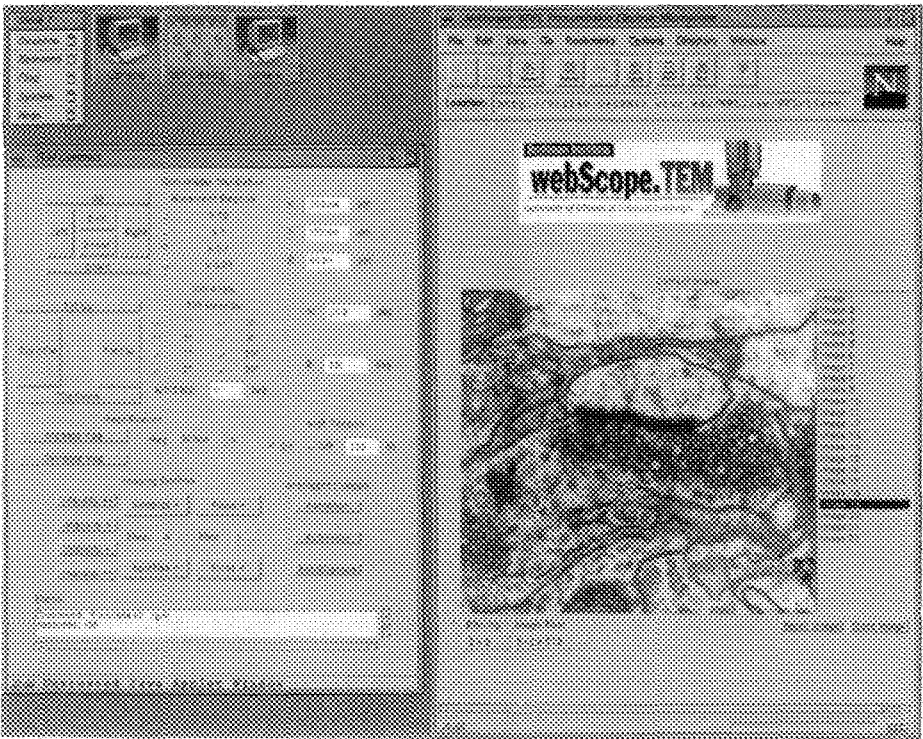
FIG. 1. A Java applet client serves as the user interface to the webScope.TEM server. Here, an in-line window on a web page allows a user to manage images from the microscope. An external frame provided by the applet serves as the control panel for the microscope.

INTEGRATED MICROSCOPY : FROM DESIGN PHILOSOPHY TO APPLICATIONS

Sébastien Tremblay*, Éric Baril*, Éric St-Pierre**, Jacques Ronaldi** and Gilles L'Espérance*.

* Centre de Caractérisation Microscopique des Matériaux, $(CM)^2$, École Polytechnique de Montréal, C.P.6079, succ. "Centre-Ville", Montréal (Qc) Canada, H3C 3A7 (Email : info@cm2.polymtl.ca)
** CLEMEX Technologies, 800 rue Guimond, Longueuil (Qc) Canada, J4G 1T5
   (Email : info@clemex.com, WebSite : www.clemex.com)

Microscopy and Objects

Object oriented programming (OOP) has been used to develop computer applications for many years. It has proven very efficient for the manipulation of data structures that share common elements and evolve over time. We observed that this approach might prove invaluable for microscopy where we, as researchers, developers and end-users, have to deal with many media (images, spectra, electrical measurements, databases, simulations, etc.) to accomplish a given characterization project. Particularly, since these media evolve as researchers find new techniques and manufacturers improve their instruments. In addition, the goals and aims of a project may also change with time. The ability to reuse information that has already been acquired/generated then becomes crucial to success since this avoids the cost of repeating an analysis when information that was considered unimportant suddenly becomes of interest. In this context all results, acquisition parameters, instrument and processing tool settings, are relevant. The need for modularity, completeness and adaptation of information guided our design for the information structure used to develop the integrated characterization system. It is based on 3 types of small data objects. The first type carries the properties of each physical object (microscope, EDX spectrometer, specimen stage, sample, etc.). The second type carries acquired data such as images, spectra, etc. Finally, the last type of small data object carries the processed results such as hardness, composition, features sizes, distribution, etc. A characterization project can then be represented like any compound document as shown in figure 1. This architecture can be used inside applications as well as with storage devices (where objects are saved in compound files). Those objects can also contain hierarchy information such as the relationship between objects (i.e. "is subset of", "is generator of" or "is defined by").

Seeing is Believing

The technological advancement of microscopy sometimes makes us forget that the initial purpose of microscopy is to image small features. This fact has been somewhat compounded by the presence of alternate techniques that provide powerful, but less visual data (e.g. X-ray spectra). To accomplish full integration of the microscopy environment, and support the objects shown in figure 1, we asked: "If we had just one program interface to carry out all aspects of a project, which one would we choose?" Our answer was : "The image analyzer". In this context the other material characterization modules and drivers are then considered tools which run in parallel or more interestingly which are embedded in, or linked to, the image analyzer (figure 2). The image analyzer then becomes the main interface component to a characterization project: the viewer and manager of all acquisition and analysis results.

The Missing Link

Only two of the many objects schematized in figure 1, image and spectrum, have proposed formats and supported standards in the microscopy community.[1] Although some attempts have partially succeeded in the area of hardware interfacing, no standard comparable to our open architecture exists for defining and exchanging configuration information, analysis commands/results, stage control patterns, etc.[2-4]

We believe that adopting comprehensive interchange standards is the key to taking telepresence microscopy from experimental and scattered implementation to nirvana without foregoing the software we enjoy. While trying to connect networks to microscopes, we should therefore provide tools that allow effective communication between various microscopy related programs running on a single computing platform.

What's Coming

The work required to integrate the hardware components is almost complete: most microscope manufacturers now implement control using a single computer. In many cases the accessories (ranging from lamps to spectrometers) can also be controlled by the same computer. Some operations, however, still require user intervention (like selecting condenser apertures on a SEM). Such features should, at a minimum, be monitored by a computer to assess the exact status of all instruments in an integrated microscopy system. Moreover, "multiple-characterization-platform" specimen holders are needed to keep track of the features of interest between two or more microscopes; some designs will be presented for optical and electron microscopy. Many applications are waiting for the automation ability and the power of a fully integrated microscopy system.[4] Examples of these will be presented from the field of materials science and engineering.

References

1. J.F. Mansfield, *Proc. of the 53rd Annual Meeting of the MSA*, (1995) 672-673.
2. L.S. Chumbley et al., *JOM*, **47** (1995) 13-17.
3. T.A.Dodson et al., *Proc. of the 53rd Annual Meeting of the MSA*, (1995) 16-17.
4. N.J. Zaluzec, *Proc. of the 53rd Annual Meeting of the MSA*, (1995) 14-15.

Figure 2
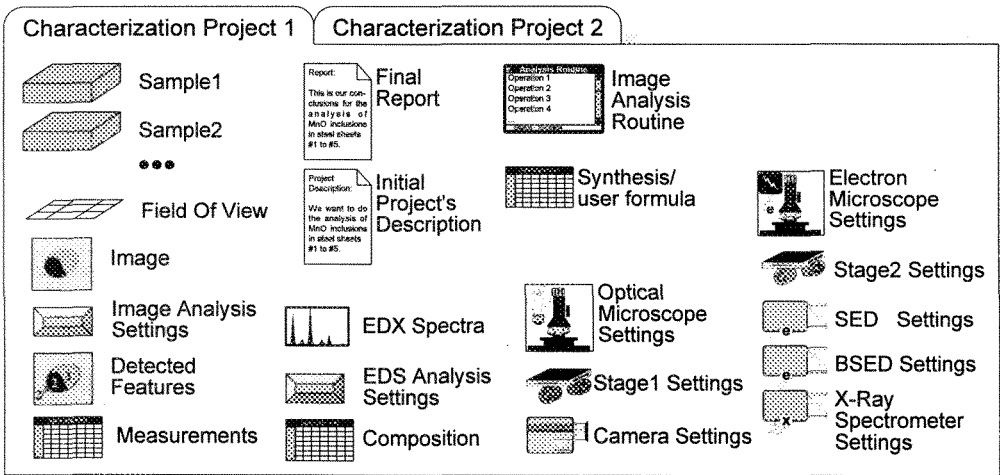
Figure 1

Figure 1. Example of the content of a compound document enabling full integration.
Figure 2. Example of software tools with the image analyzer managing the characterization project.
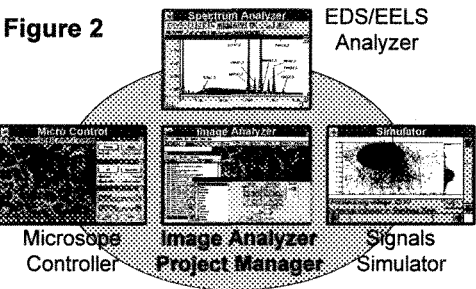
The Teaching SEM - An Example of Real-Time Remote Control SEM

John F. Mansfield
North Campus Electron Microbeam Analysis Laboratory, 413 SRB,
University of Michigan, 2455 Hayward, Ann Arbor MI 48109-2143
Email: John.F.Mansfield@umich.edu
URL: http://emalwww.engin.umich.edu/people/jfmjfm/jfmjfm.html

To introduce engineering undergraduates to one of the most widely used microstructural characterization tool, namely the scanning electron microscope (SEM), the Department of Materials Science and Engineering (MS&E) at The University of Michigan has developed the Teaching SEM. This instrument is located in the department's undergraduate teaching laboratory, however, it may be controlled from a lecture theater or classroom virtually anywhere on the University campus, or indeed, anywhere within the reach of the campus computing network and cable television network. The Teaching SEM allows MS&E to incorporate live SEM demos in the large service courses it teaches to engineering students and to show entire classes of MS&E majors how to control the microscope that they subsequently use in their laboratory practicals.

The Teaching SEM has been developed with hardware and software that is readily available, and there has been no custom software development or manufacture of specialized hardware. In addition to being a novel teaching tool, it also demonstrates the ease with which it is possible to do "Telepresence Microscopy".

The Teaching SEM is basically a Philips XL30 scanning electron microscope. The control philosophy behind Philips design of this instrument means it is one of the few, if not the only, instrument that may be currently used for real-time Telepresence Microscopy. All of the basic operating functions of the microscope are controlled by custom microprocessors and control systems, the operator's interface to the microscope is a Microsoft Windows based application. Menus, buttons, scroll bars, etc. in the graphical interface of the Windows program allow the user to control the microscope operating conditions. The application sends these commands to the dedicated instrument computers via a Small Computer Systems Interface (SCSI or scuzzy) bus. The video signal of the microscope is displayed on the screen of the Windows computer by superimposing (or keying) the video on to one of the unused colors of the VGA monitor. This video overlay is performed by using a Coreco MX video overlay frame grabber. This basic functionality of the Philips microscope is important and is illustrated in the upper portion of figure 1.

Remote control of the SEM is effected by keeping the video signal and Windows program information separate until it is displayed on the screen of the remote computer. Both the microscope Windows computer and the remote control computer are connected to the University campus-wide via a 3Com Etherlink III ISA Ethernet card. Networking software drivers for TCP/IP and the Novell IPX protocol are loaded on both computers. Remote control of the microscope computer is achieved by the use of Timbuktu Pro for Networks, a software application from Farallon Computing. Both the microscope computer and the remote control computer run Timbuktu Pro, the microscope as the master computer and the remote computer as a client.

The microscope video is transmitted to the remote computer via the University of Michigan Cable Television Network (UMTV). A Jerrold C6M cable modulator converts the microscope video signal and transmits it on a channel of the campus cable network. At the remote control location a demodulator (actually a good quality VCR) decodes the cable TV signal which is then connected to a Coreco MX video card identical the one in the microscope computer. The video is overlaid on to the Windows data with the same video keying software employed on the microscope computer. The remote control computer is illustrated in the lower part of figure 1.

The remote computer screen is almost identical to the screen that the user sees when sitting at the microscope itself. While it is obviously not possible to exchange samples remotely, a large multiple sample holder, capable of holding 10 individual sample stubs, allows the mounting of sufficient samples for most lectures and classes. Interconnection of the UMTV network with the local residential cable system and connection of the local K-12 schools to the Internet promises to allow SEM demonstrations in those schools.

Microscope Located in Undergraduate Teaching Laboratory

Remote Teaching PC Located in Lecture Theater or Classroom

Figure 1. Diagram of The Teaching SEM and how it is remotely controlled from the lecture theater or classroom.

395

THE INSTRUCTIONAL SEM LABORATORY AT IOWA STATE UNIVERSITY

L. S. Chumbley, M. Meyer, K. Fredrickson*, F.C. Laabs**

Department of Materials Science and Engineering, Iowa State University, Ames, IA 50011
*MTS, 14000 Technology Drive, Eden Prairie, MN
** Ames Laboratory, Ames, IA 50011

The Materials Science Department at Iowa State University has developed a laboratory designed to improve instruction in the use of the scanning electron microscope (SEM). The laboratory makes use of a computer network and a series of remote workstations in a classroom setting to provide students with increased hands-on access to the SEM. The laboratory has also been equipped such that distance learning via the internet can be achieved.

A view of the laboratory is shown in Figure 1. The laboratory consists of a JEOL 6100 SEM, a Macintosh Quadra computer that acts as a server for the network and controls the energy dispersive spectrometer (EDS), four Macintosh computers that act as remote workstations, and a fifth Macintosh that acts as an internet server. A schematic layout of the classroom is shown in Figure 2. The workstations are connected directly to the SEM to allow joystick and computer control of the microscope. An ethernet connection between the Quadra and the workstations allows students seated there to operate the EDS. Control of the microscope and joystick is passed between the workstations by a switch-box assembly that resides at the microscope console. When the switch-box assembly is activated a direct serial line is established between the specified workstation and the microscope via the SEM's RS-232.

A typical remote workstation is shown in Figure 3. Each workstation consists of a computer, a video monitor, a thermal printer, and a joystick control. The computers are equipped with ethernet connections and video frame grabber boards. The video monitor allows the students to continually view the SEM image and the thermal printer allows a hardcopy print to be obtained at any time. Various software programs are used to collect and analyze data and control the EDS spectrometer and microscope.

Operation of the microscope is achieved using a software program written at ISU called Scope[1]. The main screen of this program allows students to control the operating parameters of the microscope made available by the manufacturer, e.g. focus, magnification, probe current, etc. This program is resident on each computer workstation. Also available at each workstation is the shareware program Image[2], which is used for image acquisition and analysis, and a tutorial package[3]. Due to hardware connections to the Quadra, operation of the EDS system is only possible using this computer. However, operation of the EDS is possible at each station by using Timbuktu™, a program that allows remote control of the Quadra by the work stations. Using Timbuktu, students take control of the Quadra; the screen of the workstation computer replicates the Quadra screen, allowing students to acquire and analyze EDS spectra.

The entire laboratory is linked using ethernet to the campus computer network. This allows students access to data from their homes or from anywhere in the world. A video projection screen, Figure 4, is also available for classroom instruction and demonstrations. Digital cameras allow the images and operator to be viewed from any location that is running the shareware CU-SeeMe[4]. This feature is being used to bring "live" SEM images into elementary and secondary classrooms in schools around Iowa[5].

1. Written by K. Fredrickson. Copies available by FTP to 129.186.222.37.
2. Written by Wayne Rasband at the National Institute of Health.
3. Written primarily by Mary Anderson and Kari Ellingson.
4. Available from Cornell University via the world wide web.
5. The authors wish to thank Jeff Jensen and Chad Miller for their assistance.

To Internet

Server

Ethernet Connection

Joystick Cable

SEM

Sta. 4   Sta. 1

Sta. 3   Sta. 2

CU-SeeMe Server
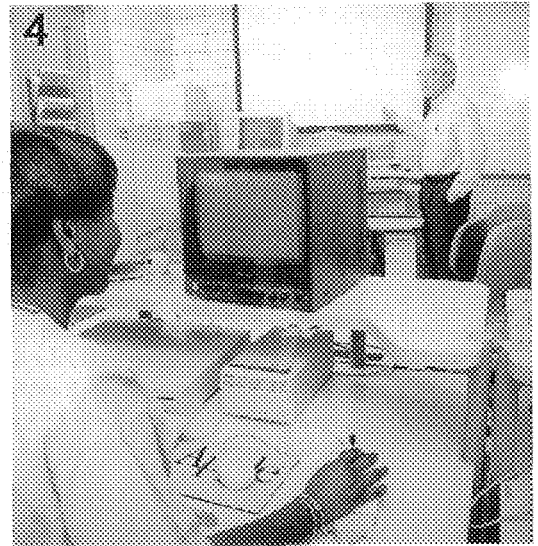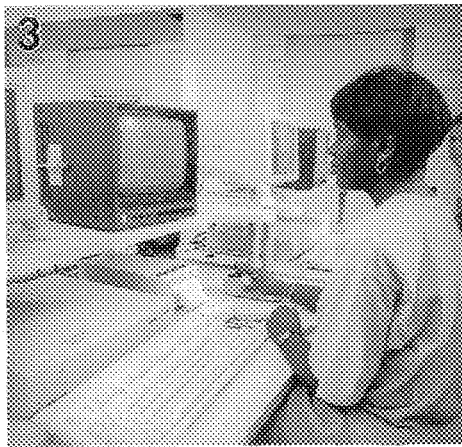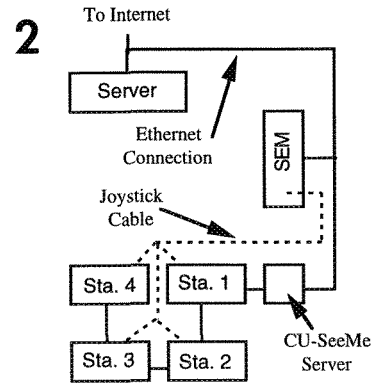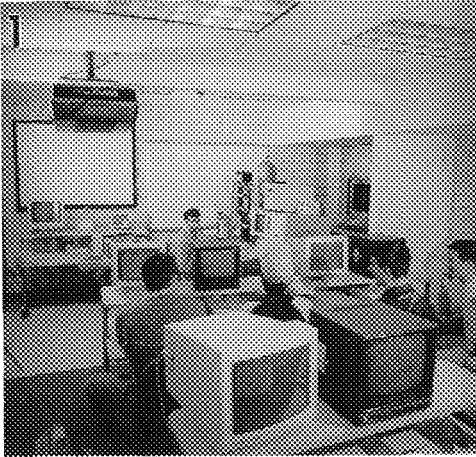
FIG 1.   Photograph showing the instructional laboratory in use at Iowa State University. Note the teaching stations and the ceiling mounted projector.

FIG 2.   Schematic layout of the laboratory showing the ethernet and joystick networks.

FIG 3.   Close-up of a typical teaching workstation. Note the computer, the TV monitor, the thermal printer, the joystick control, and the spherical digital camera.

FIG 4.   The projection system allows an instructor to display either the SEM image or a view of the computer screen.

ELECTRON MICROSCOPY OVER THE INTERNET AS AN OUTREACH TOOL

D.R. Cousens, D.Waddell, B. Cribb, M. Jones and J.Drennan
Centre for Microscopy and Microanalysis
The University of Queensland St Lucia 4072

Microscopy is an ideal medium to explore the wider applications of science and technology within the community in science and technology awareness programs. It bridges many individual disciplinary areas in science allowing many different facets of science and technology to be presented within a familiar framework.

The development of low cost video-audio conference software at Cornell University and the concurrent installation of Internet connections in Queensland schools at both primary and secondary level have provided an opportunity to enhance the science awareness and community service aspects of the Centres' operation beyond physical visits by school groups. This increases dramatically the potential audience that can be reached for a given investment of time. It also allows school communities in the more remote areas of the state to have some access to advanced scientific instruments and the applications for which they are used. The project is being initially piloted with schools in regional areas around Brisbane as this provides immediate feedback in the exploratory stages of the program.

The Centre has become involved in a program in collaboration with Key Learning Area Regional Science Coordinators in the Queensland Department of Education, the Science Teachers Association and a number of individual schools and teachers to explore and develop modules which complement and extend the school curricula at the late primary and early secondary level while simultaneously broadening the horizons. This program is being complemented by the development of teaching aids on CD-ROM which consist of packaged versions of the modules which may be used as a multimedia teaching resource by science teachers who do not have Internet access.

A number of short modules, the first of which were on the entomology of the Queensland fruit fly and the structure and fabrication of integrated circuits are under development. Further modules are planned in areas as diverse as environmental science, forensic science, fracture mechanics of materials, earth sciences. The approach has been to involve client departments with specialist expertise as well as practising teachers at the target school levels in the design and presentation of the modules.

The modules presented so far have consisted of a package of preparatory material downloadable over the net. This has varied from a full script to a series of questions with set piece answers. This is intended as preparatory material for the teachers to help prepare the students for a live session. The live sessions were initially conducted as fairly open ended session, but for practicality in a school environment, have now been limited to a one hour session. A specimen or series of specimens are examined with optical and/or scanning electron microscopy with concentration on relevant features in an overall story about the topic. The slide window capability of the Macintosh software is used to send high resolution images of selected features. As this takes between five and ten minutes, depending upon the modem speed of the slowest interconnection, the amount of material presented has to be limited and carefully selected to maintain the story line. Slides collected during the sessions are placed in the Centres web pages with explanatory text.

A major problem with the use of CU-SeeMe for these broadcasts apart from initial technical difficulties has been

398

in the generation of interactivity with the school student audience. A number of factors may account for this including unfamiliarity with the media, lack of preparation of the students for the material being presented, seeing the presenter as an authority figure, being overwhelmed by information content, technical difficulties, and too many participants to initiate dialogue on the subject material.

The least likely of these is technical familiarity on the part of the students who have no problems communicating with each other using video-conference software as the between schools chitchat before our sessions has indicated. In the last two sessions in February and March, we have attempted to prepare students for the session in advance by supplying their teachers with some preparatory material which can be discussed prior to the sessions. This has been in the form of a script outlining the session and a series of questions with set piece answers which the teachers can use as a guide and source material. Neither of these approaches has as yet succeeded in obtaining a high level of interactivity between the students and the presenter at this point. They have resulted in the stimulation of discussion at the schools with the class teachers, a step in the right direction. This has so far been most successful with primary school children, although the sample is still very small.

The lack of familiarity of the students with the presenter of the session may be addressable by providing some descriptive information with the initial information package for the session pitched at making the presenter less as a remote authority figure. The complexity of multiple interactions may be addressed by selecting a school as the primary target of the session and then rotating this status through the participants in future sessions

The use of the Internet for interschool and school-university interactions is in its infancy in Australia. By the nature of the medium itself we have the opportunity to monitor and learn from the wide experience in the United States. We do however have a different population density and population distribution which makes the use of the Internet particularly attractive for reaching remote areas.

Our experiences with the design and implementation of this program together with other applications of the Internet in our internal teaching and training functions will be presented and discussed.

DEVELOPMENT OF AN SEM DIGITAL IMAGE CAPTURE AND STORAGE SYSTEM AND ASSOCIATED DISTRIBUTED VIEWING INTERFACE

Benjamin R. Chu *, Patrick B. Moran *, Joseph B. Schaedler *

* IBM Microelectronics Division, Advanced Semiconductor Technology Center, Hopewell Junction, NY 12533

The advent of cheaper and faster network, desktop and storage products coupled with maturing digital image capture technology for microscopy tools is allowing for innovative ways to enhance the way microscopy images are captured, stored and viewed.[1-3] The SEM Laboratory at IBM's Advanced Semiconductor Technology Center (ASTC) is trying to leverage the combination of networked computing power and image capture technology to reduce costs, improve productivity and provide our internal customers with a product that better fits into their overall data analysis and documentation strategy.

ASTC's SEM Lab provides physical analysis support for over 200 semiconductor engineers working on advanced memory and logic process technologies. Over 15,000 requests (or jobs) are submitted annually to the SEM Lab which result in several hundred thousand images which are used to monitor in-line process lots, verify experimental lots and to aid in failure analysis. The original thrust of this project was to reduce the SEM Lab annual film budget (~$400K), but changing customer needs necessitated a system that would also allow for storage, retrieval and viewing of captured SEM images.

The first thing needed in developing our system was a capture system that could provide us with the same functionality, brightness/contrast quality and image aspect ratio currently available with our film cameras. The capture platform we incorporated into our 5 Hitachi SEMs is the Quartz PCI Image Capture System. The Quartz PCI system is a DOS/Windows based system which impressed us with its features, flexibility, ease of use, proven track record and large worldwide installation base. This system was developed jointly by Quartz Imaging Corp. and Nissei-Sangyo of Canada (a division of Hitachi Scientific Instruments) and can be serviced by our existing service provider, Hitachi Instruments, Inc. The workstation configured with the Quartz system is a 100Mhz Pentium with 32M of RAM, 20" monitor, 1G SCSI hard drive and a Token-Ring network connection. The other important component required to replace film is a fast, high resolution laserprinter. The configuration we decided upon is a Hewlett-Packard Laserjet 4+ with an XLI Laserjet+ resolution upgrade kit. The XLI kit increases the stock HP Laserjet 4+ resolution from 600 dpi to an effective 2400 dpi and more importantly increases print speed of our large TIFF image files dramatically. While not as good as the continuous tone resolution of Polaroid film, the XLI output has replaced 95% of our previous film needs.

The Quartz PCI system with XLI printer is an excellent stand-alone capture and print system. By itself, this system saves our organization almost $400K annually and has achieved ROI in less than 6 months. However, it became clear to us that it could be much more powerful when connected to our computer network. The ASTC accommodates a very heterogeneous computing environment consisting of office workstations, tool controllers, host mainframes and PC's. These computers also have a variety of operating systems: UNIX, OS/2, MVS and DOS/Windows. These systems are networked together using LAN technology, mainly Token-Ring and Ethernet. The only way to make these systems communicate effectively in such a varied environment is to utilize a common networking protocol, the Internet Protocol in this case. As mentioned previously, the Quartz PCI workstations are equipped with Token-Ring network interfaces and also have NetManage's ChameleonNFS TCP/IP stack installed to support the network communication to and from other systems on the network. Each Quartz PCI system is established on the network with its own TCP/IP address and hostname (i.e. nofilm1, nofilm2, etc.), and the NFS Server on each system is activated to export the appropriate image subdirectory.

The NFS server allows for direct access of the image data from a dedicated RS/6000 workstation which copies the files out to our centralized third generation network file system called the Andrew File System (AFS). In AFS, the data is stored under a central directory structure that is common to all workstations running the AFS client code (see fig. 1). Not only does AFS offer easier system administration than an NFS-only environment and

provides an accessible central repository for our data, it also offers important security functions in the form of access control lists (acl) that can be applied to the directory level. This is essential in our multi-corporate environment where access to proprietary data must be strictly controlled. While AFS maintains a full tape backup scheme every 24 hours (these tapes are kept indefinitely) our plans are to provide on-line network disk access to the original TIFF image for a period of 2 months. A reduced size JPEG rendering of the original TIFF will be available for up to 6 months. This strategy will allow our customers enough time to view, copy and print the image if they desire. By storing the images in AFS, we can provide a distributed interface for viewing of the images. Our viewing strategy is based primarily upon the use of a combination of 3rd party software and some in-house code which provides access via either RS/6000 workstations running AIX or PCs running OS/2. This allows our customers to view their images right from their desktop (see fig. 2). Since they have access to the image files via AFS, they can also embed the images into a variety of software (i.e. Lotus Notes, Applix, Microsoft Word, etc.) for documentation or annotation purposes or even maintain a copy on their local hard drive.

The major intent of this work was geared toward reducing operational costs. While we feel that we have been successful in accomplishing this, the additional result of integrating the capture systems into our network infrastructure has yet to yield its full potential. By allowing such easy access of the SEM images to our customers we feel that the future holds the promise of intranet image browsers, image databases and conference rooms equipped with computer-based overhead display units. It is our hope that this work can help guide or inspire others in their attempts to accomplish similar goals.

References
1. Nestor J. Zaluzec et al., *Tele-Presence Microscopy & the ANL LabSpace (eLab) Project*, Argonne National Laboratory.
2. T.A. Dodson et al., *Proc. 53rd Ann JMSA Meeting*, (1995)32.
3. F. He et al., *Proc. 53rd Ann JMSA Meeting*, (1995)634.
4. Grateful appreciation to IBM Microelectronics ASTC SEM Lab/PFA management and personnel (depts. 37J & 41Z), John S. Wilding Cole, Nissei Sangyo Canada and Dr. William D. Stewart, Dapple Systems
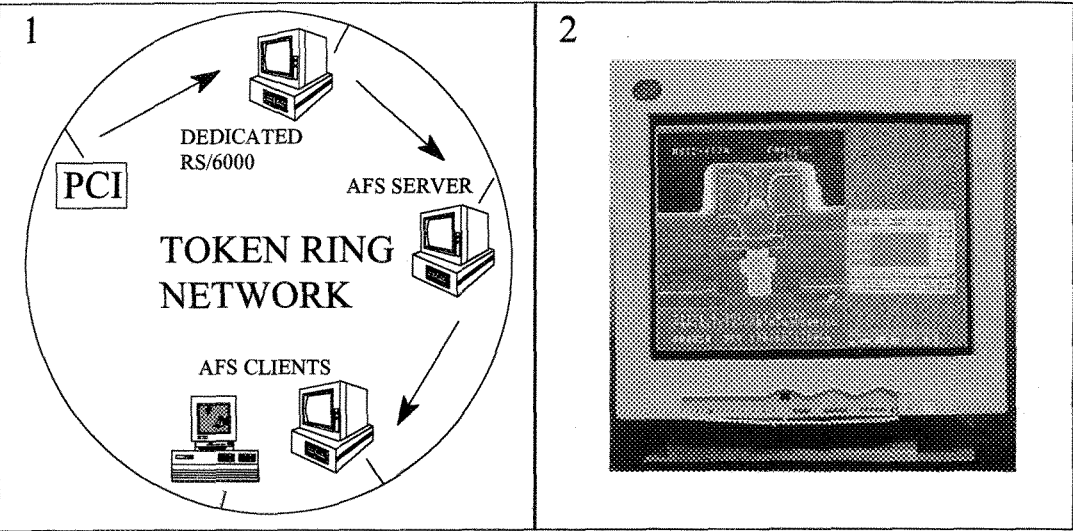
FIG. 1 - Token-Ring network schematic showing image data flow.
FIG. 2 - RS/6000 AFS client displaying captured SEM image over Token Ring network.

A WWW INTERFACE FOR VIEWING AND SEARCHING SETS OF DIGITAL IMAGES

Mary Thompson*, Jacob Bastacky**, William Johnston*

*Imaging and Distributed Computing Group, e-mail - MRThompson@lbl.gov,WEJohnston@lbl.gov
** Lung Microscopy Group, Life Sciences Division, e-mail - SJBastacky@lbl.gov
Lawrence Berkeley National Laboratory, 1 Cyclotron Rd., Berkeley CA 94720

As microscope images are increasingly being created and stored digitally, researchers are in need of tools to help them organize and quickly search these collections. Because of the large amount of storage taken up by digital images they are frequently kept on bulk storage systems remote from the microscopist's PC or workstation. The interface to these mass storage systems may be awkward and viewing large, remotely stored images can be very slow, making it difficult for the user to find a desired image.

The LBNL Image Library was designed and implemented to provide a system to help researchers organize, browse and search through digital image collections, especially collections where the original images are stored off-line in a mass storage system. We also wanted to facilitate co-operative research by allowing access to the images by specified users at local and remote sites.

An Image Library collection consists of thumbnail images and textual indexing material associated with pointers to the original images. This material is kept on-line on the machine that is running the Image Library Web Server. A user or project creates a top level collection on the server machine. Once the original beachhead is established, the collection owner is able to completely manage the collection from his local PC via Web form interfaces.

The Image Library provides the following functions:

1. Creates and stores a set of smaller "thumbnail" images that can be viewed quickly,
2. Keeps a text description file associated with each image and indexes over these files,
3. Allows the collection to be laid out in hierarchical sub-collections which can be independent of how the original images are organized or stored, and
4. Provides browsing tools to present a "view" of the thumbnail images selected by subcollection, search results, or individually by the user.

So far the Image Library has been used by two research projects. One contains about 900 scanning electron microscope images stored as 16bit grayscale TIFF images, and the other consists of about 20Gbits of X-ray video clips of coronary angiograms. In the first case, the software has enabled the researcher and his collaborators at remote sites to rapidly load and view images stored on the Lab's Unitree Mass Storage Server from desktop Macs. The second project is still in the testing stage, and is still being evaluated by the cardiologists. It has accomplished the main objective of allowing physicians at sites remote from the catherization laboratory to view the angiograms on their desktop computers.

The Image Library is implemented by a standard WWW server,[1] and a set of Perl scripts and HTML documents. A Web interface was chosen because it is graphical, platform and location independent and easily customized.[2] The server software was designed to be portable to most Unix systems and makes use of several portable libraries: pbmplus (Portable Bit Map) [3] and cjpeg for image transformations and Glimpse[4] for text indexing and searching. The client side of the application is slightly optimized for Netscape, but can generally be run by any graphic, forms-capable Web browser. Thus it runs on Unix, Windows or Mac platforms.

The Image Library can currently handle original images in 8bit or 16bit TIFF, GIF, JPEG and EPS formats. Adding images in a specialized microscope format typically requires the addition of a short script to convert the new format to a standard one. The thumbnail images are kept in either GIF or JPEG format.

To view a sample collection or to get information about downloading the software contact the URL http://www-itg.lbl.gov/ImgLib.

References
1. Robert McCool, et.al- http://hoohoo.ncsa.uiuc.edu/docs/Overview.html
2. Karen MacArthur - http://www.w3.org/hypertext/WWW
3. Jef Poskanzer - http://www.acme.com/software/pbmplus
4. Udi Manber, Sun Wu, Burra Gopal - http://glimpse.cs.arizona.edu:1994
5. This work is supported by the Director, Office of Energy Research, Office of Computation and Technology Research, Mathematical, Information, and Computational Sciences Division, of the U. S. Department of Energy under contract No. DE-AC03-76SF00098 with the University of California.
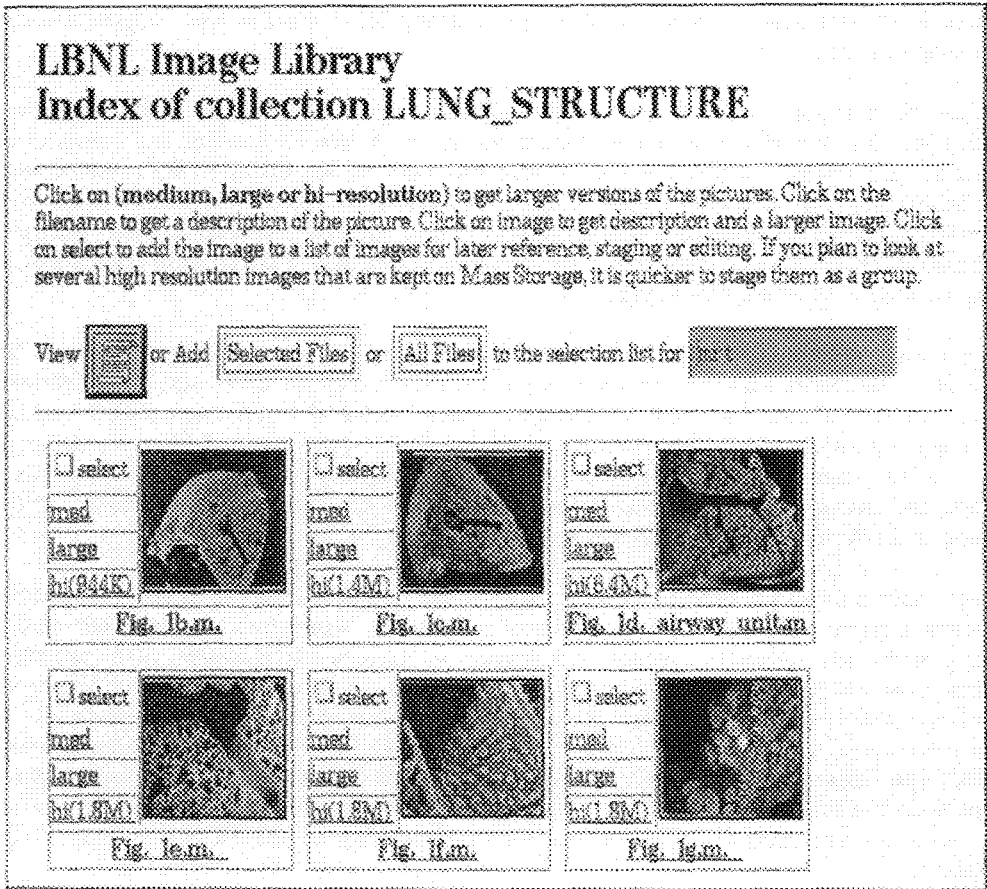
Fig. 1 Example of a browse page from the Image Library

Intranet Web System, a Simple Solution to Companywide Information-on-demand

Xiao Zhang

Technology Department, GE Plastics, Selkirk, NY, 12158

Intranet, a private corporate network that mirrors the internet Web structure, is the new internal communication technology being embraced by more than 50% of large US companies.[1] Within the intranet, computers using Web-server software store and manage documents built on the Web's hypertext markup language (HTML) format. This emerging technology allows disparate computer systems within companies to "speak" to one another using the Internet's TCP/IP protocol. A "fire wall" allows internal users Internet access, but denies external intruders intranet access. As industrial microscopists, how can we take advantage of this new technology? This paper is a preliminary summary of our recent progress in building an intranet Web system among GE microscopy labs. Applications and future development are also discussed.

The intranet Web system is an inexpensive yet powerful alternative to other forms of internal communication. It can greatly improve communications, unlock hidden information, and transform an organization. The intranet microscopy Web system was built on the existing GE corporate-wide Ethernet link running Internet's TCP/IP protocol (Fig. 1). Netscape Navigator was selected as the Web browser. Web's HTML documentation was generated by using Microsoft® Internet Assistant software. Each microscopy lab has its own home page. The microscopy Web system is also an integrated part of GE Plastics analytical technology Web system.

Information available from the Web pages includes (1) microscopy and microanalysis methods, (2) lab instrumentation, personnel, standard operation procedures (SOP), material safety data sheet (MSDS), (3) image archives and case study, (4) method development, technical reports, and project tracking sheet, (5) corporate-wide microscopy resources and internet microscopy resources (Fig. 2). On-page pointers and the search engine are connected with other departments, such as manufacturing, commercial, and customer service. It enables anyone to find information wherever it resides. All the information on the Web page is constantly updated.

With such a huge information database in hand, each lab will be able to open up virtually transparent global communication with other labs or business components, share corporate-wide microscopy resources, share best practices, reduce redundancy in method development, and centralize documentation in ISO 9000 standards, safety and environmental protection. The Web system becomes a combination of collaborative workspace, database library, and information sharing bulletin board. It really breaks down the walls and promotes people, with little, if any, training, to share the learning, share the work, and share the experience. Concepts such as virtual conferencing and virtual documentation/software distribution become a reality. In the near feature, advances in real-time CCD camera systems and streaming file-transformation software will bring remote microscopy support into real application.[2,3]

Like any new information communication system, soon the intranet Web system will, inevitably, suffer from growing pains such as over expansion of the Web. In the meantime, people need to use the Web to

receive its many benefits. The advantage and endless growth potential make the intranet Web the choice of communication models.

References

1. A. Cortese, *Business Week*, (1996)Feb.26, 76
2. C. Okon, *Advanced Imaging*, (1996)Feb., 30
3. N.J. Zaluzec, *Proc. Microscopy and Microanalysis'95*, (1995)14
4. The author is grateful to T. Stumpek for valuable discussion and excellent technical assistance.
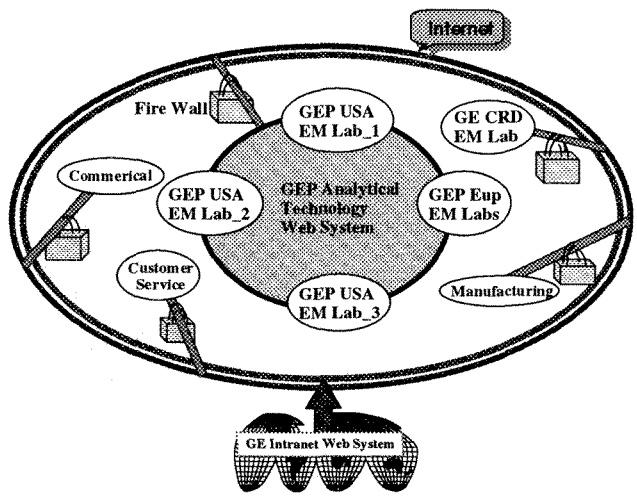
Fig. 1 Schematic view of GEP Intranet Web System.
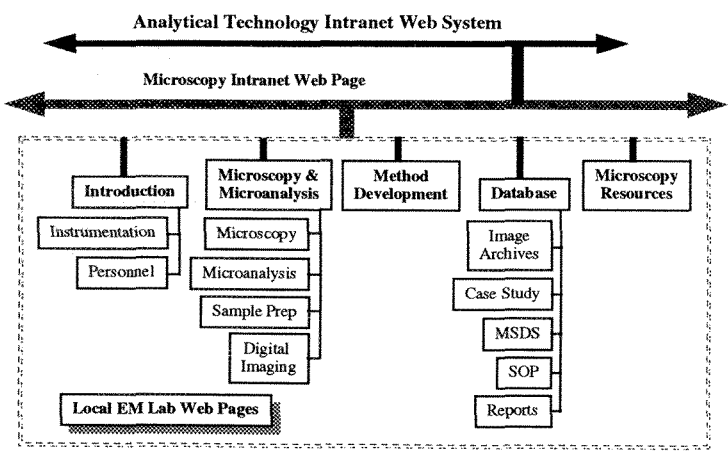
Fig. 2 Schematic view of a local GEP microscopy Web page

405

VIRTUAL SEM 1.2 - TRAINING IN SEM

B.J. Griffin & A. van Riessen*

Centre for Microscopy and Microanalysis, The University of Western Australia, Nedlands, WA, Australia 6907
* Applied Physics, Curtin University of Technology, Bentley W.A., Australia

The greatest barrier to effective training in electron microscopy is the initial apprehension within students based on the complexity and cost of the instrumentation. A second, and today more real barrier, is the actual cost of hands-on training in courses, in terms of both instrument and staff resources. The software described below was developed to eliminate these barriers, to include a 'fun' component to relax students, to improve the effectiveness of short training courses and to act as a stand-alone resource for new SEM operators.

A software package utilising multimedia components, "Virtual SEM 1.2", has been developed to simulate the use and operation of a basic scanning electron microscope (SEM). Background SEM theory is provided through introductory tutorials and an automatic assessment section allows independent evaluation of student progress. The package is appropriate for entry level operator training and also as a reference for general operation.

Digital SEM image stacks, with corresponding signal waveforms, have been recorded to demonstrate the effects of varying contrast, brightness, magnification, focus, primary beam current and accelerating voltage on a range of specimens. The specimens currently include Ag-Sn spheres on carbon tape, plant stems and the household fly. These image stacks are accessed through a screen display that simulates a SEM console. Realistic controls are provided for the user to move through the image stacks. A mandatory "filament saturation procedure", including a burn-out effect, is required prior to inspection of the "samples". An 'advanced imaging' section allows the operator to compare secondary, backscattered and cathodoluminescence images from a geological sample at a range of magnifications.

Self-assessment is provided by two multiple choice exams, each of twenty questions. On completion the software 'marks' the exam and provides the result and a grading, e.g. "Oops, are you in the right class?" for a zero score. The level is at basic, new operator standard. Results are automatically stored in a password protected file together with the date and elapsed time taken for the exam. The password protection is optional but allows 'remote' testing.

The package has been developed using the Silicon Beach package "SuperCard v1.6" and is a standalone program operable with system 7.0 and later on any MACINTOSH with a high resolution colour monitor (640x480) and a minimum of 4 megabytes of RAM. It is currently around 40 megabytes in size and will grow as additional features and specimen images are added.

The "Virtual SEM 1.2" package has now been in use, in various forms, for two years and approximately three hundred students have used it. The general feedback has been very positive and it is notable that the pervasive comment is with regard to the 'non-threatening' nature of the exercise. Currently the sample image range is being extended and a range of interactive exercises in the tutorial sections are being included. The assessment section is also being modified to provide for direct and immediate feedback to students.

"Virtual SEM 1.2" is public domain software. Unfortunately its size makes distribution difficult and so it is available from the authors on CD-ROM at a nominal price to cover the media cost (for full information: fax 619-380-1087 or email bjg@uniwa.uwa.edu.au). An earlier version (November, 1994) is available via ftp through the MSA/MAS public domain library. It is expected that an IBM-PC CD-ROM version will be available by late 1996 (hopefully in Minneapolis).
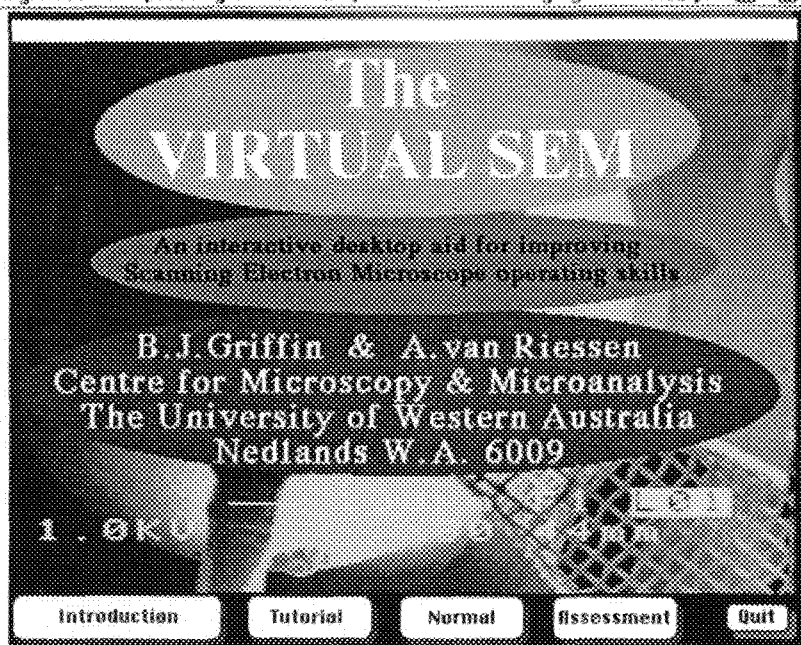
Select the required operating mode

Figure 1: Startup screen for Virtual SEM 1.2
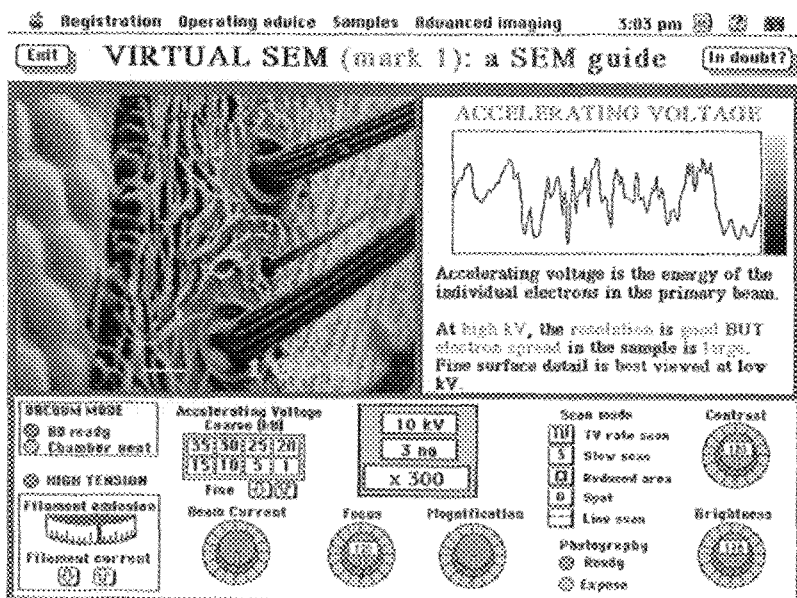
Figure 2: the 'normal' operation mode of Virtual SEM 1.2

407

Electron Microscopy and Educational Outreach on the World Wide Web

John S. Gardner*, Judy Rice**, Bill Fogt**, Kali Erickson*, and Russell Harrison*

*Microscopy Laboratory, 128 WIDB, Brigham Young University, Provo, UT 84602
**College of Education, 343 MCKB, Brigham Young University, Provo, UT 84602

For over five years, Utah Valley area high school students have been invited to the Brigham Young University Microscopy Lab to conduct individual and group research projects. This outreach program provides each student with concrete, "hands-on" experience in the field of microscopy and an application of the scientific principles learned in the high school classroom.[1] The program utilizes the expertise of university faculty, lab personnel, undergraduate research assistants, corporate professionals and public school teachers as well as microscopy facilities and equipment (Fig. 1). These elements combine in an effort to mold confident and experienced young professionals. The outreach program has produced students who have published, won contests, earned scholarships and found employment opportunities within the field. However, the program has only been able to serve a limited number of students who want to participate. With the aid of developing technology and the distributed learning model, the influence of electron microscopy can be spread more effectively.

The study of microscopy including several related subjects is now more accessible through the creation of a World Wide Web site at Brigham Young University (BYU).[2] Users can select from a variety of menus including a Library, Teaching Center, Learning Center, and Explore Your Mini-Worlds. Student research images have been collected and downloaded through the use of computerized imaging and microscopy (Fig. 2). Images from five BYU traveling Microscopy Society of America exhibits are currently accessible at the site to demonstrate how students have implemented the scientific method. The site provides a medium for publishing student research as well as a library of teaching resources. There are links to other helpful resources already available on the Internet including university libraries, contest information and regional professionals. A means is also furnished for students to submit questions directly to a microscopist through the web page. The materials provided are designed to supplement the Utah State Department of Education's core curriculum. Lesson plans are presented to help educators bring the experience of original laboratory research into their classroom.

Future improvements on the Web site include expanding the current library of images. To enable synchronous communication, a chat room will be established. Those students who demonstrate ingenuity and determination will be invited into the BYU laboratory to pursue Microscopy research. To further student access to equipment, one SEM unit has already been installed in a local Junior High School. Hopefully, other microscope systems can be obtained for interested public schools. Eventually a mobile SEM system will allow remote locations access to and experience with the outreach program. Through the combined efforts of education and technology a research environment is being created that enables students to have experience with electron microscopy as they participate in scientific studies. They will also have the opportunity to contribute not only to the enhancement of our body of general knowledge but to the advancement of their education.

References

1. W. Worthy, C&EN. 1989, 49-50.
2. http://www.byu.edu/acd1/ed/microscopy/

Fig. 1. The Distributed Learning Model for the BYU Outreach Program.

Fig. 2. Multi-faceted window allows user to choose first among insect species, second appendages, and third magnification level (Drosophila eye research submitted by American Fork High School).

MICROSCOPY OUTREACH THROUGH SHARED TECHNOLOGY

Rosemary A. Walsh, Electron Microscope Facility for the Life Sciences
The Pennsylvania State University, University Park, PA 16802

Educational Outreach at PSU's EM Facility for the Life Sciences evolved from the consolidation of multi-user laboratories and a growing demand for hands- on laboratory experiences requested by undergraduates, middle and highschool students and their teachers in central Pennsylvania. The EM lab is one of five such shared technology facilities which primarily provide university researchers with services and training.

The development of educational outreach programs grew from early work on extension projects with faculty and graduate students in the College for Agricultural Sciences. That experience and a new climate of cooperation permitted our laboratory to promote problem-based learning in funded programs such as undergraduate reasearch (independent study /honors projects) and summer institutes for pre-college students in Biology (Howard Hughes Institute) and Agricultural Sciences (Pennsylvania Governor's School, PGSAS).

In most situations we managed to match the project director with a capable student technician eager to develop laboratory skills and to structure the project design such that the training, data collection and analyis can be completed within six week summer term or the fifteen week semester. For this reason most studies utilize computer-based SEM or CRYO-SEM to document and compare samples, a description which applies to some portion of or pretest for a larger research project. One sample project on starch gelatinization was subdivided into three separate studies to fit the time constraints of three student technicians. The goal was to obtain preliminary data on three genotypes of maize starch with different polysaccharide compositions and to compare their structural changes during gelatinization. (Fig. 1, 2) One summer term study by three highschool students tested the effectiveness of irradiation in controlling bacterial growth in food products. Freshly harvested mushrooms were divided into control and treatment groups with the latter exposed to irradiation. Both sets were stored at refrigerator temperatures for 2 weeks and cap samples were taken at 3 day intervals and prepared for SEM. (Fig. 3, 4) A second set of samples were homogenized and plated and the number of colony forming units showed a positive correlation with the numbers of bacteria per unit area on the caps. Shorter programs are designed to enhance the microscopy unit in area middle schools (Plants, Cells and Viruses: Seeing the Unseeable); encourage adolescent females to consider science careers (Expanding Your Horizons in Math and Science, Women in Science and Engineering); challenge gifted students to find art in science (Engaging the Right Brain) and help teachers to examine bacteria from distinct zones in a microbial city, a cow's rumen and a cup of yogurt (Microcosmos). Programs which held the attention even of the "bored-to-tears" group concentrated on hair (straight, permed, punk-red, thick, thin, bleached), shaft appearance, difference in diameters and the elements detected by EDS.

Optimizing space, funds, equipment and faculty expertise removed the barriers which interfere with the free exchange of solutions to similar research problems, the

410

development of flexible skills and learning teams while instrumentation is still in peak condition.
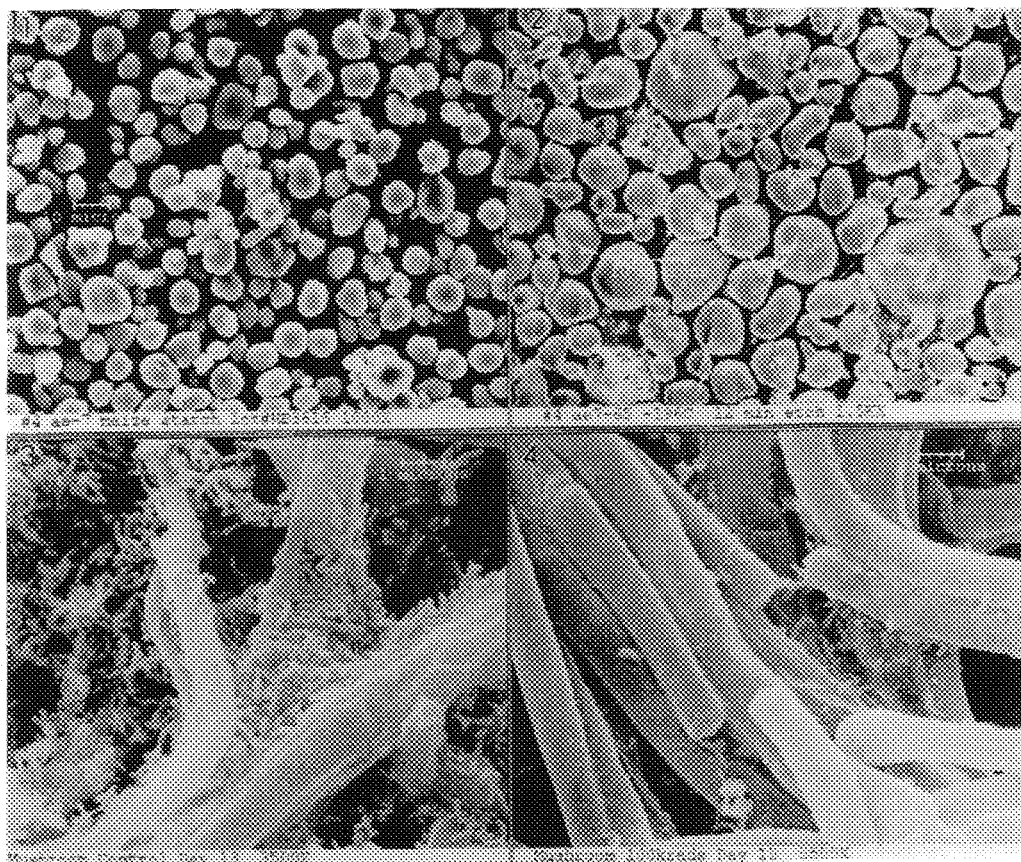
FIG. 1   ae-7 maize starch granules (70 % amylose/ 30 % amylopectin) -- Control
                imaged at 10 kV, ambient temperature, sputter-coated (10 nm AU/Pd)
FIG. 2   ae-7 maize starch granules gelatinized at 65°C, pelleted, plunge frozen (LN$_2$ slush), etched
                (-100°C), imaged at 5 kV/-196°C, uncoated
FIG. 3   Cap surface from control commercial mushroom (*Agaricus bisporous*) stored at 4°C for 13 days,
                standard EM preparation
FIG. 4   Cap surface from irradiated (100 krads) commercial mushroom (*Agaricus bisporous*) stored at
                4°C for 13 days, standard EM preparation

Bibliography:
Chen, Tom,   Particle Size Analysis of Three Maize Starch Products using the SEM. 1995. PGSAS
Hedrick, Joseph H.,   Granule Size Analysis of Gelatinized Maize Starches via CRYO-SEM. 1995 PGSAS
Branigan, Dana , Clint Fleckenstein, Fang-Tu ng,   Food Irradiation: The Effect of Low-Level Gamma
                Radiation on Shelflife of Commercial Mushrooms. 1995, PGSAS

OUTREACH OPPORTUNITIES USING THE INSTRUCTIONAL SEM AT IOWA STATE UNIVERSITY

L. S. Chumbley, M. Meyer, K. Fredrickson*, F.C. Laabs**

Department of Materials Science and Engineering, Iowa State University, Ames, IA 50011
*MTS, 14000 Technology Drive, Eden Prairie, MN
** Ames Laboratory, Ames, IA 50011

The development of a scanning electron microscope (SEM) suitable for instructional purposes has created a large number of outreach opportunities for the Materials Science and Engineering (MSE) Department at Iowa State University. Several collaborative efforts are presently underway with local schools and the Department of Curriculum and Instruction (C&I) at ISU to bring SEM technology into the classroom in a near live-time, interactive manner. The SEM laboratory is shown in Figure 1.

Interactions between the laboratory and the classroom use inexpensive digital cameras and shareware called CU-SeeMe, Figure 2. Developed by Cornell University and available over the internet, CU-SeeMe provides inexpensive video conferencing capabilities. The software allows video and audio signals from Quikcam™ cameras to be sent and received between computers. A reflector site has been established in the MSE department that allows eight different computers to be interconnected simultaneously. This arrangement allows us to demonstrate SEM principles in the classroom. An Apple Macintosh has been configured to allow the SEM image to be seen using CU-SeeMe. Two digital cameras are installed in the SEM room to show the SEM console and operator. These three signals are connected to the reflector. When a school logs in to the reflector, via modem or the internet, students in the classroom are able to see and talk to the SEM operator and view the SEM image in near live time.

Two main collaborative efforts with local schools are underway. The first, termed Project TEAMS (Teacher Education and Achievement in Math and Science) and administered by C&I, involves a three-way partnership between MSE, three pre-service student teachers in C&I and a 5th grade elementary teacher[1]. During the 1996 spring semester one TEAMS group will focus on bringing SEM technology into the elementary classroom. At the time of this writing the students are learning how to use the SEM system, Figure 3. Working with the classroom teacher they will then use this knowledge to prepare lessons (employing the CU-SeeMe connection) that are suitable for the 5th grade level. The second collaborative effort involves the MSE department and teachers[2] at the local high school. In this program cameras and software were provided to the local high school to allow them to control the SEM from the classroom. Samples are presently being selected that are suitable for the high school science curriculum. Once acquired, students will then conduct limited SEM investigations of these samples during class.

Future plans include expanding the number of interactions with schools to include all elementary and secondary schools in Iowa. The state has invested funds to install a state-wide fiber optics network that, when completed next year, will allow every school in Iowa access to the laboratory. A web page is also under development that contains tutorials on SEM operation aimed at various education levels and a library of photographs of samples submitted by students around the state, Figure 4.

Another exciting outreach aspect of the laboratory is that it should allow us to aid Iowa industry. Many companies in Iowa are relatively small (<50-100 employees) and do not have the means to obtain SEM analysis. The laboratory will allow individuals at these companies to submit samples for analysis and directly view the results as they are displayed on computers in their offices. Thus, the laboratory has enormous potential for outreach, both in the educational and industrial areas.

1. Pre-service teachers: Cassandra Green, Amy Lahr, Brad Lott, classroom teacher Mrs. Suzanne Kelly, Meeker Elementary School, Ames.
2. Science teachers Kirk Shmaltz, Ken Hartman, Bob Gibbons.
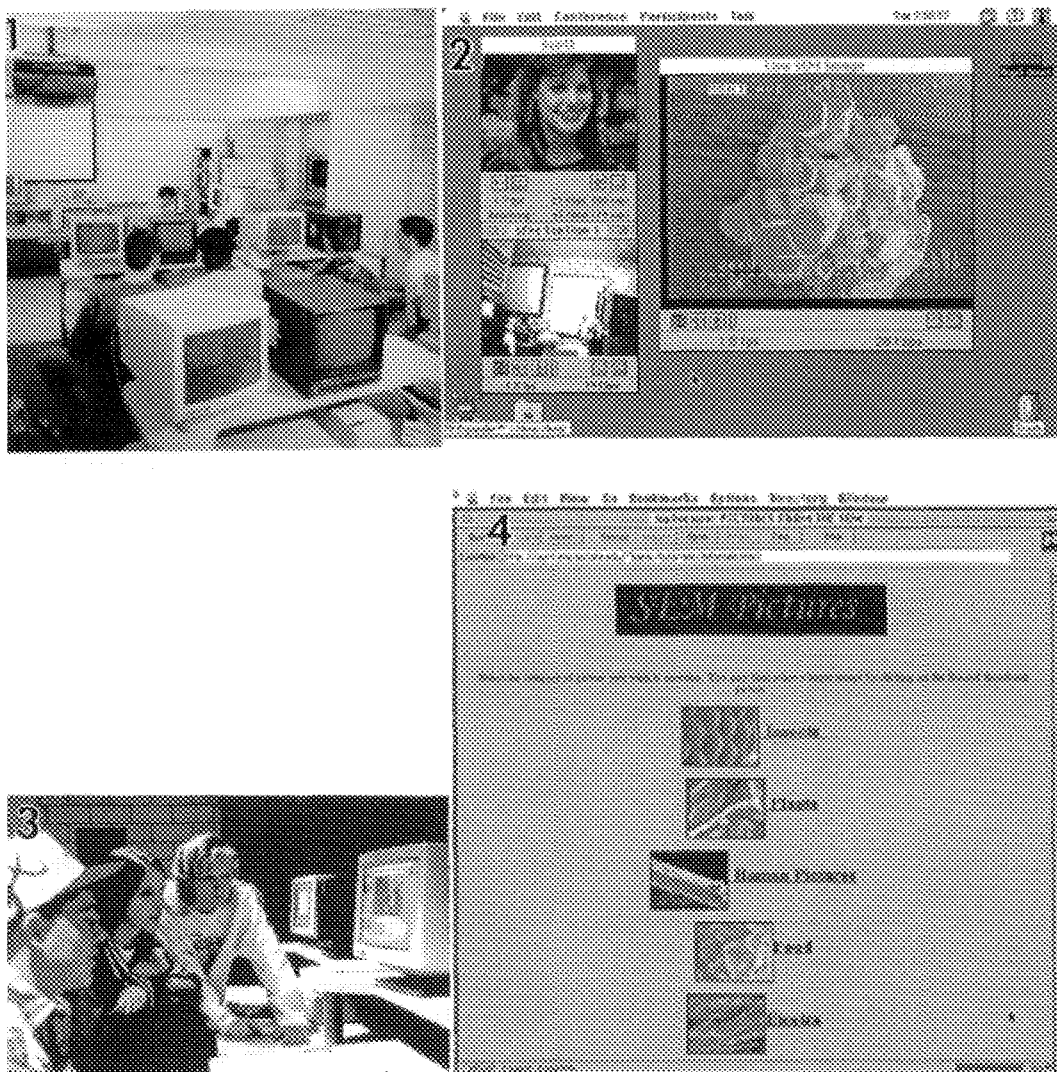
FIG 1. A photograph of the teaching laboratory.
FIG 2. A typical view of a computer screen showing the images that are available using CU-SeeMe. Three images are visible; the live SEM image, a view of the SEM console, and a student viewing the image on another computer that is linked to the MSE department reflector site.
FIG 3. Elementary education majors (from left) Brad Lott, Cassandra Green, and Amy Lahr learning to use the CU-SeeMe software and the digital cameras.
FIG 4. One screen from the web page (http://surf.eng.iastate.edu/~karie/) being developed at ISU showing different categories of sample pictures available for viewing.

REMOTE OPERATION OF A SCANNING ELECTRON MICROSCOPE (SEM) FROM DISTANT CLASSROOMS

N. R. Smith*, R. E. Tullis,* N. Fegan,** and C. L. Morgan***

*Department of Biological Sciences
**Department of Geological Sciences
***Department of Mathematics and Computer Science
California State University, Hayward, Hayward, CA 94542

California State University, Hayward (CSUH) has successfully demonstrated remote operation of a scanning electron microscope (SEM) using several networking interfaces. One of these methods is the use of highbandwidth asynchronous transfer mode (ATM). The different networking schemes have made it possible for instructors and researchers to access and control the Cal State Hayward SEM from classrooms located within the same building housing the microscope. In addition, the microscope has been remotely operated from across campus, from the local community college, and from San Jose State University.

The development of digital imaging technology provides opportunities of developing networking schemes for access and control of scientific instrumentation.[1,2,3] The ability to network microscopes offers the capability of teaching microscopy methods to a large number of students at the same time. The traditional microscopy class includes the instructor training one student at a time while other students observe the operator of the instrument.[4] Remote shared access to scientific instrumentation provides the advantages of a wider variety of resources and pooling of knowledge by a larger community.

The SEM at CSUH is a Philips XL-40 equipped with an IXRF, Inc. X-ray microanalysis and digital imaging system. The SEM is controlled by a 486 running Windows-based software to control the SEM over a SCSI interface. Symantec's pcAnywhere is used at remote sites to control the Windows software to change microscope parameters including magnification, brightness and contrast, etc. The motorized specimen stage can also be remotely positioned. Specimen insertion, tilting of the stage and Z-axis control require on-site manual manipulation.

CSUH has ATM networking capability provided through a Pacific Bell CalREN project. The small fixed-length packet size of ATM provides a basis for high speed switching and transport of video, data and audio. Using ATM it is possible to visualize images in virtual real time video. An ATM network attaches the Hayward campus to an ATM switch that also serves other CSU campuses, including San Jose, San Francisco and Fullerton. The network connection operates at DS3 speeds of 45 Mbps with 10 Mbps dedicated to the SEM.

Because of its high speed and scability, ATM is very desirable for remotely operating scientific instruments. The down side is that it is very expensive. For this reason we have also developed the use of Internet connections and campus video to import images and microscope control into classrooms.

We have used our campus video distribution system over the local cable channel to display SEM images into the local community college. Microscope control is accomplished using pcAnywhere®.

The SEM networking protocols we are using are serving as a model that will be applied to other scientific instrumentation on our campus. With these networking interfaces we are developing and using interactive curricula to better serve a wider audience of students.

References

1. N.J. Zaluzec, Proc. 52nd Meeting of MSA (1994)390.
2. T.A. Dodson, et al., Proc 53rd Meeting of MSA (1995)16.
3. M.H. Ellisman, Proc. 53rd Meeting of MSA (1995)66.
4. S. Chumbley, et al., (1995) Micro Res & Tech.32:330.
5. The authors gratefully acknowledge the networking assistance of Don Pardoe, Corinne Pelote, and Mark Honer.
6. This work is supported by the CSU DELTA/DLR/ATM. The SEM was purchased with an NSF ILI grant No. DUE-9451318.
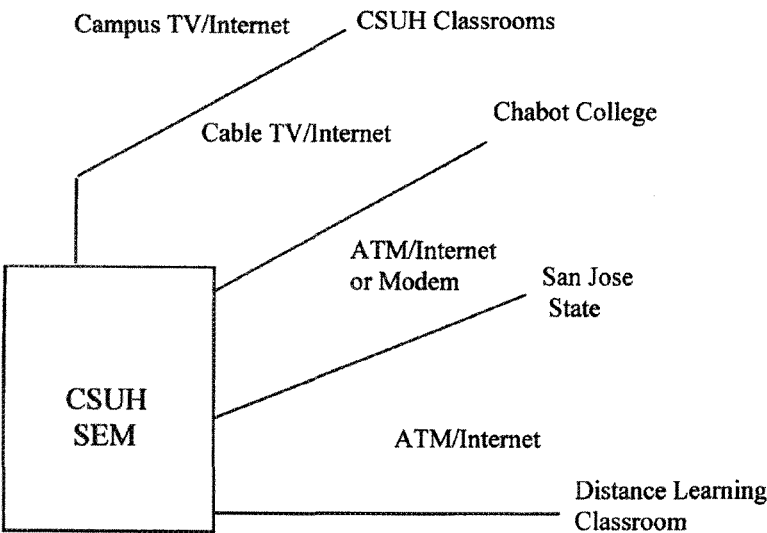
Fig. 1 Schematic diagram showing the video output mode from the CSUH Philips XL-40 SEM and the method of remote computer operation. In each case, pc Anywhere® is used at the remote site to operate the microscope controls.

A 200kV COMPREHENSIVE ANALYTICAL ELECTRON MICROSCOPE

T.Tomita,* M.Kawasaki,* M.Takeguchi,* T.Honda* and M.Kersker**
* JEOL, Ltd., 1-2 Musashino 3-chome, Akishima, Tokyo 196, Japan.
** JEOL U.S.A Inc., 11 Dearborn Road, Peabody, MA01960, U.S.A.

With the use of a high-brightness electron source, the performance of the analytical electron microscope (AEM) has significantly improved. It features a variety of sophisticated analytical functions, such as X-ray spot analysis, area analysis, electron beam energy analysis, electron diffraction, and phase analysis using a biprism for holography. Here, we report the results of our analysis using a 200kV comprehensive AEM which has an integrated ZrO/W emitter as its optic source. The AEM (JEM-2010F)[1] is equipped with an X-ray energy dispersive spectrometer (EDS), scanning image observation device (ASID), parallel detection electron energy loss spectrometer (PEELS), and TV camera.

(1) X-ray mapping using EDS and ASID

With FEG, the probe current in a 1 nm probe is increased by two-order orders of magnitude, and the background noise generated near the sample and in the illumination system is minimized. As a result, EDS analysis features high sensitivity at a minimum detection of 1% weight fraction from an ultra-micro area of 1nm diameter.

Fig.1a shows a high-resolution TEM image of the interface between a poly crystalline silicon gate (poly-Si) and a gate silicon oxide, as well as at the grain boundary in the poly-Si of a device equivalent to 64M DRAM. Fig.1b is the results of an area analysis, showing the segregation of the additives in the interface of a poly-Si gate and a gate silicon oxide.[2]

(2) EELS

Using a 1-nm-diameter probe, which has a current of 0.5nA and 0.7eV FWHM of the zero loss peak, EELS spectra were obtained with high accuracy. It is possible to detect small amounts of elements and the shift of energy level in the specimen.

Fig.2a shows a high-resolution TEM image of a SiO2/Si interface viewed in the <110> cross-section. Si-$L_{2,3}$ edges in EELS spectra, obtained at locations indicated in the TEM image, are shown in Fig.2b. Bulk Si onset (Si^0) and its chemical shift (Si^{4+}) appear in spectra C and A, respectively. The peak at 103 eV in spectrum B shows that Si atoms in an intermediate oxidation state (Si^{2+}) are present at the interface.[3]

(3) Phase analysis by electron biprism

A high-coherency electron beam was used to obtain an atomic scale potential distribution from the information on the phase. Interference fringes at 0.07 nm intervals are clearly seen in the hologram (Fig.3a) obtained by an electron biprism employing a 0.6-μ m-diameter platinum wire.

A phase map obtained from the hologram near the boundary of AlAs and GaAs is shown in Fig.3b. The comprehensive AEM, as the above examples demonstrate, supports various analytical techniques to meet a wide range of applications. Furthermore, Different analysis may be applied to a single specimen to obtain accurate quantitative/qualitative information for extensive, in-depth studies.

References

1. T.Honda, T.Tomita, K.Kaneyama and Y.Ishida, Ultramicroscopy, 54 (1994) 132-144
2. Kyung-ho Park, S.Hashimoto, M.Kawasaki and K.Ibe, Institute of Physics Conference Vol.146 Microscopy semi-conductor materials, 575-578.
3. Data courtesy of Dr.N.Igarashi, NEC Co. Ltd.
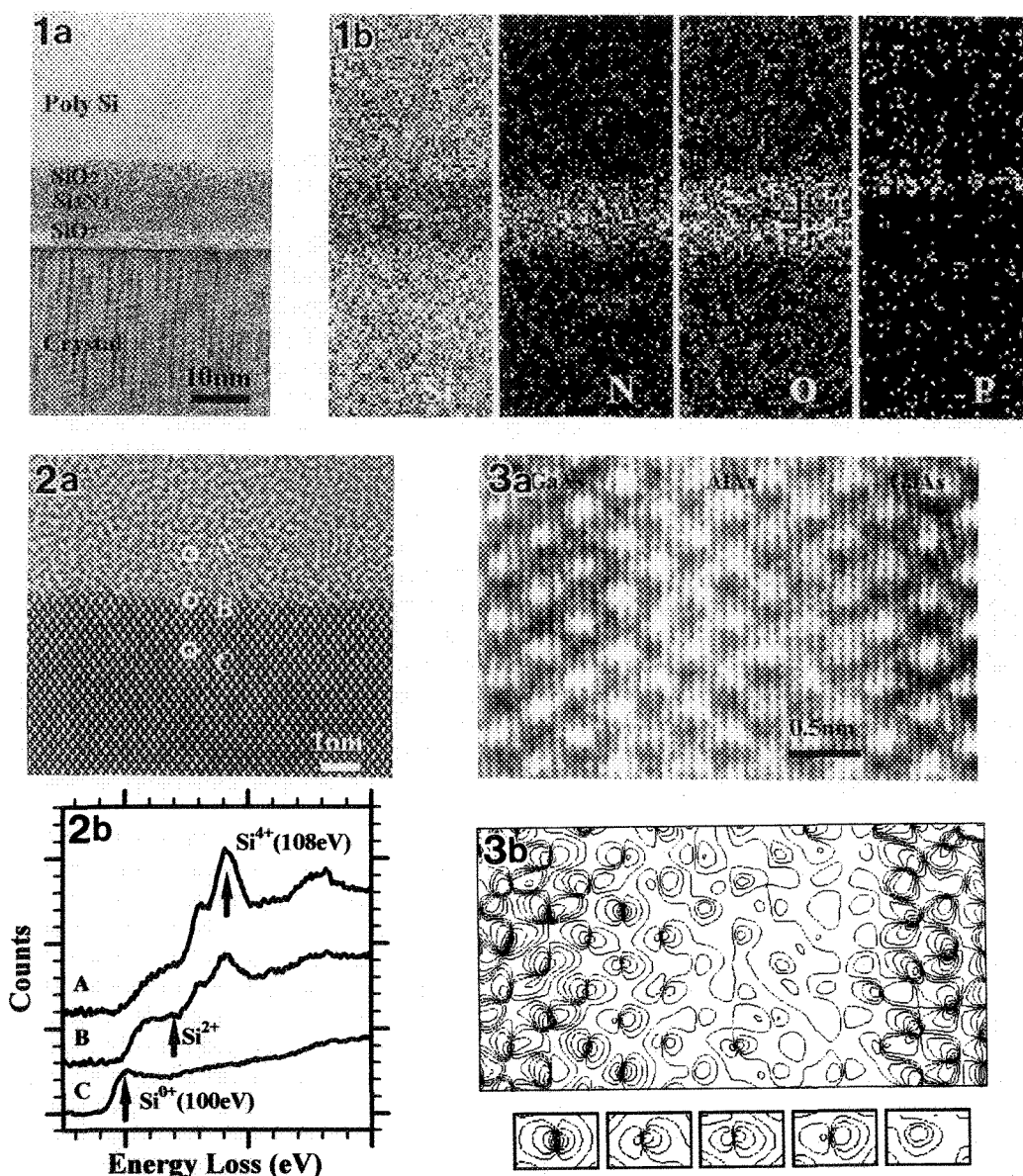
Fig.1a. High-resolution image at the interface between a poly-crystalline silicon gate and a gate
silicon oxide of a device equivalent to 64M DRAM.

Fig.1b. X-ray mapping at the interface.

Fig.2. High-resolution image of the SiO2/Si interface viewed in the <110> cross section, and
EELS spectra obtained at locations indicated in the image.

Fig.3. The hologram of AlAs/GaAs and the contour map of electric potentials.

417

PRACTICAL CORRECTION OF THREE-FOLD ASTIGMATISM IN THE PHILIPS CM TEM

Arno J. Bleeker[*], Mark H.F. Overwijk[**] and Max T. Otten[*]

[*]Philips Electron Optics, PO. Box 218, 5600 MD Eindhoven, The Netherlands
[**]Philips Research Laboratories, Prof. Holstlaan 4, 5656AA Eindhoven, The Netherlands

With the improvement of the optical properties of the modern TEM objective lenses the point resolution is pushed beyond 0.2 nm. The objective lens of the CM300 UltraTwin combines a Cs of 0.65 mm with a Cc of 1.4 mm. At 300 kV this results in a point resolution of 0.17 nm. Together with a high-brightness field-emission gun with an energy spread of 0.8 eV the information limit is pushed down to 0.1 nm. The rotationally symmetric part of the phase contrast transfer function (pctf), whose first zero at Scherzer focus determines the point resolution, is mainly determined by the Cs and defocus. Apart from the rotationally symmetric part there is also the non-rotationally symmetric part of the pctf. Here the main contributors are not only two-fold astigmatism and beam tilt but also three-fold astigmatism. The two-fold astigmatism together with the beam tilt can be corrected in a straight-forward way using the coma-free alignment and the objective stigmator. However, this only works well when the coefficient of three-fold astigmatism is negligible compared to the other aberration coefficients.[1] Unfortunately this is not generally the case with the modern high-resolution objective lenses. Measurements done at a CM300 SuperTwin FEG showed a three fold-astigmatism of 1100 nm which is consistent with measurements done by others.[2] A three-fold astigmatism of 1000 nm already sinificantly influences the image at a spatial frequency corresponding to 0.2 nm which is even above the point resolution of the objective lens. In principle it is possible to correct for the three-fold astigmatism *a posteriori* when through-focus series are taken or when off-axis holography is employed. This is, however not possible for single images. The only possibility is then to correct for the three-fold astigmatism in the microscope by the addition of a hexapole corrector near the objective lens.

We have integrated a hexapole field with the eight poles of the standard objective stigmator of the CM300 SuperTwin FEG to correct for the three-fold astigmatism. By employing custom-designed electronics and computer control we can excite each coil of the stigmator independently. This gives us the freedom to excite an octupole, a hexapole, a quadrupole and a dipole at the same time at arbitrary strengths and, excluding the octupole, of arbitrary direction. Fig. 1 shows the results of a number of measurements of the three-fold astigmatism. The open squares represent measurements over a period of one year without correction. It is seen that the three-fold astigmatism remains constant. This implies that the correction of three-fold astigmatism must be carried out only once. Lengthy daily alignment procedures can thus be avoided. The open dots represent the outcome of measurements after the mounting of the new stigmator assembly but without any correction done. During the mounting of the new stigmator the lower pole piece must be removed. We deliberately rotated the lower pole piece before rebuilding the objective lens. It is seen that only the direction but not the magnitude changed after this action. This means that the three fold-astigmatism is determined completely by the properties of the lower pole piece. Exciting the hexapole field to the correct strength and direction resultes in the solid squares in Fig. 1. The average value is well below 100 nm. This correction is sufficient to resolve 0.1 nm without distortion due to three-fold astigmatism. Fig. 2 shows a template of 16 diffractograms taken at a tilt angle of 0.34° and equally spaced azimuth. Opposing diffractograms (#n to #n+8) in this template are nearly identical demonstrating the excellent alignment.

418

References

1. A. Thust, M.H.F. *et al.*, Accepted for publication in Ultramicroscopy (1996)
2. W.O. Saxton Utramicroscopy 58 (1995) 239-243
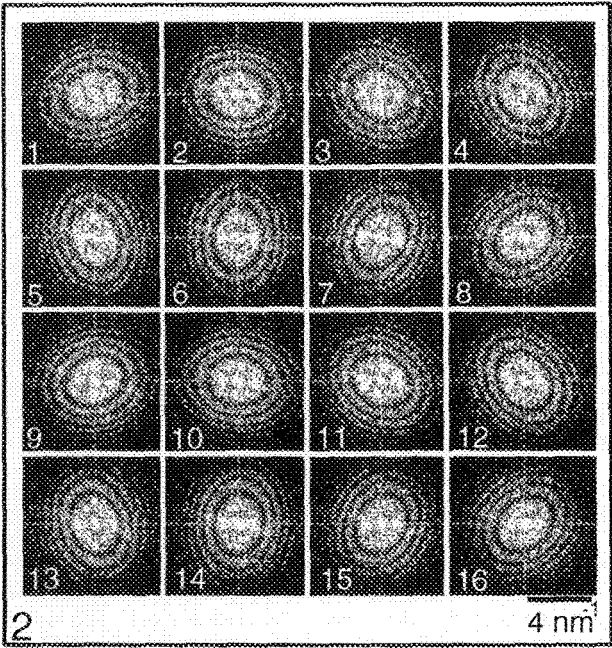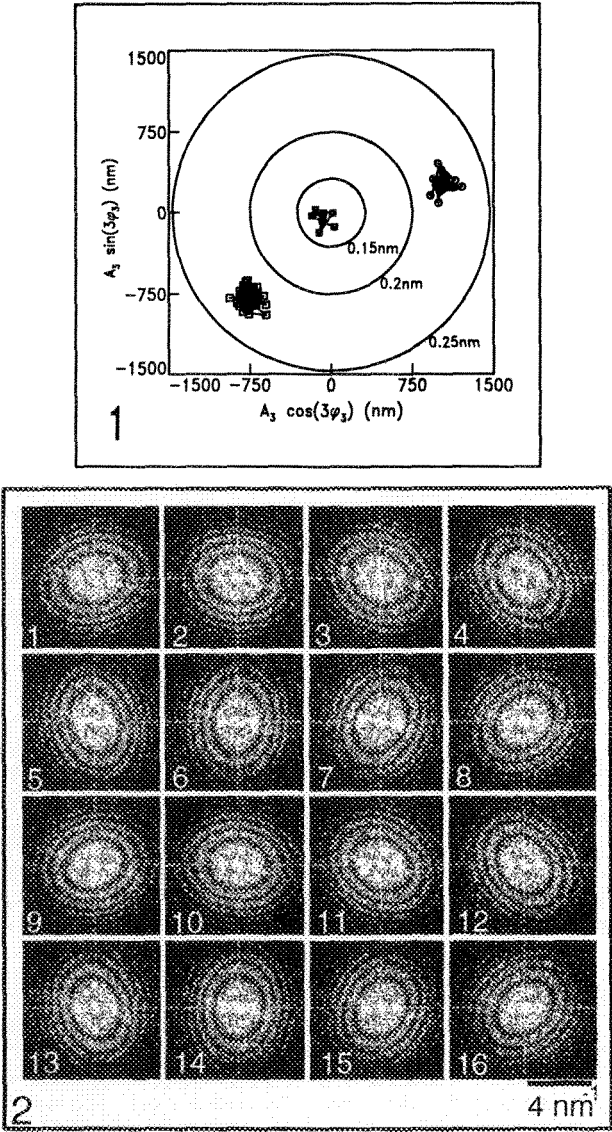
FIG.1 Measurement of the three-fold astigamtism of a CM300 ST FEG before (open squares and dots) and after correction (solid squares)

FIG.2 Diffractograms of a tilt-azimuth series with corrected three-fold astigmatism.

AN AUTOMATED PROCEDURE FOR ON-LINE MEASUREMENT OF SPHERICAL-ABERRATION COEFFICIENT OF HIGH-RESOLUTION ELECTRON MICROSCOPES

M. Pan and O.L. Krivanek

Gatan R & D, 6678 Owens Drive, Pleasanton, CA 94588

Spherical aberration coefficient (Cs) of the objective lens and electron wavelength ultimately determine the point-resolution of a high resolution electron microscope (HREM). Accurate measurement of Cs has become increasingly critical for reconstruction of structural information well beyond the point-resolution by means of either electron holography or focal series methods with a field emission gun (FEG) microscope. There are two main existing procedures for Cs measurement, i.e. (1) using diffractograms from a thin amorphous material[1,2], and (2) using beam-tilt-induced image displacement (BID)[3]. Since these procedures generally involve intensive data measurement, it is highly desirable to have an automated procedure. With an image pickup system such as CCD camera and appropriate software, we have developed an automated procedure for on-line Cs measurement. The procedure is based on analyzing diffractograms from a thin amorphous material such as amorphous carbon or germanium. The use of CCD camera allows for on-line measurement, and also for magnification to be calibrated with high precision, which is critical in Cs measurement.

The automated procedure consists of the following steps: (1) a through-focus image series is recorded from a thin amorphous material and diffractograms are calculated; (2) each diffractogram is rotationally averaged to increase signal-to-noise ratio; (3) the background of the line profile (averaged diffractogram) is correctly estimated and subtracted; (4) the damping of high frequency amplitudes due to various sources (spatial and temporal envelopes, MTF (modulation transfer function) of the CCD camera, etc.) is compensated to give equal weight for both low and high frequency amplitudes; (5) noise regions (very low and high frequencies) are excluded from the cross correlation process by using minimum and maximum fitting range which is determined automatically; (6) theoretical phase contrast transfer function (PCTF) is calculated as a function of both defocus and Cs and cross correlated with the line profile as obtained in step (2). The highest cross correlation coefficient thus corresponds to values of both defocus and the Cs. (7) the averaged Cs and the standard deviation are calculated from the through-focus series.

Since the contribution of Cs to PCTF is mainly in the high frequency range, it is very important to record images whose diffractograms show amorphous rings extending to the highest frequency. Temporal (energy spread) and spatial (beam convergence) incoherence are the main frequency damping envelopes. The damping due to spatial incoherence is dependent upon the defocus while temporal incoherence is not. So with the given beam convergence it is possible to search for a particular focus setting (called as "optimum information defocus") under which diffractogram contains the highest information transfer. This "optimum information defocus" is determined (automatically) prior to Cs measurement and used to record the through-focus image series. The value of this defocus is found to be in the range of 3-5 times Scherzer defocus.

Figure 1 shows a diffractogram of a commercial holey carbon film recorded at the "optimum information defocus" for a CM200 FEG/UltraTWIN with left half showing the original data and the right half rotationally averaged. An amorphous ring of 1.9 Å is indicated. Figure 2a is the line profile of the rotationally averaged diffractogram. Figure 2b shows the same line profile after automatic background subtraction and amplitude correction, and is used in the cross correlation process. The noise regions are excluded from the cross correlation by automatically applying a minimum and maximum fitting range (fig.2b). Figure 3a shows the 2D cross correlation function. The section of the cross correlation function containing the overall highest correlation coefficient (circled in figure 3a) is shown in figure 3b. The Cs is measured from a series of 5 images as (0.5490 ± 0.0089) mm. It is noted that the stochastic error is about 1.6%. This is most likely due to the fact that the largest amorphous ring used was only up to 1.9 Å (close to the Nyquist limit). The stochastic error in Cs measurement could be reduced by optimizing the imaging

condition, i.e. by using a higher magnification to allow higher frequency rings to be visible. Using amorphous germanium instead of amorphous carbon will extend the rings to even higher frequency due to higher atomic scattering amplitudes at high angles for germanium. Therefore the precision in Cs will be improved. Magnification calibration is found to be the main source of error in Cs measurement, for example a 1% error in magnification calibration can result in an error up to 5% in Cs measurement. The use of CCD camera and appropriate peak search (in diffractogram) routine can reduce the error in magnification calibration to less than 1% as high quality and distortion-free images are used to calculate the diffractograms[4].

In summary, an automated procedure is developed for Cs measurement based on analyzing line profiles of diffractograms from an thin amorphous material. The background subtracted line profiles are cross correlated with calculated PCTFs with variable defocus and Cs. The procedure measures Cs with high precision (~ 1%) comparable with previous diffractogram-based procedure[2]. On-line Cs measurement is made possible by using digital images from CCD cameras.

1. O.L. Krivanek, Optik 45 (1976) 97.
2. W.M.J. Coene and T.J.J. Denteneer, Ultramicroscopy 38 (1991) 225.
3. A.J. Koster and A.F. de Jong, Ultramicroscopy 38 (1991) 235.
4. W.J. de Ruijter et al., Ultramicroscopy 57 (1994) 409.
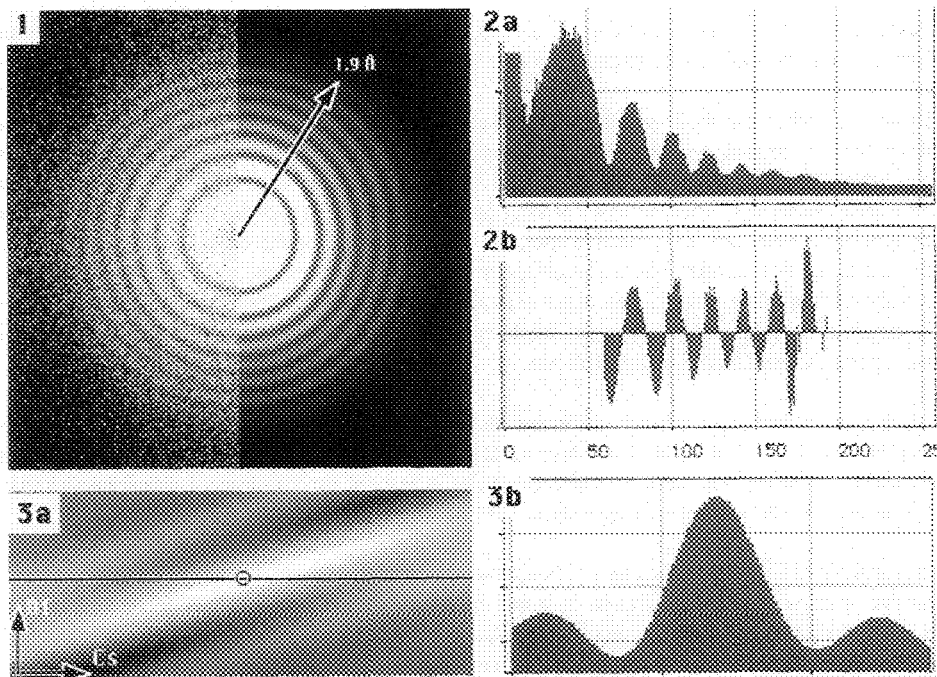
Fig.1 Diffractogram from a commercial holey carbon film recorded at "optimum information defocus" on a CM200FEG/UltraTWIN. Left half: original; Right half: rotational averaged.
Fig.2 (a) Line profile of the rotational averaged diffractogram in fig.1; (b) same line profile after background subtraction and amplitude correction. Minimum and maximum fitting range is also applied.
Fig.3 (a) 2D cross correlation function; (b) section of (a) showing the highest correlation coefficient as circled in (a).

THE CM120-BIOFILTER: DIGITAL IMAGING OF UNSTAINED SPECIMEN, A COMPARISON OF ZERO-LOSS AND UNFILTERED IMAGES

Uwe Lücken[*], A. Frank de Jong[*], Wim M. Busing[*], Jeremy Rees[*], Klaus Nadarzinski[*] and Mike K. Kundmann[**]

[*] Philips Electron Optics , PO Box 218, 5600 MD Eindhoven, The Netherlands
[**] Gatan R&D, 6678 Owens Drive, Pleasanton CA 94588, USA

A new system for energy-filtered electron microscopy (EFTEM) has been developed, adapted for the study of life science specimens. Attention has been given to integration, ease of use and the typical problems encountered while investigating unstained and cryo-specimens. Low-dose, cryo-capabilities and a high contrast objective lens have been combined with an imaging energy filter, digital image recording with phosphorus scintillator and advanced image processing capabilities. The CM120-BioFilter is an integration of the CM120-BioTWIN with the Gatan post-column imaging filter GIF100. The BioTWIN objective lens (C_s=6.2 mm, f=5.9 mm) is optimized for high-contrast imaging. The GIF100 is a computer-controlled, second- order corrected energy filter with a cooled multiscan CCD for digital image recording. Improvement of the contrast can be achieved if inelastically scattered electrons are removed. A comparison of zero-loss filtered and unfiltered images from unstained specimens is presented.

The contrast of thick, unstained specimens is limited by the high amount of inelastic scattering. Images from thick sections of unstained spleen tissue shown in Fig. 1 are compared by means of mean and standard deviation of multiscan CCD data. Figure 1a shows 8000 +/- 800 and Fig. 1b only 8000 +/- 330 counts/pixel for the same area of interest. The contrast-forming mechanism for this type of specimens is dependent on the wavelength of the electrons, the objective aperture, the focal length of the objective lens and the amount of inelastic scattering. For comparable image conditions (same voltage, same objective aperture) the zero-loss filtered shows more than twice the contrast compared to the unfiltered image. On the basis of a mean free path length of ~100 nm for carbon the thickness of this specimen has been determined by electron energy loss spectroscopy (EELS) to be 400 nm.

Figure 2 shows another example of thick unstained sections. This section of liver tissue shows hepatocytes and a single red blood cell. The light areas represents glycogen particles which are not well preserved and show only little scattering. The zero loss filtered image in Fig. 2a shows clearly better fine structure and contrast compared to the unfiltered image shown in Fig. 2b.

Imaging and analysis of biological specimens at liquid nitrogen temperature is nowadays a routine method. For phase contrast specimens (like thin frozen hydrated films) the contrast at Scherzer focus is approximately proportional to the square root of C_s so a higher C_s gives more contrast. The mean free path length for 120 kV inelastic scattered electrons in amorphous ice is ~90 nm, thus for thicker ice films zero loss filtering improves the image quality. In Figure 3 we have compared images of frozen hydrated cytoskeleton. Figure 3a shows the zero-loss filtered and Fig. 3b the unfiltered image. The inserts are the FFTs of the helical fibres and one can see in the filtered image a weak 4th layer line. The low resolution frequencies are also more pronounced in the energy-filtered image.
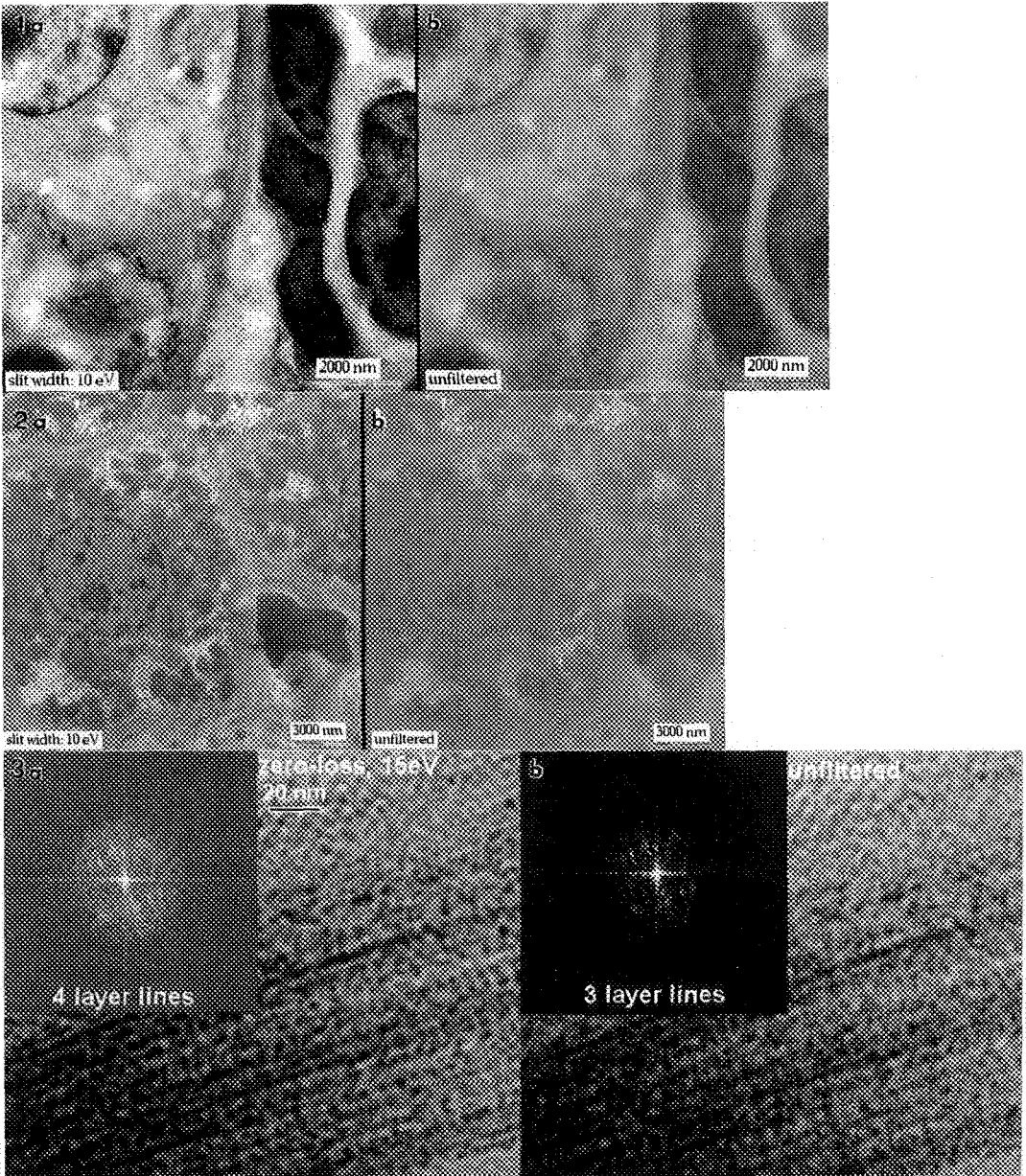
FIG. 1 Thick (~400 nm) section of spleen tissue showing a variety of cell types. No uranium and lead stain present.

FIG. 2 Thick (~350 nm) section of liver tissue showing hepatocytes and a single red blood cell. No uranium and lead stain present.

FIG. 3 Frozen hydrated cytoskeleton. The inserts represents FFT's and show a helical diffraction pattern.

MOLECULAR IMAGING: DESIGN OF THE PMP IMAGING SPECTROMETER, RESOLUTION LIMITS, AND RADIATION SENSITIVITY

M.M.G.Barfels, Y.Heng*, F.P.Ottensmeyer
Department of Medical Biophysics, U. of Toronto, 610 University Ave, Toronto, Ontario, M5G 2M9
*McMaster University, 1200 Main St. West, Hamilton, L8N 3Z5, Canada

One of the main applications of an energy filter is to obtain elemental distribution images by electron spectroscopic imaging. This technique has been pushed to the imaging of fine structure such as the sp^2 and sp^3 states of carbon at a sub-nanometer spatial resolution.[1] However, low energy loss imaging in the region of the molecular excitations has largely remained unexplored due to the limitation in the energy resolution obtainable in the energy filters. Molecular absorptions in the visible and UV regions of the spectrum occur at 1.5 eV to 10 eV. Thus it would be necessary to have an energy resolution of about 1 eV or better.

An optimized Prism-Mirror-Prism energy filter has been built by altering the straight faced pole pieces to circular curvatures.[2] See Figure 1. The optimum curvatures for each of the faces were determined iteratively. In order to simulate the electron path accurately through the Prism-Mirror-Prism filter, it was necessary to calculate the magnetic fringing fields using the Boundary Element Method as outlined by Kasper.[3] The ray-tracing procedure indicated a theoretical energy resolution of 1.3 eV for the optimized magnetic prism. This has been tested on our prototype spectrometer currently installed in the Siemens EM102. An energy resolution of 1.1 eV was obtained.

The feasibility of molecular imaging was studied by embedding a chromophore, hematin, into resin. In Figure 2 the porphyrin excitation can be seen in the difference between the hematin spectrum and resin spectrum in the low energy loss region. The absorption equivalent to the excitation in the visible region 1.5 eV to 3 eV is quite evident in the image in Figure 3.

Furthermore, the spatial resolution obtainable for imaging low energy loss electrons needed to be addressed due to the non-localized electron interactions.[4] The spatial resolution was determined by the sharpness of the edge of the hematin crystal as the image is viewed parallel to the flat side of the object. A densitometer trace taken across the edge of the crystal into the embedding resin is shown in Figure 4. The full width at half maximum of this trace after conversion to a line spread function indicates a resolution of 8 nm. The resolution using this method is dependent on the flatness of the edge measured and thus a better spatial resolution may be possible.

The radiation sensitivity of hematin was quantified with respect to dose at an incident electron energy of 60 keV. The decay was measured directly from the decrease of the electron energy loss signal at a 3 eV absorption using a 2 eV energy window. The signal decay to 1/e of its initial intensity was measured to be 120 e/A^2. See Figure 5.

References
1. Muller D.A., Tzaou Y., Raj R.& Silcox J. (1993) Nature **366**, 725-727
2. Jiang X.G. and Ottensmeyer F.P. (1993) Optik **94**, 88-95
3. Kasper E. (1987) Optik **77**, 3-12
4. Kohl H. and Rose H. (1985) Adv. in Electr. and Elect. Phys. **65**, 173-227
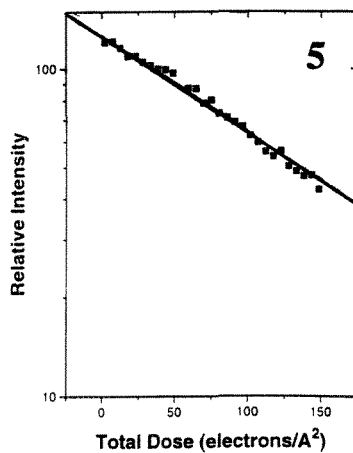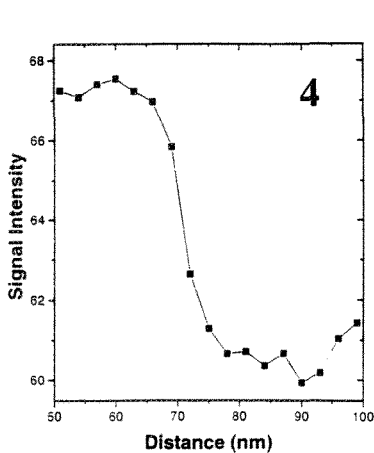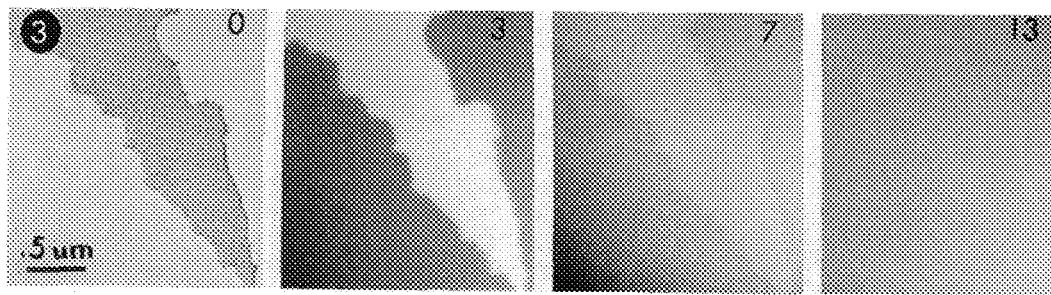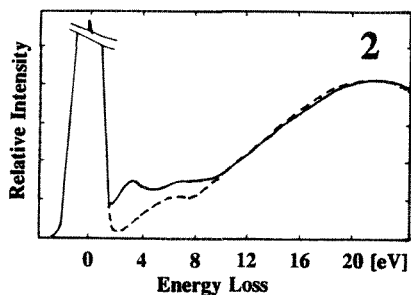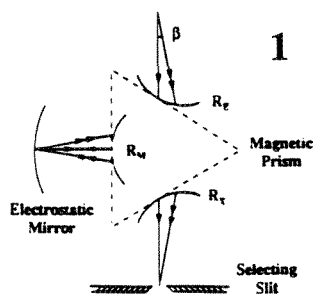
FIG. 1 Schematic diagram of the PMP imaging electron spectrometer.

FIG. 2 Spectral traces from hematin crystal section (solid line) and from embedding resin in neighboring area (dashed line).

FIG. 3 Images of the hematin crystal at energy losses indicated (in eV). The 3 eV energy loss corresponds to the energy of visible excitation of heme.

FIG. 4 Densitometer trace across a hematin edge as a measure of spatial resolution in the 3 eV energy loss region. After conversion to a line spread function, one obtains a resolution of 8 nm (FWHM).

FIG. 5 Radiation decay curve of Hematin at a 3 eV electron energy loss and an incident electron energy of 60keV. The dose$_{1/e}$ is 120 e/A^2.

425

GENERATION, PROCESSING, AND TRANSFERRING OF CCD CAMERA IMAGES IN ELECTRON CRYSTALLOGRAPHY

Z. G. Li, L. Liang, R. L. Harlow, K.E. Lehman, N. Herron
DuPont Central Research and Development, P. O. Box 80228, Wilmington, DE 19880-0228

Recently, CCD camera has been more and more used in the electron microscopy particularly for electron crystallography [1]. Use of CCD camera in this field as a recording medium possesses many significant advantages over conventional photographic films. A CCD camera has a very high dynamic range (reliable) and produces images directly in digital form which can be conveniently processed and transferred. We have initiated a program to obtain crystal structural information of plate-like materials by processing electron diffraction data from a CCD detector. As part of our program, we have developed a complete and routine procedure to convert images to diffraction data (h,k,l's and intensities).

Figure 1 is a schematic representation of the procedure. Images are initially obtained using a 1024x1024 Gatan CCD camera (model 794) which was attached to JEM-2000EX electron microscope. The collection of the images is controlled by a MAC computer which also stores the data and allows the data to be viewed. Then, the digitized electron diffraction patterns are transferred to a Sun station computer where, using Khoros software, the CCD images are processed. The Khoros system is a very complete image analysis and image processing software developed by University of New Mexico [2]. One of remarkable advantages of the Khoros system is that it provides a cantata Visual Language Programming environment (VLP), allowing users access the programs stored in Khoros libraries via a graphical user interface, and create user's specific cantata workspace. In our case of electron crystallography, a special workspace has been created to process the diffraction data. It includes steps as followed: 1) determining the center of the pattern; 2) pattern rotation; 3) measuring the positions and intensity of the diffraction spots in the pattern; 4) background subtraction; 5) output data file in the form of h,k,l's and intensities, which will be used as input into existing crystallographic software in order to solve the crystal structure [3]. Polycrystalline $Al2O3$ thin films were used to test accuracy in spatial resolution of CCD electron diffraction pattern. Signal/noise level increases significantly by averaging tens of images, something which is not practical if using conventional photographic films. For each projection, a two-dimensional potential map can be obtained.

An example of a crystal structure analysis by combining electron with synchrotron x-ray powder diffraction [4] is that of $HAlF_4$ [5] which contains relatively light elements and only exists as very thin crystals. One of biggest problems of electron crystallography is multiple scattering, due to strong electron-material interaction but, because of plate-like habit of the crystals in this case, we often were able to find some very thin crystallites where multiple electron diffraction problem was not a major one. An electron diffraction pattern in [001] projection is shown in figure 2 with a* and b* axis indicated by arrows. Trial unit cells were derived from a combination of symmetry and d-spacings obtained from the EM patterns to an accuracy of better than 1.5%. This is now routinely attainable from CCD technology. A potential map in [001] projection (figure 2b) was obtained through our routine procedure mentioned above. The detailed crystal model of $HAlF_4$ based on electron and synchrotron diffraction results will be described.

References

1. K. H. Downing, '95 Proc. Microscopy and Microanalysis, 6 (1995).
2. K. Konstantinides and J. Rasure, IEEE Transactions on Image Processing, Vol. 3, 243 (1994).
3. D. L. Dorset, Advances in Electronics and Electron Physics, Vol. 88, 111 (1994).
4. Z. G. Li et al., '95 Proc. Microscopy and Microanalysis, 152 (1995).
5. N. Herron et al., Chem. Materials, 7, 75 (1995).

plate-like crystallite

1)

electron microscope

CCD camera images
(diffraction data)

MAC Computer
(Digital Micrograph)

Sun Station (Khoros)

Structure solving software

2D potential maps

Diffraction data arrangment

diffraction spot positions
and intensities extraction

background subtraction

output file in hkl's form and
intensities
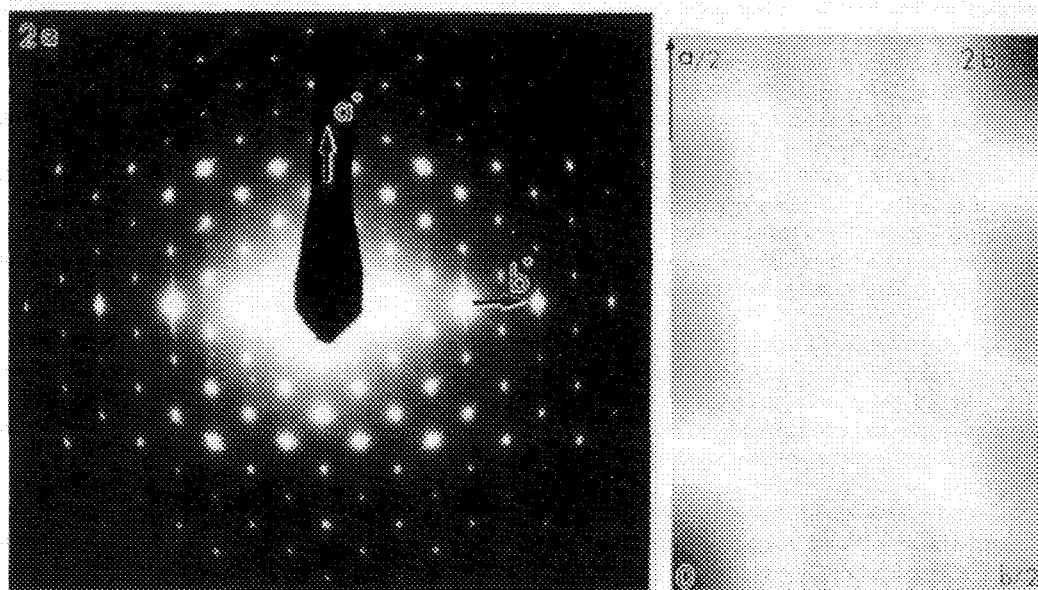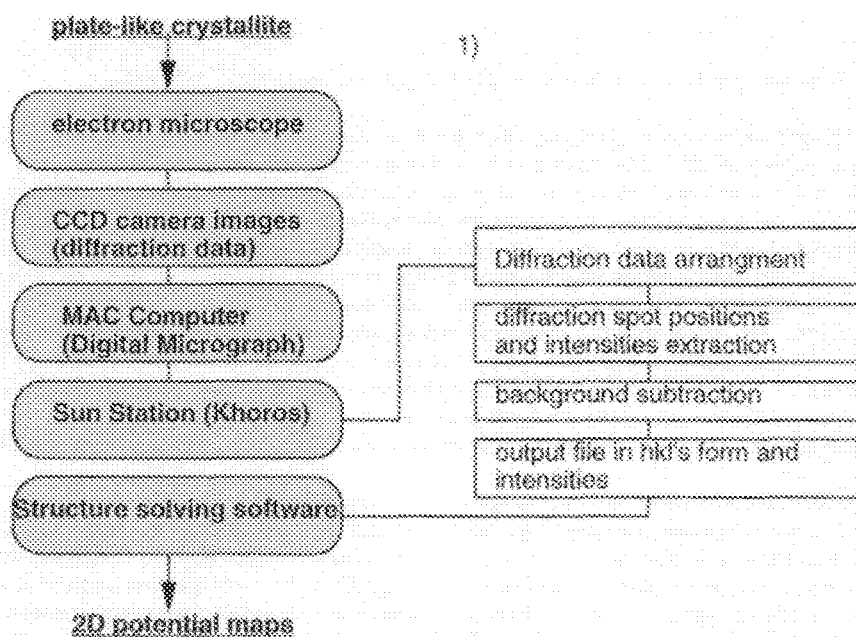
Figure 1. Schematic representation of crystal structure solving procedure using CCD camera.

Figure 2. a) Electron diffraction pattern and b) potential map of HAlF4 crystal in [001] projection.

427

TRUE COLOUR SEM IMAGING FOR PHASE RECOGNITION AND X-RAY MICROANALYSIS

Peter J.Statham

Oxford Instruments Microanalysis Group, Halifax Road, High Wycombe, Bucks HP12 3SE, U.K.

Secondary (SE) and backscattered electron (BSE) signals in the SEM provide high resolution monochrome images. BSE signal strength is modulated by mean atomic number and "false" colour can be introduced to enhance material contrast. Colour can also be introduced using multiple SE detectors, each with a different sensitivity to topographic and compositional information: by controlling signal mixtures and colours, the operator effectively has access to a powerful "studio" to generate aesthetically pleasing colour images.[1] In both these examples, the correspondence between local elemental content and colour is entirely arbitrary and under subjective control of the operator. Elemental x-ray maps can be acquired and combinations colour coded to reveal phase distributions.[2] For large numbers of maps and images, chemometric techniques such as PCA may be used to discover common relationships and assist the process of colour coding.[3] Images derived from x-ray maps are usually low resolution and the analyst has to decide which elements to include and do a fair amount of data manipulation before any conclusions can be drawn. Furthermore, local topography effects perturb any multivariate statistical analysis. This paper presents a novel imaging technique which addresses these limitations.

In cathodoluminescence (CL), the sample emits visible light, and images can be coded to reflect the "true colour", as would be seen in an optical microscope.[4] By analogy, we can use the emitted x-ray signal to generate a true colour image. Fig. 1 shows the normal human visual response to light with wavelengths from about 400 to 700 nm. To offset the visual response into the x-ray region, an energy dispersive x-ray detector and analysis system (Link ISIS) is used to assign colour to photons based on their effective wavelengths using a rainbow colour scale. For example, with a 300eV x-ray assigned red and a 5keV photon assigned blue, the offset visual response appears as in the lower graph in Fig.1. While the electron beam is resting on a point on the sample, as each photon is detected, its energy is measured and converted to a colour (r,g,b) with the condition $r+g+b=1$ and the results added to three colour accumulators which maintain totals R, G, B. At the end of the acquisition period, R,G,B effectively represents the colour sensation to the emitted x-ray spectrum which can be reproduced by display on a colour monitor. This process is repeated for all the pixels in a rectangular grid over the field of view to build up a complete full colour image in approximately 1 minute ; the acquisition can be extended for further frames to improve counting statistics. The resultant colour x-ray image effectively provides a low bandwidth chrominance signal which is combined with a high resolution monochrome electron image previously acquired from the same field of view using the same beam control hardware. As in conventional broadcast television, the combination is designed to maintain the same luminance as the electron image and thus retain high resolution image detail and topographic appearance. [5, 6]

Figure 2 still exhibits the topography and fine detail of the SE image. After the true x-ray colour is added, the tungsten-rich balls appear green, the titanium-rich balls appear blue and the carbon cement substrate is tinged red. If the red, green and blue components for each pixel are plotted on a ternary diagram the resulting scatter plot reveals clusters corresponding to the regions of similar colour (fig.3). In a multiphase sample, the numbers of pixels in each cluster can be used to calculate area % for each phase.

The multidimensional information corresponding to individual spectra at every pixel point is effectively compressed into a single true colour image and although separation of phases into different colours is not always dramatic, phase recognition is considerably easier and more intuitive than multivariate statistical analysis. Provided the same energy response band is used, the colour will be reproduced on any microscope under similar conditions so compounds will appear in memorable colours which can be learnt as for CL microscopy. Unlike pseudo-colour encoding of BSE images or signal mixing techniques, the colour is independent of beam current,

insensitive to local geometry and no user intervention is required to calibrate thresholds. Unlike conventional x-ray mapping techniques, there is no need to choose specific elements and set appropriate windows. The augmented image is intuitive and easy to interpret yet contains a considerable amount of encoded information equivalent to a multitude of x-ray images. A single image can be acquired in about one minute with sufficient statistics to give an informative "first look" at a sample. Faced with a complex analytical problem, the analyst can use this true colour x-ray imaging technique to give a useful cue for positioning the probe for subsequent microanalysis, obtain area % of phases or simply to compress topographical and compositional information into a single image for archiving. [7]

References

1. D. Scharf, U.S. Patent 5212383, May 18, 1993
2. P.J.Statham and M.Jones, Scanning, 3 (1980) 168-171.
3. R. Browning, Surface and Interface Analysis, 20 (1993) 495-502
4. G.V.Saparin and S.K.Obyden, Scanning, 10 (1988) 87-106
5. P.Statham, U.S. Patent 5357110, Oct.18, 1994
6. P.Statham, Microchimica Acta, in press , Springer Verlag (1996)
7. I am grateful to my colleagues, particularly Neville Cox for software implementation and Judith Root, Mohinder Dosanjh and Pierre Rolland for experimental work.
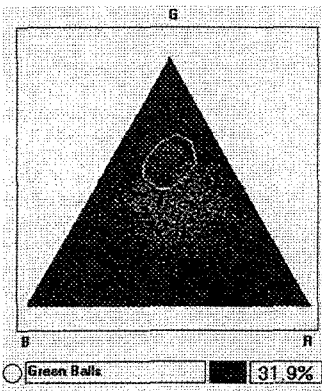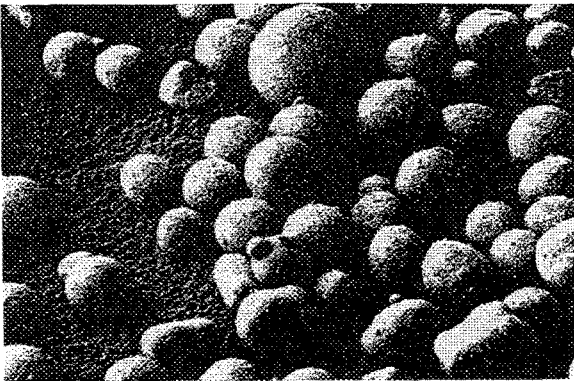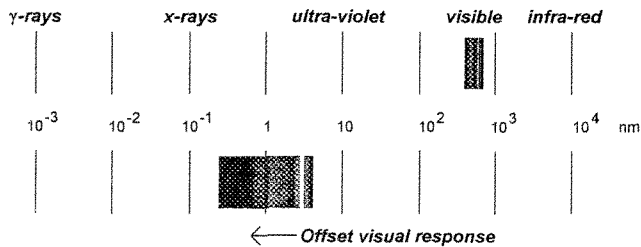
FIG.1 Electromagnetic spectrum showing region where human visual sensors normally operate to give the sensation of colour. Offsetting this visual response allows us to see a true colour x-ray image.
FIG.2 Monochrome reproduction of colour augmented image. 20kV, field width 1000 μm, acquire time 3 min..
FIG.3 Ternary scatterplot showing colour distribution for fig.2. Outlined region gives total area for W phase.

TOTAL-REFLECTION X-RAY FLUORESCENCE SPECTROMETRY (TXRF): APPLICATION TO ELEMENTAL PROFILES ON TRACE EVIDENCE AND MICROSAMPLES

Thomas A. Kubic, MS, JD, JoAnn Buscaglia, MS,** and, Ulrich Reus****

AMRAY/ATOMIKA, 160 Middlesex Turnpike, Bedford, Massachusetts 01730-1491
**TAKA Analytical Services, Inc., P. O. Box 208, Greenlawn, New York 11740-0208*
***ATOMIKA Instruments GmbH, D-85764 Oberschleissheim, Munich Germany*

Total-Reflection X-ray Fluorescence[1] spectrometry has been available as commercial instrumentation for the past few years. Since that time investigations and research has been conducted on the application of the technique particularly to problems involving micro samples such as in conservation and forensic analysis.

Elemental characterization of paint pigments, glass samples, textile fibers and liquid inclusions have been performed.

The *EXTRA IIA TXRF* spectrometer has inherent potential for the microanalysis. This instrumentation allows for simultaneous multi-element analysis for elements Phosphorus to Uranium with instrument detection levels (IDLs) less than or equal to 10 picograms for 50 of these elements.

Qualitative and semi-quantitative screening are possible with little sample preparation, while dissolved samples result in improved accuracy and precision with a dynamic range of five orders of magnitude without multiple dilutions.

This paper briefly reviews the principal and theory of *TXRF*, the operation of this instrument and its advantages over other quantitative elemental analysis techniques for these types of samples. Data demonstrating the comparable results obtained with the *EXTRA IIA* to that of ICP, AA, and NAA methods on samples supplied as proficiency tests will be presented. No difference in the quantitative results was exhibited between the reference and test data at a 95% confidence level.

Additionally, results will be presented indicating that various textile fibers made of the same material can be distinguished by their trace element *TXRF* profiles[2]. With the *TXRF* technique, preliminary data demonstrates that the correlation of single textile fibers as small as 3 mm in length with a source is possible[3].

Data from preliminary studies on the discrimination of glass samples, paint and tracing the source of pigments by their trace elemental profiles will also be discussed.

References

1. R. Klockenkamper, et al., *Analytical Chemistry* vol 64, No 23 (1992) 1115A
2. R. Klockenkamper, et al., Spectrochimica Acta Vol 48B, No 2 (1993) 239
3. A. Prange, et al., *Analytical Sciences* Vol 11 (1995) 38-1

$EN_{(new)} = \dfrac{meas. conc.}{given conc.} \times EN \ (old)$
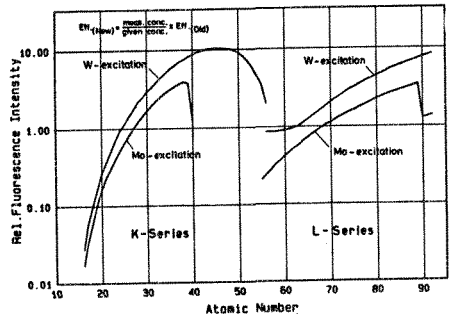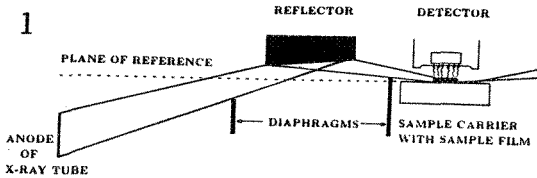
COMPARISON OF TRACE METALS IN BULLETS TEST 91-10

SAMPLE	REF Cu	EXTRA II Cu	REF Sb	EXTRA II Sb	REF As	EXTRA II As	REF Ag	EXTRA II Ag	REF Sn	EXTRA II Sn
S1a	176±14 / *163±1*	158±5	9.46±1.9 / *9.65±.06*	9.49±.1	143±6	139±15	*41.4±.5*	41.0±1.2	*.377±.003*	*.378±.01*
S1b	170±6 / *163±2*	161±4	9.55±.03 / *9.63±.11*	9.52±.1	140±12	144±13	*42.0±.4*	41.5±1.8	*.379±.008*	*.380±.01*
S1c	176±19 / *162±1*	157±4	9.54±.03 / *9.64±.09*	9.55±.1	137±3	138±15	*41.7±.5*	42.1±1.0	*.383±.005*	*.385±.01*
S2a	162±8 / *151±1*	155±6	1.32±.02 / *1.31±.01*	1.30±.09	577±10	580±26	*16.3±.5*	16.0±1.0	*.011±.001*	*.01±.001*
S2b	17±3 / *11±2*	16±3	1.56±.003 / *1.54±.01*	1.59±.12	560±8	555±30	*16.0±.3*	16.3±.8	*.096±.003*	*.092±.008*
S2c	160±4 / *149±2*	160±5	1.33±.01 / *1.29±.02*	1.30±.10	592±6	610±28	*16.0±.9*	15.9±.8	*.010±.0003*	*.01±.001*
Q1a		160±7		1.37±.10		595±22		15.8±1		.01±.001
Q1b		12±4		1.49±.15		571±27		15.6±1		.097±.001
Q1c		159±5		1.32±.10		602±30		16.2±1		.01±.001
	ppm	ppm	%	%	ppm	ppm	ppm	ppm	%	%

REF: REGULAR PRINT - NAA   ITALICS - ICP
BLANK SPACES DENOTE ELEMENT NOT DETECTED

Figure 1   Schematic of EXTRA IIA Multi Element Analyzer.

Figure 2   Response curves (x-ray intensity vs atomic number) for a three excitation sources.

Figure 3   Comparison of the trace element composition of some bullet lead by NAA, ICP, and TXRF.

SUB SURFACE IMAGING USING A TOROIDAL BACKSCATTERED ELECTRON ENERGY SPECTROMETER IN A SCANNING ELECTRON MICROSCOPE

E I Rau and VNE Robinson *

Department of Physics, Moscow State University, Moscow, Russia
*ETP Semra Pty Ltd, Sydney, Australia

In a SEM, an object under examination is scanned by a focused electron beam, of energy typically 2-30 keV. Some of the incident electrons are scattered out of the sample, carrying with them depth information from the internal structure of the sample.[1,2,3] By detecting BSEs in a definite energy range, it is theoretically possible to separate images of individual layers of a three-dimensional sample, ie, perform a kind of instrumental tomography.[4,5] Additionally, detecting BSEs on an energy separation basis gives another degree of freedom to microscopists to determine greater specimen information. To do this, a suitable BSE energy filter or spectrometer is required.

To be effective and produce high quality images, a BSE spectrometer should have a working distance of less than 40 mm. It should be axially symmetric with the electron beam passing through the center of the analyser, impinging on the specimen normal to its surface. The specimen being scanned must be placed in the space free from the analysing field of the spectrometer, which should not introduce any magnetic fields. Using these criteria, computer simulations were performed to determine the equipotentials and trajectories of electrons in cylindrical, hyperbolic, sector spherical and sector toroidal electrostatic energy analysers. The results showed that the above requirements could be satisfied by a toroidal energy analyser, which also has the advantage over the others as to the coupling coefficient, relative aperture dimensions and energy resolution capabilities.

Based upon those calculations, a suitable toroidal BSE energy spectrometer was designed and has been constructed.[6] Fig. 1 shows a cross section of the spectrometer, which is a cylinder of rotation about the central axis. This spectrometer is 20 mm thick and less than 100 mm diameter, enabling the specimen O to be at a working distance of 30 mm. The axially symmetric design of the spectrometer ensures BSEs are detected in all directions. BSEs scattered through the appropriate acceptance angles Φ and $\Delta\Phi$, pass through the input aperture S_1 and are deflected by the electric field. Only those of the appropriate energy pass through the output aperture S_2, to be detected by a specially shaped annular scintillator detector D. The energy is selected by applying a voltage (positive and negative) of only 10% of the desired energy, eliminating the need for high voltages in the specimen chamber. The energy spread of the electrons is determined by the width of the aperture S_2. Suitable operating conditions for imaging, which requires a good signal to noise, require an aperture width of approximately 0.5 mm, and gives an energy discrimination of approximately 2% of the energy of the electrons being imaged.

Fig. 2 shows a series of BSE images (primary beam energy is 20 keV) of an integrated circuit, which illustrate the capability of the BSE spectrometer. 2a is total BSE image - taken using a standard BSE detector which detects all BSEs. Although many different structures are detectable, it is not possible to tell whether they are all at the same level, or if they are at different repths. 2b is a spectrometer image, detecting the 18 keV electrons and shows primarily surface information. It should be noted that detecting the BSEs which have lost only small amounts of energy considerably enhances the atomic number contrast of the BSE image. 2c was also taken with the spectrometer, using the 14 keV electrons, and shows sub surface information. Fig. 2 clearly illustrates the ability of the BSE energy spectrometer to separately image surface and sub surface detail. From Fig. 2, we can readily see that the structures shown in Fig. 2 (b) are above those shown in Fig. 2 (c). This ability to image separate layers in a multi-layer specimen could open new fields of application for the scanning electron microscope, where until now, it has only been possible to image surface structures by using low beam accelerating voltages or the low loss BSE technique, with sub surface structures being deduced.[7] Sub surface structures have been deduced from the difference between high and low voltage images.

References

1. H Niedrig, J. Appl. Phys. 53 (1982) R15
2. L Reimer, R Bongeler, M Kassens, F Liebsher, R Senkel, Scanning, **13** (1991) 381
3. N N Dreomova, S I Zaitsev, E I Rau, E V Yakimov, Bulletin of the Russian Academy of Sciences. Physics., **57** (1993) 1305
4. S Likharev, A Kramarenko, V Vyborhov, Proc 52 Annual Meeting, EMSA, San Francisco Press (1994) 488
5. E I Rau, N N Dreomova, A N Matvienko, V O Savin, D O Savin, Izvestija Academii nauk, Physics N2 (1995) 87 (in Russian)
6. EI Rau, VNE Robinson, Scanning (1996) In Press
7. OC Wells, Appl. Phys. Lett. **19** (1971) 232
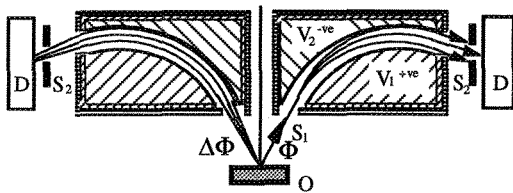
FIG. 1 Schematic Illustration of the sector torroidal spectrometer.
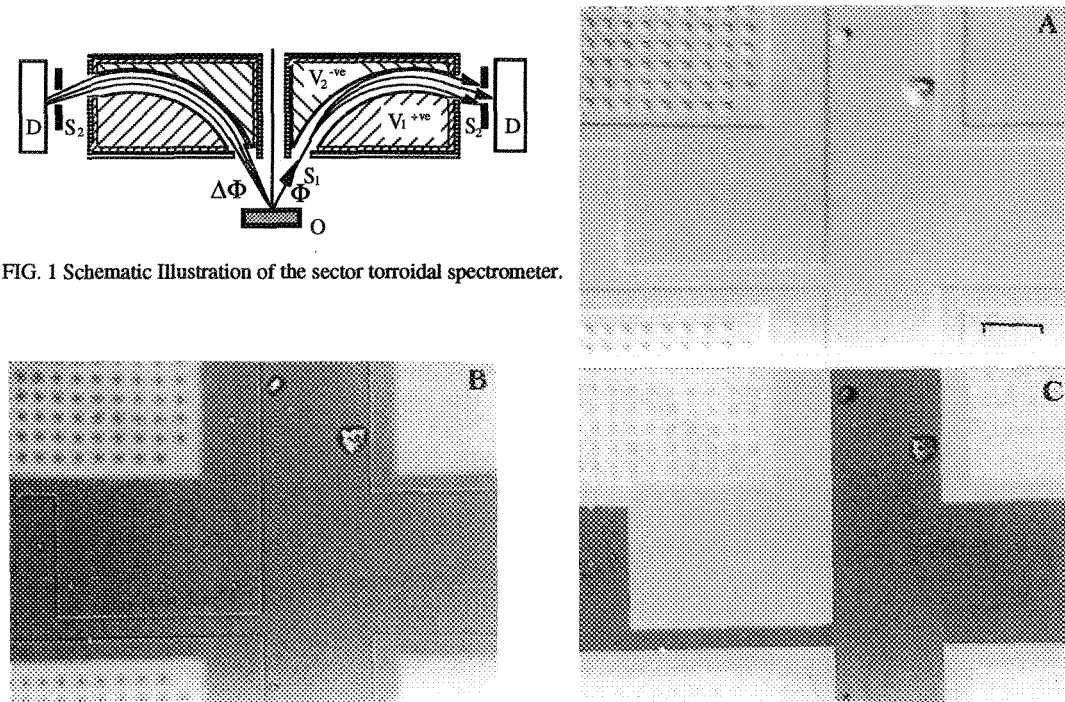
FIG 2.   20 keV BSE images of an integrated circuit.   The total BSE image (a) shows a number of different structures. The 18 keV spectrometer image (b) shows surface detail, while the 14 keV spectrometer image (c) shows sub surface information, with almost no detection of the surface features.   Magnification marker is 40 μm.

Gapless Single-Pole Magnetic Lens for Low-Voltage SEM

F.C. Tsai, A.V. Crewe

Enrico Fermi Institute and Department of Physics, The University of Chicago, Chicago, IL 60637

An unconventional single pole lens design has attracted attention because it promises a highly confined strong field distribution which in turns results in smaller third aberrations than that of the conventional lenses.[1] However in this type of lens heat dissipation becomes crucial. In the low electron energy range (less than 5 KV), however, we can keep all the benefits from the single pole piece without being concerned about the cooling requirement.

The key to the design is to avoid the unnecessary strong fields in any region away from the axis, which can absorb a lot of applied magnetomotive force (MMF) if this off-axis region happens to be in the air. This implies that a reasonable design is a gapless geometry. In our design (Fig. 1), a hemisphere tip sits on the top of a central pole. At the rim between the boundary of the central tapered pole and the tip is a 45° semi-angle funnel-shaped exterior pole. These three parts physically contact each other and form a gapless geometry. The central and exterior poles also contact each other at the bottom of the lens to form the high permeability magnetic circuit loop. The cross section of each part of the lens has been chosen in such a way that the region close to the tip will saturate first.

The field distribution of the lens has been calculated by the OPERA2D package which uses a finite element method to solve electromagnetic problems. The results show that the axial field is highly confined at the tip surface and it starts to saturate at about 1600 Amp.turns (Fig.2). The calculated axial field is used in the calculations of paraxial ray tracing and the third order aberration coefficients. Fig. 3 shows the required electron voltages to form the probe at different positions in front of the tip. The corresponding spherical and chromatic aberrations are shown in Fig. 4 and 5 respectively. Our data shows the chromatic aberration dominates the spherical aberration when we choose an electron source with 0.2 eV energy spread. Fig. 6 is the optimized chromatic aberration.[2] This data shows that we can easily reach a probe size better than 2.3 nm for an electron energy at 1 KeV. The ultimate probe size is 0.623 nm for electron energy less than 5 KeV. This is a big improvement in resolution compared with the conventional SEMs.

We also expect the gapless geometry can be applied to the conventional lens design.

References

1. T. Mulvey, "Unconventional Lens Design", *Magnetic Electron Lenses*, ed. by P.W. Hawkes (Springer-Verlag Berlin Heidelberg New York 1982).
2. A.V. Crewe, *Ultramicroscopy* 23 (1987) 159.
3. The authors gratefully acknowledge the helps from Dr. Lee C. Teng, Dr. Kenneth Thompson and Dr. Suk H. Kim, and the use of the facilities at the Accelerator System Division, Argonne National Laboratory.
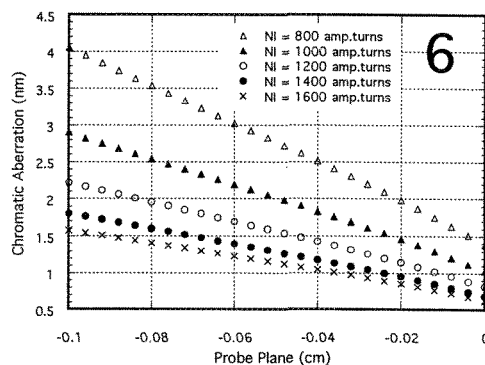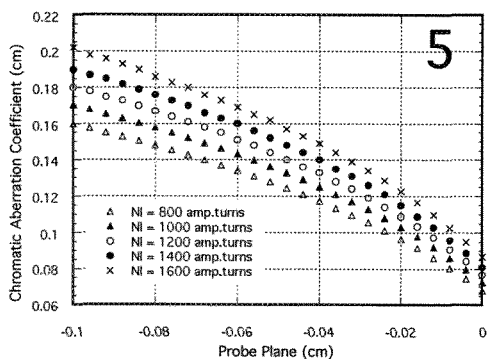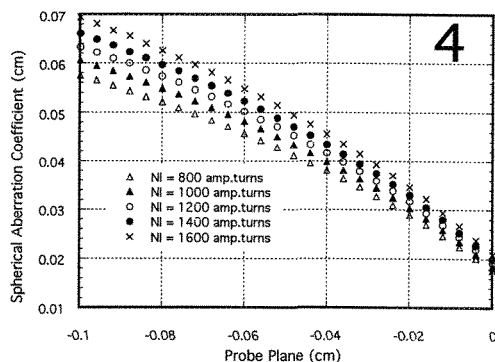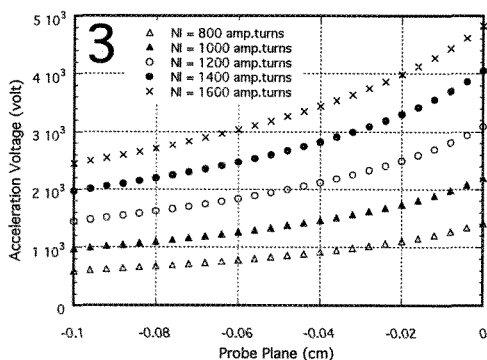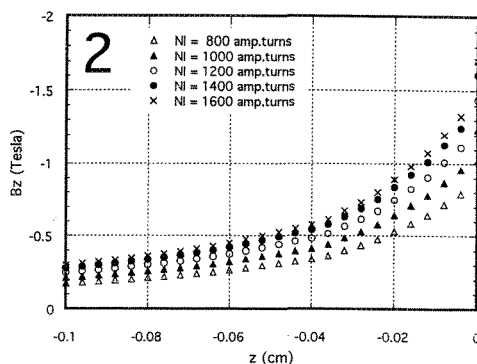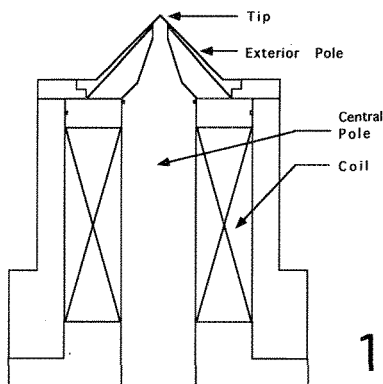
Fig. 1 The Gapless Single-Pole Magnetic Lens.
Fig. 2 The axial field around the tip. The tip surface is at z = 0.00 cm. It starts to saturate at 1600 Amp.turns.
Fig. 3 The required electron energies to from the probe at different positions in front of the tip.
Fig. 4 The spherical aberration coefficient corresponding to Fig. 3 .
Fig. 5 The chromatic aberration coefficient corresponding to Fig. 3.
Fig. 6 The optimized chromatic aberration corresponding to Fig. 3.

DEVELOPMENT OF A SEMI-IN-LENS DIGITAL FE-SEM

Y. Yamamoto*, A. Yamada*, T. Negishi*, T. Kobayashi*, N. Watanabe*, T. Miyokawa*, N. Tamura* and C.Nielsen**

* JEOL Ltd., 1-2 Musashino 3-chome, Akishima, Tokyo, JAPAN
* * JEOL U.S.A. Inc., 11 Dearborn Road, Peabody, MA 01960

Observation of new materials such as semiconductor, polymer and compounds, with a Field Emission Scanning Microscope (FE-SEM) has been increasingly important in recent years. As the integration scale of semiconductor device as well as nanometer fabrication scale of the new materials are increasing, a high resolution FE-SEM became indispensable for research and development. Since these new materials are often non-conducting and charging, metal coating, minimum electron dose technique or rapid scanning must be used to observe the surface morphology. Furthermore, all the operational sequences have been required to be drastically simplified.

We have developed a semi-in-lens fully digital FE-SEM which can obtain high resolution secondary electron images (SEI) with minimum influence of charging at the specimen. An outline of this new FE-SEM is shown in Fig.1. The electron optical system (EOS) is based on the conventional FE-SEM (H. Kazumori et al, 1994[1]) with a cold field emission gun (C-FEG), giving a guaranteed resolution of 2.5 nm at an accelerating voltage of 1kV. It is possible to select ten scan speeds from 0.28s to 121s in the vertical direction with 1280 x 1024 pixels and average and integrate the SEI signals at the ambient scan speed. Higher scan speeds for a reduced area on the "viewing" CRT can also be set for adjustment of the image, together with mode numbers "0", "1" and "2", in which the voltages of the accelerating and retarding electrodes on the objective lens are different. The mode number, incident dose and scan speed must be selected according to changes in the sample surface potential. Images with 1280 x 1024 pixels x 8bits can be observed on a 17" viewing CRT. Mouse, keyboard and a simple operation panel are used to operate the FE-SEM with user friendly software functions. The hardware can be connected to a PC using an ethernet cable. SEI's at 1280 x 1024 pixels can be output to a video printer and SEI's at 2048 x 2048 pixels to the recorder for scanning image (RSI). Figure 2(a) and (b) show SEI's of resist in mode "2" with an emission current of 12 μ A, where (a) illustrates the SEI with one scan at a scan speed of 80s, and (b) with an integration of 30 times at an scan speed of 0.5s in vertical direction. In (b), an influence of charging at the sample is removed. To eliminate charging from the incident electron beam, it is necessary to use minimum dose for observation. Averaging or integration can be set for each scan speed and typically those at fast scan speeds are most useful for observing nonconducting samples.

REFERENCES
1. H. Kazumori, et al (1994) Proc. 13th Int. Cong. on Electron Microscopy Paris 1, pp 61-62
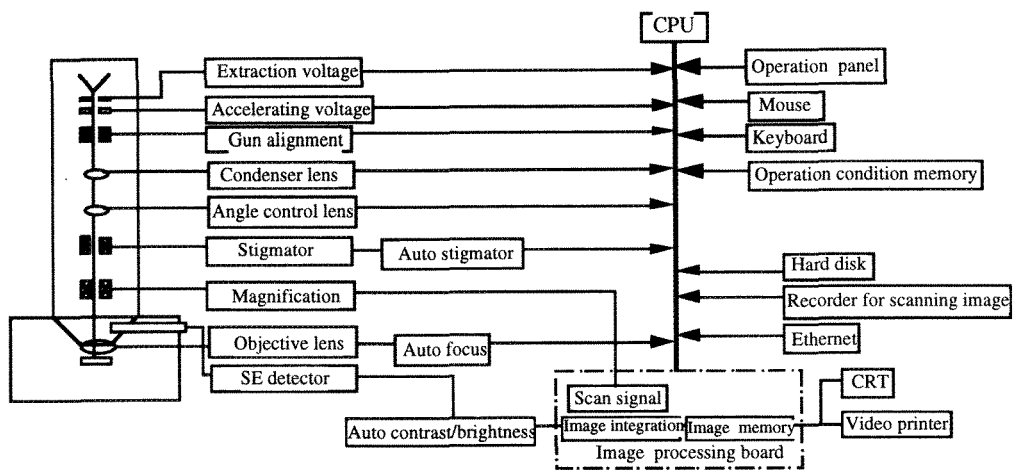
Fig. 1

Fig. 2(a)   2(b)

FIG.1 Schematic outline of the FE-SEM, showing the main controls

FIG. 2(a) SEI of resist with one scan at a scan speed of 80s in the vertical direction. Accelerating voltage is 1kV, WD 2mm and magnification 35,000x.

FIG. 2(b) SEI of resist at a scan speed of 0.5s at an integration of 64 times. Accelerating voltage is 1kV, WD 2mm and magnification 35,000x.

MOSAIC MAPPING: A MEANS OF TILING IMAGES TO SHORTEN ACQUISITION SPEED FOR LOWER - MAGNIFICATION SEM IMAGES AND WAVELENGTH DISPERSIVE SPECTROMETERS (WDS) X-RAY MAPS

J.D. Geller and C.R. Herrington

Geller MicroÅnalytical Laboratory, 426e Boston St., Topsfield, MA 01983-1212.

The minimum magnification for which an image can be acquired is determined by the design and implementation of the electron optical column and the scanning and display electronics. It is also a function of the working distance and, possibly, the accelerating voltage. For secondary and backscattered electron images there are usually no other limiting factors. However, for x-ray maps there are further considerations. The energy-dispersive x-ray spectrometers (EDS) have a much larger solid angle of detection that for WDS. They also do not suffer from Bragg's Law focusing effects which limit the angular range and focusing distance from the diffracting crystal. In practical terms EDS maps can be acquired at the lowest magnification of the SEM, assuming the collimator does not cutoff the x-ray signal. For WDS the focusing properties of the crystal limits the angular range of acceptance of the incident x-radiation. The range is dependent upon the 2d spacing of the crystal, with the acceptance angle increasing with 2d spacing. The natural line width of the x-ray also plays a role. For the metal layered crystals used to diffract soft x-rays, such as Be - O, the minimum magnification is approximately 100X. In the worst case, for the LIF crystal which diffracts Ti - Zn, ~1000X is the minimum.

If lower magnifications are needed for either electron imaging or WDS maps manufacturers have provided computer control systems which raster the specimen stage with a stationary electron beam. In principle the minimum magnification is limited to the specimen stage's range of travel. For a 25mm diameter specimen (displayed on a 100mm X 100mm image) a 4X magnification is required. The acquisition speed for a stage mapped electron image with 640 X 417 pixels is in excess of 4 hours. To shorten the acquisition time the image is normally acquired with the stage moving bi-directionally. The actual data acquisition time for 50ms/pixel is 13 seconds, with the remaining ~3.75 hours being overhead from stage movement. Using "Mosaic Macpping" this almost prohibitively long time can be shortened by more than 10X.

Mosaic Mapping is a hybrid technique which combines electron beam scanning of multiple fields-of-view with mechanical stage movement. Consider the above situation using the minimum available magnification of 40X (2.5mm X 2.5mm) on our JEOL-733 electron probe microanalyzer. A matrix of 10 X 10 images or "tiles" with each image having 64 X 42 pixels are required to completely cover the 25mm diameter specimen. We have developed a new capability in our computer control program, called dPICT (digital photo image tool), which rasters the electron beam at each of the 100 (10 X 10) stage positions to form a complete image. The secondary (SEI) and backscattered (BEI) electron images in figure 1 were collected in less than 25 minutes (~10% of the time required for the stage mapped image). The tiled data, which is also collected with the stage moving bi-directionally, is manipulated by the program to form one continuous TIFF (tagged image file format) image. The data can also be stored in 16 bit binary file, if necessary.
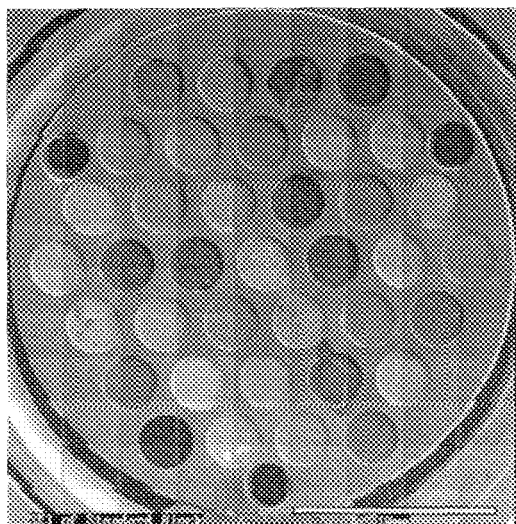
FIG. 1a
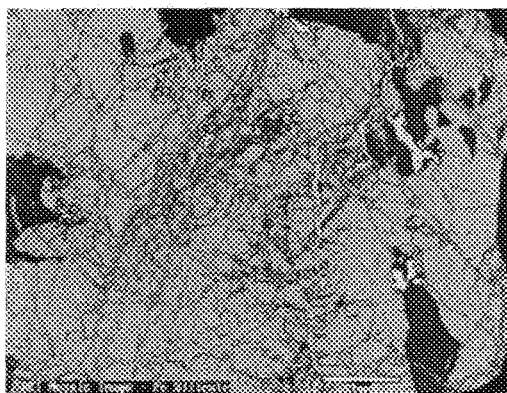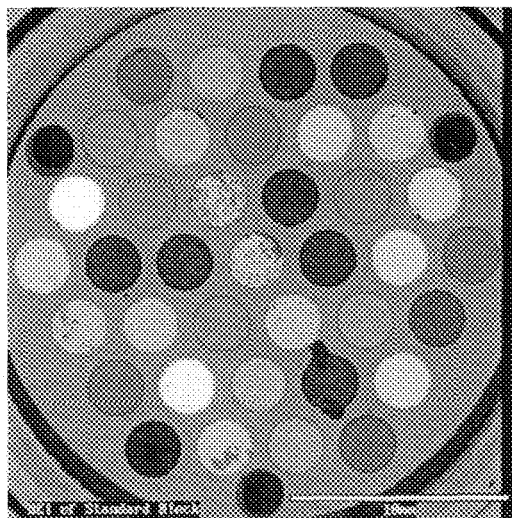
FIG. 2a
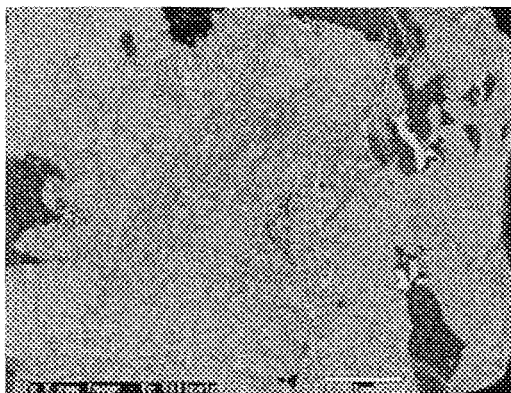
FIG. 2b

The brightness difference of the SEI images is related to the change in SEI detector efficiency as the specimen stage moves from tile to tile. Since the BEI efficiency is constant it does not show this effect.

Figure 2 shows BEI and FeKα Mosaic Map of an iron silicate mineral with an original magnification of 17X, rather low for a WDS map. The images were acquired with 59 X 59 tiles composed of 10 X 8 pixels each at a 1,000X magnification. Using a 1 msec. dwell time the overhead from stage motion for the 3,481 tiles was about 90 of the 94 minutes. Increasing the dwell time would add about 5 minutes for each additional 1 msec. The program automatically calculates the details for image acquisition after being given the electron beam image magnification desired as well as the stage coordinates representing the opposite corners of the specimen.

The time savings using Mosaic Mapping for gathering low magnification SEI and BEI images is much greater than that for WDS x-ray maps. This is due the higher electron beam scanning magnifications (which increases the number of tiles) required due to the focusing characteristics of the WDS system.

COMPUTATIONAL MICROGRAPH REGISTRATION WITH SIEVE PROCESSES

P.J. Phillips[1], J. Huang[2] and S. M. Dunn[2]

[1]US Army Research Laboratory, Ft. Belvoir, VA 22060
[2]Dept. of Biomedical Engineering, Rutgers University, Piscataway, NJ 08855

In this paper we present an efficient algorithm for automatically finding the correspondence between pairs of stereo micrographs, the key step in forming a stereo image. The computation burden in this problem is solving for the optimal mapping and transformation between the two micrographs. In this paper, we present a *sieve* algorithm for efficiently estimating the transformation and correspondence.

In a sieve algorithm, a sequence of stages gradually reduce the number of transformations and correspondences that need to be examined, i.e., the analogy of sieving through the set of mappings with gradually finer meshes until the answer is found. The set of sieves is derived from an image model, here a planar graph that encodes the spatial organization of the features. In the sieve algorithm, the graph represents the spatial arrangement of objects in the image. The algorithm for finding the correspondence restricts its attention to the graph, with the correspondence being found by a combination of graph matchings, point set matching and geometric invariants.

The geometric invariants identify and prioritize potential correspondences between vertices in the two graphs. The graph matching algorithm examines each of these correspondence in order, starting with the pair with the highest priority. Graph matching establishes an initial mapping between the vertices and their neighboring vertices in both graphs (images), which were identified by the geometric invariants. The initial mapping is local because it is computed using vertex neighborhoods. Point set matching extends the local mapping to a global mapping. An integral part of this extension process the goodness of the global mapping is evaluated and the mapping is rejected if the goodness criteria is not met. In this case, the local mapping with the next highest priority is examined.

This technique is demonstrated by registering stereo pairs and was compared with the registration systems of Peach and Heath[1] and Huang et al[2]. The Peachy and Heath system reconstructs depth maps from stereo pairs, however, it requires a human operator that views the two images stereoscopically and manually performs the 3D reconstruction. The Huang et al algorithm finds the alignment between micrographs using geometric invariants and geometric hashing. All possible geometric invariants are computed, unlike the sieve algorithm.

The sieve algorithm was run on five pairs of micrographs (Figure 1). The correspondence mapping for each pair of images was compared with the ground truth for that pair; that being derived by visual inspection. On average, there were 130 nodes in each image of each of the five pairs; on average 99% were matched correctly, 0.05% were multiple matches and 0.05% were incorrect matches (Figure 2). Whereas it takes one week to register 12 stereo pairs using the system of Peachy and Heath, both the system of Huang et al and the sieve algorithm can compute the processing in less than one day's time, the sieve algorithm being the superior.

References
1. L. Peachy and J. Heath., *J. Micros.*, 153 (1989).
2. J. Huang, S. Dunn, S. Wiener, P. DeCosta., *J. Comp. Assist. Micros.*, 2 (1994).

Figure 1. An example of the gray level micrographs used: (a) Image A and (b) Image B.

(a)

(b)

(a)

(b)
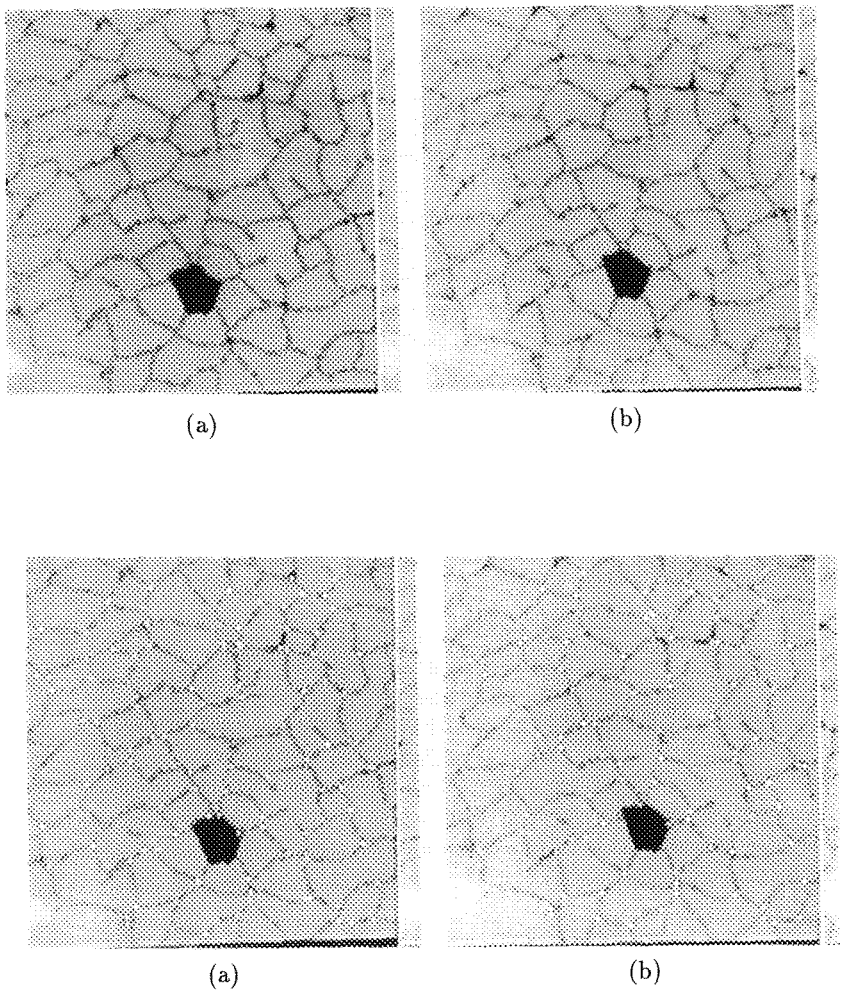
Figure 2. The results of matching the two micrographs shown in Figure 1. The vertices matched are marked as white squares.

DEVELOPMENT OF A HIGH-SPEED OPTICAL MICROSCOPE AUTO-FOCUS CONTROL SYSTEM FOR EPMA

S. Notoya*, M.Saito*, M.Matsuya*, T.Ishii*, K.Murakami*, H.Ohashi* and C.Nielsen**
*JEOL Ltd., 1-2 Musashino 3-chome, Akishima, Tokyo, JAPAN
* * JEOL U.S.A. Inc., 11 Dearborn Road, Peabody, MA 01960

This paper reports the new development of an optical microscope automatic focus control system (OMAFD) for the JXA-8800/8900 series Electron Probe Microanalyser (EPMA). In recent years, a method called "wide area mapping" has been increasingly used with EPMA for measurement of X-rays by moving the specimen to obtain 2-dimensional element distributions over large analysis areas. In mapping, the simultaneous acquisition of multiple elements is required. Using an optical microscope, which has a very small (about $\pm 1 \mu$ m) depth of focus, the specimen surface needs to be vertically adjusted to the Rowland circle of a wavelength dispersive X-ray spectrometer. Even with flat specimens, actual analysis points often show some inclination. Specimens are often inclined accidentally during sample preparation and mounting. Moreover, requirements of specimen analysis with curved or irregular surfaces have been increasing.

The OMAFD consists of an illuminator, a sensor, an Auto-focus (AF) controller, a stage controller and so on (Fig.1). Contrast of a pattern on the specimen surface projected from the illuminator is detected by the sensor as two different images, coming through two different optical paths. The AF controller receives these signals detected by the sensor and recognize if it is at the focus position or if it is displaced up or downward. Using the pattern projection, this system can do auto-focusing even with polished flat specimens. It also allows continuous focusing control with other specimens, detecting direction of displacements.

The OMAFD has two kinds of automatic height correction functions, "search" and "trace" (Fig.2). The "search" function is to find the focus position, scanning the specimen vertically. By the use of this function, setting of analysis points can be automated. The analysis points can be selected by only observing secondary or back scattered images and saved, without requiring verification of the specimen height with optical microscope, and both qualitative and quantitative analysis of these selected points can be automatically carried out. The "trace" is a function for continuously keeping the focus position with the specimen surface while driving the specimen at high speed while acquiring a wide area stage map. Using the "trace" function, the line and area analysis can be carried out for specimens with smoothly curved surface. The accuracy of focus is about $\pm 1 \mu$ m.

Applications for mapping with the OMAFD are shown in Fig.3, Fig.4, Fig.5 and Fig.6. Figure 4 illustrates the map of a Cu specimen with cylindrical surface. Figure 6 shows the map of a non-flat edge of a steel specimen. For comparison, examples of measurements without height correction are also shown. Uniform and correct distribution of a main element is obtained with the OMAFD, whereas without height correction accurate element distribution can not be obtained.
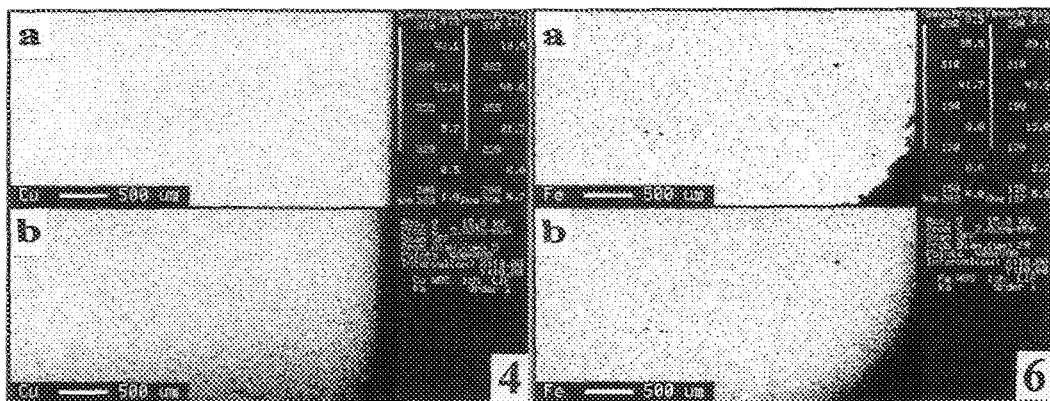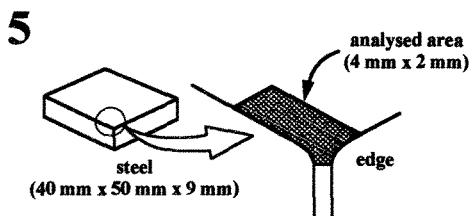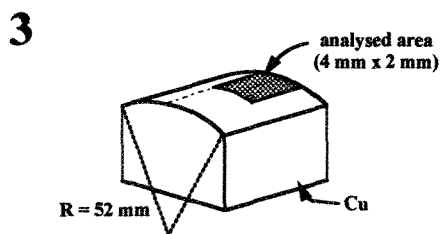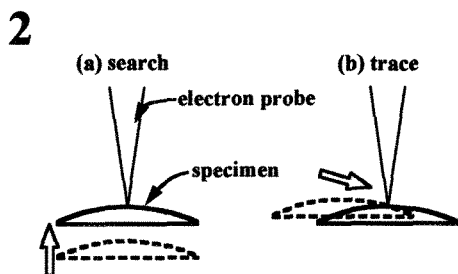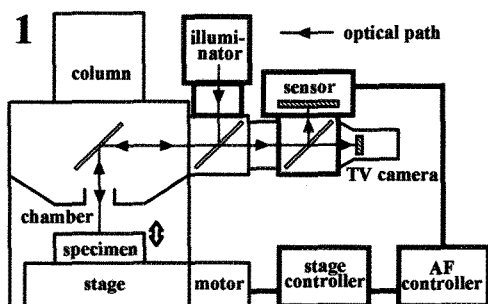
FIG. 1 -- Block diagram of OMAFD.

FIG. 2 -- Actions of OMAFD, (a) search and (b) trace.

FIG. 3 -- Cu specimen with cylindrical surface.

FIG. 4 -- Cu-Kα Maps of analysed area arrowed in Fig. 3, (a) corrected with OMAFD and (b) without correction.

FIG. 5 -- Non-flat edge of steel specimen.

FIG. 6 -- Fe-Kα Maps of analysed area arrowed in Fig. 5, (a) corrected with OMAFD and (b) without correction.

STEM DARK-FIELD IMAGE USING A 200-kV AEM

T. Tomita*, T. Honda* and M. Kersker**

* JEOL, Ltd., 1-2 Musashino 3-chome, Akishima, Tokyo 196 Japan

** JEOL U.S.A. Inc., 11 Dearborn Road, Peabody, MA 01960, U.S.A.

Interpretation of the high resolution transmission image typically requires simulation since the contrast changes in a complicated way due to changes in focus and specimen thickness. The contrast in images formed by collecting high angle forward scattered electrons in STEM does not change with changes in thickness or defocus.

Until recently, high angle annular dark field (HADF) images were obtained only from instruments using cold field emission guns.[1] Recently we have attempted to obtain HADF images using Schottky (ZrO/W(100)) thermal field emission and using a 200kV instrument designed as a comprehensive TEM/STEM.[2] Advantages of the ZrO/W emitter are easy operation, very good short and long term stability, high brightness, and narrow energy spread. This microscope, The JEM2010F with thermal field emission, allows subnanometer analysis with EDS(spot, line, and mapping), EELS, holograms, etc, and has a standard TEM imaging system for high resolution imaging and for various diffraction modes, viz., CBED, selected area, Tanaka, etc.

A ray diagram of HADF is shown in Figure 1. The annular darkfield (ADF) detector is attached to the diffraction chamber which is located between the projector lens and the viewing chamber. The detection half angle is variable from 10mrad - 30 mrad to 50 100mrad by varying the camera length. If a large diameter detector is used, an angle greater than 150mrad can be used. The detector is a scintillator (P47) to a photomultiplier through a refractive type photo guide.

Figure 2 shows a HADF image of GaAs/AlAs. The semiangle of detection is 50 - 100mrad, an angle large enough to achieve Z contrast images clearly showing the boundary between GaAs and AlAs. The lattice image showing 0.33nm and 0.28nm is also clearly shown.

We have demonstrated that it is possible to achieve atomic resolution using HADF imaging with thermal field emission. Higher resolution may be achieveable. Additional experiments are underway including subnanometer PEELS analysis of individual atomic layers.

References:

1. S.J. Pennycook, D.E. Jesson, and M.F. Chisholm, Microsc. Semicond. Mater. Conf. Oxford. 10 - 13 April, 1989.

2. T. Honda, T. Tomita, K. Kaneyama, and Y. Ishida, Ultramicroscopy, 54(1994) 132-144.
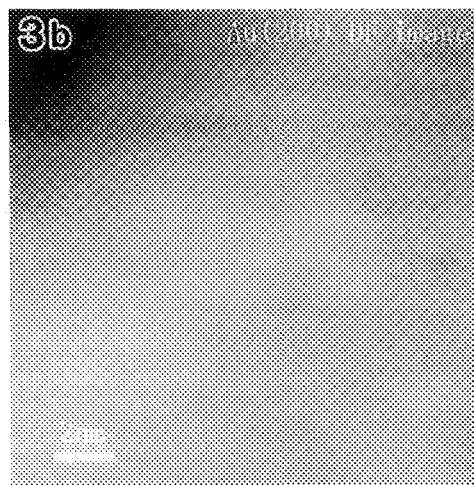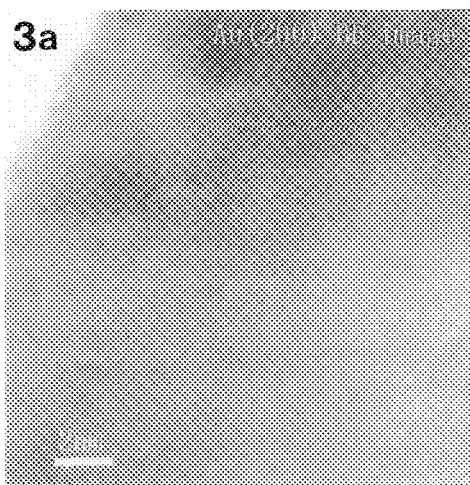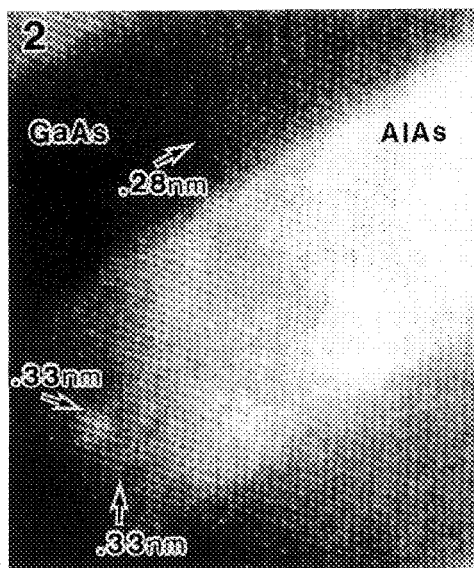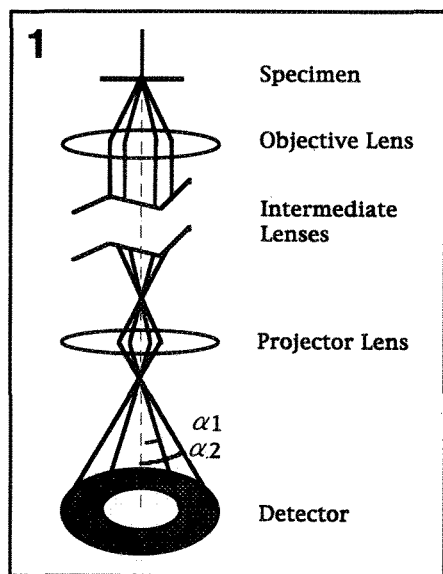
Fig.1. Ray path for the electrons detected by HADF detector.
Fig.2. Dark field STEM image of the GaAs/AlAs obtained by HADF detector.
Fig.3a. Bright field STEM images of Au (200) lattice.
Fig.3b. Dark field STEM images of Au (200) lattice.

DEVELOPMENT OF A COMPUTER-CONTROLLED 120kV HIGH-PERFORMANCE TEM

H.Kobayashi,* I.Nagaoki,* E.Nakazawa** and T. Kamino* *

* Instrument Division, Hitachi Ltd., 882 Ichige, Hitachi-naka, Ibaraki, 312 Japan
**Hitachi Instruments Engineering Co., Ltd., 882 Ichige, Hitachi-naka, Ibaraki, 312 Japan

A new computer controlled 120kV high performance TEM has been developed(Fig. 1). The image formation system of the microscope enables us to observe high resolution, wide field,and high contrast without replacing the objective lens pole-piece. The objective lens is designed for high-contrast (HC) and high-resolution(HR) modes, and consists of a double gap and two coils. A schematic drawing of the objective lens and the strength of the magnetic field of the lens is described in Fig.2. When the objective lens is used in HC mode, upper and lower coils are operated at a lens current of same polarity to form the long focal length. The focal length(fo) , spherical aberration coefficient(Cs) and chromatic aberration coefficient (Cc) in HC mode at 100kV are 6.5, 3.4 and 3.1mm, respectively. Magnification range at HC mode is $\times$ 700 to $\times$ 200,000. The viewing area with an objective aperture of a diameter of 10μm is 160mm in diameter. In HR mode, the polarity of lower coil current is reversed to form a shorter focal length for high resolution image observation. The fo, Cs and Cc of the objective lens in HR mode at 100kV are 3.1, 2.8 and 2.3mm, respectively. The highest magnification in HR mode is $\times$ 600,000.

The Image formation system, consisting of 6-lenses, is computer controlled, and it allows rotation-free-TEM images through out the magnification range in both HC and HRmodes. Ray diagrams in HC and HR modes are shown in Fig. 3. Operation system of the microscope is fully computer-aided, and all important operation conditions such as accelerating voltage, lens currents, beam deflectors, specimen stage, vacuum sequence and other major functions of the microscope are computer controlled, and all the conditions are displayed on the status monitor. Additional computer can be connected for external microscope control or data communication.

A motor controlled eucentric side entry specimen goniometer stage with a maximum specimen tilting angle of $\pm 20°$ in full specimen position is employed. For operators comfort,the speed of specimen traverse is linked with magnification automatically. With the aid of a newly developed anti-vibration system for the microscope column, the drift rate of the specimen stage is reduced to less than 1nm/min.

An example of thin section of a radish leaf which is fixed with glutaraldehyde and osmium tetroxide is shown in Fig.4. The image shows high contrast at a low magnification.

specimen

objective lens

1st int. lens

2nd int. lens

1st proj. lens

2nd proj. lens

HC mode

HR mode

strength of magnetic field

upper coil

lower coil

HC mode

HR mode

20 μm
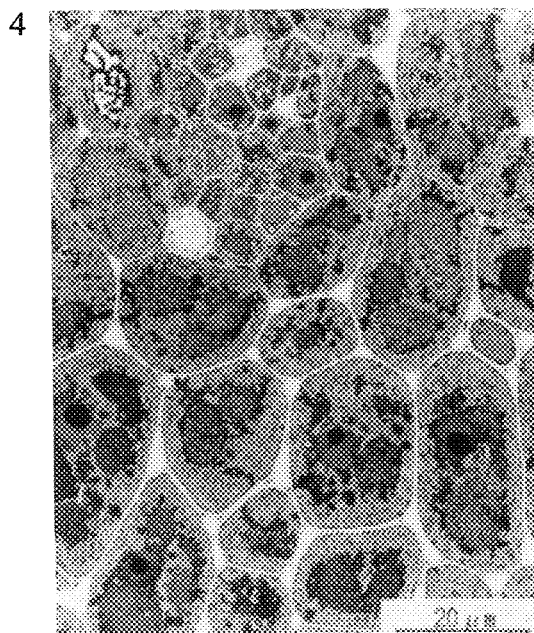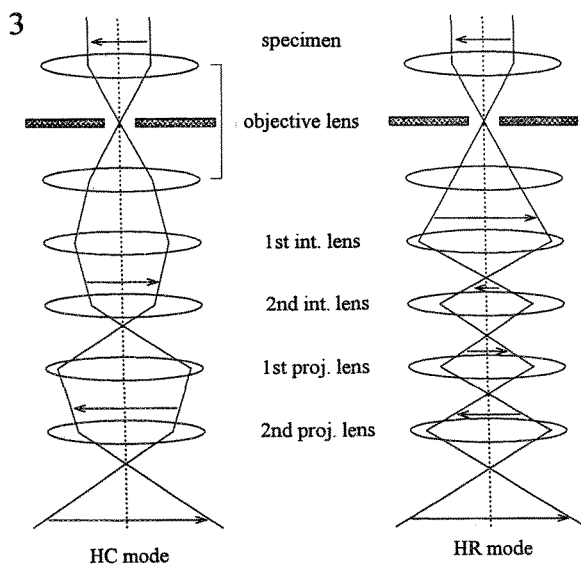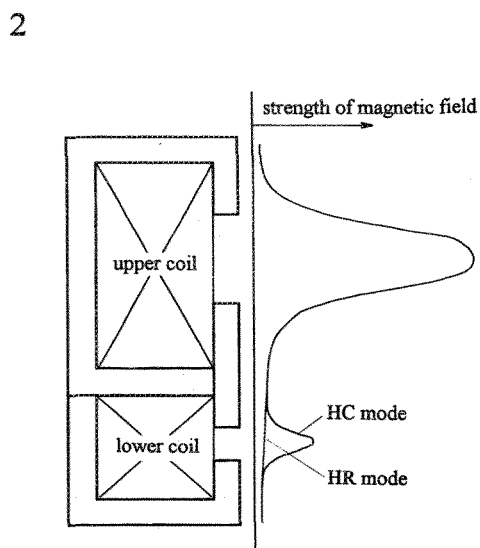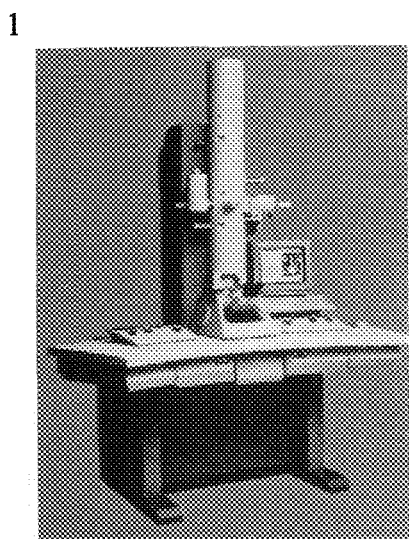
FIG. 1   New 120kV high performance TEM
FIG. 2   Schematic drawing of the objective lens and its magnetic field.
FIG. 3   Ray diagram of the image formation system in HC and HR modes.
FIG. 4   Example of low magnification-high contrast image observation of a thin section of radish leaf.

THE CM200 FEG-TWIN OPTIMIZED FOR CRYO-ELECTRON MICROSCOPY

Uwe Lücken and Max T. Otten

Philips Electron Optics, Applications Laboratory, Building AAE, 5600 MD Eindhoven, The Netherlands

The requirements for cryo-electron microscopy are: good vacuum, high resolution under low-dose conditions at low magnification, low drift with cooled cryo-transfer holders and, in some cases, fast spotscan imaging. For our cryo microscopes we have introduced special factory tests in which these specifications will be met.

In order to obtain high spatial frequencies at low magnification an appropriate specimen with a statistical distribution of small spacings and a fine-grained recording film is needed. We used amorphous tungsten on carbon as specimen and overexposed and underdeveloped Agfa Scienta film (Fig. 1). The laser diffractogram in Fig. 2 presents Thon rings out to 0.19 nm in a one-second exposure flood-beam image. The result of a similar experiment done with a cooled cryo-transfer holder is shown in Fig. 3. Flood-beam images of gold islands and carbon black on a thin carbon film were taken at 66 000x at liquid-nitrogen temperature with one second exposure under low-dose conditions. The laser diffractogram clearly shows Thon rings out to 0.2 nm.

The combination of the CompuStage together with the objective-lens anticontaminator and additional Philips cryo blades leads to a complete shielding of the cryo specimen with almost no open solid angles towards warm surfaces. This results in ice growth of less than 1 nm water/hour. These cryo blades, combined with a special objective-aperture holder, allow tilting up to +/- 70 degrees with the shield in place. The high tilt and low drift are especially important for automatic tomography procedures of cryo specimens. A drift rate experiment (Fig. 4) shows a rate of 0.5 to 1.5 nm/min. The measurement was started 5 min after the final stable temperature was reached.

Fast spotscan imaging may reduce the effect of beam-induced movement and specimen drift. The experiment in Fig. 5 shows images taken with a beam diameter of 100 nm at 10 msec exposure per spot. The corresponding laser diffractogram of one spot shown in Fig. 6 presents Thon rings out to 0.235 nm.

FIG. 1 Image of amorphous tungsten film taken at 66 000x under low-dose conditions at room temperature.
FIG. 2 Laser diffractogram of Fig. 1, showing Thon rings out to 0.19 nm.
FIG. 3 Laser diffractogram of a 1 sec flood-beam image of gold islands and carbon black on a thin holey carbon film taken with a cooled cryo transfer holder at a primary magnification of 66 000x. The 0.204 nm refections as well as Thon rings are visible.
FIG. 4 Cryo-drift-experiment: slow scan CCD images of gold islands and carbon black at 500 000x are taken every min and the cross-correlation peak is marked in the first image taken. The drift rate varies from 0.5 to 1.5 nm/min.
FIG. 5 Spotscan images of a cross-grating taken with a 100 nm wide beam using a fast spotscan routine at a magnification of 66 000x with 10 msec exposure time under cryo-conditions.
FIG. 6 Laser diffractogram of one spot from Fig. 5 showing 0.204 nm reflections and Thon rings out to 0.235 nm.
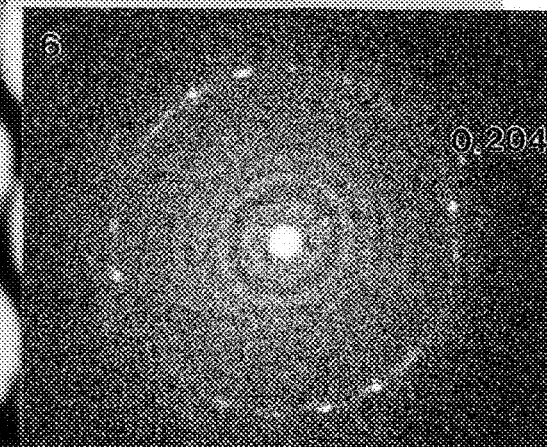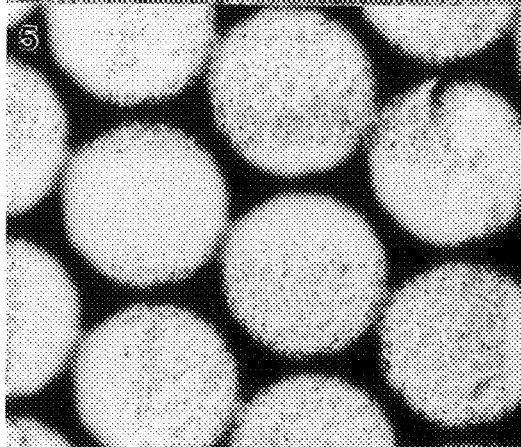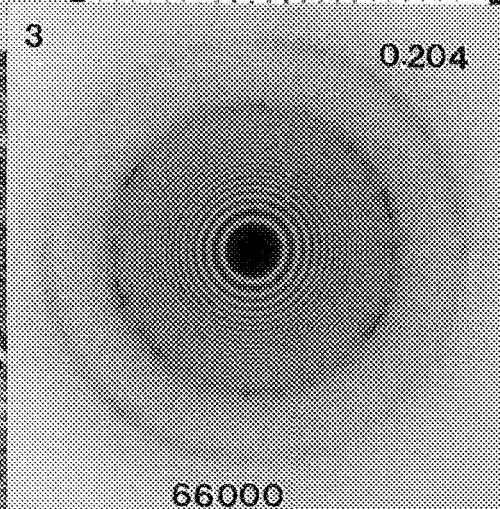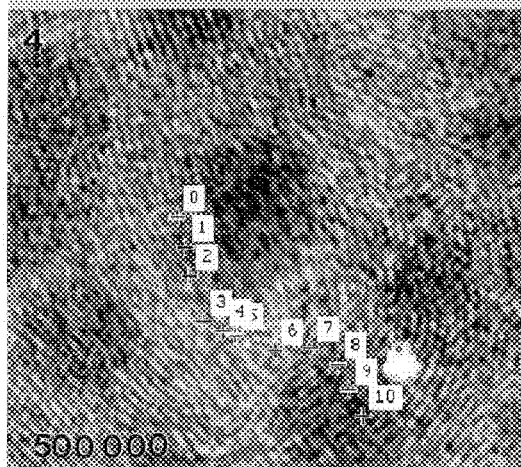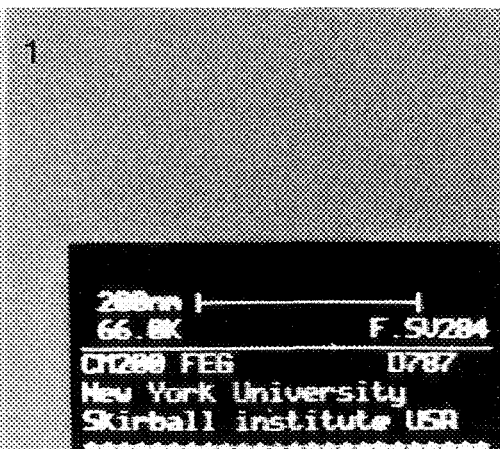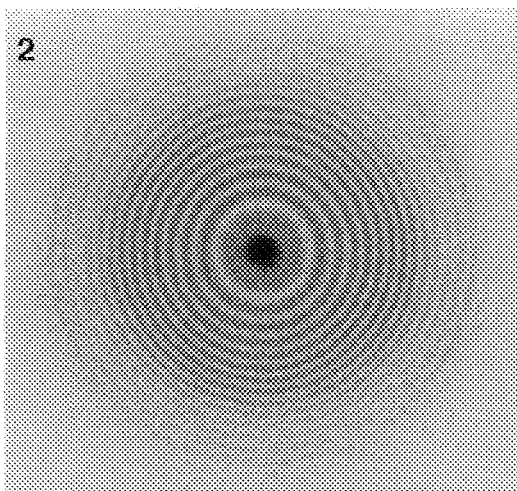
WINDOWS REMOTE CONTROL FOR THE PHILIPS CM MICROSCOPE

Max T. Otten

Philips Electron Optics, Applications Laboratory, Building AAE, 5600 MD Eindhoven, The Netherlands

New software has been developed to make it possible to control the CM microscope under Windows. The software structure is such that all programs communicate through a dynamic link library CMREMOTE.DLL and communication program SECS2.EXE with the microscope (Fig. 1). Due to this structure, the amount of memory required is minimised since functional duplication is avoided, and the remote control handling is simplified because the user programs do not need to handle the complicated communication protocol but instead use simple functions such as Get Alignment and CompuStage Goto Position. Several sets of programs are finished, with further additions planned to replace currently available software running under MS-DOS.

Available at the moment is the Windows CM Remote Control package which contains the Windows CM Monitor, a program to read alignments, stigmator settings and mode settings from microscope and store them in a file on the PC. With the file are stored an operator name and comments to allow identification who stored the data and for what reason. In addition, there are tags at the end of each file to safeguard against corruption (e.g. by someone accidentally reading the file into a wordprocessor and then saving after modification). Later these settings can be read from disk file and restored to the microscope.

Additionally the Windows CM Remote Control package contains two Tutor programs, one for Borland Pascal, the other for Visual Basic, which make it easy to build user programs. For C the LIB and H(eader) file for the dynamic link library are also supplied. The Tutor programs contain all remote control functions, either in the menu where they are arranged by topic (File, Info, Pushbutton, Goniometer, etc.) or accessible in three child windows that represent the left-hand and right-hand TEM panels and STEM panels with their knobs and buttons. Pressing any of the controls in these three panel windows performs the same action on the microscope. The Tutor programs come with complete source code, including that used for building the Help files for the CM Borland Pascal Tutor. Both Tutor programs employ a wide variety of Windows control elements like sliders, buttons and check boxes, providing easy-to-follow examples of how to handle programming for Windows.

A set of Windows CM Remote Control freeware programs is available (free from the author, e-mail mto@eo.ie.philips.nl, or by downloading from the Philips Electron Optics World-Wide Web site http://www.peo.philips.com). The programs cover the following topics:
CM Alignment Help: emulates the CM Microcontroller with its alignment procedures. The Help file will show information relevant to the active alignment step. In addition, the Help file contains a general background about the electron optics of the CM microscope, describing the gun, lenses, deflection coils, stigmators, and the TWIN-type lens. The program can be run either on-line or off-line.
CM Beam Blanker: displays a button on the monitor. Pressing the button toggles the CM microscope beam blanker on and off. Useful for keeping the beam off the specimen during breaks, e.g. to evaluate EDX results.

CM CompuStage Control: read or set the CompuStage position, read or set the registers or tilt to preset values for stereo pictures. Positions and register contents can be saved in a file. Registers settings can be read in again and restored to the microscope.

CM FEG Registers: reads out the contents of the FEG gun registers for a FEG microscope, stores the settings in a file and allows resetting them to the microscope.

CM Free Lens Control: stores Free Lens Control settings in a file from which the settings can be downloaded into the six registers on the microscope.

CM List: makes it possible to log vacuum pressures, lens currents and/or FEG settings continuously. The program logs the data in a text file with tab separators (easy read into spreadsheet program). It can be run in the background or minimised to an icon.

CM Profile: allows stepping a profile (for EDX or EELS) in TEM or Nanoprobe mode. Start and end points are set and number of points defined. Thereafter the program steps through the profile by clicking a button. Recentring the beam to correct for drift and stepping back is also possible.

CM Crystal: a program that does not use remote control but, on the basis of lattice parameters input by the user, can calculate d spacings (one by one or a table with spacings within a specified range), interplanar angles, angles between vectors in real and reciprocal space, and can index a diffraction pattern.

CBED Thickness: also an off-line program, to calculate thickness of the crystalline specimens on the basis of fringes in CBED patterns. Analysis can be based on either minima alone or maxima and minima.

All programs run under Windows 3.1 or higher, Windows NT and Windows 95. In addition some of the freeware programs such as CM FEG Registers and CM CompuStage Control have been found to run on Apple Macintosh under SoftWindows emulation. Further tests will be done to see if all programs can be made to run under the SoftWindows emulation.
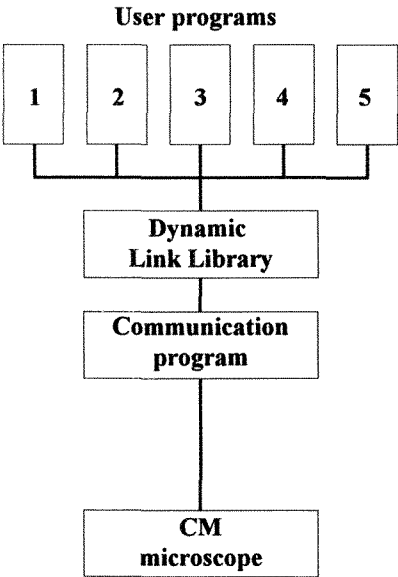
FIG. 1 Schematic representation of the software structure of the Windows CM Remote Control.

SMARTTILT: THE SENSIBLE WAY OF TILTING

Max T. Otten

Philips Electron Optics, Applications Laboratory, Building AAE, 5600 MD Eindhoven, The Netherlands

Tilting a crystalline material in the Transmission Electron Microscope to bring it to a particular crystallographic orientation can be an experience that varies from the almost trivial (e.g. in the case of a large single-crystal piece of silicon in a semiconductor specimen) to something that frustrates even the most experienced operator (e.g. in the case of nanometre-sized crystals in a polycrystalline matrix). The problems encountered during such tilting experiments have to do mostly with the following characteristics of the double-tilt holder and goniometer of the microscope:

- the second tilt is not eucentric
- the mechanical characteristics of the goniometer and specimen holder are such that the forces applied by the tilt drive mechanism can lead to displacements ranging from a few to hundreds of nanometres
- the tilt required commonly involves a combination of α and β tilts.

Normally the operator has to juggle to keep the crystal within the beam (by applying corrections to the x and/or z goniometer axes), set or adjust the tilt speeds for the α and β tilts, judge how much to tilt with α and β, and assess the result on the diffraction pattern. As a consequence, the whole procedure is normally done in increments, with many intermediate steps, corrections for overshoots, and so on. The time taken to tilt a particular crystal is inversely related to its size. For an experienced operator who knows the relative orientations of the diffraction pattern and the tilt direction, tilting a very small crystal sometimes can take up to tens of minutes. For an inexperienced operator, the procedure commonly results in losing track of the crystal and having to start over with another one.

Although for most TEM operators the above is part of life, there is a more sensible way of doing things once a number of pre-conditions are fulfilled.

In principle it is possible to model the behaviour of the goniometer and the specimen holder and on the basis of such a model make corrections for movement of the non-eucentric β tilt axis. As a first step, one can take a simplified model, assuming the holder and goniometer are perfect, and calculate what corrections for x and z displacement are required to counteract the x and z changes induced by tilting on the β axis. This procedure is the basis for what has been called compucentricity: pseudo-eucentricity achieved by computer-generated corrections on the movements of the goniometer. A more accurate way of achieving compucentricity is by acknowledging that no holder or goniometer is perfect, with deviations from ideal behaviour that are systematic (and therefore can be corrected) and random (the ultimate limits tolerances on positioning). The mechanistic model then incorporates those imperfections and corrects for them as well. In order to allow such corrections to be made, it is of course absolutely necessary that all five goniometer axes are under computer control (as it is with the current Philips goniometer, the CompuStage).

The next step is to enable software to make the link between an apparent displacement of a diffraction pattern and the tilts required to bring the origin of the displacement onto the optical axis. If the diffraction pattern displacement can be read out, then a simple calibration procedure will allow the determination of the relation between the x,y shifts of the diffraction pattern and the α and β tilts of the goniometer.

452

On the basis of these two principles we are performing the following:
- a change has been made to the tilting mechanism of the double-tilt holder to improve the tolerances on the β tilt in order to make the behaviour of the holder less susceptible to the incorrigible random movements
- software is developed for compucentricity on the basis of an elaborate model, based on developments in mechatronics robotics, with calibration of the individual holder and goniometer and thus allowing corrections on the β tilting
- the software of the CM microscope is being modified to allow reading out of the displacement of the diffraction pattern
- the SMARTTILT program is being developed, which combines all previous elements into a sensible procedure for tilting

The SMARTTILT program will be a Windows Remote Control program for the CM microscope, running on a PC connected to the microscope (any PC will do, the only requirement is the Remote Control function inside the microscope). It will work on the following basis.

The first step is to perform a number of calibrations:
- the compucentric behaviour of the specimen holder and goniometer
- the relation between size of x,y shifts of the diffraction pattern and the tilts of the goniometer

Next on the unknown crystal, simply shift the diffraction pattern (with the diffraction shift) from a centred position to one where the new position of the optical axis should lie and tell the program to tilt. The program will then recentre the diffraction pattern and tilt the CompuStage, with speed, increments and user corrections as specified to allow the operator to interfere when the crystal threatens to be lost form view, all done with compucentric corrections.

Tilting will be possible in two ways, either to the new position specified or along a perpendicular. In the latter case it is possible to tilt around a systematic row to search for a zone axis pattern. The two methods are indicated schematically in Fig. 1.
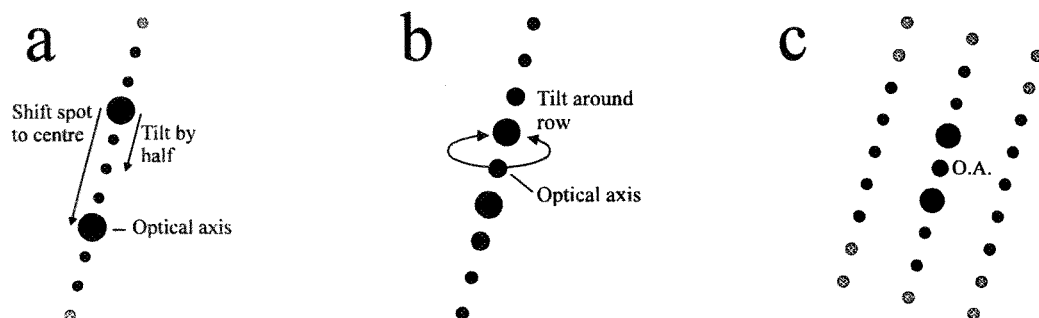
FIG. 1 Schematic steps in SMARTTILTing: a) original diffraction pattern with a non-symmetrical systematic row visible. b) systematic row tilted to symmetrical condition. c) zone axis found by tilting around systematic row. The size and intensity of the disks is used as an indication of the intensity of the beams.

453

METHODS TO MONITOR AND IMPROVE THE PERFORMANCE OF SPECIMEN HOLDERS FOR TRANSMISSION ELECTRON CRYOMICROSCOPY

B. L. Armbruster*, B. Kraus** and M. Pan*

*Gatan Inc., 6678 Owens Drive, Pleasanton CA 94588, and **Gatan GmbH, Ingolstädter Straße 40, D-80807 Munich, Germany

One goal in electron microscopy of biological specimens is to improve the quality of data to equal the resolution capabilities of modern transmission electron microscopes. Radiation damage and beam-induced movement caused by charging of the sample[1], low image contrast at high resolution[2], and sensitivity to external vibration and drift in side entry specimen holders limit the effective resolution one can achieve. Several methods have been developed to address these limitations: cryomethods are widely employed to preserve and stabilize specimens against some of the adverse effects of the vacuum and electron beam irradiation, spot-scan imaging reduces charging and associated beam-induced movement, and energy-filtered imaging removes the "fog" caused by inelastic scattering of electrons which is particularly pronounced in thick specimens.[3]

Although most cryoholders can easily achieve a 3.4Å resolution specification, information perpendicular to the goniometer axis may be degraded due to vibration. Absolute drift after mechanical and thermal equilibration as well as drift after movement of a holder may cause loss of resolution in any direction. Methodology to examine the response of side entry cryoholders to external vibration has been described by Henderson and Faruqi.[4] Their study of six cryoholders allowed identification of modes due to the combination of the microscope and goniometer, the holders and goniometer, and modes specific to the holders. Whereas the photomultiplier used by Henderson and Faruqi can be adapted to any microscope to study vibration response, a CCD camera and appropriate software which we describe in this paper can provide information on the drift performance of a specimen holder.

In this report digital imaging was used to monitor the drift performance and stability of commercially available cryoholders. Standard graphite-holey carbon and oriented gold calibration grids were loaded into Model 626 cryoholders and, as a comparison, a single tilt holder in a Philips CM200 TEM. Drift performance at ambient and low temperatures was measured by means of cross-correlation analysis of digital images recorded on a Model 794 MultiScan camera bottom-mounted to the microscope column. Two drift measurement scripts run in DigitalMicrograph™ software were available for this analysis: Script 1 sequentially numbered the sampling points and displayed them on the original image for easy reference to the orientation of the sample in the microscope, Script 2 automatically rescaled the image if sample drift was greater than the field of view present in the original imaging field and displayed the result against a neutral background.

Representative results from running drift measurement scripts 1 and 2 are shown in Figures 1 and 2, respectively. Both scripts operate by cross-correlation of a sequence of images taken on a CCD camera. When Script 1 is activated, a reference image is taken with the center point numbered zero and marked by a cross. The change in position of the initially central feature is automatically calculated, marked and numbered at successive timepoints. The number 10 and the marker at the lower left of the annotation denote the last measurement in this series, with zero through nine represented by the cluster of markers under the last reading. When Script 2 is activated to study the stabilization of a single tilt holder, the first measuring point is denoted in the center of the image field in Figure 2. Successive timepoints establish the speed and vector of drift, shift the initial central marker and indicate the drift vector with an arrow. The final measurement in the sequence is located at the arrowhead. Computer control of the microscope's image shift coils will relocate the specimen to maintain the initial features in the camera field of view. Measurements of relative and total drift are displayed in a results window of the software. The scripts allow the user to determine whether drift rates are increasing or decreasing, if the direction of drift is along or at an angle to the axis of the goniometer, and whether the holder has achieved an equilibration state. The user can customize the scripts by choosing the number of

measurements taken by the CCD camera, exposure time, the delay between measurements, image binning and image size. Although the scripts described here were written for a Macintosh-based imaging system, similar protocols could be developed for cameras operated on PC-based platforms.

The possibility to assess specimen quality and cryoholder stability on-line gives feedback that facilitates undertaking immediate modifications to optimize specimen holder performance. Several practical suggestions to achieve best cryoholder performance include removing any particulates and excess vacuum grease from the o-ring, removing nucleation points on the inner surface of the cryoholder dewar with a cotton applicator, and filtering out ice crystals in liquid nitrogen while filling the specimen holder dewar.

1. J. Brink and W. Chiu, *J. Microscopy*, 161(1991) 279.
2. R. Henderson, *Ultramicroscopy*, 46(1992) 1.
3. K.F. Han et al., *J. Microscopy*, 178(1995) 107.
4. R. Henderson and A. R. Faruqi, *Ultramicroscopy*, 60(1995) 375.
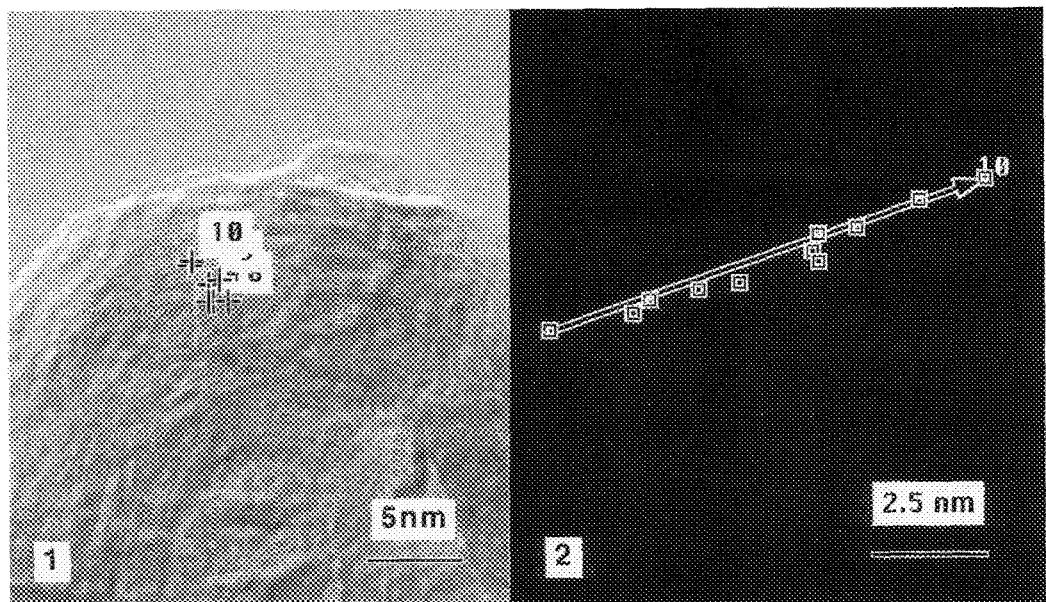
Figure 1. A drift performance of 20Å/min is demonstrated by the overlapping markers on the image of a calibration grid at a cryoholder temperature of -185°C. Drift measurement is based on cross correlation of successive digital images taken with a CCD camera. The position of a central feature is automatically tracked and indicated by a numbered cross on the initial image. The number 10 and assocated cross at the lower left of the annotation indicate the last measurement point of the series. Measurements 0-9 are represented by the cluster of crosses under the annotation.

Figure 2. With a single tilt holder at ambient temperature, the second script indicates with an arrow and markers the relative speed and direction of specimen drift immediately after movement of the holder. This drift measurement script is also based on cross correlation of successive digital images but the specimen image is not displayed. The first measuring point is represented by the square at left at the base of the arrow with successive timepoints along the shaft of the arrow. The number 10 represents the last timepoint in the series.

DETECTIVE QUANTUM EFFICIENCY OF 25μm PIXEL IMAGING PLATE

A.Taniyama*, D.Shindo*, T. Oikawa** and M.Kersker***

* Institute for Advanced Materials Processing, Tohoku University, Katahira 2-1-1, Aoba-ku, Sendai 980-77, Japan
** JEOL Ltd., 1-2 Musashino 3-Chome, Akishima, Tokyo 196, Japan
*** JEOL USA Inc., 11 Dearborn Road, Peabody, MA 01960

The 25μm pixel Imaging Plate (IP) [1] is expected to apply to high-resolution transmission electron microscopy (HRTEM) because of its higher spatial resolution than the 50μm pixel IP. It seems that the 25μm pixel IP, which has wide dynamic range and good linearity, is effective for HRTEM with low exposure to reduce electron radiation damage. In order to apply the IP to the HRTEM appropriately, it is necessary to understand the detective efficiency of the IP. In this paper, signal to noise (S/N) ratio and detective quantum efficiency (DQE) of the 25μm pixel IP at accelerating voltages of 100, 200 and 1250kV are presented and a suitable amount of electron exposure for HRTEM is discussed.

DQE is expressed as the comparative noise level (σ_i^2/σ_o^2) measured by the ratio of the mean-square fluctuation of incident electrons (σ_i^2) to that of output signal (σ_o^2).[2] In this experiment, the distribution of the incident electrons was assumed to be Poisson statistics. The fluctuation of output signal was calculated with signal intensity recorded on the IPs. The IPs (Fuji film FDL-UR-V : 25μm pixel) were uniformly exposed to incident electrons with JEM-2010 (100 and 200kV) and JEM-ARM1250 (1250kV) electron microscopes. The amount of incident electrons was measured with a Faraday cup. The exposed IPs were kept for 24hr at 20℃ in a dark room after the exposure. The signal intensity recorded on the IPs was converted into digital data with the FDL5000 / PIXsysTEM II Imaging Plate reader system.

Figure 1 shows the signal intensity as a function of the number of incident electrons. The 25μm IP has good linearity in electron exposure for the accelerating voltages of 100 and 200kV. A part of data in the case of 1250kV is also indicated in Fig.1. Figure 2 shows the $(S/N)^2$ of the output signal intensity of the 25μm pixel IP as a function of the number of incident electrons. The $(S/N)^2$ increases with increasing incident electrons but tends to saturate in high exposure region, although the good linearity between the number of incident electrons and output signal is reserved in the region. This saturation seems to be caused by the fixed noise of IP reader system. Figure 3 shows the DQE of the 25 μm pixel IP as a function of the number of incident electrons. The DQE curves have maximum values at about 20, 20 and 200 e/pixel for the accelerating voltages of 100, 200 and 1250kV, respectively. The above results indicate that the high quality images can be obtained, if the exposure is more than 20 e/pixel for the accelerating voltages of 100 and 200kV and it is more than 200 e/pixel in the case of 1250kV. Figure 4 shows an example of HRTEM images of α-AlB₁₂ observed at 1250kV. Exposure and a direct magnification were about 300 e/pixel and ×800K, respectively. The fine structure of α-AlB₁₂ can be observed under this condition. Thus, the high quality TEM images can be observed with the 25μm pixel IP under the optimum exposure condition taking account of the S/N ratio and the DQE.

References
1. N.Ogura et al., Proc. 13th ICEM (Paris), (1994) 219.
2. A.Rose, J. Soc. Motion Picture Engrs., 47 (1946) 273.
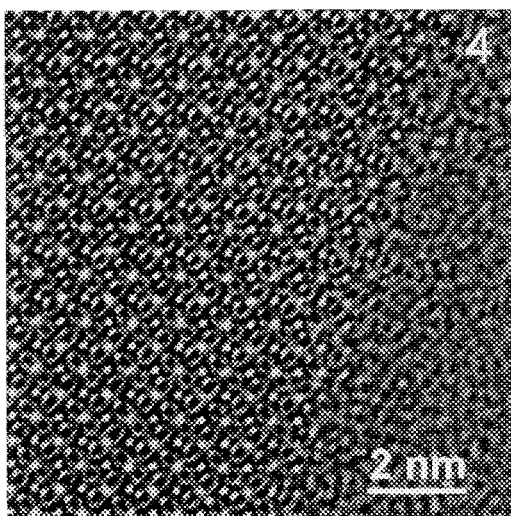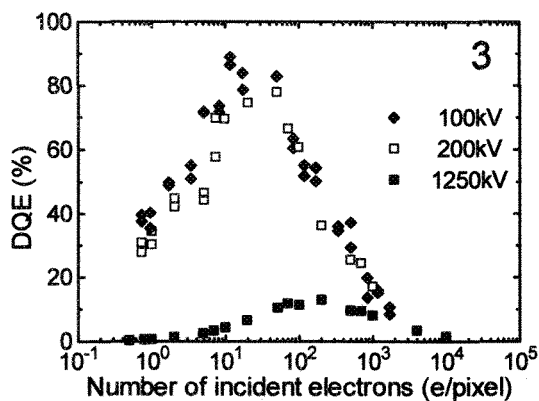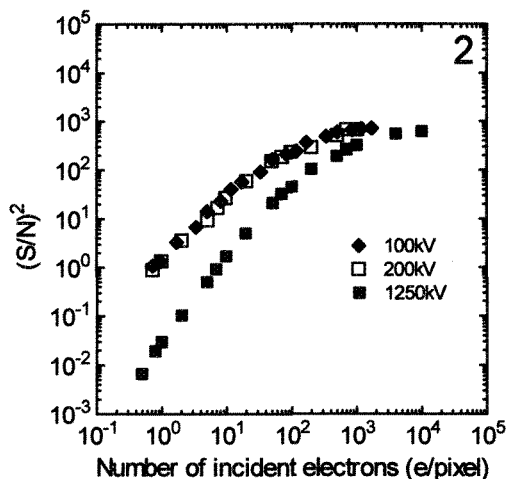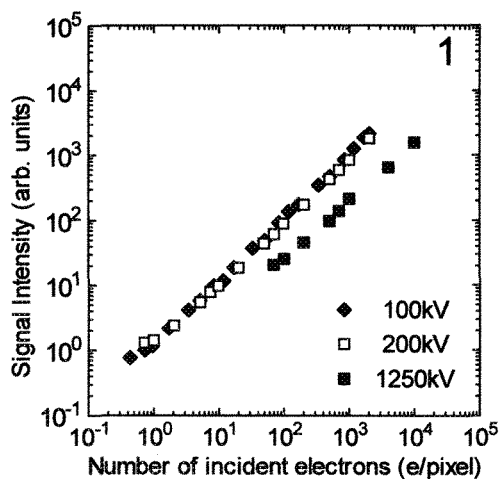
Fig. 1. Signal intensity as a function of the number of incident electrons of 25μm pixel IP.

Fig. 2. Signal to noise ratio (S/N)² of the 25μm pixel IP.

Fig. 3. Detective Quantum Efficiency of the 25μm pixel IP.

Fig. 4. HRTEM image of α-AlB₁₂ observed with the 25μm pixel IP.

DEVELOPMENT OF HIGH-DEFINITION IMAGE PROCESSING SYSTEM FOR A FE-SEM

M. Yamada*, T. Yoshihara*, H.Arima*, Y. Nimura*, T. Kobayashi* and C.Nielsen**

*JEOL Ltd., 1-2 Musashino 3-chome, Akishima, TOKYO, JAPAN and
** JEOL U.S.A. Inc., 11 Dearborn Road, Peabody, MA 01960

This paper presents the development of a new, fully digital image processing system for a field emission SEM (FE-SEM) which can eliminate fluctuations in the emission current. The system can display, in real time, images with 1280 x 1024 pixels on a viewing CRT, allowing direct observation of high definition SEM images on the FE-SEM.

In the past, even though image was acquired and recorded (photographed) with the resolution higher than 1,000 x 1,000 pixels, it was generally observed on the viewing CRT at the resolution of only about 500 x 500 pixels for real-time observation. This created a difference in image quality between the two CRT's. Using a CRT of the same pixel resolution for observation as on the recording CRT, the difference in image quality can be minimised, provided that the characteristics (speed and resolution) of the image processing and scan generator system are improved and optimised for digital processing.

In this new system, image signals detected by the photo-mutiplier are amplified and converted into 10 bit digital data while the detected emission current signals are simultaneously converted into 10 bit digital data. The image signal data is then divided by the emission current data, added according to the brightness of each element, and compressed to 8 bits with a limiter (Fig.1). The advantages of the digital operation are that no offset error occurs and that high integration becomes possible.

Frame averaging is performed on a 16 bit multiplier-accumulator during image signal transfer from an input-frame-buffer to an output-frame-buffer. An address generator makes it possible to form an accumulated image at a desired position of the output-frame-buffer. A scan generator counts the repetition time and a blanking time set by a computer in both horizontal and vertical directions and a 12 bit D/A converter outputs

a sawtooth-like scan signal. This image processing system and scan generator are synchronised to one clock signal using a pipeline process, thus improving the reliability of the system by avoiding critical timings between functions.

To observe images in real time, a D/A conveter with a built-in look-up table composes both the output-frame-buffer plane and overlay plane and provides RGB video signals with 1280 x 1024 pixels onto the CRT.

All the hardware is integrated on a single board so that the wiring length is kept to a minimum and so that the clock signals can be distributed stably to all digital operation chips. The control and operation logic is implemented on FPGA (3,000 to 9,000 gates) chips, with 8 FPGA chips in total.

Control response and software development efficiency are improved by the employment of a real-time multitasking operating system in the signal control software. Using windows software for the graphics controller, the SEM operating menu can be displayed with an imaging overlay plane.
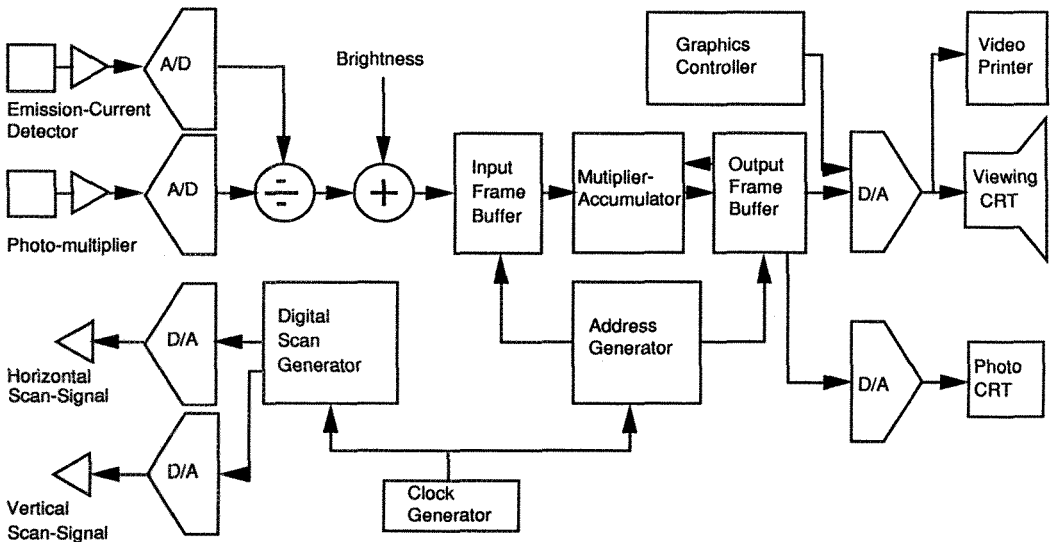
FIG. 1. The Digital Image processing system.

EVALUATION OF COMMERCIAL TRITIUM STANDARDS: A SIGNIFICANT SOURCE OF ERROR IN QUANTITATIVE AUTORADIOGRAPHY

J. Nissanov* and L.Rioux**

*Biomedical Engineering and Science Institute, Drexel University, Philadelphia, PA 19104

**Department of Pharmacology, University of Pennsylvania, Philadelphia, PA 19104

Using quantitative receptor autoradiography (QAR), it is possible to investigate the distribution of ligand binding sites as well as binding affinity[1]. Accuracy in this technique is critically dependent on the quality of available radioactive calibration standards. For autoradiography using tritiated ligands, commercial ^3H standards are available. These are also used, after cross-calibrating, as convenient standards for short-lived radioisotopes for which commercial standards are not available[2]. A common practice in QAR is to appose these standards, each a slide containing 14 plastics of known radioactive concentration, along with the tissue sections on each sheet of x-ray film and to use these to produce a calibration curve and assign absolute concentration to densitometric measurements taken from the film. Typically, experimenters use multiple standards in their studies and directly compare data calibrated using different calibration sets. To our knowledge, only one study[2] has tested the implicit assumption that the standards, once corrected for decay, are equivalent. That study concluded that the variability among standards is low. We revisit the issue.

We compared ten ART-123A standards (American Radiolabeled Chemicals, St. Louis, MO) manufacture on the same date (6/23/89). The experiment was run in triplicate. For each run, the standards were apposed to Hyperfilm (Amersham) for an exposure period of 24 hours. The films were digitized (7.7 μm/pixel) using a Sony XC-77 CCD camera and DataTranslation DT2255 capture board and analyzed using the image processing software Brain for Macintosh[3]. A number of precautions were followed to minimize densitometric variability arising during capture. First, a mask was used to reduce flare. The mask encompassed an area of 4.4 cm by 1.9 cm, just sufficient to view all 14 concentration values of a single standard. Second, shading correction was applied to all images to reduce the effects of spatial nonuniformity in illumination and in camera response[3].

For each calibration plastic on a standards set, a large ROI was defined and the average gray value determined. The number of saturated pixels, pixels of gray value equal to 255 on the opaque end of the scale and equal to the film background on the transparent end, was determined. No standard plastic having 5% or more of its ROI saturated was further analyzed. The standards were compared using a single calibration curve. The curve was defined using the standard closest to the mean value for all the standards. To identify which of the ten standards fitted this criteria, for each value, the average of all the standards was computed and the squared difference between the average and the individual values determined. For each standard, the sum of these squares was found and the standard having the minimum difference from the average employed for construction of the curve. A curve was fitted to the data from this standard using a 2nd degree polynomial. Using this curve, the gray value of all the standards were converted to concentration values. Considerable variability was found (Table 1). The difference, as a ratio of the average, between the minimum and maximum value among the standards ranged from 15 % for the highest calibration value used 2000 μCi/g to a high of 39 % for the 1000 μCi/g plastic.

Could the observed variation be due to temporal instability of the imaging system? To evaluate this possibility, four glass optical standards (0.2, 0.4, 0.6 and 0.8 OD units; Melles Griot, Irvine, CA)

460

were simultaneously imaged every 2 minutes for a period of 1 hour, the one hour total duration of this experiment exceeds the time required to image all the radioisotope standards. Because of known spatial nonuniformity of the optical standards themselves, the same ROI was examined for each of the standard at each time point. The gray value was converted to equivalent concentration value using the isotope calibration curve described above. The greatest instability was observed for the 0.8 OD. The standard deviation of all the time samples for this standard was 2.12 μCi/g while the range between the lowest and highest value was 1% of the average. Clearly, then, the observed variability in the ^{3}H standards are not explained by temporal instability of the imaging system but instead reflect variability among the standards themselves.

The large magnitude of this variability can dramatically affect accuracy of QAR. However, the problem can be partially resolved by cross–calibrating one's radioisotopes standards. This would permit comparison of data calibrated with different standards. However, absolute quantitation requires more reliable standards.

References

[1] L. Rioux and J. Joyce. J. Neural Transm. P-D Sect (1993) 6:199-210.

[2] R. Artymyshyn et al., J. Neurosci. Meth (1990) 32:185-192.

[3] J. Nissanov and D.L. McEachron, J. Chem. Neuroanat. (1991) 4:329-342.

[4] This work was supported by NIH award P41 RR01638 to JN and a NRSA (NINDS) to LR.

Table 1-Comparison of calibration standards.

Calibration Value (μCi/g)	Average (μCi/g)	Stdev (μCi/g)	(max-min)/average (%)
2000	2023	103	15
1000	911	99	39
489	635	61	37
243	253	21	28
138	108	15	38
63.1	56	3	18
36.3	46	3	16

* For one of the ten standards, more than 5% of the pixels at this value were saturated. This value for this standard was consequently not used

CORRECTIONS FOR SEVERAL FACTORS THAT LIMIT QUANTITATIVE ANALYSIS OF 3-D DATA SETS COLLECTED USING SCANNING-LASER CONFOCAL MICROSCOPY

S. Kayali*, H. Ancin*, B. Roysam*, D.H. Szarowski**, W. Shain***, J.N. Turner***

*Depts. of Biomedical Engineering and ECSE, Rensselaer Polytechnic Institute, Troy, NY, 12180
**Wadsworth Center, NYS Dept. of Health, Albany, NY
***Wadsworth Center and School of Public Health, University at Albany, Albany, NY

The confocal microscope collects high contrast 2-D images at different depths from thick (≥ 100 µm) tissues samples, thus providing data for quantitative measurements of 3-D objects. There are several factors that may limit quanititative analysis[1-3] including photobleaching of fluors, attenuation of measured signal, mismatch in the various refractive indeces of the sample, and the width of the point spread function. We have addressed the first three of these limitations by using acriflavine-stained 100-µm thick sections of rat hippocampus and our 3-D automated analysis software[4]. The laminar structure of the hippocampus provides tissue sections with areas of high and low nuclear density (pyramidal and extra-pyradmidal cell regions, respectively). Corrections for these limitations were made to samples from rat testes where developing spermatogonia provide nuclei of different DNA content .

The contribution of photobleaching to signal degradation was determined by collecting multiple 3-D images (z-series) of the same field. Twenty-one images of 50 planes each were collected (total scans= 1050). A decrease of intensity was observed as a function of tissue depth (Fig 1); however, no significant photobleaching was observed until more than five images (250 scans) were recorded. Intensity continued to decrease with the number of images collected. The greatest effect was observed in focal planes closest to the objective (laser source). Thus, conditions for studying signal attenuation and refractive index mismatch should not be compromised by photobleaching.

An empirical correction for signal attenuation was made using an exponential fit to the average intensity of nuclei as a function of distance from the objective. No significant differences were observed for fitting pyramidal and extra-pyramidal regions (Fig 2). This correction procedure was verified by imaging the same field from opposite z-directions (Fig 3). No significant differences in the exponential components were observed. When the average intensity for each nucleus is corrected, the average intensities of nuclei differed according to tissue distribution, e.g. pyramidal vs extra-pyramidal, but not tissue depth. A test of our attenuation correction using testes samples indicated that two major, overlapping populations of nuclei were discriminated (Fig 4).

Refractive index mismatch was studied using the z-diameter of extra-pyramidal cell nuclei. The z-diameter of the nuclei decreased linearly with z-dimension (distance from the objective). When the raw data were corrected, a single population of nuclei (diameter≈ 11µm) was observed (Fig 5).

References
1. Rigaut et al, *Visualization in Biomedical Microscopies*, New York:VCH (1992)205.
2. Hell et al, *J. Microsc.* 169 (1993)391.
3. Majlof and Forsgren, *Meth. Cell Biol.* 38 (1993)79.
4. Roysam et al, *J. Microsc.* 173 (1994)103.
5. This work was supported in part by NIH grants RR01219 and RR10957.
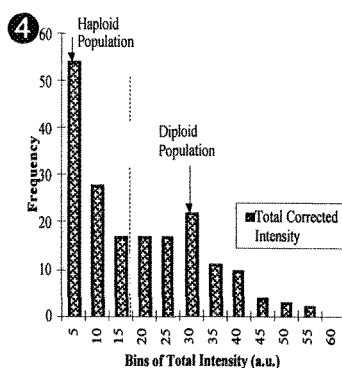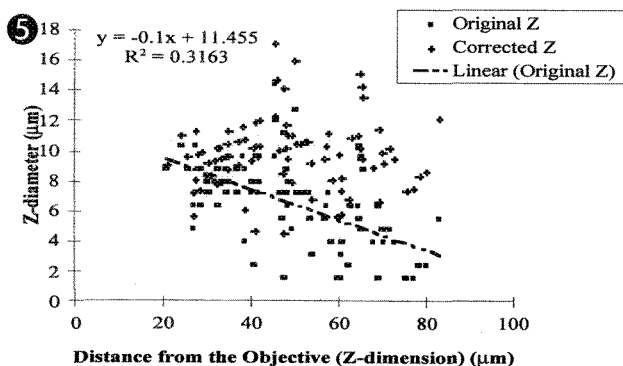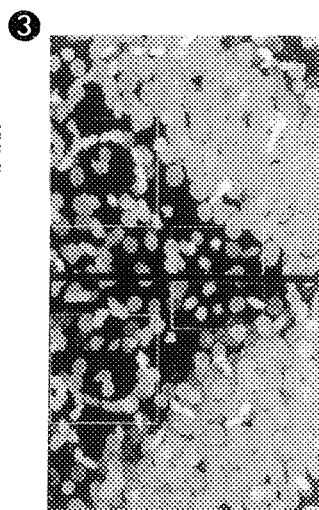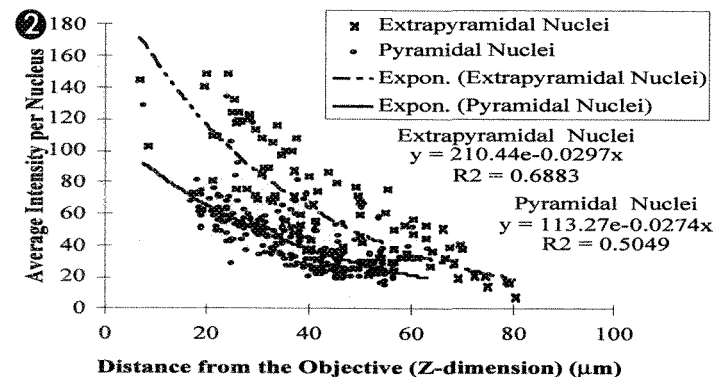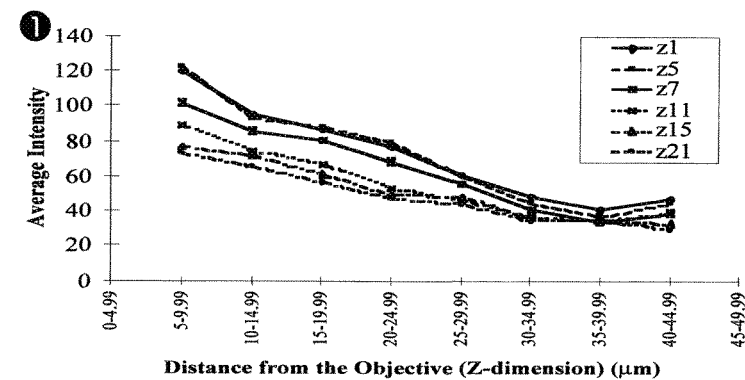
Fig 1. Photobleaching of fluorescence as a function of scans and tissue thickness (z-dimension).

Fig 2. Exponential attenuation of nucelar signals as a function of z-dimension.

Fig 3. Field of a hippocampus section imaged from opposite z-directions. Squares delineate regions where extra-pyramidal nuclei were identified. The width of the large boxes is 48 μm.

Fig 4. Histogram of attenuation corrected nuclear intensities from rat testes samples.

Fig 5. Correction of z-diameter data of the extra-pyramidal cell nuceli for refractive index mismatch.

463

ULTRA-HIGH RESOLUTION WITH THE JEM-2010F FIELD-EMISSION TEM

F.Hosokawa*, T.Tomita*, T.Honda* and M.Kersker**

*JEOL Ltd., 1-2, Musashino 3-chome, Akishima, Tokyo,196 JAPAN
**JEOL(U.S.A) Inc., 11 Dearborn Road, Peabody, MA 01960

Historically, high probe current in small probes has been the principal virtue of the field emission TEM. Analytical performance is greatly enhanced[1] and fine probe mapping an important analytical tool for trace element segregation and very fine scale high resolution chemical imaging. Less appreciated is the enhanced high resolution capability due to the small energy spread of the electron source and higher coherency due to reduced primary and virtual source size. The envelope function of the phase contrast transfer function (PCTF) is drastically improved reducing image blurring due to both chromatic aberration and specimen illumination angle. This is especially true for the high spatial frequencies beyond the first zero. Intensities sufficient for image formation can be obtained from these higher frequency regions. Since the PCTF does not change its form, photographing images at the Scherzer condition will yield higher resolution with higher coherency, however, the transfer of the specimen potential corresponding to contrast enhanced regions is in the oscillations form beyond the first zero. Changes in the defocus will lead to changes in transferred frequencies beyond the first zero and possible extinctions of otherwise transferred information since the oscillations will pass through zero contrast. Interpretation of images under these conditions will, therefore, require accurate measurement of the optical parameters of the microscope and especially accurate measurements of the defocus conditions. It is also important to calculate images under these conditions for comparison with measured images which give the insurance of defocus conditions supposed to be presented.

We present the results of a series of high resolution images of standard high resolution samples. An auto-adjustment system[2] of Windows version was used to facilitate taking the micrographs. This system permits the beam alignment, astigmatism correction, and defocus step to be quantitatively controlled.

Figure 1(a) and Figure 2(a) show the ultrahigh resolution image of H-Nb2O5 and β-Si3N4 respectively. The multislice calculated images corresponding to these actual defocused images are superimposed inside of the micrographs. The images show good correspondence. The black spots in the H-Nb2O5 micrograph correspond to Nb atoms. In the β-Si3N4 micrograph, white spots in the medium intensity surrounding the 6 fold axis correspond to the Si and N atoms, the weak white spots correspond to the N atoms. Figure 1(b) and Figure 2(b) shows the calculated image and superimposed atom site in black . For further works, we intend to do image reconstruction by Wiener filtering and Schiske filtering.

REFERENCES.
1. T.Tomita, M.Kawasaki and R.Ravel-Chapuis Proc. 13th Int. EM Congress **1**, 215-216
2. F.Hosokawa, Y.Kondo, T.Honda and R.C.Hertsens Proc. 13th Int. EM Congress **1**, 207-208

FIG. 1   a   b
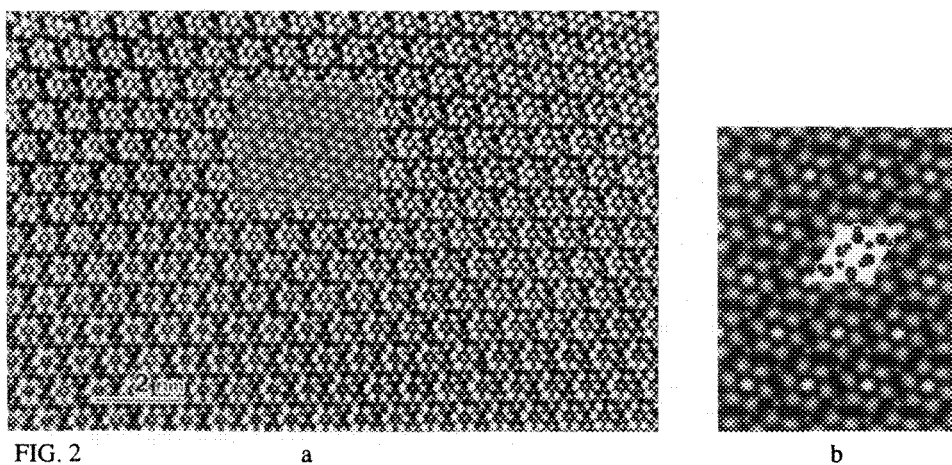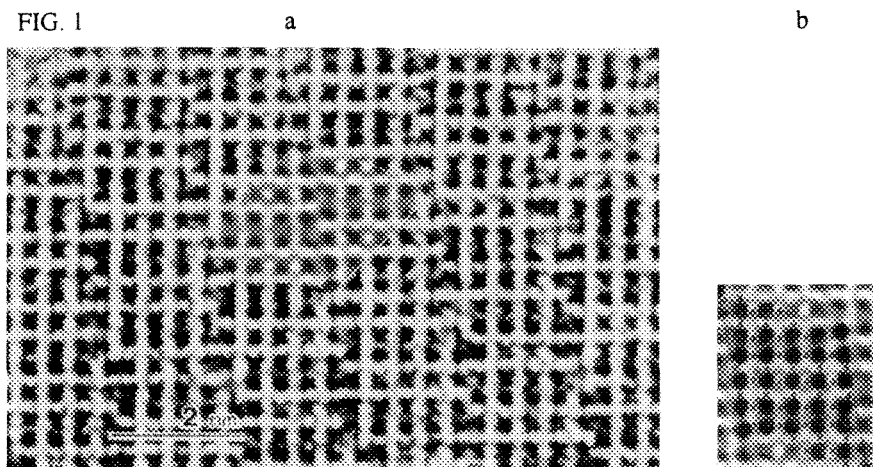
FIG. 2   a   b

FIG.1 : a) High resolution micrograph of H-Nb2O5<010>. Calculated image is superimposed. The black spots correspond to Nb atoms.
b) Calculated image and superimposed atom site in black.

FIG. 2: a) High resolution micrograph of β-Si3N4<001>.Calculated image is superimposed.
b) Calculated image and superimposed atom site in black.

465

AN INTEGRATED ENERGY-FILTERING TEM FOR THE LIFE SCIENCES

A.F. de Jong[a], H. Coppoolse[a], U. Lücken[a], M.K. Kundmann[b], A.J. Gubbens[b] and O.L. Krivanek[c]

[a]Philips Electron Optics, P.O. Box 218, 5600 MD Eindhoven, The Netherlands
[b]Gatan R&D, 6678 Owens Drive, Pleasanton CA 94588, USA
[c]Microstructure Physics, Cavendish Laboratory, Cambridge, CB3 0HE, United Kingdom

Energy-filtered transmission electron microscopy (EFTEM) has many uses in life sciences[1]. These include improved contrast for imaging unstained, cryo or thick samples; improved diffraction for electron crystallography, and elemental mapping and analysis. We have developed a new system for biological EFTEM that combines advanced electron-optical performance with a high degree of automation. The system is based on the Philips CM series of microscopes and the Gatan post-column imaging filter (GIF). One combination particulary suited for the life sciences is that of the CM120-BioTWIN[2] and the GIF100[3]: the CM120-BioFilter. The CM120-BioTWIN is equipped with a high-contrast objective lens for biological samples. Its specially designed cold-trap, together with low-dose software, supports full cryo-microscopy. The GIF100 is corrected for second-order aberrations in both images and spectra. It produces images that are isochromatic to within 1.5 eV at 120 keV and distorted by less than 2% over 1k x 1k pixels. All the elements of the filter are computer controlled. Images and spectra are detected by a TV camera or a multi-scan CCD camera, both of which are incorporated in the filter. All filter and camera functions are controlled from Digital Micrograph running on an Apple Power Macintosh.

The design philosophy has been to develope an integrated system dedicated to user-friendlyness and high-quality performance. Being mainly concerned with samples, microscopy and applications, the user should be able to operate the system directly from the microscope. The system should appear to the user almost as a normal TEM, equipped with a CCD camera that records energy-filtered images and diffraction patterns. At the same time, control from the Macintosh side is possible, supporting more complicated filter functions and image processing.

Several operating and set-up pages for energy filtering are added to the microscope software. They provide control of all the essential features of the filter from the microscope console. An example of a BioFilter set-up page that appears on the microscope control monitor is shown in Fig. 1. Camera and filter control are achieved by single push-button actions. Pressing a button on the CM sends a remote-control message from the CM to the Macintosh, which then performs the required actions. Similar operation is possible from an icon-based button command pallette (Fig. 2) on the Macintosh. All normal operating modes and possibilities on the CM are still available. The full flexibility of the Digital Micrograph software for e.g. three-window mapping and image processing is available on the Macintosh.

The integration also has consequences for the optics of the microscope. Low magnifications and short camera lengths are provided by newly developed imaging lens regimes, to accomodate the extra magnification factor of the filter. The CM software automatically switches from the normal magnification regime to the special BioFilter regime when the fluorescent screen is lifted, reducing the magnification by a factor of about 10, while maintaining image alignment. Magnifications as low as 1200x on the filter's CCD (with the objective lens on) are achieved in

in CM120-BioFilter. An example of a low-magnification image is given in Fig. 3. When operating with low magnifications or camera lengths, the size and position of the cross-over in the microscope's pumping aperture become important, as this crossover is imaged onto the spectrum plane[4]. Special software is provided to align the crossover position, assuring alignment of the zero-loss peak in the spectrum upon a change of magnification or camera-lenght. In addition, displacements of the zero-loss peak because of instrumental drift (HT, filament or prism current) can be adjusted automatically by a "centre zero-loss" routine in the filter software. The ALIGN ZERO button is available both on the CM and on the Macintosh.

In summary, the *CM120-BioFilter* is an easy-to-use energy filter for Life Science TEM, with advanced automation, high-quality optical performance and fully integrated digital imaging. It is *one* system which can be operated from the microscope at the touch of a soft key or, at the user's choice, from the Apple Power Macintosh at the click of a mouse.

References

1. Proc. European Workshops on Electron Spectroscopic Imaging: Ultramicroscopy 32 (1990) number 1, J. of Microscopy 162 (1991) part 1 and 166 (1992) part 3.
2. U. Lücken et al., Proc. Microscopy and Microanalysis (MSA) 1995, p. 584.
3. O.L. Krivanek et al., Ultramicroscopy 59, 267-282 (1995).
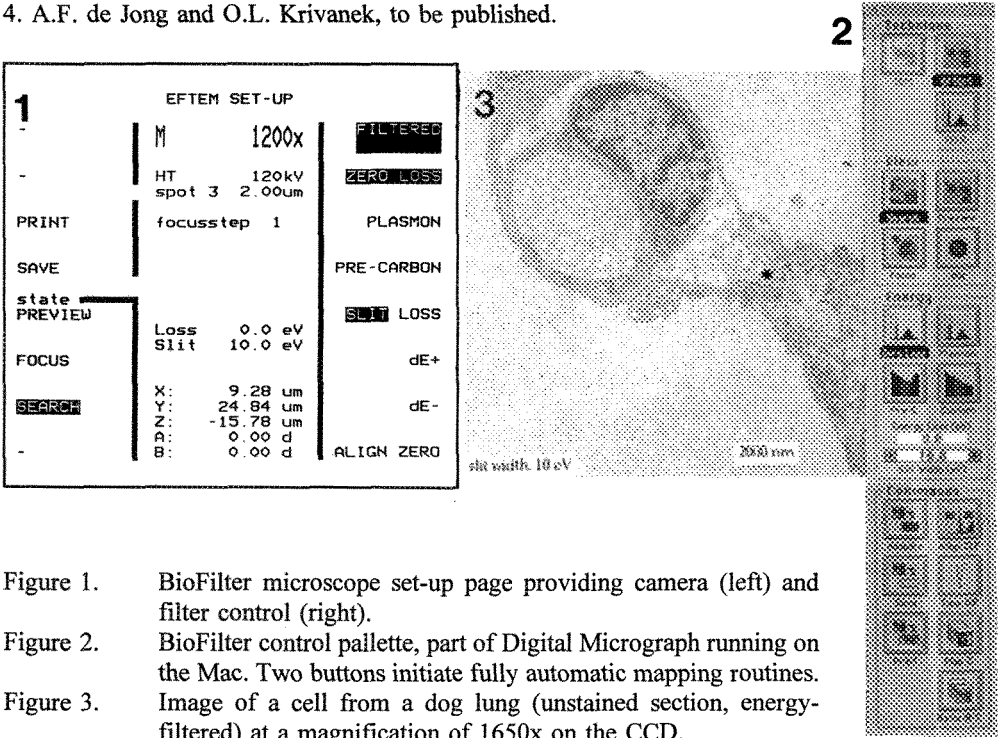4. A.F. de Jong and O.L. Krivanek, to be published.

Figure 1.   BioFilter microscope set-up page providing camera (left) and filter control (right).

Figure 2.   BioFilter control pallette, part of Digital Micrograph running on the Mac. Two buttons initiate fully automatic mapping routines.

Figure 3.   Image of a cell from a dog lung (unstained section, energy-filtered) at a magnification of 1650x on the CCD.

A STUDY OF ELECTROSTATIC PHASE PLATES USING ELECTRON HOLOGRAPHY

A. Mohan, B. G. Frost *, and D. C. Joy *

EM Facility, University of Tennessee, Knoxville, TN 37996
* and Oak Ridge National Laboratory, Oak Ridge, TN 37831

Contrast in transmission electron microscopy is normally provided by variations in the intensity of the transmitted electron beam, but weakly scattering objects such as biological tissue and polymers may not cause a sufficient change in amplitude to provide a useful image. The phase of the electron beam, however, is altered and if the phase change can be made to yield amplitude variation then the imaging can be carried out as desired. This can be accomplished by the use of some phase shifting device which alters the phase of the scattered wave by $\pi/2$ with respect to the unscattered wave.[1] A number of such devices have been discussed in the literature but their design has typically been optimized empirically.[2] One of the methods for performing Phase Contrast Microscopy in the TEM is by using an electrostatic phase plate in the back focal plane of the objective lens.[3] This device consists of a charged fiber which causes small deviations in the ray paths of the scattered and the unscattered waves thus introducing a suitable phase shift between them.[4]

In this paper we have used the technique of electron holography to study the charging behavior of an electrostatic phase plate in the TEM. The phase plate was constructed by drawing a fine glass capillary to a diameter of 0.9μm and mounting it across a 30μm disc aperture. This was then coated with a layer of gold a few hundred angstroms in thickness. The microscope used to study the phase plate was a Hitachi HF-2000 field emission TEM operated at 200kV, equipped with an electrostatic biprism. The phase plate was inserted in the specimen plane of the microscope and allowed to charge under the beam. The illumination in the microscope was then set to perform low resolution holography.[5] The objective lens was turned off to provide a larger field of view and the sample focused using the intermediate lens.

Figure 1 (a &b) shows a hologram of the phase plate and the reconstructed phase image. The equipotential lines in the reconstructed phase image (Fig. 1b) show a cylindrical symmetry on one side of the fiber and a radial symmetry on the other. The parallel phase lines are due to a uniform charge on the fiber while the radial phase lines are due to charge concentration at a point. Assuming the phase shift is produced as a result of the potential, an estimate can be made of the charge on the fiber. This was found to be approximately 270 electrons/μm along the length of the fiber and an additional 70 electrons in the region of the charge concentration. Further, the cylindrical phase lines are not visible on one side of the fiber because of the influence of the field on the reference wave. Figure 2 shows a four times phase amplified image and the influence of the radial field on the cylindrical component can be clearly seen. The charging behavior of the phase plate was modeled and a simulation of the phase lines is shown in Figure 3.

As shown in the reconstructed phase image, the field around the fiber is the sum of a cylindrical field due to a uniform charge and a spherical field due to a point charge. For the fiber to act as an effective phase shifting device, the charge on it must be concentrated at a point so as to set up a radially symmetric field. The cylindrical component of the field will distort the image obtained by using this device as a phase plate and this component can be minimized by varying the thickness of the gold on the fiber. Electron holography allows us to image the net field around the fiber and hence predict the behavior of the phase plate.[6]

References

1. Zernicke, F., Physica, 9 (1942) 686
2. Blackson, J., Phd Dissertation, University of Tennessee (1995)
3. Unwin, P. N. T., Phil. Trans. Roy. Soc. Lond., B261 (1971) 95
4. Krakow, W., and Siegel, B., Optik, 42 (1975) 245
5. Frost, B. G., Voelkl, E., and Allard, L.F., Submitted to Ultramicroscopy
6. This work was performed at the Oak Ridge National Laboratory, managed for the DOE by Lockheed Martin Energy Systems, Inc. under contract DE-AC05-84OR21400.
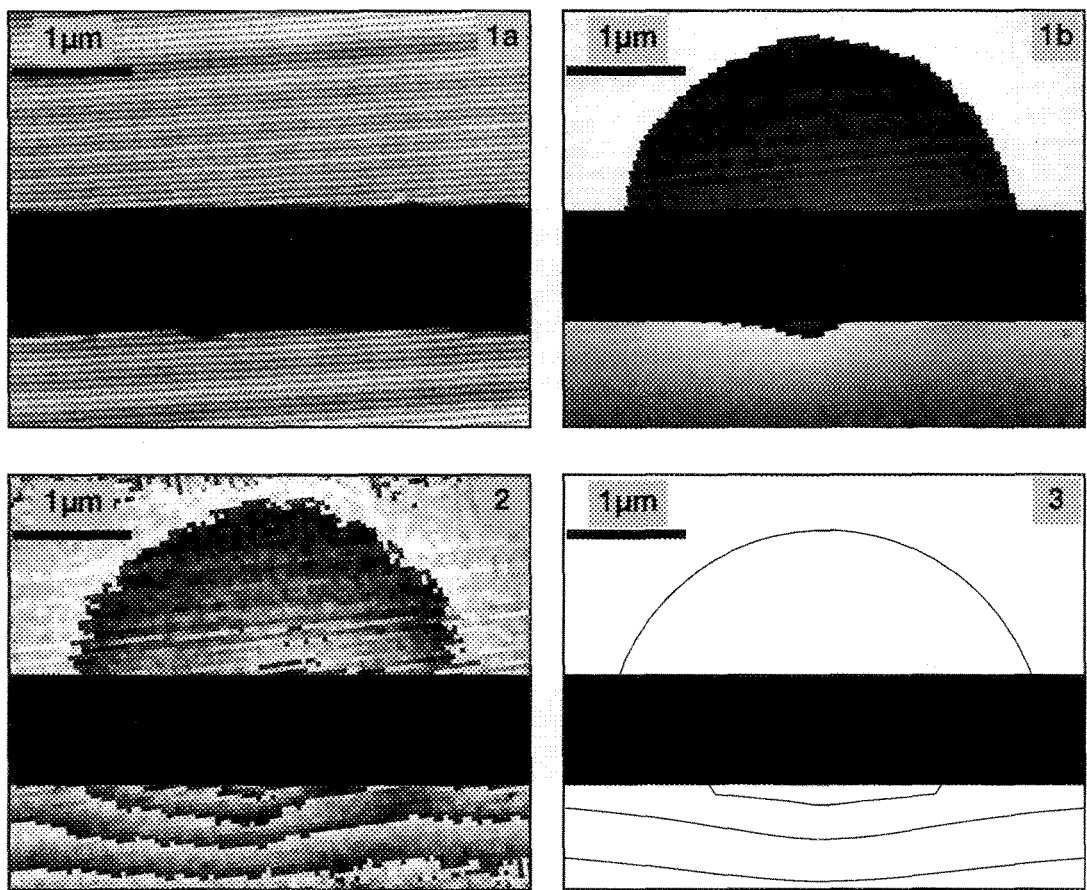
FIG. 1a Hologram of an electrostatic phase plate.
FIG. 1b Reconstructed phase image of the hologram.
FIG. 2   Four times phase amplified image.
FIG. 3   Simulation of the phase lines around an electrostatic phase plate.

ZAF, PAP, φ(ρz), *a*-FACTOR...: A COMPARISON OF THE RELATIVE ACCURACIES OF THE ALPHABET SOUP OF CORRECTION FACTORS FOR "NON-OPTIMIZED" SAMPLES

John T. Armstrong

Division of Geological and Planetary Sciences, California Institute of Technology, Pasadena, CA 91125; *currently at:* Surface and Microanalysis Science Div., National Institute of Standards and Technology, Gaithersburg, MD 20899

The ultimate practical test of the utility of a correction procedure for quantitative x-ray microanalysis is how well the analyses of standards of interest conform to their known compositions. Many papers have been published testing various correction algorithms by processing data from sets of quantitative analyses through the corrections and then comparing the resulting error histograms[1] (*e.g.*, Fig. 1). The best correction procedure is usually considered to be the method that results in error histograms with the minimum mean relative error and the smallest standard deviation for the distribution of relative errors. Such evaluations can be misleading for a number of reasons: (1) the correction procedure may have been "adjusted" by adding empirical factors to produce superior results for a particular type of specimen. If the test data either include these data or include samples of similar composition to those employed for the refinement, the results may appear artificially good and may not work nearly as well for other types of specimens. (2) The analytical data used for testing may itself be flawed, either because the samples were not actually the compositions they were thought to be (or the sample surface analyzed was not the same composition as that published for the bulk material); or because the surface or the sample was contaminated, rough or charging; or because the analytical conditions were not well controlled. (*Many of the published k-factors used in evaluating correction procedures [e.g., ref. 1] were obtained in the early days of microbeam analysis, using instruments having poor control over high voltage and beam current stability with low spectrometer take-off angles.*) (3) The analytical data may contain specimens analyzed under unusual conditions (*e.g.*, very high or very low accelerating potentials) that may have very large corrections dominating the data set that may never be encountered in normal analysis.

A better procedure for evaluating the relative effectiveness of correction procedures for a particular type or types of specimens is to evaluate the functional behavior of the corrections over the range of compositions of interest. One way of doing this is to plot the magnitude of the correction factors as a function of sample composition for a range of binary (or more complicated) compositions (*e.g.*, Fig. 2), such as plotting C/K vs. C (where C is the relative concentration and K is the calculated ratio of intensity for the element in the sample compared to that in a pure element, oxide or end member composition) or, similarly, plotting the *a*-factor ($a = [(C/K) - C] / [1 - C]$) vs. C.[2] Previous work has shown that in all cases, such plots can be well expressed by 0, 1st, or 2nd order polynomials.[2] By analyzing one or more intermediate compounds in the system, the shape and position of such curves can be readily determined. Systems with similar absorption, fluorescence and atomic number corrections should exhibit similar C/K vs. C behavior. The quality of analytical data used for evaluating correction procedures can itself be tested for internal consistency by being plotted in this fashion.

References
1. K. F. J. Heinrich and D. E. Newbury, Eds., *Electron Probe Quantitation*, Plenum Press, (1991).
2. J. T. Armstrong, Proc. 50th Ann. MSA Meeting (1992) 1656 and 1744.
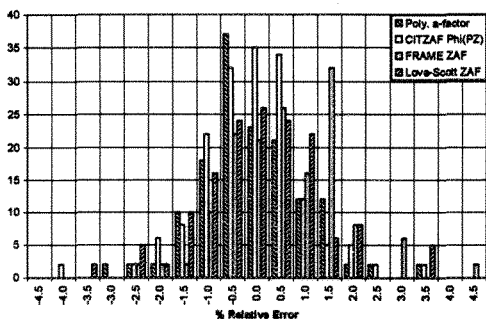
Error Histograms for Shaw Silicate Analyses

Poly. a-factor
CITZAF Phi(PZ)
FRAME ZAF
Love-Scott ZAF

% Relative Error

1b

Error Histograms for Shaw Silicate Analyses

PAP-XPP
PROZA Phi(PZ)
Packwood Phi(PZ)
Duncumb-Reed ZAF

% Relative Error

2a

Si K-Ir L (20 keV, 40 deg.)

C/k – Si K-alpha

C (Si) – el. wt. %

CITZAF
Frame
ZAF
PAP
XPP
Pack/Br
Proza
Cor2
Riveros
'LoveScott
Sewell

2b

a-factors for Si Ka in Si-Ir

a-factor

C (Si)

CITZAF
Frame
ZAF
PAP
XPP
Pack/Br
Proza
Cor2
Riveros
LoveScott
Sewell

2c

SiK - Ir L (20 keV, 40 deg.)

C/k – Ir L-alpha

C (Ir) – el. wt. %

CITZAF
Frame
ZAF
PAP
XPP
Pack/Br
Proza
Cor2
Riveros
LoveScott
Sewell

2d

a-factors for Ir La in Si-Ir

a-factor

C (Ir)

CITZAF
Frame
ZAF
PAP
XPP
Pack/Br
Proza
Cor2
Riveros
LoveScott
Sewell
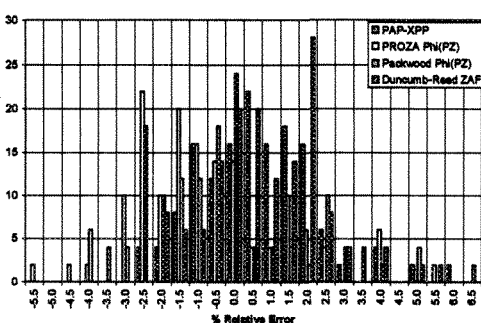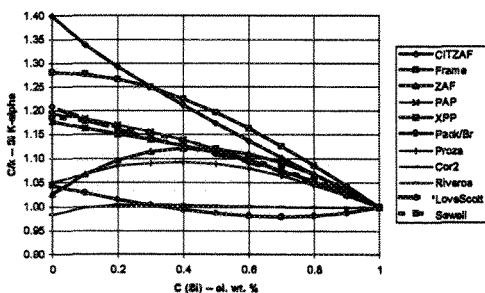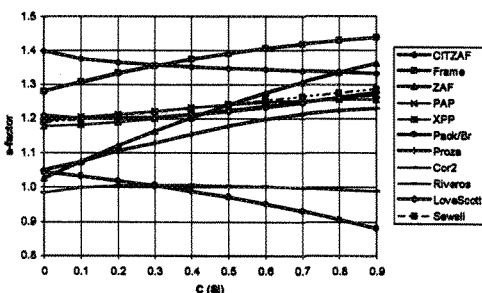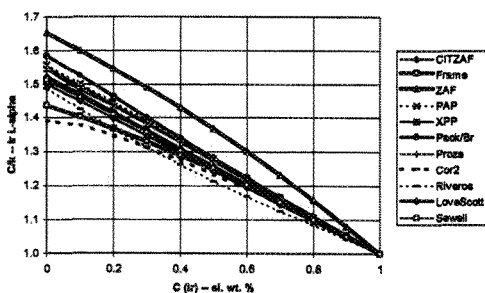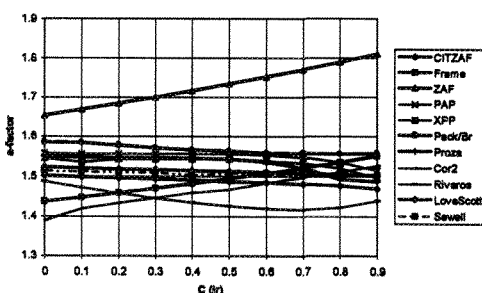
FIG. 1 Histograms of percentage relative errors obtained from measurement of a suite of oxide and silicate mineral standards containing Mg, Al, Si and/or Ca. The various histograms are obtained by processing the same data through different correction algorithms. Analyses were performed at 15 keV using MgO, Al_2O_3, SiO_2 and $CaSiO_3$ as standards.

FIG. 2 Plots of calculated correction factors (C/k: a,c and *a*-factors: b,d) vs. composition (C in element wt. %) for Si Kα and Ir Lα in Si-Ir alloys (a,c) using different algorithms.

"STANDARDLESS" QUANTITATIVE ELECTRON PROBE X-RAY MICROANALYSIS WITH ENERGY-DISPERSIVE SPECTROMETRY: WHAT IS THE DISTRIBUTION OF ERRORS?

Dale E. Newbury

National Institute of Standards and Technology, Gaithersburg, MD 20899

Conferences on quantitative electron probe X-ray microanalysis are typically highlighted by presentations which seek to advance the state of analytical science in this field through improvements in knowledge of the fundamentals of electron/X-ray-specimen interactions, inter-element (matrix) corrections, corrections for irregular specimen geometry, etc. However, in light of recent developments in computer-assisted, energy dispersive X-ray spectrometry analytical systems, we need to re-evaluate what is actually taking place in the everyday application of this analytical technique. The central paradigm in quantitative electron probe X-ray microanalysis, as established in the earliest work of Castaing and built upon by generations of contributors, is the measurement of the ratio of the intensity of an element in the unknown to the intensity for the same element in a standard under constant conditions of beam energy, known dose, and spectrometer performance.[1] The set of such "k-values" determined for all constituents in the unknown is then converted into a set of concentrations through the use of matrix correction factors calculated through one of several schemes, e.g., "ZAF", $\phi(\rho z)$, etc. The great power of electron-excited X-ray microanalysis derives from the simplicity of the standards required. Pure elements and simple stoichiometric compounds will suffice, although homogeneous multi-element mixtures can be readily employed when available. Extensive testing and refinement of this standards-based method has established a reliable estimate of the error distribution which arises in its application to a wide variety of problems. An example of an error distribution for ZAF analysis with pure element standards is shown in Figure 1, derived from data reported in a study made more than 20 years ago.[2] Typically, most errors are less than ±5% relative, with ±2% relative achievable in a large fraction of analyses. Recent research in quantitative analysis has led to further narrowing of this error distribution.[3] The k-value approach was developed because the efficiency of wavelength dispersive spectrometers used in early work varied strongly with energy and other variables, making it difficult to predict. The intensity ratio eliminated this uncertainty, as well as several physical factors. Energy dispersive spectrometry (EDS) permitted continual observation of the complete X-ray spectrum with an efficiency which was both predictable and reasonably stable over time. Since all elements could be measured simultaneously, it was perhaps inevitable that in the quest for operational productivity and simplicity, a quantitative analysis method based on comparing one element to another, rather than itself, should be developed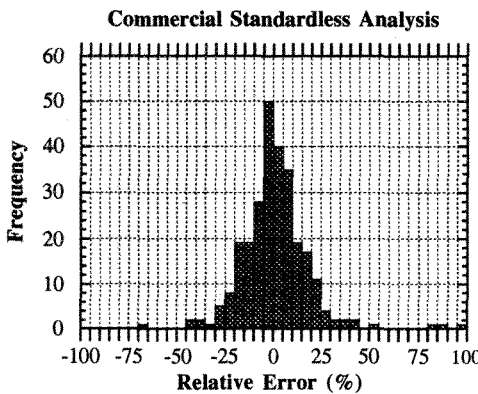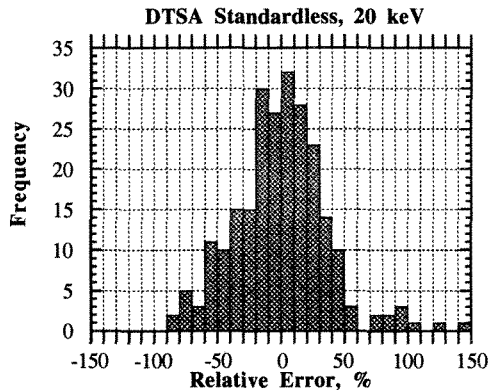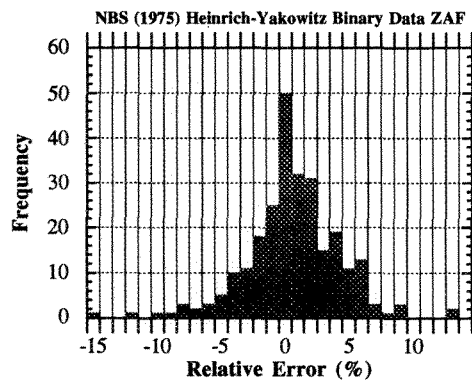. Such "standardless" methods fall into two general classes. The most ambitious approach, true standardless analysis, is based on "first principles" calculations of all physical factors involved in X-ray generation, propagation, and EDS detection with no reference to measured standards. Error distributions that result from standardless analysis procedures are likely to be much broader than those for the standards-based ZAF approach. An example of an error distribution produced by a true standardless procedure embedded in the NIST-NIH Desktop Spectrum Analyzer program is shown in Figure 2.[4,5] This error distribution is so broad that it is not possible to reliably deduce stoichiometric compound formulas from such "quantitative" results. An intermediate case, which probably forms the basis for most commercial "black box" implementations of "standardless" analysis, is the "fitted standards" approach. Actual experimental measurements of pure element standard intensities are recorded for a specific beam energy and detector configuration. These intensities are mathematically fitted for each shell. When standard intensities are required for elements not directly measured, at a

different beam energy, or for a different detector configuration, the first principles equations for X-ray generation, propagation, and detection are utilized to make appropriate corrections to the fitted intensity values. Because of the closer relationship to actual measurements, the fitted standards approach should provide better accuracy. An example of an error distribution obtained with a commercial "black box" standardless analysis scheme is shown in Figure 3. While "fitted standards" yields a narrower error distribution than true standardless, both error distributions are much broader than that obtained with conventional standards-based ZAF analysis. The widespread use of "quantitative" results obtained from procedures with such broad error distributions is diminishing the reputation of X-ray microanalysis.[5]

References
1. Goldstein, J., et al., Scanning Electron Microscopy and X-ray Microanalysis, Plenum: New York, (1992) 395.
2. Heinrich, K. and Yakowitz, H., Anal. Chem. **1975**, *47*, 2408.
3. Heinrich, K. and Newbury, D., eds., Electron Probe Quantitation (Plenum, New York, 1991).
4. Fiori, C. E. and Swyt, C.R., "NIST-NIH Desktop Spectrum Analyzer", Standard Reference Data Program, National Institute of Standards and Technology, Gaithersburg, Md, 20899.
5. Newbury, D. E., Swyt, C. R., and Myklebust, R. L., Analyt. Chem, 67 (1995) 1866.

NBS (1975) Heinrich-Yakowitz Binary Data ZAF

DTSA Standardless, 20 keV

Commercial Standardless Analysis

Relative errors observed with various procedures:
Figure 1. Conventional approach, k-values and ZAF.[2]
Figure 2. True "first principles" standardless analysis.[4,5]
Figure 3. Commercial "fitted standards" approach.

FUNDAMENTAL PARAMETERS FOR MICROANALYSIS

David C Joy
EM Facility University of Tennessee, Knoxville, TN 37996-0810 and
Oak Ridge National Laboratory, Oak Ridge, TN 37831

In order to perform quantitative X-ray microanalysis many parameters, representing the various stages of Xray generation and transport through the specimen at the chosen experimental conditions, must be known for all of the elements that might be encountered. Although ideally quantification is done by reference to standards so that only the functional variation of these parameters is required, in current practice it is increasingly necessary to work in situations where standardization is impossible and consequently where absolute magnitudes must be known. The quality and quantity of data that is now available varies widely.

Ionization cross sections
Although the amount of experimental data is limited, particularly in the energy range between 1 and 20keV, a critical assessment has concluded that for K-shell excitations both the magnitude of the cross-section σ and its variation with energy are adequately well known for overvoltages greater than about 2.[1,2] For L- and M-shell excitations, however, and in all cases when the operational overvoltage is less than 2, the situation is much less satisfactory. In the energy range below 100keV there are only published L-shell ionization cross-sections for six elements (compared with data for 18 K-shells), and none at all for M-shells. With the increasing interest in performing X-ray microanalysis at low beam energies, and consequently at low over-voltages, there is a demonstrated need for systematic work in this topic. While the measurement of cross-sections at high beam energies is relatively straightforward, since the use of electron transparent foils simplifies the calculations particularly when bremsstrahlung production is employed as an internal standard, at low beam energies detailed simulations must be performed in order to extract the desired data from experimental measurements. An additional problem is that

Fluorescent yields
are the least well known parameters amongst those that are of interest. Since the X-ray yield is proportional to the product of the fluorescent yield ω and the cross-section σ the uncertainty in the fluorescent yields directly impacts the accuracy of absolute cross-section determinations. Although the variation of fluorescent yields for K-shell excitations is fairly well established for atomic numbers greater than 10, for lower atomic numbers, and for the L- and M-shell excitations there is little theoretical or published experimental data. An additional complexity, that has so far not be taken seriously into account, is the likelihood that the magnitude of the fluorescent yield is itself chemically sensitive. Estimates of the variation suggest that a 20% change between the value for an element and the corresponding value for that element in a compound are possible.[3] Since the measurement of the fluorescent yield is a complicated matter it may be preferable to consider only the product of $\sigma\omega$ rather than to attempt to separate the two.

Electron stopping power
The electron stopping power determines the depth and lateral distribution of X-ray production within the specimen, and hence affects the magnitude of the generation, absorption and the backscatter cor-

rection terms. Experimental stopping power data for a variety of elements and compounds are now available over the energy range from 1eV to 10keV.[1] A comparison of the measured data for elements with stopping power values computed from the Bethe expression and employing one of the accepted expressions for the mean ionization potential J shows that the simple analytic model is adequately accurate down to energies of the order of 3J, but for lower energies significantly underestimates the stopping power. The application of the Bethe expression to compounds, using values of J derived from the mean average atomic number of the material, results in stopping power values which can be substantially in error at all energies compared to measured values. However, the experimental data shows that stopping powers are additive at all except perhaps the lowest energies (<100eV) and hence if a comprehensive collection of elemental data can be assembled then the necessary values for any arbitrary compound can be generated as needed.

Backscattered and Secondary Electron yields

Although neither the backscattered electron yield η nor the secondary electron yield δ appear directly in the computations for microanalysis, these parameters are an important metric of the electron-solid interaction and a sensitive test of the accuracy of Monte Carlo and other simulations of the interaction. A survey of published data contains values of η and δ for about half of the elements in the periodic table over at least some of the energy range from 10eV to 20keV.[1] The spread in experimental values is generally higher than desirable, and even for the most exhaustively studied materials such as aluminum or copper it is still not possible to state a value of either η and δ with a precision of better than ±5%. It is thus still not possible to answer even such longstanding questions as to whether the variation of η with atomic number is smoothly monotonic or if there are discontinuities as shells are filled.[4] There are apparently no more than a couple of measurements of η and δ for compounds, and consequently there is no way to test any of the various predictions of these parameters for complex materials as compared to their elemental constituents.

In summary, a considerable body of experimental data on ionization cross-sections, fluorescent yields, stopping powers, and electron yields is now in place, but the coverage of the data with respect to atomic number and energy is usually sparse and for many quite common elements there is apparently still no measured data at all. For compounds, again even those of technological or industrial importance, the situation is much worse as there is insufficient data even to make it possible to evaluate the accuracy of analytic approximations or fits to the desired parameters. A systematic program to measure the parameters discussed here is urgently required, particularly to obtain values at the low energies and low over-voltages which characterize much of the current applications of electron-beam microanalysis

1. Joy DC, SCANNING **17**, (1995), 270. A complete copy of this compilation is available on request from the author. SE and BSE data may be accessed at http://www.nsctoronto.com/nissei-sangyo
2. C J Powell, NBS Special Publication 460, (1976), 97
3. C A Quarles and L Estep, Phys.Rev.**A34**, (1986), 2488
4. H Bishop, Ph.D Thesis, University of Cambridge, 1963
5. Oak Ridge National Laboratory is operated by Lockheed Martin Energy Research Corp. for the U.S. Department of Energy under contract number DE-AC05-96OR22464

THE LIMITATIONS OF QUANTITATIVE EDS ANALYSIS AT LOW VOLTAGE

C. E. Nockolds

E.M. Unit, University of Sydney, NSW 2006, Australia

There are several reasons for carrying out x-ray microanalysis at low beam energies. In conventional electron probe microanalysis with wavelength dispersive spectrometers (WDS) there has been a considerable effort in recent years to improve the accuracy of quantitative analysis of the "light" elements B, C, N and O.[1] The shapes of the low energy K x-rays and the L x-rays of the first transition series metals are also being studied with the aim of determining the chemical environments of the atoms in a sample. In most materials these soft x-rays suffer from very high absorption, and reducing the depth of the interaction volume by lowering the beam voltage to 5kV or below leads to a much reduced absorption correction. In scanning electron microscopy the introduction of thin window energy dispersive spectrometers (EDS) has made it possible to look at low energy x-rays and here the main interest in working at low voltages is in the improvement of the resolution of analysis.[2,3]

In this paper the limitations of SEM/EDS low voltage analysis will be examined, and possible solutions to some of the problems explored. It will be assumed that the aims are to achieve quantitative analysis at the best possible spatial resolution. Various types of samples fall into this area; for example, sub-micron grains in a polished specimen, small particles on a surface, or a diffusion profile across a boundary in a bulk specimen. In many cases these problems are either difficult or not possible by other methods (such as thin film analysis in a scanning transmission E.M.) and it may well be worth putting in a considerable effort to obtain a reasonable quantitative analysis.

At low voltages a thin coating on the surface can have a significant effect on quantitative and qualitative analysis. The coating could be a conductive layer of carbon or metal applied to the surface of the sample by the analyst, a thin oxide layer, or some unknown contamination on the specimen. These samples can be described as thin films on substrates, and technically they should be analysed as such. If the parameters of the coating are known (composition, mass thickness) then the effects of the coating can be calculated using "thin film on substrate" (TFOS) software and the k-ratios for the elements in the substrate can then be corrected before applying the bulk matrix matrix corrections.[4,5] However, when the details of the coating are not known, the sample needs to be treated as a true TFOS sample. If the composition of the coating is not known, or if there is a common element between the coating layer and the substrate it will be necessary to collect a full set of k-ratios at more than one beam energy. The most difficult surface effect to deal with is the carbon contamination generated by the electron beam interacting with hydrocarbon molecules at the surface of the sample. The surface contamination changes with time, and the rate of contamination depends on the cleanliness of both the specimen and the chamber vacuum. This problem can not be dealt with effectively by the TFOS approach and the only thing that can be done is to minimise the contamination rate in the microscope. Beam induced carbon contamination severely limits the possibility of analysing low concentrations of carbon in a sample and it can also introduce systematic errors for the analysis of other elements.

At 5 kV many of the x-ray lines that are routinely used for analysis are no longer generated by the beam. For atomic numbers above 20 the K-lines are not excited effectively and the only lines that are available are the L-lines. It has been pointed out by Armstrong that for the elements Ti through Ga these L-lines may be unsuitable for EDS quantitative analysis using currently available correction procedures because the $L\beta/L\alpha$ ratio is a function of the composition of the sample.[6] The elements Ge through to about Sb provide L-lines that can be used for quantitative analysis, albeit with a steadily diminishing overvoltage ratio and a consequent loss of intensity. For atomic numbers above 51 we would hope that M-lines were becoming available in the low energy range, however, for atomic numbers 52(Te) to 57(La) the $M\alpha$ and $M\beta$ lines are not generated because the N_{VI} and N_{VII} electron shells are empty,

and these shells are not fully populated until atomic number 70(Yb). There is also an indication from line and edge energies that for elements up to Pt there may be a problem with the $M\beta/M\alpha$ ratio (as for the L-lines).

One way of resolving these problems with the low energy L and M-lines is to go back to using higher energy lines. In order to maintain the spatial resolution of analysis it will then be necessary to work at low overvoltages. As an example we can consider the analysis of Ti in a sample; at 5kV the K lines will not be excited, however, if we go to 8kV, with an overvoltage of approximately 1.6, and assume that the sample is pure Ti, then the depth for the generation of TiK x-rays is about $0.35\mu m$.[5] The major disadvantages of this approach are: (1) k-ratios will have to be collected for at least two voltages (2) the matrix correction software must be able to handle k-ratios with different voltages. Another approach is to collect data at several voltages and use Monte Carlo calculations to model the interaction. This is similar to the TFOS method, with the extra complication of a more geometrically complex sample e.g. small spherical particles embedded in a matrix, or regularly shaped crystals on a smooth substrate. The development of a modelling program of this type would allow the low voltage analyst to overcome the limitation of having to contain the x-ray generation within the region of interest.

1. G.F. Bastin and H.J.M. Heijligers, *Electron Probe Quantitation*, eds K.F.J. Heinrich and D.E. Newbury, Plenum Press, New York, (1991)145
2. E.D. Boyes, *Proc. Int . Congr. on E.M.*, (1994)55
3. C.E. Nockolds, *Microbeam Analysis*, (1994)185
4. J.L. Pouchoir and F. Pichoir, *Electron Probe Quantitation*, eds K.F.J. Heinrich and D.E. Newbury, Plenum Press, New York, (1991)
5. R.E. Waldo, *Microbeam Analysis*, (1991)31
6. J.T. Armstrong, *Microbeam Analysis*, (1995)189

LOW-VOLTAGE EDS OF MAGNESIUM FERRITE DENDRITES IN A FEG-SEM

Matthew T. Johnson,* Ian M. Anderson,[†] Jim Bentley,[†] and C. Barry Carter*

*Dept. of Chemical Engineering & Materials Science, University of Minnesota, Minneapolis, MN 55455
†Metals & Ceramics Division, Oak Ridge National Laboratory, PO Box 2008, Oak Ridge TN 37831-6376

Energy-dispersive X-ray spectrometry (EDS) performed at low (≤ 5 kV) accelerating voltages in the SEM has the potential for providing quantitative microanalytical information with a spatial resolution of ~100 nm.[1,2] In the present work, EDS analyses were performed on magnesium ferrite spinel [$(Mg_xFe_{1-x})Fe_2O_4$] dendrites embedded in a MgO matrix, as shown in Fig. 1. The spatial resolution of X-ray microanalysis at conventional accelerating voltages is insufficient for the quantitative analysis of these dendrites, which have widths of the order of a few hundred nanometers, without deconvolution of contributions from the MgO matrix. However, Monte Carlo simulations indicate that the interaction volume for $MgFe_2O_4$ is ~150 nm at 3 kV accelerating voltage and therefore sufficient to analyze the dendrites without matrix contributions.

Single-crystal {001}-oriented MgO was reacted with hematite (Fe_2O_3) powder for 6 h at 1450°C in air and furnace cooled. The specimen was then cleaved to expose a clean cross-section suitable for microanalysis. Single-crystal MgO and polycrystalline B2-ordered $Fe_{55}Al_{45}$ were ground and polished for use as microanalysis standards. Specimen and standards were mounted onto an aluminum SEM stub with carbon dag and sputter-coated with ~1 nm of platinum. EDS spectra were acquired with a Philips XL30-FEG operated at 3 kV and an Oxford Super-ATW detector with XP3 pulse processor, and analyzed using DTSA with the 4pi interface. The spectra were acquired with an untilted specimen and a take-off angle of 35°. Three spectra from different regions were acquired for each of the dendrites and standards and the extracted characteristic X-ray intensities were averaged as a measure of the statistical precision.

An EDS spectrum characteristic of the spinel-structured dendrites is shown in Fig. 2. The continuum background of the spectrum extends to the 3 kV accelerating voltage, indicating no significant retardation of the probing electrons due to specimen charging. Such retardation was evident for uncoated specimens. The characteristic peaks of the O-K (525 eV) and Fe-L (705 eV) X rays overlap considerably, whereas the Mg-K (1254 eV) X-ray peak stands alone. Minor X-ray peaks are also evident for the Pt (2047 eV) coating and for a carbon (277 eV) contamination layer and were present in all spectra acquired from both specimen and standards. The only other extraneous feature was a low energy shoulder on the Fe L peak of the $Fe_{55}Al_{45}$ standard, indicating the presence of a thin oxide scale. These minor peaks illustrate the surface sensitivity of low voltage microanalyses. Within DTSA, multiple linear least squares (MLLSQ) fitting was found to be more robust for extraction of the characteristic intensities than simplex fitting, for which the small carbon peak effected large variations in the background fit from one spectrum to the next. Gaussian-shaped MLLSQ references were acquired from simplex fitting of the MgO and $Fe_{55}Al_{45}$ standards. The oxygen contribution to the Fe-L reference was removed with the DTSA calculator using the O-K reference. Microanalysis k-ratios were calculated from the measured intensities and correction factors were calculated with Flextran ZAF correction software.

The average intensities and ZAF correction factors from specimen and standards, and the calculated k-ratios and concentrations for the spinel dendrite are shown in Table 1, along with the concentrations for stoichiometric $MgFe_2O_4$ for comparison. The excellent precision (~1%) of the measured characteristic intensities indicates a low statistical scatter in the fitted background with the MLLSQ procedure. The sum of the concentrations for the spinel dendrite is 0.981 ± 0.008. That this sum is within 2% of unity is heartening, but the standard error indicates that the statistical scatter in the measured intensities is not the limiting factor in the analysis. Possible sources of systematic error include variations in beam current, absorbing effect of the oxide scale on the $Fe_{55}Al_{45}$ standard (which was ignored), and differences in the Fe Lα/Lβ intensity ratios between specimen and standard due to self absorption.[3] Analyses are planned using a stoichiometric $MgFe_2O_4$ microanalysis standard in order to minimize the corrections and sources of systematic error.[4]

478

References
1. E. Boyes, *Proc. 13th ICEM: Electron Microscopy 1994* 1(1994)51.
2. C.E. Nockolds, *Microbeam Analysis* 3(1994)185.
3. J.T. Armstrong, *Microbeam Analysis* 4(1995)S189.
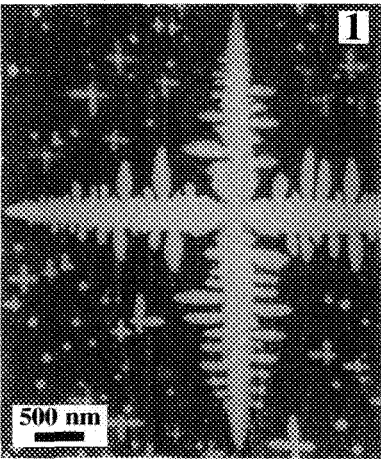
TABLE 1 - Results of EDS analysis.

Specimen		O-K	Fe-L	Mg-K
MgO	<I>	111001 ± 448		93205 ± 434
	ZAF	1.010		1.054
$Fe_{55}Al_{45}$	<I>		89600 ± 505	
	ZAF		1.070	
dendrite	<I>	92848 ± 481	61281 ± 625	19559 ± 273
	ZAF	0.887	1.246	0.983
	k-ratio	0.332 ± 0.002	0.490 ± 0.006	0.127 ± 0.002
	weight %	29.2 ± 0.2	57.1 ± 0.7	11.8 ± 0.2
$MgFe_2O_4$	weight %	32.0	55.8	12.2
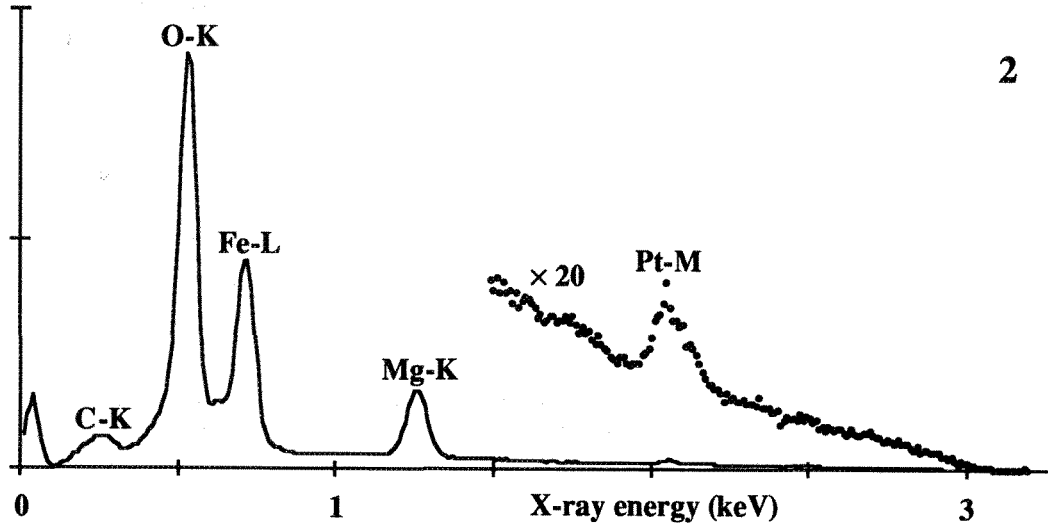
FIG 1 - SEM backscattered electron image of spinel-structured dendrites in MgO matrix.
FIG 2 - EDS spectrum acquired from spinel-structured dendrites. Full scale is 50000 counts per channel.

A SIMULATION PROGRAM FOR QUANTITATIVE PROCEDURE IN EPMA

Claude Merlet

ISTEEM, FU 16, CNRS, Université de Montpellier II, Sciences et Techniques du Languedoc, Pl. E. Bataillon, 34095 Montpellier Cedex 5, France.

In the last ten years the development of new X-ray depth distribution models in electron probe microanalysis (EPMA), has allowed to obtain accurate quantitative programs for stratified and massive samples. With these new quantitative methods, for the energy lines greater than 1keV and for massive samples, the results of the quantification are independent of the accelerating voltage (for an excited line). Nevertheless, for light elements, and for soft X-ray emission in complexe compounds, the choice of these optimum experimental conditions is not trivial. Moreover, the physical parameters and boundary conditions of the measurements are not well known.

In an attempt to choose the optimum accelerating voltage, and to solve some difficulties in the quantification of low energy lines, a software (freeware) has been developed on PC and under the WINDOWS operating system. The calculation procedure is based upon the double partial gaussian profile[1] $\phi(\rho z)$ (recently developed for massive compounds). This description, flexible, precise and mathematically simple allows to compute rapidly the X-ray intensities. The program, which has been designed mainly for WDS electron probe, uses graphic simulations, and includes two sections:
- The first simulations group concerns the calculation and the plot, for the analysed lines in a compound, versus accelerating voltages of: - the normalised intensities (Fig. 1), - the quantification factors [Z], [A] and [F], - the intensity ratio with respect to a standard, - and the ultimate ionisation depths before and after absorption (Fig. 2). For the measure of microparticles, characteristic lines strongly absorbed, or stratified samples, the knowledge of the measured depth is an important data.

- The second point is the calculation and the plot of the quantification factors within a small energy domain at the location of the analysed characteristic X-ray emission peaks (Fig.3.). This point is fundamental in the soft X-ray measurements[2], for the estimate of the continuum[3, 4] (Fig. 4), the interference subtraction[5, 6] as well as the peak area calculation[5, 6].

These simulations are well illustrate on figures 1-4 with example of the vanadium oxide. The difficulties of oxygen quantification in vanadium compounds are due to: - a) the presence of the interference line Lα of the vanadium, - b) the strong mass absorption coefficient of the oxygen in the vanadium, - c) the presence of the absorption edge, which gives rise discontinuity in the background. The simulation program puts well in obviousness these different phenomena and allows the user to choose a correct accelerating voltage and to calculate in a realistic way the area of the peak of oxygen after subtraction of the background and of the vanadium Lα line.

References

1. C. Merlet, Mikrochim. Acta, 114/115 (1994), 363.
2. G. Remond et al., Proc. 4Th EMAS (1995), 117.
3. C. Merlet and Bodinier, Chemical Geology, 83 (1990), 55.
4. J. A. Small et al., J. Appl. Phys., 61 (1987), 459
5. M. Fialin et al., Scanning Microscopy Supplement 7 (1993), 153.
6. G.F. Bastin and H.J.M. Heijligers, Scanning, 13 (1991), 325
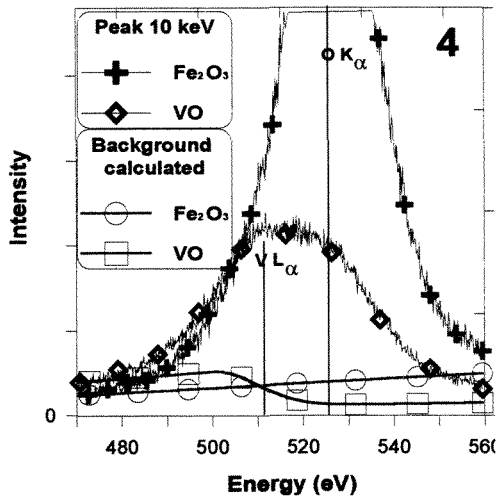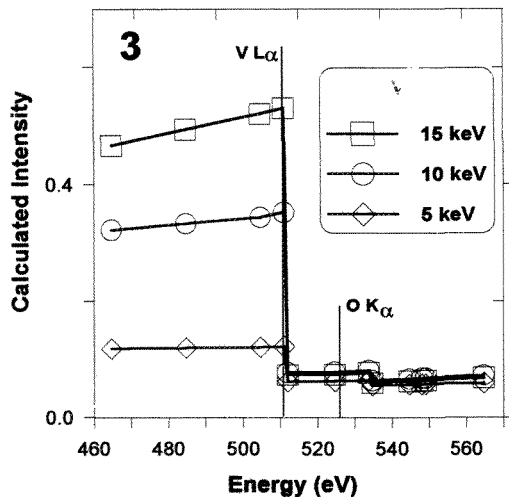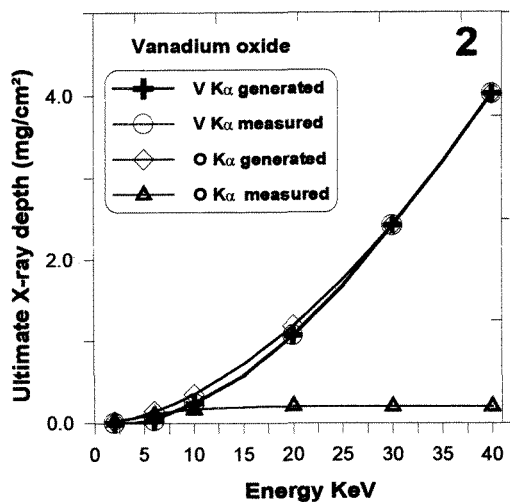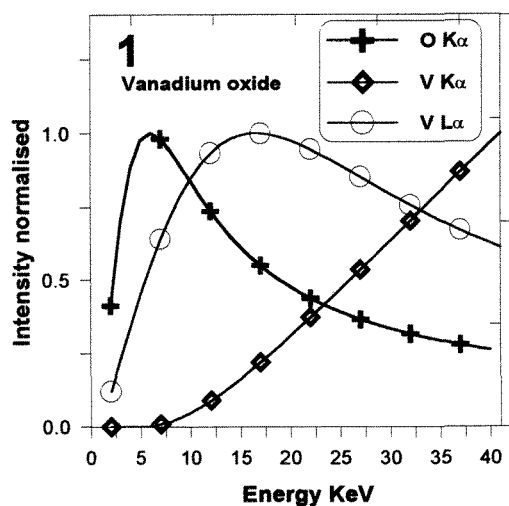
FIG. 1. Normalised intensities versus accelerating voltage for O Kα, V Lα and V Kα in vanadium oxide
FIG. 2. Ultimate X-ray depth, with and without absorption for O Kα, V Lα and V Kα in vanadium oxide
FIG. 3. Calculated intensity in the vicinity of the energy domain of O Kα in vanadium oxide
FIG. 4. Background computation in the range 470-560 eV in vanadium oxide.

LIGHT-ELEMENT EPMA—CORRELATIONS, CONVOLUTIONS, AND TRUE CONCENTRATIONS

Alfred Kracher[1], Joel F. Flumerfelt[2], and Iver E. Anderson[2]

[1]Geological Sciences and [2]Ames Laboratory, DOE, Iowa State University, Ames, IA 50011

Analyses of small concentrations of light elements by electron microprobe are complicated by a number of factors, including low signal strength and line overlap. Obtaining reliable data may require techniques that are uncommon in wavelength-dispersive (WDS) x-ray analysis. A case in point is the investigation of alloys that contain small amounts of nitrogen. Nitridation of Al metal and Al alloys with N-bearing gaseous species is being studied as a way to form *in situ* nitride precipitates, which is of interest for altering the mechanical properties of these materials. It was found, for example, that one specific alloy with 1.7 wt% Ti and 7.7 wt% Y retains much larger N concentrations on nitridation than pure Al, using the same processing conditions for both alloys. Nitrogen may be present in $TiAl_3$ precipitates, YAl_3 precipitates, or the matrix. Identifying the N-bearing compound by EPMA has proven difficult, however, because of the interference of Ti $L\ell$ on N Ka, combined with the low peak/background ratio of the N Ka peak.

Line overlap is usually not a major problem in x-ray analysis. Although we have found that some mineral systems (e.g., the ore minerals in gold telluride deposits) may show interference in as many as 8 element pairs in the same analysis, the line overlap can be easily accounted for by a small linear correction. Such a correction is built into the PROBE software used in this study.

In light element analysis the situation may be less favorable. A linear overlap correction is not satisfactory for the interference of Ti $L\ell$ on N $K\alpha$. Moreover, the presence of other Ti L-series lines makes it impossible to determine the background at N $K\alpha$ by linear background correction, since measurements of the x-ray continuum cannot be performed sufficiently close to the peak. Standard methods for off-peak background determination result in significant *negative* net counts for N on Ti-free samples, and a non-linear relationship between apparent N counts (due to Ti $L\ell$) and Ti $K\alpha$ counts (Fig.1). Routine data reduction thus fails to provide accurate N concentrations. However, the computing power of recent spreadsheet programs makes it possible to perform more complex calculations on individual analyses with reasonable speed.

1. Background subtraction. The true shape of the x-ray background in WDS results from a combination of the x-ray continuum, given by the Kramers equation, and the geometric relation-ship within the WDS spectrometer, which changes continuously with wavelength. Although the complex theoretical equation could in principle be fit to existing background data, a simple polynomial fit is usually adequate. In principle, the background over the entire range of a WDS spectrometer, which covers a factor of about 3.5 in wavelength, can be subtracted in this way.

2. Peak deconvolution. In energy-dispersive (EDS) analysis, where peak overlaps are a more serious problem, spectra are routinely subjected to "peak stripping" algorithms. In WDS it is less common to deal with spectra covering over large wavelength ranges. However, because of the high resolution of WDS spectrometers, it is possible to detect small concentrations of elements even in the presence of other elements whose lines overlap. We have found that simple peak stripping routines following background subtraction are useful in WDS analysis for a range of problems. In the case of N analysis, although too time-consuming for point-by-point application, it can be used to assess the accuracy of the interference correction.

3. Non-linear interference calculation. In the case of Ti Lℓ and N Kα it is necessary to determine the apparent N Kα counts on materials of varying Ti content, and fit a polynomial to the data. An interference correction has to be applied each analysis on the unknown sample.

Although the more complicated data reduction methods can potentially introduce additional errors in the determination of light elements, preliminary data indicate that the detectability of light elements is often reduced only slightly relative to "ideal" conditions.
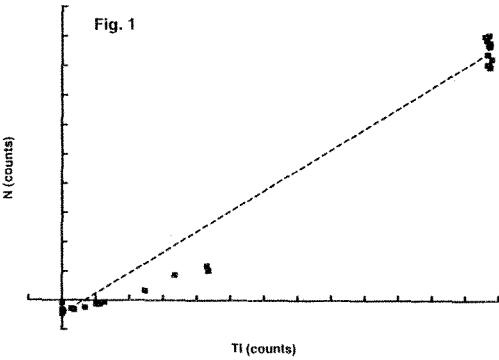

FIG. 1 Apparent N Kα counts due to Ti Lℓ *versus* Ti Kα counts. Scale: x-axis from -1×10^5 to $+13\times10^5$ counts, y-axis from -5×10^3 to $+50\times10^3$ counts. Dashed line is a linear correlation of all data points. Both the deviation from linearity and the non-zero intercept are obvious.

SEM/EDS ANALYSIS OF BORON IN WASTE GLASSES WITH ULTRATHIN WINDOW DETECTOR AND DIGITAL PULSE PROCESSOR

J.S. Luo, S.F. Wolf, W.L. Ebert, and J.K. Bates

Chemical Technology Division, Argonne National Laboratory, Argonne, IL 60439

Borosilicate glass has been selected for immobilizing radioactive wastes because of its chemical durability and ability to incorporate many different elements.[1] Boron is an important component in the borosilicate waste glass: its addition facilitates the processibility of glass by lowering its viscosity. In addition, the release of boron is used to measure the corrosion progress during laboratory tests that determine the durability of a glass. Analysis of boron that is present in waste glasses and in the reaction products that form during the reaction of glass is important for understanding the reaction kinetics and mechanism of glass corrosion.

Waste glasses have been previously analyzed for B in our laboratory by wavelength-dispersive spectrometry (WDS) in SEM. As can be deduced from Fig. 1, WDS analysis of waste glasses with B concentrations up to 4 wt% yields a line with a slope of 0.4 counts/s/wt%, with a resolution of ~0.5 wt%. However, EDS is analytically more convenient and advantageous because its high detection efficiency and its ability to simultaneously acquire an entire spectrum. The innovation of the ultra-thin window has made it possible for an EDS to detect soft x-rays, which are absorbed by a normal Be window. Unfortunately, the detection sensitivity is still poor for elements lighter than C; boron is only detectable when analyzing B-rich (>20 wt%) samples, such as BN, with a traditional analog x-ray pulse processor (APP) (see Fig. 2). The technique cannot be readily employed to analyze B in waste glasses which have low B contents (typically <5 wt%). However, the sensitivity can be greatly improved by using the recently introduced digital pulse processor (DPP) (see Fig. 2), with which the preamplifier output is digitized and the resulting data stream is digitally processed.[2] In this paper, we report the detection of B in borosilicate waste glasses with a Noran Voyager III EDS system equipped with a DPP, which is interfaced with a Topcon ABT 60 SEM operating at 5 kV.

Two waste glasses selected for analysis include glass LD6-5412, developed by Pacific Northwest National Laboratory (PNNL) and glass EA, developed by Savannah River Technology Center (SRTC). These glasses contain 1.55 wt% and 3.47 wt% B, respectively. A blank test has also been carried out on a quartz sample containing no B to rule out possible artifacts. For waste glasses, the B peaks are clearly distinguishable in the EDS spectra acquired at 5 kV for 100 s (see Fig. 3a). To our knowledge, this probably is the lowest B concentration (1.55 wt%) detected with an EDS that has been reported. It should be noted, however, that the B peaks severely overlap with the C peaks, which are due to the carbon film coated on the sample surface to produce a conductive layer. The presence of the C peak could limit the detection of lower B concentrations, as evidenced in the spectrum for 1.55 wt% B where the B peak is only barely visible (Fig. 3a). This problem can be solved by subtracting the C peaks as shown in Fig. 3b, which still has a good peak-to-noise ratio for 1.55 wt % B. This result suggests that even lower B content could be detected by EDS with DPP if the C peaks are subtracted as done in Fig. 3b. By plotting the peak intensity against the weight percent of boron in the glass, we also found a nearly linear relationship, similar to that observed with WDS (see Fig. 1).[3] Calibration of this curve will allow us to quantify the B contents in waste glasses.

References

1. J.C. Cunnane et al., DOE/EM-0177 (1994).
2. J.J. Friel and R.B. Mott, Adv. Mater. & Proc. 145(1994)35.
3. This research was sponsored by the U. S. Department of Energy, Office of Environmental Management, under Contract W-31-109-ENG-38.
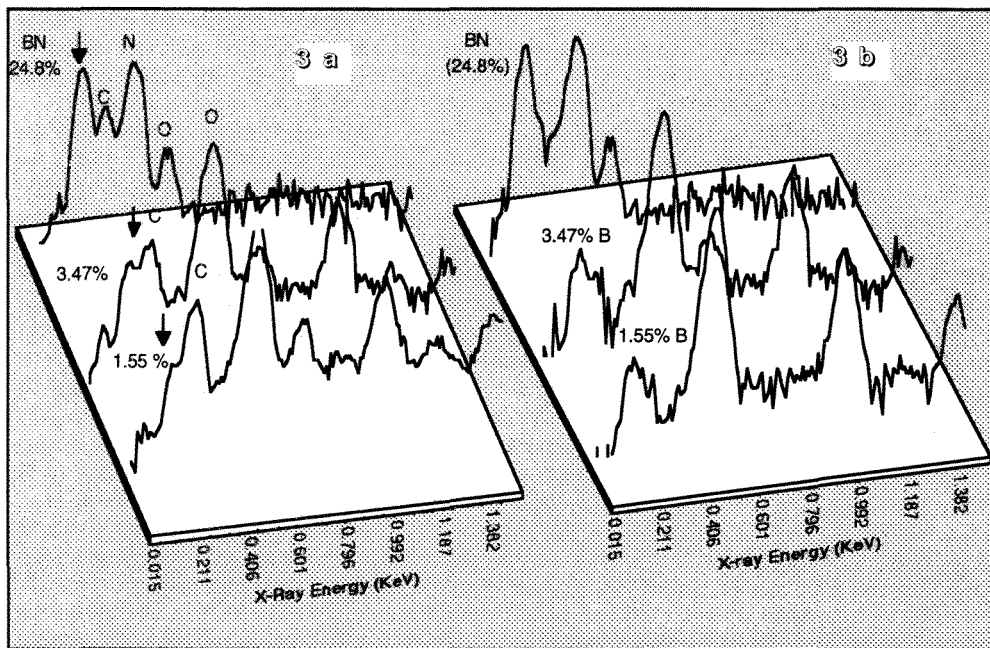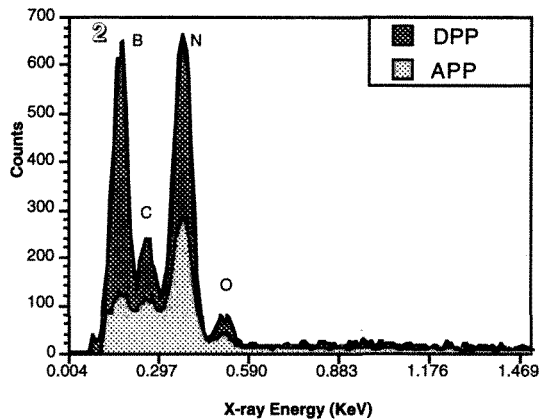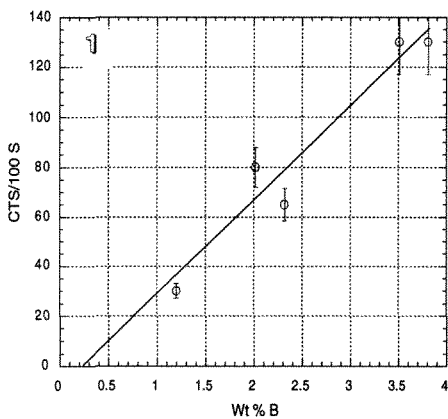
FIG.1. Beer-Lambert plot showing number counts vs. B wt% in glass analyzed by WDS.
FIG.2. EDS spectra of BN comparing DPP vs. APP processing.
FIG.3. EDS spectra of BN and two waste glasses with less than 5 wt% B: (a) as-acquired spectra and (b) spectra with carbon peaks subtracted. The result demonstrates a detectability of less than 1.5 wt% B if C peaks can be properly subtracted.

PROCEDURES FOR X-RAY MICROANALYSIS OF LAYERED STRUCTURES: ACCURACY AND LIMITS

J. L. Pouchou* and J. F. Thiot**

*Department of Materials Science, ONERA, 92320 Châtillon, France
**SAMx, 78280 Guyancourt, France

The procedures presently available for X-ray microanalysis (*XRMA*) of layered structures derive more or less directly from the semi-empirical $\phi(\rho z)$ models proposed in the 80's.[1,2] In the last years, the spreading of advanced computer programs such as *Strata* made more people aware than these methods were effective, and could be used in many cases as a complement or a substitute to near-surface analysis methods. New approaches for $\phi(\rho z)$ reconstruction, based on the angular and energetic distributions of the electrons, are emerging (e.g. IntriX model[3]). They should enable to describe more accurately structures with strong atomic number variations. Monte-Carlo simulations (*M-C*) are useful to assess $\phi(\rho z)$ models, but for daily work their effectiveness seems presently restricted to the elaboration of calibration charts to be used for repetitive situations.

The basic data processed are values of the relative intensity k for each element, measured at varying voltage. For good performance, procedures should accept homogeneous or layered bulk standards, and account for fluorescence by characteristic lines and continuum. At a given voltage, the depth distribution of ionization $\phi(\rho z)$ enables to determine the mass of an element per cm² near the specimen surface. The basic check of a model is to verify its capability to predict the correct values of k in a wide voltage range for a surface layer of known mass thickness. Fig. 1 compares the k curves given by *PAP* and *XPP* models to *M-C* and to experimental data[4] for Al films (~ 100 to 2000 nm) on Si. Table 1 shows that thicknesses given by *Strata* (iteration with *PAP* and *XPP* applied to the whole set of data) deviate from nominal (*RBS*) by a few % or less (i.e. ~ the accuracy of *RBS* itself). However, deviation may exceed 10 % in particular regions (*XPP* for thick layers, *M-C* at low voltage).

XRMA is able to detect thin surface segregations and to measure them with reasonable accuracy, even when the atomic numbers of the film and the substrate strongly differ. For very thin gold layers (~ 0.5 and 1.5 nm), we obtained ~ 10 % or less deviation between *XRMA* and *RBS* mass thicknesses (Table 2). Measurements of a thin carbon film (~ 4.8 µg/cm²) on substrates from B to Au confirms that the thickness found with *Strata* is almost constant whatever the substrate, while the measured k-ratio increases by a factor ~ 2 (Fig. 2).

Structures with strong Z variation are difficult for semi-empirical models, especially when the discontinuity is near the diffusion depth, because when the excitation depth increases they assume a progressive variation of $\phi(\rho z)$ shape, from that of the layer material to that of the substrate material. *M-C* calculations[5] first, and recently the IntriX model,[3] have shown the weakness of this assumption. Fig. 3 shows typical discrepancies between *PAP* and *M-C*[6] for a fictitious B film on Ga at 20 kV. Taking also into account the predictions for the standards, it comes that *PAP* would overestimate the layer thickness by ~ 5 % compared to *M-C*. In the layer, the concentration of a minor element similar to Ga (e.g. As measured with its Lα line) would be underestimated by ~ 4 %. In the substrate, the concentration of a light element comparable to B would be overestimated by ~ 10 % compared to *M-C*. The best agreement between *PAP* and *M-C* would be for the Ga Lα k-ratios of the substrate.

For complex multilayer structures, the difficulty is that different specimen descriptions may lead to almost identical curves of k vs. voltage. Hence, it is usual that the problem of determining precisely an unknown structure cannot be solved completely if one element exists in several layers. Fig. 4 shows the example of a TiN / SiO_2 / Si sandwich with possible surface oxidation. Measuring nitrogen is too difficult here because of the spectral interference with Ti. Hence, TiN stoichiometry had to be assumed. A TiO_2 native surface oxide had also to be postulated to explain the increase of O k-ratio at low voltage. Table 3 shows that for the outer layers, *Strata* results differ from *RBS* ones,[7] because the insufficient depth resolution of *XRMA* was limiting the capability to detect the presence of N in the surface oxide layer and the deviation of the underlying TiN from stoichiometry. However, the good point is that if one considers the total mass per cm² of every segregating element, *XRMA* is in satisfactory agreement with *RBS* (10 % deviation for Ti and 2 to 4 % for the other elements).

References
1. R.H. Packwood and J.D. Brown, *X-Ray Spectrom.*, 10(1981)138
2. J.L. Pouchou and F. Pichoir, *J. Physique C2*, 45(1984)47
3. P.-F. Staub, *ANRT Group#8 meeting*, Paris (1996), to be published.
4. W. Reuter et al., *J. Phys. D: Appl. Phys.*, 11(1978)2633
5. P. Karduck and N. Ammann, *Electron Microscopy*, 2(1990)14
6. J. Hénoc et al., *ANRT Group#8 meeting*, Paris (1996), to be published.
7. C. Hitzman, Evans & Associates, *personal communication*, (1995)
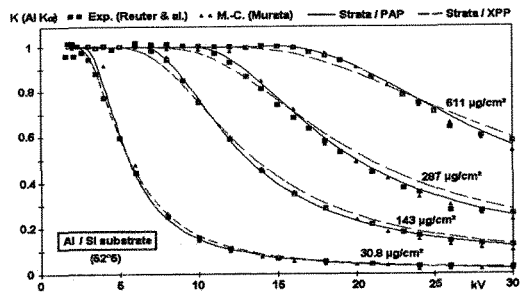
TABLE 1 - Al layers on Si substrate. Deviation of *PAP* and *XPP* results from *RBS* nominal Al thicknesses.

µg/cm² Al (*RBS*[6])	30.8	143	287	611	
Strata / PAP % deviation	2.3	0.7	-3.1	-2.5	mean -0.7
Strata / XPP % deviation	-1.0	-4.9	-6.6	-1.3	mean -3.5

FIG. 1 - Al films on Si substrate. Comparison of *PAP* and *XPP* curves with experimental data [6] and *M-C*.

TABLE 2 - Comparison of X-ray microanalysis (take-off 40°) with *RBS* for Au thin films on Si substrate.

	Experimental k (pure Au standard)									Au mass thickness (µg/cm²)		
kV	3	3.5	4	4.5	5	6	7	8	10	Strata/PAP	Strata/XPP	*RBS*
Au / Si #1	0.0443	0.0308	0.0215	0.0166	0.0132	0.0094	0.0071	0.0057	0.0037	0.98	0.98	1.08
Au / Si #2	-	-	0.0690	-	-	-	-	0.0165	0.0106	2.83	2.80	2.91
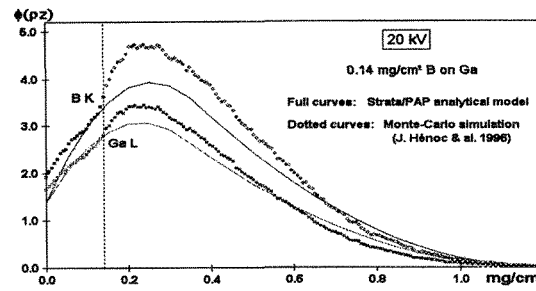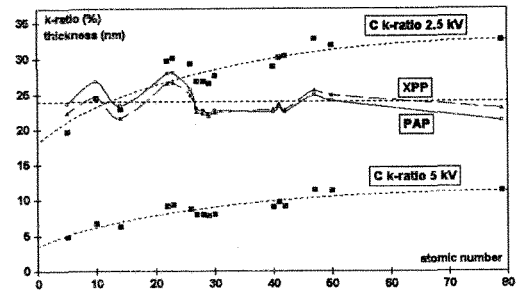
FIG. 2 - 4.8 µg/cm² C film on various substrates.

FIG. 3 - *PAP* and *M-C* φ(ρz) for 0.14 mg/cm² B on Ga.

FIG. 4 - TiO₂/TiN/SiO₂/Si. Experimental k and *PAP* curves for the description of Table 3.
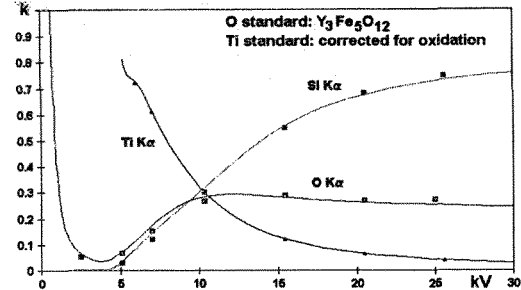
TABLE. 3 - Top: *PAP* and *RBS*[7] descriptions for the specimen of Fig. 4. Bottom: segregated mass per cm².

	XRMA	RBS
layer #1	2.3 nm Ti 33 O 67	5 nm Ti 37 N 43 O 20
layer #2	112 nm Ti 50 N 50	100 nm Ti 47 N 53
layer #3	552 nm Si 33 O 67	555 nm Si 33 O 67
substrate	Si	Si
Ti	46.4 µg/cm²	42.2 µg/cm²
N	13.4 µg/cm²	14.0 µg/cm²
O	69.6 µg/cm²	68.5 µg/cm²
Si	61.6 µg/cm²	59.8 µg/cm²

EDS X-RAY MICROCALORIMETERS WITH 13 eV ENERGY RESOLUTION

D. A. Wollman, G. C. Hilton, K. D. Irwin, and J. M. Martinis

National Institute of Standards and Technology, Boulder, CO 80303

Although Si- and Ge-based Energy Dispersive Spectroscopy (EDS) detectors are by far the most commonly used x-ray spectrometers for microanalysis, they are limited by energy resolutions on the order of 100 eV. This low energy resolution is insufficient to clearly resolve many peak overlaps between K_α x-ray lines of different elements. In addition, many L and M lines of heavier elements fall in the 100 eV to 2 keV energy range, making it difficult in complicated spectra to identify and quantify the presence of technologically important lighter elements. Higher energy resolution and good count rates are necessary to provide improved limits of detectability.

We are developing a cryogenic x-ray microcalorimeter with significantly improved energy resolution and a count rate and detector area suitable for EDS microanalysis. In a calorimeter, the energy of an x-ray is converted to heat, and a measurement of the temperature rise of the detector gives the deposited photon energy. Our microcalorimeter detector consists of a normal-metal x-ray absorber which is in thermal and electrical contact with a superconducting transition-edge sensor (TES). The temperature of the superconducting film is held constant within its transition by means of electrothermal feedback[1] (ETF), so that the Joule power dissipated in the film equals the thermal energy conducted to the low temperature heat bath. The energy of an x-ray absorbed and converted to heat in the normal-metal film is obtained by measuring the resulting reduction in feedback Joule power through the TES using a low-noise SQUID (Superconducting Quantum Interference Device) amplifier. In addition to having an improved theoretical energy resolution limit (~ 1 eV for a 1 mm by 1 mm by 1 μm Au absorber), the partial electronic regulation of temperature in an ETF-TES microcalorimeter makes it up to 100 times faster than other calorimeters.[1] Achievable count rates of 1000 to 10 000 counts per second for the ETF-TES microcalorimeter are compatible with the requirements of EDS microanalysis.

To demonstrate the potential of the ETF-TES microcalorimeter for EDS microanalysis, we have designed and constructed a compact and portable spectrometer, which is shown mounted on a commercial Scanning Electron Microscope (SEM) column in Fig. 1. An ETF-TES detector is located at the end of a cold finger extending into the SEM, and is cooled to an operating temperature of 100 mK by a small adiabatic demagnetization refrigerator (ADR). Although the spectrometer cryostat requires liquid helium, the ADR is easy to use and its operation can be fully computerized. X-rays produced inside the SEM are admitted to the detector through a thin x-ray window.

Using this ETF-TES portable spectrometer, we have obtained an SEM x-ray spectrum of titanium with an energy resolution of 13 eV (FWHM) for the Ti K_α (4.511 keV) and K_β (4.931 keV) lines, as shown in Fig. 2. The figure inset shows that the spectrum has no troublesome artifacts which result from incomplete energy collection.

The detector used to obtain this spectrum had a small-area Ag absorber with dimensions 250 μm by 250 μm by 2 μm. Due to a conservative design, the detector had a very slow time constant of 750 μs. This time constant can be easily improved by at least a factor of 10 without loss of energy resolution by simply increasing the thermal conductance between the device and the heat bath. Although the performance of this ETF-TES microcalorimeter was far from optimum, we have demonstrated a new and promising technology for higher energy resolution EDS microanalysis.

References

1. K. D. Irwin, *Appl. Phys. Lett.*, **66** (1995) 1998.
2. Contribution of the US Government; not subject to copyright. This work was supported by NASA under grant No. NAGW-4170, and in part by the ONR under contract No. N000014-94-F-0087.
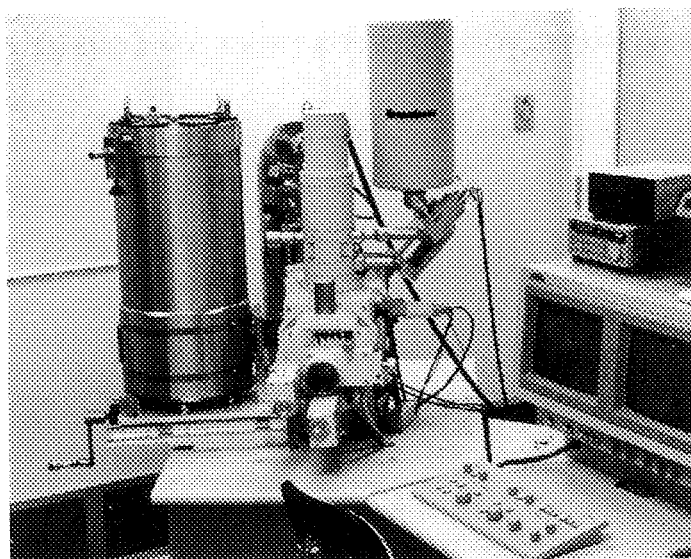
Fig. 1. Photograph of our portable spectrometer mounted on the left side of a commercial SEM column. For comparison, a commercial EDS system is shown installed on the right side of the column.

SEM X–ray Spectra of Ti sample
EDS Si(Li) Detector vs. ETF–TES Microcalorimeter

Fig. 2. SEM x-ray spectra of titanium obtained with our ETF-TES microcalorimeter and a commercial EDS Si(Li) detector. A more complete spectrum for our ETF-TES microcalorimeter is presented in the figure inset, demonstrating the absence of spectrum artifacts.

489

A NEW NUMERICAL MODEL FOR ELECTRON-PROBE ANALYSIS AT HIGH DEPTH RESOLUTION

P.-F. Staub[*,**], C.Bonnelle[**], F.Vergand[**], P.Jonnard[**]

*Cameca, 103 bd St-Denis, 92403, Courbevoie cedex, France

**Laboratoire de Chimie Physique-Matière et Rayonnement, Université Paris VI, 11 rue P. et M. Curie, 75231 Paris cedex 05, France
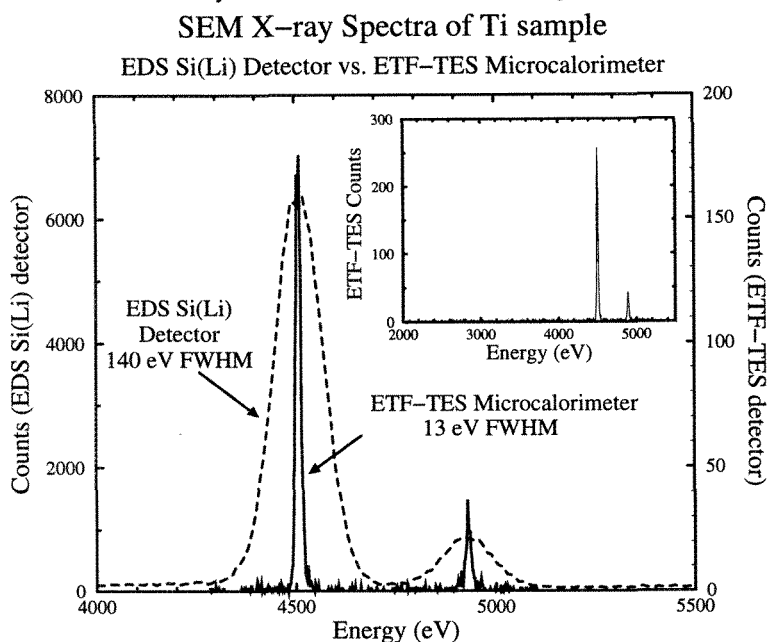
Characterizing dimensionally and chemically nanometric structures such as surface segregation or interface phases can be performed efficiently using electron probe (EP) techniques at very low excitation conditions, i.e. using small incident energies ($0.5 < E_0 < 5$ keV) and low incident overvoltages ($1 < U_0 < 1.7$).[1,2] In such extreme conditions, classical analytical EP models are generally pushed to their validity limits in terms of accuracy and physical consistency, and Monte-Carlo simulations are not convenient solutions as routine tools, because of their cost in computing time. In this context, we have developed an intermediate procedure, called IntriX, in which the ionization depth distributions $\Phi(\rho z)$ are numerically reconstructed by integration of basic macroscopic physical parameters describing the electron beam/matter interaction, all of them being available under pre-established analytical forms. IntriX's procedure consists in dividing the ionization depth distribution into three separate contributions: $\Phi(\rho z) = \sum_{i=1}^{3} \Phi_i(\rho z)$, with each contribution $\Phi_i(\rho z)$ corresponding to the ionizations produced by the electrons during their i^{th} crossing of the elementary layer dz, as pictured in figure 1 (i=1 is transmission, i=2 is back-scattering, etc..). Orders i>3 are neglected. The physical insight and accuracy allowed by IntriX procedure are illustrated in figures 2 and 3 where computed $\Phi(\rho z)$ functions and their various components $\Phi_i(\rho z)$ are compared to experimental data by Brown and Parobeck, respectively for ionization of Si K level at high overvoltage ($U_0 = 5.43$) and Cu K level at low overvoltage ($U_0 = 1.33$) in Ag matrixes.[3]

IntriX computes $\Phi(\rho z)$ functions using empirical parameters directly derived from beam/thin films or beam/bulk targets experiments, such as the electron transmission and back-scattering rates and their associated energetic and angular distributions.[4] This kind of approach grants a natural ability to modelize the characteristic X-ray emitting behavior of film/substrate samples[5], as illustrated in figure 4 (measurements from ref.[6]). Moreover, as IntriX parameters are expressly fitted on data acquired at energies as low as 0.5 keV, good performance is maintained in the low energy region, as confirmed by the X-ray intensity measurements we have made on layered structures in the range $1.5 < E_0 < 5$ keV (cf.figure 5), even for characterizing nanometric deposits (~ 1 µg/cm^2). An IntriX session runs tens to hundreds times faster than do a Monte-Carlo code.

References

1. C.Bonnelle and F.Vergand, *J.Chimie Physique*, 86 (1989) 1293.
2. J.-L. Pouchou, F.Pichoir, *Electron Probe Quantitation*, Ed. K.F. Heinrich & D.E.Newbury, Plenum Press, (1991) 31.
3. J.D. Brown and L.Parobeck, *X-ray Spectrom.*, 5 (1976) 36.
4. P.-F. Staub, *J.Phys D:Appl.Phys.*, 27(1994) 1533 and *J.Phys D:Appl.Phys.*, 28(1995) 252.
5. H.J. August and J. Wernisch, *X-Ray Spectrom.*, 20 (1991) 131.
6. G.F. Bastin and H.J.M. Heijligers, *Proc. 28th annual MAS meeting*, Ed. J.J.Friel, New-Orleans, LA,(1994) 43.
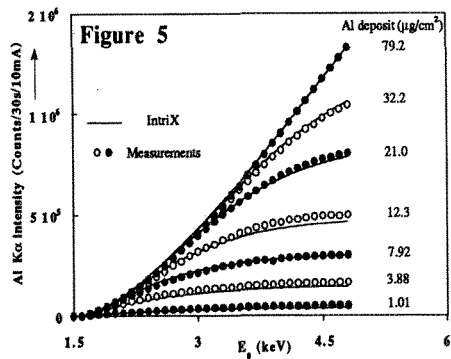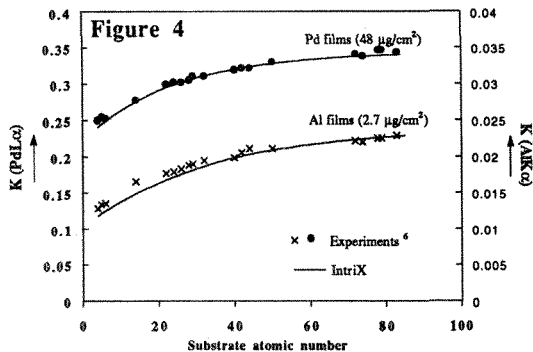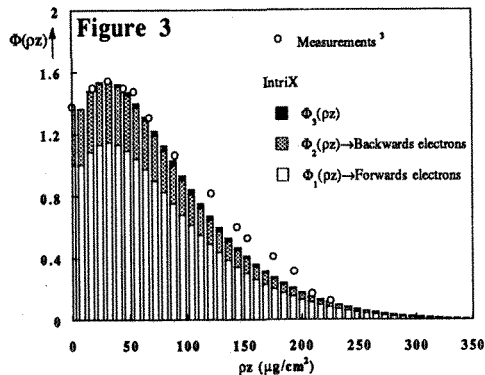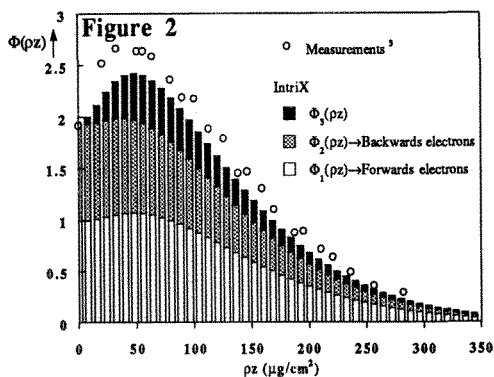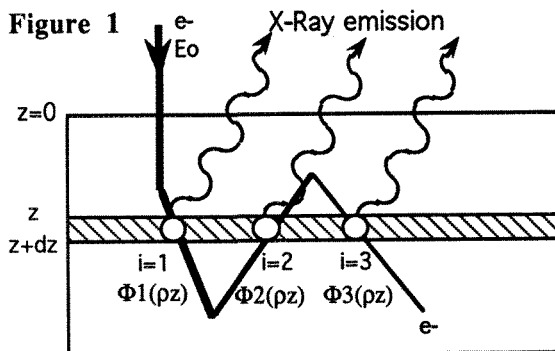
FIG. 1 IntriX schematic display of contributions i=1, 2, 3 to ionization at depth z inside the target.

FIG. 2 IntriX computed $\Phi(\rho z)$ function and attached contributions i=1,2,3 for the Si K level ionization in an Ag matrix (E0=10 keV, U0=5.43) and comparison with corresponding measurements (ref.3).

FIG. 3 Same as figure 2, but for Cu K level ionization (E0=12 keV, U0=1.33).

FIG. 4 Comparison between measured (ref.6) and IntriX computed K-ratios for PdLα and AlKα lines emitted respectively by Pd films and Al films deposited on a wide variety of substrates (E0=10 keV).

FIG. 5 Computed and measured AlKα intensities for Al deposits on Mn substrate at low energies.

491

THE EXPERIMENTAL DETERMINATION OF THE SURFACE IONIZATION VALUE φ(0) FOR Al-Kα RADIATION

G.F. Bastin, J.M. Dijkstra and H.J.M. Heijligers

Laboratory for Solid State Chemistry and Materials Science, University of Technology, P.O. Box 513, NL-5600 MB Eindhoven, The Netherlands.

The surface ionization value ($\varphi(0)$) plays a crucial role in matrix correction procedures, not only in bulk applications under extreme conditions (ultra-light element radiations) but certainly also in thin-film applications. By definition the $\varphi(0)$ value for the x-radiation of a particular element is the ratio between the x-ray intensity emitted by an infinitely thin film of that element on a substrate and the intensity emitted from the same unsupported film. In an earlier publication we described our work on setting up data bases of systematic thin-film measurements[1]. In this work we deposited several elements (Al, Pd) in six different thicknesses (10 to 320 nm) onto a wide variety of polished substrates (Be up to Bi) and the x-ray intensities of the film elements were measured over a wide range in accelerating voltage (3 to 30 kV). In the same deposition runs the same films were deposited onto rock salt crystals. These specimens could not only be used for independent determinations of the film thicknesses (by Rutherford Backscattering, TEM cross-sections) but they also gave access to the determination of the x-ray intensities emitted by the unsupported films. To this end the rock salt was dissolved in water and the films were picked up on a TEM grid, in order to be measured in an electron probe micro-analyzer (JEOL 733, JEOL 8600). In this way the ratio between the supported and the unsupported emitted intensity can be determined for each film/substrate combination, for each particular accelerating voltage and for each of the six film thicknesses. If for a fixed accelerating voltage and a fixed substrate element this ratio is plotted as a function of film thickness a graph is obtained which allows the ratio supported/unsupported intensity to be extrapolated towards zero thickness, a condition where the definition of $\varphi(0)$ is satisfied. Fig. 1 shows an example of such a plot for Al on a Be substrate at 30 kV. Only a small variation (of the order of 1.5 %) is observed for these conditions. Stronger curvatures and larger variations at this voltage are observed when the atomic number of the substrate is increased: 3.5 % for a Mo and 3.7 % for a Bi substrate. With decreasing voltage these effects tend to become stronger. These observations are fully consistent with the predictions based on calculations with existing thin-film software[2]. Fig 2 shows a number of $\varphi(0)$ values for Al-Kα radiation on a variety of substrates determined in this way. The data could well be fitted by an equation of the type proposed earlier by Rehbach[3]:

$$\varphi(0) = 1 + [\ 1 - (U_0)^{-\frac{1}{2}}\ ]^\alpha \bullet \beta$$

in which U_0 is the overvoltage ratio (E_0 / E_c). The parameters α and β could be fitted in terms of the atomic number Z of the matrix as follows :
$\ln(\alpha) = (a + cZ)/(1 + bZ)$, with a = 1.1018998, b = 0.069529433, and c = - 0.030489602
$\beta = (a + cZ)/(1 + bZ)$, with a = -0.16159369, b = 0.048986588, and c = 0.093307075
Similar work is under way for Pd-Lα radiation and it is our intention to compare our measured $\varphi(0)$ values to the predictions based on a variety of existing $\varphi(0)$ expressions from literature.

References

1. G.F. Bastin and H.J.M. Heijligers, *Proc. 28th MAS Meeting*, New Orleans, (1994) 43.
2. G.F. Bastin, H.J.M. Heijligers and J.M. Dijkstra, *Proc. XIIth Intern. Congress for Electron Microscopy*, Vol. 2, (1990) 216.
3. W. Rehbach, *Ph. D. Thesis*, University of Technology, Aachen (W-Germany), (1987).
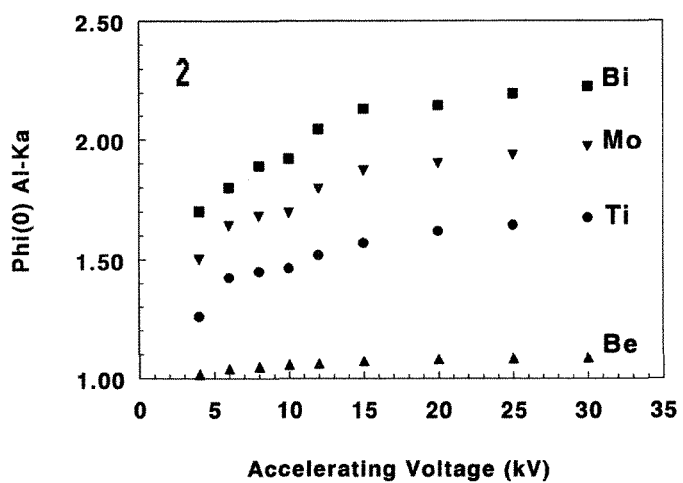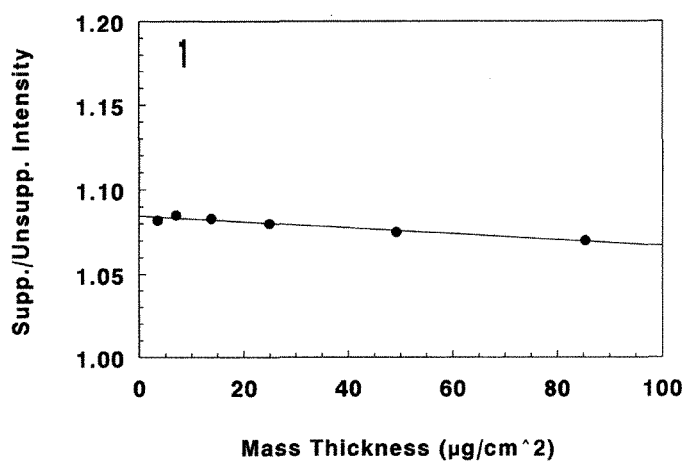
FIG. 1 Variation in the ratio of the emitted Al-Kα intensity between supported and unsupported film as a function of mass-thickness at 30 kV for a Be-substrate.

FIG. 2 Measured φ(o) values for Al-Kα radiation on four different substrates between 4 and 30 kV.

493

The Determination of the Thickness and Composition of Multilayered Thin Films in the SEM by x-Ray Microanalysis with Monte Carlo Simulations

By: Raynald Gauvin[1], Mario Caron[2] , Pierre Hovington[1], Dominique Drouin[1], Gilles Gagnon[2] and John F. Currie[2]

1: Département de Génie mécanique, Université de Sherbrooke,
   Sherbrooke, Québec, Canada, J1K 2R1
2: LISA, Département de génie physique, École Polytechnique de Montréal,
   Montréal, Québec, Canada, H3V 3A7

X-Ray microanalysis is now a well established technique to determine the composition and the thickness of multilayer structures of different materials. The most popular software used to quantify such system are based on analytical $\varphi(\rho z)$ curves which are approximation of the x-Ray generation process. The computed $\varphi(\rho z)$ curves of multilayered samples are based on mixtures rules and weight functions which are not always accurate. In this paper, Monte Carlo simulations of electron trajectories in solids are used to compute $\varphi(\rho z)$ curves in multilayered specimens directly and then used to computed the K ratios.

To validate this procedure, a TiN(100 nm)/Ti(10 nm) multilayer metallization structure deposited on SiO_2(100 nm)/Si substrate was used in conjonction with a TiN(400 nm)/Si standard sample. This system is a very active field of research and development in the microelectronics industry[1]. The thicknesses, composition and microstructure of both systems were fully characterized by Elastic Recoil Detection (ERD), X-ray diffraction (XRD) and Transmission Electron Microscopy (TEM).

In addition, EDS X-ray microanalysis was performed on the same structures in order to obtain the experimental K ratio of Ti $L\alpha$ and N $K\alpha$ X-ray lines for different incident electrons energies. Using the totality of these experimental data, it is possible to compute the theoretical K ratio by Monte Carlo simulations using the CASINO program[2]. The net intensity of both lines were deconvoluated using the program DECON.PH[3]. Figure 1 shows a comparison of experimental and theoretical K ratios in the range between 1 and 7.5 keV. These results illustrate that experimental and theoretical values are in excellent agreement with each other. This excellent agreement between computed and measured K ratio in a system of known composition and thickness prove the utility of using Monte Carlo simulations to quantify multilayered specimens.

Also, it is important practically to determine the stochiometry of the TiN deposit on the Ti/SiO_2/Si system. Figure 2 shows computed K ratios of Ti $L\alpha$ and N $K\alpha$ X-ray lines for an atomic ratio of N/Ti ranging from 0,8 to 1,2 as a function of beam energy with the same parameters as above. From these simulations, it is clear that the greatest sensitivity of the K ratio as a function of composition is at 5 keV for Ti $L\alpha$ and at 1 keV for N $K\alpha$.

REFERENCES
1 L. Ouellet, Y. Tremblay, G. Gagnon, M. Caron, J. F. Currie, S. C. Gujrathi, M. Biberger and R. Reynolds (1996) "The effect of an oxygen plasma exposure on the reliability of a Ti/TiN/(oxygen plasma exposure)/AlSiCu/TiN contact metallization", accepted for publication in J. Appl. Phys.

2 R. Gauvin, P. Hovington and D. Drouin (1995) "Quantification of Spherical Inclusion in the Scanning Electron Microscope Using Monte Carlo Simulations", SCANNING, Vol. 17, pp. 202-219.

3 P. Hovington, G. L'Espérance and E. Baril (1993) "Processing and Quantification of Low Energy EDS Spectra and Modelling of the DODE with Time", Proceedings of the 1993 MAS meeting, VCH Publisher, New York, PP. 226-227.
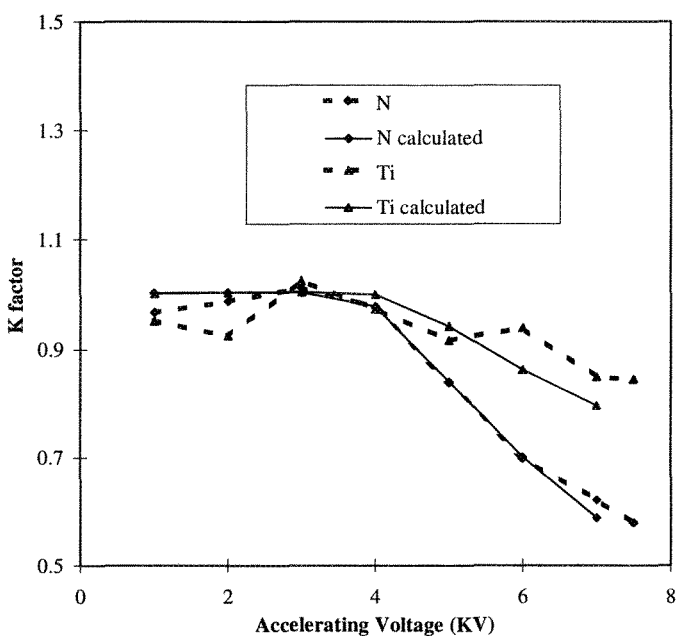
Fig. 1

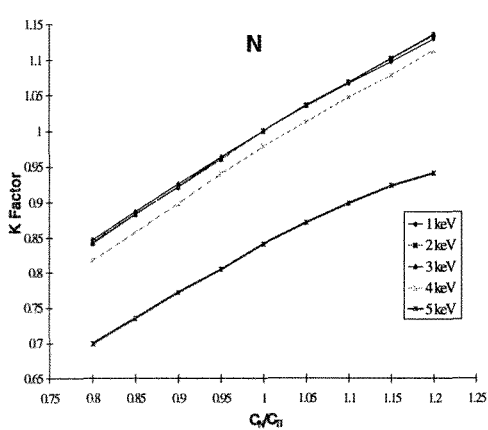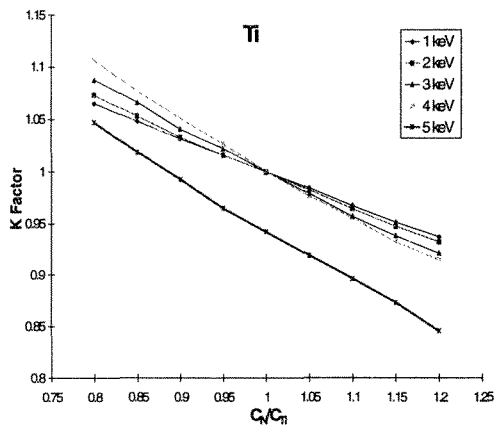Fig. 2

Fig. 3

Fig. 1 Experimental and calculated K ratio of the N Kα and Ti Lα as a function of the accelerating voltage
Fig. 2 K ratio of the N Kα as a function of the concentration ratio of N/Ti
Fig. 3 K ratio of the Ti Lα as a function of the concentration ratio of N/Ti

QUANTITATIVE PARTICLE ANALYSIS: FACT OR FICTION

J.A. Small, and J.T. Armstrong

Surface and Microanalysis Science Division, National Institute for Standards & Technology, Gaithersburg, MD 20899

In conventional microprobe analysis, the samples and standards have a controlled geometry, i.e. flat polished, and infinitely large with respect to the electron beam interaction volume. As a result, the measured x-ray intensities for the analyzed elements vary in a predictable manner with composition and the various elemental concentrations can be calculated from a choice of several analytical algorithms[1]. Unlike conventional analysis, the quantitative analysis of particles with the electron probe presents a very difficult analytical challenge. Most particles are irregularly shaped and do not have controlled geometries. In addition, depending on their size, they may not be "infinitely" thick with respect to the electron beam. Because of the random sizes and shapes, the emitted x-ray intensity from particles may be greater than or less than the intensities from a flat conventional sample of the same composition. A diagram from Armstrong of the interaction between an electron beam and a particle is shown in Fig. 1 and illustrates the "particle" effects that make quantitative particle analysis so difficult.[2] The first effect is that electrons may scatter out the bottom and sides of particles without producing x-rays, A & A'. This results in a decrease of x-ray intensity for all elements in the particle. The second effect is due to the unpredictable and variable absorption path length between the point of x-ray generation and the detector B-C & B'-C'. Depending on the particle shape, x-ray absorption pathlengths in particles may be greater than, less than, or equal to pathlengths in a conventional sample. The result of these "particle" effects is that both x-ray generation and absorption for particles not only vary with composition as in bulk specimens but also with particle size and shape. To perform credible quantitative particle analysis by comparing particles to standards, we must be able to correct for the effects of the particle's shape and size on x-ray generation and emission.

Over the years several different methods have been developed for quantitative particle analysis.[3] The purpose of this paper is to compare and contrast several of these methods by looking at the error distributions from the analyses of particles with known compositions. For example, one relatively common method for particle analysis is to use a conventional analysis program with bulk standards, analyze oxygen by stoichiometry, and normalize the results to 100%. A refinement of this method is to substitute particle standards, similar in composition to the sample, for the bulk standards. Figs. 2-4 show the error histograms for the EDS analysis of a series of bulk analytical glasses and particles of the glasses analyzed with both conventional and particle standards. Randomly shaped particles were made by grinding the bulk glasses and were analyzed with the electron beam in spot mode. The conventional standards were compounds (pure elements & oxides) used for the bulk glass analysis, and the "particle" standard was made by averaging the analyses of several particles from one of the glasses in the series. All bulk and particle analyses were normalized to 100%. The histogram in Fig. 2 shows the error distribution for 2800 analyses on the bulk glasses. The width of distribution is typical of bulk sample analysis with 98% of the errors within ± 4%. Figs. 3 & 4 show the error histograms for normalized particle analysis with conventional standards and with "particle" standards respectively. The widths of the two particle histograms are similar but as expected are much broader than the bulk distribution with about 98% of the analyses falling between ± 20%. The particle histogram with conventional standards shows a pos-

itive shift of about 5%, which is similar to results from Armstrong.[4] In contrast, the particle histogram with "particle" standards is centered around zero with no shift and for this system provides more accurate results than conventional standards. Extending this comparison to other particle systems and analysis methods will make it possible to estimate the overall quality of particle analysis and to evaluate each method independently on different particle systems.

References

1. J. I. Goldstein et al., *Scanning Electron Microscopy and X-Ray Microanalysis*, Plenum Press, New York (1992)397.
2. J. T. Armstrong, *Scanning Electron Microscopy*, SEM Inc., Chicago (1981)455.
3. J. A. Small, *Scanning Electron Microscopy*, SEM Inc., Chicago (1981)447.
4. J. T. Armstrong, Electron Probe Quantitation, K.F.J. Heinrich and D.E. Newbury editors, Plenum Press, New York (1991)261.
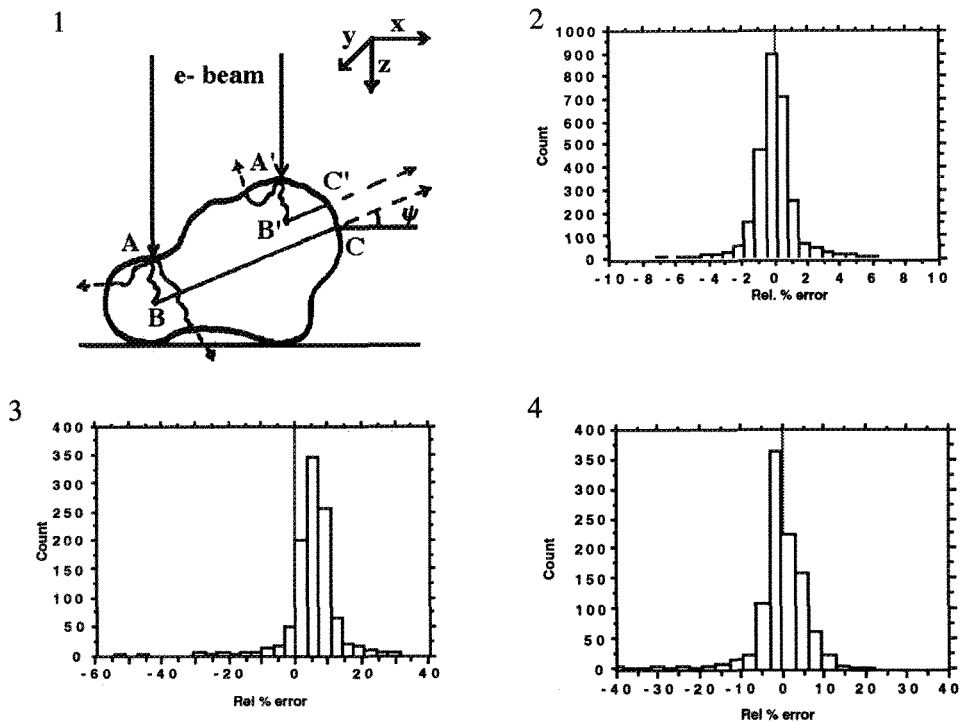
FIG. - 1 Diagram of electron beam interaction with a particle.
FIG. - 2 Relative percent error histogram for bulk glass analysis.
FIG. - 3 Relative percent error histogram for particles analyzed with conventional standards.
FIG. - 4 Relative percent error histogram for particles analyzed with particle standard.

CHARACTERIZATION OF SMALL INCLUSIONS: SEM vs TEM, OR IS IT EVEN WORTH CONSIDERING SEM?

Carl Blais*, Gilles L'Espérance*, Éric Baril*, Clément Forget**

*Center for Microscopy and Characterization of Materials, (CM)^2, École Polytechnique de Montréal, C.P. 6079, succursale « Centre-Ville », Montréal, (Qué.), CANADA, H3C 3A7.

** CLEMEX Technologies inc., 800 rue Guimond, Longueuil, (Qué.), CANADA, J4G 1T5.

Inclusions of technological importance are often in the size range from 0.1 to 1 µm [1]. These inclusions are generally too thick for EEL-spectrometry and require the use of EDS to characterize their chemical composition. Recent Monte Carlo simulations indicated that scanning electron microscopes (SEM's) equiped with a field emission gun (FEG) might challenge transmission electron microscopes (TEM's) for the charaterization of small inclusions [2]. In the light of these results, we investigated the possibility of using a FEGSEM to characterize inclusions found in micro-alloyed steel welds used for arctic applications. The main setbacks of using EDS for such a task are due to the presence of small phases of unknown thicknesses, non-homogeneity of the X-ray generation volumes, variation in absorption along the path length of the X-rays, etc. [3]. Even though these problems are encoutered in both the SEM and the TEM, the relative ease of imaging the very small inclusions in TEM confers a definite advantage to this technique. Furthermore, TEM allows to obtain convergent-beam electron diffraction patterns (CBED) which complement the chemical composition characterization, thereby allowing the unambiguous identification of the phases present (chemistry and crystal structure).

Figure 1 shows a TEM-micrograph of an inclusion found in a steel weld. In order to minimize the matrix effects on the X-ray spectra, carbon extraction replicas on Ni-grids were used. The inclusion is clearly constituted of many small phases. It is believed that some of the phases found at the periphery of the inclusions promote the formation of acicular ferrite which increases the toughness of the material [4]. Thus, we were interested to confirm the presence of TiO and/or TiN on the surface of inclusions which basically consisted of a core of $MnTiO_3$ + SiO_2. Figure 2 shows a X-ray spectrum obtained in TEM from the phase arrowed in figure 1. The main elements are Ti and O. The strong Ni peak arises from the grid. Figures 3 and 4 respectively show a micrograph of the same inclusion (as in figure 1) and a X-ray spectrum from the same region, this time obtained in SEM. The spectrum of figure 4, acquired at 15 keV, clearly shows the effect of beam broadening in the SEM. Thus, the net intensity ratios, MnKα/TiKα and SiK/TiKα are higher in the SEM (0.21 and 0.21 respectively) than in TEM (0.13 and 0.04 respectively). Finally, figure 5 shows a convergent-beam electron diffraction pattern which confirms that the region of interest is basically composed of TiO-fcc. This paper will compare the results of the characterization of small inclusions in TEM and FEGSEM as a function of accelerating voltage, with an emphasis on low voltages. The advantages and limitations of each technique will be discussed. The use of ultramicrotomy to prepare thin sections of these inclusions will also be covered. Finally, the deconvolution of X-ray spectra, especially for light elements, will be presented.

REFERENCES:

1. S. St-Laurent, G. L'Espérance, *Mat. Sci. Eng.* A149(1992)339.
2. R. Gauvin et al., *Proc. Ann. Conf. Microbeam Analysis Society*, (1995)355.
3. J.T. Armstrong, *Electron Probe Quantitation*, (1991)261.
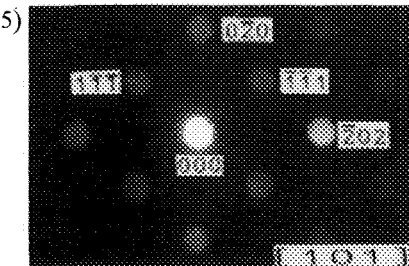4. A.G. Mills et al., *Mat. Sci. Tech.*, dec.(1987)1051.
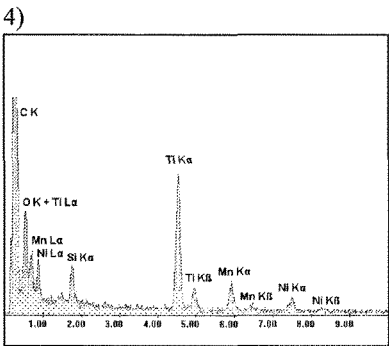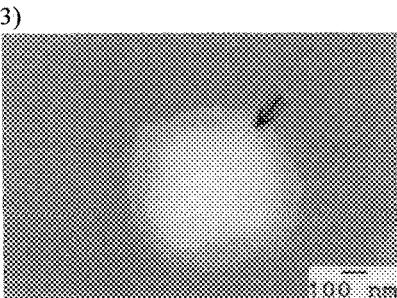
1)

2)

3)

4)

5)
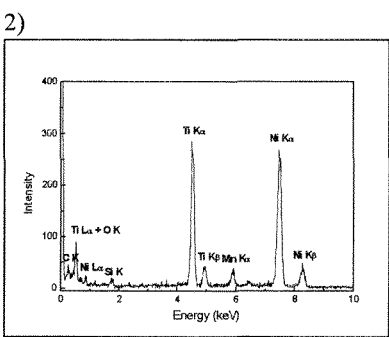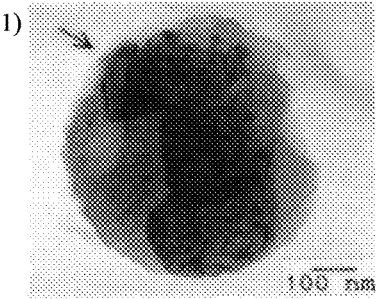
Figure 1:   TEM micrograph of a mutiphase inclusion found on a carbon extraction replica of a steel weld.

Figure 2:   TEM X-ray spectrum of the region shown by the arrow in figure 1. The large Ni peak arises from the grid. (E_0=300 keV, spot =24 nm, ϕ=50 μm, θ=35°).

Figure 3:   SEM micrograph of the same inclusion found in figure 1.

Figure 4:   SEM X-ray spectrum of the region shown on figure 1. The Si and Mn peaks are due to the broadening of the beam in the inclusion. (E_0= 15 keV, I= 1 nA).

Figure 5:   CBED of the region highlighted in figures 1 and 3. TiO-c.f.c.

AUTOMATED FINE-PARTICLE ANALYSIS USING SCANNING ELECTRON MICROSCOPY

Catherine A. O'Keefe and Tina M. Watne

Energy & Environmental Research Center, University of North Dakota, Grand Forks, North Dakota 58202-9018 USA

Owing to analytical advances, submicron particles as small as 0.1 µm can be characterized for chemical composition, size, and shape using scanning electron microscopy (SEM). Once these characteristics are determined, the individual particles can be grouped into categories that provide size, shape, and chemical/mineral distributions of the fine particle fraction.

An important application of submicron particle analysis is in solving ash-related problems in coal combustion and gasification systems. The Energy & Environmental Research Center (EERC) at the University of North Dakota is involved in an international consortium formed by the Electric Power Research Institute (EPRI), with U.S. Department of Energy Morgantown Energy Technology Center support, to study ash-related problems associated with the cleaning of hot gases in advanced energy systems. Before the gases are sent through a gas turbine to produce electricity, the particulates are removed with ceramic filters. Filters designed to trap the ash have a tendency to become plugged with ash, eventually causing operational problems. The focus of the project is to characterize the ashes from several filter systems to determine the mechanisms by which difficult-to-clean ash is formed and how it blinds hot-gas filters.

Submicron particles need to be adequately dispersed to properly analyze individual particles because of the analysis volume when the particle is hit by the SEM beam. Thus an aqueous solution with a set sample-to-solvent ratio was used. An aliquot of solution was drawn while being sonicated, and a few drops were placed on a vitreous carbon substrate, allowing for dispersion of the particles on the surface of a smooth substrate.

The particles were analyzed by the fine particle technique (FPT). This technique employs a JEOL 35-U SEM equipped with a Tracor Northern (TN) 5500 energy-dispersive spectrometry (EDS) system with an ultrathin Be window detector. A TN particle recognition and characterization program (PRC), which is a "seek-and-find" method for locating and analyzing individual particles using live images, was used to determine the size and shape of the individual particles. Then an EDS spectrum, using an accelerating voltage of 10 kV, was collected on each particle.

The elements routinely analyzed by the FPT are Na, Mg, Al, Si, P, S, Cl, K, Ca, Fe, Ba, and Ti. The size, shape, and composition of 750 to 1500 particles per sample are required. The raw FPT results are manipulated by a data reduction program called Finepart to provide normalized weight percents for six particle-size bins ranging from 0.1 to 100 µm in average diameter. The particles are also classified into 33 different mineral categories, which are based on previous ash characterization work performed at the EERC.

The bulk elemental results for Finepart were reduced using the normalized x-ray counts for each region of interest (ROI) in the SEM spectrum and reported as weight percents. Bulk composition was

determined to compare the FPT to standard analytical techniques, like x-ray fluorescence (XRF). The weight percents were obtained by normalizing the x-ray counts for each ROI, multiplying by a density factor, and dividing the product by the volume of the particles. A ZAF correction was not necessary because of the particle size and the dispersion of the particles on the vitreous carbon substrate. The results indicated that the ROI and density factor cause a greater analytical variation in the elemental weight percent for the FPT than for the XRF technique for Ca and Fe. The comparison of the other elements showed similar results between the FPT and XRF. The discrepancies in the Fe and Ca values are probably due to the low accelerating voltage used in the FPT.

Samples were also prepared in triplicate to test the repeatability of the sample preparation technique. Five hundred particles were analyzed for size, ranging from 0.1 to 100 μm in diameter (Figure 1). Figure 1 shows good repeatability for the sample preparation technique for the six different size bins.

In conclusion, FPT can be used to provide the size, shape, and chemistry/mineralogy of individual fine particles. This information can be utilized to solve ash-related problems in coal combustion and gasification systems by focusing on the mechanism by which difficult-to-clean ash is formed and how it blinds hot-gas filters.
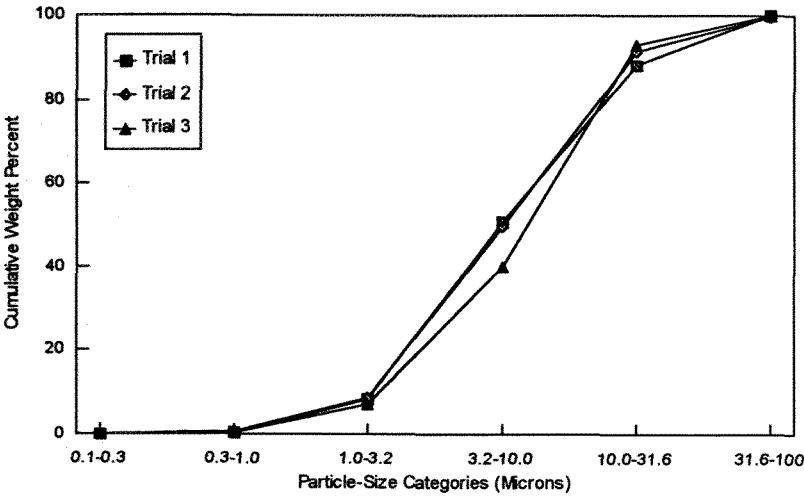

FIG. 1 - Repeatability of sample preparation for FPT.

ANALYSIS OF COMPLETED COMMERCIAL SEMICONDUCTORS USING EPMA

R. Packwood*, M.W. Phaneuf**, V. Weatherall*, I. Bassignana***

*   Materials Technology Laboratory, NRCan, 568 Booth St., Ottawa, Ontario CANADA
**   Chipworks Inc., 205 Catherine St., Ottawa, Ontario CANADA
***   Advanced Technology Laboratory, Bell-Northern Research Ltd., Ottawa, Ontario CANADA

The development of specialized analytical instruments such as the SIMS, XPS, ISS etc., all with truly incredible abilities in certain areas, has given rise to the notion that electron probe microanalysis (EPMA) is an old fashioned and rather inadequate technique, and one that is of little or no use in such high technology fields as the semiconductor industry. Whilst it is true that the microprobe does not possess parts-per-billion sensitivity (ppb) or monolayer depth resolution it is also true that many times these extremes of performance are not essential and that a few tens of parts-per-million (ppm) and a few tens of nanometers depth resolution is all that is required. In fact, the microprobe may well be the second choice method for a wide range of analytical problems and even the method of choice for a few.

The literature is replete with remarks that suggest the writer is confusing an SEM-EDXS combination with an instrument such as the Cameca SX-50. Even where this confusion does not exist, the literature discusses microprobe detection limits that are seldom stated to be as low as 100 ppm[1], whereas there are numerous element combinations for which 10-20 ppm is routinely attainable. At the same time, the microprobe is quickly being recognized as the only reliable method available to many labs for the accurate analysis of submicron deposits. Fig. 1 shows that EPMA can be used as an independent calibration source "equal to the very best physical technique in (GaAl)As work"[2]; similar work has been done on WSi films. In our lab, EPMA is used routinely to reliably measure differences in silicon content between metal layers of aluminum alloy metallizations, often when the average silicon content in each layer may be 0.2 and 0.5 atomic percent respectively, and this on a completed device surrounded by silicon-based inter-layer dielectrics, sitting on a silicon substrate. Similar techniques can be used to measure the copper content in these metallizations.

Source and drain level and even well level concentrations of ion-implanted n-type (eg. As and P) dopants may be quantified or possibly mapped, even for relatively shallow implants. Fig. 2 shows an EPMA trace across the input protection structure of a commercial integrated circuit deprocessed to leave the polysilicon layers standing proud above the bare substrate. This figure, showing an approximately half-micron thick P doped polysilicon line sitting on a deeper As doped well structure, illustrates the sort of detail that can be achieved in relatively routine fashion. This style of analysis would be very difficult in an SED-EDXS instrument; even in the SX50 considerable care must be taken, and count times may reach into the thousands of seconds per point.

Fig. 3 shows a final example, where concentrations have been measured by EPMA at the bottom of three SIMS craters of different depths into an As implanted SIMS standard. The EPMA As concentrations have been computed on the assumption of a uniform concentration of As through the analysis depth (E_0 = 10kV). Data taken at different acceleration voltages or a knowledge of the actual concentration profile expected would permit a more accurate calculation of the dopant concentration, based on a more realistic distribution with respect to depth of the dopant species. Earlier work[3,4] on the MSG$\Phi(\rho z)$ has shown the way to quantification in this manner of a variety of non-uniform concentration vs. depth profiles.

References
1. K.F.J. Heinrich, D.E. Newbury, *Metals Handbook* Vol 10 (1985)517 "Electronprobe X-ray Microanalysis"
2. D.A. Macquistan, I.C. Bassignana et al., *Adv. In X-Ray Anal.*, Vol 36 (1993)221
3. R. Packwood, G. Remond, *Int. Met. Soc. Symp. On Anal. Tech.*, June 21-25, 1995 *To Be Published*
4. G. Remond, R.H. Packwood, et al., *Microbeam Anal.* (1992)1652.